CO$_2$ Capture by Aqueous Absorption
Summary of 3rd Quarterly Progress Reports 2009

Supported by the Luminant Carbon Management Program

and the

Industrial Associates Program for CO$_2$ Capture by Aqueous Absorption

by Gary T. Rochelle

Department of Chemical Engineering

The University of Texas at Austin

October 31, 2009

Introduction

This research program is focused on the technical obstacles to the deployment of CO$_2$ capture and sequestration from flue gas by alkanolamine absorption/stripping and on integrating the design of the capture process with the aquifer storage/enhanced oil recovery process. The objective is to develop and demonstrate evolutionary improvements to monoethanolamine (MEA) absorption/stripping for CO$_2$ capture from coal-fired flue gas. The Luminant Carbon Management Program and the Industrial Associates Program for CO$_2$ Capture by Aqueous Absorption support 16 graduate students. These students have prepared detailed quarterly progress reports for the period July 1, 2009 to September 30, 2009. We have attached presentations made by Xi Chen and Rochelle at the IEA workshop in Regina. Also included are paper manuscripts submitted by Freeman, Nguyen, and Plaza.

Conclusions

At 120 to 150 °C, partial pressure of PZ is from 0.2 to 1.6 kPa for 5.5 m PZ; At 120 and 140 °C, PZ partial pressure is 0.7 and 1.8 kPa for 8.7 m aqueous PZ, and 0.8 to 2.1 for 10.5 m PZ.

The volatility of unloaded amines at 40 °C is in the order: 16 m DGA (1.5 Pa), 8 m PZ (~8-10), 7 m MEA (10), 5 m AMP (14.2), 8 m EDA (17.2).

The normalized flux, k$_g$', of CO$_2$ in MEA and PZ solutions is represented by activity-based kinetics with a second order dependence on the activity of the free amine. At constant loading, the k$_g$' is mostly independent of amine concentration and temperature because of canceling effects on the components of the flux expression. The diffusion of reactants and products ecome important at greater T and CO$_2$ loading.

10 m DGA® is not competitive with 7 m MEA or 8 m PZ. 10 m DGA® has a capacity much smaller than 8 m PZ, about 80% that of 7 m MEA. 10 m DGA® absorbs CO$_2$ at a rate 20% less than 7 m MEA. The heat of CO$_2$ absorption of 10 m DGA® is 81 kJ/mol at average operational CO$_2$ loading, the same as that of 7 m MEA.

The mass transfer area of structured packing is strongly related to packing size (125–500 m^2/m^3) and liquid load (2.5–75 m^3/m^2·h). Surface tension (30–72 mN/m) had a weaker but significant effect. Liquid viscosity (1–15 mPa·s) and flow channel configuration had essentially no impact. The ratio of mass transfer area to specific area (a_e/a_p) was correlated by:

1

$$\frac{a_e}{a_p} = 1.339 \left[\left(\frac{\rho_L}{\sigma} \right) g^{\frac{1}{3}} \left(\frac{Q}{L_p} \right)^{\frac{4}{3}} \right]^{0.116}$$

The June 2009 thermodynamic model for PZ accurately predicts VLE and heat capacity but fails to provide adequate predictions of PZ volatility, heat of CO_2 absorption, and speciation.

Less complex stripper configurations were modeled for 9 m MEA. The double matrix using only single-stage flashes required an equivalent work of 33.8 kJ/mole CO_2, compared to 35.8 for one single-stage flash and 35.3 for a simple stripper.

Normalized density of EDA solution is not a strong function of amine concentration, and can be predicted only using CO_2 concentration.

Metal concentrations in EDA samples that have been thermally degraded are much higher than those in PZ and about twice those of MEA, suggesting that EDA will corrode stainless steel.

The C_p of loaded 12 m EDA is lower than that of 8 m PZ and 7 m MEA. High amine concentration with high loading helps to reduce the sensible heat requirement.

8 m 2-PE thermally degrades more slowly than 7 m MEA and EDA, but much more significantly than PZ. The dimer of 2-PE is the main thermal degradation product. There is colloidal suspension in thermally degraded 2-PE samples .

With 7 m MDEA the amine loss rate was 61%/week when cycled between 55 and 120 $^{\circ}$C. We have hypothesized that entrained oxygen from the oxidizer at 55 °C is entrained and reacts with the MDEA at 120 $^{\circ}$C.

When DEA is reacted wth PZ or Methyl-PZ at150 $^{\circ}$C we observe the expected dimers with masses of 173.1 and 187.1, corresponding to thermal degradation products also observed in the degradation of MDEA/PZ.

When MEA was degraded in two successive steps to represent absorber and stripper conditions, the degradation rate was comparable to that expected from the respective oxidative and thermal degradation experiments.

The reaction of monoethanolamine (MEA) with formate to form N-formyl-ethanolamine reached equilibrium in 12 to 2 hours at studied at 55–130 °C.

Dissolved chromium was a mild catalyst of MEA oxidation. Degradation occurred at an average rate of 0.5 mM/hr and was unaffected by Cr concentration (0.01–1 mM). Equimolar addition of EDTA reduced the degradation rate by 50%.

Iron-catalyzed degradation of 8 m PZ is greatly reduced by 100 mM A. With 0.4 mM Fe^{2+}/0.1 mM Cr^{3+}/0.05 mM Ni^{2+}, the apparent loss of PZ was negligible with some products. With the addition of 10 mM A, the yield of degradation products was significantly reduced.

In 15 weeks at 175 °C, 8 m PZ degradation produced about 600 mM total formate, and 43 mM EDA as well. Total formate reached 560 and 690 mM total formate andwhile EDA reached 42 and 45 mM. Accumulation of Fe^{++}, Ni^{++}, and Cr^{++} was less than 12 mM, suggesting that 316SS is resistant to corrosion by 8 m loaded PZ.

The designed skid for a two-stage flash with 0.1 MW nominal capacity will have a footprint of 9 x 6 feet. The major equipment was purchased for $60,000.

1. VLE Study of Aqueous Piperazine at High T   *p. 12*

by Qing Xu

In this quarter a high temperature VLE experimental apparatus was built, tested, and modified. Experiments were conducted with water and 5, 8, 10 m PZ solutions at 120, 140, and 150 °C. 5 runs for 8 m PZ with about 0.4 CO_2 loading were conducted at 140 and 150 °C. At 120–150 °C, partial pressure of PZ ranges from 0.2 to 1.6 kPa for 5.5 m PZ; at 120 and 140 °C, PZ partial pressure is 0.7 and 1.8 kPa for 8.7 m aqueous PZ, and 0.8 to 2.1 for 10.5 m PZ.

A 500 mL stainless steel autoclave was used as the equilibrium cell, the vapor sample was continuously analyzed by FTIR, and liquid samples were taken before and after each run. For CO_2 loaded aqueous PZ solutions, liquid samples were also taken during the experiment. Liquid samples were analyzed by TIC and total alkalinity titration.

Several improvements have been made: 1, 3, and 5 min sampling times were selected in Calmet® software for FTIR analysis and 1 min was found to be the best. The RTD thermometer was replaced with a low noise K-type thermocouple. The thermal well inside the autoclave was replaced with a new one. Heating tapes and thermostats were added around the top of the autoclave and the vapor sampling tubes to avoid condensation in the vapor line. Bigger SS bombs were used to obtain liquid samples.

2. Volatility and heat capacity of amine alternatives   *p. 25*

by Bich-Thu Nguyen

The volatility of aqueous amine-water systems is explored in this report. A number of amines was studied at varying concentrations, from very dilute to highly concentrated conditions, at temperatures from 40–70 ℃. While it is not currently possible to compare amine volatilities in general due to differences in the conditions studied in each case, it is relevant to observe volatility at the working concentration of each amine (~30–50 wt %) at 40 ℃. The amines studied are ranked as follows in order of increasing volatility: DGA® (diglycolamine – 16 m) ~1.5 Pa; PZ (piperazine – 8 m) < 17.1 Pa (~8–10 Pa); MEA (monoethanolamine – 7 m) ~10 Pa; AMP (2-amino-2-methyl-1-propanol – 5 m) ~14.2 Pa; EDA (ethylenediamine – 8 m) ~17.2 Pa. At a most basic level of scientific analysis, DGA® is much less volatile than EDA, the most volatile amine studied, due to the former being more polar overall (-OH group present) and therefore is more water-friendly with little to no tendency to leave the solution (volatilize). Amine volatility is a complex phenomenon dependent on several properties of the molecule, including its boiling point, molecular weight, and most certainly its polarity as determined by chemical group contribution and arrangement. In future studies, amine volatility will be explained in depth in the context of UNIQUAC (a group contribution theory) in an effort to understand and validate experimental observations.

3. Rate Measurements for MEA and PZ   *p. 38*

by Ross E. Dugas

A Ph.D. dissertation on this work is in preparation. Chapter 5 on modeling is attached.

Using the wetted wall column rate data and available literature data, MEA and PZ spreadsheet models were created to explain observed rate behavior. The resultant liquid film mass transfer coefficient, k_g', expressions use termolecular (base catalysis) kinetics and with an activity-based rate expression. The k_g' expressions were shown to accurately represent rate behavior over the very wide range of experimental conditions. The model fully explains rate effects with changes in amine concentration, temperature, and CO_2 loading. These models allow for rate behavior to be predicted at any set of conditions as long as the parameters in the k_g' expressions can be accurately estimated.

An Aspen Plus® RateSep^{TM} model for MEA was created to model CO_2 flux in the wetted wall column. The model was able to fairly accurately calculate CO_2 flux over the wide range of experimental conditions but included a systematic error with MEA concentration. The systematic error results from an inability to properly represent the activity coefficient of MEA. Due to this limitation, the RateSep^{TM} model is most accurate when finetuned to one specific amine concentration. This Aspen Plus® RateSep^{TM} model allows for scale up to industrial conditions to examine absorber or stripper performance.

4. Wetted Wall Column Rate Measurements   *p. 121*

by Xi Chen

The CO_2 solubility and adsorption/desorption rate were measured in the wetted wall column for 10 m Diglycolamine® (DGA®) with varied CO_2 loading (mol CO_2/mol alkalinity). VLE models of CO_2 were regressed from experimental data to calculate CO_2 capacity and enthalpy of CO_2 absorption (ΔH_{abs}). The liquid film mass transfer coefficients (kg') and CO_2 partial pressures (P*) obtained were compared to those of 8 m piperazine (PZ) and 7 m monoethanolamine (MEA) as well as other amines studied in the previous quarter. The capacity of DGA® is about 20% less than that of 7 m MEA. DGA® has about the same heat of absorption for CO_2 (ΔH_{abs}=81 kJ/mol) as MEA, much higher than PZ (70 kJ/mol).

5. Influence of Liquid Properties on Effective Mass Transfer Area of Structured Packing   *p. 127*

by Robert Tsai
(also supported by the Separations Research Program)

The quarterly effort is included in the attached manuscript.

The mass transfer area of nine structured packings was measured in a 0.427 m ID column via absorption of CO_2 from air into 0.1 kmol/m^3 NaOH. The area was most strongly related to packing size (125–500 m^2/m^3) and liquid load (2.5–75 m^3/m^2·h). Surface tension (30–72 mN/m) had a weaker but significant effect.   Liquid viscosity (1–15 mPa·s) and flow channel configuration had essentially no impact on the mass transfer area. Surface texture (embossing) increased the effective area by 10% at most. The ratio of mass transfer area to specific area (a_e/a_p) was correlated within limits of ±13% for the entire experimental database:

$$\frac{a_{e}}{a_{p}} = 1.339 \left[\left(\frac{\rho_{L}}{\sigma} \right) g^{\frac{1}{3}} \left(\frac{Q}{L_{p}} \right)^{\frac{4}{3}} \right]^{0.116}$$

6. Modeling Stripper Performance for CO₂ Removal   p. 162

by David Van Wagener

Since Hilliard developed thermodynamic models for various amine solvents, additional experimental data have been collected at new conditions. The data primarily of interest have been for concentrated piperazine (PZ). The Hilliard model performed well for low PZ concentrations, 0.9 m–5 m, but 8 m PZ will be used in future simulations. This model was previously updated with high amine concentration data, resulting in the June 2009 PZ model. The property predictions by this model were investigated to evaluate the overall accuracy of the model for 8 m PZ. The VLE and heat capacity predictions showed little deviation from laboratory data. The volatility predictions were difficult to scrutinize because there are few data points from the lab. The Aspen Plus® predictions were systematically lower than the available lab data, but the deviations may be reduced when new data are collected with new FTIR software. Unlike these properties, the speciation and heat of absorption predictions are not yet acceptable. The bicarbonate concentration was large compared to other solvents, but no data are available for 8 m PZ. The heat of absorption predictions were questionable for two reasons. First, the predictions did not approximate the magnitude of laboratory data collected at NTNU. However, there was agreement between the calculated values using the Gibbs-Helmholtz equation with the measured VLE and Aspen Plus® predictions using this model. The Aspen Plus® predictions and Gibbs-Helmholtz calculations both have values around 60–70 kJ/mol CO₂, whereas the laboratory data is 20–30 kJ/mol CO₂ higher with +/-10 kJ/mol CO₂ scatter for all temperatures. The second concern with heat of absorption predictions in Aspen Plus® was whether the Gibbs-Helmholtz calculations are consistent with calorimetric results. Prior analysis with MEA demonstrated a slight difference between these two calculation methods, but the difference is more severe for 8 m PZ.

Next, analysis of various stripper configurations with different complexity levels using 9 m MEA was initiated. The most efficient configuration thus far is equilibrium flashes in a double matrix arrangement. The double matrix configuration has only been evaluated using all equilibrium flashes, but it had a 4.2% improvement over a simple stripper, with 35.3 kJ/mol CO₂ and 33.8 kJ/mol CO₂ for the simple stripper and double matrix, respectively. A configuration developed by Fluor consisting of a simple stripper with an adiabatic flash on the lean stream also performed better than the simple stripper, but only reduced the equivalent work requirement to 34.4 kJ/mol CO₂. Other evaluated configurations which did not outperform the simple stripper included 1-stage and 2-stage flashes.

7. CO₂ Absorption Modeling Using Aqueous Amines   p. 176

by Jorge M. Plaza

Work continued on the development of an absorber model for 8 m PZ. The thermodynamic model was updated by Van Wagener from version 02/06/09 to version 06/16/09. This update required re-regression of the density data. A density subroutine was implemented to calculate

this property independent of speciation. However, the developed subroutine could not adequately represent the density data due to issues related to the average molecular weight. Density was re-regressed satisfactorily using the Clarke model for liquid molar volume for electrolyte solutions in Aspen Plus®. The resulting parameters are presented in this report.

The behavior of the activity coefficient of CO_2 was corrected using the N_2O analogy with a correlation for Henry's constant presented in Cullinane (2005) for N_2O-water and regression work by Dugas (in progress) for N_2O-MEA. A linear relation for the activity of CO_2 and loading and temperature has been proposed. Previous work had shown a maximum value around a loading of 0.30. The activity coefficient was modified using the CO_2-ion local contribution parameters (τ) in the e-NRTL model. Resulting values are included in this report.

8. Modeling Absorber/Stripper Performance with MDEA/PZ   p. 185
by Peter Frailie

The goal of this study is to evaluate the performance of an absorber/stripper operation that utilizes the MDEA/PZ blended amine. Before analyzing unit operations and process configurations, the thermodynamic framework for the blended amine must be satisfactorily constructed. The approach used in this study is first to construct separate MDEA and PZ models that can later be reconciled via cross parameters to accurately model the MDEA/PZ blended amine. Once the MDEA/PZ model has been completed it must be incorporated into separate absorber and stripper models similar to those developed by Van Wagener and Plaza. This study is currently in the process of developing the MDEA/PZ model based on thermodynamic data.

Preliminary correlations are presented for density, viscosity, CO_2 solubility and heat capacity in 7 m MDEA/2 m PZ. The MDEA model has already been completed, but the PZ model is in need of some major corrections. The goal for the next quarter is to complete the MDEA/PZ thermodynamic model and begin constructing a rate-based model for the absorber.

9. Solvent Management of MDEA/Piperazine   p. 191
by Fred Closmann

(also supported by the Process Science & Technology Center)

The integrated solvent cycling/degradation apparatus (ISDA) was modified in the third quarter to obtain accurate temperature and oxidation-reduction potential (ORP) measurements. Three cycling experiments were completed in the quarter. At conditions of 55 °C in the oxidative reactor and 120 °C in the thermal reactor, we measured a formate production rate of 0.6 mM/hr. When we reversed the formation of amides in samples from this same experiment, we observed a formate production rate of 0.98 mM/hr. When the same solvent was cycled at conditions of 55 °C in the oxidative reactor and thermal reactors, the formate production rate was 0.004 mM/hr. The measured amine loss rate at the 55/120 °C condition was ~61%/wk, which was over an order of magnitude greater than the rate (0–2.5%/wk) observed in thermal cylinder experiments conducted at 120 °C.

Using thermal cylinder experiments and LC-MS analytical detection equipment, we confirmed the presence of DEA degradation products expected in the presence of strong nucleophiles including piperazine (PZ) and methyl-PZ. The mass of those degradation products were 173.1 and 187.1, respectively, when DEA was reacted with PZ and methyl-PZ in CO_2 loaded samples degraded at 150+ °C.

10. Solvent Management of Concentrated Piperazine   *p. 227*

by Stephanie Freeman

Iron-catalyzed degradation of 8 m PZ is reduced with the addition of 100 mM Inhibitor A. PZ in the presence of iron loses 10% of the initial amine within 500 hours but A reduces this to effectively no loss. With 10 mM of A in the presence of stainless steel metals (Fe^{2+}, Cr^{3+}, Ni^{2+}), the loss of PZ was not reduced while fewer degradation products were produced

At 175 °C, 8 m PZ lost 71.5 and 73% over 15 weeks with 0.3 and 0.4 mol CO_2/mol alkalinity, respectively. This degradation produced large amounts of formate, total formate, and EDA. Total formate reached 560 and 690 mM while EDA reached 42 and 45 mM for the two loadings, respectively. The degradation in these experiments seen in the first 5 weeks matched the rate observed in previous experiments at this temperature. Despite the high rate of degradation observed in these two experiments, metal concentrations were low for Fe^{2+}, Cr^{3+}, and Ni^{2+}, all staying below 7 and 12 mM in the two experiments. Unique to these two experiments, Ni^{2+} was found in the highest concentration, not iron as was expected.

The behavior of 16 PZ derivatives was observed in the Cation IC-MS. Most of the amines, AcPZ, AEPZ, AMPZ, DFPZ, DMPZ, EDA, EPZ, FPZ, HEEDA, HEP, HEMP, MPZ, and TEDA, behaved as expected producing a single peak with the expected m/z ratio for that analyte. Doublet signals (m/z = 2*MW+1) were observed in 7 analytes as well. Three species, 2-Imidazolidone, 2-Methyl-2-Imidazoline, and 2,5-piperazindione, produced very weak signals without the expected m/z ratio.

Cation IC-MS analysis of 11 oxidation and one thermal degradation sample was performed. In those where PZ degraded, namely OE2, OE4, and TE9, peaks of EDA and N-Formyl PZ were identified. Experiments with Inhibitor A both have the same unidentified peak that must be an adduct of A.

ICP-OES will be used for metals analysis rather than AA because of ability to detect multiple metals in the same sample, reducing the volume of sample needed for analysis.

11. Ethylenediamine as a solvent for CO_2 capture   *p. 261*

by Shan Zhou

The density of 8 m and 12 m ethylenediamine (EDA) with different CO_2 loadings was measured. The solution density has a linear relationship with CO_2 concentration in the solutions (mol CO_2/kg solution).

8 m EDA samples which had been degraded for 8 weeks in thermal degradation experiments were measured by atomic absorption. 8 m EDA is more corrosive than MEA and piperazine (PZ).

The heat capacity of 12 m EDA was measured. With less water in the solution, the heat capacity of loaded 12 m EDA is lower than both 8 m PZ and 7 m MEA.

Thermal degradation experiments of 2-Piperidineethanol (2-PE) were performed at 120–150 °C. Thermal degradation of 2-PE is slower than that of MEA, but 2-PE polymerized in the thermal degradation process.

12. Oxidative Degradation of MEA   *p. 271*

by Alex Voice

The degradation of MEA was carried out in two successive steps to represent absorber and stripper conditions. Amine loss was 17.4% after 13 days at 135 ^{o}C, before being transferred to the oxygen environment at 55 ^{o}C. Degradation in this environment was initially 1.8%/week, but dropped off steeply to 0.3%/week by the third week. These rates were consistent with previous thermal (Davis, 2009) and oxidative (Sexton, 2008) degradation work.

The reaction of monoethanolamine (MEA) with formate to form N-formyl-ethanolamine was studied at temperatures of 55–130 ^{o}C. The activation energy of this reaction was determined to be 48±6 kJ/mol

Samples from an industrial CO_2 capture process were analyzed for heat stable salts (HSS). The lean solution contained 11 mM of total HSS (glycolate and formate were the highest, with 6 and 3 mM, respectively). The reclaimer waste contained 326 mM of HSS and their respective amide derivatives (N-carboxyl-ethanolamine). Formate and N-formyl-ethanolamine were found at concentrations of 64 mM and 170 mM, respectively.

Dissolved chromium was found to catalyze oxidation of MEA in the high gas flow apparatus. Degradation occurred at an average rate of 0.5 mM/hr and was unaffected by Cr concentration (0.01–1 mM). Equimolar addition of EDTA reduced the degradation rate by 50%.

13. Dynamic Operation of CO_2 Capture   *p. 290*

by Sepideh Ziaii

This work presents the dynamic behavior of the amine absorption/stripping system in response to the changes in the capture or steam cycle operating conditions. This dynamic simulation was run in a flow sheet of Aspen Custom Modeler® by integrating the dynamic models of the absorber and the stripper and including simplified steady state models of the cross heat exchanger, the lean solvent cooler, and pumps.

The dynamic results demonstrate that, in the absence of any control system, CO_2 capture reaches steady state in less than 30 minutes smoothly after making a step change in the steam rate and flue gas rate. However the CO_2 capture continues to vary slowly because no control action is bringing the water content back to balance.

Regulating the temperature of lean solvent recycling to the absorber is presented as an alternative strategy to control water balance, however it is not proposed as an instantaneous control action.

In addition, controlling the levels in the inventories in an acceptable range is indicated as a mandatory control action. It should be considered for amine systems to make sure that thermal and oxidative degradation and liquid/vapor separation criteria will always be satisfied.

14. Electric Grid Level Implications of Flexible CO_2 Capture Operation
p. 298

by Stuart Cohen

A first-order model of hourly electric grid dispatch and pricing has been adapted in order to investigate the implications of flexible carbon dioxide (CO_2) capture over a multi-year time

frame with annually varying fuel prices, CO_2 prices, electricity demand, and power plant fleet. Preliminary analysis of the Electric Reliability Council of Texas (ERCOT) electric grid over a 21-year period with six natural gas and CO_2 price path combinations shows that coal-fired plants continue to be dispatched at base load regardless of the availability of CO_2 capture unless natural gas prices are low and CO_2 prices are high. Operation of flexible CO_2 capture in response to demand-induced electricity price variations depends on complex interactions of fuel and CO_2 prices, operating costs, and the current power plant fleet. When the emissions cost penalty of partial-load CO_2 capture is only a few dollars per megawatt-hour, flexibility can be used for modest operating profit improvements, but these improvements could be offset by any operating cost penalty for using a flexible system. However, by eliminating the need for new capacity to replace output lost to full-load CO_2 capture, flexibility can greatly improve the net present value of a CO_2 capture investment.

The same dispatch and market model has also been expanded for use in a comparative study of flexible CO_2 capture in the United Kingdom (UK) and ERCOT electric grids. The two grids are similar in market structure and size, but differences in capacity mix, demand variations, and fuel markets will likely produce diverging behaviors of flexible CO_2 capture systems.

15. Measurement of Packing Liquid Phase Film Mass Transfer Coefficient p. 315

by Chao Wang

Packings are widely used in distillation, stripping, and scrubbing processes because of their relatively low pressure drop, good mass transfer efficiency, and ease of installation. Packings are also are also being investigated for the post combustion carbon capture process for these reasons. Research continues to focus on development of high performance packing, especially on minimizing pressure drop, maximizing mass transfer efficiency, and minimizing costs. The design of packed absorbers for carbon dioxide capture will require the reliable measurement and accurate prediction of the effective area, gas and liquid film mass transfer coefficient. A variety of experimental methods for measuring effective area, gas and liquid film mass transfer coefficient k_La have been reported. Consistent measurements of these important design parameters will be tried this summer and will continue in the fall.

Absorption of CO_2 with NaOH is applied to measure the effective area of packings. Atmospheric carbon dioxide is used as gas phase and 0.1 M NaOH is used as liquid phase. The effective area can then be determined by the measured overall volumetric gas phase mass transfer coefficient ($K_{og}a$, Henry's constant, carbon dioxide diffusivity, free OH concentration, and the predicted reaction rate constant). These measurements have been obtained on a wide variety of random and structured packings by the UT/SRP. In recent years, Robert Tsai has obtained additional gas/liquid contact area data by adjusting the surface tension and viscosity of the system.

The absorption of SO_2 into NaOH solution will be used to measure the gas phase film volumetric mass transfer coefficient. Sulfur dioxide (SO_2), blended with ambient air at a composition of approximately 80 ppm, will be absorbed by 0.1 M NaOH solution. The gas phase film mass transfer coefficient may be determined from the measured gas phase volumetric mass transfer coefficient (k_ga) and the previously measured gas/liquid contact area (a).

The stripping of toluene from water with air is applied to measure the liquid phase volumetric mass transfer coefficient (k_La). Ambient air is used to strip soluble toluene from water. The liquid phase mass transfer coefficient can be determined from the measured liquid phase volumetric mass transfer coefficient and the previously measured gas/liquid contact area.

In this quarter, a new SO_2 analyzer has been installed and incorporated into the UT/SRP air/water pilot plant and DeltaV control system. The SO_2 analyzer underwent testing and troubleshooting separately. In addition, a gas chromatographic system was set up to allow measurements of ppm levels of toluene in water. The analytical system has also been checked out and trouble-shooted. Three structured packings will be studied in the upcoming quarter: Raschig-Jaeger RSP250, Sulzer Mellapak 2X, and Koch-Glitsch Flexipac 1.6Y HC. These packings were obtained during this quarter.

16. Pilot Plant Testing of Advanced Process Concepts using Concentrated Piperazine p. 327

by Eric Chen

Pilot plant testing of 8 m piperazine in a two-stage heated flash is planned for the spring of 2010. Substantial modifications to the existing pilot plant at SRP will be needed. The process flow diagrams (PFD) and piping and instrument diagrams (P&ID) were updated. The high pressure pump, cross-exchanger, two pressure vessels, and two steam heaters were designed and ordered. Three-dimensional models of the skid equipment are being developed and will be used to design the layout of the skid structure and process piping. A list of process instrumentation and control valves was developed and quotes were obtained.

17. Nitrosamine Formation in CO$_2$ Capture Plant p. 346

by Mandana Ashouripashaki (Civil Engineer co-supervised by Howard Liljestrand)

The purpose of this work is to investigate nitrosamine formation in CO_2 capture plants from coal-fired power plant flue gas.

Nitrosamines are important, because of their carcinogenic effect on animals and humans. Almost all studies related to nitrosamines have been done in acidic conditions which are compatible with *in vivo* conditions.

The project is going to determine whether nitrosation reagents are present in the system, and, if there are sufficient nitrosation compounds, what is the possibility of nitrosamine formation in a basic medium, because amine solutions in CO_2 capture plants have alkaline and basic properties.

The specific objectives of this work will be:
- Develop an appropriate method for measuring and detecting nitrosamine to monitor nitrosamine production reaction in CO_2 capture plants.
- Qualify the nitrite sources in CO_2 capture plants: flue gas, absorber, and stripper.
- Determine nitrite and amine reaction rates to qualify nitrosamine formation in basic solution.
- Analyze amine oxidation and thermal degradation products and their effects on amine and nitrite reaction to examine if they are nitrosamine formation catalysts or inhibitors.
- Investigate piperazine behavior in reaction with nitrites and nitrosopiperazine inhibition methods.

Attachments

VLE Study of Aqueous Piperazine at High T

Quarterly Report for July 1 – September 30, 2009

by Qing Xu

Supported by the Luminant Carbon Management Program

and the

Industrial Associates Program for CO_2 Capture by Aqueous Absorption

Department of Chemical Engineering

The University of Texas at Austin

October 7, 2009

Abstract

In this quarter a high temperature VLE experimental apparatus was built, tested, and modified. Experiments were conducted with water and 5, 8, 10 m PZ solutions at 120, 140, and 150 °C. 5 runs for 8 m PZ with about 0.4 CO_2 loading were conducted at 140 and 150 °C. At 120–150 °C, partial pressure of PZ ranges from 0.2 to 1.6 kPa for 5.5 m PZ; At 120 and 140 °C, PZ partial pressure is 0.7 and 1.8 kPa for 8.7 m aqueous PZ, and 0.8 to 2.1 for 10.5 m PZ.

A 500 mL stainless steel autoclave was used as the equilibrium cell, the vapor sample was continuously analyzed by FTIR, and liquid samples were taken before and after each run. For CO_2 loaded aqueous PZ solutions, liquid samples were also taken during the experiment. Liquid samples were analyzed by TIC and total alkalinity titration.

Several improvements have been made: 1, 3, and 5 min sampling times were selected in Calmet® software for FTIR analysis and 1 min was found to be the best. The RTD thermometer was replaced with a low noise K-type thermocouple. The thermal well inside the autoclave was replaced with a new one. Heating tapes and thermostats were added around the top of the autoclave and the vapor sampling tubes to avoid condensation in the vapor line. Bigger SS bombs were used to obtain liquid samples.

Introduction

For concentrated PZ solutions, thermal degradation is negligible up to 150 ºC (Freeman et al., 2008). Many stripper configurations operate more efficiently at elevated temperature and pressure. Thus for concentrated PZ, better energy performance may be obtained by increasing stripper temperature without degradation of PZ (Rochelle et al., 2008a). The stripper pressure of the pilot plant campaign in 2008 approached 60 psia (Rochelle et al., 2008b).

The high temperature VLE measurement also has applications for other amines. For thermal resistant amines like AMP and DGA®, the stripper temperature can be increased; for amines with relative high thermal degradation rates (for instance, MEA), stripper temperature is limited but thermal reclaimers must operate at a much higher temperature. VLE research at high T and P can help understand these processes.

Experimental Methods

In this period, the apparatus for high temperature range VLE measurement was set up and tested by water, 5, 8 and 10 m aqueous PZ and 8 m PZ with about 0.4 CO_2 loading. Temperature for PZ solution was from 120 to 150°C, for water it was from 100 to 204°C. Water tests were conducted because of cleaning, calibration and testing for FTIR and needle valves, etc.

Apparatus

The apparatus is shown in Figure 1. Solid lines represent actual tubes while dashed lines represent electric wire connections. An autoclave (ZipperClave®, by Autoclave Engineers) was used as the equilibrium cell. Its designed operating range is up to 2000 psia and 232 ºC. The 500 mL pressure vessel is made of 316SS stainless steel. Closure is effected by a resilient spring member (the "Zipper") inserted through a circumferential groove in the body and cover (Autoclave Engineers). A quick release/safety lock ensures that the spring is fully inserted and makes it easy to open and close the equilibrium cell. A magnetic agitator (MAG075, MagneDrive II Series, by Autoclave Engineers) was used to get equilibrium without leaking to the atmosphere. It was driven by a compressed air motor (2AM-NCC-16, by Gast®). The agitator is good for both liquid and vapor phases. It has a hollow shaft, which draws the gas into the middle of the shaft when the agitation starts. It is then dispersed through the impeller hub and mixes with the liquid.
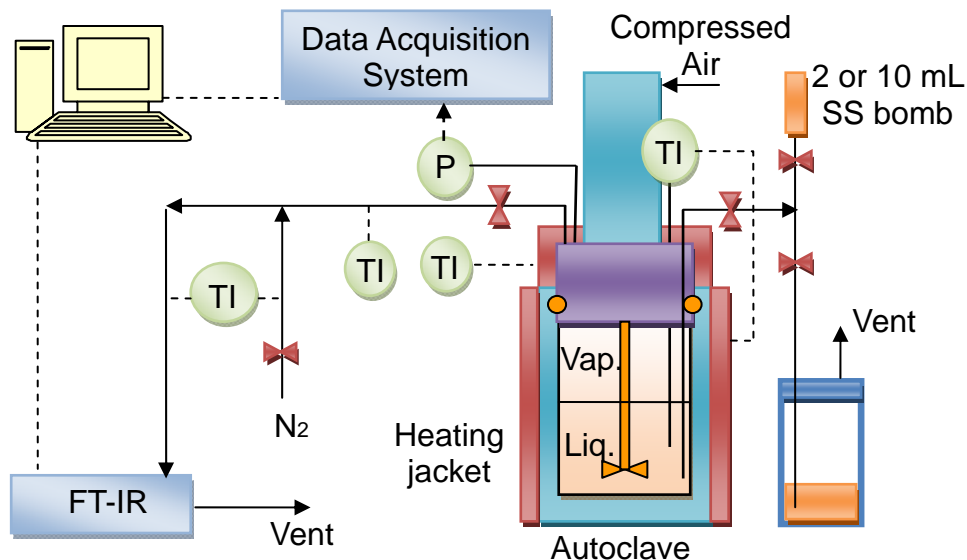
Figure 1: High Temperature VLE Apparatus

A low noise K-type thermocouple with miniature connector (model GKMQ-SS-062-U-6, by Omega®) was installed inside the thermal well of the vessel for temperature measurement. It was connected to a Fuji Electric PXZ-4 temperature controller. A pressure transducer (Druck® PTX 611, 0–30 bar absolute pressure) was used for pressure measurement. It was connected to a signal converter and a data logger NI USB 6009; LabView® SignalExpress® software was used for data recording. The pressure reading system was calibrated by a dead weight pressure tester (S/N 19189/278, by Budenberg Volumetrics, Inc.). Temperature measurement was calibrated by measuring pure water vapor pressure from 100 to 204 °C and pressure output conversion was adjusted to match the data from DIPPR Chemical Database (BYU DIPPR, Thermophysical

Properties Laboratory, 1998). The calibration data and plots are in the results section of this report. The top and surrounding of the equilibrium cell lid were covered by thermally conductive adhesive heating tapes from Clayborn Lab® and the temperature was kept between 160 and 175 °C by disc thermostats from Selco Products Company.

One Swagelok® valve and one Parker HR0 needle valve were in the vapor sampling line. Two 2 μ Swagelok® filters were installed before and after the needle valve. The valves and vapor sampling tube were wrapped with heating tape from Thermo Scientific®, and the temperature on the tubing surface was controlled by an Omega® K-type thermocouple and a temperature controller by Omega®. To obtain good data the T was set at 170–180 °C. N_2 at 1–5 L/min flow rate was preheated to 180 °C and joined the sample gas; the mixed gas was kept at 180 °C by the same heating line.

A Gasmet™ DX-4000 multicomponent FTIR gas analyzer and Calcmet® software were used for vapor analysis.

Procedures
Before each run, 250 to 300 mL solution was prepared and added into the autoclave. To avoid the effects of O_2, N_2 or CO_2 was used to purge air and then the cell was sealed and heating started. Data recording of pressure started when the system reached the target T. The agitation rate varied from 1500 RPM to 2500 RPM, depending on the viscosity of the mixture.

After the temperature and pressure had been stable for about 30 min, the vapor sampling valve was opened. Sample gas was diluted by 2–3 L/min N_2 and then the mixed gas entered the FTIR analyzer. The needle valve opening and N_2 flow rate were adjusted to get proper concentrations. The sample gas flow rate was kept above 80 mL/min at standard pressure. Calcmet® software was used for analyzing vapor sample on line. After the concentration has been relatively constant for a certain time, the vapor sampling stopped and the autoclave was heated to the next target temperature.

Liquid samples were collected before and after each experiment and analyzed by TIC and acid titration. For experiments with loaded CO_2, 2 to 5 more liquid samples were collected into 2 or 10 mL SS bomb during the run.

Liquid sample analysis

Total Inorganic Carbon (TIC)
The concentration of CO_2 in solution was determined by TIC analysis. The liquid samples were diluted by a factor of 50. About 10–15 μL diluted sample was injected into a CO_2 analyzer (Model 525, Horiba PIR 2000). Details can be found in Appendix B.2 of Hilliard's dissertation (2008).

Acid Titration
The total alkalinity of solution was determined by acid titration using a Metrohm-Peak 835 Titrando equipped with an automatic dispenser, Metrohm-Peak 801 stirrer, and 3M KCl pH probe. Details are available in Appendix A.3 of Hilliard (2008) and Appendix F of Sexton (2008).

Results

Pressure and Thermocouple Calibration

The pressure transducer was calibrated with a dead weight tester. The calibration curve is shown in Figure 2.

Pressure Transducer Calibration

$y = 14.724593x - 7.386030$

$R^2 = 0.999774$
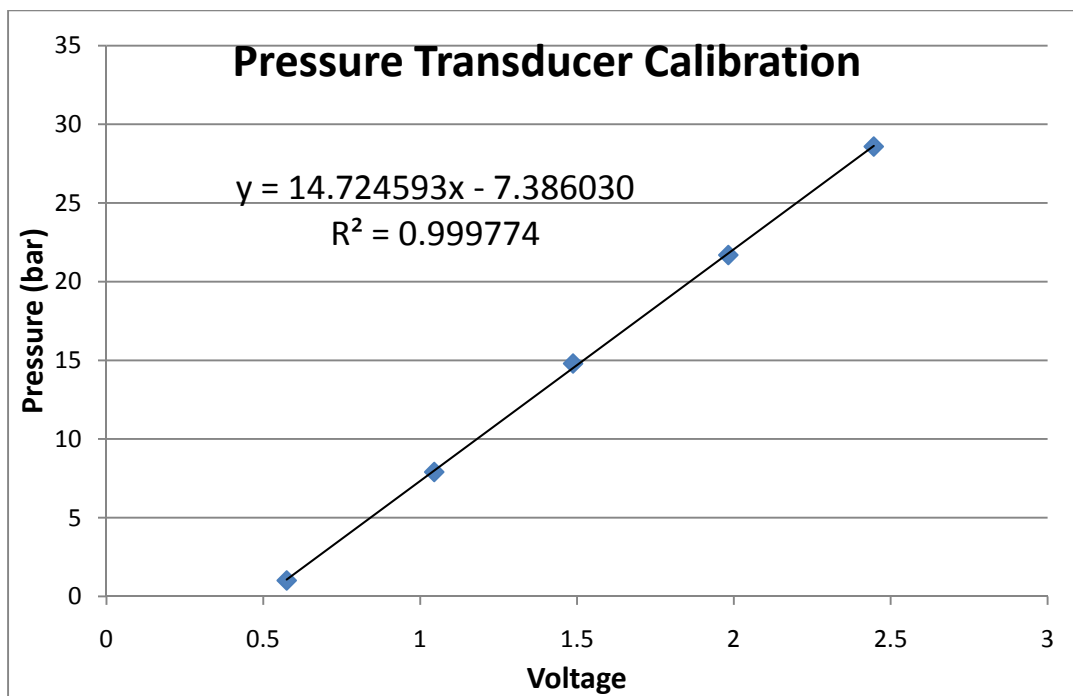
Figure 2: Pressure Transducer Calibration

LabView® SignalExpress® scales voltage to pressure data using the equation in Figure 2 for the experiments before September 25. After that an Omega® K-type low noise thermocouple replaced the normal thermocouple and further pressure calibration associated with temperature measurement was performed. Pure water vapor pressure was measured at 100 to 204 °C and compared with literature data from DIPPR chemical databank. The correlation is shown in Figure 3 below.
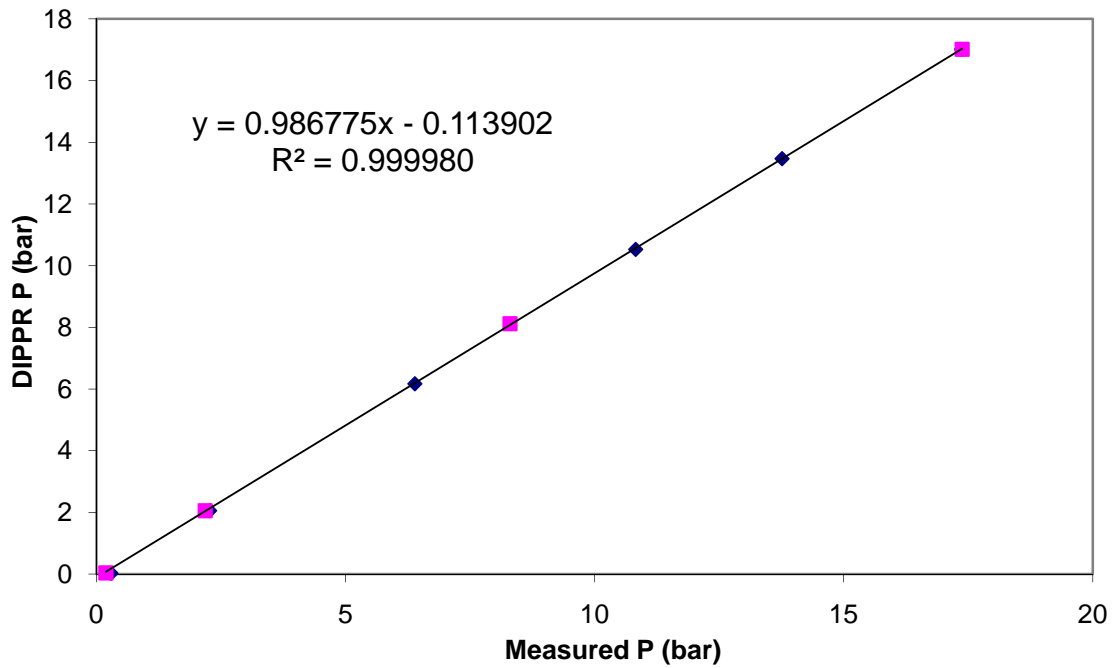
Figure 3: Calibration of Pressure Transducer with Thermocouple

For the experiments after September 25^t, a combination of the above two equations was input into Signal Express® and will be used from now on.

$$y = 14.529860x - 7.400745 \qquad (1)$$

y - pressure, bar.
x - voltage, V.

Pressure Measurement
Figure 4 shows a typical pressure graph during the 5 m PZ run.
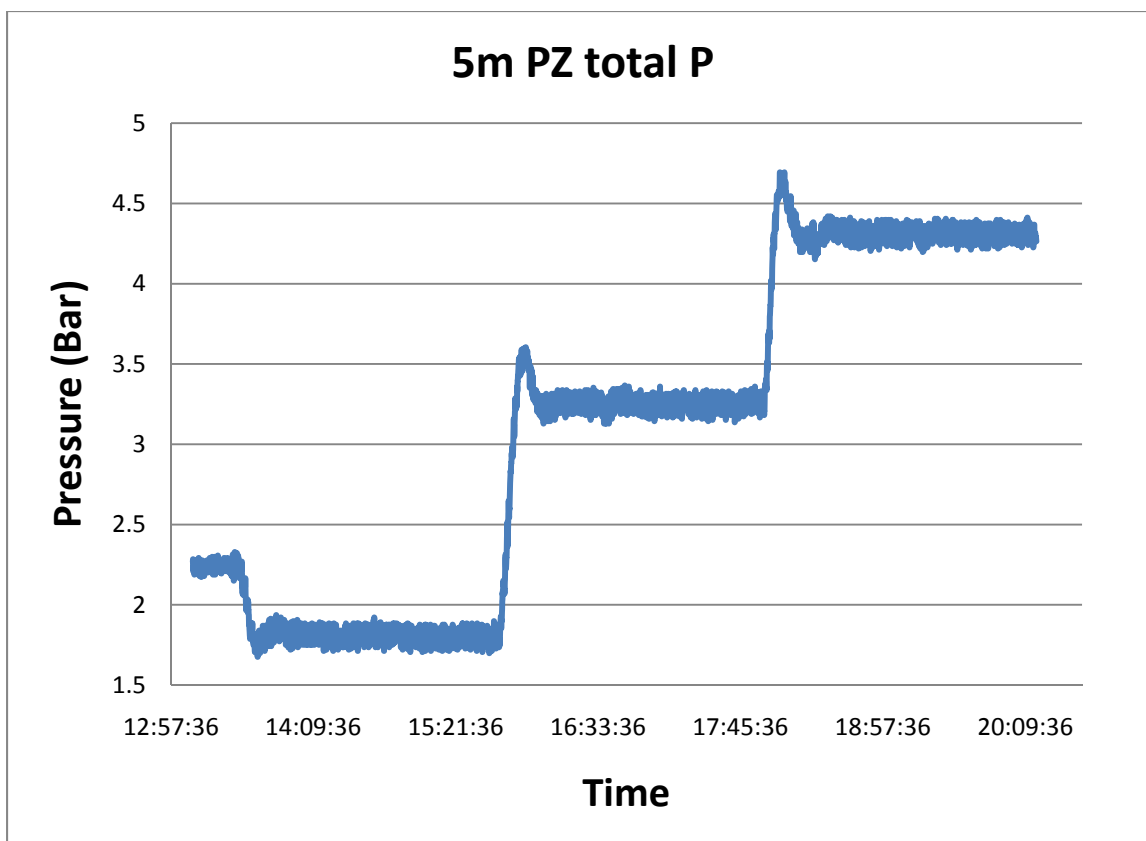
Figure 4: Total Pressure of 5 m PZ at 120, 140, and 150 °C

There are 4 basic stages in the pressure curve and they are at 120, 120, 140, and 150 °C. At the beginning there was N_2 in the equilibrium cell so the pressure is a little higher than stage 2. The fluctuation at the beginning of each temperature results from the sudden pressure change at the opening of the vapor sampling valve. Because of composition changing in the cell, there is a small incline at each stage. Average pressure was calculated for each stage after P became stable. The total pressure data generated in this period are shown in Table 1 in the following section.

FTIR Measurement – Concentration and Partial Pressure

Results for Aqueous PZ with CO₂:
Figure 5 shows the concentration for water, CO_2, and PZ in vapor for run PZ-3 which was 7.9 m PZ with 0.4 CO_2 loading. The vapor sampling valve was open during 2 periods in this run: one started from 14:42, the other started from about 16:00 and the temperatures were 140 and 150 °C, respectively. The CO_2 concentration is relatively constant at each temperature. However PZ and water concentrations peak from time to time.
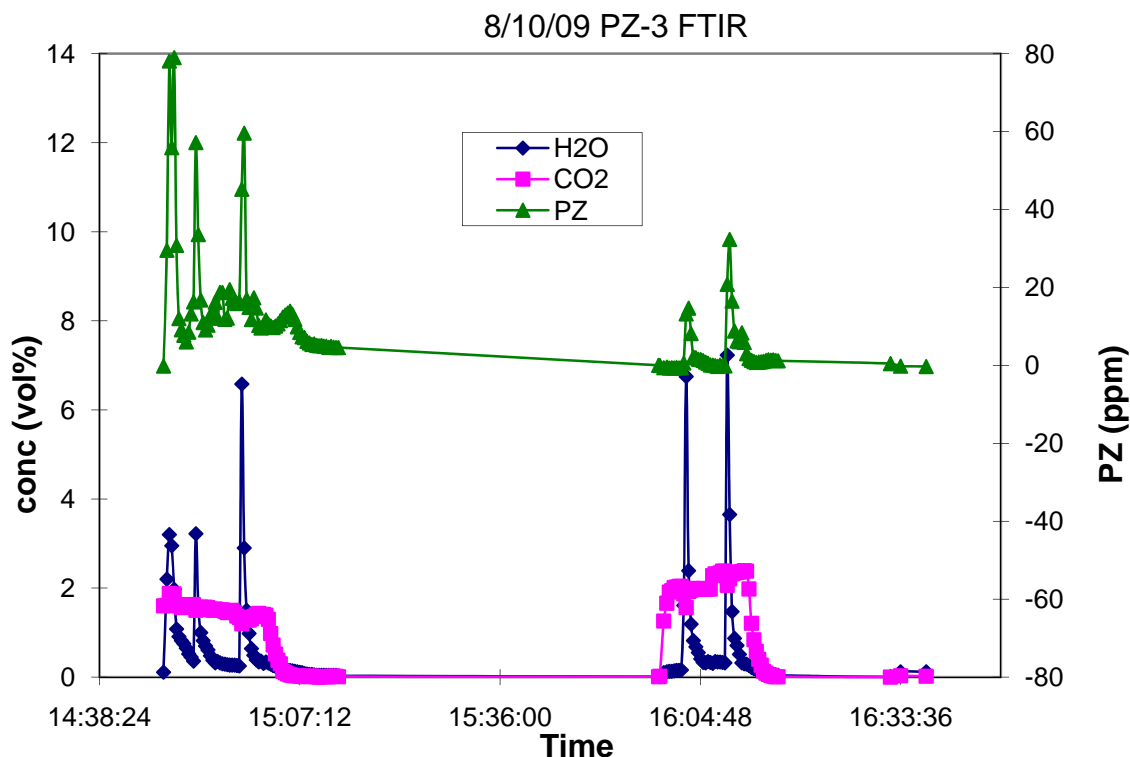
Figure 5: FTIR Plot for Run PZ-3, 7.9 m PZ, 0.4 CO_2 Loading, 140 and 150 °C

Much effort was expended to solve this problem. In the beginning of setting up this apparatus the vapor sampling line was insulated but not heat traced. One hypothesis was PZ and water condensation in the vapor sampling line. From experience we know that PZ shows peaks more readily in the FTIR graph, which indicates that PZ condenses more easily in the sampling line. Therefore heating tapes, thermostats, and temperature controllers were added to maintain the top of the equilibrium cell and the vapor sampling line at an appropriate temperature to avoid condensation. Experiments were conducted with water and aqueous PZ for testing this new system and better results were achieved. Another hypothesis was liquid entrainment going into the vapor line. This can be solved by adding an entrainment stopper and will be investigated in the next quarter.

Analyzing methods were also modified. Longer sampling time in FTIR and the calculation of rolling average concentrations could help to reduce noise. The disadvantage of using longer FTIR sampling times is that it would be hard to distinguish an entrainment, if any occurred. Up to now, the best sampling time found is 1 min.

Results for Aqueous PZ without CO_2:
Figure 6 shows a typical FTIR plot for 3 temperatures: 120, 140, and 150 °C.
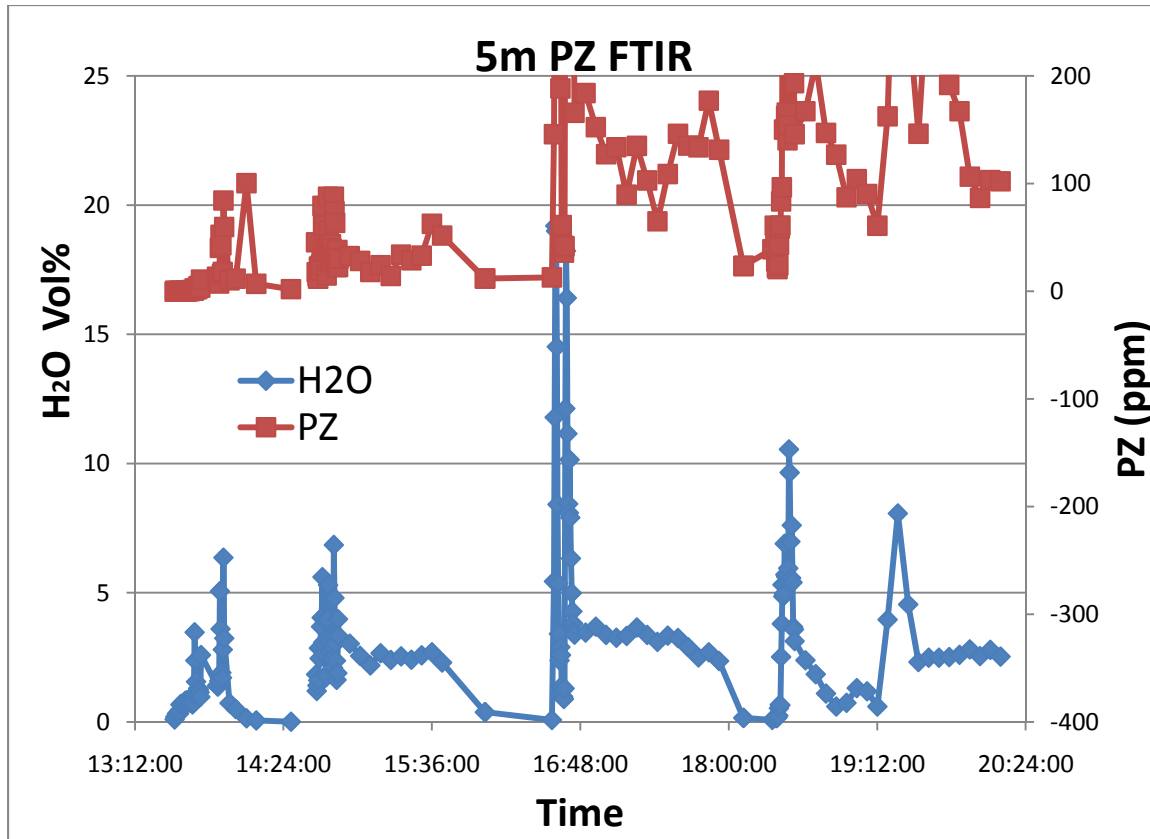
Figure 6: FTIR Plot for 5 m PZ at 120, 140, and 150 °C

At each temperature the partial pressures of H_2O and PZ were calculated from concentrations using equations 2 and 3:

$$P_{H_2O} = P_t \cdot y_{H_2O} \tag{2}$$

$$P_{PZ} = P_t \cdot y_{PZ} \tag{3}$$

P_t - total pressure, kPa.

P_{H_2O} - partial pressure of H_2O, kPa.

P_{PZ} - partial pressure of PZ, kPa.

y_{H_2O} - mole fraction of H_2O in vapor.

y_{PZ} - mole fraction of PZ in vapor.

Then P_{H_2O} and P_{PZ} were plotted for each temperature:
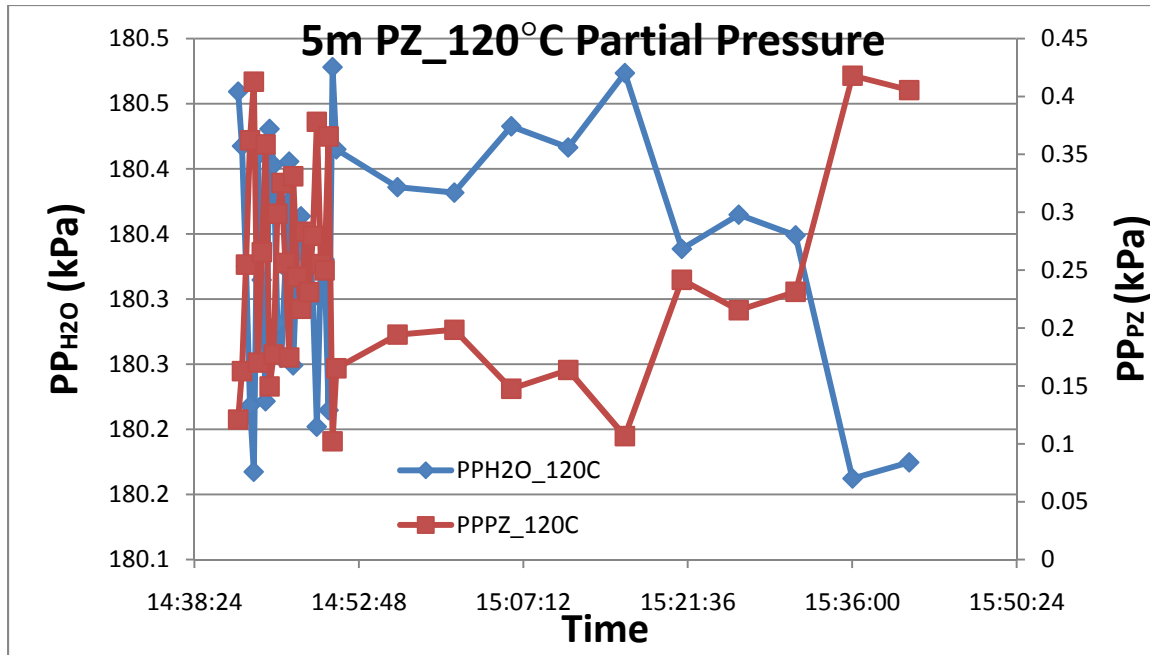
Figure 7: Partial Pressure of Water and PZ at 120 °C in 5 m PZ Experiment

In Figure 7 the points before 14:50 were taken at 20 sec sampling time, while the rest points were taken at 5 min sampling time. According to the trend curves the partial pressure of water is about 180.35±0.15 kPa and the partial pressure of PZ is about 0.23±0.15 kPa. More accurate average values were calculated in Excel. Similar processing was done with other data at different T and PZ concentration. Only data at relatively stable status were taken into calculation. Figures 8 and 9 show the partial pressure plots of water and PZ at 140 and 150 °C for 5 m PZ solution.
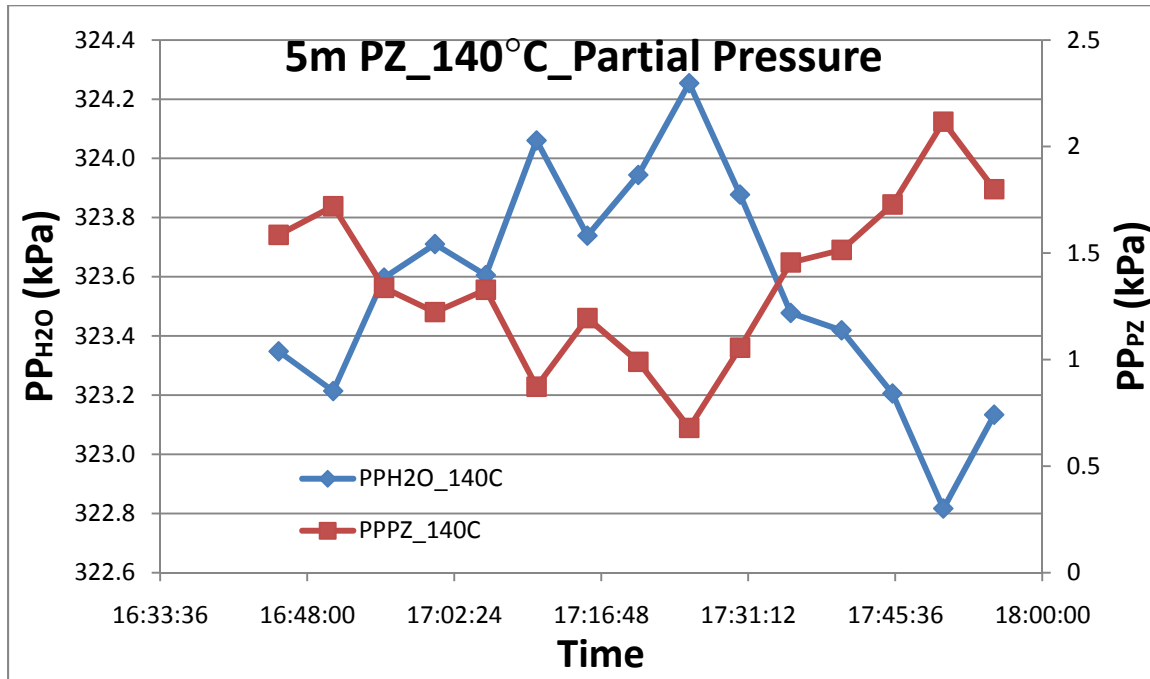
Figure 8: Partial Pressure of Water and PZ at 140 °C in 5 m PZ Experiment
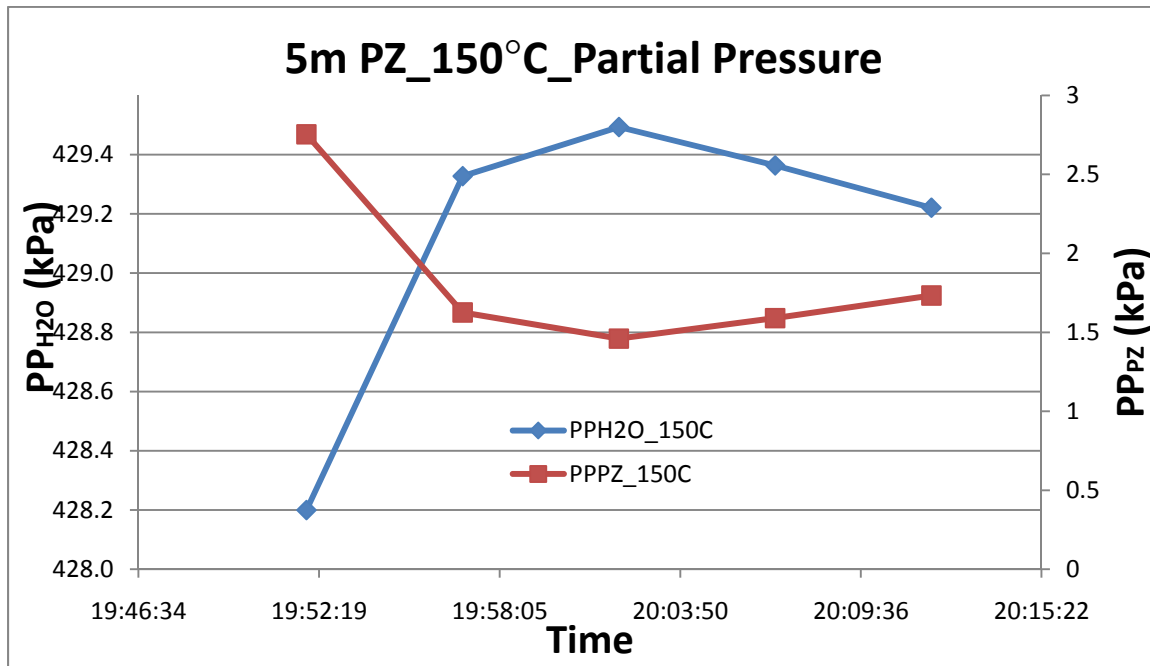
Figure 9: Partial Pressure of Water and PZ at 150 °C in 5 m PZ Experiment

Figures 10 to 12 show the partial pressure plots of water and PZ for 10 m PZ solution.
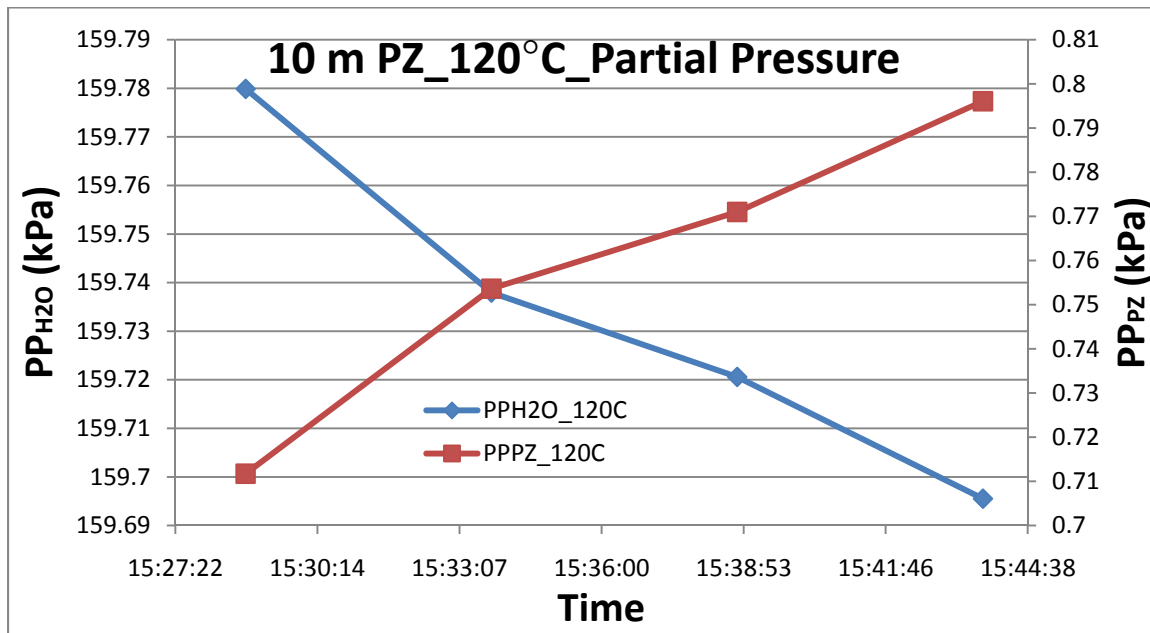
Figure 10: Partial Pressure of Water and PZ at 120 °C in 10 m PZ Experiment
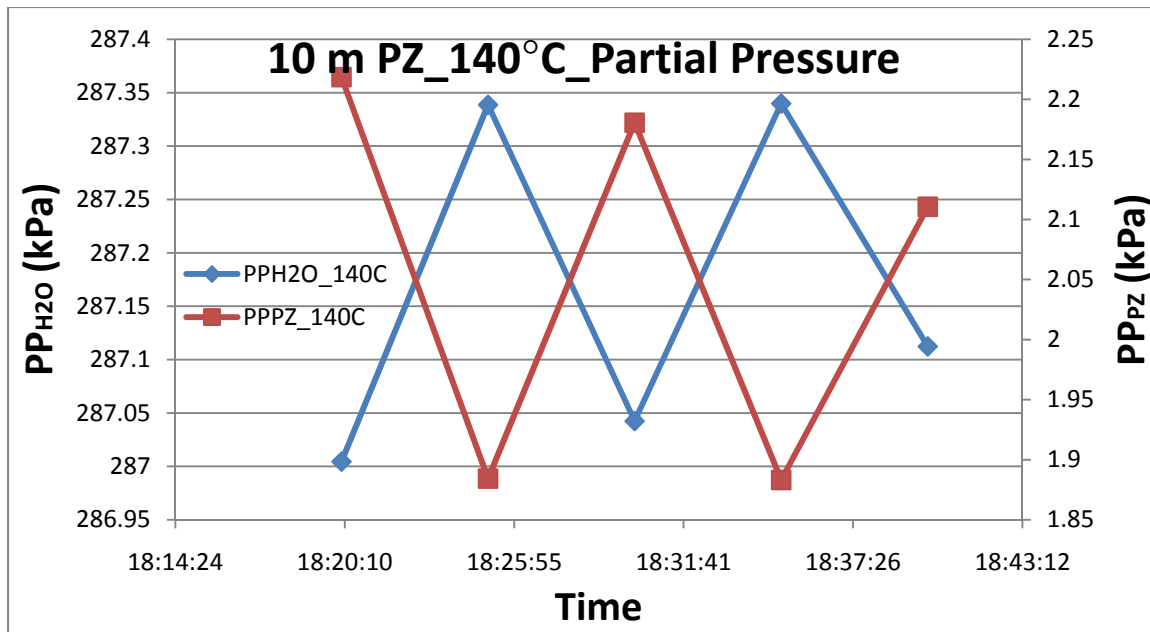
Figure 11: Partial Pressure of Water and PZ at 140 °C in 10 m PZ Experiment
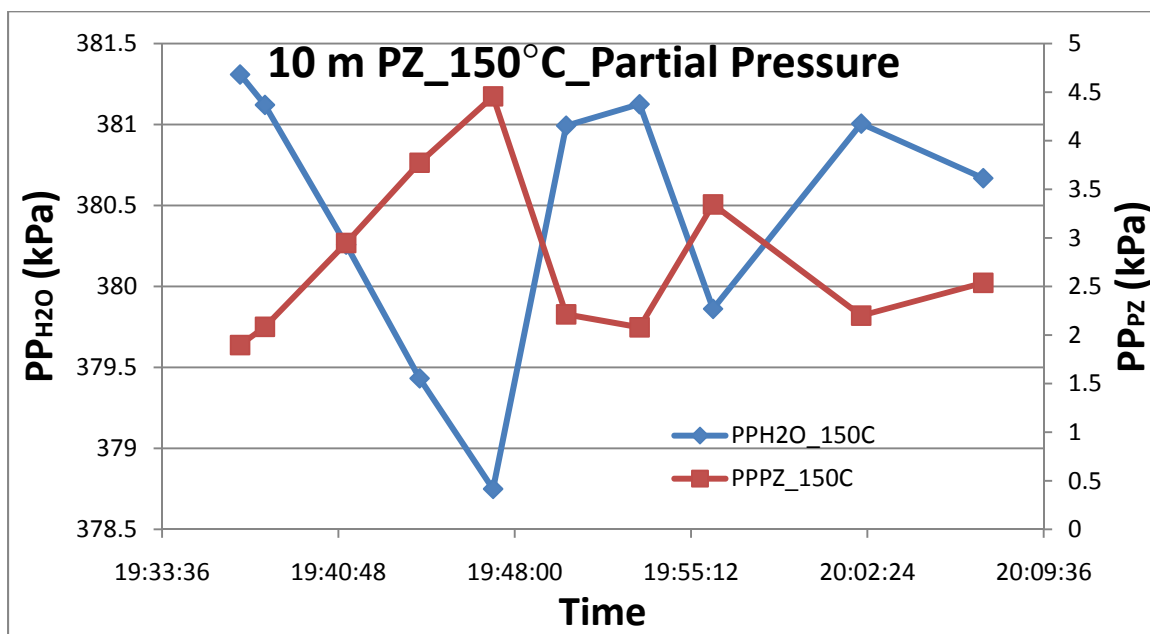
Figure 12: Partial Pressure of Water and PZ at 150 °C in 10 m PZ Experiment

In Figure 12 the water and PZ partial pressures fluctuate a lot so no data was usedfrom this graph. This may result from the high concentration of PZ in the vapor phase. Higher N_2 flow for dilution and a higher vapor sample flow rate should be applied in future when PZ concentration is high.

Table 1 gives a summary of the total pressure and partial pressure measurements in this period.

Table 1: Total Pressure and Partial Pressure Summary of Aqueous PZ

Date	Temperature(°C)	PZ(m)	Total Pressure (kPa)	P_{H2O} (kPa)	P_{PZ} (kPa)
20090922	140	8.7	325.81	324.03	1.770
	140	9.4	321.28	319.09	2.193
20090924	120	8.7	179.58	179.27	0.307
20090929	120	5.31	180.58	180.35	0.229
	140	5.62	324.93	323.65	1.284
	150	5.93	430.95	429.35	1.602
	92.2	5.93	77.67	N/A	N/A
20091001	120	10.37	160.49	159.73	0.758
	140	10.73	289.22	287.17	2.055
	150	11.12	383.21	N/A	N/A
	92.2	11.12	66.65	N/A	N/A

Conclusions and Recommendations

In this period a high temperature VLE experimental apparatus was built, tested, and modified. Experiments were conducted with water and 5, 8, 10 m PZ solutions at 120, 140, and 150 °C. 5 runs for 8 m PZ with about 0.4 CO_2 loading were conducted at 140 and 150 °C. At 120 to 150 °C, partial pressure of PZ is from 0.2 to 1.6 kPa for 5.5 m PZ; At 120 and 140 °C, PZ partial pressure is 0.7 and 1.8 kPa for 8.7 m aqueous PZ, and 0.8 to 2.1 for 10.5 m PZ.

Equilibrium could be well obtained in the 500 mL stainless steel autoclave. FTIR analyzed diluted vapor sample continuously; CO_2 concentration was relatively constant while H_2O and PZ concentration peaked from time to time. By heat tracing of the lid and the top surrounding of the autoclave, as well as the vapor sampling line, part of this issue was solved for aqueous PZ runs. It was found that the flow rate of the vapor sample should be kept higher than 80 mL/min at 1 atm to generate good data. Higher N_2 flow for dilution and a higher vapor sample flow rate should be applied when PZ concentration is high. 1 min was found to be the best sampling time for FTIR analysis. The low noise K-type thermocouple worked more consistently than the RTD thermometer when there is magnetic agitation inside.

Issues and Future Work

There are several problems unsolved for this high temperature VLE apparatus and these will be investigated in future. More experiments will be performed using this apparatus.

In vapor sampling, getting constant concentrations for PZ and water is still a problem. Heat tracing can solve part of it, but when the PZ concentration increases, there is a tendency for PZ to condense more easily. Entrainment also needs to be avoided by installing a mist eliminator.

Another problem is the liquid sampling. Samples collected during a run were not very consistent. Because the agitator shaft circulates bubbles into the liquid phase and does a good job in mixing, a certain time would be taken for liquid-vapor separation after agitation stops. However during this time, equilibrium may be disturbed due to the lack of mixing. The liquid sampling line should also be flushed after each 2 samples. In the future a baffle bar will be added into the equilibrium cell to accelerate bubble braking; a vacuum pump will be used to assist liquid sampling. This pump will also be used to vacuum the equilibrium cell before each run.

There may be temperature gradients inside the vessel, but it is difficult to determine whether this is the case, since there is only one measuring point inside the vessel.

More experiments will be performed with 1 to 10 m PZ at temperatures varying from 120 to 150 °C. PZ solution with CO_2 loading will also be tested and both vapor and liquid samples will be analyzed.

Activity of water, PZ, and CO_2 will be studied based on the experimental VLE data and compared with literature values. An Aspen Plus® PZ model will be used to generate VLE data as a comparison to the experimental results.

References

Autoclave Engineers®, Zipperclave® 500&1000 mL stirred reactor, http://www.autoclaveengineers.com/ae_pdfs/SR_500_1000_Zip.pdf

DIPPR, 1998-Provo, UT: BYU DIPPR, Thermophysical Properties Laboratory, 1998-Version 13.0.

Freeman SA et al. "Carbon dioxide capture with concentrated, aqueous piperazine." *GHGT-9*. Washington D.C. 2008.

Hilliard MD. *A Predictive Thermodynamic Model for an Aqueous Blend of Potassium Carbonate, Piperazine, and Monoethanolamine for Carbon Dioxide Capture from Flue Gas.* The University of Texas at Austin. Ph.D. Dissertation. 2008;1083.

Rochelle GT et al. "CO_2 Capture by Aqueous Absorption, Third Quarterly Progress Report 2008." Luminant Carbon Management Program. The University of Texas at Austin. 2008a.

Rochelle GT et al. "CO_2 Capture by Aqueous Absorption, Fourth Quarterly Progress Report 2008." Luminant Carbon Management Program. The University of Texas at Austin. 2008b.

Sexton AJ. *Amine Oxidation in CO_2 Capture Processes*. The University of Texas at Austin. Ph.D. Dissertation. 2008.

Amine Volatility for Binary Aqueous Amine-H₂O Systems

Progress Report for July 1– September 30, 2009

by Thu Nguyen

Supported by the Luminant Carbon Management Program

and the

Industrial Associates Program for CO$_2$ Capture by Aqueous Absorption

Department of Chemical Engineering

The University of Texas at Austin

October 1, 2009

Abstract

The volatility of aqueous amine-water systems is explored in this report. A number of amines were studied at varying concentrations, from very dilute to highly concentrated conditions, at temperatures from 40 ℃–70 ℃. While it is not currently possible to compare amine volatilities in general due to differences in the conditions studied in each case, it is relevant to observe volatility at the working concentration of each amine (~30–50 wt %) at 40 ℃. The amines studied are ranked as follows in order of increasing volatility: DGA® (diglycolamine – 16 m) ~1.5 Pa; PZ (piperazine – 8 m) < 17.1 Pa (~8–10 Pa); MEA (monoethanolamine – 7 m) ~10 Pa; AMP (2-amino-2-methyl-1-propanol – 5 m) ~14.2 Pa; EDA (ethylenediamine – 8 m) ~17.2 Pa. At a most basic level of scientific analysis, DGA® is much less volatile than EDA, the most volatile amine studied, due to the former being more polar overall (-OH group present) and therefore is more water-friendly with little to no tendency to leave the solution (volatilize). Amine volatility is a complex phenomenon dependent on several properties of the molecule, including its boiling point, molecular weight, and most certainly its polarity as determined by chemical group contribution and arrangement. In future studies, amine volatility will be explained in depth in the context of UNIQUAC (a group contribution theory) in an effort to understand and validate experimental observations.

Introduction

The volatility of amines in various amine-H$_2$O systems are studied for scientific understanding. The amine partial pressure is an indicator of its volatility – also to be analyzed in terms of its apparent activity coefficient. Amine volatility is to be explained in terms of chemical group contribution theory as presented by UNIQUAC. This report examines the following aqueous amine systems from 40 ℃–70 ℃ (typical operating temperature range of the absorber): MEA – 3.5 m, 7 m, 11 m, 23.8 m; PZ – 2 m, 5 m, 8 m, 10 m; AMP – 0.3 m, 1 m, 5 m, 12 m; EDA – 0.5 m, 8 m, 20.5 m; DGA® – 0.3 m, 5 m, 17 m. The concentration ranges were chosen to encompass conditions close to infinite dilution of the amine up to highly concentrated. Amine volatility measurements at unloaded condition will later be supplemented by measurements at loaded conditions to present a complete description of the CO$_2$ Capture scenario. Recall that amine

volatility at 40ºC and lean loading is of greatest interest as this is the existing condition at the top of the absorber where amine is either vented or is directed into a water wash system.

Experimental Apparatus

Amine Volatility Measurement

Amine volatility was measured in a stirred reactor coupled with a hot gas FTIR analyzer (Fourier Transform Infrared Spectroscopy, Temet Gasmet Dx-4000) as shown in Figure 1.
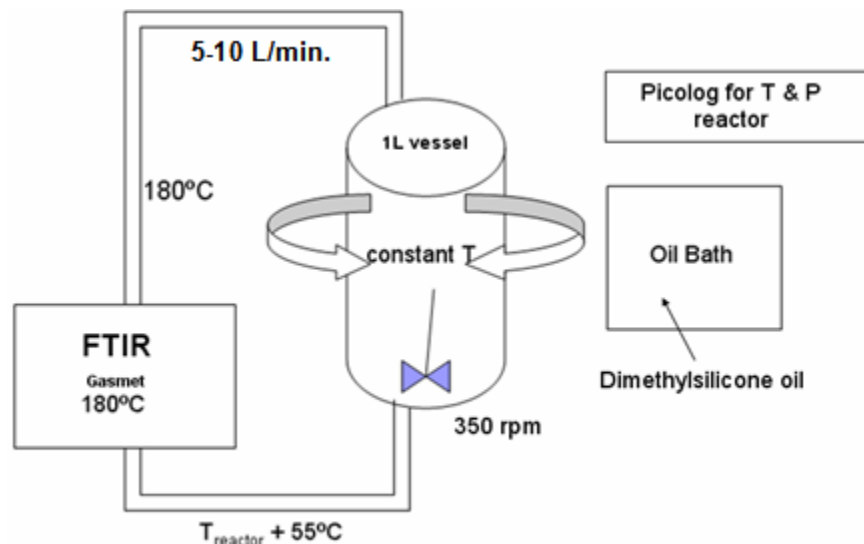

Figure 1: Amine Volatility Experimental Setup

The 1L glass reactor was agitated at 350 rpm. Temperature in the reactor was controlled by circulating dimethylsilicone oil. The reactor was insulated with thick aluminum insulation material. Vapor from the headspace of the reactor, primarily 5–10 L/min. nitrogen, was circulated by a heated sample pump to the FTIR through a heated Teflon line. Both the line and analyzer were maintained at 180 ºC to prevent possible condensation or adsorption of amine. The FTIR measured amine, CO_2, and water concentration in the gas. After the gas passed through the FTIR, it was returned to the reactor through a heated line maintained ~55 ºC hotter than the reactor. It was determined that the 55 ºC difference was sufficient to ensure that the return gas does not upset the solution that is in equilibrium with the gas inside the reactor, and to prevent potential heat loss at the bottom of the reactor.

Amine Concentration

The amine concentration was determined by acid titration (Hilliard, 2008) with an automatic Titrando series titrator with automatic equivalence point detection. A 300X diluted sample was titrated with 0.1 N H_2SO_4 to a pH of 2.4. The amount of acid needed to reach the equivalence point at a pH of 3.9 was used to calculate the total amine concentration.

Theory

Amine volatility is quantified by an apparent activity coefficient (γ_{amine}) as defined by the modified Raoult's law.

$$\gamma_{amine} = P_{amine} / [x_{amine} * P^{\circ}_{amine}]$$

(1)γ_{amine} is the apparent activity coefficient of the amine

P_{amine} is the partial pressure of the amine in the gas

x_{amine} is the liquid phase mole fraction of the amine

P°_{amine} is the vapor pressure of the amine at a given temperature

The reference value for γ_{amine} is 1 which is the case of a solution having ideal species interaction. Note that the activity coefficients presented in this paper are apparent values, instead of being actual values, as they are computed using x_{amine} that are not the true liquid phase mole fractions of free amine present in solution. The liquid composition of the amine in this case assumes total amine concentration in the presence of total CO_2 unspeciated.

Data

Table 1: Binary MEA-H$_2$O Volatility

MEA (m)	T (C)	P$_{MEA}$ (Pa)	γ_{MEA}
3.5	45.9	5.88	0.391
3.5	51.2	8.00	0.366
3.5	58.9	13.5	0.367
3.5	65.3	19.0	0.343
3.5	42.7	4.51	0.379
3.5	49.4	7.29	0.378
3.5	56.3	11.2	0.362
3.5	65.5	18.2	0.325
3.5	60.0	13.2	0.334
3.5	40.0	4.19	0.431
7.0	72.7	79.0	0.483
7.0	64.7	33.6	0.333
7.0	42.1	10.6	0.493
7.0	49.3	15.6	0.433
7.0	52.8	20.5	0.445
7.0	56.8	21.0	0.349
7.0	61.4	28.3	0.346
7.0	39.8	10.0	0.553
7.0	59.9	27.1	0.365
11.0	60.0	40.2	0.364
11.0	40.0	12.0	0.443
23.8	42.8	24.3	0.402
23.8	49.9	44.7	0.441

23.8	53.9	61.1	0.460
23.8	61.7	141	0.633

Table 2: Binary PZ-H$_2$O Volatility

PZ (m)	T (C)	P$_{PZ}$ (Pa)	γ_{PZ}
1.9	40	2.18	0.055
1.9	50	3.98	0.057
1.9	60	6.79	0.057
1.9	70	13.2	0.067
5.0	40	5.12	0.055
5.0	44.7	5.40	0.043
5.0	53.3	10.8	0.054
5.0	60	17.2	0.061
7.9	50	17.1	0.067
7.9	55	27.9	0.084
7.9	60	34.2	0.079
7.9	65	53.4	0.096
7.9	70	84.8	0.119
10.0	50	29.9	0.097
10.0	55	39.8	0.099
10.0	60	61.5	0.117
10.0	65	97.3	0.144
10.0	70	139.8	0.162

Table 3: Binary AMP-H$_2$O Volatility

AMP (m)	T (C)	P$_{AMP}$ (Pa)	γ_{AMP}
0.29	40	1.55	1.66
0.29	45.5	2.23	1.54
0.29	50.1	3.55	1.73
0.29	55	4.99	1.70
0.29	60	7.09	1.70
0.29	65	10.2	1.76
0.29	70	15.0	1.88
0.92	40	4.10	1.40
0.92	45	6.09	1.39
0.92	50	8.49	1.33

0.92	55	12.9	1.40
0.92	60	18.1	1.39
0.92	65	27.3	1.50
0.92	70	40.2	1.61
4.6	40	14.2	1.03
4.6	45	19.1	0.93
4.6	50	31.9	1.06
4.6	55	48.0	1.11
4.6	60	64.3	1.05
11.5	40	28.8	0.93
11.5	45	40.5	0.88
11.5	50	63.3	0.94
11.5	55	88.6	0.91
11.5	60	120	0.87
11.5	65	183	0.96
11.5	70	261	0.99

Table 4: Binary EDA-H_2O Volatility

EDA (m)	T (C)	P_{EDA} (Pa)	γ_{EDA}
0.48	40	0.560	0.016
0.48	45	0.869	0.020
0.48	50	1.26	0.022
0.48	55	1.87	0.025
0.48	60	2.74	0.029
0.48	65	5.90	0.050
7.8	40	17.2	0.035
7.8	45.5	26.1	0.040
7.8	50	35.2	0.043
7.8	55	51.5	0.049
7.8	60	69.4	0.051
7.8	65	112	0.066
7.8	70	157	0.074
20.6	35	225	0.277
20.6	40	282	0.262
20.6	45	380	0.270
20.6	50	509	0.280

20.6	55	687	0.294
20.6	60	909	0.306
20.6	65	1258	0.337
20.6	70	1720	0.368

Table 5: Binary DGA$^®$-H$_2$O Volatility

DGA$^®$ (m)	T (C)	P$_{DGA}$ (Pa)	γ_{DGA}
0.2	46.5	0.100	1.46
0.2	50	0.179	1.97
0.2	55	0.219	1.62
0.2	60	0.269	1.35
0.2	65	0.329	1.14
0.2	70	0.588	1.42
4.8	40	1.27	1.47
4.8	45	1.54	1.16
4.8	50	2.09	1.04
4.8	55	2.24	0.745
4.8	60	2.46	0.557
4.8	65	3.28	0.513
4.8	70	5.71	0.624
16.0	40	1.50	0.617
16.0	45	2.17	0.578
16.0	50	3.29	0.580
16.0	55	4.74	0.561
16.0	60	6.72	0.541
16.0	65	9.13	0.507
16.0	70	13.9	0.542

Results

Figure 2 shows the apparent activity coefficient for 3.5 m , 7.0 m, 11.0 m, and 23.8 m MEA.
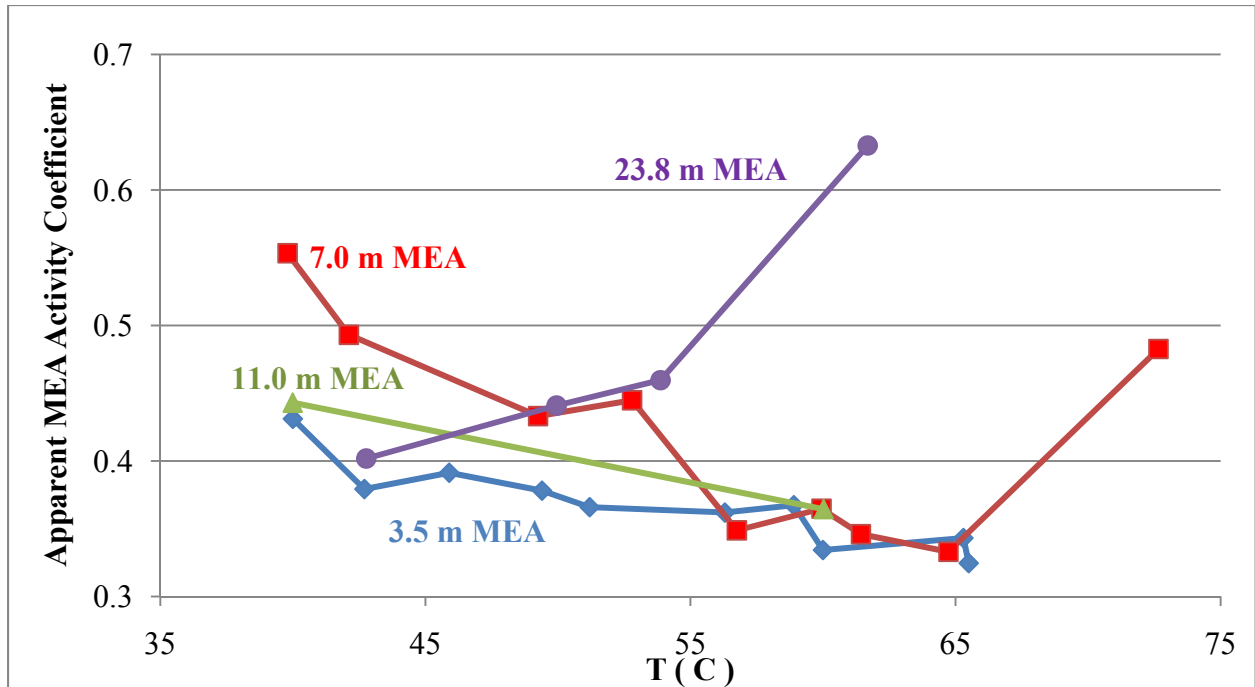
Figure 2: Apparent Activity Coefficient of 3.5 m, 7.0 m, 11.0 m, 23.8 m MEA

The vapor pressure of liquid MEA is given as (DIPPR):

$$P^o_{MEA} \text{ (Pa)} = \exp [92.6 + (-1.04 \times 10^4 / T) - (9.47 \ln T) + (1.9 \times 10^{-18} T^6)] \qquad (2)$$

The concentration of MEA in a given solution affects its volatility. For low concentrations, in this case 3.5 m and 7.0 m MEA, the volatility increases with higher amine concentration as 7.0 m MEA is more volatile than 3.5 m MEA. Practically speaking, at 40 ºC, the apparent activity coefficient of 7 m MEA (~0.55) is greater than that of 3.5 m MEA (~0.43). However, for more concentrated MEA solutions, 11.0 m and 23.8 m MEA, volatility is seen to decrease with higher amine concentration. 23.8 m MEA has a lower apparent activity coefficient than 11 m MEA at ~40 ºC. This is likely due to the possibility that MEA has a greater tendency to stay in solution (less volatile) when it is increasingly surrounded by more of its own kind, as opposed to being predominantly surrounded by water molecules in the case of dilute solutions which tend to drive volatility. A competing effect on volatility is temperature as exhibited by the directions of trends shown. Primarily speaking, temperature drives amine vapor pressure. For 3.5 m, 7.0 m, and 11.0 m MEA, the volatility of amine in these cases is not high enough to offset the rapid increase in vapor pressure with temperature; therefore, the apparent activity coefficient decreases with temperature. For a solution as concentrated as 23.8 m MEA, the volatility is great enough to keep pace with the rising vapor pressure of the liquid with temperature; thus the apparent activity coefficient in this case is seen to increase with T.

Figure 3 displays the apparent activity coefficient for 2 m, 5 m, 8 m, and 10 m PZ.
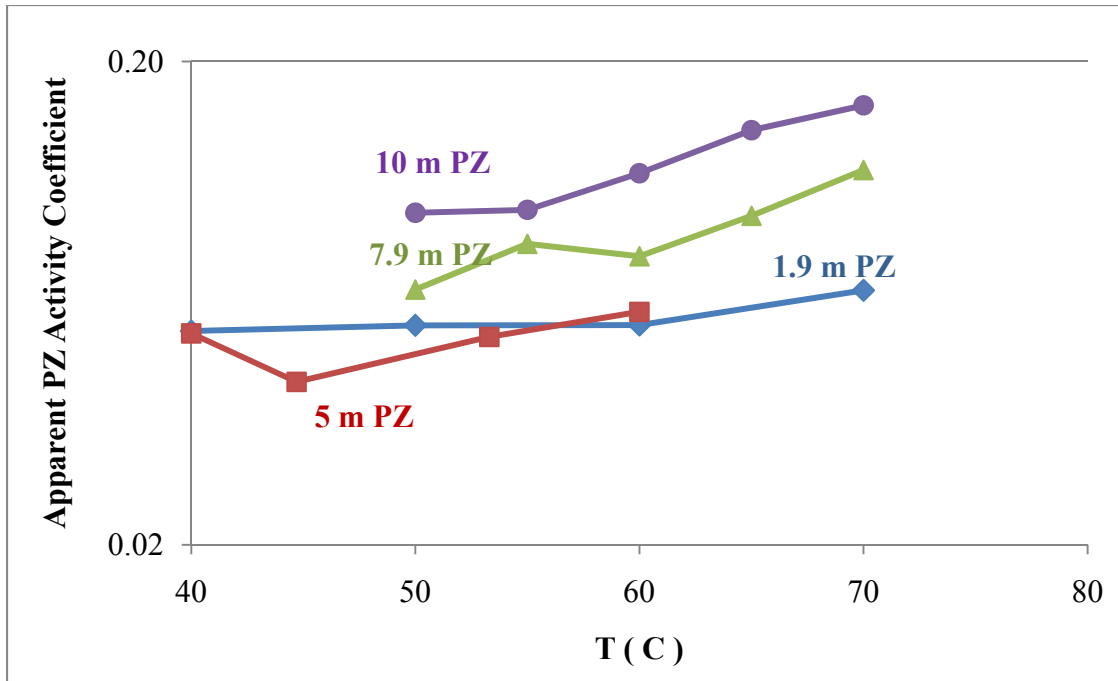
Figure 3: Apparent Activity Coefficient of 2 m, 5 m, 8 m, 10 m PZ

PZ vapor pressure is computed per the following (DIPPR):

$$P^o_{PZ} \text{ (Pa)} = \exp[70.5 - (7914.5/T) - (6.65\ln T) + (5.2 \times 10^{-18} T^6)] \tag{3}$$

The apparent activity coefficient increases with PZ concentration. With increasing PZ concentration, there is more free amine present in solution to volatilize, thereby increasing its apparent activity coefficient. Amine volatility also increases with temperature in this case. Finally, it appears that PZ is as volatile as MEA, if not less volatile at lower amine weight percentages.

Figure 4 shows volatility for 0.3 m, 1 m, 5 m, and 12 m AMP.
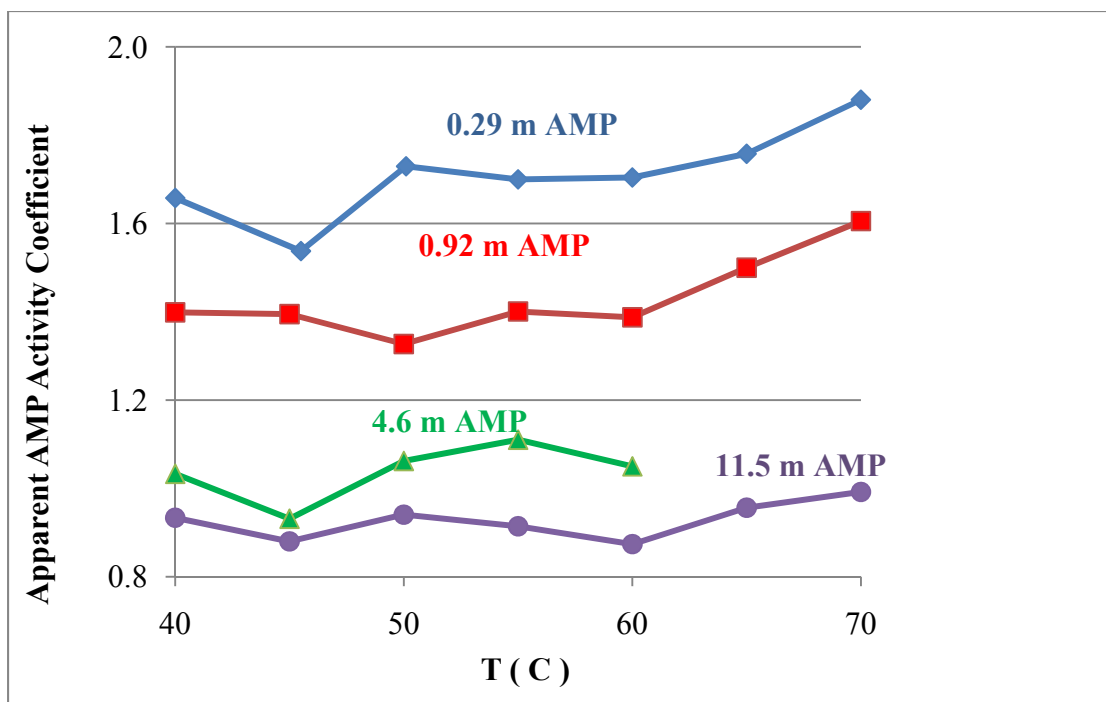
Figure 4: Apparent Activity Coefficient of 0.3 m, 1.0 m, 5.0 m, 12 m AMP

The vapor pressure of AMP is provided as follows (Pappa et al., 2006):

$$P^o_{AMP} (kPa) = \exp[\ 15.155 - (3472.6 / (T - 107.32))\ ] \tag{4}$$

AMP volatility decreases as the amine concentration increases. This is likely due to the possibility that AMP has a greater tendency to stay in solution as it is increasingly surrounded by its own kind in more concentrated solutions. Also AMP does not show a very strong temperature behavior as its volatility remains rather constant over the temperature range noted. This phenomenon suggests that AMP heat of solution is rather independent of temperature. Additionally, AMP in water is seen to be much more volatile than either aqueous MEA or PZ as indicated by the high magnitude of the former's apparent activity coefficient. Unlike PZ, AMP volatility is not a strong function of its concentration as its apparent activity does not vary much given the wide range of concentrations shown.

Figure 5 displays the apparent activity coefficient of 0.5 m, 8.0 m, and 20 m EDA.
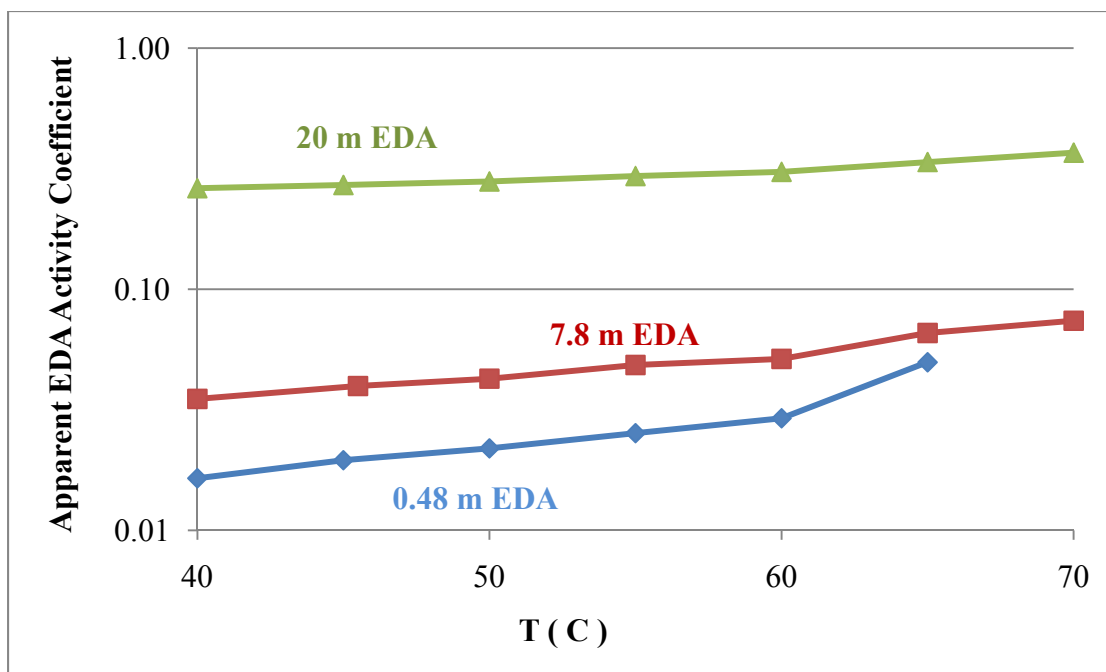
Figure 5: Apparent Activity Coefficient of 0.5 m, 8 m, 20 m EDA

EDA vapor pressure is given by the following (DIPPR):

$$P^o_{EDA} (Pa) = \exp[73.5 - (7572.7 / T) - (7.14 \ln T) + (1.21 \times 10^{-17} T^6)] \qquad (5)$$

EDA volatility is a strong function of its concentration, unlike AMP. Its apparent activity coefficient increases by at least an order of magnitude going from very dilute to highly concentrated solution, whereas the same is not observed for AMP over the same range of concentrations. However, like AMP, EDA volatility does not appear to be a very strong function of temperature as it remains relatively constant at each given concentration over the temperature range studied. This suggests that EDA heat of solution is rather independent of temperature.

Figure 6 displays volatility in 0.2 m, 4.8 m, 16 m DGA®.
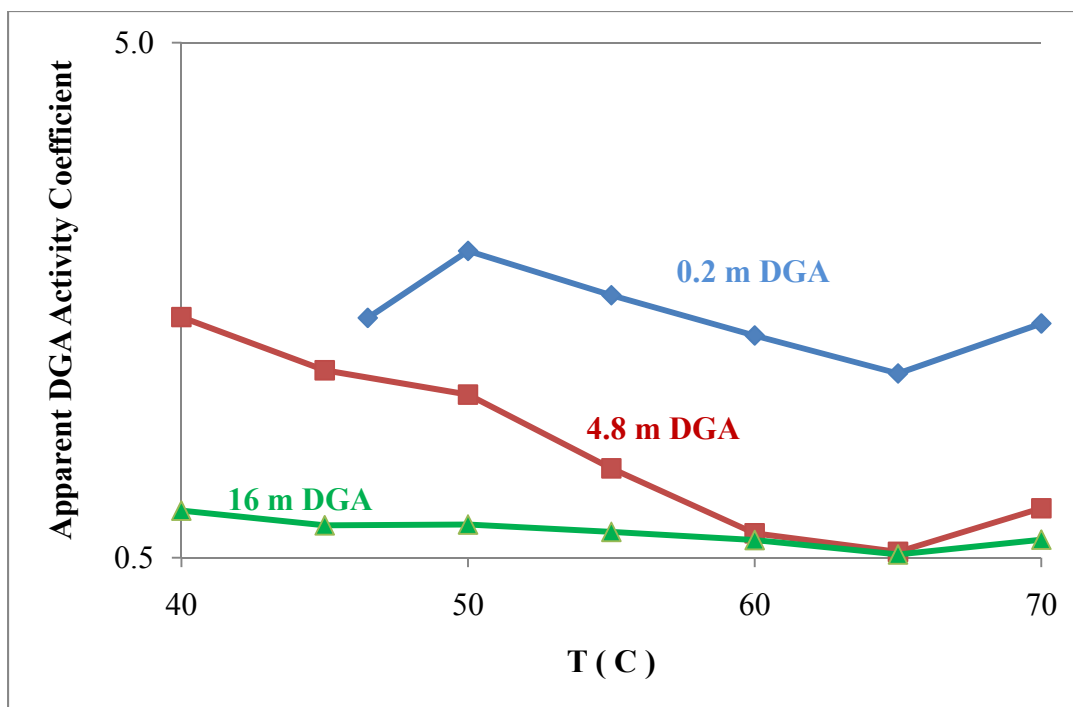
Figure 6: Apparent Activity Coefficient of 0.2 m, 5 m, 16 m DGA®

The vapor pressure of DGA® is determined as follows (DIPPR):

$$P^o_{DGA} \text{ (Pa)} = \exp[107.3 - 12{,}191/T - 11.5 \ln T + 4.15 \times 10^{-18} T^6] \tag{6}$$

The apparent activity coefficient of DGA® does not appear to be a strong function of amine concentration. Indeed, the apparent activity changes by less than an order of magnitude going from condition close to infinite dilution (0.2 m DGA®) to highly concentrated (16 m DGA®). Also, DGA® appears to be more volatile in dilute solutions than in more concentrated solutions. This is perhaps due to the possibility that DGA® tends to stay in solution (i.e. less volatile) as it is increasingly surrounded by more of its own molecules as opposed to water. Finally, DGA® volatility also appears to be a strong function of temperature, at least for low to medium concentration solutions. Note that the apparent activity coefficient of DGA® decreases steadily with temperature for 0.2 m and 4.8 m DGA® as its partial pressure is not able to keep pace with rising vapor pressure. For 16 m DGA®, however, volatility is rather constant with temperature as there is just so much free amine present to volatilize in such a way that it evens out the steadily increasing vapor pressure. Please refer Eq 1 in the Theory section for theoretical context.

Conclusions

There is no standardized basis at which one can rank the volatilities of the amines studied. The amine volatilities are all measured at different concentrations, making it difficult to compare them on an equivalent basis. With each amine though, it is possible to select a working concentration and temperature to minimize volatility; however, the operating conditions chosen must also be conducive to high capacity, high reaction rates, and high CO_2 heat of absorption.

Also, it must be noted that volatility is only a concern at the top of the absorber (40 ºC and nominal lean loading) as it is here that there is a risk of venting fugitive amine into the atmosphere if a water wash tower is not designed adequately.

Although it is not yet possible to compare these amines on exactly the same basis due to varying conditions studied, it is useful to examine their volatilities at nominal working concentrations at 40 ºC. Table 6 summarizes the volatilities of the amines for the condition described above.

Table 6: Unloaded Amine Volatility at Working Concentrations and 40 ºC

Amine	Concentration (m)	$P_{amine\ 40ºC}$ (Pa)
DGA®	16	1.5
PZ	8	< 17.1 (~8-10)
MEA	7	10
AMP	5	14.2
EDA	8	17.2

The amines in the table are listed in order of increasing volatility. The working concentrations shown are typically between 30%–45% wt % amine. DGA®, however, can be prepared at 16 m (~62 wt %) without experiencing viscosity issues. Interestingly enough, at such a high concentration, DGA® still shows minimal volatility of only ~1.5 Pa. The rest of the amines studied, though ranked, have roughly the same volatilities on the same order of magnitude. It is believed that the volatility of an amine is dependent upon several competing factors, including its molecular weight, boiling point, and degree of polarity which is determined by its chemical structure and placement of groups. This report does not attempt to provide an in-depth analysis of the chemical basis for amine volatility. However, at a cursory level, it is sufficiently clear that DGA® (the least volatile amine) is more polar than EDA (the most volatile) due to the presence of an –OH group attached at one end of the molecule. The alcohol group makes the DGA® molecule more polar relative to its amine counterpart, and essentially this enables DGA® to be more water-friendly with little to no tendency to leave the solution (or to be volatile). UNIQUAC, a group contribution theory, will be utilized in the future to explain and validate the experimental amine volatilities measured.

Future Work

Continuing effort will be made toward screening new amines for their volatilities. Some amines to be studied in the near future include: 1-methyl piperazine, diaminopropane, 2-piperidine ethanol (2-PE), hydroxyethyl piperazine (HEP), and an equimolal blend of 1-methyl piperazine and piperazine. Initially, only binary aqueous solutions of these amines will be studied to satisfy a scientific interest in understanding amine-water volatility. Effort will be made to explain and justify these empirical measurements per chemical group contribution theory as outlined by UNIQUAC. There is also a plan to measure the volatility of these amines at loaded conditions

for practical applications. Ultimately, the empirical measurements will be incorporated into Aspen Plus® for amine system modeling using e-NRTL. The main modeling focus, however, will be on constructing a robust thermodynamic framework for MDEA/PZ blend.

References

DIPPR 801: Thermophysical Property Database for Pure Chemical Compounds.

Hilliard MD. *A Predictive Thermodynamic Model for an Aqueous Blend of Potassium Carbonate, Piperazine, and Monoethanolamine for Carbon Dioxide Capture from Flue Gas.* The University of Texas at Austin. Ph.D. Dissertation., 2008.

Pappa G, Anastasi C, Voutsas, E. "Measurement and thermodynamic modeling of the phase equilibrium of aqueous 2-amino-2-methyl-1-propanol solutions." *Fluid Phase Equilibria.* 2006;243:193–197.

Chapter 5: Modeling

5.1 SPREADSHEET MODELING

As Section 2.2.3 on film theory shows, the liquid film mass transfer coefficient, k_g',
results from both reaction and diffusion resistances. These resistances in the liquid film can be
separated using a series resistance.

$$\frac{1}{k_g^{'}} = \frac{1}{k_g^{"}} + \frac{1}{k_{l,prod}^{o}} \left(\frac{\Delta P_{CO2}^{*}}{\Delta [CO_2]_T} \right)$$

(5.1)

In Equation 5.1, the first term refers to the reaction resistance which is characterized by
the pseudo first order condition. The second term incorporates the slope of the equilibrium line
and the physical mass transfer coefficient of the reactants and products.

An analytical expression to calculate k_g' at highly concentrated, highly loaded conditions
has previously remained elusive and thus required experimentation to determine CO$_2$ mass
transfer rates. This approach attempts to identify and re-evaluate the assumptions in the typical
treatment of calculating k_g'.

The reaction portion of Equation 5.1 requires the reaction rate of CO_2. This can be defined generically by Equation 5.2. In Equation 5.2, the order of the reaction with respect to the amine is variable. The value of "x" will be determined by evaluating experimental data.

$$r_{CO2} = -k\gamma_{Am}^x [Am]^x \gamma_{CO2} ([CO_2] - [CO_2]_e)$$
(5.2)

Solving the material balance and using the proper boundary conditions with the pseudo first order assumption results in Equation 5.3, which is more complex than the traditional expression (Equation 2.30).

$$k_g^" = \frac{\sqrt{k\gamma_{Am}^x [Am]^x D_{CO2}}}{\gamma_{CO2}^{0.5} H_{CO2,H2O}}$$
(5.3)

The more complex expression requires an understanding of the rate constant, the activity coefficients of both the amine and CO_2, the order of the amine and the diffusion coefficient of CO_2. Equation 5.3 can only represent the reaction resistance. Experimental conditions with significant diffusion resistances also require an accurate representation of the slope of the equilibrium line and the mass transfer coefficient of the products and reactants. All of the varying parameters for both monoethanolamine and piperazine systems are explored in the following sections. Equation 5.4 combines Equation 5.1 and 5.3 to give the full expression for calculating k_g'.

$$\frac{1}{k_g'} = \frac{\gamma_{CO2}^{0.5} H_{CO2,H2O}}{\sqrt{k\gamma_{Am}^x [Am]^x D_{CO2}}} + \frac{1}{k_{l,prod}^o} \left(\frac{\Delta P_{co2}^*}{\Delta [CO_2]_T} \right)$$
(5.4)

5.1.1 Monoethanolamine Systems

5.1.1.1 Activity Coefficients

The rate expression will use the activities of the reactants, not the concentrations. It cannot be assumed that activity coefficients are near 1.0 in highly loaded, highly concentrated MEA solutions. These solutions are highly ionic and should be treated so.

MEA activity coefficients can be obtained from amine volatility experiments. CO_2 activity coefficients can be obtained from Henry's solubility data.

5.1.1.1.1 Monoethanolamine Activity Coefficient

Hilliard (2008) provides data for volatility of 3.5, 7, and 11 m MEA. These experiments coincide with the CO_2 partial pressure experiments Hilliard conducted in an equilibrium cell. The FTIR analyzer he used simultaneously measured gas phase concentrations of multiple components.

The MEA volatility data were treated by the modified Raoult's Law in Equation 5.5. Reported values of 164 and 666 Pa were used for the equilibrium partial pressure of pure MEA at 40 and 60 °C (DIPPR, 1979).

$$y_{MEA}P = P_{MEA} = \gamma_{MEA}x_{MEA}P_{MEA}^*$$
(5.5)

Equation 5.5 requires the mole fraction of MEA. The mole fraction of MEA is easy to determine accurately below 0.4 CO_2 loading by assuming each mole of CO_2 reacts with 2 moles of MEA. Above a 0.45 mol_{CO2}/mol_{alk}, bicarbonate concentration can become significant while free MEA concentration becomes very small. At these high CO_2 loadings it is very difficult to accurately determine the free MEA concentration. Due to this uncertainty, no data from Hilliard (2008) above 0.45 CO_2 loading were used in the determination of MEA activity coefficients. Figure 5.1 shows the calculated MEA activity coefficients using the modified Raoult's law.
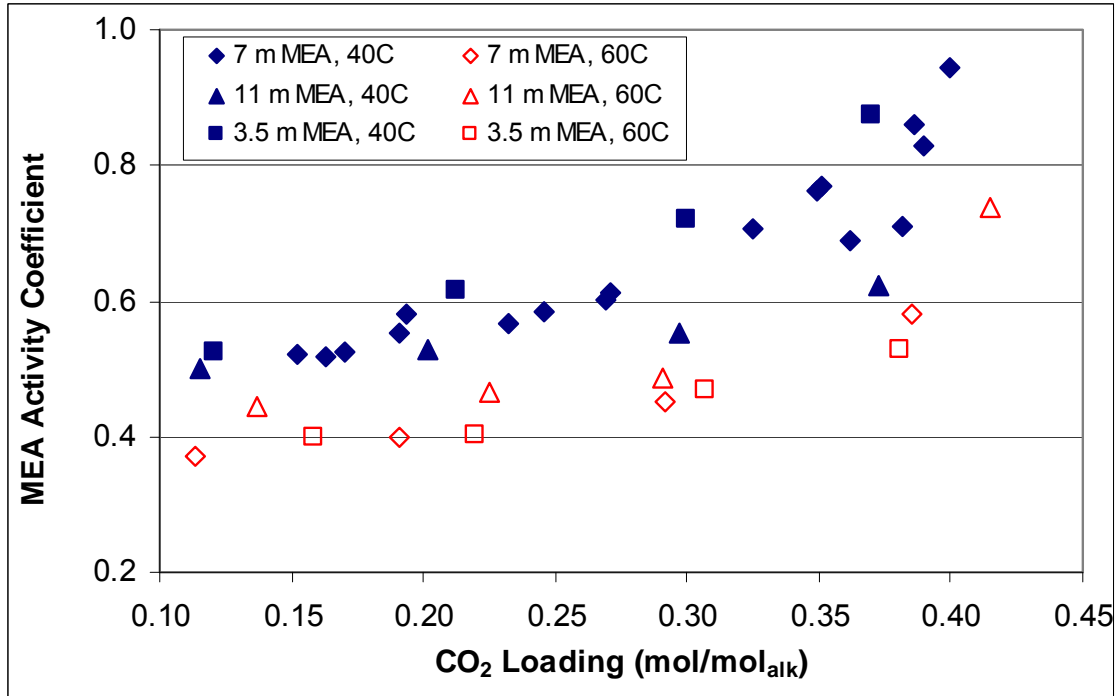
Figure 5.1: Calculated MEA activity coefficients for 3.5, 7, and 11 m MEA at 40 and 60 ˚C (Hilliard, 2008).

The Hilliard data show an increasing MEA activity coefficient with increasing CO_2 loading. The MEA activity coefficient is also a function of temperature, with higher temperatures having lower activity coefficients. Amine concentration does not seem to be a major factor in the determination of the activity coefficient. The 3.5, 7, and 11 m MEA data sets each tend to mostly overlap.

The data in Figure 5.1 were regressed to produce an expression for MEA activity coefficient. The expression in Equation 5.6 is plotted as lines in Figure 5.2 to show regressed values at 40, 60, 80, and 100 ˚C. Equation 5.6 uses CO_2 loading in terms of mol/mol$_{alk}$ and temperature in Kelvin.

$$\ln \gamma_{MEA} = -5.71 + 1.74(CO_2 Loading) + \frac{1503}{T} \qquad (5.6)$$
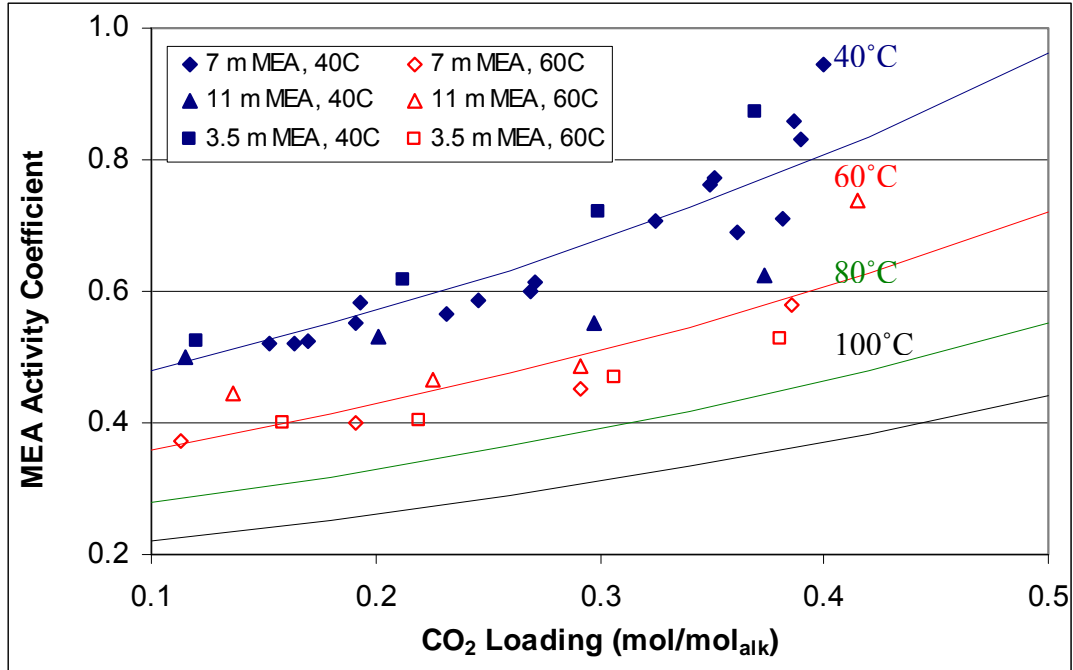
Figure 5.2: **Calculated MEA activity coefficients for 3.5, 7, and 11 m MEA at 40 and 60 ˙C (Hilliard, 2008) with regressed lines at 40, 60, 80, and 100 ˙C.**

5.1.1.1.2 Carbon Dioxide Activity Coefficient

The activity of CO_2 in loaded MEA solutions can be obtained the physical solubility of N_2O. Unfortunately, very few N_2O solubility data have been reported in concentrated, CO_2 loaded MEA systems. Browning and Weiland (1994) present 12 N_2O solubility data points in 10, 20, and 30 wt % MEA solutions up to 0.4 CO_2 loading at 25 ˙C. No other N_2O solubility data varying amine concentration and CO_2 loading are known. The N_2O solubility data were regressed into Equation 5.7. Equation 5.7 includes the MEA concentration in wt %.

$$\ln H_{N2O,25C} = \begin{pmatrix} 8.3194 + 4.52 \cdot 10^{-3}(MEA) - 4.78 \cdot 10^{-2}(CO_2 Ldg) \\ + 4.56 \cdot 10^{-2}(MEA)(CO_2 Ldg) \end{pmatrix} \tag{5.7}$$

Figure 4.14 shows the N_2O solubility data points from Browning as well as the regressed curves for 10, 20, and 30 wt % MEA.
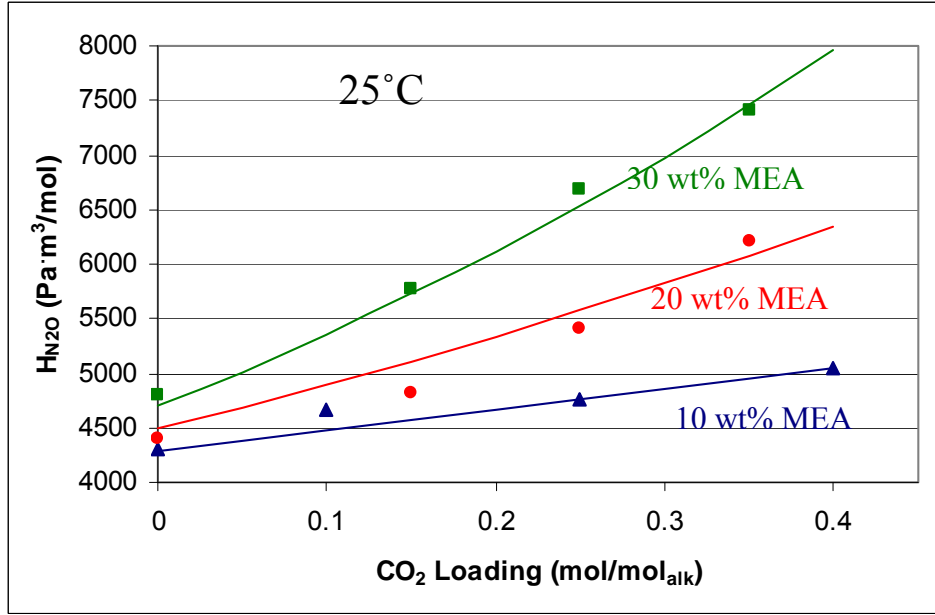
Figure 5.3: N$_2$O solubility data (Browning and Weiland, 1994) and model (lines) in 10, 20, and 30 wt % MEA solutions at 25 ˚C.

Figure 5.3 shows that Equation 5.7 does a very good job of predicting the N$_2$O solubility as a function of amine concentration and CO$_2$ loading. Figure 5.3 also illustrates how drastically the N$_2$O solubility decreases with increasing loading and amine concentration. It is imperative that both the amine concentration and CO$_2$ loading are considered in the estimation of the Henry's constant. Equation 5.7 allows for the calculation of the solubility of CO$_2$ in MEA solutions via the N$_2$O analogy, but only at 25 ˚C. Laddha (1981) showed that the ratio of N$_2$O and CO$_2$ solubilities remained constant for various organic solutions and that the N$_2$O analogy can be applied to estimate the solubility of CO$_2$ in aqueous alkanolamine solutions. It is not possible to directly measure CO$_2$ solubility in these amine systems since CO$_2$ will react with the amine.

$$\left(\frac{H_{CO2}}{H_{N2O}} \right)_{so\ln} = \left(\frac{H_{CO2}}{H_{N2O}} \right)_{H2O} \tag{5.8}$$

The CO$_2$ and N$_2$O solubility data in water as a function of temperature have been compiled and regressed (Versteeg and Van Swaaij, 1988).

$$H_{CO2,H2O} = 2.82 \cdot 10^6 \exp(-2044/T) \ Pa \cdot m^3 mol^{-1} \tag{5.9}$$

$$H_{N2O,H2O} = 8.55 \cdot 10^6 \exp(-2284/T) \ \ Pa \cdot m^3 mol^{-1} \qquad (5.10)$$

The traditional implementation of the N_2O analogy assumes that N_2O and CO_2 solubility in concentrated, loaded amines has the same temperature dependence as N_2O and CO_2 in water. Fortunately this assumption is no longer required for MEA solutions. Hartono (2009) recently published N_2O solubility data in loaded 30 wt % (7 m) MEA solutions. Hartono measured N_2O solubility from 25–87 ˚C for 0, 0.2, 0.4, and 0.5 CO_2 loading solutions. Figure 5.4 illustrates the N_2O solubility results for each of the 4 CO_2 loadings.
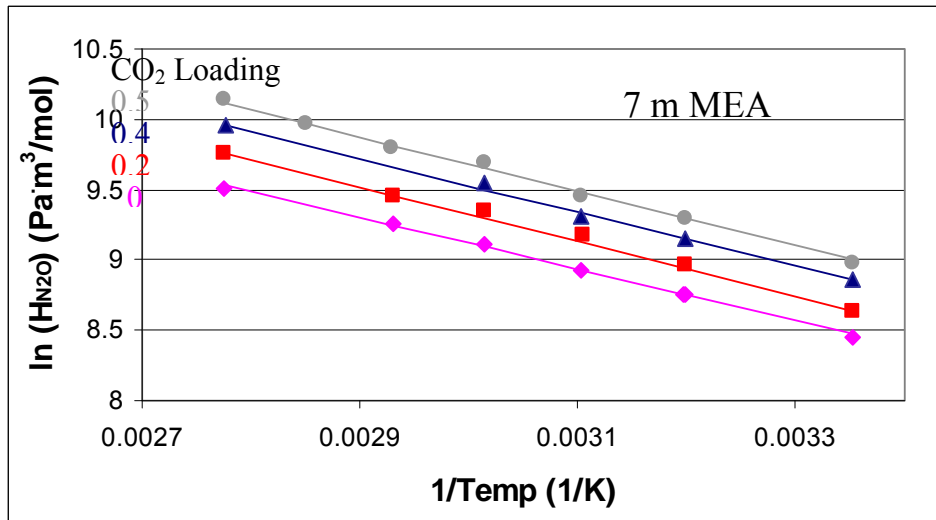
Figure 5.4: N_2O solubility data (points) and trend lines for 0, 0.2, 0.4, and 0.5 CO_2 loaded 7 m MEA solutions (Hartono, 2009)

The natural log of the N_2O solubility plotted against inverse temperature yields straight lines for each of the 4 CO_2 loadings. The slope of the lines corresponds to the temperature behavior of N_2O solubility in 7 m MEA. The slopes of the four lines are approximately equal with an average value of -1905/T. The N_2O solubility temperature dependence in loaded MEA solutions can be added to Equation 5.7 which is valid only at 25 ˚C. Equation 5.11 should be valid from 25 to at least 87 ˚C, the temperature range of the regressed data.

$$H_{N2O} = \exp\left[\left(\begin{array}{l} 8.3194 + 4.52 \cdot 10^{-3}(MEA) - 4.78 \cdot 10^{-2}(CO_2 Ldg) \\ + 4.56 \cdot 10^{-2}(MEA)(CO_2 Ldg) \end{array}\right) - 1905\left(\frac{1}{T} - \frac{1}{298.15}\right)\right] \quad (5.11)$$

Similar to the N_2O solubility from Browning (1994), Hartono shows the N_2O solubility decreasing with increasing CO_2 loading. Unfortunately, the data do not agree completely. Both Hartono and Browning measure N_2O solubility at 25 °C for 7 m MEA. Figure 5.5 shows the disagreement in the two data sets.
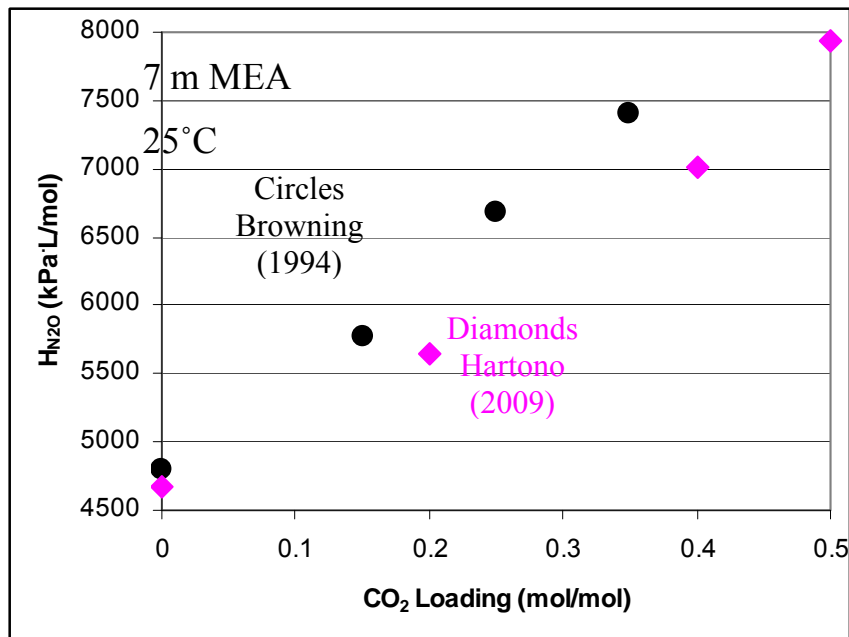
Figure 5.5: N_2O solubility in 7 m MEA at 25 °C (Browning and Weiland, 1994; Hartono, 2009)

Since these are the only two data sets for N_2O solubility in loaded MEA solutions, it is not possible to tell which data set is erroneous. In this work, the Browning (1994) data set has been used to quantify the effects of CO_2 loading and MEA concentration on N_2O solubility. The Hartono (2009) data set has been used to quantify the effect of temperature on N_2O solubility.

Using the N_2O analogy, the solubility of CO_2 in loaded MEA solutions can be determined using Equation 5.11 along with the solubility of CO_2 and N_2O in water at the experimental temperature. The calculation of the Henry's constant of CO_2 allows for the determination of the activity coefficient of CO_2 via Equation 5.12. The activity coefficient of CO_2 is assumed to be equivalent to the activity coefficient of N_2O due to the nature of the analogy.

$$\gamma_{N2O} = \frac{H_{N2O}}{H_{N20,H2O}} = \frac{H_{CO2,}}{H_{CO2,H2O}} = \gamma_{CO2}$$

(5.12)

H_{CO2} gives the effective solubility of CO_2 in the solution. $H_{CO2,H2O}$ is the true thermodynamic Henry's constant which refers to the solubility of CO_2 in pure water. The activity coefficient of CO_2 varies between 1.3 and 3.2 for 7–13 m MEA wetted wall column experiments at 40 to 100 °C.

5.1.1.2 Diffusion Coefficient of CO_2

Work by Versteeg and Van Swaaij (1988) has shown that the diffusion of N_2O and CO_2 in aqueous amines generally follows the viscosity dependence in Equation 5.13.

$$\left(D_{N2O}\eta^{0.8}\right)_{so\ln} = CONSTANT = \left(D_{N2O}\eta^{0.8}\right)_{Water}$$

(5.13)

The N_2O and CO_2 diffusivity relationship in Equation 5.13 was confirmed with MDEA solutions but resulted in less satisfactory results for AMP (Tomcej and Otto, 1989; Xu, Otto et al., 1991). Diaphragm cell experiments in loaded MEA and PZ solutions yield a viscosity dependence of 0.72 compared to the 0.8 obtained by Versteeg and Van Swaaij (1988) for N_2O (Figure 4.1). Although the 0.72 dependence obtained from the diaphragm cell experiments does not necessarily represent CO_2 diffusion, or diffusion of any other specific species, the 0.72 dependence was used for calculation of the diffusion coefficient of CO_2.

$$\left(D_{CO2}\right)_{so\ln} = \frac{\left(D_{CO2}\eta^{0.72}\right)_{Water}}{\left(\eta^{0.72}\right)_{so\ln}}$$

(5.14)

The diffusion coefficient of CO_2 in water was calculated via Versteeg (1988).

$$D_{CO_2} = 2.35 \cdot 10^{-6} \exp\left(-2119/T\right) \quad m^2 \cdot s^{-1}$$

(5.15)

The viscosity of water at the wetted wall column experimental temperatures was obtained from tabulated data by Watson (1986). MEA solution viscosity values were obtained from Weiland (1998).

$$\eta = \eta_{H2O} \exp\left(\frac{[(a\Omega + b)T + (c\Omega + d)] \cdot [\alpha(e\Omega + fT + g) + 1]\Omega}{T^2}\right)$$

(5.16)

Table 5.1:   Parameters for MEA viscosity (Weiland, Dingman et al., 1998)

a	b	c	d	e	f	g
0	0	21.186	2373	0.01015	0.0093	-2.2589

5.1.1.3 Free MEA Concentration

The free MEA concentration in molarity, [MEA], was determined using the fraction of the free amine in the Hilliard (2008) model at each wetted wall column condition. The Hilliard model is a sequential regression thermodynamic model capable of handling systems containing H_2O, CO_2, MEA, PZ, and K^+. Required density data was obtained from the Weiland (1998) density correlation for MEA solutions.

$$\rho = \frac{x_{Am}M_{Am} + x_{H_2O}M_{H_2O} + x_{CO_2}M_{CO_2}}{V} \tag{5.17}$$

$$V = x_{Am}V_{Am} + x_{H_2O}V_{H_2O} + x_{CO_2}V_{CO_2} + x_{Am}x_{H_2O}V^* + x_{Am}x_{CO_2}V^{**} \tag{5.18}$$

$$V_{Am} = \frac{M_{Am}}{aT^2 + bT + c} \tag{5.19}$$

$$V^{**} = d + e \cdot x_{Am} \tag{5.20}$$

Table 5.2:   Parameters for MEA density (Weiland, Dingman et al., 1998)

a	b	c	d	e	M_{Am}	V_{CO2}	V^*
-5.35162E-07	-4.51417E-04	1.19451	0	0	61.09	0.04747	-1.8218

5.1.1.4 Monoethanolamine Order

With accurate estimations for the activity coefficients of MEA and CO_2, the MEA concentration dependence on k_g' can be examined. It was found that the rate data show a 2nd order dependence on the MEA concentration. This 2nd order dependence can be satisfied from either the zwitterion or termolecular mechanism, although the termolecular mechanism is more likely for MEA. The termolecular mechanism allows for the following base catalysis reaction expression.

$$r_{CO2} = -\left(k_{MEA}[MEA] + k_{H2O}[H_2O]\right) \cdot [MEA] \cdot [CO_2] \tag{5.21}$$

For the 2nd order dependence to be observed $k_{MEA}[MEA]$ must be much greater than $k_{H2O}[H_2O]$. Crooks and Donnellan (1989) report k_{MEA} and k_{H2O} values based on 0.02–0.06 M MEA rate data. They report k_{MEA} values about 2200 times larger than k_{H2O}. Bronsted theory which relates base pKa's to rate constants would also predict a k_{MEA} value orders of magnitude larger than k_{H2O}. If k_{MEA} is 2200 times larger than k_{H2O}, more than 99% of the amine in 7 m MEA would have to be reacted before the water catalysis significance approached the MEA catalysis significance. In this analysis with high MEA concentrations, water catalysis has been neglected.

Density function theory calculations have also shown that water catalysis of the zwitterion species is thermodynamically implausible due to an increase of energy in the water catalyzed products (Billet, Schultes et al., 1999). MEA catalyzed products were shown to have a favorable decrease in energy compared to the zwitterion species.

In order for the 2nd order amine dependence to match the zwitterion mechanism, k_r must be much greater than $\sum k_b[B]$ in Equation 5.22 yielding Equation 5.23. This is generally not accepted as true for MEA (Danckwerts, 1979). However, in the previous treatment of literature data leading to this conclusion, activity coefficients and the Henry's constant of CO_2 were not considered rigorously. At least in these highly concentrated, highly loaded MEA systems, these parameters are very important.

$$r_{CO2} = -\frac{[Am][CO_2]}{\dfrac{1}{k_f} + \dfrac{k_r}{k_f \sum k_b[B]}} \qquad (5.22)$$

$$r_{CO2} = -\frac{k_f}{k_r}[MEA][CO_2]\sum k_b[B] \qquad (5.23)$$

This section has been written with respect to concentration for simplicity. However, the model is activity-based so activity coefficients can be input into these equations.

The majority of the literature data on MEA rates report kinetics with a first order MEA dependence. These data are generally unloaded and at dilute MEA concentrations using concentration based kinetics. Concentrated MEA rate experiments evaluated using concentration based kinetics have shown a greater than 1.0 dependence on the MEA concentration (Aboudheir, Tontiwachwuthikul et al., 2003). Therefore, it is not unrealistic to observe 2nd order MEA kinetics for highly loaded, concentrated MEA using activity-based kinetics.

5.1.1.5 *Liquid Phase Mass Transfer Coefficient of Reactants and Products,* $k^0_{l,prod}$

The liquid phase mass transfer coefficient of the reactants and products, $k^0_{l,prod}$, was calculated as shown in Section 3.2.2.2. Since the reactants and products are limiting rather than CO_2, the diffusion coefficient of the reactants and products must be incorporated.

$$k^o_{l,prod} = \left(\frac{3^{1/3}2^{1/2}}{\pi^{1/2}} \right) \left(\frac{Q^{1/3}h^{1/2}W^{2/3}}{A} \right) \left(\frac{g\rho}{\mu} \right)^{1/6} D^{1/2}_{prod} \qquad (5.24)$$

The diffusion coefficients of the products were obtained by utilizing the diaphragm cell diffusion experiments. Equation 5.25 was obtained from a curve fit of Figure 4.1. The diffusion coefficient is represented in m^2/s and viscosity is in cP.

$$D_{prod} = 8.2 \cdot 10^{-10} \mu^{-0.72} \qquad (5.25)$$

Viscosity and density parameters required for Equation 5.26 were once again obtained by the Weiland (1988) correlations for MEA.

5.1.1.6 *Slope of the Equilibrium Line*

The slope of the equilibrium line in Equation 5.1 results from converting a concentration-based mass transfer coefficient to a partial pressure basis. The slope can be difficult to accurately determine due to the sensitivity at high loading or temperatures. Recall partial pressure curves are plotted on a log-based y-axis. This produces very high values for the slope. In cases where diffusion limits CO_2 mass transfer, a poor estimation of the slope of the equilibrium can drastically affect the expected mass transfer.

The equilibrium partial pressure can be uniformly predicted from an empirical expression developed by Xu (Rochelle, Sexton et al., 2009) using literature data. The empirical relationship in Equation 5.26 is valid for MEA solutions between 40 and 160 ˚C. Equation 5.26 defines the partial pressure in Pascals with temperature in Kelvin.

$$\ln P_{CO2} = 44.2 + (-116,000 J/mol) \cdot \frac{1}{RT} - 29.7\alpha + 11,600\frac{\alpha}{T} + 17.3\alpha^2 \quad (5.26)$$

Figure 5.6 shows the fit to previously referenced CO_2 partial pressure data in Figure 4.2.
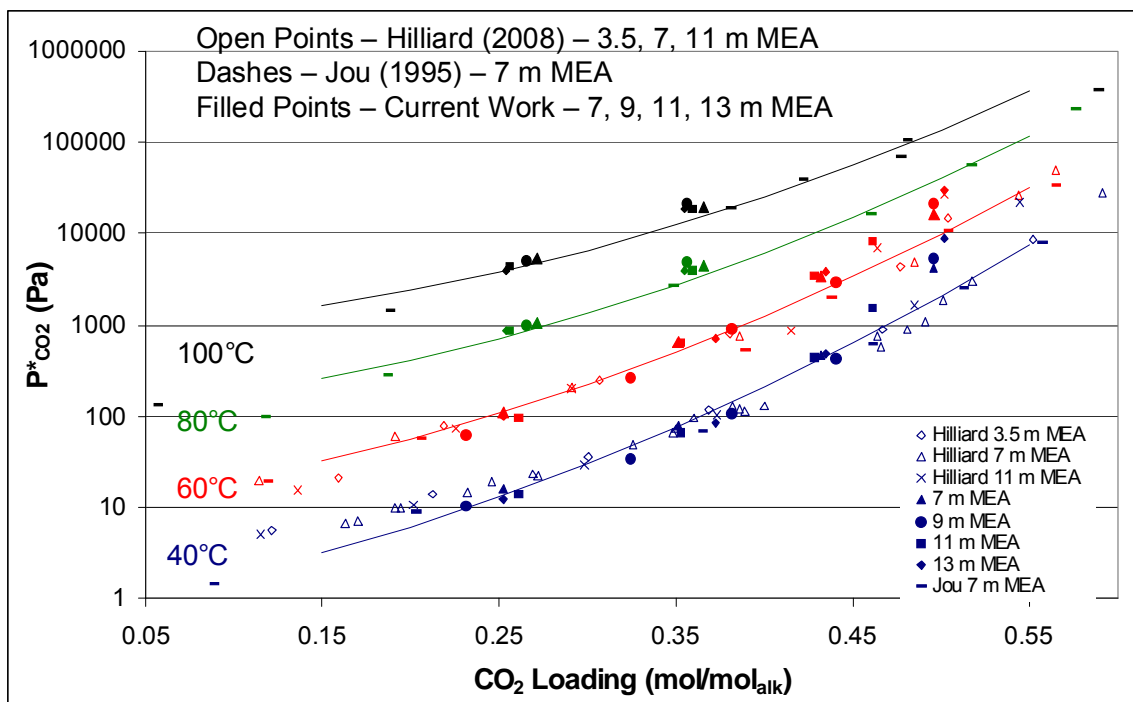
Figure 5.6: Equilibrium CO_2 partial pressure measurements in MEA solutions at 40, 60, 80, and 100 ˚C (Jou, Mather et al. 1995; Hilliard 2008). Lines – Equation 5.26.

Taking the derivative of Equation 5.26 with respect to CO_2 loading yields a term which can be multiplied by the alkalinity concentration to obtain the slope of the equilibrium line in the required units. This analytical approach provides a fairly consistent representation of the slope of the equilibrium line over a wide range of experimental conditions.

5.1.1.7 Rate Constant

The rate constant for MEA has been reported as Equation 5.27 based on a review of the available literature data (Versteeg, Van Dijck et al., 1996).

$$k_{MEA} = 4.4 \cdot 10^8 \exp\left(-\frac{5400}{T}\right) \; m^3 mol^{-1} s^{-1} \tag{5.27}$$

The temperature dependence of Equation 5.27 has been used in this model although the equation is only valid up to 40 ˚C. No reliable literature data were available at higher temperatures to verify Equation 5.27 at higher temperatures (Versteeg, Van Dijck et al., 1996). Regardless, this temperature dependence has been extrapolated up to 100 ˚C for this model.

Equation 5.27 assumes a first order MEA dependence which is not supported by the wetted wall column experiments in this work. Since a 2nd order amine concentration dependence was found, the pre-exponential constant required readjustment. It was adjusted until the expression in Equation 5.28 was minimized.

$$\sum\left(\frac{k'_{g,calc} - k'_{g,meas}}{k'_{g,meas}}\right)^2 \tag{5.28}$$

The obtained value of k_{MEA} is 2.4*10^6 m^{6}mol^{-2}s^{-1} based on the final rate expression shown in Equation 5.29. This rate expression leads to the following expression for k_g' in MEA solutions.

$$r_{CO2} = -k_{MEA}\gamma_{MEA}^2 [MEA]^2 \gamma_{CO_2}[CO_2] \tag{5.29}$$

$$\frac{1}{k'_g} = \frac{\gamma_{CO2}^{0.5} H_{CO2,H2O}}{\sqrt{k\gamma_{MEA}^2 [MEA]^2 D_{CO2}}} + \frac{1}{k^o_{l,prod}}\left(\frac{\Delta P^*_{CO2}}{\Delta[CO_2]_T}\right) \tag{5.30}$$

The evaluation of the model is presented in Section 5.2.

5.1.2 Piperazine

5.1.2.1 Activity Coefficients

The rate expression is determined by the activity of the reactants, not the concentration. It cannot be assumed that activity coefficients are near 1.0 in highly loaded, highly concentrated PZ solutions. These solutions are highly ionic and should be treated so.

5.1.2.1.1 Piperazine and Piperazine Carbamate Activity Coefficients

In the MEA analysis, the MEA activity coefficient was obtained via amine volatility data analyzed by the modified Raoult's law. Using the modified Raoult's law for PZ presents a problem since pure PZ is a solid at the experimental temperatures. Piperazine partial pressure data from pure liquid piperazine can be extrapolated to 40 ˚C although the PZ correlation is limited to temperatures greater than 106 ˚C. PZ volatility data from Hilliard (2008) utilizing the modified Raoult's law approach yield Figure 5.7. The free PZ concentration in Figure 5.7 was obtained from the Hilliard model.

$$y_{PZ}P = P_{PZ} = \gamma_{PZ}x_{PZ}P_{PZ}^* \qquad (5.31)$$
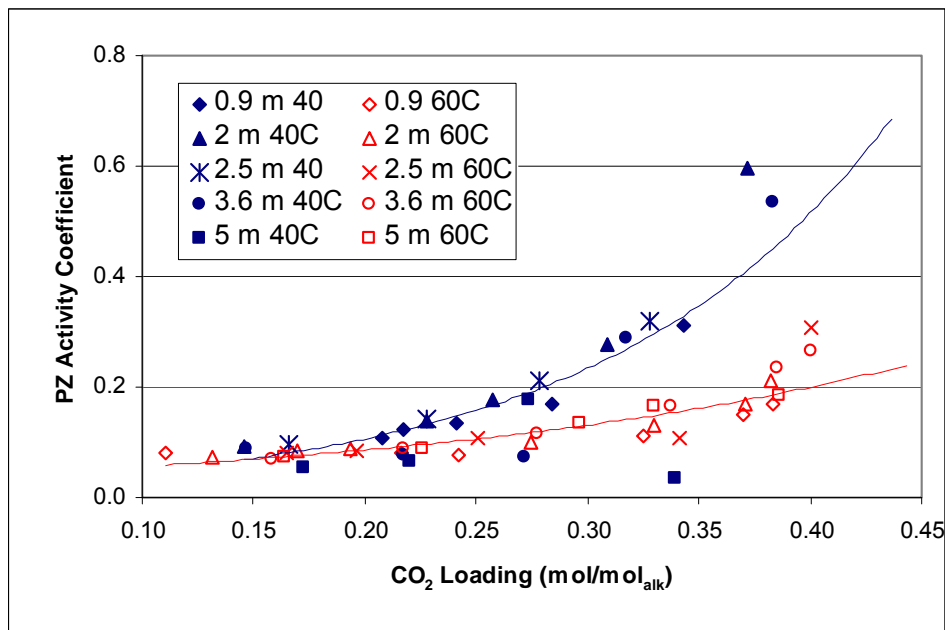
Figure 5.7: PZ volatility data evaluated using the modified Raoult's law with an extrapolated P_{PZ}^*

Results in Figure 5.7 do not seem to be reliable since it is somewhat unrealistic to believe that the activity coefficient of PZ varies a factor of 7 from 0.15 to 0.4 CO_2 loading at 40 ˚C. Since PZ and PZ carbamate concentrations do not change a factor of 10 over this range, implementing this activity coefficient data would result in a higher PZ activity and a faster CO_2 reaction rate at 0.4 than 0.1 CO_2 loading. Rate experiments have clearly shown that rates are significantly faster at lower CO_2 loading.

This phenomenon results from the modified Raoult's law form which only considers free piperazine. The free piperazine drops significantly at higher CO_2 loading and produces very high PZ activity coefficients. The data generally show a PZ volatility drop about a factor of 2 from low to high loading. Meanwhile the free piperazine concentration may change a factor of 20 or more.

Since PZ has 2 reactive nitrogen groups, the Raoult's law approach may not be a trustworthy approach to predicting reaction activity coefficients. Considering the case of PZ carbamate where one nitrogen group has reacted with CO_2, the Raoult's law approach for volatility yields a zero thermodynamic activity due to its ionic nature and inability to enter the vapor phase. The reaction activity is certainly not zero since the 2nd nitrogen group is known to react very quickly with either CO_2 or a proton.

Since PZ volatility data cannot be used to predict PZ activity coefficients another approach needed to be found. The Hilliard (2008) model was used to predict the PZ and PZ carbamate activity coefficients at wetted wall column conditions. The Hilliard model is based on the electrolyte non-random two liquid (e-NRTL) model which minimizes the excess Gibbs free energy in determining interaction parameters. Figure 5.8 shows obtained activity coefficients in 5 m PZ at 60 ˚C.
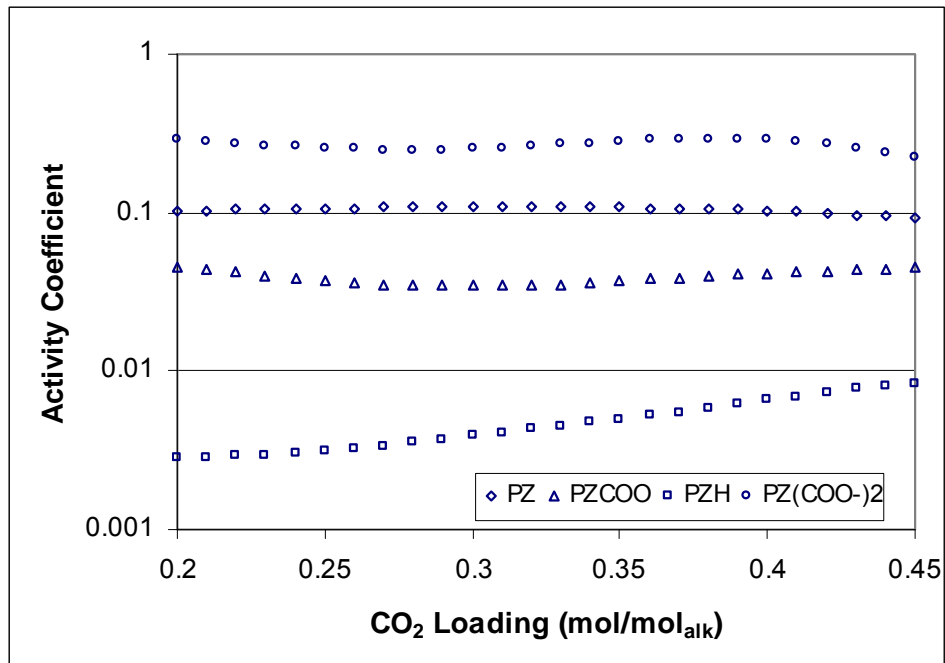
Figure 5.8: Activity coefficient results of the Hilliard (2008) model for 5 m PZ at 60 ˚C

Table 5.3 shows a summary of the obtained PZ and PZCOO⁻ activity coefficient values at 2 and 5 m at 40 and 60 ˚C. The wetted wall column experiments for PZ ranged from 0.22 to 0.41 CO_2 loading. Table 5.3 shows the minimum and maximum values over that loading range.

Table 5.3: PZ and PZCOO⁻ activity coefficients from the Hilliard (2008) model for 2 and 5 m PZ at 40 and 60 C between 0.22 and 0.41 CO_2 loading

	PZ		PZCOO⁻	
	Min	Max	Min	Max
2 m 40C	0.054	0.062	0.033	0.048
2 m 60C	0.075	0.082	0.035	0.042
5 m 40C	0.071	0.077	0.029	0.043
5 m 60C	0.101	0.109	0.034	0.042

It is important to note that the PZ activity coefficients in Table 5.3 are similar to the values in Figure 5.7 at very low loading. Near zero loading, the modified Raoult's law should be able to accurately determine the activity coefficient of PZ since PZCOO⁻ is not present.

Both PZ and PZCOO⁻ are relatively constant with changes in CO_2 loading at each condition. The small variance in γ_{PZ} does not seem to be directly correlated with CO_2 loading. However, the PZ activity coefficient increased significantly with increases in amine

concentration and temperature. PZCOO⁻ activity coefficients were mostly constant despite varying experimental conditions.

The Hilliard model contains data from 0.9 to 5 m PZ and is accurate at temperatures up to 60 ˚C (Hilliard, 2008). Above these conditions the model produces some activity coefficients which were not deemed reliable. Rather than extrapolating the model for 8, 12 m PZ and 80, 100 ˚C, the data within the reliable range of the model were extrapolated. This was done by regressing the average PZ activity coefficients to Equation 5.32. Equation 5.32 was used to extrapolate to 8, 12 m PZ and 80, 100 ˚C conditions. PZ activity coefficients were regressed on a wt% amine basis with temperature in Kelvin. Since PZCOO⁻ activity coefficients were relatively constant, an average value was used for all conditions.

$$\ln \gamma_{PZ} = 2.325 + 0.172(PZ) - \frac{1702}{T} \qquad (5.32)$$

$$\gamma_{PZCOO^-} = 0.038 \qquad (5.33)$$

5.1.2.1.2 Carbon Dioxide Activity Coefficient

No N_2O solubility data in concentrated or CO_2 loaded PZ solutions are available in the literature. Therefore, the activity coefficient of CO_2 in PZ solutions cannot be determined via experimental data. For lack of a better estimate, the N_2O solubility in CO_2 loaded concentrated PZ solutions was assumed to be identical to CO_2 loaded concentrated MEA. Equation 5.11, obtained from solubility data in MEA, was used with one modification. The CO_2 loading in Equation 5.11 was multiplied by 2 since the CO_2 loading is in terms of mol_{CO2}/mol_{alk}. Multiplying the CO_2 loading by 2 allows Equation 5.34 to represent the solubility based on the CO_2 concentration. The PZ concentration in Equation 5.34 is represented in wt %. Equation 5.34 was used to determine the Henry's solubility of N_2O in PZ solutions.

$$H_{N2O} = \exp\left[\left(\begin{array}{c} 8.3194 + 4.52 \cdot 10^{-3}(PZ) - 4.78 \cdot 10^{-2}(2 \cdot CO_2 Ldg) \\ + 4.56 \cdot 10^{-2}(PZ)(2 \cdot CO_2 Ldg) \end{array}\right) - 1905\left(\frac{1}{T} - \frac{1}{298.15}\right)\right] \qquad (5.34)$$

Again, the CO_2 and N_2O solubility data in water as a function of temperature have been compiled and regressed (Versteeg and Van Swaaij, 1988). These equations were used along with the N_2O analogy to predict the activity coefficient of CO_2 in PZ solutions.

$$H_{CO2,H2O} = 2.82 \cdot 10^6 \exp(-2044/T) \ Pa \cdot m^3 mol^{-1} \qquad (5.35)$$

$$H_{N2O,H2O} = 8.55 \cdot 10^6 \exp(-2284/T) \ Pa \cdot m^3 mol^{-1} \qquad (5.36)$$

$$\gamma_{N2O} = \frac{H_{N2O}}{H_{N20,H2O}} = \frac{H_{CO2,}}{H_{CO2,H2O}} = \gamma_{CO2} \qquad (5.37)$$

H_{CO2} gives the effective solubility of CO_2 in the solution. $H_{CO2,H2O}$ is the true thermodynamic Henry's constant which refers to the solubility of CO_2 in pure water. The activity coefficient of CO_2 varies between 1.1 and 5.6 for the 2–12 m PZ wetted wall column experiments.

5.1.2.2 Diffusion Coefficient of CO_2

The diffusion coefficient of CO_2 in PZ solutions was calculated identically to the diffusion coefficient of CO_2 in MEA solutions.

PZ solution viscosity values were obtained from regressing 5–12 m PZ viscosity measurements at 25, 40, and 60 ˚C from Freeman (Rochelle, Sexton et al., 2008). Details on the PZ viscosity regression can be found in Appendix E.

5.1.2.3 Piperazine and Piperazine Carbamate Concentrations

Piperazine and piperazine carbamate concentrations were estimated using mole fractions from the Hilliard (2008) model at each wetted wall column condition. Required density data was obtained from regressing 2–12 m PZ density measurements at 20, 40 and 60 ˚C from Freeman (Rochelle, Sexton et al. 2009). Details on the PZ density regression can be found in Appendix E.

5.1.2.4 Piperazine Order

With estimations for the activity coefficients of PZ, PZCOO⁻ and CO_2, the PZ concentration dependence on k_g' can be examined. A base catalysis reaction expression similar to the expression for the MEA system is written below. Equation 5.38 is written generically.

$$r_{CO2} = -(k_{Am}[Am] + k_{H2O}[H_2O]) \cdot [Am] \cdot [CO_2] \qquad (5.38)$$

Like the MEA analysis, catalysis by water was ignored. In concentrated PZ solutions, the water catalysis should be even more insignificant than in MEA systems because both PZ and PZ carbamate have a higher pKa than MEA and more free amine is present at the highest loading conditions.

Neglecting water catalysis but accounting for activity coefficients and both bases in the PZ system allows Equation 5.38 to be expanded into Equation 5.39. The rate expression could also be written as Equation 5.40 which clearly shows each reaction permutation.

$$r_{CO2} = -\left(\begin{matrix} k_{PZ}\gamma_{PZ}[PZ] \\ + k_{PZCOO^-}\gamma_{PZCOO}[PZCOO^-] \end{matrix} \right) \cdot \left(\begin{matrix} \gamma_{PZ}[PZ] \\ + \gamma_{PZCOO}[PZCOO^-] \end{matrix} \right) \cdot [CO_2] \qquad (5.39)$$

$$r_{CO2} = -\left(\begin{matrix} k_{PZ}\gamma_{PZ}^2[PZ]^2 + k_{PZ}\gamma_{PZ}[PZ]\gamma_{PZCOO}[PZCOO^-] \\ + k_{PZCOO}\gamma_{PZCOO}[PZCOO^-]\gamma_{PZ}[PZ] \\ + k_{PZCOO}\gamma_{PZCOO}^2[PZCOO^-]^2 \end{matrix} \right) \cdot [CO_2] \qquad (5.40)$$

It is not obvious that this expression is 2ⁿᵈ order with respect to the PZ activities but the expression is analogous to the MEA expression which results in a 2ⁿᵈ order MEA dependence. Ignoring activity coefficients, Equation 5.40 suggests that doubling PZ and PZCOO⁻ concentrations would lead to a rate expression 4 times larger. Although the expression is more complex than the expression for MEA systems, the PZ rate expression is also about 2ⁿᵈ order.

5.1.2.5 Liquid Phase Mass Transfer Coefficient of Reactants and Products, $k_{l,prod}^0$

The liquid phase mass transfer coefficient of the reactants and products, $k_{l,prod}^0$, was calculated as shown in Section 3.2.2.2.

Density data was obtained from regressing 2–12 m PZ density measurements at 20, 40 and 60 ˚C from Freeman (Rochelle, Sexton et al., 2009). PZ solution viscosity values were obtained from regressing 5–12 m PZ viscosity measurements at 25, 40, and 60 ˚C from Freeman (Rochelle, Sexton et al., 2008a). Details on the PZ density and viscosity regressions can be found in Appendix E.

5.1.2.6 Slope of the Equilibrium Line

The slope of the equilibrium line in Equation 5.1 results from converting a concentration-based mass transfer coefficient to a partial pressure basis. The slope can be difficult to accurately determine due to the sensitivity at high loading or temperatures. Recall partial pressure curves are plotted on a log-based y-axis. This produces very high values for the slope. In cases where diffusion limits CO_2 mass transfer, a poor estimation of the slope of the equilibrium can drastically affect the expected mass transfer.

The equilibrium partial pressure can be uniformly predicted from an empirical expression developed by Xu (Rochelle, Sexton et al., 2009) using literature data. The empirical relationship in Equation 5.41 is valid for PZ solutions between 40 and 190 ˚C. Equation 5.41 defines the partial pressure in Pascals with the temperature in Kelvin.

$$\ln P_{CO2} = 38.4 + (-102,000J/mol) \cdot \frac{1}{RT} - 20.6\alpha + 13,200\frac{\alpha}{T} + 3.23\alpha^2 \quad (5.41)$$

Figure 5.9 shows show the fit to previously referenced CO_2 partial pressure data (Figure 4.3).
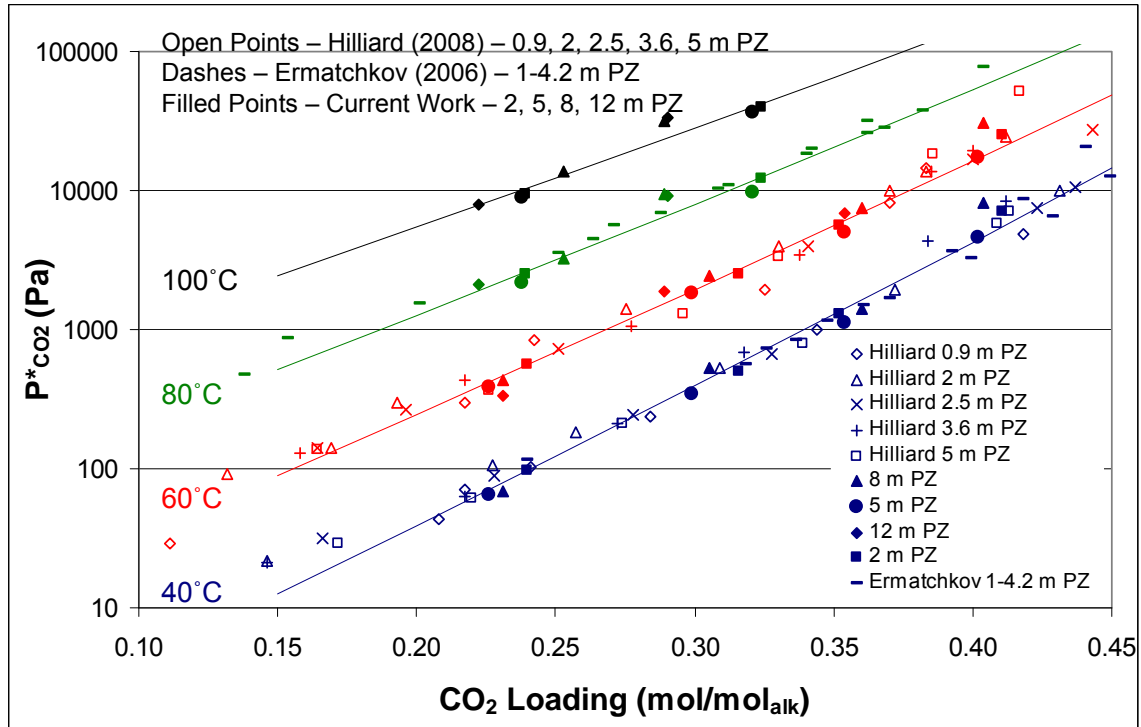
Figure 5.9: Equilibrium CO$_2$ partial pressure measurements in PZ solutions at 40, 60, 80, and 100 $^{\circ}$C (Ermatchkov, Perez-Salado Kamps et al., 2006; Hilliard, 2008). Lines – Equation 5.41.

Taking the derivative of Equation 5.41 with respect to CO$_2$ loading yields a term which can be multiplied by the alkalinity concentration to obtain the slope of the equilibrium line in the required units. This analytical approach provides a fairly consistent representation of the slope of the equilibrium line over a wide range of experimental conditions.

5.1.2.7 Rate Constant

The rate constant for PZ is not quite as simple as MEA. Bishnoi (2000) reported a rate expression with first order PZ dependence leading to Equation 5.42.

$$k_{PZ} = 4.14 \cdot 10^7 \exp\left(-\frac{33,600}{RT}\right) \; m^3 mol^{-1} s^{-1} \tag{5.42}$$

Derks (2006) also reported a rate expression with a first order PZ dependence. Derks suggests the rate constant expression in Equation 5.43.

$$k_{PZ} = 6.57 \cdot 10^7 \exp\left(-\frac{34,100}{RT}\right) \; m^3 mol^{-1} s^{-1} \tag{5.43}$$

Cullinane uses a rigorous kinetic model to interpret rate constants. Cullinane reports a 2nd order PZ dependence but reports a separate rate constant for each amine-base pairing. The rate expression used by Cullinane is similar to the expression (Equation 5.40) used in this work and is shown below.

$$r_{CO_2} = \sum_B k_{Am-B}[Am][B][CO_2] \qquad (5.44)$$

The Cullinane model cannot be compared to the first order models by Derks (2006) and Bishnoi (2000). It is also difficult to compare to the current model because the current model is activity-based while the Cullinane model is concentration-based.

Cullinane reports an activation energy of 35 kJ/mol which compares nicely to the 33.6 and 34.1 kJ/mol reported by Bishnoi and Derks. The current model also utilizes an activation energy of 35 kJ/mol.

The rate expression (Equation 5.39 or 5.40) has 2 pre-exponential constants. The value for k_{PZCOO} was assumed to be 70% of k_{PZ}. This 70% value was used by Cullinane for the reported k_{PZ-PZ}, $k_{PZ-PZCOO}$, $k_{PZCOO-PZ}$ and $k_{PZCOO-PZCOO}$ rate constants. The 70% ratio is based on Bronsted theory which relates the pKa of a base to its rate constant. With k_{PZCOO} ratioed to k_{PZ}, the k_{PZ} pre-exponential rate constant was adjusted until the expression in Equation 5.45 was minimized.

$$\sum \left(\frac{k'_{g,calc} - k'_{g,meas}}{k'_{g,meas}} \right)^2 \qquad (5.45)$$

The values of k_{PZ} and k_{PZCOO} are $6.9*10^7$ and $4.8*10^7$ $m^6mol^{-2}s^{-1}$, respectively, in the final rate expression shown in Equation 5.46. This rate expression leads to the following expression for k_g' in PZ solutions.

$$r_{CO2} = - \begin{pmatrix} k_{PZ}\gamma_{PZ}^2[PZ]^2 + k_{PZ}\gamma_{PZ}[PZ]\gamma_{PZCOO}[PZCOO^-] \\ + k_{PZCOO}\gamma_{PZCOO}[PZCOO^-]\gamma_{PZ}[PZ] \\ + k_{PZCOO}\gamma_{PZCOO}^2[PZCOO^-]^2 \end{pmatrix} \cdot [CO_2] \qquad (5.46)$$

$$\frac{1}{k_g'} = \frac{\gamma_{CO2}^{0.5} H_{CO2,H2O}}{\sqrt{\left(\begin{array}{l} k_{PZ}\gamma_{PZ}^2[PZ]^2 + k_{PZ}\gamma_{PZ}[PZ]\gamma_{PZCOO}[PZCOO^-] \\ + k_{PZCOO}\gamma_{PZCOO}[PZCOO^-]\gamma_{PZ}[PZ] \\ + k_{PZCOO}\gamma_{PZCOO}^2[PZCOO^-]^2 \end{array}\right)D_{CO2}}} + \frac{1}{k_{l,prod}^o}\left(\frac{\Delta P_{CO2}^*}{\Delta[CO_2]_T}\right) \quad (5.47)$$

5.2 Excel Model Analyses

With the framework for the MEA and PZ spreadsheet models defined, each model can now be analyzed. This section looks at how each parameter in the modified k_g' expression is affected by changes in temperature, amine concentration, and CO_2 loading. Wetted wall column experiments have shown that neither temperature nor amine concentration changes significantly affect k_g' for MEA and often PZ systems (Figures 4.7 and 4.8). This section shows why k_g' is relatively unaffected.

This section also extrapolates the model to explore the resultant k_g' for a 20 °C case which could be feasible in cold locations such as the North Sea.

The final form of the k_g' expressions can be written as Equation 5.48 and 5.49 for MEA and PZ, respectively. The first term in the k_g' expressions represents the pseudo first order condition. The second term includes the mass transfer resistance due to diffusion of reactants and products near the reaction interface.

$$\frac{1}{k_g'} = \frac{\gamma_{CO2}^{0.5} H_{CO2,H2O}}{\sqrt{k\gamma_{MEA}^2[MEA]^2 D_{CO2}}} + \frac{1}{k_{l,prod}^o}\left(\frac{\Delta P_{CO2}^*}{\Delta[CO_2]_T}\right) \quad (5.48)$$

$$\frac{1}{k_g'} = \frac{\gamma_{CO2}^{0.5} H_{CO2,H2O}}{\sqrt{\left(\begin{array}{l} k_{PZ}\gamma_{PZ}^2[PZ]^2 + k_{PZ}\gamma_{PZ}[PZ]\gamma_{PZCOO}[PZCOO^-] \\ + k_{PZCOO}\gamma_{PZCOO}[PZCOO^-]\gamma_{PZ}[PZ] \\ + k_{PZCOO}\gamma_{PZCOO}^2[PZCOO^-]^2 \end{array}\right)D_{CO2}}} + \frac{1}{k_{l,prod}^o}\left(\frac{\Delta P_{CO2}^*}{\Delta[CO_2]_T}\right) \quad (5.49)$$

5.2.1 Monoethanolamine

5.2.1.1 Parameter Dependences

This section shows how each of the parameters in Equation 5.48 change with temperature, amine concentration, and CO_2 loading.

The rate constant is independent of amine concentration and CO_2 loading. Figure 5.10 shows the temperature effect on the rate constant.
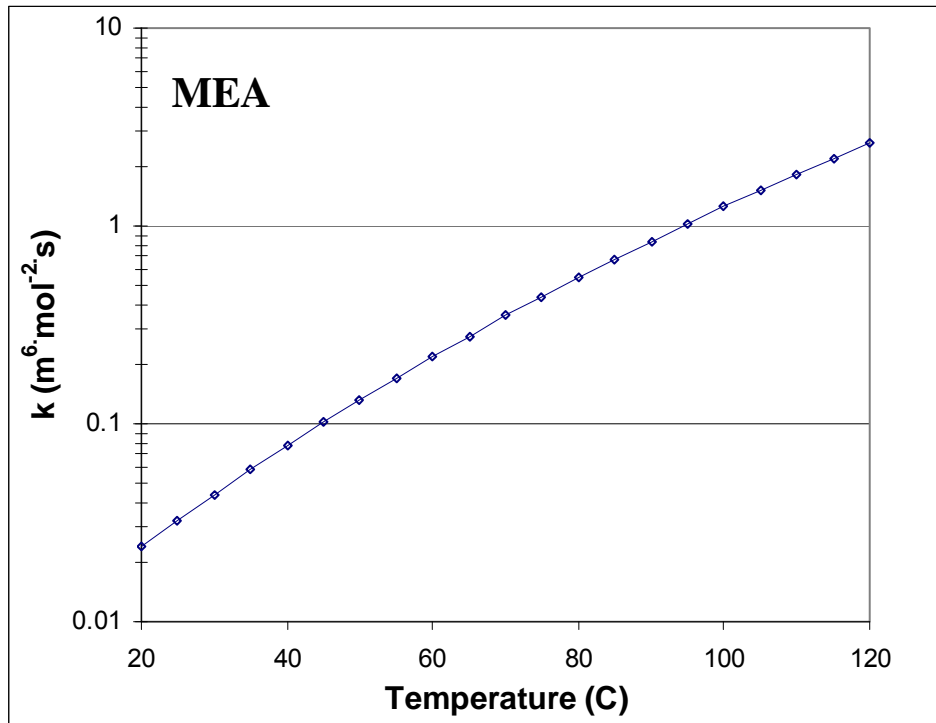
Figure 5.10: Calculated MEA rate constant from 20–120 ˚C

It is important to note that the MEA rate constant increases drastically with increasing temperature, 2 orders of magnitude from 20–120 ˚C. The rate constant has a 0.5 order dependence on the pseudo first order term in Equation 5.48.

The MEA activity coefficient is also independent of amine concentration. Figure 5.11 shows how the MEA activity coefficient is affected by changes in temperature and CO_2 loading.
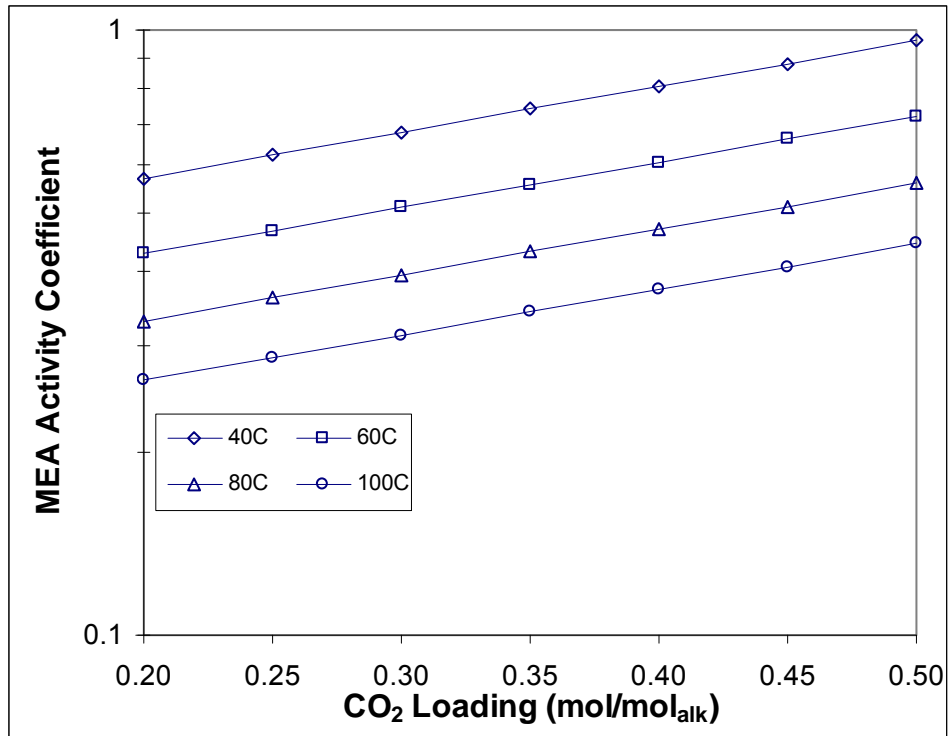
Figure 5.11: Calculated MEA activity coefficients from 40–100 °C at CO_2 loadings from 0.2 to 0.5

The MEA activity coefficient increases with CO_2 loading and decreases with temperature. Values vary about a factor of 3 over the plotted range. The pseudo first order portion of the k_g' expression has a 1st order dependence on the MEA activity coefficient.

The CO_2 activity coefficient is a function of CO_2 loading, temperature and amine concentration. Figure 5.12 plots calculated data for 7 and 13 m MEA.
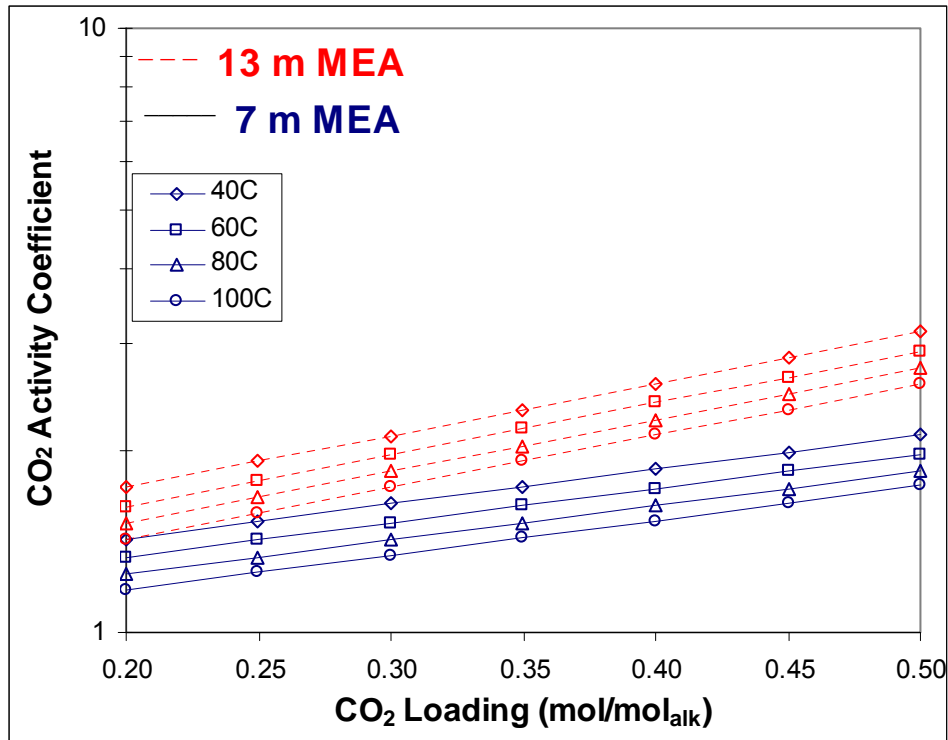
Figure 5.12: Calculated CO_2 activity coefficients from 40–100 $^{\circ}$C at CO_2 loadings from 0.2 to 0.5 in 7 and 13 m MEA

The activity coefficient of CO_2 increases with MEA concentration and CO_2 loading and decreases with increasing temperature. CO_2 activity coefficient values vary about a factor of 2 over the plotted range. The CO_2 activity coefficient has a -0.5 order effect on the pseudo first order k_g' expression.

The free MEA concentration is a function of CO_2 loading and amine concentration. The free MEA concentration is also a very slight function of temperature due to the speciation of the Hilliard (2008) model. Figure 5.13 plots the data for 7 and 13 m MEA.
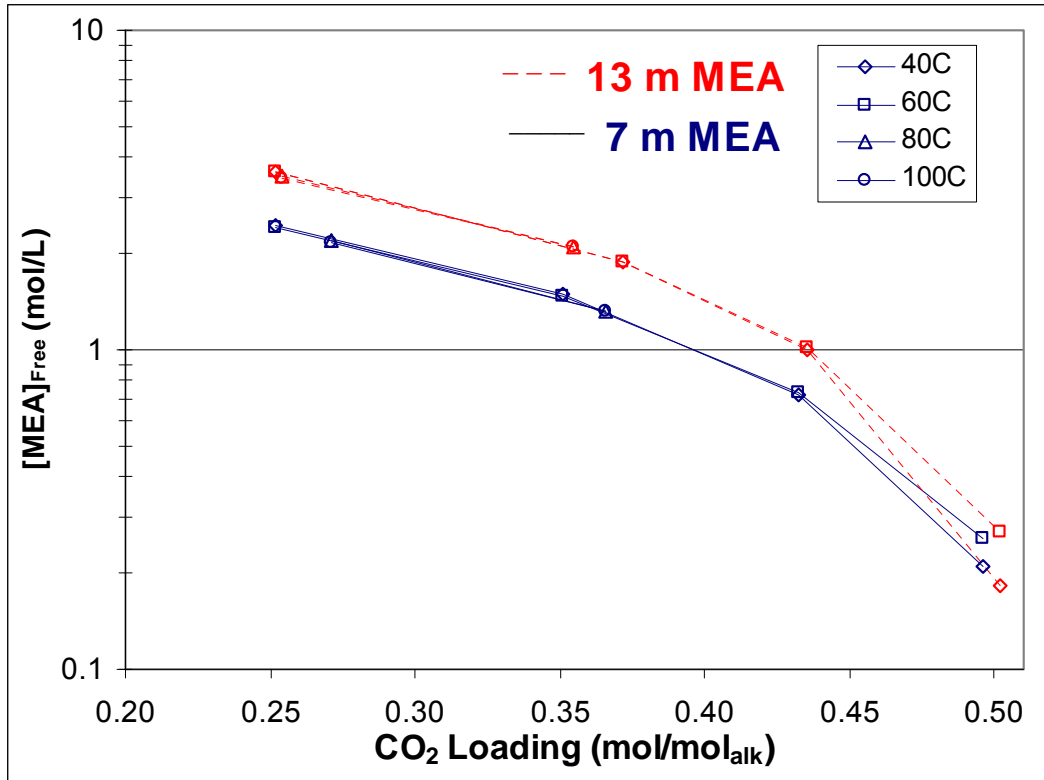
Figure 5.13: Free MEA concentration from 40–100 ˙C for 7 and 13 m MEA (Hilliard, 2008).

Figure 5.13 shows a nearly negligible effect of temperature on free MEA. Of course, the free amine concentration decreases with both increasing CO_2 loading and decreasing total MEA concentration. The change with CO_2 loading is particularly important since the free MEA concentration can change more than 1 order of magnitude from over the lean to rich CO_2 loading range. The free MEA concentration has a 1st order effect on the pseudo first order portion of the k_g' expression in Equation 5.48.

The diffusion coefficient of CO_2 is affected by CO_2 loading, temperature, and amine concentration since each of these parameters affect viscosity. Figure 5.14 shows how the calculation of the diffusion coefficient of CO_2 is affected by changes in each of the three parameters.
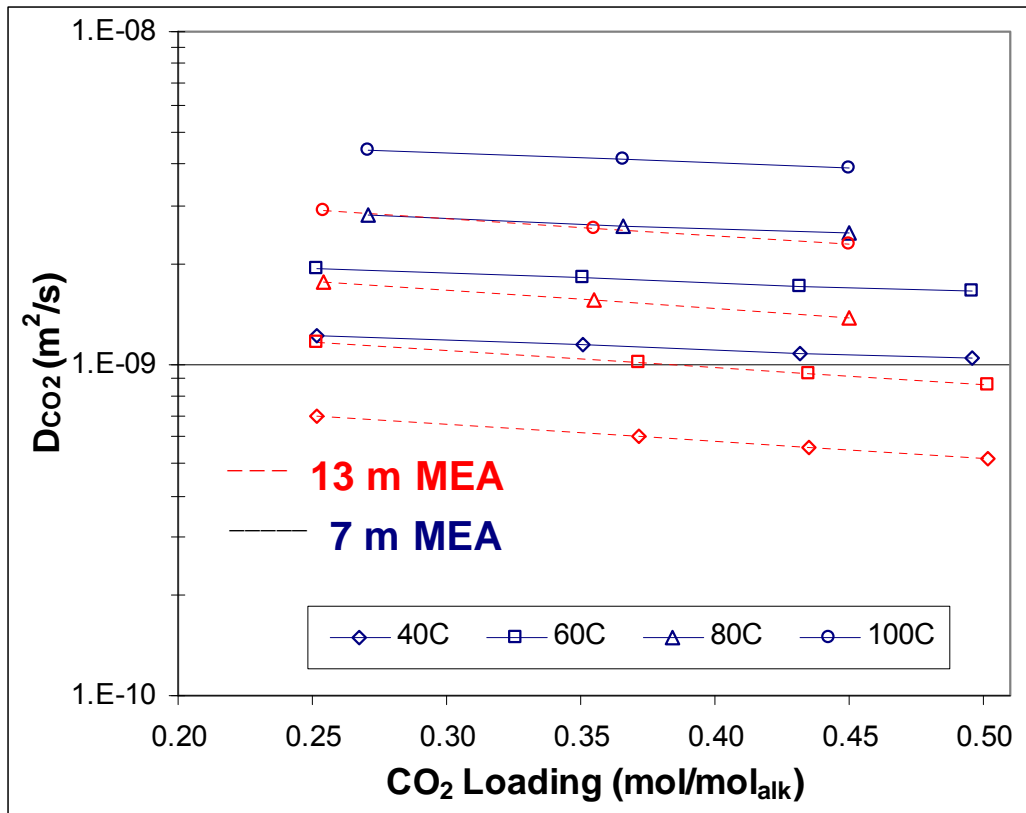
Figure 5.14: Calculated diffusion coefficient of CO_2 for 40–100 $^\bullet$C at 0.2–0.5 CO_2 loadings in 7 and 13 m MEA

CO_2 loading has a fairly minor effect on the diffusion coefficient of CO_2. Both amine concentration and temperature have strong effects on D_{CO2}. The data shown in Figure 5.14 exhibit a full order of magnitude difference between the lowest and highest D_{CO2} values. The diffusion coefficient of CO_2 has a 0.5 order dependence on the pseudo first order portion of the k_g' expression.

5.2.1.2 Parameter Significance

The previous section has shown how each of the parameters in Equation 5.48 varies with changes in CO_2 loading, temperature, and MEA concentration. However, many of the parameters have different effects on the k_g' expression. This section attempts to compare the significance of each parameter by showing the changes in each parameter at common conditions. Note that the order of the parameters is only significant to the pseudo first order portion of

Equation 5.48. If diffusion becomes a significant resistance at a given condition, the pseudo first order part of Equation 5.48 becomes less meaningful.

Figures 5.15–5.17 are plotted against CO_2 loading for some extreme conditions: 7 and 13 m MEA. For each parameter the correct dependence in Equation 5.48 is incorporated. Since Figures 5.15–5.17 each have stated temperatures, only the free MEA concentration, diffusion coefficient of CO_2, and the activity coefficients vary. The values of the rate constant and the Henry's solubility in water are constant in each graph.
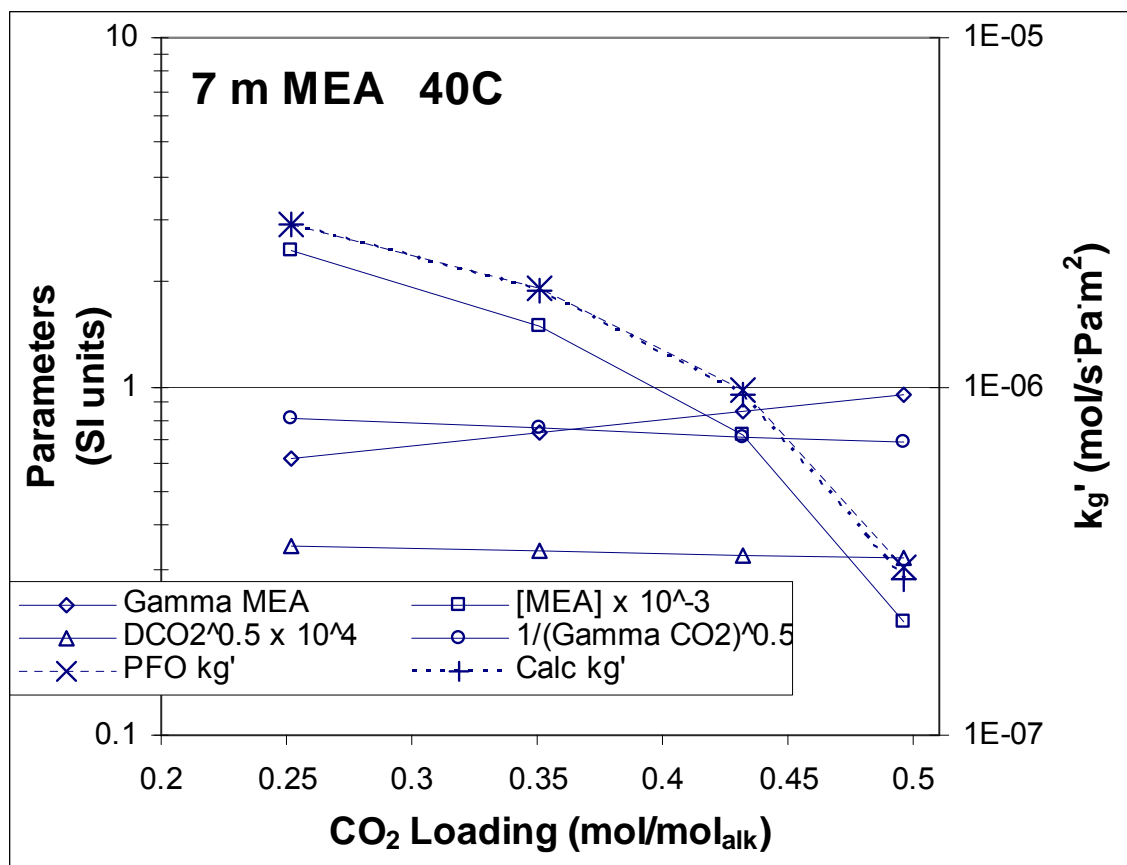
Figure 5.15: Parameter significance versus CO_2 loading for 7 m MEA at 40 ˚C

Figure 5.15 shows that the free MEA concentration has nearly the same shape as the calculated k_g' curves. The mass transfer rate is almost completely controlled by the free amine concentration for 7 m MEA at 40 ˚C. Each of the other parameters is nearly constant over the relevant CO_2 loading range. At 40 ˚C the pseudo first order k_g' and the calculated k_g' are nearly

identical. This is expected because diffusion resistances are very small at low temperature due to the slope of the equilibrium line.
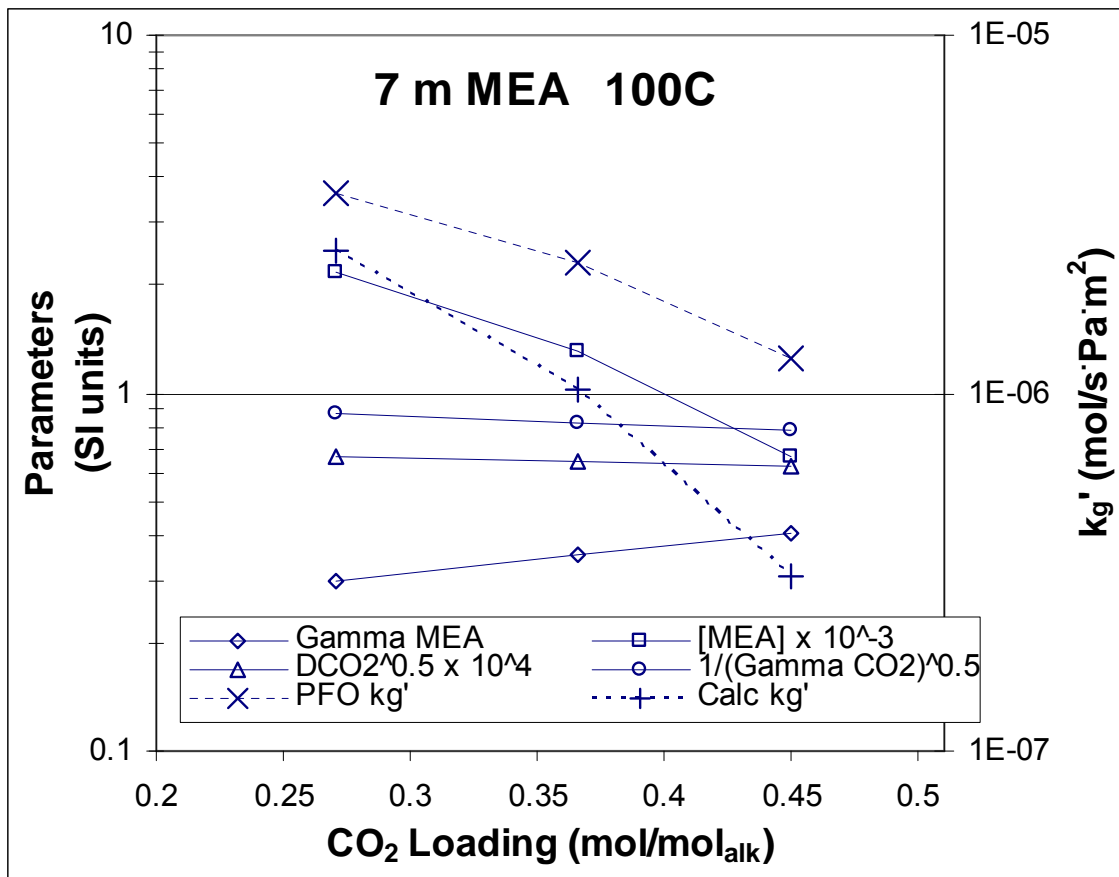
Figure 5.16: Parameter significance versus CO_2 loading for 7 m MEA at 100 ˚C

Figure 5.16 again shows the parameter significances for 7 m MEA but this time at 100 ˚C. The diffusion coefficient and activity coefficient of CO_2 contributions both decrease slightly with increasing CO_2 loading. At 100 ˚C, the activity coefficient of MEA has a stronger effect than at 40 ˚C. Again, changes in k_g' result primarily from the change in free MEA. It is also important to note that the pseudo first order k_g' and the calculated k_g' vary significantly at low loading and even more at higher loading. At 100 ˚C, MEA solutions encounter significant diffusion resistances which limit CO_2 mass transfer.
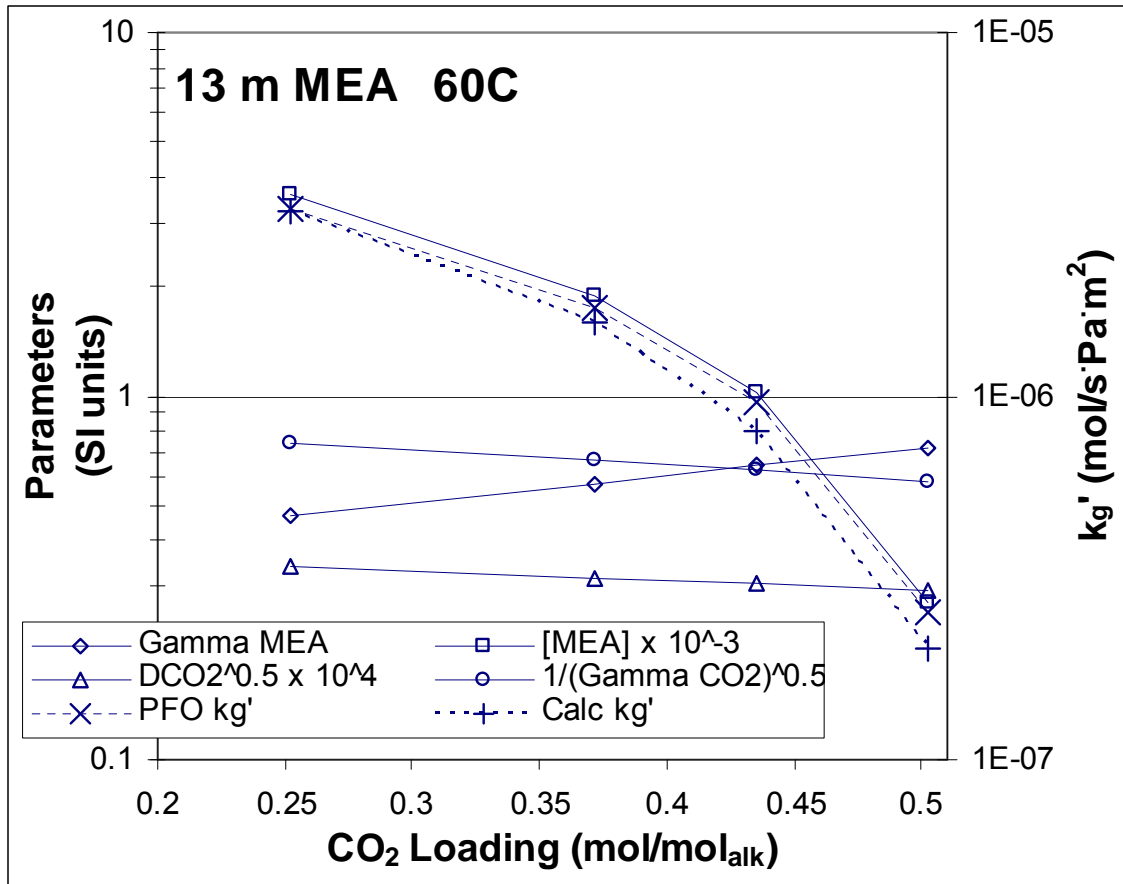
Figure 5.17: Parameter significance versus CO_2 loading for 13 m MEA at 60 ˚C

In 13 m MEA at 60 ˚C, both the activity and diffusion coefficients of CO_2 have a decreasing dependence which essentially cancels the increasing effect of the MEA activity coefficient. Again, the free amine concentration is the main parameter which affects the k_g' of the system. At 60 ˚C, there is a small but significant diffusion resistance on the system. This resistance causes the pseudo first order k_g' and the calculated k_g' to diverge slightly at the higher CO_2 loading conditions.

Figure 5.18 directly looks at the effect of the parameters as a function of temperature. An intermediate condition of 9 m MEA, 0.3 CO_2 loading was selected for this analysis.
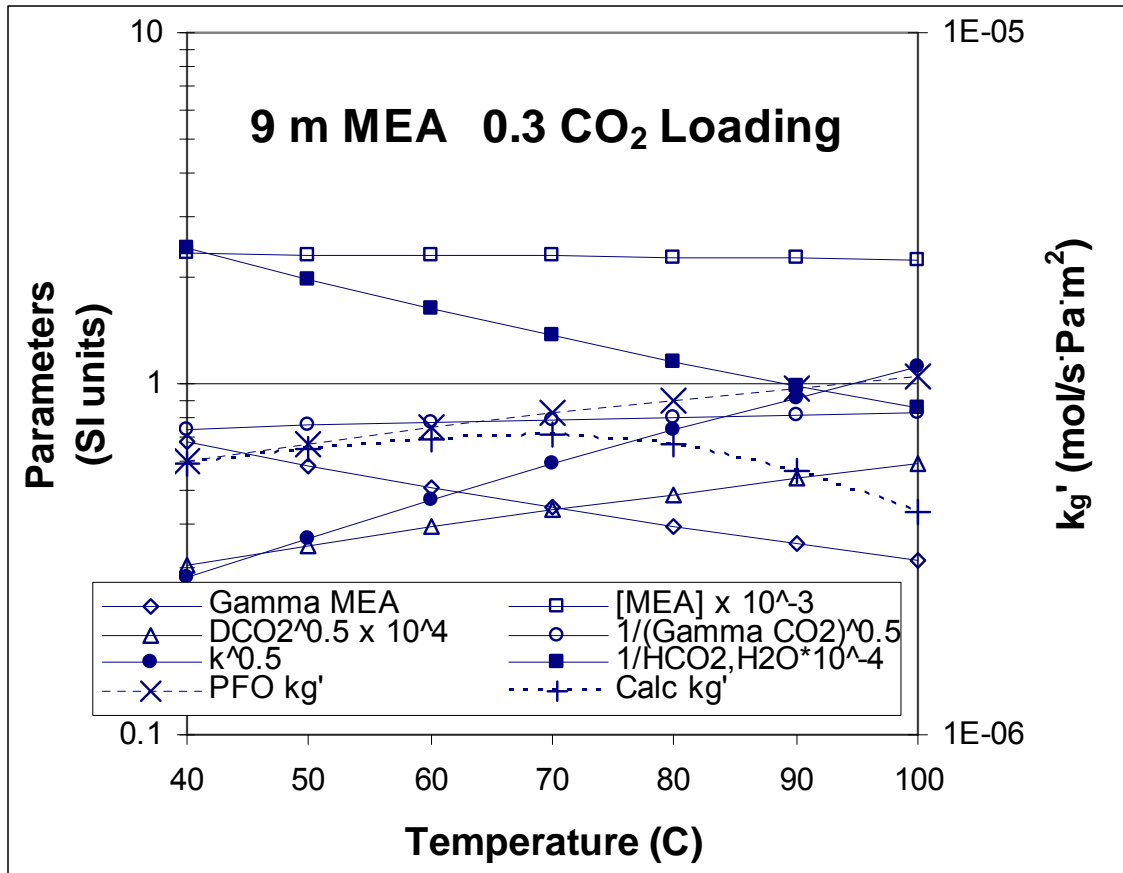
Figure 5.18: Parameter significance versus temperature for 9 m MEA at 0.3 CO2 loading

Figure 5.18 has shown that k_g' is mostly independent of temperature in MEA solutions. However, the parameters which comprise the k_g' expression have very strong temperature dependences. The Henry's solubility in water, the rate constant, the activity coefficient of MEA, and the diffusion coefficient of CO_2 are all strongly affected by temperature. However, these positive and negative dependences mostly cancel each other. The pseudo first order k_g' shows about a 50% increase over the temperature range but that increase is negated by the increased diffusion resistance at higher temperature. The calculated k_g' is more or less constant but does have a maximum at intermediate temperatures. A close look at Figure 4.7 shows that this phenomenon was often seen for MEA experiments in the wetted wall column.

Figure 5.19 shows the significance of each parameter with changes in amine concentration. 60 ˚C solutions with a 0.4 CO_2 loading were selected for this analysis.
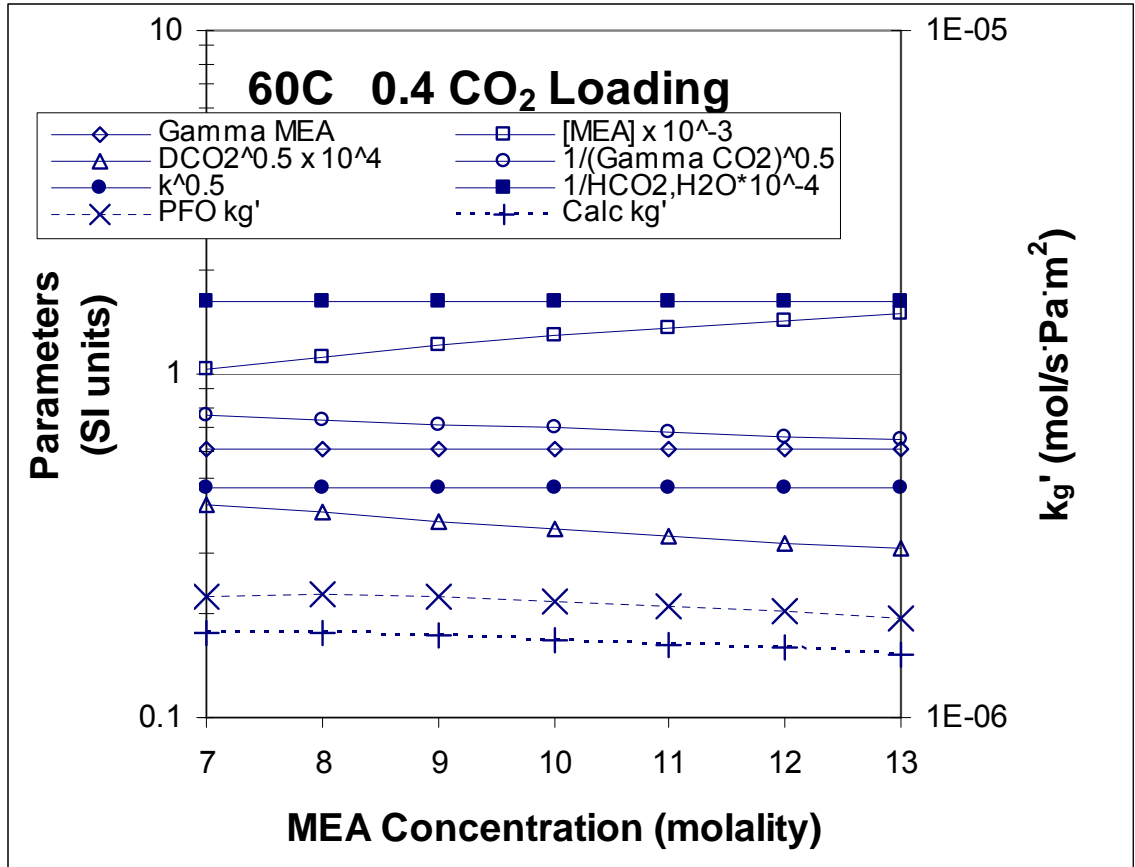
Figure 5.19: Parameter significance versus MEA concentration for 60 ˚C and 0.4 CO₂ loading

Figure 5.19 explains exactly why wetted wall column experiments have shown that k_g' is independent of MEA concentration. With changes in MEA concentration, most of the parameters are relatively constant in their effect on k_g'. Only the diffusion coefficient of CO_2, the activity coefficient of CO_2, and the free amine concentration vary significantly and those dependences essentially cancel each other.

Figure 5.20 shows the importance of the of the diffusion resistance in 7 and 13 m MEA over the range of experimental temperatures.
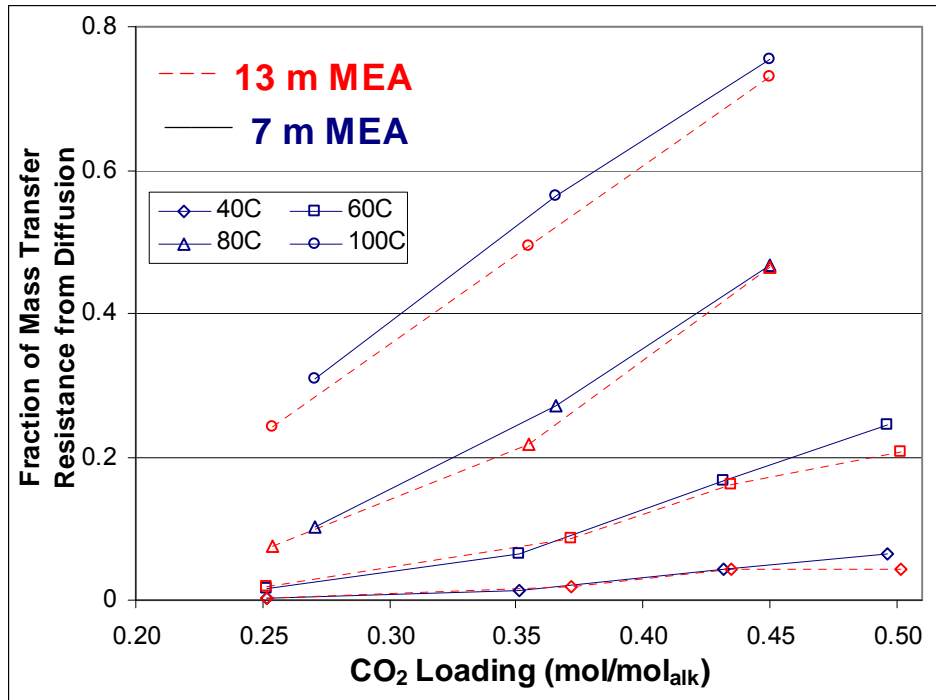
Figure 5.20: Fraction of mass transfer resistance from diffusion for 40–100 ˚C, 7 and 13 m MEA

The amine concentration does not affect the ratio of the resistances due to kinetics and diffusion in Equation 5.48. Figure 5.19 shows that the pseudo first order k_g' does not change significantly with MEA concentration. This implies that the value of the diffusion resistance does not change very much either with amine concentration changes. At higher concentrations, the physical liquid film mass transfer coefficient, k_l^o, decreases due to viscosity changes. However, the slope of the equilibrium line also has a concentration term since it must be defined in $Pa/(mol/m^3)$. The increased concentration decreases the slope of the equilibrium line. The diffusion term in Equation 5.48 divides k_l^o by the slope and that term is mostly unchanged with changes in total MEA concentration.

At high temperatures, particularly 100 ˚C, diffusion limits mass transfer even at moderate CO_2 loadings. This is mainly due to a drastic increase in the slope of the equilibrium line in Equation 5.48.

5.2.1.3 *Error Analysis*

This analysis seeks to show that systematic error has been removed from the model with respect to changing temperature and MEA concentration. The lack of systematic error provides a better confidence in the estimation of the parameters which comprise the k_g' expression, Equation 5.48.

Figure 5.21 shows an overall graph of all the wetted wall column data: 7–13 m MEA, 40–100 ˚C, 0.23–0.50 CO_2 loading. A parity plot is used to compare measured wetted wall column k_g' values to the calculated k_g' from Equation 5.48.
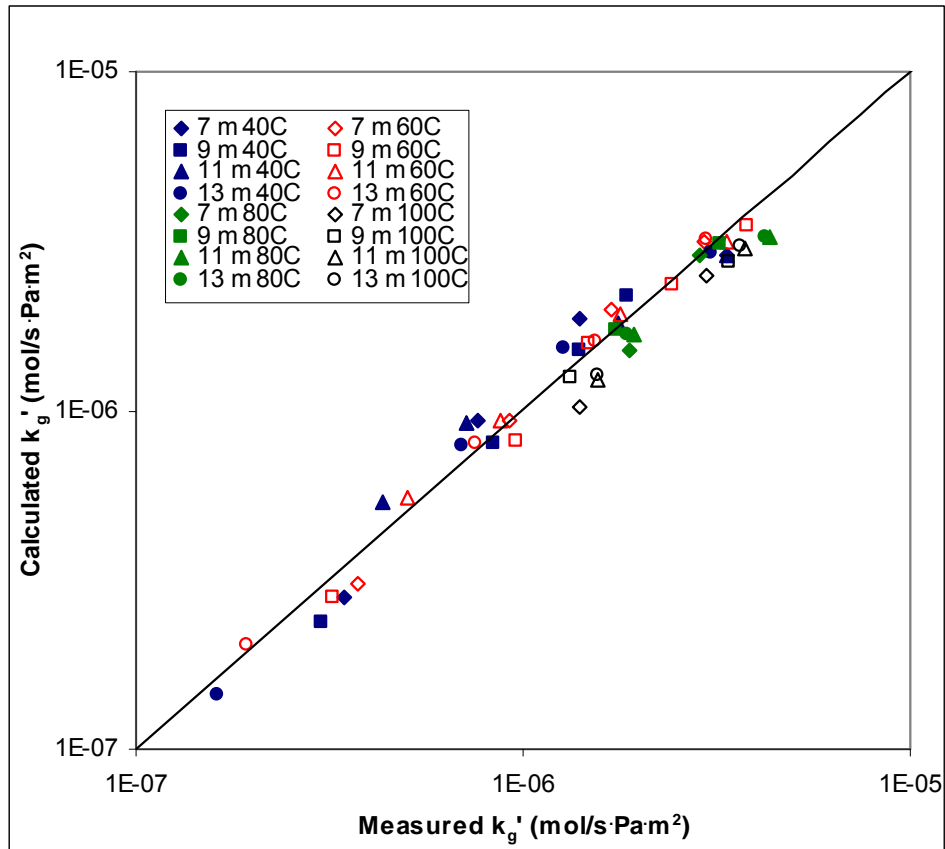
Figure 5.21: Parity plot comparing experimentally measured MEA k_g' values to k_g' values calculated from Equation 5.48

Figure 5.21 shows that k_g' values vary about a factor of 30 from the lowest loading to the highest loading conditions. A brief view shows that all of the points fall relatively close to the

parity line. Equation 5.48 represents the measured k_g' in MEA solutions with an average error of 13%.

Figure 5.22 includes all the data in Figure 5.21 but is plotted differently to show systematic trends in CO_2 loading. The y-axis is presented on a log scale so that percentage errors either positive or negative are visually represented clearly.
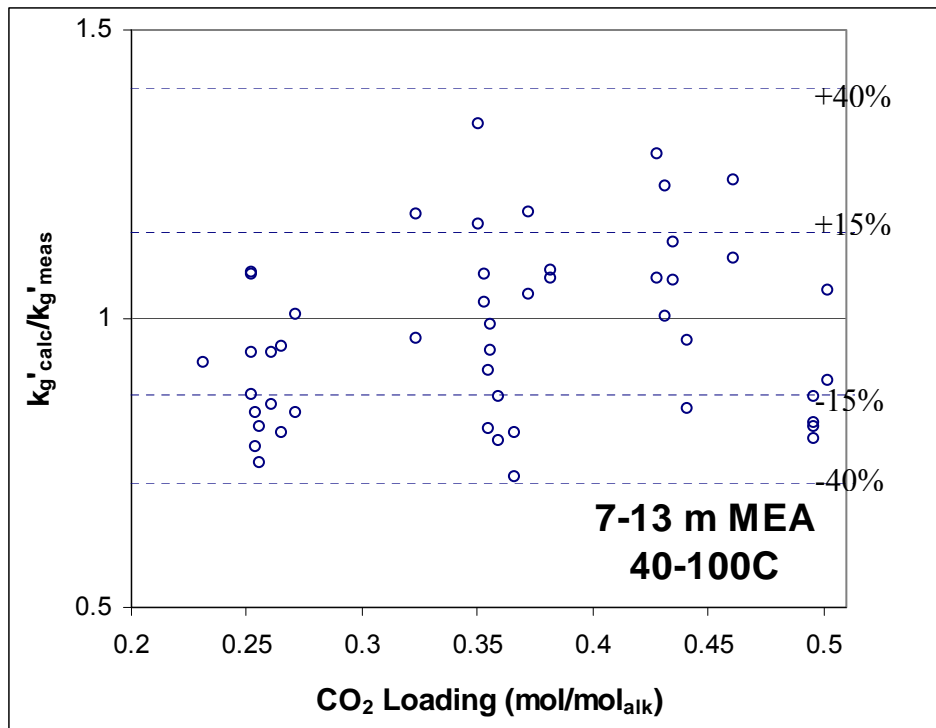
Figure 5.22: Calculated/measured k_g' versus CO_2 loading for all MEA wetted wall column conditions

Figure 5.22 has dotted lines to show ±40% error in the estimation of k_g'. All of the data fall within 40% of the measured k_g' values. This is impressive since k_g' values vary about a factor of 30. Many of the parameters comprising the k_g' expression change drastically with changes in temperature, MEA concentration, and CO_2 loading. Overall, there does not seem to be a systematic trend with changes in CO_2 loading since the points are centered around the y=1 line.

Figure 5.23 plots all the experimental data against temperature.
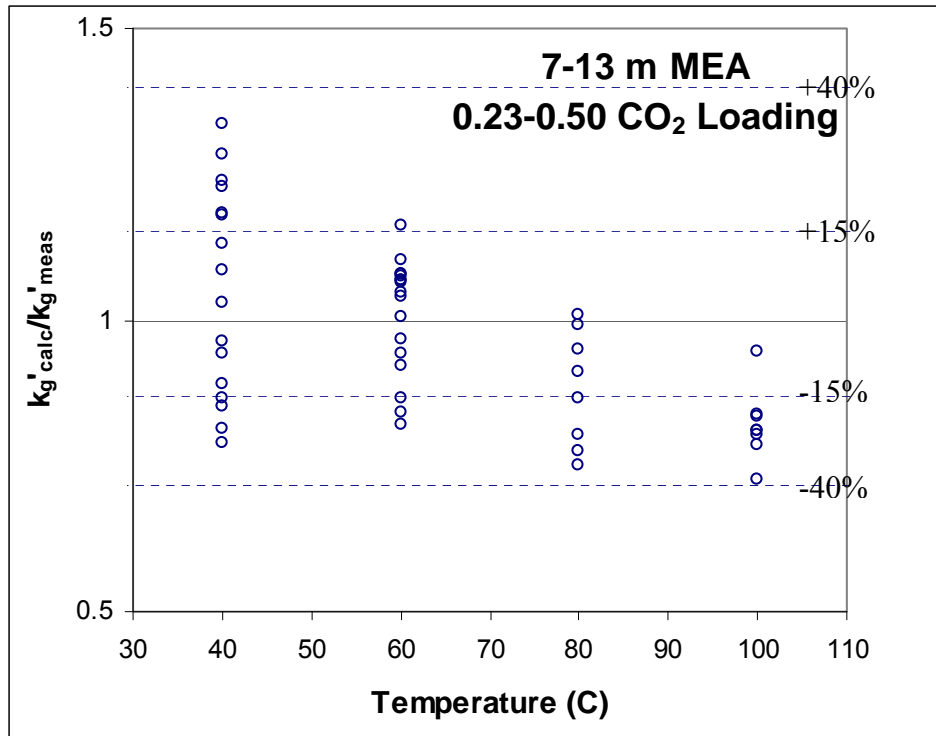
Figure 5.23: Calculated/measured k_g' versus temperature for all MEA wetted wall column conditions

Figure 5.23 shows a slight systematic error with increasing temperature. Recalling Figure 5.18, many of the parameters comprising k_g' vary wildly with changes in temperature. The slope of the equilibrium line is also extremely sensitive to temperature. Considering how sensitive Equation 5.48 is to changes in temperature, the systematic error shown in Figure 5.23 is quite small. The systematic temperature error in Figure 5.23 is about 4 kJ/mol. This can be compared to the MEA activation energy of 45 kJ/mol (Equation 5.27). However, the activation energy should not be adjusted to remove the error since the activation energy is known with more certainty than the other temperature dependent terms in the k_g' expression.

Figure 5.24 plots all the experimental data with MEA concentration on the x-axis.
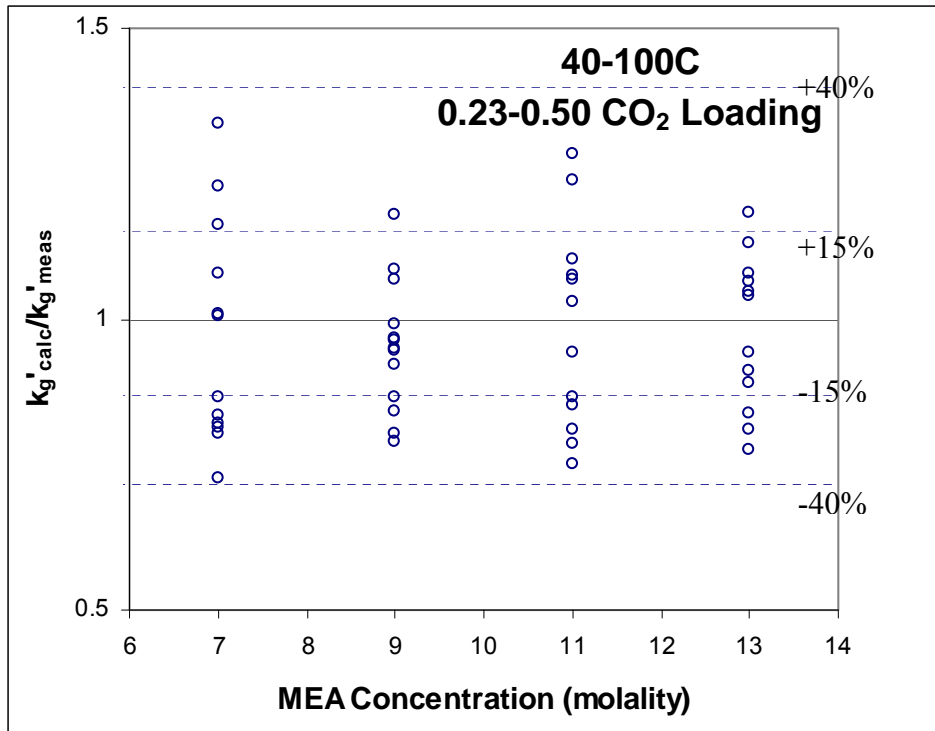
Figure 5.24: Calculated/measured k_g' versus MEA concentration for all MEA wetted wall column conditions

Figure 5.24 shows no systematic error in the calculated k_g' values with MEA concentration. Recall that Figure 5.19 showed that only a few parameters had mild dependences with changes in amine concentration.

Figures 5.22–5.24 show that systematic error with respect to CO_2 loading, temperature, and MEA concentration has mostly been removed from the model. The absence of significant systematic error increases confidence both in the model and in the determination of each parameter in the k_g' expression.

5.2.2 Piperazine

5.2.2.1 Parameter Dependences

This section shows how each of the parameters in Equation 5.49 change with temperature, PZ concentration, and CO_2 loading.

The PZ and PZCOO⁻ rate constants are independent of PZ concentration and CO_2 loading. Figure 5.25 shows the temperature effect on the rate constant.
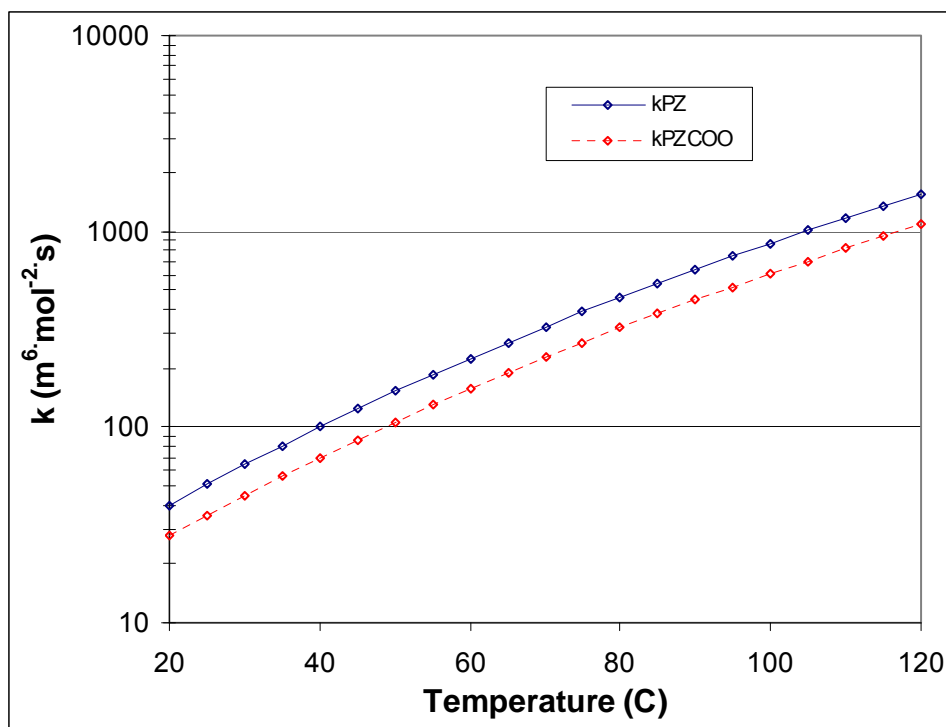
Figure 5.25: Calculated PZ and PZCOO⁻ rate constants from 20–120 ˚C

The PZ and PZCOO⁻ rate constants increase drastically with increasing temperature, about 1.5 orders of magnitude from 20–120 ˚C. The PZCOO⁻ rate constant has been set at 70% of the PZ rate constant based on work by Cullinane (2005). The rate constant dependence in Equation 5.49 approximates to the 0.5 power of the pseudo first order portion of Equation 4.49. Due to the complexity of the equation, the dependence cannot be explicitly stated since it will change as speciation changes.

The PZ activity coefficient is independent of CO_2 loading. Figure 5.26 shows how the PZ activity coefficient is affected by changes in temperature and total PZ concentration. The PZ carbamate activity coefficient is essentially independent of temperature, CO_2 loading, and amine concentration. This model defines it as a constant, 0.038. PZ and PZ carbamate activity coefficients were obtained from the Hilliard model (2008).
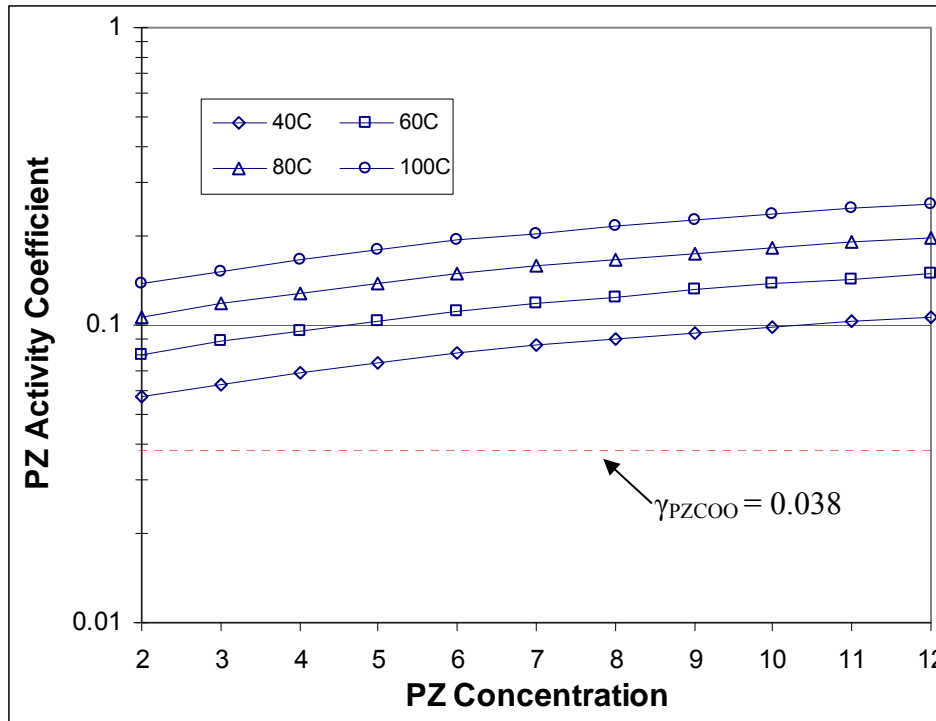
Figure 5.26: PZ activity coefficients for 2–12 m PZ from 40–100 ˚C (Hilliard, 2008)

The PZ activity coefficient increases with total PZ concentration and temperature. Values vary about a factor of 2 over the plotted range. Like the rate constants, Equation 5.49 does not define an explicit order for the PZ activity coefficient, but it is approximately 1st order in the pseudo first order expression.

The CO_2 activity coefficient is a function of CO_2 loading, temperature, and amine concentration. Figure 5.27 plots the calculations for 2 and 12 m PZ.
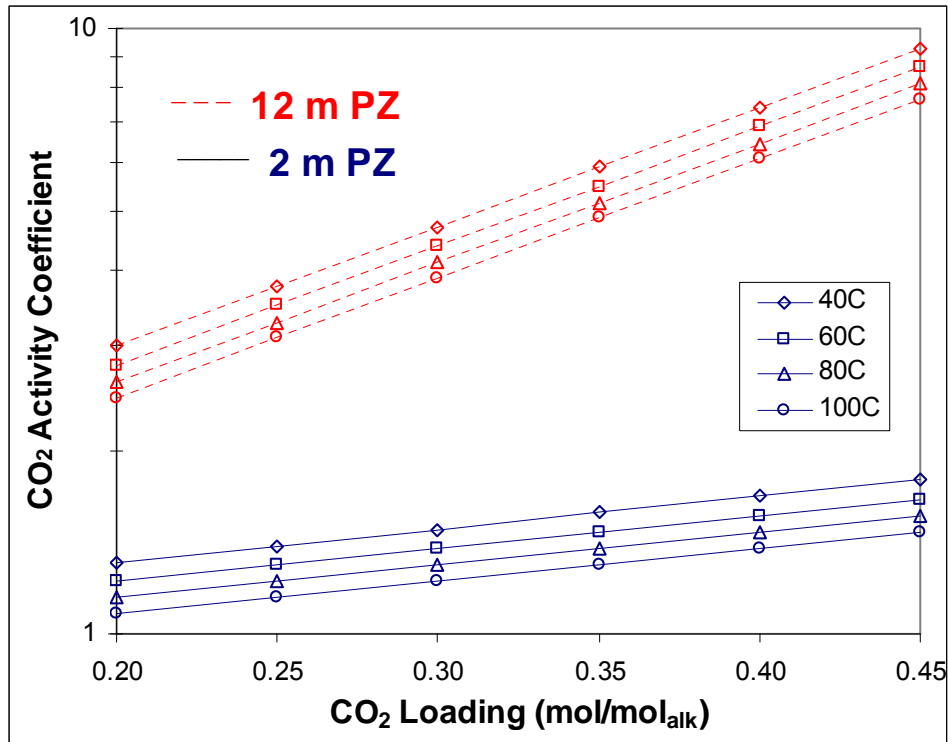
Figure 5.27: Calculated CO_2 activity coefficients at 40–100 $^\circ$C with 0.2 to 0.45 CO_2 loadings in 2 and 12 m PZ

The activity coefficient of CO_2 increases with PZ concentration and CO_2 loading and decreases with increasing temperature. CO_2 activity coefficient values vary about a factor of 10 over the plotted range. The CO_2 activity coefficient has a -0.5 order effect on the pseudo first order portion of the k_g' expression.

The free PZ and PZCOO⁻ concentrations are a function of CO_2 loading and amine concentration. They are also a function of temperature since the solution speciation changes with temperature. Figure 5.28 plots the free PZ concentrations for 2 and 8 m PZ. Figure 5.29 plots the free PZCOO⁻ concentrations for 2 and 8 m PZ. These values were obtained from the Hilliard model.
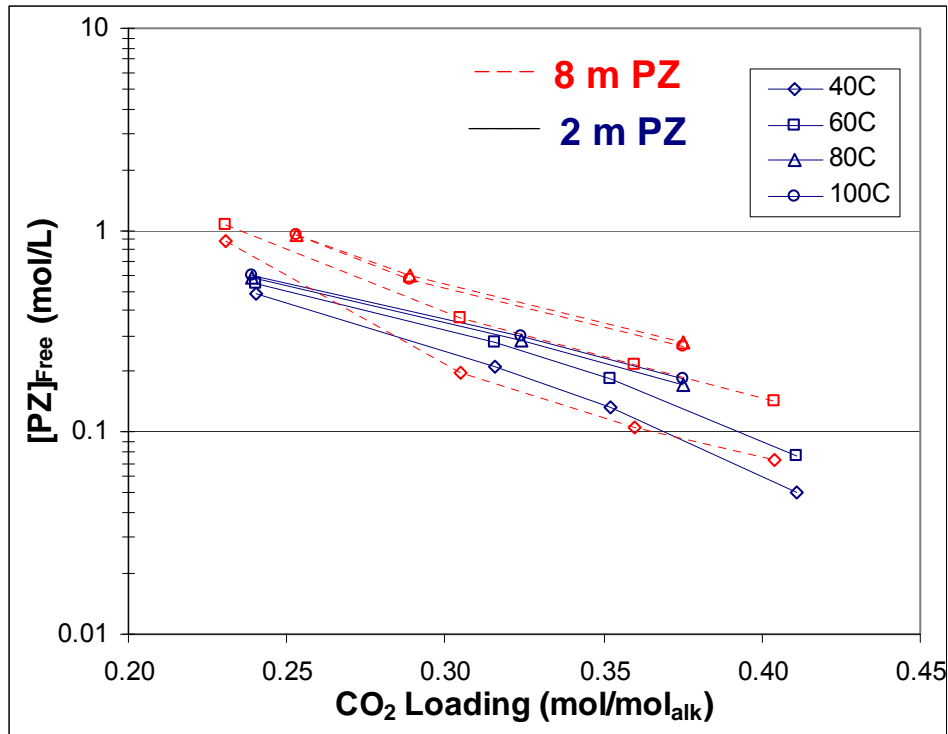
Figure 5.28: Free PZ concentration from 40–100 °C for 2 and 8 m PZ (Hilliard, 2008)

Oddly enough, free PZ concentrations for 2 m and 8 m PZ are roughly equivalent at constant CO_2 loading. This suggests that the total amine concentration plays a large part in the speciation of PZ solutions. Overall the free PZ concentration varies about a factor of 10 from the lean to the rich conditions.
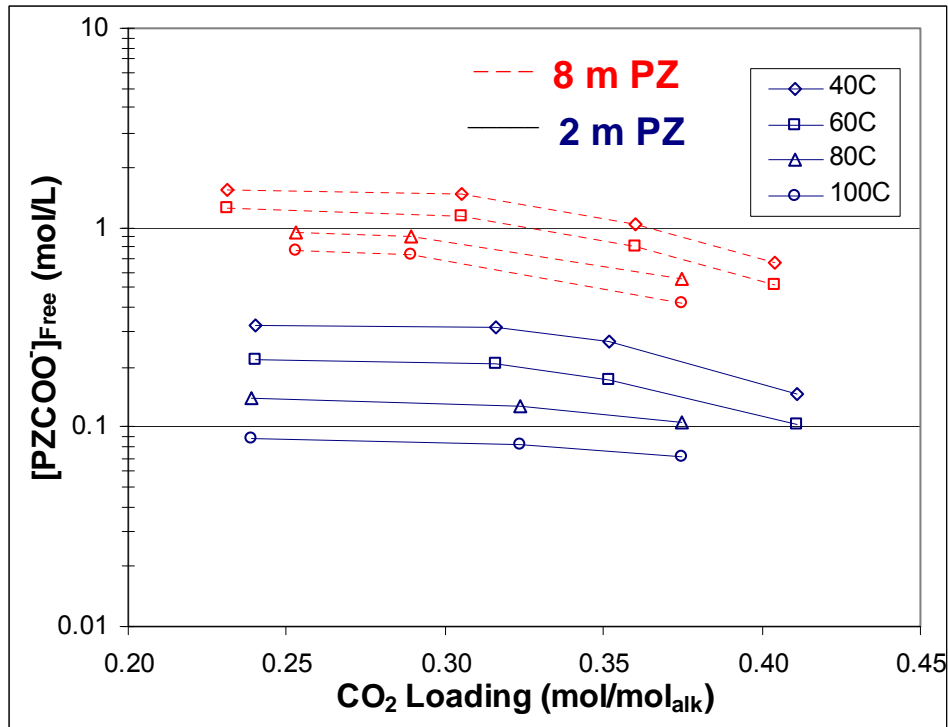
Figure 5.29: PZCOO⁻ concentration from 40–100 ˚C for 2 and 8 m PZ (Hilliard, 2008)

Figure 5.29 shows a very large difference in the PZCOO⁻ concentrations for 2 and 8 m PZ. This was expected since free PZ concentrations are fairly similar in the Hilliard model. The PZ material balance must be satisfied. The free PZ concentration is also a significant function of temperature, especially for the 2 m solution. Again, the order of the free PZ and PZCOO⁻ concentrations in Equation 5.49 is not explicit but they are approximately 1st order since concentrations are squared under the square root.

Figure 5.30 shows the total free amine concentrations in 2 and 8 m PZ.
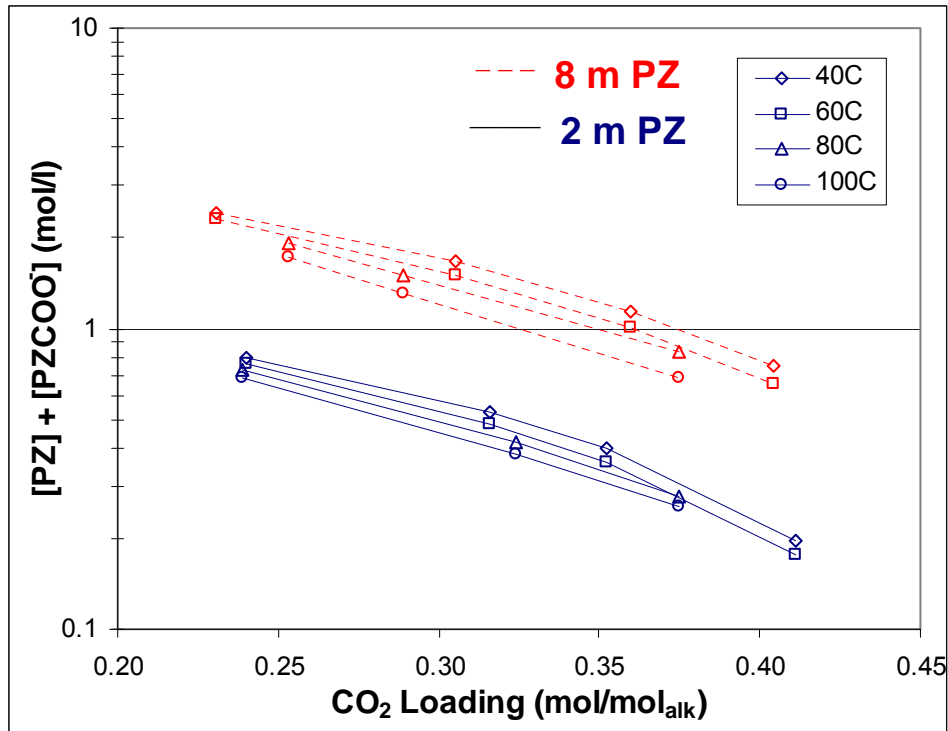
Figure 5.30: Free amine concentrations in 2 and 8 m PZ at 40–100 ˚C (Hilliard, 2008)

The diffusion coefficient of CO_2 is affected by CO_2 loading, temperature, and amine concentration since each of these parameters affects viscosity. Figure 5.31 shows how the calculation of the diffusion coefficient of CO_2 is affected by changes in each of the three parameters.
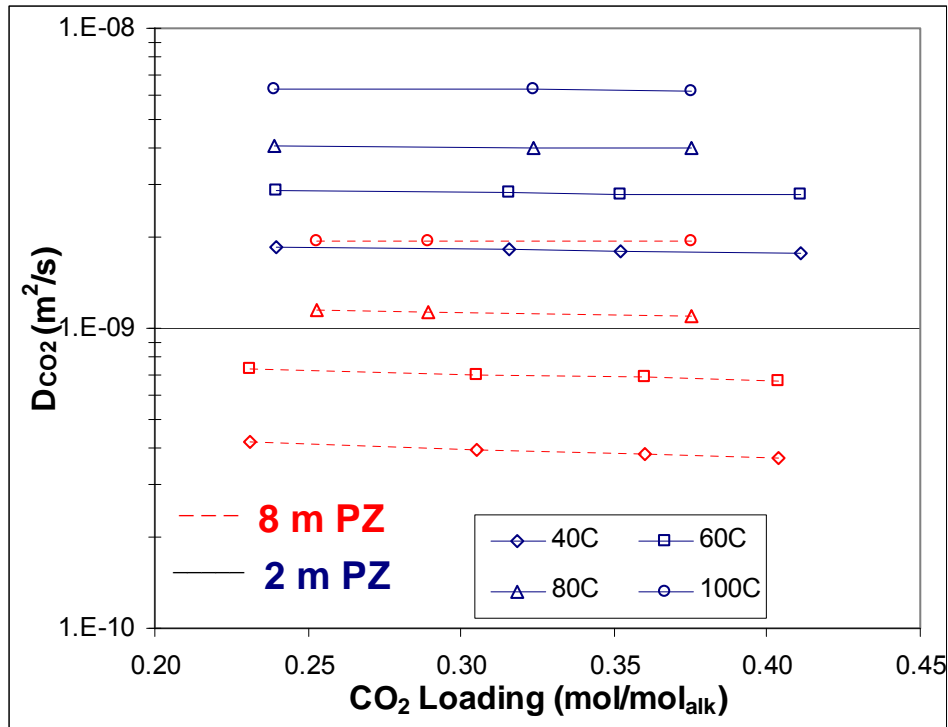
Figure 5.31: Calculated diffusion coefficient of CO_2 from 40–100 $^{\circ}$C in 2 and 8 m PZ

CO_2 loading has a fairly minor effect on the diffusion coefficient of CO_2. Both amine concentration and temperature have very strong effects on D_{CO2}. Higher amine concentration and lower temperature increase viscosity and thus lower diffusion coefficients. The data shown in Figure 5.31 exhibit more than a full order of magnitude difference between the lowest and highest D_{CO2} values. The diffusion coefficient of CO_2 has a 0.5 order effect on the pseudo first order portion of the k_g' expression, Equation 5.49.

5.2.2.2 Parameter Significance

The previous section has shown how each of the parameters in Equation 5.49 varies with changes in CO_2 loading, temperature, and MEA concentration. However, many of the parameters have different dependences on the k_g' expression, and some of these dependences must be approximated due to the form of Equation 5.49. This section attempts to compare the significance of each parameter by showing the changes in each parameter at common conditions. Note that the order of the parameters is only significant to the pseudo first order portion of

Equation 5.49. If diffusion becomes significant at a given condition, the pseudo first order part of Equation 5.49 becomes less meaningful.

Figures 5.32–5.34 are plotted against CO_2 loading for some extreme conditions: 7 and 13 m MEA. For each parameter the explicit or approximated dependence in Equation 5.49 is incorporated. Since Figures 5.32–5.34 each have stated temperatures, only the free PZ and PZCOO$^-$ concentrations, diffusion coefficient of CO_2, and the activity coefficient of CO_2 vary. The rate constant and the Henry's solubility in water are constant in each graph.
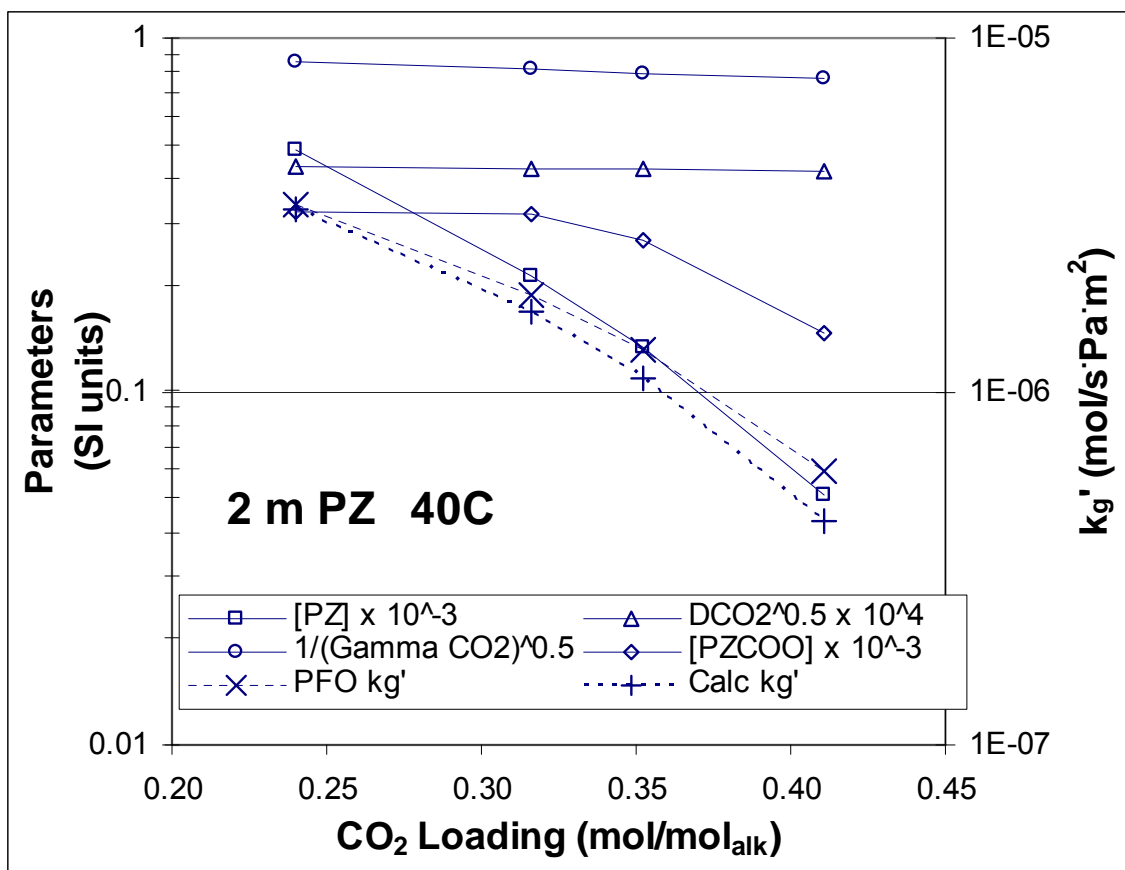
Figure 5.32: Parameter significance versus CO_2 loading for 2 m PZ at 40 ˚C

Figure 5.32 shows that for 2 m PZ at 40 ˚C, the dependences in Equation 5.49 for the activity and diffusion coefficients of CO_2 are minor with CO_2 loading changes. The change in the liquid film mass transfer coefficient, k_g', with increased CO_2 loading is almost completely controlled by the free amine concentrations. The calculated and pseudo first order k_g'

calculations are almost identical at this 40 ˚C condition. This implies that diffusion resistances are negligible. At 40 ˚C, the slope of the equilibrium line is very small making the 2nd term in Equation 5.49 of minimal importance.
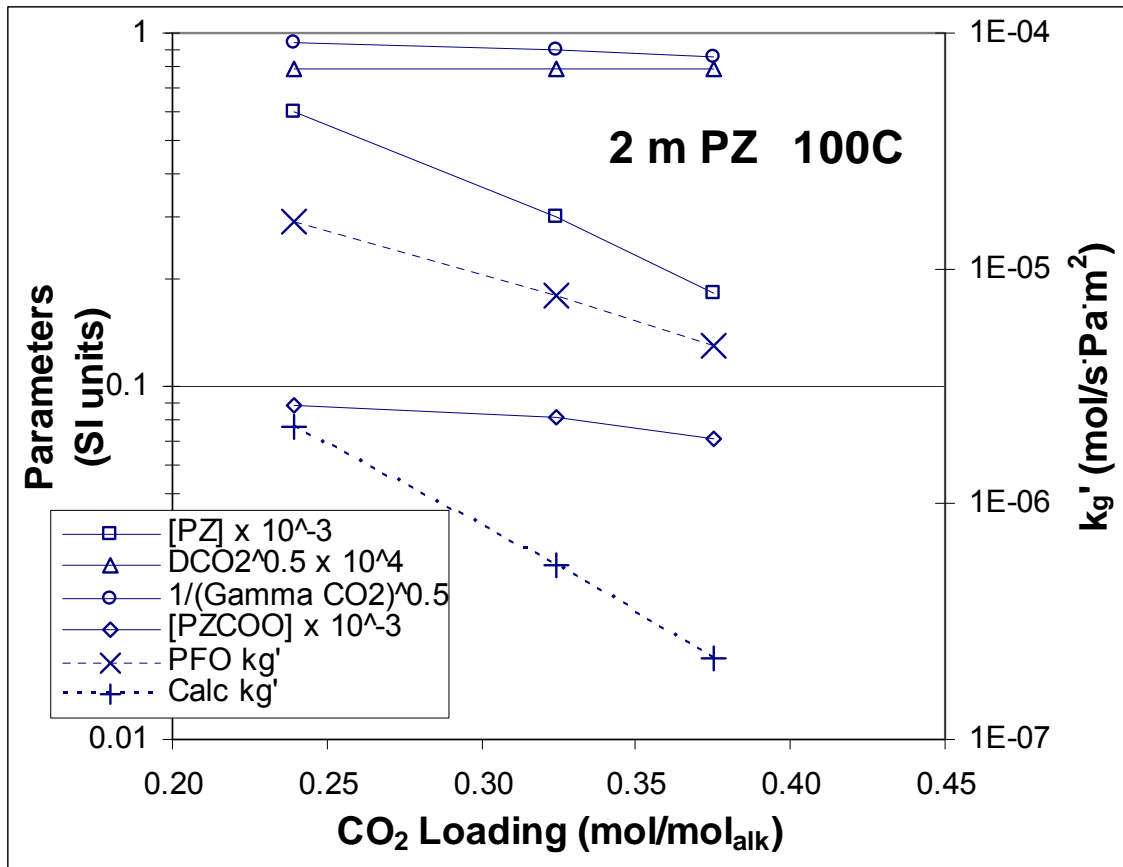
Figure 5.33: Parameter significance versus CO_2 loading for 2 m PZ at 100 ˚C

Figure 5.33 shows the significance of parameters in 2 m PZ but this time at 100 ˚C. Only low loading data are shown here since high loading, high temperature experiments could not be performed in the wetted wall column. Again, the diffusion and activity coefficients of CO_2 change insignificantly with CO_2 loading. At low loading, $PZCOO^-$ concentration remains relatively unchanged. The change in the pseudo first order slope is almost completely due to the change in the free PZ concentration. Note that the parameters range 2 decades in Figure 5.33 while the k_g' scale includes 3 decades. Since this 100 ˚C condition is significantly affected by diffusion resistances, the calculated k_g' values fall far below pseudo first order k_g' values. The

drop is even more marked at the higher loading since less free amine is available. The diffusion of fresh amine to the interface limits mass transfer in this case.
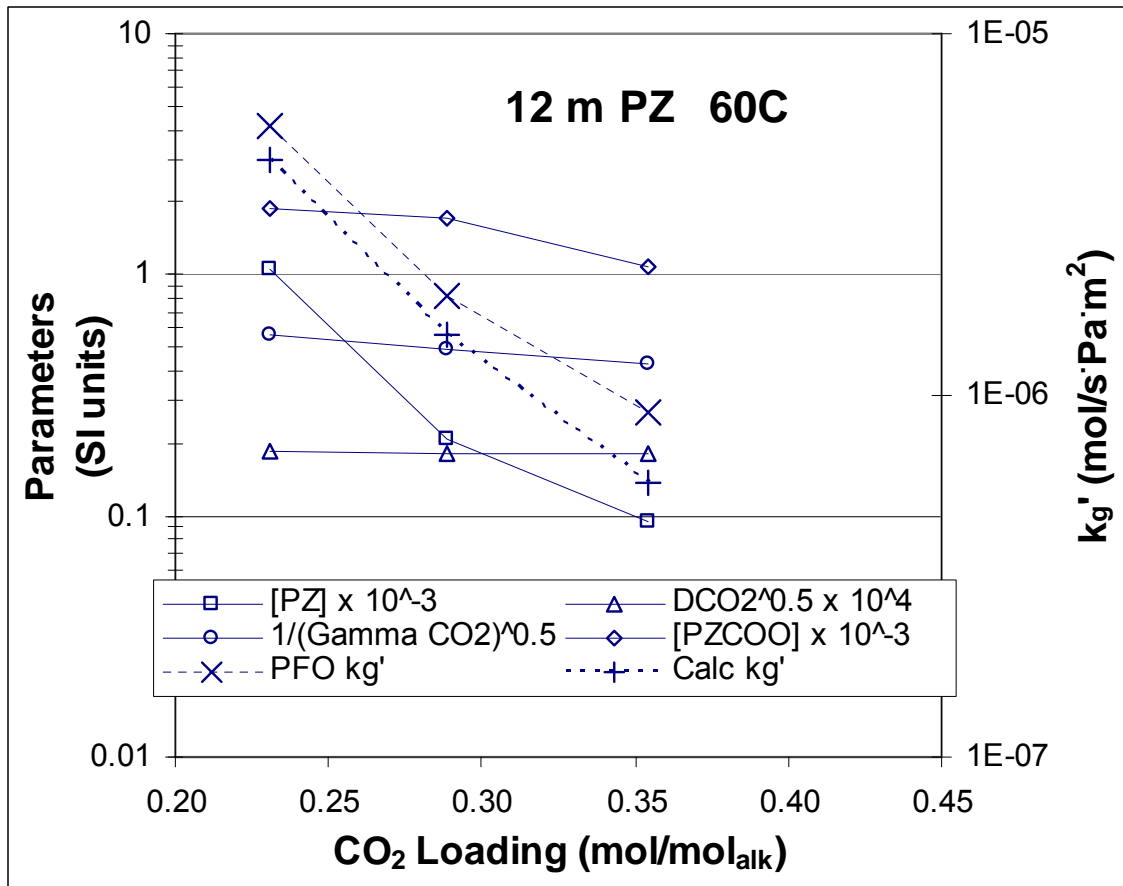
Figure 5.34: Parameter significance versus CO_2 loading for 12 m PZ at 60 ˚C

Figure 5.34 shows the parameter significance as a function of CO_2 loading at 12 m PZ, 60 ˚C. This condition is not soluble at 0.4 loading so that point is not included. Very similar to the previous 2 graphs, k_g' is almost completely controlled by the change in the free PZ concentration. The free PZ carbamate concentration begins to contribute to the drop in k_g' near 0.35 loading. Since this solution is at 60 ˚C, there is only a minor diffusion resistance which increases slightly with increasing CO_2 loading.

Figure 5.35 looks at the effect on the parameters as a function of temperature. Intermediate conditions of 5 m PZ at 0.3 CO_2 loading were selected for this analysis.
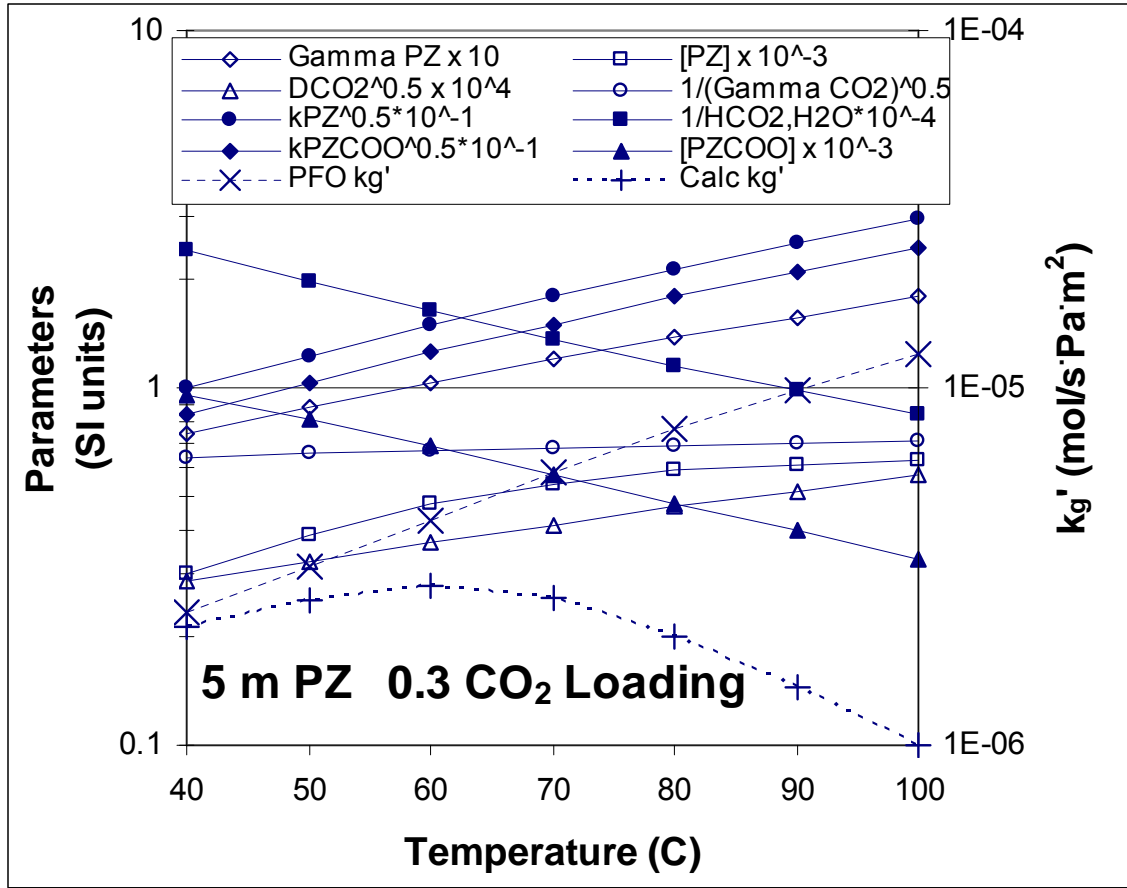
Figure 5.35: Parameter significance versus temperature for 5 m PZ at 0.3 CO₂ loading

Figure 5.35 shows that nearly all the parameters in Equation 5.49 are strongly affected by temperature. Only the activity coefficient of CO_2 dependence remains mostly constant with changes in temperature. The contributions of the PZ activity coefficient, both rate constants, the free PZ concentration, and the diffusion coefficient of CO_2 each increase significantly with increasing temperature. The thermodynamic Henry's constant ($H_{CO2,H2O}$) and the PZCOO⁻ concentration dependences each decrease significantly with increasing temperature. Those 8 parameters give a significant increase in the pseudo first order rate expression with increasing temperature. However, the higher temperature increases the diffusion resistance. The increased diffusion resistance causes k_g' to remain relatively constant from 40 to 70 °C before it begins to decrease. Overall, the predicted k_g' varies a factor of 2 despite 7 parameter dependences which

vary factors of 2–3. The fact that the model accurately predicts the correct temperature behavior is remarkable considering the wide variance in the parameters.

Figure 5.36 shows the significance of each parameter with changes in total PZ concentration. Only 5 parameters are included in Figure 5.36 since the Henry's constant, and rate constants are constant with temperature.
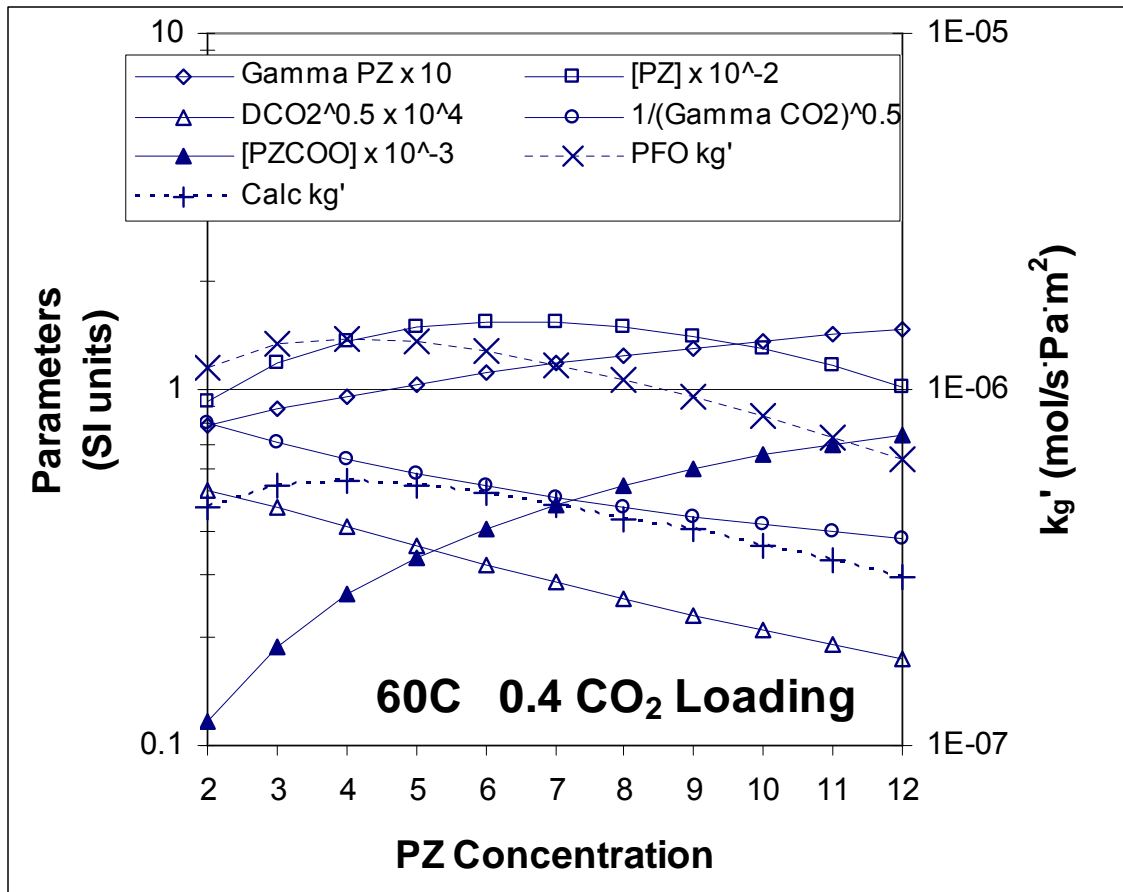
Figure 5.36: Parameter significance versus PZ concentration for 60 °C and 0.4 CO_2 loading

Overall, the parameters do not depend on PZ concentration as much as they depend on temperature. k_g' varies less than a factor of 2 over the 2–12 m PZ range. One interesting point in Figure 5.36 is that the pseudo first order k_g' and the non pseudo first order k_g' remain evenly spaced. This implies that PZ concentration does not affect the fraction of the diffusion resistance. Essentially, the ratio of the 2 terms in Equation 5.49 is unaffected by the PZ concentration.

Figure 5.37 explicitly shows the fraction of diffusion resistance for 2 and 8 m PZ.
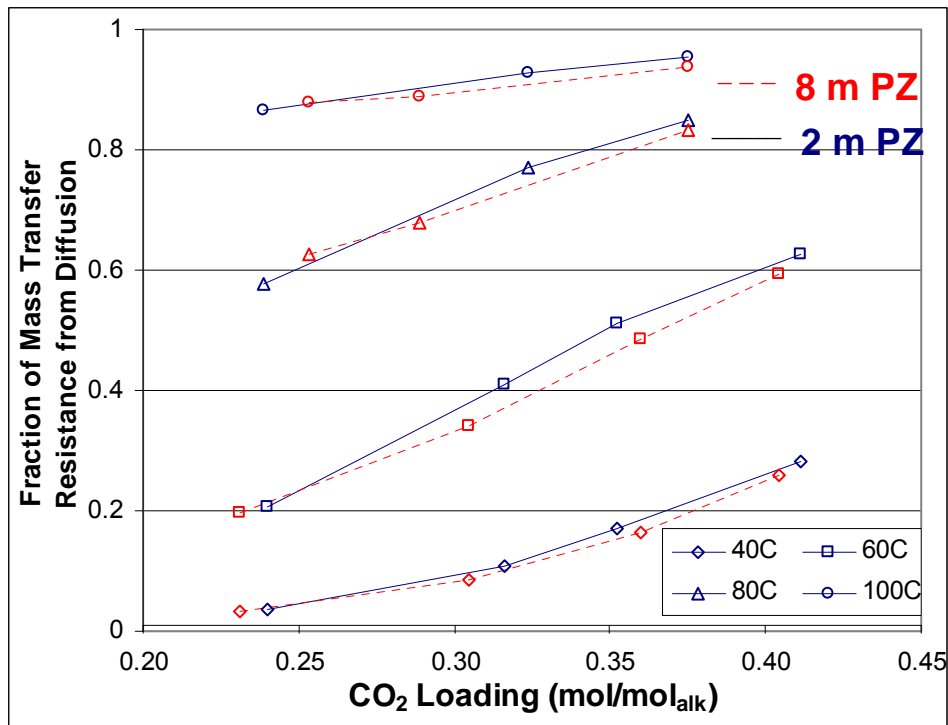
Figure 5.37: Fraction of mass transfer resistance from diffusion for 40–100 °C in 2 and 8 m PZ

As previously stated, the total PZ concentration does not affect the relative importance of the 2 terms in Equation 5.49. The fraction of resistance due to diffusion remains independent of PZ concentration. At higher concentrations, the physical liquid film mass transfer coefficient, k_l^o, decreases due to viscosity changes. However, the slope of the equilibrium line has a concentration term since it is defined in $Pa/(mol/m^3)$. The increased concentration decreases the slope of the equilibrium line. The diffusion term in Equation 5.49 divides k_l^o by the slope and that term is mostly unchanged with changes in total PZ concentration.

5.2.2.3 Error Analysis

Like the MEA error analysis, this is not a typical error analysis. It seeks to show that most of the systematic error has been removed from the model. The lack of systematic error provides a better confidence in the estimation of the parameters which comprise the k_g' expression, Equation 5.49.

Figure 5.38 shows an overall graph of all the wetted wall column data: 2–12 m PZ, 40–100 ˚C, 0.22-–0.41 CO_2 loading. A parity plot is used to compare measured wetted wall column k_g' values to the calculated k_g' from Equation 5.49.
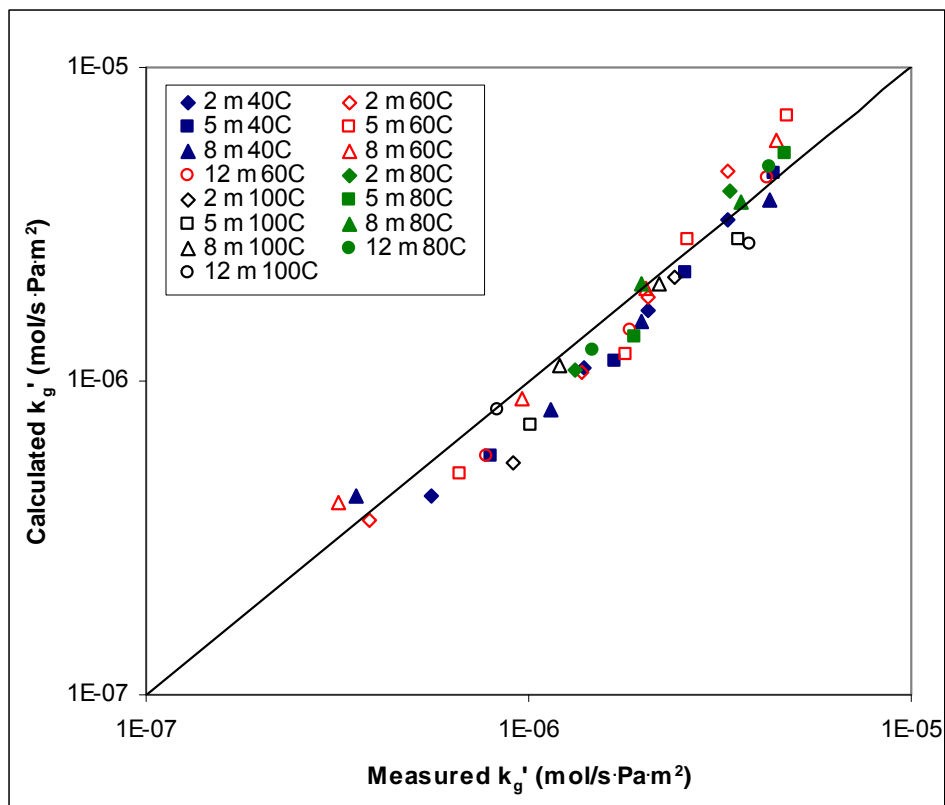
Figure 5.38: Parity plot comparing experimentally measured PZ k_g' values to k_g' values calculated from Equation 5.49.

Figure 5.38 shows that k_g' values vary about a factor of 20 from the lowest loading to the highest loading conditions. A brief view shows that all of the points fall relatively close to the parity line. There are no obvious trends with temperature or amine concentration. However, to analyze and detect the systematic error, a closer look into the data is required. Equation 5.49 represents the measured k_g' in PZ solutions with an average error of 19%.

Figure 5.39 includes all the data in Figure 5.38 but is plotted differently to show systematic trends in CO_2 loading. The y-axis is presented on a log scale so that percentage errors either positive or negative are visually represented clearly.
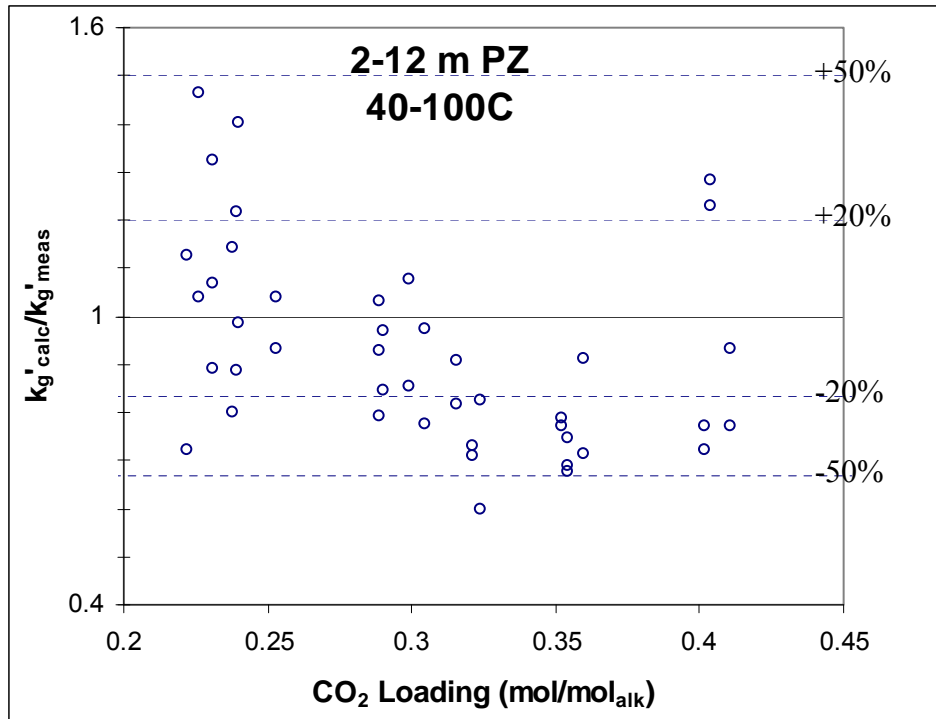
Figure 5.39: Calculated/measured k_g' versus CO_2 loading for 2–12 m PZ wetted wall column conditions

Figure 5.39 has dotted lines to show ±50% error in the estimation of k_g'. All but one of the data points fall within 50% of the measured k_g' values. This is impressive considering the range of conditions. k_g' values vary about a factor of 20. Many of the parameters comprising the k_g' expression change drastically with changes in temperature, PZ concentration, and loading. Overall, there seems to be a minimal systematic trend with CO_2 loading. Intermediate CO_2 loading conditions slightly underestimate k_g' while low and high loading conditions seem to be relatively evenly spaced around the y=1 line.

Figure 5.40 also plots all the experimental data but plots temperature on the x-axis.
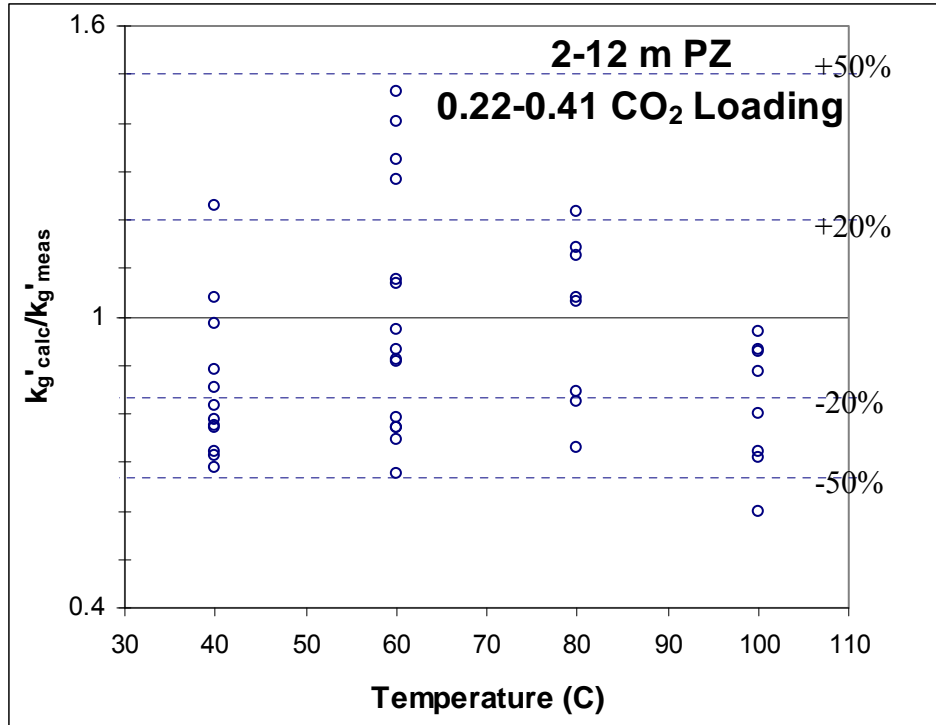
Figure 5.40: Calculated/measured k_g' versus temperature for 2–12 m PZ wetted wall column conditions

Figure 5.40 shows no significant systematic error with increasing temperature. Recalling Figure 5.35, many of the parameters comprising k_g' vary wildly with changes in temperature. The slope of the equilibrium line is also extremely sensitive to temperature. Considering how sensitive Equation 5.49 is to changes in temperature, the lack of systematic error is suggests that the temperature dependent terms are being represented accurately.

Figure 5.41 plots all the experimental data with PZ concentration on the x-axis.
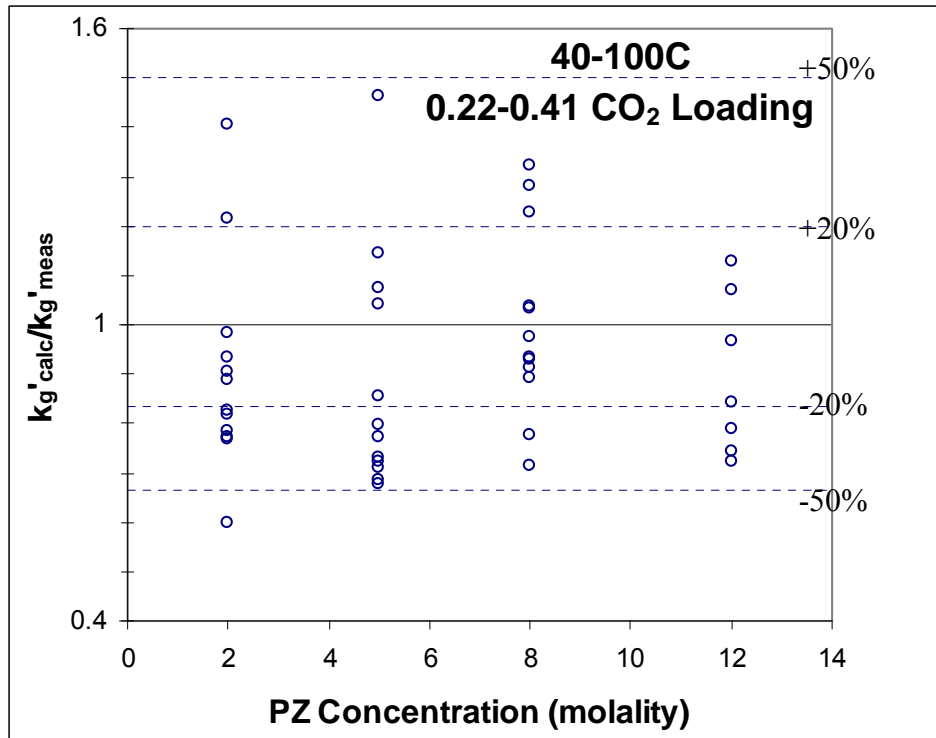
Figure 5.41: Calculated/measured k_g' versus PZ concentration for 2–12 m PZ wetted wall column conditions

Figure 5.41 shows no systematic error in the calculated k_g' values with PZ concentration. Recall that Figure 5.43 showed that many of the parameters vary significantly with changes in amine concentration. Regardless, the concentration dependent terms seems to be properly represented.

Figures 5.39–5.41 show that systematic error with respect to CO_2 loading, temperature, and PZ concentration have essentially been removed from the model. The absence of significant systematic error increases confidence both in the model and in the determination of each parameter in the k_g' expression.

5.2.3 Model Comparisons to Literature Data

5.2.3.1 MEA Model Comparisons to Literature Data

Figure 5.42 shows a comparison of the model to concentrated MEA rate data by Aboudheir (2002) and Hartono (2009). Aboudheir uses a laminar jet absorber which has a very

fast liquid film physical mass transfer coefficient due to short contact times. To compare to this pseudo first order condition, the pseudo first order results of the model are plotted in Figure 5.42. The Hartono data can also be compared to the pseudo first order model results since the diffusion of reactants and products is unimportant at concentrated, unloaded conditions.
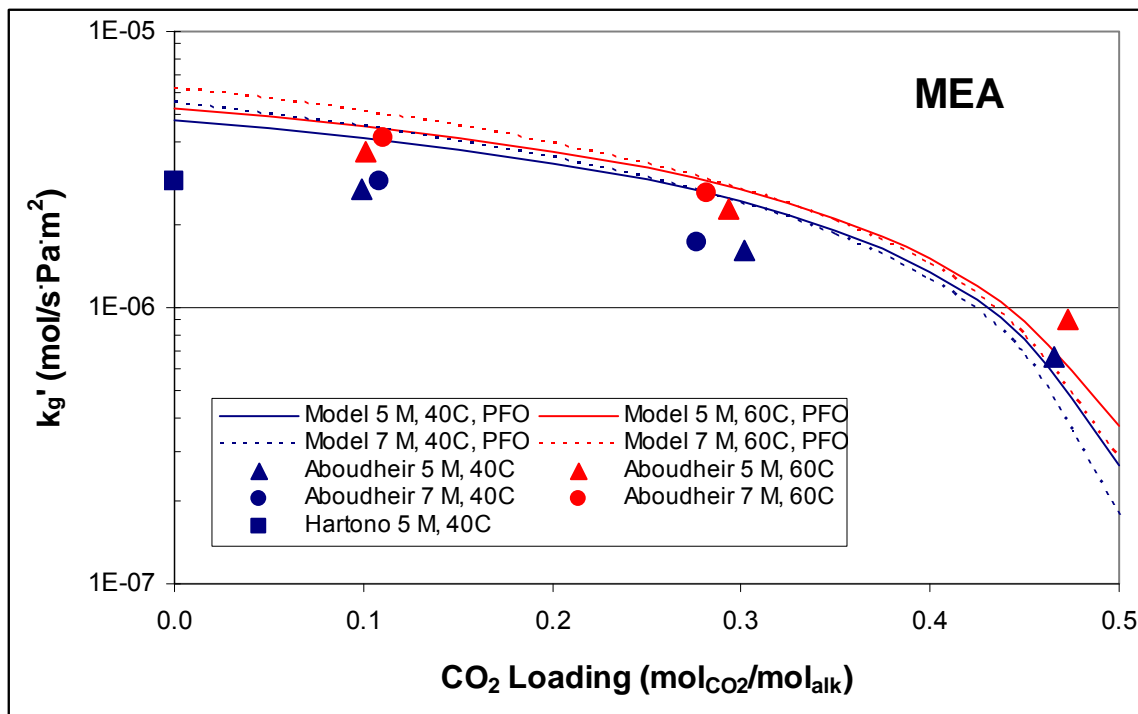
Figure 5.42: Pseudo first order model results compared to 5 and 7 m MEA literature data (Aboudheir 2002; Hartono 2009)

The pseudo first order model results for both 7 and 13 m show temperature trends similar to the Aboudheir data. The model also matches the k_g' values fairly well over the entire CO_2 loading range. The model shows a more drastic change in kg' at higher loading. This was seen in all the experimental data (Figure 4.10). The wetted wall column experimental data could not justify the flattening of the k_g' values at lower CO_2 loading. The model predicts this observed trend.

The model can also be extrapolated to 0 loading and more dilute MEA concentrations to evaluate recent data by Hartono (2009).
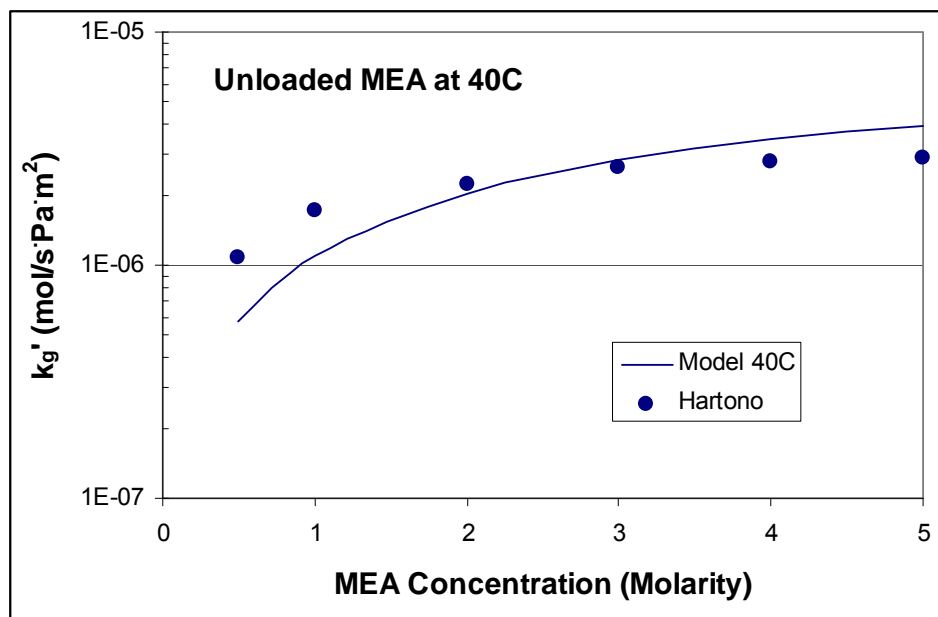
Figure 5.43: MEA model comparison to Hartono (2009) at 40 ˚C

Overall, the data seem to match the Hartono data fairly well. Rates are under-predicted at low MEA concentrations and slightly over-predicted at high MEA concentrations. The model neglects base catalysis by water. This could be significant to the rates at very low MEA concentrations.

5.2.3.2 Comparison to Cullinane (2006) Piperazine Rate Constants

Figure 4.12 has shown that 1.8 m PZ from the Cullinane model (2005) compares very favorably to 2 m PZ experiments in the wetted wall column. This analysis seeks to compare the rate expressions also.

Due to differences in the form of the Cullinane rate expression and the form of the rate expression used in this work (Equation 5.40), it is difficult to make a straightforward rate constant comparison. An attempt has been made to compare unloaded 1 M PZ.

Cullinane (2006) reports an overall rate constant of 102,000 s^{-1} at 25 ˚C for unloaded 1 M PZ. This value results from the combination of the k^o_{PZ-PZ} and $k^o_{PZ-H_2O}$ rate constants multiplied by the PZ and water molarity, respectively. This model ignores the water catalysis effect. At 1

M PZ this effect can be significant. It is easier to exclude the water catalysis from the Cullinane expression to obtain a 70,100 s^{-1} rate expression only considering PZ catalysis.

The current model can be extrapolated to 1 M but the difference in the form of the expression must be considered, particularly the activity coefficients. Cullinane utilized a concentration-based model. Effectively, the Cullinane rate constants include MEA and CO_2 activity coefficients used in this model. The CO_2 activity coefficient approaches 1 for unloaded, dilute solutions. The unloaded 25 ˚C PZ activity coefficient was estimated as 0.0393 by the model. This model predicts the rate constant times the square of the PZ activity coefficient to yield 78,600 s^{-1} at 25 ˚C. This compares very favorably to the 70,100 s^{-1} value reported by Cullinane (2006).

5.2.3.3 *Piperazine Model Comparisons to Literature Data*

Figure 5.44 compares the PZ model to work done by Cullinane. Two unloaded, 1.2 M PZ data points are compared. A 1.8 m PZ model developed by Cullinane is also compared. Although Cullinane did not measure rates in CO_2 loaded aqueous PZ, he was able to build the model using unloaded PZ and loaded K_2CO_2/PZ rate data.
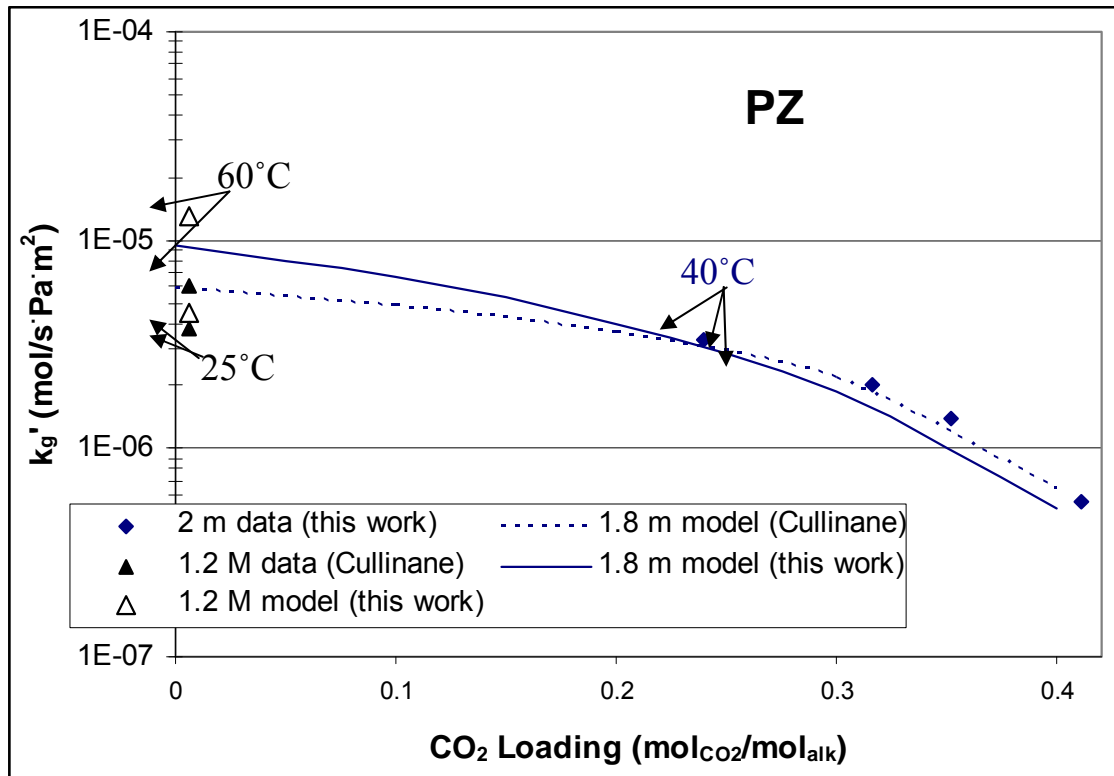
Figure 5.44: PZ model comparison to Cullinane (2005) model and data

Figure 5.44 shows an excellent match between the two 1.8 m PZ models and the 2 m PZ rate data. The PZ model also does a fair job of predicting k_g' for unloaded PZ solutions. Both 25 and 60 °C experiments by Cullinane are adequately represented by the PZ model. The model was unable to accurately represent the 0.06–0.30 M PZ data from Bishnoi (2000). The Hilliard (2008) model did not seem to accurately speciate the dilute PZ solutions. The model predicted almost all the CO_2 being converted to bicarbonate, rather than $PZCOO^-$.

5.2.4 Significant Case: 20 °C Absorber Operation

Experiments included in this work test a large range of amine concentrations. MEA concentrations greater than 13 m and PZ concentration greater than 12 m are unlikely to be relevant for industrial use. The 40–100 °C temperatures tested also exhibit a large range of conditions. 120 °C is not a particularly interesting condition because mass transfer in those solutions would be almost completely controlled by diffusion resistances. Special equipment designs, such as using trays instead of packing, could be used to increase the physical liquid film

mass transfer coefficient, k_l^o. This model is not particularly useful in evaluating that condition because k_l^o in this model would be very different than the industrial k_l^o. Amine solutions at 20 ˚C could be analyzed accurately by this model since diffusion resistance would be negligible.

In some locations such as the North Sea it may be feasible to cool amine solutions down to 20 ˚C. The colder amine solution would allow for a richer solution at the bottom of the absorber. This analysis uses the spreadsheet model to explore the kinetic implications of operating an absorber at 20 ˚C. The analysis has been carried out with 3 solutions, 7 and 13 m MEA and 8 m PZ.

The bottom of an absorber with flue gas from coal combustion will be approximately 12% CO_2 near atmospheric pressure. This 12 kPa partial pressure must be significantly more than the partial pressure of the amine solution for significant absorption to occur. Due to the reduction of CO_2 driving force and the slower rates at the bottom of the absorber it is unlikely that the amine solution would have a CO_2 loading exhibiting more than a 6 kPa partial pressure. Therefore 20 ˚C amine solutions are analyzed up to a CO_2 loading which has a 6 kPa CO_2 partial pressure.

None of the 20 ˚C conditions encounter significant diffusion limitations so no adjustment in k_l^o is required to adjust to an industrial design.

5.2.4.1 7 and 13 m MEA

Using the spreadsheet model, the CO_2 partial pressure and liquid film mass transfer coefficient has been calculated for 0.25–0.6 loading in 7 and 13 m MEA. The results are included in Table 5.4.

Table 5.4: Calculated CO$_2$ partial pressure and k$_g$' for 7 and 13 m MEA at 20 ˚C

MEA	Temp	CO$_2$ Loading	P*$_{CO2}$	k$_g$'
m	C	mol$_{CO2}$/mol$_{alk}$	Pa	mol/s·Pa·m^2
7	20	0.25	1.2	2.5E-06
		0.3	3.1	2.1E-06
		0.35	8.8	1.7E-06
		0.4	28	1.2E-06
		0.45	95	6.3E-07
		0.5	353	1.7E-07
		0.55	1433	3.7E-08
		0.6	6345	1.5E-08
13		0.25	1.2	2.5E-06
		0.3	3.1	2.0E-06
		0.35	8.8	1.5E-06
		0.4	28	1.0E-06
		0.45	95	5.3E-07
		0.5	353	8.7E-08
		0.55	1433	1.2E-08
		0.6	6345	5.6E-09

The values in Table 5.4 at 20 ˚C are compared to 40–100 ˚C conditions in Figure 5.45.

7 m MEA conditions are denoted by solid lines while 13 m MEA is represented by dashed lines.
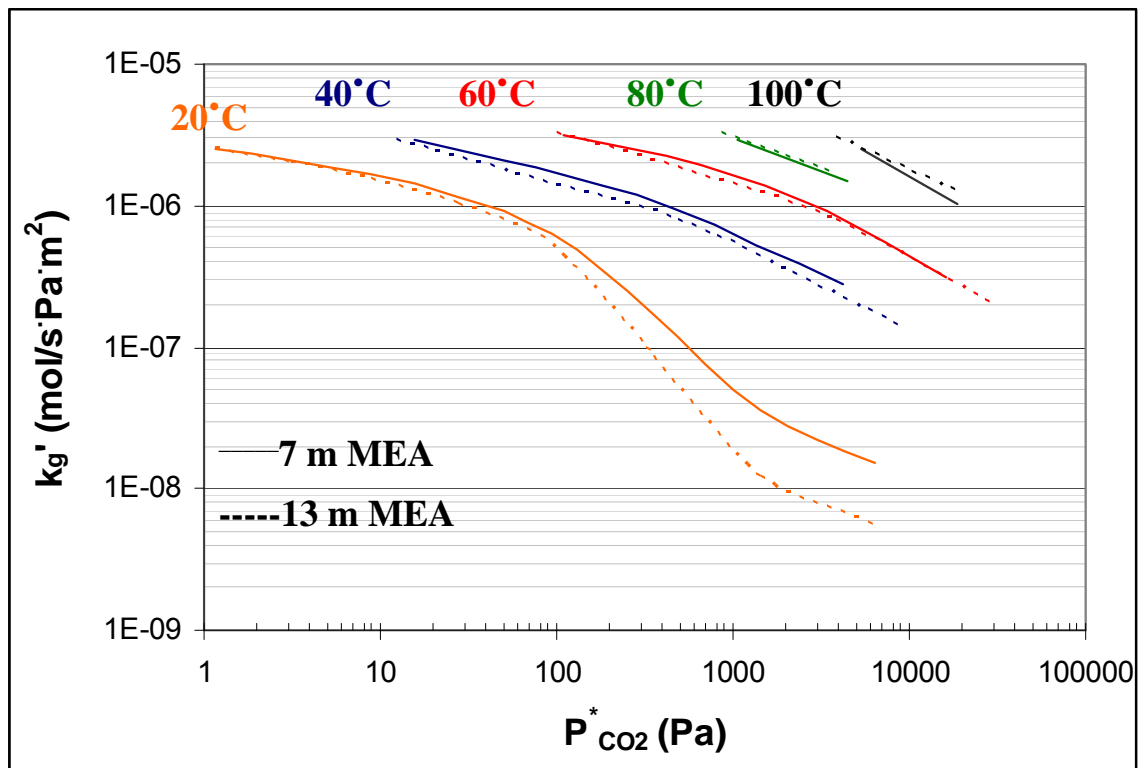
Figure 5.45: Predicted CO$_2$ absorption/desorption rates in 7 and 13 m MEA at 20–100 ˚C

Figure 5.45 shows that the 20 ˚C solutions actually perform similarly to the higher temperature data until near a 100 Pa partial pressure, 0.45 CO_2 loading. Above this loading the free amine concentration seems to be too small to produce significant rates. Rates at the rich end of the absorber in the 2–5 kPa range are 10 times slower than rates at 40 ˚C.

The 20 ˚C case is interesting because the colder temperatures allow for the amine solution to achieve higher CO_2 loading at the bottom of the absorber. The higher CO_2 loading leads to a lower energy consumption in the stripper. However, for MEA, CO_2 loadings at 20 ˚C seem too rich to produce acceptable rates. Operating with a 20 ˚C rich solution at the bottom of the absorber does not seem to be advantageous for MEA solutions.

5.2.4.2 8 m PZ

Ignoring possible PZ solubility issues, 8 m PZ has also been analyzed at 20 ˚C by the spreadsheet model. Table 5.5 includes the obtained CO_2 partial pressure and k_g' results.

Table 5.5: Calculated CO_2 partial pressure and k_g' for 8 m PZ at 20 ˚C

PZ	Temp	CO_2 Loading	P^*_{CO2}	k_g'
m	C	mol_{CO2}/mol_{alk}	Pa	$mol/s\,Pa\,m^2$
		0.2	4.8	1.7E-06
		0.25	17	1.7E-06
		0.3	65	1.1E-06
8	20	0.35	243	6.7E-07
		0.4	932	3.7E-07
		0.45	3627	1.4E-07
		0.5	14344	1.1E-08

The values in Table 5.5 at 20 ˚C are compared to 40–100 ˚C conditions in Figure 5.46.
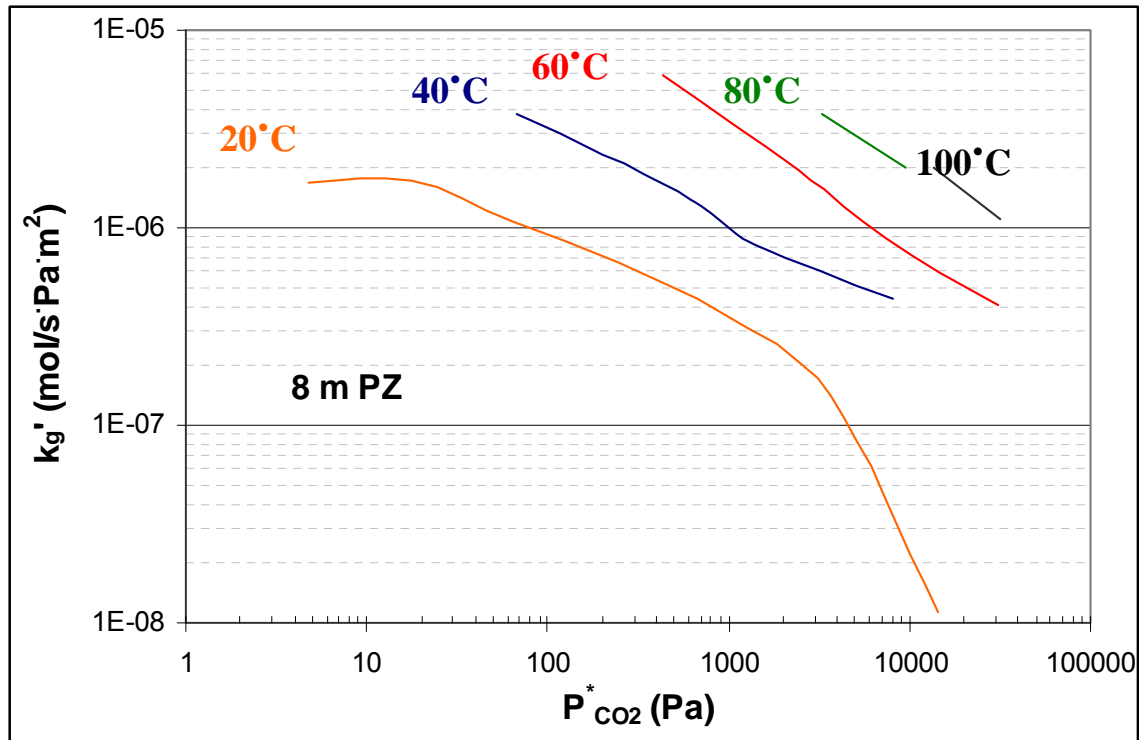
Figure 5.46: Predicted CO_2 absorption/desorption rates in 8 m PZ at 20–100 ˚C

8 m PZ rates at the rich end of the absorber in the 2–5 kPa range are about 3 times slower than rates at 40 ˚C. However, the 20 ˚C case achieves higher CO_2 loadings and a larger CO_2 capacity which may yield enough energy savings to offset the slower rates. A comprehensive absorber/stripper model incorporating both capital and operating costs would be required to quantify if the 20 ˚C case were more economically favorable than the 40 ˚C condition. This analysis ignores PZ solubility issues.

5.3 ASPEN PLUS® RATESEP™ MODELING

In addition to the spreadsheet model, an Aspen Plus® RateSep™ model was created. Rather than predicting the mass transfer coefficient, k_g', the Aspen Plus® RateSep™ model can predict CO_2 flux. This model can be fitted to wetted wall column data and then scaled up to industrial conditions.

As a starting point the e-NRTL thermodynamic framework of the Hilliard (2008) model was used. However, this model is not capable of handling the high amine concentration and high

temperature conditions which were tested in the wetted wall column experiments. Hilliard regressed data up to 11 m MEA and 5 m PZ. CO_2 partial pressure estimates are reliable up to 60 ˚C. Wetted wall column experiments utilized amine concentrations up to 13 m MEA and 12 m PZ at 100 ˚C. The Hilliard model did not accurately extrapolate to these higher amine concentrations.

5.3.1 Physical design

The wetted wall column is modeled as an Aspen Plus® RateSep™ column. The actual wetted wall column has an annulus geometry since the liquid film flows over a rod and the gas flows around it. The Aspen Plus® RateSep™ module cannot mimic this geometry. The column in the model is designed as a typical, cylindrical column. The diameter was adjusted so the column would have the same cross-sectional area as the wetted wall column. This results in equivalent gas velocities in the wetted wall column and the model. The design height of the column is the height of the wetted wall column, 9.1 cm.

Mimicking the wetted area of the column requires a similar manipulation. In the wetted wall column, the contact area is the surface area of a metal rod which is coated with a thin film of liquid. The model assumes an arbitrary packing. An interfacial area Fortran subroutine was written to ensure that the wetted area of the wetted wall column, 38.52 cm^2, would be duplicated in the model.

The model operates with 3 countercurrent stages. The model does not consider pressure drop.

5.3.2 Primary Monoethanolamine Data Regression

A modified VLE model was created with the same sequential regression approach that Hilliard employed. Hilliard (2008) used heat of absorption, nuclear magnetic resonance, heat capacity, amine partial pressure, and CO_2 partial pressure data to regress thermodynamic parameters. This model neglects the heat of absorption data.

The main MEA data regression includes nuclear magnetic resonance, heat capacity, amine partial pressure, and CO_2 partial pressure from Hilliard. Increased importance was placed on the MEA partial pressure data since these data lead to MEA activity coefficients which are very important to the rate behavior. CO_2 partial pressure data from Jou (1995) and Dugas (Rochelle, Sexton et al., 2009) were also included in the regression. The 6 highest CO_2 loading data points from Dugas were excluded from the regressed data because they did not match Hilliard and Jou data very well, recall Figure 4.2. The MEA VLE model includes data ranging from 3.5 m MEA to 13 m MEA with temperatures from 25 to 120 ˚C. Only data with CO_2 loadings between 0.25 and 0.6 mol_{CO2}/mol_{MEA} were included in the regression.

In an effort to simplify the regressions and obtain better CO_2 partial pressure predictions, significantly fewer parameters were regressed in this work than that of Hilliard. Some binary interaction parameter pairings were deemed insignificant and deleted. The complexity of the temperature dependence of the molecule, anion-cation pairings was also simplified by deleting some of the temperature dependent terms.

Table 5.6 gives the regressed parameters for the system. Heat of formation, free energy of formation, heat capacity and molecule, anion-cation binary interaction parameters were regressed. Figures 5.47–5.50 show the CO_2 partial pressure fit of the model against 7, 9, 11, and 13 m MEA. In each figure, the points include various amine concentrations since amine concentration does not seem to affect the CO_2 partial pressure, at least at CO_2 loadings below 0.45.

Table 5.6: Regressed Thermodynamic Parameters for the MEA/CO₂/H₂O System

Parameter	Component i	Component j	Value (SI units)	Std Dev
DGAQFM/1	MEACOO-		-496158959	1.74E+11
DHAQFM/1	MEACOO-		-697951174	1.74E+11
CPAQ0/1	MEACOO-		130947.417	1.74E+11
GMELCC/1	H2O	(MEA+,HCO3-)	14.8093684	0.64199251
GMELCD/1	H2O	(MEA+,HCO3-)	-86.190984	186.650961
GMELCC/1	(MEA+,HCO3-)	H2O	-5.0211477	0.13851185
GMELCC/1	H2O	(MEA+,MEACOO-)	14.5192817	1.37165807
GMELCD/1	H2O	(MEA+,MEACOO-)	-296.81634	433.860025
GMELCC/1	(MEA+,MEACOO-)	H2O	-5.2861271	0.06415175
GMELCC/1	MEA	(MEA+,MEACOO-)	59.9691675	3962.31577
GMELCD/1	MEA	(MEA+,MEACOO-)	1058.22129	1.74E+11
GMELCC/1	(MEA+,MEACOO-)	MEA	4.36696398	26.194822
NRTL/1	H2O	MEA	-126.92543	23.7472366
NRTL/2	H2O	MEA	4058.34113	1007.37814
NRTL/5	H2O	MEA	20.7342464	3.92797305
NRTL/6	H2O	MEA	-0.0243425	0.0061571
NRTL/1	MEA	H2O	0.58508807	5.29404778
NRTL/2	MEA	H2O	774.507514	1775.65575
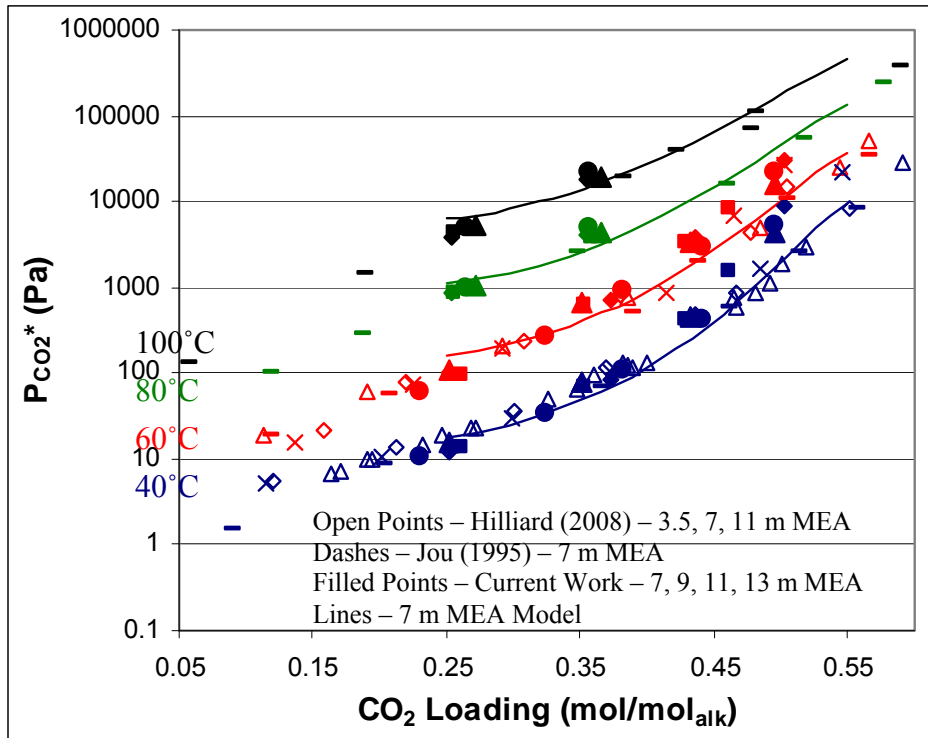
Figure 5.47: CO₂ Partial Pressure Regression Results – 7 m MEA
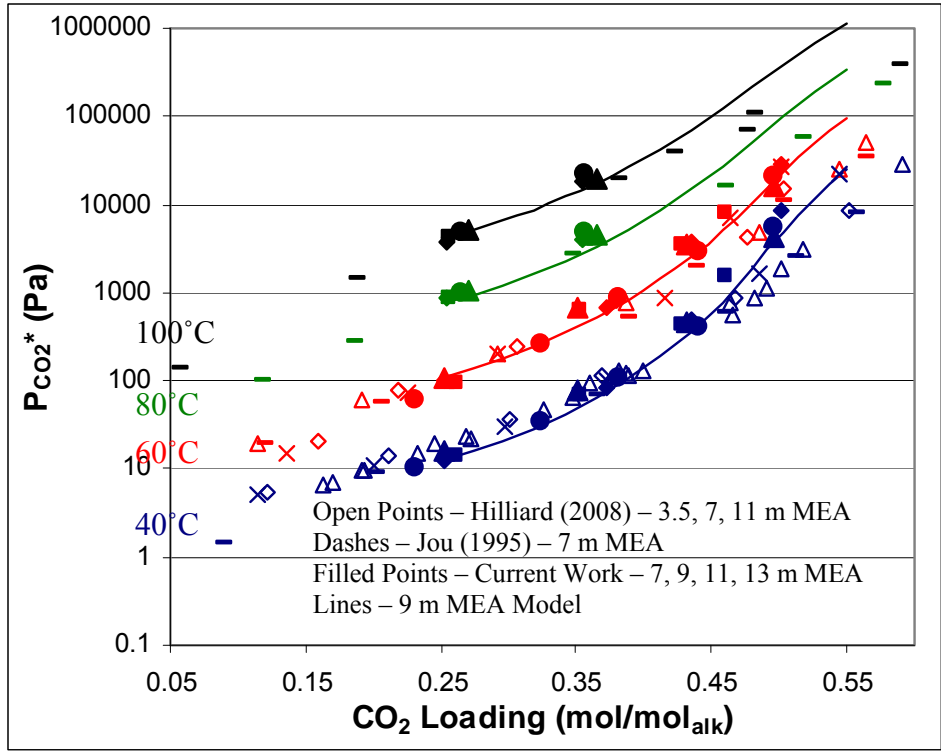
Figure 5.48: CO_2 **Partial Pressure Regression Results – 9 m MEA**
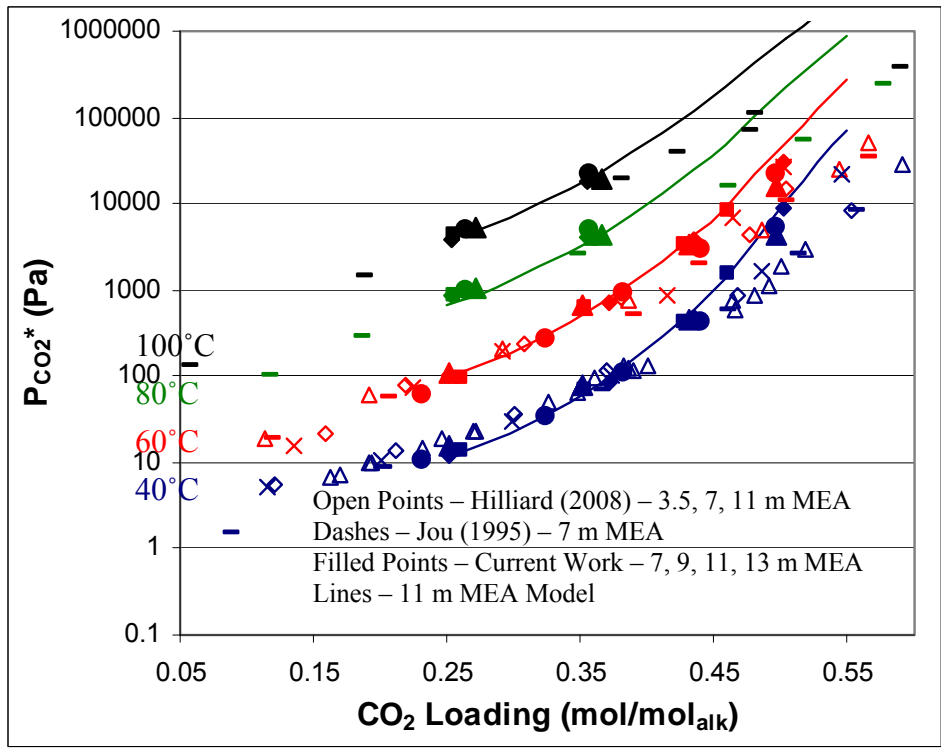
Figure 5.49: CO_2 **Partial Pressure Regression Results – 11 m MEA**
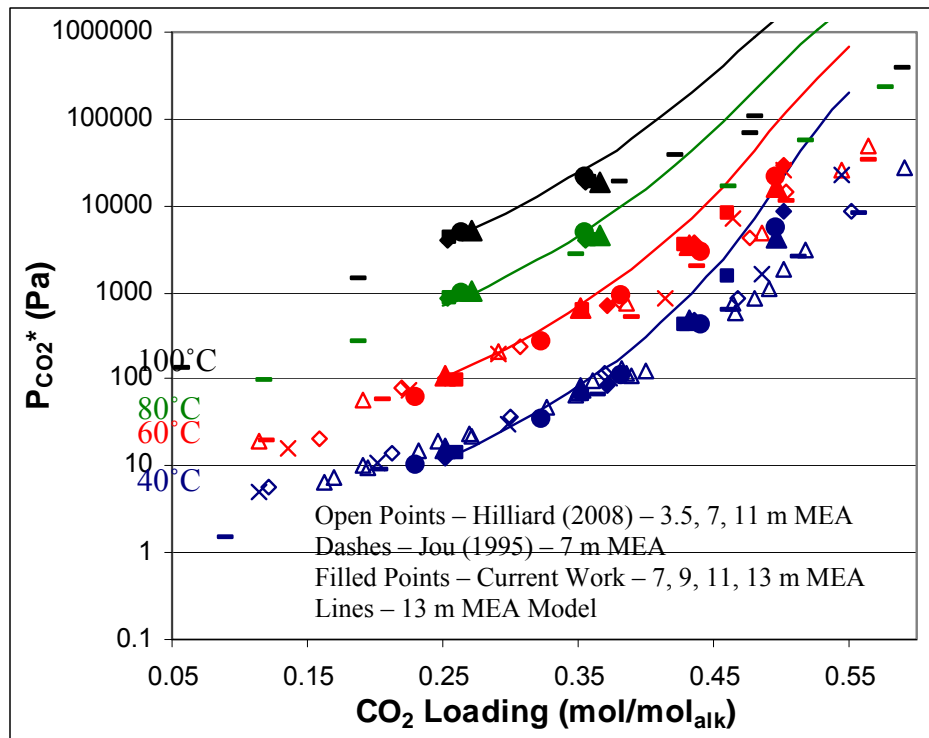
Figure 5.50: CO₂ Partial Pressure Regression Results – 13 m MEA

The regression fits the 7 m MEA data at each of the temperatures. At higher amine concentrations the regression accuracy declines, particularly at the rich loadings. The model is least accurate where the bicarbonate concentration is highest, 13 m MEA at high CO_2 loading. Although the regressed CO_2 partial pressure fit is not exceptional, it seems to be the best that can be achieved.

5.3.3 Primary Piperazine Data Regression

A satisfactory regression of the PZ data was not obtained. PZ and PZ carbamate activity coefficients could not be represented properly. Since the rate model has a very strong dependence on the activity coefficients, a significant error in the PZ and PZ carbamate activity coefficient representation undermines the integrity of the model. CO_2 activity coefficients could not be manually adjusted to desired values by adjusting electrolyte pair parameters. An Aspen Plus® RateSep™ model for PZ solutions was not created.

5.3.4 CO$_2$ loading adjustment

Since the predicted CO$_2$ partial pressure does not always fit the experimental data, the model has the capability to predict CO$_2$ absorption when desorption should be occurring. Any conditions operating near the CO$_2$ equilibrium partial pressure will also produce drastically incorrect CO$_2$ fluxes. In a model designed to predict flux, this is unacceptable. Therefore, the CO$_2$ loading of the inlet amine solutions was adjusted to fit the CO$_2$ partial pressure exactly. This solves the unacceptable CO$_2$ driving force issue at the expense of adjusting the free amine concentration. The error introduced into the model by adjusting the free amine concentration is very much less than not correcting the erroneous CO$_2$ partial pressure. Table 5.7 gives the MEA wetted wall column conditions and the adjusted Aspen Plus$^\circledR$ loading that was used to match the measured equilibrium partial pressure.

Table 5.7: Wetted wall column conditions with the adjusted Aspen Plus$^\circledR$ CO$_2$ loading to fit CO$_2$ partial pressure data

MEA	Temp	Experimental CO$_2$ Loading	Adjusted Aspen CO$_2$ Loading	P*$_{CO2}$	MEA	Temp	Experimental CO$_2$ Loading	Adjusted Aspen CO$_2$ Loading	P*$_{CO2}$
m	C	mol/mol$_{alk}$	mol/mol$_{alk}$	Pa	m	C	mol/mol$_{alk}$	mol/mol$_{alk}$	Pa
7	40	0.252	0.218	15.7	11	40	0.261	0.268	14.0
		0.351	0.379	77			0.353	0.355	67
		0.432	0.456	465			0.428	0.426	434
		0.496	0.522	4216			0.461	0.461	1509
	60	0.252	-	109		60	0.261	0.249	96
		0.351	0.383	660			0.353	0.361	634
		0.432	0.460	3434			0.428	0.428	3463
		0.496	0.516	16157			0.461	0.455	8171
	80	0.271	0.237	1053		80	0.256	0.271	860
		0.366	0.387	4443			0.359	0.359	3923
	100	0.271	-	5297		100	0.256	0.261	4274
		0.366	0.375	19008			0.359	0.354	18657
9	40	0.231	0.228	10.4	13	40	0.252	0.253	12.3
		0.324	0.329	34			0.372	0.349	84
		0.382	0.389	107			0.435	0.414	491
		0.441	0.440	417			0.502	0.485	8792
		0.496	0.507	5354		60	0.252	0.248	100
	60	0.231	-	61			0.372	0.349	694
		0.324	0.324	263			0.435	0.414	3859
		0.382	0.391	892			0.502	0.472	29427
		0.441	0.438	2862		80	0.254	0.264	873
		0.496	0.501	21249			0.355	0.343	3964
	80	0.265	0.279	979		100	0.254	0.248	3876
		0.356	0.384	4797			0.355	0.337	18406
	100	0.265	0.268	4940					
		0.356	0.376	21534					

In most cases the change in loading is insignificant. At the highest CO_2 loadings, near 0.5, even relatively small changes in the CO_2 loading can drastically affect the free MEA concentration. This introduces a very large amount of error into the Aspen Plus® RateSep™ results for these high CO_2 loading conditions.

Three conditions did not produce Aspen Plus® CO_2 loadings which match the partial pressure. These solutions suffer from CO_2 partial pressure curves which flatten at lower CO_2 loading. The Aspen Plus® CO_2 loading could either not be calculated or was drastically different in these three cases.

5.3.5 CO₂ Activity Coefficients

CO_2 activity coefficients were not represented correctly by the main data regressions because no data concerning CO_2 activity coefficients were included in the regression. CO_2 activity coefficients in MEA solutions were characterized outside of Aspen Plus® using experimental data (Browning and Weiland, 1994; Hartono, 2009). The regressed dependences (Equation 5.11) were implemented into the model by manually adjusting 2 electrolyte pair interaction parameters. Table 5.8 shows the obtained fit of the Aspen Plus® calculated CO_2 activity coefficient with the calculated CO_2 activity coefficient from Equation 5.11.

Table 5.8:   Adjusted electrolyte pair interaction parameters to fit CO₂ activity coefficient data

	Component i	Component j	Value	Default Value
GMELCC	MEA+,MEACOO	CO2	-10.25	-8
GMELCE	MEA+,MEACOO	CO2	175	0

Table 5.9: CO_2 activity coefficient fit in MEA solutions

MEA	CO_2 Loading	Temp	Calc γ_{CO2}[1]	Model γ_{CO2}	Calc γ_{CO2}[1]/Model γ_{CO2}
m	mol/mol$_{alk}$	C			
7	0.25	40	1.54	1.45	0.95
7	0.25	60	1.43	1.16	0.81
7	0.25	80	1.34	1.12	0.83
7	0.25	100	1.26	1.21	0.96
7	0.35	40	1.72	1.68	0.98
7	0.35	60	1.60	1.29	0.81
7	0.35	80	1.50	1.27	0.85
7	0.35	100	1.41	1.44	1.02
7	0.45	40	1.90	1.92	1.01
7	0.45	60	1.76	1.42	0.81
11	0.25	40	1.76	1.90	1.08
11	0.25	60	1.63	1.41	0.86
11	0.25	80	1.53	1.36	0.89
11	0.25	100	1.44	1.53	1.06
11	0.35	40	2.01	2.20	1.10
11	0.35	60	1.87	1.56	0.84
11	0.35	80	1.75	1.54	0.88
11	0.35	100	1.65	1.88	1.14
11	0.45	40	2.26	2.36	1.05
11	0.45	60	2.10	1.62	0.77
13	0.25	40	1.84	2.14	1.16
13	0.25	60	1.71	1.54	0.90
13	0.25	80	1.61	1.48	0.92
13	0.25	100	1.52	1.71	1.12
13	0.35	40	2.12	2.41	1.14
13	0.35	60	1.97	1.66	0.84
13	0.35	80	1.85	1.65	0.89
13	0.35	100	1.75	2.07	1.19
13	0.45	40	2.40	2.48	1.03
13	0.45	60	2.23	1.65	0.74

1 - Calculated from Equation 5.11

Adjusting the 2 parameters in Table 5.8 does not significantly affect the CO_2 partial pressure. Interaction parameters are implemented on a mole fraction basis and dissolved CO_2 concentrations are extremely small. CO_2 partial pressure is mainly dependent on interaction parameters such as H_2O/MEA^+,MEACOO$^-$ and MEA/MEA$^+$,MEACOO$^-$ since MEA and CO_2 comprise the majority of the solvent mole fraction. Only interaction pairings containing CO_2 will be considered for the calculation of the CO_2 activity coefficient.

5.3.6 Physical Properties

Correctly representing density and viscosity solutions in the model is particularly important because they affect other important parameters. Density values affect the thickness of the liquid film which is important for the liquid film mass transfer coefficient. The density also plays into the viscosity calculation so it is important to regress density parameters before

viscosity parameters. Viscosity parameters will have a strong effect on the diffusion coefficients of the species in solution. Diffusion coefficients are sometimes strongly tied to mass transfer rates, drastically limiting mass transfer.

5.3.6.1 Density

Monoethanolamine density values were obtained from a correlation produced by Weiland (1998). MEA density values were calculated for 7, 9, 11, and 13 m MEA at loadings ranging from 0.1 to 0.5 at 0.05 increments. Densities were calculated at 40, 60, 80, and 100 ˚C.

Density values for the nonionic species (MEA, H_2O, CO_2) are determined using the Rackett liquid molar volume model. Density values for ionic species are determined using the Clarke liquid density model which uses cation-anion pairing parameters.   Detailed information and the equations used in these models can be found in the Aspen Plus® help files.

Since the Clarke liquid density model uses apparent electrolyte mole fractions, not every anion-cation species pairing needs to be regressed. Only the species combinations that are both present in significant concentration are important to predict density. The regressed density parameters for MEA are shown in Table 5.10.

Table 5.10: Regressed Monoethanolamine Density Parameters

Parameter	Component i	Component j	Value (SI units)	Std Dev
RKTZRA/1	MEA		0.2403	0.0003
VLCLK/1	MEA+	MEACOO-	0.1311	0.0016
VLCLK/2	MEA+	MEACOO-	-0.0628	0.0075
VLCLK/1	MEA+	HCO3-	0.0568	0.0211
VLCLK/2	MEA+	HCO3-	0.1548	0.0977

Figures 5.51 and 5.52 graphically show how well the regressions fit 7 and 13 m MEA. For all cases, the fit is satisfactory.
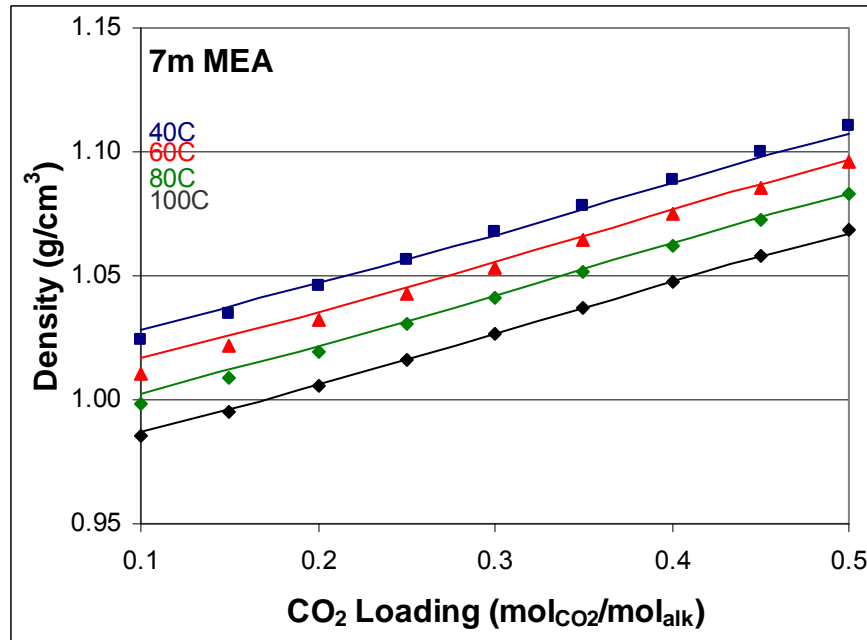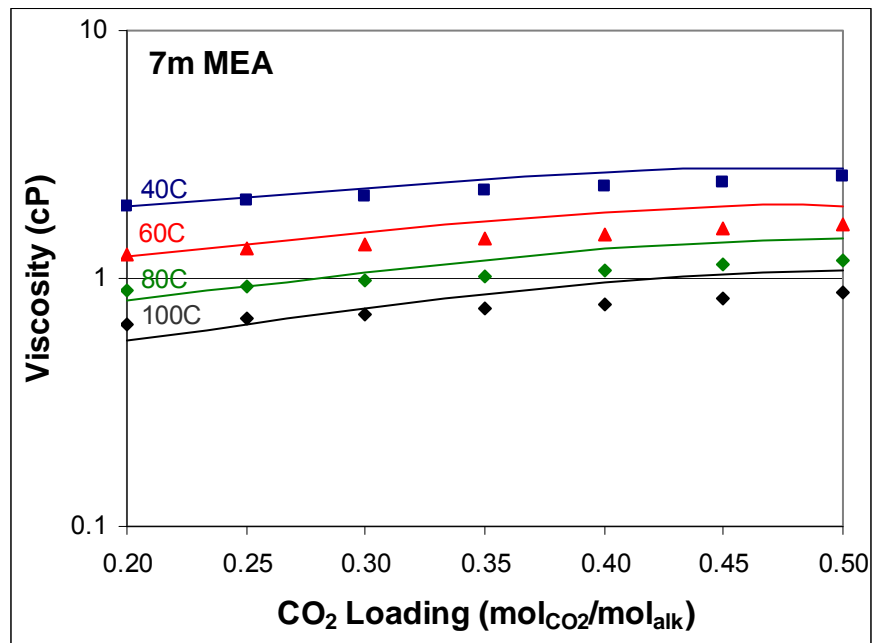
Figure 5.51: 7 m MEA Density Regression: Points - Weiland Correlation (1998); Lines - Aspen Plus® Regression
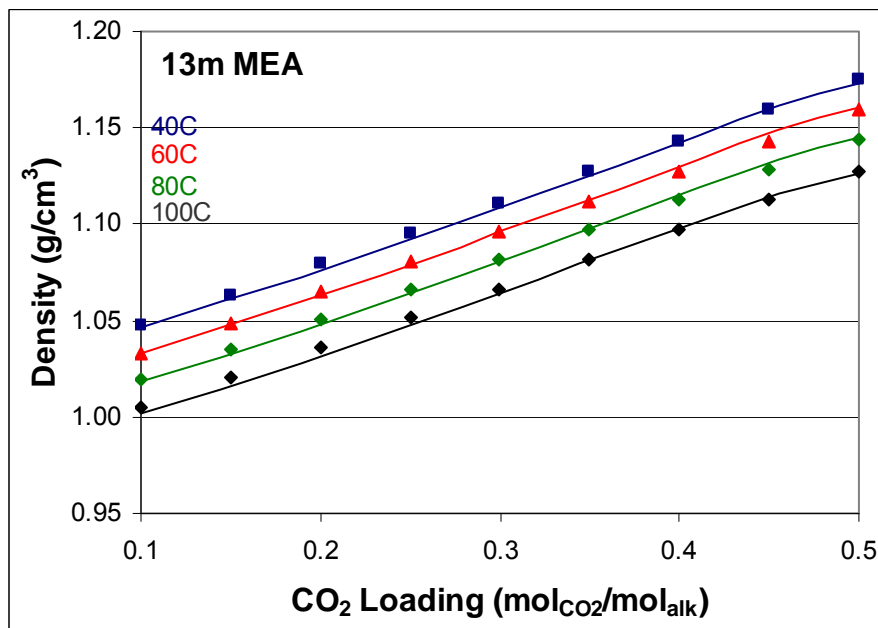
Figure 5.52: 13 m MEA Density Regression: Points - Weiland Correlation (1998); Lines - Aspen Plus® Regression

5.3.6.2 Viscosity

Monoethanolamine viscosity data for the regression was again obtained from Weiland (1998) correlations. MEA viscosity values were calculated for 7, 9, 11, and 13 m MEA at 40, 60, 80, and 100 ˚C with loadings ranging from 0.2 to 0.5 at 0.05 increments.

Viscosity values for nonionic species are determined using the DIPPR liquid viscosity model. The Jones-Dole electrolyte model is used to account for the viscosity contributions of the ionic species. Table 5.11 summarizes the regressed viscosity parameters for the MEA system. Figures 5.53 and 5.54 show how well the regression was able to match the 7 and 13 m MEA data.

Table 5.11: Regressed Monoethanolamine Viscosity Parameters

Parameter	Component i	Value (SI units)	Std Dev
IONMUB/1	MEA+	-23.57	4.09
IONMUB/1	MEACOO-	24.13	4.09
MULDIP/1	MEA	-43.21	3.38
MULDIP/2	MEA	13411	1087

Figure 5.53: 7 m MEA Viscosity Regression: Points - Weiland Correlation (1998); Lines - Aspen Plus® Regression
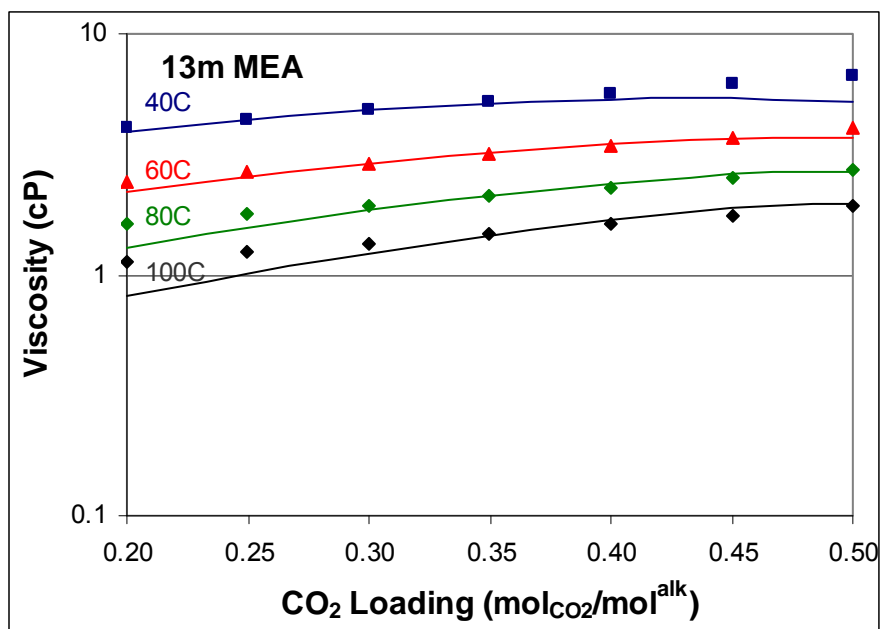
Figure 5.54: 13 m MEA Viscosity Regression: Points - Weiland Correlation (1998); Lines - Aspen Plus® Regression 5.3.7 Mass Transfer Coefficients

The gas and liquid film mass transfer coefficient correlations obtained from the wetted wall column were coded into a Fortran subroutine. This causes Aspen Plus® to use the same gas and liquid film mass transfer coefficients as the wetted wall column. k_g and k_l^o correlations are discussed in Section 3.2.2.

5.3.8 Reactions

The reactions for the $MEA/CO_2/H_2O$ system are shown in Table 5.12. Two pairs of forward and reverse kinetic reactions and 5 equilibrium reactions were used.

Table 5.12: Kinetic and Equilibrium Reactions of the MEA/CO₂/H₂O System

Rxn No.	Reaction type	Stoichiometry
1	Kinetic	2 MEA + CO2 --> MEACOO- + MEA+
2	Kinetic	MEACOO- + MEA+ --> 2 MEA + CO2
3	Kinetic	MEA + CO2 + H2O --> MEACOO- + H3O+
4	Kinetic	MEACOO- + H3O+ --> MEA + CO2 + H2O
5	Equilibrium	2 H2O <--> H3O+ + OH-
6	Equilibrium	CO2 + 2 H2O <--> H3O+ + HCO3-
7	Equilibrium	HCO3- + H2O <--> H3O+ + CO3--
8	Equilibrium	MEA+ + H2O <--> MEA + H3O+
9	Equilibrium	MEACOO- + H2O <--> MEA + HCO3-

This analysis uses the same rate expression as the spreadsheet model, repeated in Equation 5.50. Recall the expression is actually activity-based, not concentration-based. The ratio between k_{MEA} and k_{H2O} was set at 2192, based on termolecular rate constants in MEA solutions (Crooks and Donnellan, 1989). $r_{CO2} = -(k_{MEA}[MEA] + k_{H2O}[H_2O]) \cdot [MEA] \cdot [CO_2]$

$$(5.50)$$

K_{eq} can be calculated by the activities of the species in each reaction when the solution is in equilibrium. At equilibrium, the total forward reaction must be equal to the reverse reaction. The K_{eq} is coupled with the activities of the species and the rate constants as shown in Equation 5.51.

$$K_{eq} = \frac{k_f}{k_r} = \frac{a_{products}}{a_{reactants}} \qquad (5.51)$$

K_{eq} was calculated at 40, 60, 80, 100 °C for each of the forward reactions. The temperature dependence of K_{eq} is shown in Equation 5.52. Calculated K_{eq} values can be fitted to this form accurately.

$$\ln K_{eq} = A + B/T + C \cdot \ln(T), \text{ T in (K)} \qquad (5.52)$$

Aspen Plus® uses a power law rate expression as shown in Equation 5.53 where k is the pre-exponential constant, T is the temperature, T_0 is a reference temperature, E_A is the activation energy, and R is the gas constant.

$$r = k \left(\frac{T}{T_0}\right)^n \exp\left[\frac{-E_a}{R}\left(\frac{1}{T} - \frac{1}{T_0}\right)\right] \qquad (5.53)$$

The equilibrium constant form relates nicely to the power law rate expression form. The A in the K_{eq} expression can be related to the rate constant while B and C can be related to Ea/R and n, respectively. A simple equation can be implemented inside a design specification in the model to ensure that the reverse rate expression is always thermodynamically consistent with the forward rate expression.

The activation energy was input as 44.9 kJ/mol, based on the value reported by Versteeg (1996). The reference temperature is 298.15 K. Fitting the rate constant to the data produced a value of 6.1×10^6 for the MEA catalysis reaction.

5.3.9 Model Results

Figures 5.55–5.57 show the error in the flux with respect to the MEA concentration, CO_2 loading, and temperature. The final model balances the negative and positive flux errors by adjusting the rate constant until the sum of the squares of the errors was minimized. The final pre-exponential rate constant obtained was $6.1*10^6$ based on the form of Equation 5.53.

$$\sum \left(\frac{Flux_{model} - Flux_{meas}}{Flux_{meas}} \right)^2 \tag{5.54}$$

Not all the wetted wall column conditions have been plotted in Figures 5.55–5.57. Some conditions introduce very large, expected errors so they were excluded from the analysis. Data points at the highest CO_2 loading, near 0.5, were excluded because the model cannot accurately predict the correct free amine concentration after the CO_2 loading is adjusted to fit the partial pressure data. The 0.46 CO_2 loading data for 11 m MEA was retained in the analysis. At each experimental condition, 6 inlet CO_2 partial pressures were tested in the wetted wall column. This analysis only includes the 2 extremes, the most absorption and the most desorption cases. Any points which had inlet CO_2 partial pressures within 25% of the equilibrium partial pressure were excluded. Also, 7 m MEA, 60 ˚C at 0.252 loading; 7 m MEA, 100 ˚C at 0.271 CO_2 loading; and 9 m MEA, 60 ˚C at 0.231 CO_2 loading were excluded from this analysis. Each of these conditions presented very large changes in CO_2 loading when the partial pressure was matched. These errors resulted from a flattening of the CO_2 partial pressure curve at low CO_2 loading.
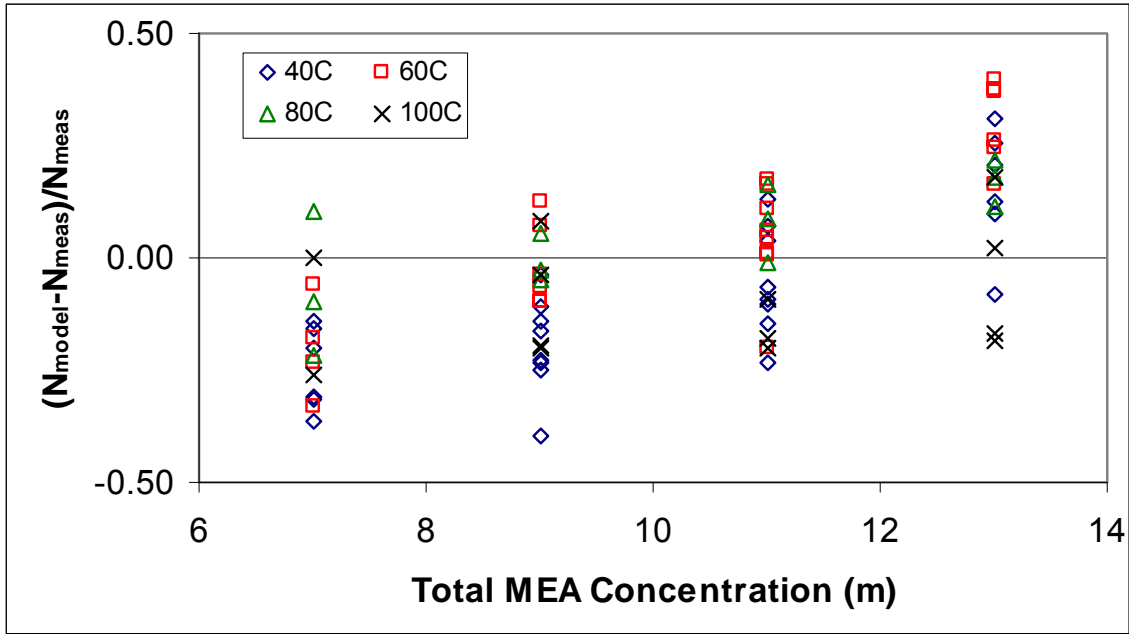
Figure 5.55: Aspen Plus® RateSep™ model error versus total MEA concentration for wetted wall column experimental conditions
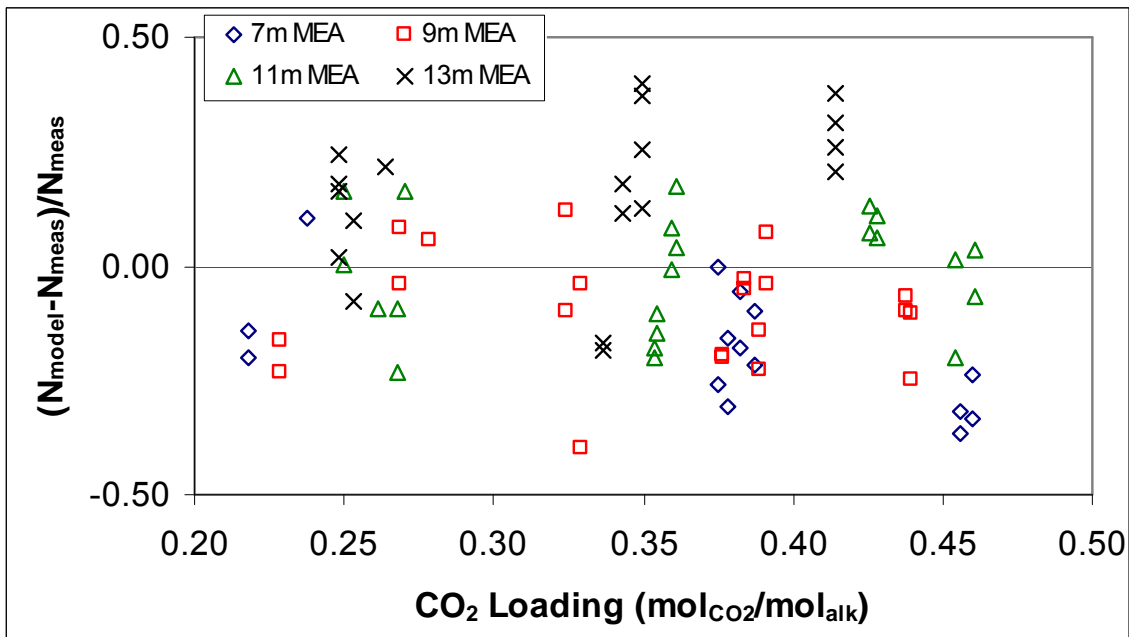
Figure 5.56: Aspen Plus® RateSep™ model error versus CO_2 loading for wetted wall column experimental conditions
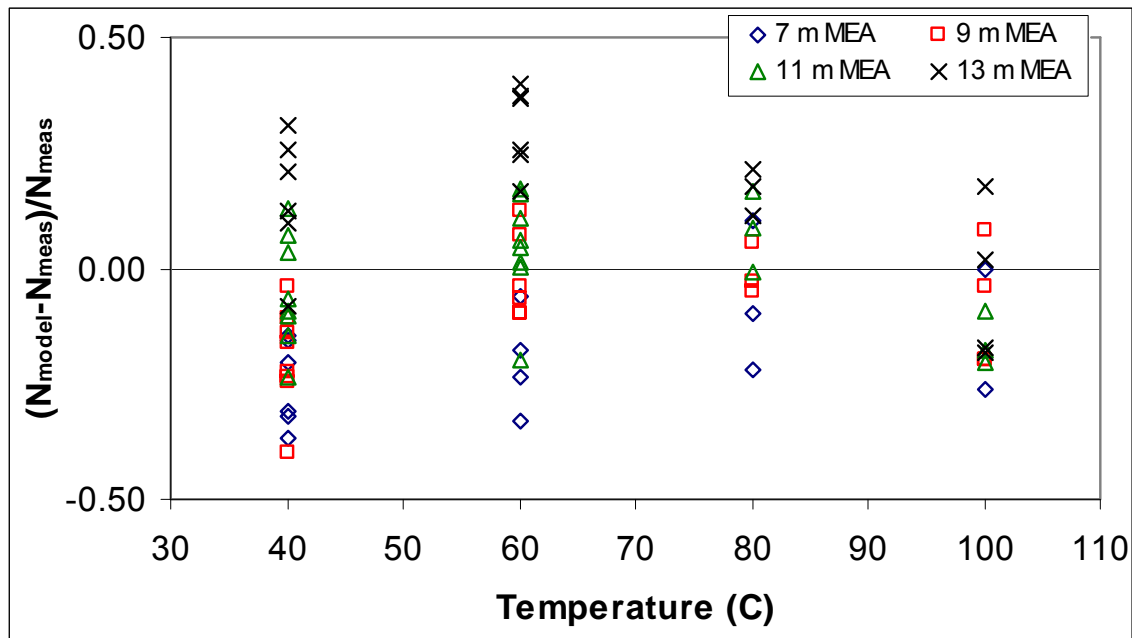
Figure 5.57: Aspen Plus® RateSep™ model error versus temperature for wetted wall column experimental conditions

Errors in the flux calculated by the model are always within 50% of the wetted wall column measured fluxes. This is not bad, considering the magnitude of the flux varies about a factor of 100. Absorption and desorption runs are both considered. Model errors seem to spread evenly with changes in CO_2 loading and temperature. There is a significant systematic error in the predicted flux with changes in amine concentration.

The MEA model has a flaw in its ability to predict flux with changing MEA concentration because of an inability to properly regress MEA activity coefficients. Figure 5.2, utilizing MEA volatility data from Hilliard (2008), showed that the MEA activity coefficient was independent of amine concentration. The spreadsheet model showed no systematic trend with MEA concentration, suggesting that MEA dependent parameters in the k_g' rate expression (Equation 5.48) are likely correct. Although the MEA volatility data had 3 times the emphasis as other data in the main MEA regression, the model still shows significant MEA concentration dependences in the MEA activity coefficient. Figure 5.58 includes the same conditions as in

Figure 5.2 but the activity coefficients are from the model rather than the modified Raoult's law equation.
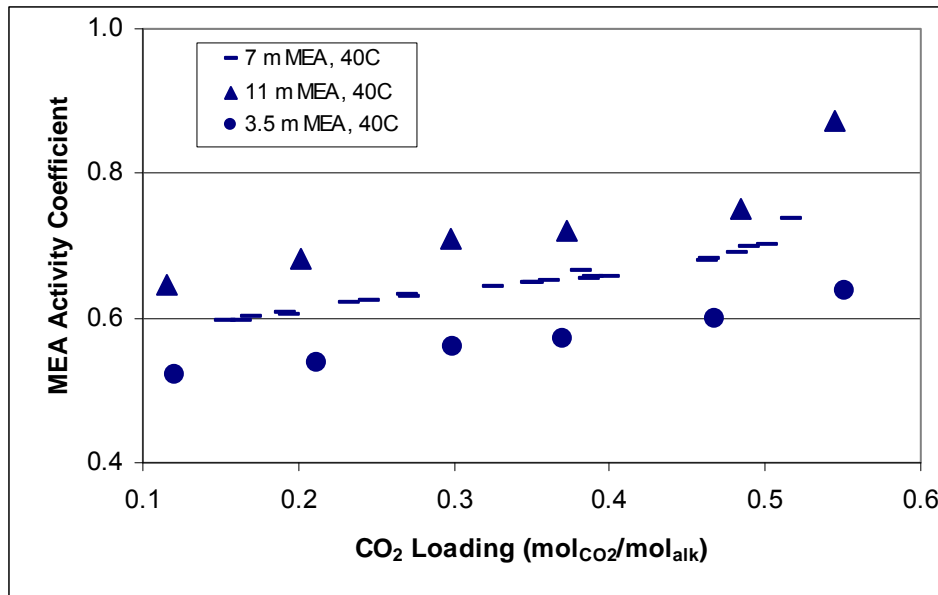
Figure 5.58: Aspen Plus® RateSep™ model prediction of MEA activity coefficients at Hilliard MEA volatility experiment conditions.

The increasing activity coefficient with increasing MEA concentration ensures that the model under-predicts rates at low MEA concentrations while over-predicting CO_2 mass transfer rates at the highest MEA concentrations.

Due to the limitation in representing the MEA activity coefficient, the RateSep™ model is most accurate when finetuned to one specific amine concentration. The error in the predicted flux seems to be about 25% for each amine concentration.

References

Aboudheir, A., P. Tontiwachwuthikul, et al. (2003). "Kinetics of the reactive absorption of carbon dioxide in high CO_2-loaded, concentrated aqueous monoethanolamine solutions." Chemical Engineering Science **58**: 5195-5210.

Aboudheir, A. A. (2002). Kinetics, Modeling, and Simulation of Carbon Dioxide Absorption into Highly Concentrated and Loaded Monoethanolamine Solutions. Chemical Engineering. Regina, Saskatchewan, Canada, University of Regina. **Ph.D.:** 364.

Billet, R., M. Schultes, et al. (1999). "Billet-Schultes model. Calculation model for holdup, pressure loss, and HELP in packed towers." Kemikaru Enjiniyaringu **44**(12): 969-979.

Bishnoi, S. and G. T. Rochelle (2000). "Absorption of Carbon Dioxide into Aqueous Piperazine: Reaction Kinetics, Mass Transfer and Solubility." Chem. Engr. Sci. **55**: 5531-5543.

Browning, G. J. and R. H. Weiland (1994). "Physical Solubility of Carbon Dioxide in Aqueous Alkanolamine via Nitrous Oxide Analogy." Journal of Chemical and Engineering Data **39**: 817-822.

Crooks, J. E. and J. P. Donnellan (1989). "Kinetics and Mechanism of the Reaction Between Carbon Dioxide and Amines in Aqueous Solution." J. Chem. Soc. Perkin Trans. II: 331-333.

Cullinane, J. T. (2005). Thermodynamics and Kinetics of aqueous piperazine with potassium carbonate for carbon dioxide absorption. Chemical Engineering. Austin, TX, The University of Texas at Austin**:** 295.

Cullinane, J. T. and G. T. Rochelle (2006). "Kinetics of Carbon Dioxide Absorption into Aqueous Potassium Carbonate and Piperazine." Industrial & Engineering Chemistry Research **45**(8): 2531-2545.

Danckwerts, P. V. (1979). "The reaction of CO_2 with ethanolamines." Chemical Engineering Science **34**(4): 443-446.

Derks, P. W. J., T. Kleingeld, et al. (2006). "Kinetics of Absorption of Carbon Dioxide in Aqueous Piperazine Solution." Chem. Engr. Sci. **61**(20): 6837-6854.

DIPPR (1979). Vapor Pressures and Critical Points of Liquids XIV: Aliphatic Oxygen-Nitrogen Compounds. Item 79030. London, Engineering Sciences Data.

Ermatchkov, V., A. Perez-Salado Kamps, et al. (2006). "Solubility of Carbon Dioxide in Aqueous Solutions of Piperazine in the Low Gas Loading Region." Journal of Chemical and Engineering Data **51**(5): 1788-1796.

Hartono, A. (2009). Characterization of diethylenetriamine (DETA) as absorbent for CO_2. Chemical Engineering. Trondheim, Norway, Norwegian University of Science and Technology. **Ph.D.:** 243.

Hilliard, M. (2008). A Predictive Thermodynamic Model for an Aqueous Blend of Potassium Carbonate, Piperazine, and Monoethanolamine for Carbon Dioxide Capture from Flue Gas. Chemical Engineering. Austin, The University of Texas at Austin. **Ph.D.:** 1025.

Jou, F.-Y., A. E. Mather, et al. (1995). "The Solubility of CO_2 in a 30 Mass Percent Monoethanolamine Solution." The Canadian Journal of Chemical Engineering **73**(1): 140-147.

Laddha, S. S. and P. V. Danckwerts (1981). "Reaction of CO_2 with Ethanolamines: Kinetics from Gas Absorption." Chem. Engr. Sci. **36**: 479-482.

Rochelle, G. T., A. Sexton, et al. (2008). "CO_2 Capture by Aqueous Absorption - 3rd Quarterly Progress Reports 2008."

Rochelle, G. T., A. Sexton, et al. (2008a). "CO_2 Capture by Aqueous Absorption - 3rd Quarterly Progress Reports 2008."

Rochelle, G. T., A. Sexton, et al. (2009). "CO_2 Capture by Aqueous Absorption - 4th Quarterly Progress Reports 2008."

Tomcej, R. A. and F. D. Otto (1989). "Absorption of Carbon Dioxide and Nitrous Oxide into Aqueous Solutions of Methyldiethanolamine." AIChE Journal **35**(5): 861-864.

Versteeg, G. F., L. A. J. Van Dijck, et al. (1996). "On the Kinetics Between CO_2 and Alkanolamines Both in Aqueous and Non-aqueous Solutions. An Overview." <u>Chem. Engr. Comm</u> **144**: 113-158.

Versteeg, G. F. and W. P. M. Van Swaaij (1988). "Solubility and diffusivity of acid gases (carbon dioxide, nitrous oxide) in aqueous alkanolamine solutions." <u>Journal of Chemical and Engineering Data</u> **33**(1): 29-34.

Watson, J. R. and J. V. Sengers (1986). "Improved International Formullations for the Viscosity and Thermal Conductivity of Water Substance." <u>J. Phys. Chem. Ref. Data</u> **15**: 1291.

Weiland, R. H., J. C. Dingman, et al. (1998). "Density and Viscosity of Some Partially Carbonated Aqueous Alkanolamine Solutions and Their Blends." <u>Journal of Chemical and Engineering Data</u> **43**(3): 378-382.

Xu, S., F. D. Otto, et al. (1991). "Physical Properties of Aqueous AMP Solutions." <u>Journal of Chemical and Engineering Data</u> **36**(1): 71-75.

Wetted Wall Column Rate Measurements for DGA®

Quarterly Report for July 1 – September 30, 2009

by Xi Chen

Supported by the Luminant Carbon Management Program

and the

Industrial Associates Program for CO₂ Capture by Aqueous Absorption

Department of Chemical Engineering

The University of Texas at Austin

October 1, 2009
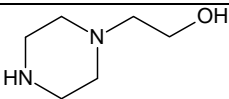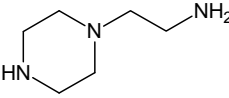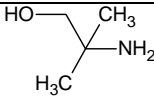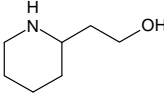
Abstract
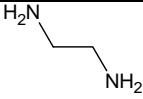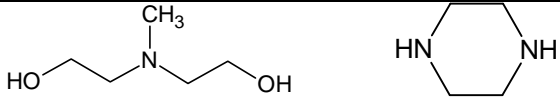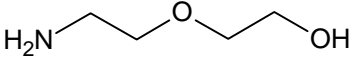
The CO_2 solubility and adsorption/desorption rates were measured in the wetted wall column for 10 m Diglycolamine® (DGA®) with varied CO_2 loading (mol CO_2/mol alkalinity). VLE models of CO_2 were regressed from experimental data to calculate CO_2 capacity and enthalpy of CO_2 absorption (ΔH_{abs}). The liquid film mass transfer coefficients (kg') and CO_2 partial pressures (P*) obtained were compared to those of 8 m piperazine (PZ) and 7 m monoethanolamine (MEA) as well as other amines studied in the previous quarter. The capacity of DGA® is about 20% less than that of 7 m MEA. DGA® has about the same heat of absorption for CO_2 (ΔH_{abs}=81 kJ/mol) as MEA, much higher than PZ (70 kJ/mol).

Introduction

This quarter the measurement with the wetted wall column (WWC) focused on 10 m DGA®. The names and chemical structures of amines that have been studied so far are shown in Table 1.

Table 1: Name and chemical structure of the amines screened in this work

Name	Chemical structure
N-(2-hydroxyethyl)piperazine (HEP)	
1-(2-Aminoethyl)piperazine (AEP)	
2-amino-2-methyl-1-propanol (AMP)	
2-piperidineethanol (2-PE)	

Ethylenediamine (EDA)	
Methyldiethanolamine (MDEA) /Piperazine (PZ)	
DGA®	

Experimental Methods

Experimental apparatus, procedure, and analytical methods have been described in previous reports and will not be repeated here. DGA® (Diglycolamine®, 98%, Acros), CO_2 (99.99%, Matheson Tri-Gas), and deionized water (Millipore, Direct-Q) were used in this study.
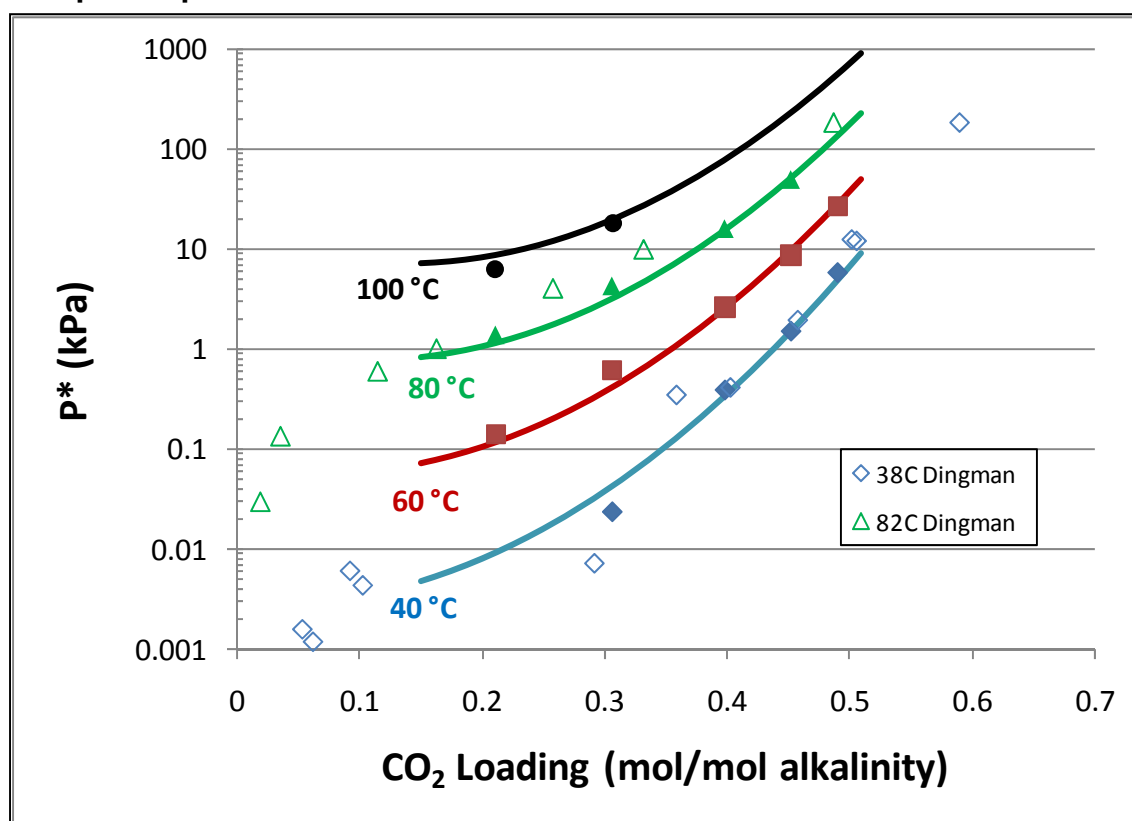
Results and Discussion

CO_2 partial pressure

Figure 1: CO_2 solubility for 10 m DGA®

As shown in Figure 1, the filled points are experimental data for 10 m DGA® from this work. Parameters for the following semi-empirical VLE equation were regressed and the model is presented as solid curves in the figure.

$$\ln P = a + b/T + c \cdot \alpha + d \cdot \alpha/T + e \cdot \alpha^2 \tag{1}$$

The curves fit the points satisfactorily. The data from Dingman et al. (1983) for 17.7 m DGA® at 38 °C and 82 °C are represented by those empty points. Values at 38 °C from Dingman agree with our values at 40 °C reasonably well. The slight difference in solubility could be attributed to the difference in amine concentration and temperature.

Heat of CO_2 absorption

Heat of absorption was calculated from the model by applying the following thermodynamic equation:

$$\Delta H_{abs} = -R \frac{d(\ln P)}{d(1/T)} \tag{2}$$

Absorption/Desorption rates
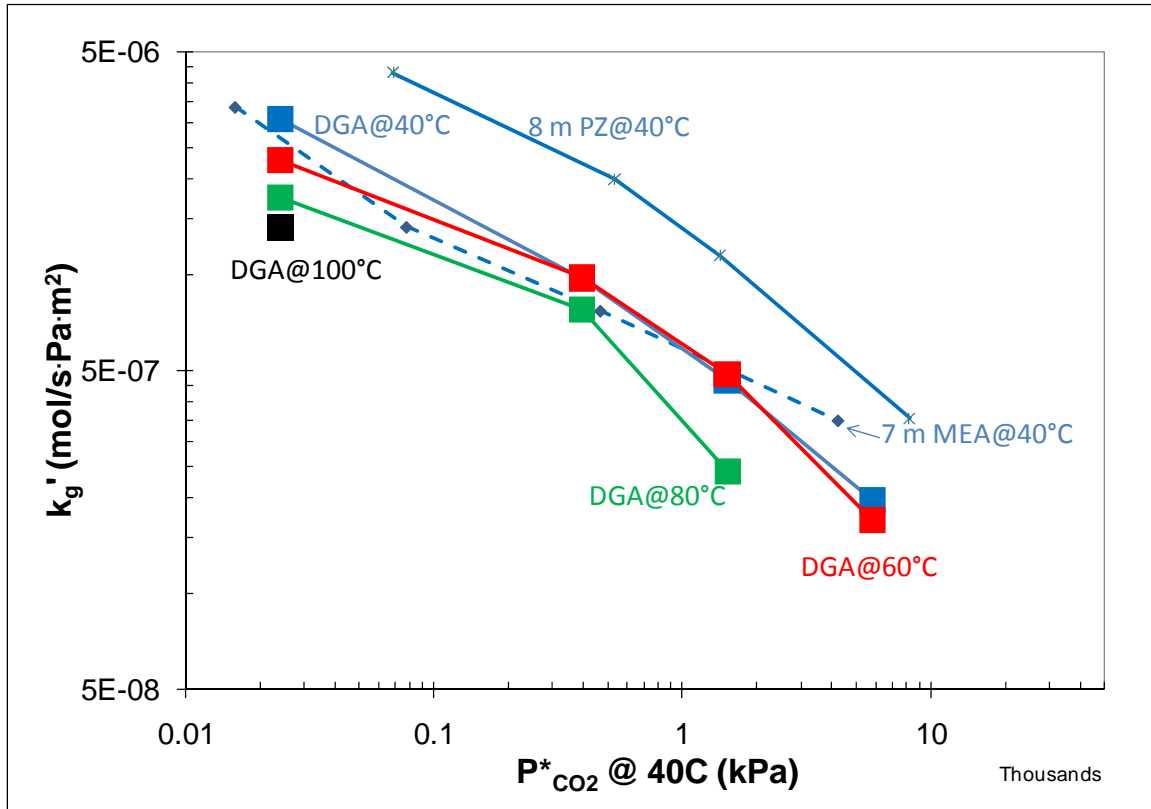
Figure 2: kg' vs. CO_2 partial pressure @ 40 °C for 10 m DGA®

kg' vs. CO_2 partial pressure at 40 °C was plotted for 10 m DGA® in Figure 2. The rate at 40 °C was compared to that of 7 m MEA and 8 m PZ. At 40 °C, 10 m DGA® has a similar kg' as MEA when $P*_{CO2}$ < 1 kPa but becomes slower than MEA at higher $P*_{CO2}$. For the same loaded DGA® solution, a change in temperature from 40 °C to 60 °C did not affect the value of kg'.

The data for VLE and kg' are also tabulated in Table 2.

Table 2: CO$_2$ solubility and kg' at different temperatures for DGA$^®$

[DGA$^®$] (m)	Temp (°C)	CO$_2$ Loading (mol/mol alka)	P$_{CO2}$ (kPa)	kg' ($\times 10^7$ mol/s·Pa·m^2)
10	40	0.307	0.02	30.7
10	40	0.399	0.39	9.7
10	40	0.453	1.51	4.6
10	40	0.491	5.79	2.0
10	60	0.212	0.15	37.1
10	60	0.307	0.63	22.8
10	60	0.399	2.67	9.8
10	60	0.453	8.87	4.9
10	60	0.491	26.93	1.7
10	80	0.212	1.42	31.4
10	80	0.307	4.36	17.4
10	80	0.399	16.27	7.7
10	80	0.453	50.09	2.4
10	100	0.212	6.25	24.5
10	100	0.307	18.04	14.0

Figure 3 compares the kg' values for the amines that have been tested so far. DGA$^®$ shows a performance comparable to 8 m 2-PE at CO$_2$ partial pressures from 0.5 kPa to 5 kPa. In addition, DGA$^®$ is a slower solvent than MDEA/PZ and HEP.
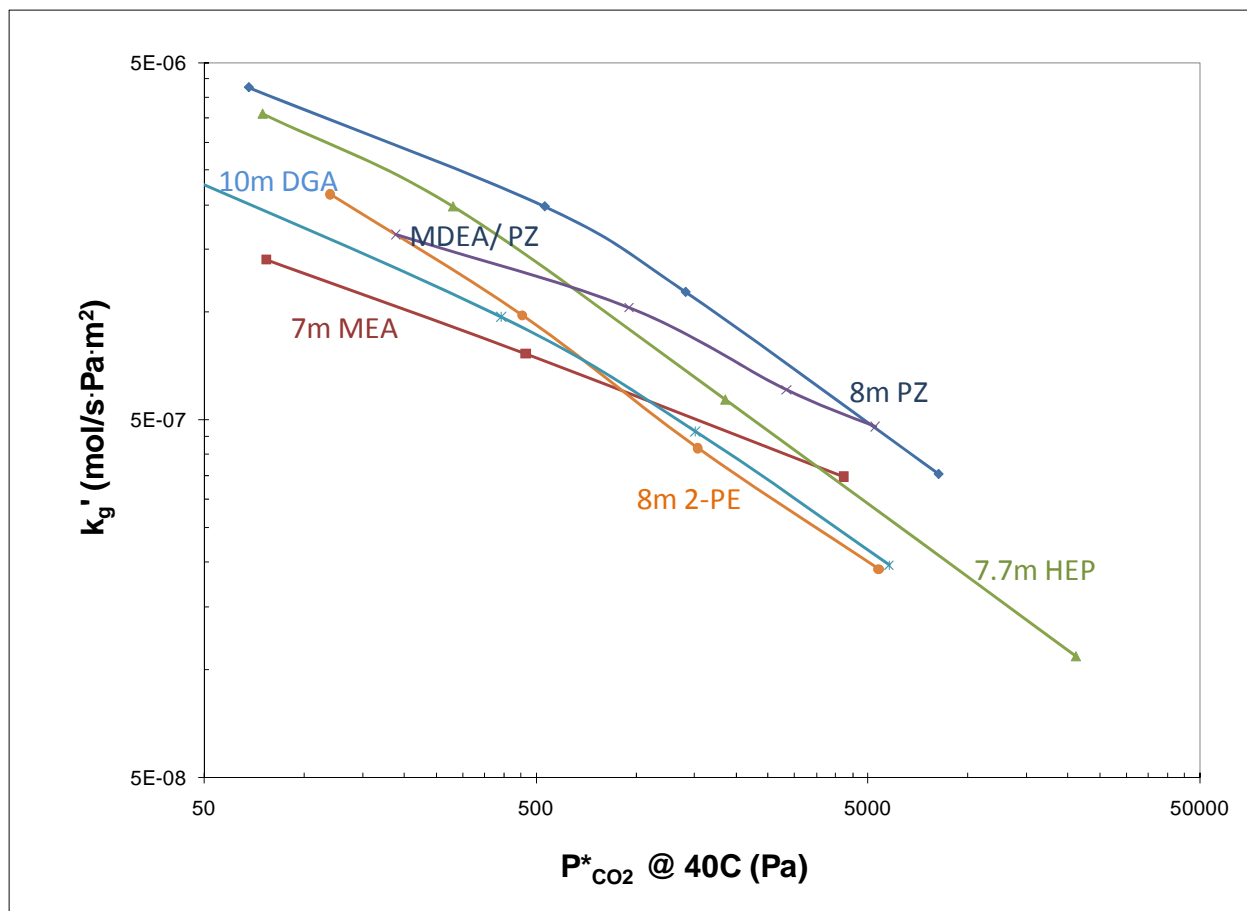
Figure 3: Comparison of CO₂ mass transfer at 40 °C for some of the amines studied so far.

Table 3: Summary table for all the tested amines

Amine	Conc. (m)	CO$_2$ Capacity (mol/kg (water+amine))	kg' @PCO$_2$ =5kPa (×10^{7}mol/s·Pa·m^2)	ΔH_{abs}@PCO$_2$ =1.5kPa (kJ/mol)
MDEA/PZ	7/2	0.71	5.7	67
PZ	8	0.79	5.3	70
MEA	7	0.47	3.1	82
HEP	7.7	0.68	2.9	69
AEP	6	0.66	2.3	72

2-PE	8	1.23	2	73
AMP	4.8	0.96	1.7	73
EDA	12	0.78	1.6	80
DGA®	10	0.38	2.4	81

In Table 3, cyclic capacity, kg' at rich conditions, and average heat of absorption of CO_2 are compared among MEA, PZ, DGA® as well as other amines. DGA® has a smaller capacity and is a slower solvent than MEA and PZ. ΔH_{abs} for DGA® is about the same as MEA, presumably because they are both primary amines.

Conclusions

CO_2 solubility and absorption rate for 10 m DGA® were measured with the WWC in this quarter and compared to those amines tested previously. 10 m DGA® has a capacity much smaller than 8 m PZ, about 80% that of 7 m MEA. 10 m DGA® absorbs CO_2 at a rate 20% less than 7 m MEA. Heat of CO_2 absorption of 10 m DGA® is about 81 kJ/mol at average operational CO_2 loading, the same as that of 7 m MEA. Results show that 10 m DGA® is not competitive as a solvent candidate in comparison to 7 m MEA or 8 m PZ.

Future Work

A proprietary amine was also tested successfully this quarter. Those results will be presented at the research review meeting in January 2010. An amino acid salt and N-Methyl-1,3-Propanediamine will be tested using the wetted wall column in the next quarter.

References

Dingman JC, Jackson JL et al. "Equilibrium data for the hydrogen sulfide-carbon dioxide-diglycolamine agent-water system". Proceedings, Annual Convention - Gas Processors Association. 1983;62:256–68.

A Dimensionless Model for Predicting the Mass Transfer Area of Structured Packing

Robert E. Tsai, A. Frank Seibert, R. Bruce Eldridge, and Gary T. Rochelle

Department of Chemical Engineering, The Separations Research Program, The University of Texas at Austin, Austin, TX, 78712-1062

Abstract

The mass transfer area of nine structured packings was measured in a 0.427 m ID column via absorption of CO_2 from air into 0.1 kmol/m^3 NaOH. The area was most strongly related to packing size (125-500 m^2/m^3) and liquid load (2.5-75 m^3/m^2·h). Surface tension (30-72 mN/m) had a weaker but significant effect. Liquid viscosity (1-15 mPa·s) and flow channel configuration had essentially no impact on the mass transfer area. Surface texture (embossing) increased the effective area by 10% at most. The ratio of mass transfer area to specific area (a_e/a_p) was correlated within limits of ±13% for the entire experimental database:

$$\frac{a_e}{a_p} = 1.339 \left[\left(\frac{\rho_L}{\sigma} \right) g^{1/3} \left(\frac{Q}{L_p} \right)^{4/3} \right]^{0.116}$$

Topical heading

Separations

Keywords

Absorption, mass transfer, structured packing, effective area

Introduction

Packing is commonly used in absorption and distillation columns to promote efficient gas-liquid contacting. For CO_2 capture by aqueous amine absorption, structured packing is an attractive option because of its favorable mass transfer and hydraulic characteristics.[1,2] In this application, the CO_2 absorption rate is typically independent of conventional mass transfer coefficients (k_G or k_L^0) but remains directly proportional to the effective mass transfer area (a_e). Therefore, a reliable structured packing area model is especially critical for the analysis and design of these processes.

Wang et al.[3] performed an extensive review of the numerous structured packing area correlations that have been proposed and noted that the problem has not been satisfactorily solved. Various issues with the models are apparent. Many rely on packing-specific constants, which limit their adaptability and also imply a degree of discontinuity between the seemingly relatable packings. The different correlations predict contrasting effects of properties like liquid viscosity and surface tension as well, indicating that the internal fluid flow behavior is not well understood. It is evident that there is ample margin for improvement in current predictive capabilities.

The correlations of Rocha et al.[4] and Billet and Schultes[5] are two widely used structured packing mass transfer area models. Both were based on large experimental databases of "lumped" (e.g. HETP) mass transfer data and were validated accordingly. In other words, the capability of the models to handle overall mass transfer performance was tested; however, the specific mass transfer parameters (k_G, k_L^0, a_e) themselves were never independently verified. Consequently, it is possible that the individual parameter correlations have been inherently confounded by interacting effects. For instance, during the model development, a viscosity

impact on mass transfer efficiency may have been correlated with the effective area, when it really should have been associated with the mass transfer coefficient. This issue makes it difficult to use these correlations with a high level of confidence.

Recently, there has been a drive toward characterization methods that decouple the mass transfer parameters via appropriate test system selections, thereby facilitating a cleaner interpretation of the mass transfer performance.[6,7] The present work was in consensus with this approach, with the specific objective being the development of an improved mass transfer area model for structured packing. The basis of this *area* model was a comprehensive set of *area* data; effective areas of a variety of packings were evaluated as a function of liquid load, liquid viscosity, and surface tension. The experiments were planned with the physical property ranges of amine solvents in mind,[8-12] although the test conditions were certainly of general relevance as well. Measurements were made via the absorption of dilute CO_2 into aqueous NaOH. This method has been identified by Sharma and Danckwerts,[13] among many others, as a convenient means by which gas-liquid interfacial areas can be determined. With sufficient free hydroxide, the concentration of bicarbonate (HCO_3^-) is negligible, and the overall reaction may be written as:

$$CO_2(aq) + 2OH^- \rightarrow CO_3^{2-} + H_2O \qquad (1)$$

The reaction can be considered as practically irreversible, with a rate expression given by equation 2.

$$r = k_{OH^-}[OH^-][CO_2] \qquad (2)$$

When CO_2 partial pressures are low and hydroxide ion is present in relative excess, the reaction can be treated as pseudo-first-order. Equation 2 consequently simplifies to:

$$r \cong k_1[\text{CO}_2] \qquad\qquad (3)$$

Experimental

Materials

The NaOH solutions for wetted-wall column experiments were purchased from Fisher Scientific (certified grade). The solutions for packed column tests were prepared using solid NaOH pellets (PHARMCO-AAPER, 98.5% or EMD Chemicals Inc., 97.0%). A nonionic surfactant, Tergitol[TM] NP-7 (Dow), was used to reduce the surface tension of solutions. POLYOX[TM] WSR N750 (Dow) – essentially, poly(ethylene oxide) with a molecular weight of 300,000 – was employed as a viscosity enhancer. With both of these reagents, suppression of foam was found to be necessary, particularly during packed column experiments. Dow Corning[®] Q2-3183A antifoam was utilized for this purpose in concentrations typically ranging from 50-100 ppm$_\text{w/v}$.

Packed column

The packed column had an outside diameter of 0.46 m, an inside diameter of 0.427 m, and a 3-m packed height. Operation was countercurrent, with ambient air entering below the packing bed and flowing upward through the tower. The liquid (typically 0.75 m^3 inventory) was pumped in a closed loop and was distributed at the top of the column using a pressurized fractal distributor with 108 drip points/m^2. Additional details about the equipment are in Tsai et al.,[14] and a complete procedural description can be found in Tsai.[15]

Wetted-wall column (WWC)

The wetted-wall column (WWC) was a bench-scale gas-liquid contactor with a known interfacial area (38.52 cm^2) that was used the measure the kinetics of various systems. The

apparatus has previously been used and described by Bishnoi and Rochelle,[16] Cullinane and Rochelle,[17] and Tsai et al.[14]

Supplementary equipment

The goniometer (ramé-hart Inc., model #100-00) included an adjustable stage, a syringe support arm, a computer-linked camera for live image display, and a light source. This system was used with FTA32 Video 2.0 software (developed by First Ten Angstroms, Inc.) to make surface tension measurements via pendant drop analysis.

A Physica MCR 300 rheometer (Anton Paar, USA) equipped with a cone-plate spindle (CP 50-1) was used for viscosity measurements. Temperature was regulated ($\pm 0.1°C$) with a Peltier unit (TEK 150P-C) and a Julabo F25 water bath unit (for counter-cooling). Measurement profiles consisted of a logarithmically ramped or decremented shear rate (100-500 s^{-1}), with a minimum of 10 points taken at 15 second intervals.

Governing equations and data analysis

The performance of both the WWC and the packed column was modeled by series resistance (equation 4). The overall mass transfer resistance is the sum of the gas- and liquid-side resistances.

$$\frac{1}{K_G} = \frac{1}{k_G} + \frac{1}{k_g'} \tag{4}$$

For the WWC experiments, the overall mass transfer coefficient (K_G) was determined from the CO_2 flux and the partial pressure driving force. The gas-side mass transfer coefficient (k_G) was a function of physical properties and was calculated using a WWC-specific correlation.[16] Equation 4 was solved for k_g', which has been defined as a liquid-side mass transfer coefficient expressed in terms of a CO_2 partial pressure driving force (equation 5).

$$N_{CO_2} = k_g' \left(P_{CO_2}^i - P_{CO_2}^* \right) = k_g' P_{CO_2}^i \tag{5}$$

In equation 5, P^*_{CO2} is zero because of the irreversibility of the CO_2-NaOH reaction. Under the assumption of pseudo-first-order conditions, surface renewal theory may be used to present the flux as:[16,18]

$$N_{CO_2} = k_L^0 \sqrt{1 + \frac{k_1 D_{CO_2,L}}{\left(k_L^0\right)^2}} \frac{P_{CO_2}^i}{H_{CO_2}} \tag{6}$$

The Hatta number (Ha) for pseudo-first-order reactions has been defined in various sources:[19,20]

$$Ha = \frac{\sqrt{k_1 D_{CO_2,L}}}{k_L^0} \tag{7}$$

For $Ha^2 \gg 1$ equation 6 can be simplified to:

$$N_{CO_2} = \frac{\sqrt{k_1 D_{CO_2,L}}}{H_{CO_2}} P_{CO_2}^i \tag{8}$$

Combination of equations 5 and 8 leads to the following theoretical expression for k_g':

$$k_g' = \frac{\sqrt{k_1 D_{CO_2,L}}}{H_{CO_2}} = \frac{\sqrt{k_{OH^-}[OH^-]D_{CO_2,L}}}{H_{CO_2}} \tag{9}$$

Experimental k_g' values from the WWC (equation 4) were compared with calculated ones (equation 9), evaluated using the correlations of Pohorecki and Moniuk[21] for the diffusion coefficient ($D_{CO2,L}$), Henry's constant (H_{CO2}), and reaction rate constant (k_{OH-}).

For the packed column experiment, gas-side resistance was intentionally limited by using dilute caustic solution (0.1 kmol/m^3) and operating at high superficial air velocities (0.6, 1, or 1.5 m/s). This resistance was calculated from the correlation of Rocha et al.[4] to account for 1-2% of the overall mass transfer resistance on average; measurements consisting of the absorption of SO_2 into caustic solution have supported this estimate. The $1/k_G$ term in equation 4 was

neglected, and K_G was assumed to be equal to k_g'. This approximation enabled the effective area (a_e) to be determined by separating it from the volumetric mass transfer coefficient ($K_G a_e$).

$$a_e = \frac{u_G \ln\left(\dfrac{y_{CO_2,in}}{y_{CO_2,out}}\right)}{ZK_G RT} \approx \frac{u_G \ln\left(\dfrac{y_{CO_2,in}}{y_{CO_2,out}}\right)}{Zk_g' RT} = \frac{u_G \ln\left(\dfrac{y_{CO_2,in}}{y_{CO_2,out}}\right)}{ZRT} \cdot \frac{H_{CO_2}}{\sqrt{k_{OH^-}[OH^-]D_{CO_2,L}}} \qquad (10)$$

To legitimately interpret k_g' in the manner outlined above (equation 9), Ha^2 must be large, and there must be minimal interfacial depletion of reactants. Haubrock et al.,[20] among others, quantified these requirements:

1. $Ha > 2$

2. $E_\infty / Ha > 5$

The enhancement factor for an instantaneous, irreversible reaction (E_∞) is expressed in equation 11.

$$E_\infty = 1 + \frac{D_{OH^-,L}[OH^-]H_{CO_2}}{D_{CO_2,L}P_{CO_2}^i} \qquad (11)$$

All of the experiments performed in this work satisfied these conditions. For reference, Ha^2 for the WWC was on the order of 10^2. k_L^0 was estimated from the theory of Pigford,[22] Hobler,[23] and Bird et al.,[24] which Pacheco[25] found to be in good agreement (within 15%) with experimental values. The large Ha^2 criterion was slightly weaker for the packed column tests. Ha^2 was 12 in the absolute worst case, but it was at least 30 for 95% of the recorded data points. Here, k_L^0 was calculated from the correlation of Rocha et al.[4]

Wetted-Wall Column (WWC) Results

The WWC was used to evaluate the baseline CO_2-NaOH kinetics or essentially, k_g' values. It was also utilized to test for potential impacts of the property-modifying additives (Tergitol NP-7 or POLYOX WSR N750) on k_g'. The WWC results are summarized in Table 1,

expressed as a normalized k_g' (experimental k_g' / calculated k_g'). For the base case and surfactant systems, the calculated k_g' was simply the "Pohorecki" k_g'. For the POLYOX system, a different $D_{CO2,L}$ was applied to account for the polymer-based viscosity enhancement, in accordance with the work of Lohse et al.[26] This rather interesting modification was discussed in detail in Tsai et al.[27]

Table 1. Summary of WWC Results (Experimental Conditions: 27-35°C, 0.15-0.32 m/s (Gas), 1.5-4.2 cm^3/s (Liquid), 150-630 Pa CO$_2$ at Inlet)

Test system	Approx. μ_L and/or σ	Number of data points	Normalized k_g'
0.1 kmol/m^3 NaOH (Baseline)	0.8 mPa·s, 70 mN/m	111	1.10 ± 0.09
0.1 kmol/m^3 NaOH + 125 ppm$_v$ Tergitol NP-7 + 50 ppm$_{w/v}$ Dow Corning Q2-3183A antifoam	30 mN/m	32	1.08 ± 0.07
0.1 kmol/m^3 NaOH + 1.25 wt % POLYOX WSR N750	8 mPa·s	10	0.94 ± 0.05

The baseline measurements gave values of flux (k_g') that were 10% higher than predicted by Pohorecki and Moniuk.[21] Nevertheless, the disparity was not believed to be drastic enough to reject their model. The Pohorecki k_g' was therefore presumed to be acceptable for the interpretation of the packing mass transfer area measurements (equation 10). There was no statistically confirmable impact of surfactant and antifoam, implying that the same k_g' could be applied in this case as well; explanations for this result were offered in Tsai et al.[14] The WWC data with POLYOX were in good agreement with the Lohse-corrected Pohorecki k_g' values; this combined k_g' model was consequently used for packing experiments involving this system.

Packing Mass Transfer Area Results

Effect of air rate (M125Y/M250Y/F1Y/M500Y)

As stated in the Experimental Section, three air velocities (0.6, 1.0, or 1.5 m/s) were generally run within a given experiment. The results in Figure 1 are distinguished accordingly. The mass transfer area data for three Mellapak^{TM} packings (M125Y/M250Y/M500Y), as well as

Flexipac^{TM} 1Y (F1Y), are shown at the maximum operating liquid load for the high velocity (1.5 m/s) condition for each packing – basically, nearing the upper limit of the pre-loading region, where gas flow rate might be more likely to affect the results. One could possibly argue that there was a slight increase in area with velocity, particularly considering the lowest M250Y measurement, but it was believed that this point was somewhat anomalous and that inferring a trend would be an incorrect interpretation of the results. The mass transfer area was concluded to be insensitive to the air rate. Thus, it was considered acceptable to treat all of the data obtained at a given liquid load on equivalent terms. Figure 2 displays the baseline M250Y measurements, where the points at each liquid load have been averaged for clarity. For reference, most of the figures that follow will show results that have been consolidated in this manner.
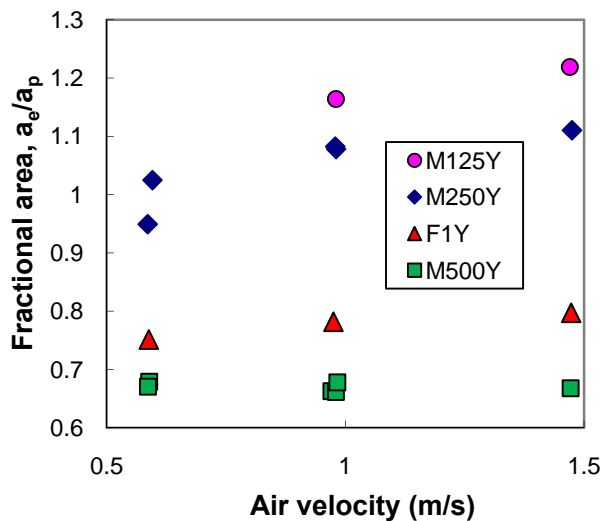
Figure 1. Mass transfer area data at maximum operating liquid load for gas velocity of 1.5 m/s for M125Y (a_p = 125 m^2/m^3, 61.1 m^3/m^2·h), M250Y (a_p = 250 m^2/m^3, 61.1 m^3/m^2·h), F1Y (a_p = 410 m^2/m^3, 36.7 m^3/m^2·h), and M500Y (a_p = 500 m^2/m^3, 18.3 m^3/m^2·h).
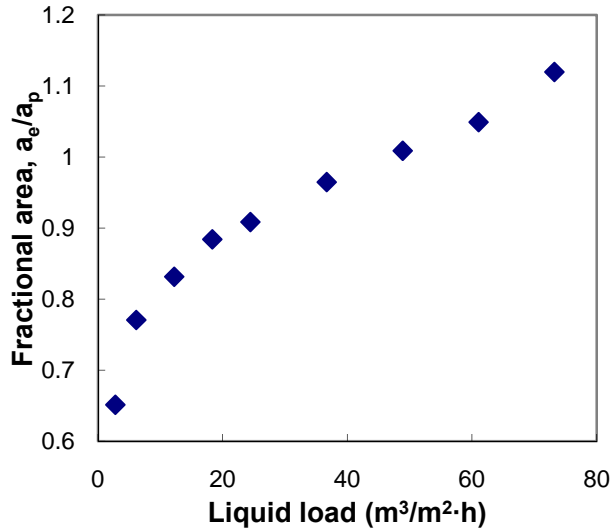
Figure 2. Averaged mass transfer area data for M250Y (a_p = 250 m^2/m^3).

Global model

Table 2 lists the packings included in the mass transfer area database, along with their relevant physical dimensions and approximate conditions at which they were tested. The low surface tension (30 mN/m) and high viscosity (10 mPa·s) conditions were simulated using the same additives as tested in the WWC – that is, 125 ppm$_v$ Tergitol NP-7 and 1.25 wt % POLYOX WSR N750, respectively. Moderate viscosity (5 mPa·s) cases were run using a slightly lower POLYOX concentration (0.85 wt %); this system was not explicitly investigated in the WWC but was assumed to fall under the same model as the high viscosity scenario. Antifoam concentration sometimes varied (50-100 ppm$_{w/v}$) compared to the specific WWC experiments, but this was not believed to affect the k_g' interpretation. The channel dimensions (S, B, h) were defined in the same fashion as in other publications.[28,29] All packings were manufactured by Sulzer Chemtech, with the exception of Flexipac 1Y (Koch-Glitsch Inc.) and the prototype 500-series packing. Every packing was perforated.

Table 2. Structured Packing Database

Packing	Specific area, a_p (m²/m³)	Corrugation angle, α (°)	Channel side, S (mm)	Channel base, B (mm)	Crimp height, h (mm)	Parameter source(s)	Conditions: $\mu_L{}^a$ (mPa·s) / σ^b (mN/m)
Mellapak 250Y (M250Y)	250	45	17	24.1	11.9	Petre et al.[30]	1/73, 0.8/31, 4/58, 14/44
Mellapak 500Y (M500Y)	500	45	8.1	9.6	6.53	Aroonwilas[31]	1/73, 0.9/31, 4/45, 10/42
Mellapak 250X (M250X)	250	60	17	24.1	11.9	Measured	1/73, 1/30, 11/42
MellapakPlus™ 252Y (MP252Y)	250	45	17	24.1	11.9	Measured	0.8/71, 0.8/30, 8/42
Mellapak 250Y (smooth) (M250YS)	250^c	45	17	24.1	11.9	Measured	1.1/73, 1/31
Mellapak 125Y (M125Y)	125	45	37	55	24.8	Measured	0.9/72, 0.8/31
Mellapak 2Y (M2Y)	205	45	21.5	33	13.8	Sulzer Measured	0.9/72
Flexipac 1Y (F1Y)	410	45	9	12.7	6.4	Koch-Glitsch Petre et al.[30]	0.8/71, 6/63
Prototype 500 (P500)	500	45	8.1	9.6	6.53	Assumed same as M500Y	0.9/72, 0.9/31

^{a} For base case system (0.1 kmol/m³ NaOH), calculated from correlation of Moniuk and Pohorecki[32]
^{b} For base case system (0.1 kmol/m³ NaOH), assumed same as water and calculated from fit of data in Haar et al.[33]
^{c} Denotes uncertainty in actual specific area

The mass transfer area model first presented in Tsai et al.[27] is displayed in equation 12 in its most updated form.

$$\frac{a_e}{a_p} = 1.339\left[(We_L)(Fr_L)^{-\frac{1}{3}}\right]^{0.116} \tag{12}$$

The standard errors from the regression were: $(a_e/a_p) \pm 6.5\%$, $1.339 \pm 0.9\%$, and 0.116 ± 0.002. The dimensionless $(We_L)(Fr_L)^{-1/3}$ grouping, with characteristic length (δ) defined by the "classical" Nusselt film thickness,[24] is shown expanded in equation 13.

$$(We_L)(Fr_L)^{-1/3} = \left(\frac{\rho_L}{\sigma}\right) g^{1/3} \left(\frac{Q}{L_p}\right)^{4/3} = \left(\frac{\rho_L}{\sigma}\right) g^{1/3} \left(\frac{Q}{A} \cdot \frac{Bh}{4S}\right)^{4/3} \qquad (13)$$

Figure 3 is a plot of the entire packing mass transfer area database, along with the global model (equation 12) and dashed lines denoting two standard deviations (±13%). The data can be found in detailed, tabulated form in Tsai.[15]
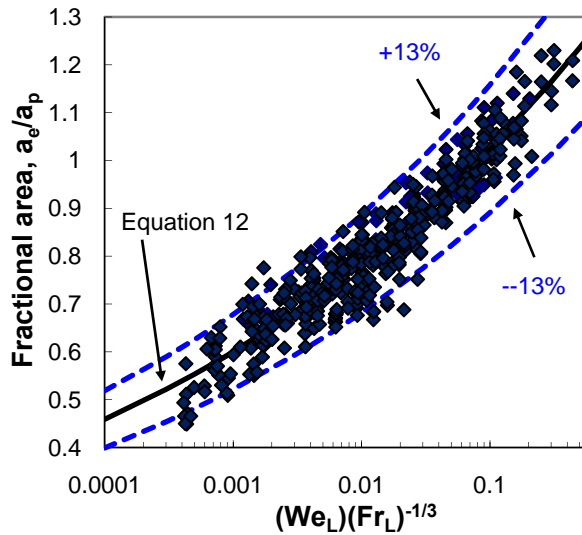

Figure 3. Structured packing mass transfer area database, compared with global correlation (equation 12).

The fit of the model was quite acceptable given the broad scope of the database, which as indicated in Table 2, consisted of packing sizes ranging from 125-500 m^2/m^3, viscosity from roughly 1-15 mPa·s, and surface tension from 30-72 mN/m. The liquid load and specific area, reflected in the flow rate per wetted perimeter term (Q/L_p) in equation 13, most strongly dictated the mass transfer area. Surface tension and liquid density were also correlated as relevant parameters, although the latter was never explicitly varied. Notably absent from the model was liquid viscosity, which, over the range of values tested, was concluded to have a negligible effect on area. Also not included were terms involving the packing corrugation angle (M250X), element interface (MP252Y), and surface texture (M250YS), since none of these features were

found to appreciably affect the effective area. These results are all discussed in detail in the subsequent sections.

Effect of liquid load and packing size (M125Y/M250Y/F1Y/M500Y)

Figure 4 illustrates the strong influence of both liquid load (2.5-75 $m^3/m^2 \cdot h$) and packing size (125-500 m^2/m^3) on the mass transfer area. Every packing exhibited an increase in effective area with increasing liquid load. This was naturally attributable to a greater portion of the packing being wetted and therefore available to participate in the mass transfer process. It could be speculated, based on rivulet flow studies,[34,35] that the effective area was governed by the ability of the liquid to spread within the individual flow channels. When considering both the relatively small geometric boundaries (S < 40 mm) and the surface tension-related results (covered in the next section), it seems more reasonable to infer that the trend with liquid load was dictated by the distribution of liquid to the channels themselves – not necessarily the degree of coverage within a singular channel.

The standard M250Y packing performed well on a fractional area (a_e/a_p) basis; measured values ranged from 0.65 to 1.12. Its specific area was clearly being well utilized, but as might be expected of a structured packing, there was little mass transfer occurring beyond the packing surface. This is in contrast with random packing, where the effective area often exceeds the nominal area, sometimes by more than 50%.[36] It was quite interesting, then, that M125Y exhibited higher (10%) fractional areas than M250Y, approaching a value of 1.3 at the high-end loads. Mass transfer from the column wall (9.3 m^2/m^3) was not accounted for, but it would have a greater relative effect for M125Y (7.5%) than for M250Y (3.7%) and therefore could have factored into the observed deviation in fractional area. Still, it alone was not enough to justify the 10% difference. Hence, it would seem that as structured packings become coarser, their

fractional area efficiency tends toward that of random packings. Henriques de Brito et al.[37] speculated that low a_p packings could be more prone to liquid flow instabilities such as rippling or formation of satellite droplets due to longer film running lengths. These phenomena certainly could have contributed to the M125Y mass transfer areas. The fractional area efficiency of the finer packings (F1Y and M500Y) was notably lower; both were found to plateau far below unity. The trend with liquid load also appears to differ from the coarser packings, in that a more distinct fractional area asymptote was reached at the highest liquid loads. While F1Y and M500Y could have been less subject to mass-transfer-enhancing film instabilities, the capillary phenomena hypothesis proposed by Tsai et al.[14] was thought to provide the best explanation for these results. Essentially, the poorer efficiencies could be attributed to detrimental liquid bridging and pooling between packing sheets, which could be a foreseeable problem for fine packings due to their high internal density. This could justify the asymptotic behavior too – a reflection of the packings becoming clogged near their upper capacity limits and therefore unable to benefit from additional liquid throughput.
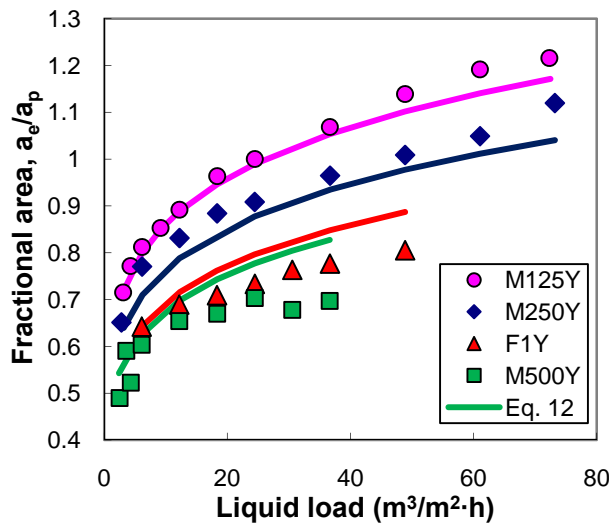
Figure 4. Comparison of mass transfer area data for M125Y (a_p = 125 m^2/m^3), M250Y (a_p = 250 m^2/m^3), F1Y (a_p = 410 m^2/m^3), and M500Y (a_p = 500 m^2/m^3).

14

To demonstrate the ability of equation 12 to collapse the various data sets, the results in Figure 4 have been re-plotted in dimensionless form in Figure 5. The model captures the overall combination of liquid load and geometry well, but it misses subtle aspects like the tendency of F1Y and M500Y to flatten out. Thus, while it is satisfactory in its current form, further improvements can obviously be made. An additional term could be required to account for the liquid accumulation induced by the narrow, constricted sheets of the finer packings, although it would not necessarily make sense to use the Nusselt film thickness as the characteristic dimension here, since the film is basically unbounded. Instead, it would perhaps be more logical to use a geometric parameter – for instance, the sheet spacing – for the length scale. This is all just speculation, however; progress has yet to be made in this regard.
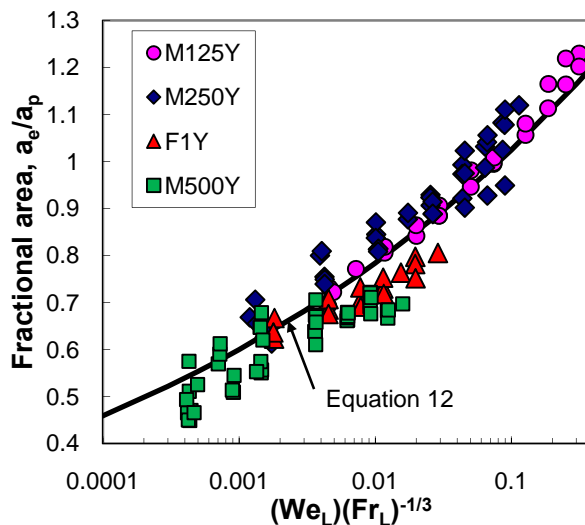
Figure 5. Representation of M125/M250Y/F1Y/M500Y data on dimensionless basis.

Effect of surface tension (M250Y/M500Y/P500)

Extensive tests showed that the mass transfer area was always enhanced by a reduction in surface tension (30 mN/m), regardless of packing geometry. A greater effect of surface tension on finer packings (500-series) relative to coarser ones (250-series and lower) was observed. Effective areas were higher by 15-20% on average for the fine packings, whereas the increase

15

was 10% or less for the coarse ones. The data sets for M250Y (Figure 6) and M500Y/P500 (Figure 7) are shown for illustration. It is unclear why P500 slightly outperformed M500Y for the base case but then overlapped at low surface tension. It could be possible that the geometry (e.g. surface texture) of P500 was less conducive to undesirable liquid bridging but lost its advantage when the surface tension was reduced. Regardless, the purpose of the P500 experiment was to verify the stronger linkage of high a_p packings to surface tension, which was indeed affirmed even though the difference was smaller than the one observed with M500Y.

A lower surface tension would intuitively be associated with a lower contact angle – a relation confirmed in Tsai et al.[14] – and hence, better liquid spreading. If spreading were a valid explanation for the increase in wetted area, though, then one would expect a substantially bigger deviation from the base case at low liquid loads (i.e. 10 $m^3/m^2 \cdot h$ and below), due to surface coverage limitations. This was not reflected in the data. The mass transfer area improvement was fairly constant for every packing as a function of liquid load, with the greatest departure actually occurring at the upper capacity limit of the 500-series packings. This consistency suggests that the enhancement was attributable to a common mechanism other than liquid spreading, such as creation of satellite droplets or wave formation. This same idea was proposed in the previous section when discussing the M125Y results. Thus, it could be that increasing packing coarseness or decreasing surface tension induces similar instabilities to the liquid films on the packing surface. The additional 5-10% distinction between coarse and fine packings was believed to be related to capillary phenomena. As with the asymptotic trend, it should be emphasized that the model presently fails to account for this difference but perhaps could be corrected with the incorporation of an additional parameter.

It should be recognized that Tsai et al.[14] presented mass transfer area data for M250Y and M500Y and concluded that a reduction in surface tension (35 mN/m) from the base case (72 mN/m) had no impact on M250Y and a dramatic effect (50%) on M500Y. Improvements to the experimental set-up since then (see Tsai[15]) could explain the discrepancy between the more recent data and this previous report. The past mass transfer area data were not included in the current database.
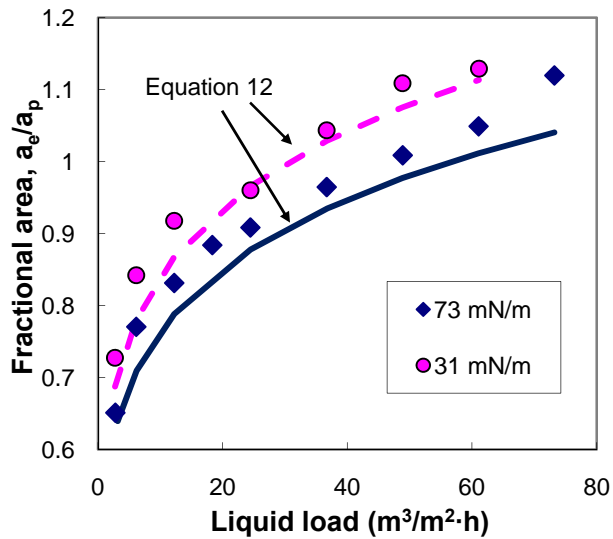

Figure 6. Comparison of baseline and low surface tension mass transfer area data for M250Y (a_p = 250 m^2/m^3).
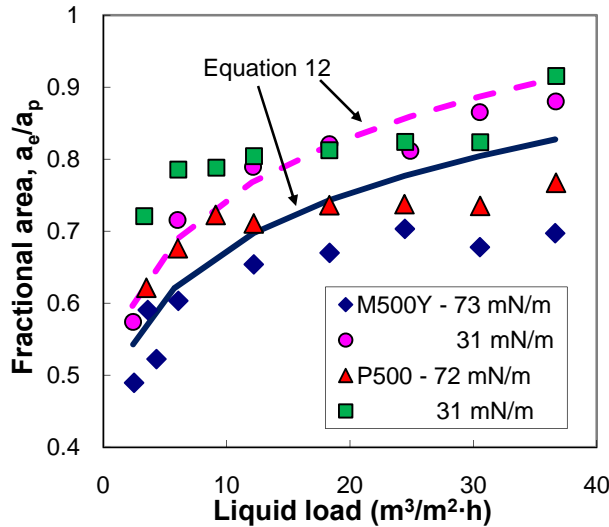
Figure 7. Comparison of baseline and low surface tension mass transfer area data for M500Y and P500 (a_p = 500 m^2/m^3).

Effect of liquid viscosity (M250Y/M500Y)

Figure 8 compares results with M250Y at low viscosity (baseline), moderate viscosity (4 mPa·s, 58 mN/m), and high viscosity (14 mPa·s, 44 mN/m). It was not possible to increase viscosity without also changing surface tension because POLYOX WSR N750 affects both parameters. The results are plotted in dimensionless form to remove the expected effect of surface tension. The area at high viscosity appears to be about 5% less than that at low viscosity. However, this deviation is well within the experimental noise limits, and therefore, it is logical to conclude that there is a negligible effect of viscosity on the mass transfer area.

The M500Y results confounded the matter somewhat. Baseline, moderate viscosity (4 mPa·s, 45 mN/m), and high viscosity (10 mPa·s, 42 mN/m) data are displayed in Figure 9. If viscosity were assumed to have no influence, the viscous points would be expected to fall somewhat above the baseline, owing to the inability of the $(We_L)(Fr_L)^{-1/3}$ grouping to fully capture the surface tension effect for M500Y. The moderate viscosity data were reasonable in this context. The high viscosity results, in contrast, aligned with the baseline, which would

18

imply there to be a negative impact of viscosity equal to the gain from the reduced surface tension (on the order of 10%). Since the majority of related data suggested that viscosity was basically irrelevant, however, it was decided to not over-analyze this one data set, which was perhaps exacerbated by other factors like minor foaming (particularly at high liquid loads).

The lack of a viscosity effect was not overly surprising. The elevated viscosities presumably resulted in slightly thicker liquid films on the packing surface. In the idealized scenario of a smooth, inclined plate, this change would merely raise the gas-liquid contact line further above the surface. It would not affect the interfacial area of the two fluids in any way.
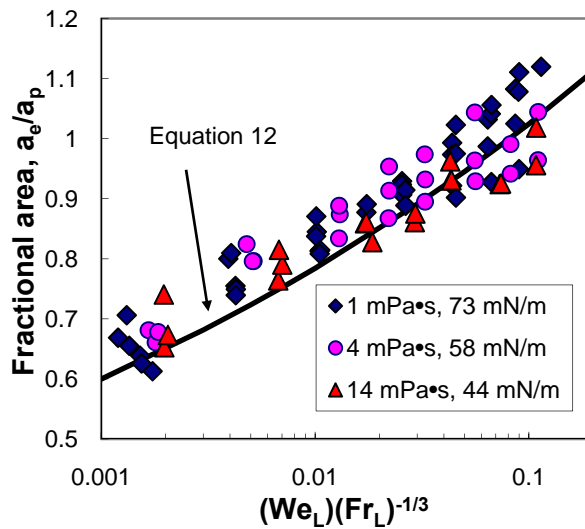
Figure 8. Comparison of baseline and viscous mass transfer area data for M250Y (a_p = 250 m^2/m^3).
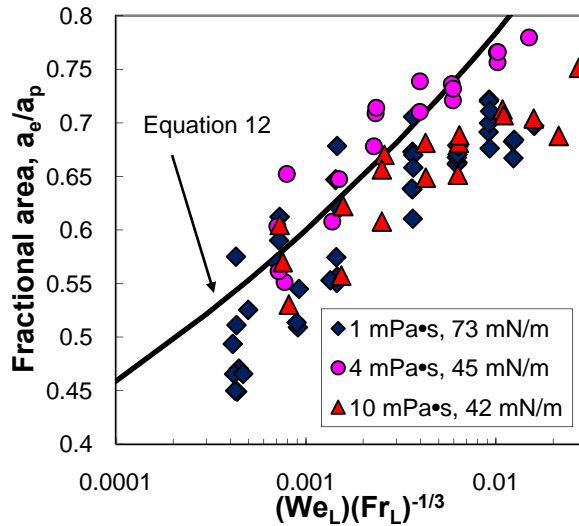
Figure 9. Comparison of baseline and viscous mass transfer area data for M500Y (a_p = 500 m^2/m^3).

Effect of corrugation angle (M250Y/M250X) and element interface (M250Y/MP252Y)

The M250Y, M250X, and MP252Y mass transfer area data are shown in Figure 10. M250X had steeper flow channels (60°) than M250Y (45°) but otherwise was geometrically equivalent. Its measured area appears to be lower than M250Y but by less than 5% – insufficient to be distinguished from the experimental noise – and consequently, it was concluded that the two packings had the same effective area. While this result would seemingly contradict past investigations[38,39] that reported a 20-30% decrease in mass transfer performance when shifting from a 45° to a 60° inclination, it is important to realize that the literature studies were interpreted on an HETP basis and therefore could be more reflective of the mass transfer coefficient than the effective area. Olujic et al.[38] found that Montz B1-250 (45°) had a 20% lower HETP than Montz B1-250.60 (60°). However, the model of Rocha et al.[4] would also predict the 45° packing to have a 15-20% greater gas-side mass transfer coefficient (k_G). Hence, the poorer HETP of Montz B1-250.60 could have been entirely attributable to a lower k_G, which

would imply that the wetted areas of the Montz packings were the same – just as the results in Figure 10 would indicate.

The concept of high capacity packings has been discussed in the literature.[40] Essentially, the idea is to expand the operational limits of packing by smoothing the sheets near the interface between elements, often referred to as the joint and cited as a problem-spot possessing much higher liquid hold-up than the element bulk,[41] from the standard 45° inclination to a vertical (90°) orientation. Our particular high capacity packing (MP252Y) resembled M250Y except for the aforementioned modification, which occurred at the top/bottom 1.25-cm of each 21-cm tall element. The channel dimensions (*S, B, h*) were measured to be the same as for M250Y, and the specific area was assumed to be 250 m^2/m^3 as well. (It should be noted that Alix and Raynal[42] listed slightly different dimensions for MP252Y than the values in Table 2, but even if their numbers were used, the calculated wetted perimeters of MP252Y and M250Y would still be within 3% of each other.) The M250Y and MP252Y data were practically indistinguishable, which would suggest that the joint does not tangibly contribute to the mass transfer area. It is worth noting that the majority of data was collected far from the loading region, where one would not expect there to be a great deal of gas-liquid turbulence or mixing between elements. This could explain the lack of a joint effect. That is, the two packings could possibly only deviate (in terms of mass transfer area) near flooding, where M250Y might be anticipated to exhibit greater mass transfer (at the expense of pressure drop) because of its more abrupt joint transition.
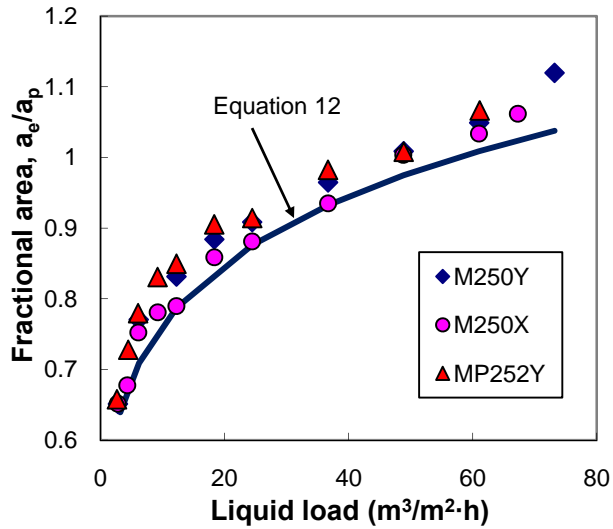
Figure 10. Comparison of mass transfer area data for M250Y, M250X, and MP252Y ($a_p =$ 250 m²/m³).

The fact that the mass transfer areas of the three 250-series packings was identical was especially striking in the context of their pressure drop behavior. Figures 11 and 12 respectively compare the dry and irrigated (24.4 m³/m²·h, with water) pressure drop for the packings. The results have been normalized by equation 14, a simple power law expression obtained from a regression of the M250Y dry pressure drop data as a function of the gas flow factor (F_s).

$$\frac{\Delta P_{dry,M250Y}}{Z} = 30.92 F_s^{1.856} \tag{14}$$
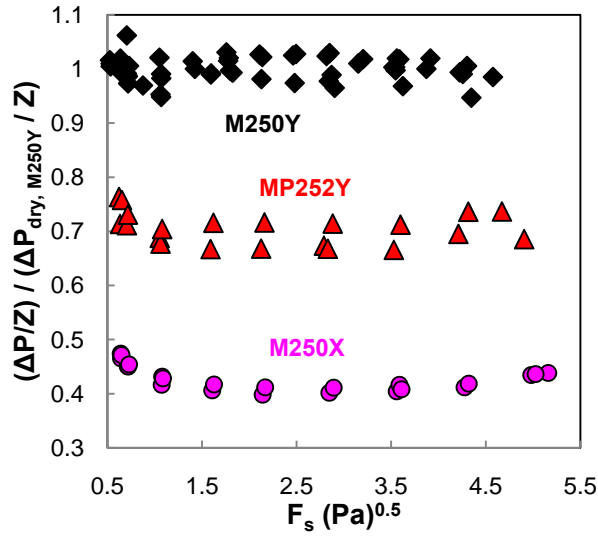
Figure 11. Comparison of dry pressure drop data for M250Y, M250X, and MP252Y.
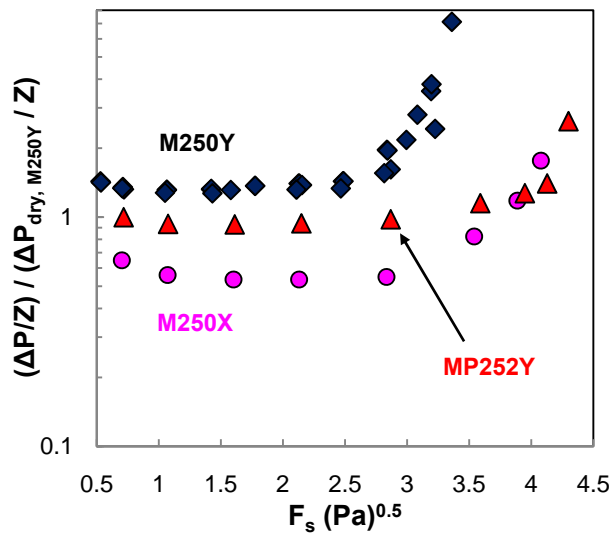
Figure 12. Comparison of pressure drop data at liquid load of 24.4 m³/m²·h for M250Y, M250X, and MP252Y.

The M250X and MP252Y dry pressure drops were 40% and 70% of those of M250Y; this relative ratio was maintained even under irrigated conditions (pre-loading). Given that the packings exhibited very similar wetted areas, it would seem that the channel configuration has a far greater impact on the vapor flow path than on the liquid.

23

On the sole basis of effective area, it obviously would not make sense to select M250Y over M250X or MP252Y, on account of its significantly poorer hydraulic performance. The M250X/MP252Y tradeoff is not as straightforward; the former offered lower pressure drops but the latter seemed to better resist flooding (10% greater capacity). Based on these findings, geometric designs not currently commercially available but seemingly worth pursuing might include a packing with channels steeper than 60° or possibly a hybrid 60°/smoothed joint packing ("MellapakPlus 252X").

Effect of texture (M250Y/M250YS)

M250YS was an untextured (smooth) version of M250Y. The two packings were otherwise geometrically identical and were both assumed to have a specific area of 250 m^2/m^3. Figure 13 displays the mass transfer area results for the packings.

McGlamery[34] speculated that surface texture could increase mass transfer via two mechanisms: greater liquid spreading and enhanced turbulence. While the M250YS points were lower than the M250Y points, the difference between the two data sets was constant (10%) over the investigated liquid loads, which, based on prior arguments, would favor turbulence as the explanation when interpreting the results.

Alternatively, it is possible that because the surface of M250YS was not embossed, it had an appreciably lower (at least 10%) specific area than M250Y. In this case, we would conclude the impact of texture on the effective area to be negligible. Hydraulic measurements showed the M250YS pressure drops to be 15-20% lower under dry and irrigated (pre-loading) conditions, which would coincide with M250YS possessing less surface area. Frictional differences were considered as a possible theory, but it seemed unlikely that they alone would account for such a large discrepancy. Hydraulic data with other packings suggested a fairly direct scaling of

pressure drop with specific area, so both area (10-15%) and friction (5-10%) could be contributing to the 15-20% effect.

While the latter premise appears to have credibility, there is nothing to disprove the first theory, about enhancement from turbulence. Thus, the only definite conclusion that can be made is that texture has at most a weak effect on the mass transfer area.
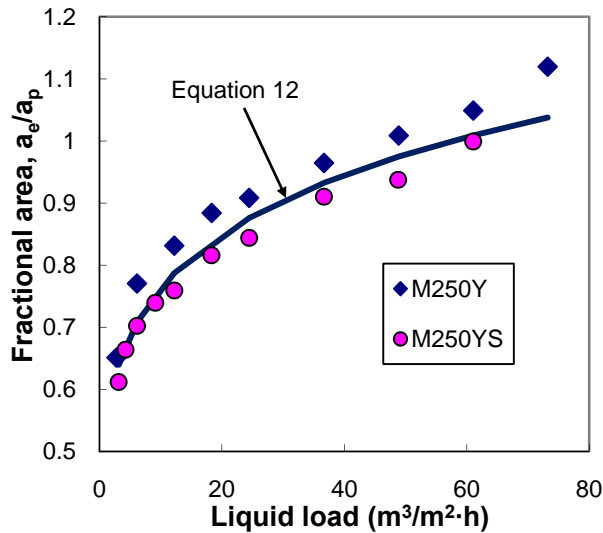

Figure 13. Comparison of mass transfer area data for M250Y and M250YS (a_p = 250 m^2/m^3).

Comparison with literature models

Tsai et al.[27] demonstrated the models of Rocha et al.[4] and Billet and Schultes[5] to be notably poor in their handling of aqueous systems and speculated that this could be due to their reliance on distillation data (Rocha et al. especially), which generally consist of very low surface tension systems. An important objective of this entire research project was to address this shortcoming and establish a model suitable for aqueous solvents. Ideally, though, this model would be universal, capable of bridging the apparent gap between hydrocarbon and aqueous systems. To test this, equation 12 was evaluated at conditions reported in a distillation study (cyclohexane/n-heptane) conducted by the Separations Research Program at the University of

Texas.[38] The highest pressure scenario (414 kPa) deviated most from water and was selected to offer the most rigorous assessment of the model. Liquid loads were between 2.5 and 50 $m^3/m^2 \cdot h$, and the relevant physical properties (averaged at the column bottom) were: $\rho_L = 561$ kg/m^3, $\mu_L = 0.16$ mPa·s, and $\sigma = 8$ mN/m. Figure 14 compares equation 12 with the literature correlations for this distillation condition and for water. For this analysis, the assumed properties of water were: $\rho_L = 1000$ kg/m^3, $\mu_L = 1$ mPa·s, and $\sigma = 72$ mN/m. The mass transfer areas of the cyclohexane/n-heptane system were predicted to be 20% higher than the areas with water for M250Y. This was a somewhat liberal extrapolation of the 10% effect observed during the low surface tension experiments, but at the very least, the predicted fractional areas were plausible, ranging from 0.74 to 1.18. The model was undoubtedly more flexible than Rocha et al. and Billet and Schultes, which clearly do not handle aqueous conditions well. Nevertheless, it should be emphasized that because equation 12 was developed using aqueous systems, it is still best suited for applications of this nature. As with any model, caution should be exercised when extrapolating beyond the databank upon which it was based.

It was interesting to note that the two literature models converged for cyclohexane/n-heptane, which was perhaps indicative of their common source basis. Also worth pointing out was the much better agreement of the models with equation 12 (relative to the water scenario), particularly at moderate liquid loads (25-50 $m^3/m^2 \cdot h$). Thus, while the use of the Rocha et al. or Billet and Schultes correlations for the analysis of aqueous systems is not recommended, they could actually be acceptable when applied toward the distillation-type systems from which they were developed.
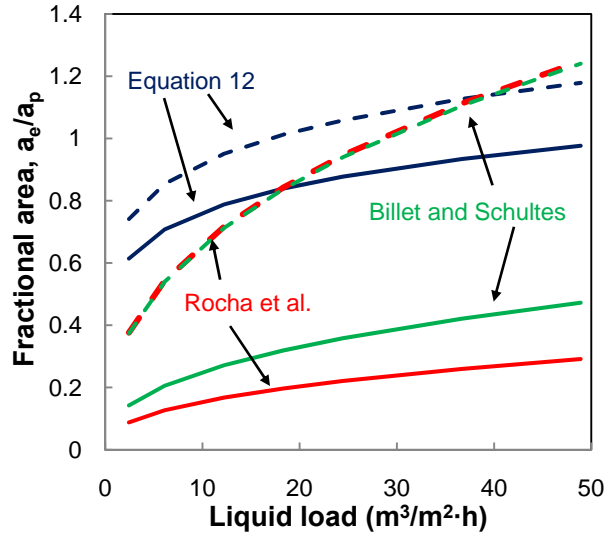
Figure 14. Predicted M250Y mass transfer areas from various models. Lines denote water (—) or cyclohexane/*n*-heptane system at 414 kPa (– –).

Conclusions

Rates of absorption of CO_2 into 0.1 kmol/m^3 NaOH were measured. The k_g' models for the base case, low surface tension (125 ppm$_v$ Tergitol NP-7 + 50 ppm$_{w/v}$ Dow Corning Q2-3183A antifoam), and high viscosity (1.25 wt % POLYOX WSR N750) systems were found to match the data within 10% and were therefore believed to be acceptable for use with no further modifications.

The mass transfer area of nine structured packings was measured via absorption of CO_2 into 0.1 kmol/m^3 NaOH. The global model that was regressed as a function of $(We_L)(Fr_L)^{-1/3}$ was capable of representing the entire database with acceptable accuracy (±13%). It was also satisfactory in its treatment of both aqueous and hydrocarbon systems, unlike the Rocha et al.[4] and Billet and Schultes[5] correlations. The model was certainly not without flaws, though, and most notably was unable to account for two features that distinguished the high a_p packings from the others: a more prominent asymptote with liquid load and a stronger dependence on surface

tension. Both were suspected to be a function of internal liquid bridging and could possibly be captured with appropriate adjustments to the correlation.

Packing size (125-500 m^2/m^3) and liquid load (2.5-75 $m^3/m^2 \cdot h$) had the largest influence on the mass transfer area. A greater area was generally always associated with a higher liquid load, and fractional area (a_e/a_p) efficiency increased with increasing coarseness.

A reduction in surface tension (30 mN/m) enhanced the mass transfer area. The difference was more pronounced for the finer packings (15-20%) than for the coarser ones (10%). No significant dependence on liquid viscosity (1-15 mPa·s) was observed.

Flow channel configuration (45° vs. 60° or smoothed element interfaces) had essentially no bearing on the effective area but drastically affected the hydraulics. Dry and pre-loading pressure drops for the 250-series packings were in the order: M250X (0.4) < MP252Y (0.7) < M250Y, with the numbers in parentheses representing the values relative to M250Y.

The effect of surface texture on the mass transfer area was debatable but was weak at best; the gain from embossing (vs. smooth) was a maximum of 10%.

Acknowledgments

Notation

A = cross-sectional area of column, m^2

a_e = effective area of packing, m^2/m^3

a_p = specific (geometric) area of packing, m^2/m^3

B = packing channel base, m

$D_{CO2,L}$ = diffusion coefficient of CO_2 in solution, m^2/s

$D_{OH^-,L}$ = diffusion coefficient of OH^- in solution, m^2/s

F_s = gas flow factor, $(m/s)(kg/m^3)^{0.5}$ or $(Pa)^{0.5}$

g = gravitational constant; 9.81 m/s^2

H_{CO2} = Henry's constant of CO_2, $m^3 \cdot Pa/kmol$

h = packing crimp height, m

K_G = overall mass transfer coefficient, $kmol/m^2 \cdot Pa \cdot s$

k_1 = pseudo-first-order reaction rate constant, s^{-1}

k_G = gas-side mass transfer coefficient, $kmol/m^2 \cdot Pa \cdot s$

k_g' = liquid-side mass transfer coefficient, $kmol/m^2 \cdot Pa \cdot s$

k_L^0 = physical liquid-side mass transfer coefficient, m/s

k_{OH^-} = second-order reaction rate constant, $m^3/kmol \cdot s$

L_p = wetted perimeter in cross-sectional slice of packing, m

N_{CO2} = molar flux of CO_2, $kmol/m^2 \cdot s$

P = pressure, Pa

P_{CO2}^* = equilibrium partial pressure of CO_2, Pa

P_{CO2}^i = partial pressure of CO_2 at gas-liquid interface, Pa

Q = volumetric flow rate, m^3/s

R = ideal gas constant, $m^3 \cdot Pa/kmol \cdot K$

r = chemical reaction rate, $kmol/m^3 \cdot s$

S = packing channel side, m

T = temperature, K

u_G = superficial gas velocity, m/s

$y_{CO2,in/out}$ = mole fraction of CO_2 at inlet/outlet

Z = packed height, m

Greek letters

α = corrugation angle (with respect to the horizontal), deg

ΔP = pressure drop, Pa

δ = characteristic length, m

μ_L = liquid viscosity, kg/m·s or Pa·s

ρ_L = liquid density, kg/m^3

σ = surface tension, N/m

Dimensionless groups

a_f = fractional area of packing, a_e/a_p

Fr_L = Froude number for liquid, $\dfrac{u_L^2}{g\delta}$

We_L = Weber number for liquid, $\dfrac{\rho_L u_L^2 \delta}{\sigma}$

Literature Cited

(1) Aroonwilas A, Tontiwachwuthikul P, Chakma A. Effects of operating and design parameters on CO_2 absorption in columns with structured packings. *Sep. Purif. Technol.* 2001;24:403-411.

(2) Luo S, Li H, Fei W, Wang Y-d. Liquid Film Characteristics on Surface of Structured Packing. *Chin. J. Chem. Eng.* 2009;17:47-52.

(3) Wang GQ, Yuan XG, Yu KT. Review of Mass-Transfer Correlations for Packed Columns. *Ind. Eng. Chem. Res.* 2005;44:8715-8729.

(4) Rocha JA, Bravo JL, Fair JR. Distillation Columns Containing Structured Packings: A Comprehensive Model for Their Performance. 2. Mass-Transfer Model. *Ind. Eng. Chem. Res.* 1996;35:1660-1667.

(5) Billet R, Schultes M. Predicting Mass Transfer in Packed Columns. *Chem. Eng. Technol.* 1993;16:1-9.

(6) Hoffmann A, Maćkowiak JF, Górak A, Haas M, Löning J-M, Runowski T, Hallenberger K. Standardization of Mass Transfer Measurements: A Basis for the Description of Absorption Processes. *Chem. Eng. Res. Des.* 2007;85:40-49.

(7) Rejl JF, Linek V, Moucha T, Valenz L. Methods standardization in the measurement of mass-transfer characteristics in packed absorption columns. *Chem. Eng. Res. Des.* 2009;87:695-704.

(8) Freeman SA, Dugas RE, Van Wagener D, Nguyen T, Rochelle GT. Carbon dioxide capture with concentrated, aqueous piperazine. *Int. J. Greenhouse Gas Control.* 2009 (in press).

(9) Weiland RH, Dingman JC, Cronin DB, Browning GJ. Density and Viscosity of Some Partially Carbonated Aqueous Alkanolamine Solutions and Their Blends. *J. Chem. Eng. Data.* 1998;43:378-382.

(10) Henni A, Hromek JJ, Tontiwachwuthikul P, Chakma A. Volumetric Properties and Viscosities for Aqueous AMP Solutions from 25°C to 70°C. *J. Chem. Eng. Data.* 2003;48:551-556.

(11) Vázquez G, Alvarez E, Navaza JM, Rendo R, Romero E. Surface Tension of Binary Mixtures of Water + Monoethanolamine and Water + 2-Amino-2-methyl-1-propanol and Tertiary Mixtures of These Amines with Water from 25°C to 50°C. *J. Chem. Eng. Data.* 1997;42:57-59.

(12) Derks PW, Hogendoorn KJ, Versteeg GF. Solubility of N_2O in and Density, Viscosity, and Surface Tension of Aqueous Piperazine Solutions. *J. Chem. Eng. Data.* 2005;50:1947-1950.

(13) Sharma MM, Danckwerts PV. Chemical methods of measuring interfacial area and mass transfer coefficients in two-fluid systems. *Br. Chem. Eng.* 1970;15:522-528.

(14) Tsai RE, Schultheiss P, Kettner A, Lewis JC, Seibert AF, Eldridge RB, Rochelle GT. Influence of Surface Tension on Effective Packing Area. *Ind. Eng. Chem. Res.* 2008;47:1253-1260.

(15) Tsai RE. Influence of Viscosity and Surface Tension on the Mass Transfer Area of Structured Packing. Ph.D. Thesis (in preparation), University of Texas at Austin, Austin, TX, 2010.

(16) Bishnoi S, Rochelle GT. Absorption of carbon dioxide into aqueous piperazine: reaction kinetics, mass transfer, and solubility. *Chem. Eng. Sci.* 2000;55:5531-5543.

(17) Cullinane JT. Kinetics of Carbon Dioxide Absorption into Aqueous Potassium Carbonate and Piperazine. *Ind. Eng. Chem. Res.* 2006;45:2531-2545.

(18) Danckwerts PV. *Gas-Liquid Reactions*. New York: McGraw-Hill, 1970.

(19) Kucka L, Kenig EY, Gorak A. Kinetics of the Gas-Liquid Reaction Between Carbon Dioxide and Hydroxide Ions. *Ind. Eng. Chem. Res.* 2002;41:5952-5957.

(20) Haubrock J, Hogendoorn JA, Versteeg GF. The Applicability of Activities in Kinetic Expressions: a More Fundamental Approach to Represent the Kinetics of the System CO_2-OH- in Terms of Activities. *Int. J. Chem. React. Eng.* 2005;3:1-17.

(21) Pohorecki R, Moniuk W. Kinetics of Reaction between Carbon Dioxide and Hydroxyl Ions in Aqueous Electrolyte Solutions. *Chem. Eng. Sci.* 1988;43:1677-1684.

(22) Pigford RL. Counter-Diffusion in a Wetted Wall Column. Ph.D. Thesis, University of Illinois at Urbana-Champaign, Urbana, IL, 1941.

(23) Hobler T. *Mass Transfer and Absorbers*. Oxford: Pergamon Press, 1966.

(24) Bird RB, Stewart WE, Lightfoot EN. *Transport Phenomena* (2nd edition). New York: John Wiley & Sons, Inc., 2002.

(25) Pacheco MA. Mass Transfer, Kinetics and Rate-based Modeling of Reactive Absorption. Ph.D. Thesis, University of Texas at Austin, Austin, TX, 1998.

(26) Lohse M, Alper E, Quicker G, Deckwer WD. Diffusivity and Solubility of Carbon Dioxide in Diluted Polymer Solutions. *AIChE J.* 1981;27:626-631.

(27) Tsai RE, Seibert AF, Eldridge RB, Rochelle GT. Influence of viscosity and surface tension on the effective mass transfer area of structured packing. *Energy Procedia*. 2009;1:1197-1204.

(28) Olujic Z, Kamerbeek AB, de Graauw J. A corrugation geometry based model for efficiency of structured distillation packing. *Chem. Eng. Process.* 1999;38:683-695.

(29) Sidi-Boumedine R, Raynal L. Influence of the viscosity on the liquid hold-up in trickle-bed reactors with structured packings. *Catal. Today*. 2005;105:673-679.

(30) Petre CF, Larachi F, Iliuta I, Grandjean BPA. Pressure drop through structured packings: Breakdown into the contributing mechanisms by CFD modeling. *Chem. Eng. Sci.* 2003;58:163-177.

(31) Aroonwilas A. Mass-Transfer with Chemical Reaction in Structured Packing for CO_2 Absorption Process. Ph.D. Thesis, University of Regina, Regina, Saskatchewan, 2001.

(32) Moniuk W, Pohorecki R. Viscosity and Density of Sodium and Potassium Alkaline Solutions. *Hung. J. Ind. Chem.* 1991;19:175-178.

(33) Haar L, Gallagher JS, Kell GS. *NBS/NRC Steam Tables: Thermodynamic and Transport Properties and Computer Programs for Vapor and Liquid States of Water in SI Units.* Washington, D.C.: Hemisphere Publishing Corporation, 1984.

(34) McGlamery GG. Liquid Film Transport Characteristics of Textured Metal Surfaces. Ph.D. Thesis, University of Texas at Austin, Austin, TX, 1988.

(35) Nicolaiewsky EMA, Tavares FW, Rajagopal K, Fair JR. Liquid film flow and area generation in structured packed columns. *Powder Technol.* 1999;104:84-94.

(36) Wilson I. Gas-Liquid Contact Area of Random and Structured Packing. M.S. Thesis, University of Texas at Austin, Austin, TX, 2004.

(37) Henriques de Brito M, von Stockar U, Bangerter AM, Bomio P, Laso M. Effective Mass-Transfer Area in a Pilot Plant Column Equipped with Structured Packings and with Ceramic Rings. *Ind. Eng. Chem. Res.* 1994;33:647-656.

(38) Olujic Z, Seibert AF, Fair JR. Influence of corrugation geometry on the performance of structured packings: an experimental study. *Chem. Eng. Process.* 2000;39:335-342.

(39) Fair JR, Seibert AF, Behrens M, Saraber PP, Olujic Z. Structured Packing Performance - Experimental Evaluation of Two Predictive Models. *Ind. Eng. Chem. Res.* 2000;39:1788-1796.

(40) Olujic Z, Jansen H, Kaibel B, Rietfort T, Zich E. Stretching the Capacity of Structured Packings. *Ind. Eng. Chem. Res.* 2001;40:6172-6180.

(41) Green CW, Farone J, Briley JK, Eldridge RB, Ketcham RA, Nightingale B. Novel Application of X-ray Computed Tomography: Determination of Gas/Liquid Contact Area and Liquid Holdup in Structured Packing. *Ind. Eng. Chem. Res.* 2007;46:5734-5753.

(42) Alix P, Raynal L. Liquid distribution and liquid hold-up in modern high capacity packings. *Chem. Eng. Res. Des.* 2008;86:585-591.

Modeling Stripper Performance for CO$_2$ Removal with Amine Solvents

Quarterly Report for July 1 – September 30, 2009

by David Van Wagener

Supported by the Luminant Carbon Management Program

and the

Industrial Associates Program for CO$_2$ Capture by Aqueous Absorption

Department of Chemical Engineering

The University of Texas at Austin

October 1, 2009

Abstract

Since Hilliard developed thermodynamic models for various amine solvents, additional experimental data have been collected at new conditions. The data primarily of interest have been for concentrated piperazine (PZ). The Hilliard model performed well for low PZ concentrations, 0.9 m–5 m, but 8 m PZ will be used in future simulations. This model was previously updated with high amine concentration data, resulting in the June 2009 PZ model. The property predictions by this model were investigated to evaluate the overall accuracy of the model for 8 m PZ. The VLE and heat capacity predictions showed little deviation from laboratory data. The volatility predictions were difficult to scrutinize because there are few data points from the lab. The Aspen Plus® predictions were systematically lower than the available lab data, but the deviations may be reduced when new data are collected with new FTIR software. Unlike these properties, the speciation and heat of absorption predictions are not yet acceptable. The bicarbonate concentration was large compared to other solvents, but no data are available for 8 m PZ. The heat of absorption predictions were questionable for two reasons. First, the predictions did not approximate the magnitude of laboratory data collected at NTNU. However, there was agreement between the calculated values using the Gibbs-Helmholtz equation with the measured VLE and Aspen Plus® predictions using this model. The Aspen predictions and Gibbs-Helmholtz calculations both have values around 60–70 kJ/mol CO$_2$, whereas the laboratory data is 20–30 kJ/mol CO$_2$ higher with +/-10 kJ/mol CO$_2$ scatter for all temperatures. The second concern with heat of absorption predictions in Aspen Plus® was whether the Gibbs-Helmholtz calculations are consistent with calorimetric results. Prior analysis with MEA demonstrated a slight difference between these two calculation methods, but the difference is more severe for 8 m PZ.

Next, analysis of various stripper configurations with different complexity levels using 9 m MEA was initiated. The most efficient configuration thus far is equilibrium flashes in a double matrix arrangement. The double matrix configuration has only been evaluated using all equilibrium

flashes, but it had a 4.2% improvement over a simple stripper, with 35.3 kJ/mol CO_2 and 33.8 kJ/mol CO_2 for the simple stripper and double matrix, respectively. A configuration developed by Fluor consisting of a simple stripper with an adiabatic flash on the lean stream also performed better than the simple stripper, but only reduced the equivalent work requirement to 34.4 kJ/mol CO_2. Other evaluated configurations which did not outperform the simple stripper included 1-stage and 2-stage flashes.

Introduction

Piperazine (PZ) is of interest as a solvent for CO_2 capture because it has significantly higher capacity than 7 m monoethanolamine (MEA), the baseline and industry standard. A PZ molecule has two amine groups, which leads to this increased capacity. High solvent capacity results in less solvent being circulated between the absorber and stripper, so the stripper reboiler duty decreases because the sensible heat input for the solvent is lowered. The CO_2 absorption rate for piperazine is enhanced over MEA as well, also possibly due to the two amine groups per molecule. As an added benefit, PZ has no detectable thermal degradation up to 150 °C. Many explored stripper configurations operate more efficiently at high temperatures, so it is expected that PZ will perform better than MEA (Freeman et al., 2008).

Previously, a thermodynamic model was developed for PZ (Hilliard, 2008) and it was used to simulate a simple stripper with the accompanying rich and lean pumps, cross heat exchanger, and multi-stage compressor. The simulations produced results with few convergence errors; however, the behavior while varying the lean loading specification was unexpected. Typically the calculated equivalent work of the stripper has a single distinct optimum lean loading (Oyenekan, 2007), but in this case, the PZ stimulation demonstrated both a local and global optimum (Van Wagener, 2008) . The local optimum was at a lean loading of 0.30, an expected value based upon the measured VLE at absorber conditions. The global optimum was at a lean loading of 0.15, and the temperature profile was very hot; reaching temperatures over 120 °C. A suggested source for this unusual behavior was the accuracy of the model predictions of thermodynamic values for the solvent. The predictions that seemed particularly questionable were the solvent heat capacity and heat of absorption of CO_2. Prior work generated heat capacity data for 8 m PZ by using trends in lower concentration PZ solvents. The model parameters were regressed to better predict heat capacity. However, the fit was not improved. The heat capacity data used for the regression were extrapolated from values at lower PZ concentrations. Though not an ideal source of data, these values were the only ones available at the time.

More recently, heat capacity data for 8 m PZ were collected by Nguyen. These data were used to improve the heat capacity predictions in a new regression incorporating A-E heat capacity parameters. In addition to regressing the parameters for the electrolytes in the system, the dielectric constant for PZ was also included to improve the fit of the VLE. This inclusion seemed to greatly benefit the accuracy of the Aspen Plus® predictions, though it was an atypical set of parameters to regress because the values of dielectric constants are generally known from lab experiments. However, these data were not readily available for PZ, and the values used by Hilliard took the values for piperidine and were corrected using one available data point for PZ. Piperidine was used because it has similar structure to PZ; it is a cyclic molecule with only one amine group. In this quarter, the accuracy of the June 2009 PZ model is further assessed.

It has been hypothesized that there is a relation between configuration complexity and performance that can be correlated. Determining this relation will be the bulk of this Ph.D. project, and some preliminary work in this area has been conducted this quarter. Since complexity is a broad undertaking, the analysis starts at the most simple separation method, a single heated flash, and progresses systematically to more complex configurations.

Methods and Results

Assessment of PZ Thermodynamic Model Accuracy

Last quarter, a PZ model was developed, called the June 2009 model (061609 PZ Model). By the time of the last quarterly report, the VLE and heat capacity data were compared against experimental data and the model was shown to offer a significant improvement in predictions for these properties for 8 m PZ over the original Hilliard PZ model. The fit of these properties are shown below in Figure 1 and Figure 2.
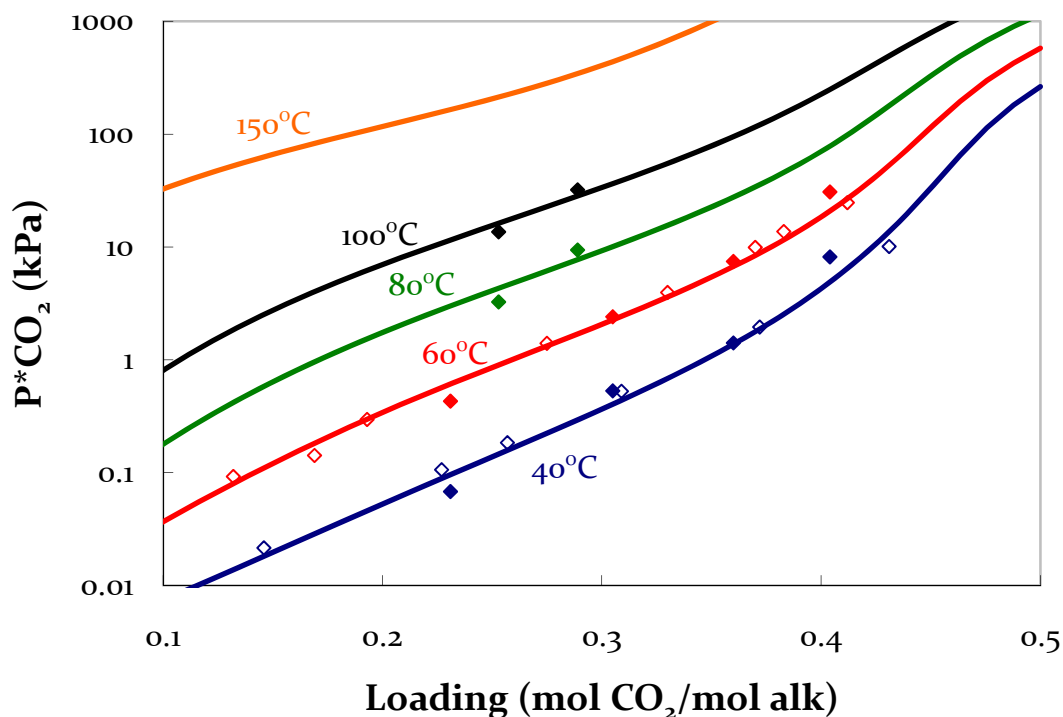
Figure 1: CO$_2$ solubility predictions for 8 m PZ. Points: data collected by Hilliard and Dugas, Lines: model predictions.
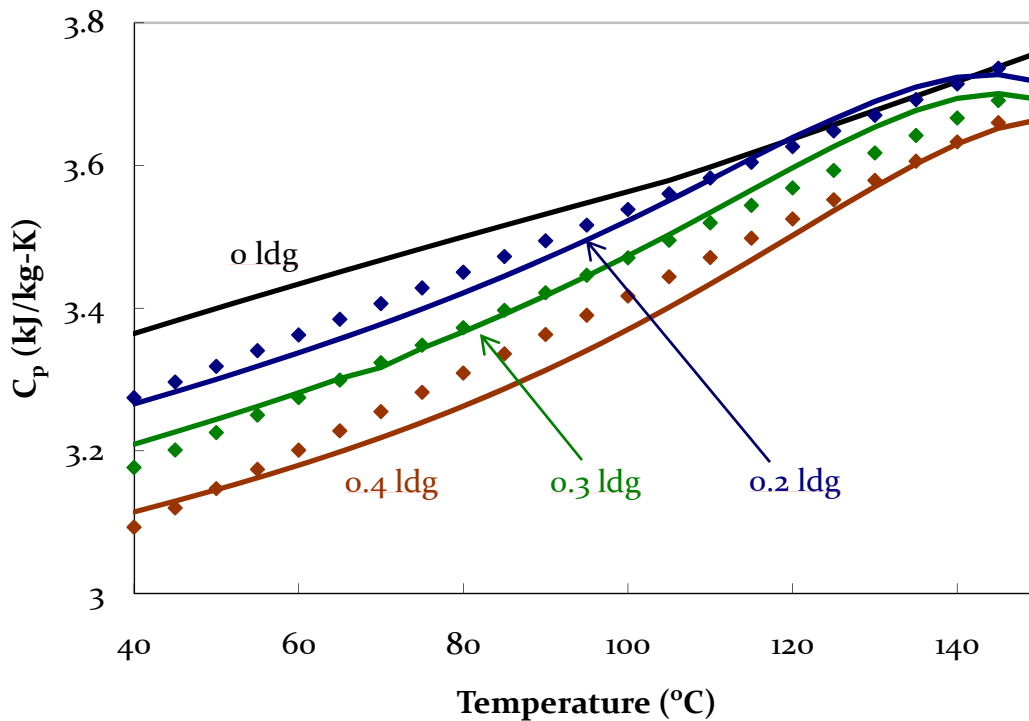
Figure 2: Liquid mixture heat capacity predictions for 8 m PZ. Points: data collected by Nguyen, Lines: model predictions.

The accuracy of the volatility predictions was investigated this quarter. Only a few laboratory measurements have been gathered thus far by Nguyen. Additionally, the software in the FTIR used for collecting volatility measurement has since been updated to improve the accuracy, suggesting that the current data points need to be replaced by data collected with the new software. The more recent data for other solvents collected with the new software have generally been lower than previous measurements at similar conditions, so the same could be expected for the 8 m PZ data. A plot of the Aspen Plus® volatility predictions along with the old volatility measurement is shown in Figure 3.
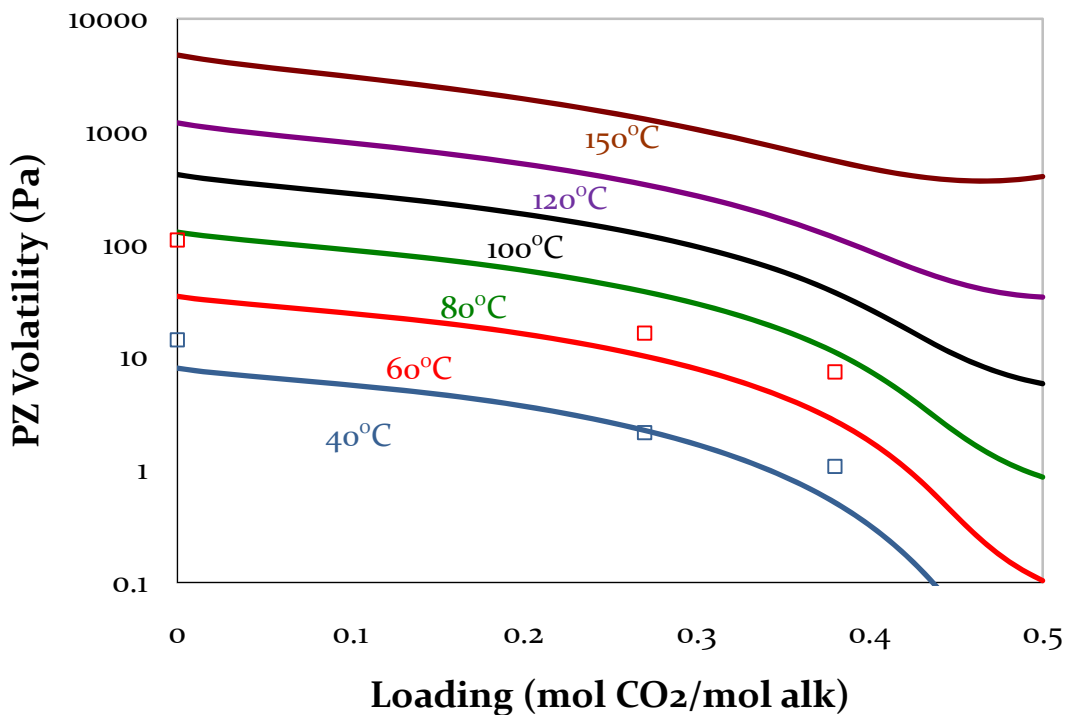
Figure 3: Solvent volatility for 8 m PZ. Points: data collected by Nguyen, Lines: model predictions.

Two properties without reliable laboratory data are heat of absorption and speciation. Heat of absorption has been measured by Freeman using the apparatus at NTNU, but there is excessive scatter in the measurements and the values are 30–40% higher than what is expected by estimating the heat of absorption using the VLE and the Gibbs-Helmholtz relation. The heat of absorption is expected to be 60–70 kJ/mol CO_2, which can be used as a basis for analyzing the heat of absorption predicted by the Aspen Plus[®] model. The speciation is predicted by the Aspen Plus[®] model in order to fit all other thermodynamic properties. Next, the speciation of 8 m PZ has not been measured, but the trends approximately follow what is expected. As no data were available, speciation was not used for the regression, though, and its accuracy is essential because all other properties depend on it in some form. Comparing the predicted speciation of 8 m PZ to previous data for other solvents (Hilliard, 2008) suggests that the bicarbonate concentration is far too high. This will be an important point for improvement in future regressions. The heat of absorption and speciation predictions are shown below in Figures 4 & 5, respectively.
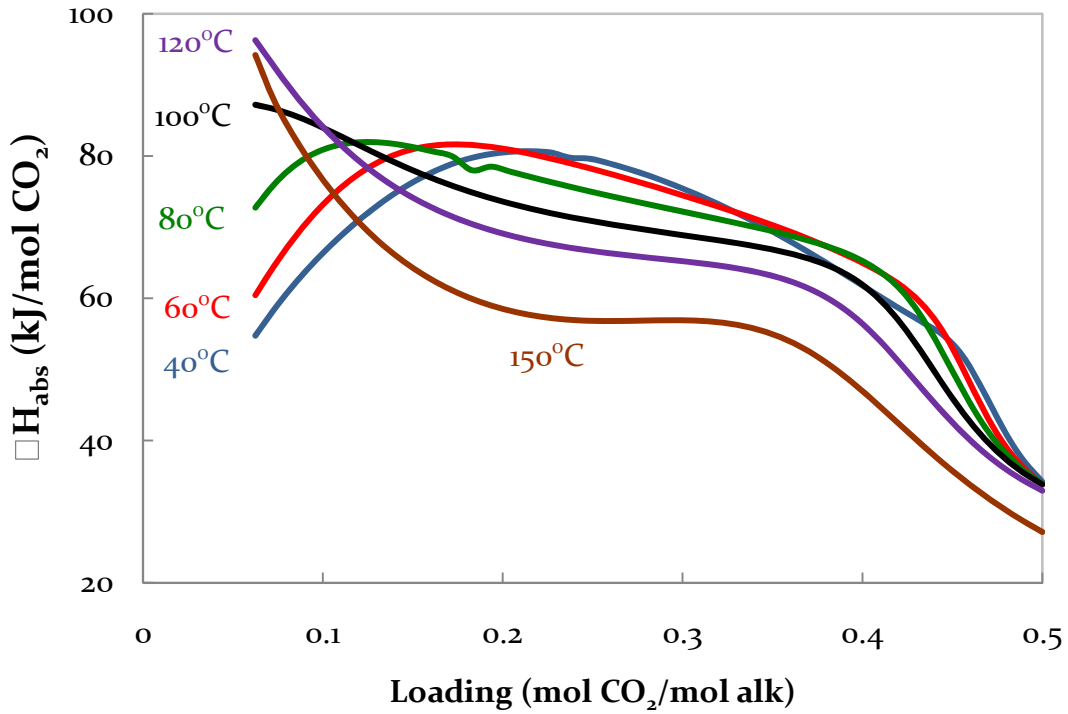
Figure 4: Aspen Plus® model heat of absorption predictions for 8 m PZ.
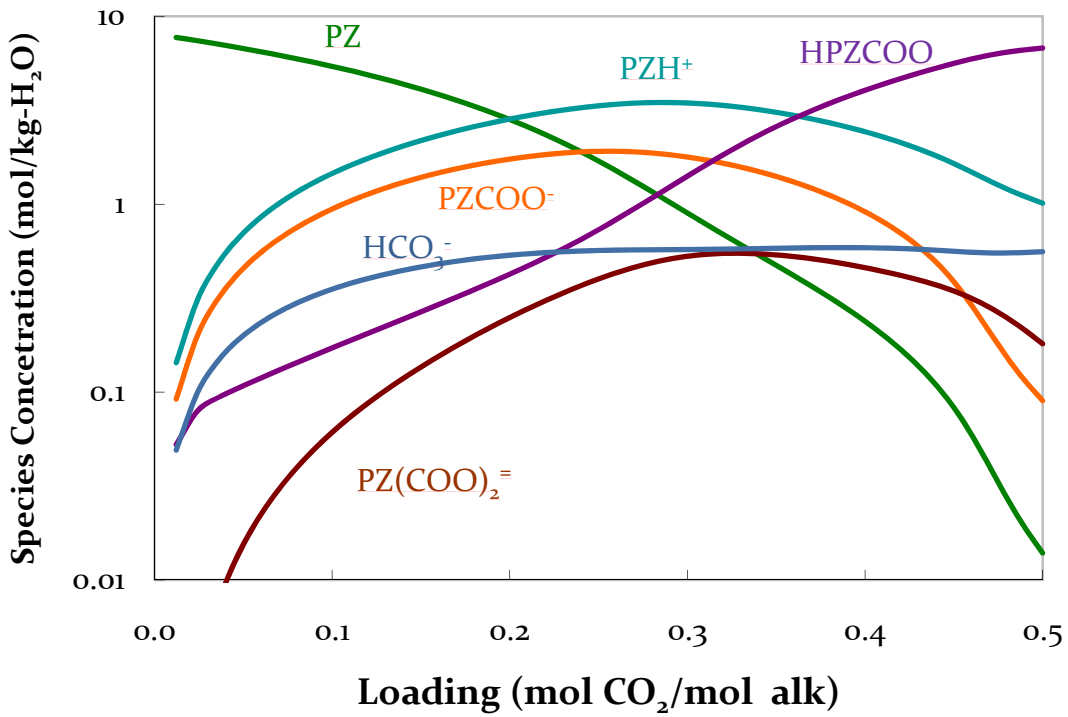
Figure 5: Aspen Plus® model predictions for liquid phase speciation in 8 m PZ.

In addition to recognizing the potential speciation issue, the heat of absorption predictions have also become a concern. Heat of absorption predictions in Aspen Plus® can be calculated using the calorimetric method as well as the Gibbs-Helmholtz equation. The calorimetric method utilizes a flash to absorb a differential amount of gaseous CO_2 into the amine solvent at a specific temperature and loading. The amount of absorbed CO_2 is kept low to prevent a significant change in loading or speciation. The heat duty required to absorb the CO_2 while maintaining the temperature and pressure is equal to the heat of absorption when normalized by the CO_2 rate:

$$\Delta H_{abs} = {Q_{abs}}/{n_{CO_2}} \tag{1}$$

The Gibbs-Helmholtz equation can be naturally transformed to directly calculate the heat of absorption. The traditional form of equation uses the heat of vaporization when considering a pure liquid, but this term becomes the heat of absorption when there are multiple components and a reaction is occurring in the liquid phase. The equation is as follows:

$$\frac{d(\ln P_{CO_2})}{d(1/T)} = -\frac{\Delta H_{abs,CO_2}}{R} \tag{2}$$

These two methods should provide equivalent results; however, the PZ model predictions are not consistent. Previous MEA models, like the one by Hilliard, also demonstrated this issue, but only to a small extent. As shown in Figure 6 the difference between the two calculation methods is exaggerated for the PZ model. The results for 40 °C are selectively shown, but the trends are similar for 60 °C–150 °C. A collaboration with AspenTech is currently trying to resolve this issue to ensure that the regressed model is behaving accurately.
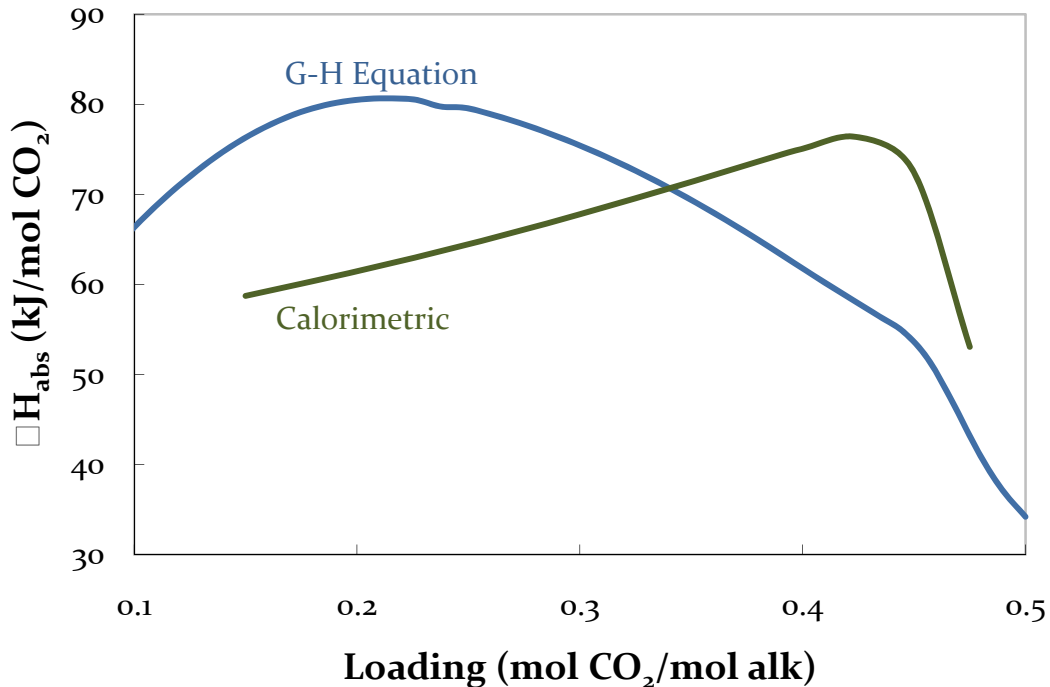
Figure 6: Aspen Plus® model predictions of heat of absorption for 8 m PZ at 40 °C using Gibbs-Helmholtz and calorimetric calculations.

Complexity Modeling

In this quarter, the analysis of the effect of configuration complexity on performance has started. The definition of complexity is still loose, but it is expected that the number of process units in the configuration is roughly related to a complexity "value". At this point, the complexity is calculated as the total number of major pieces of equipment, excluding typical pumping and compression equipment. For example, a single-stage heated flash has a value of 2 (a heater and separation vessel), and a simple stripper has a value of 3 (a heater, vessel, and packing). The end goal will be to analyze the performance of a wide range of configurations with varying levels of complexity. It is expected that more complex configurations will improve performance but have a diminishing return at higher complexity. It is also expected that different configurations with similar complexity values will perform differently according to how efficiently the process units are arranged. A systematic justification for the arrangement of process units as it relates to performance may be possible.

The analysis has begun at the most simple separation method, a 1-stage flash, and is building upward in total number of pressure stages. Each stage has a number of options: flash vs. packing, heated vs. adiabatic, and recompression of the vapor to the prior stage. The configurations that have been modeled thus far are: 1-stage flash, 2-stage flash (isothermal, only heat stage 1, and only heat stage 2), simple stripper, stripper with adiabatic flash on lean (patented configuration by Fluor), and double matrix configuration with equilibrium flashes. The diagrams of these configurations can be found in Figures 7–11.
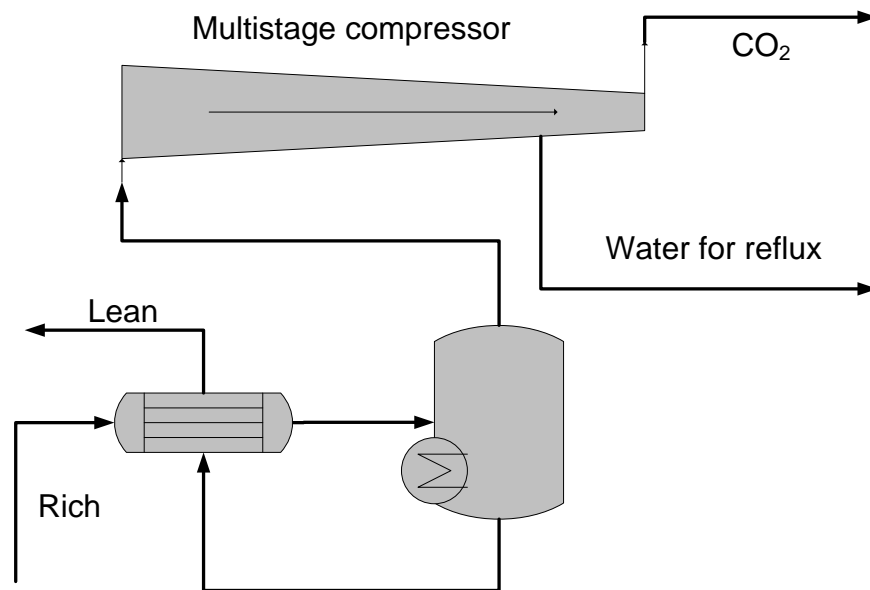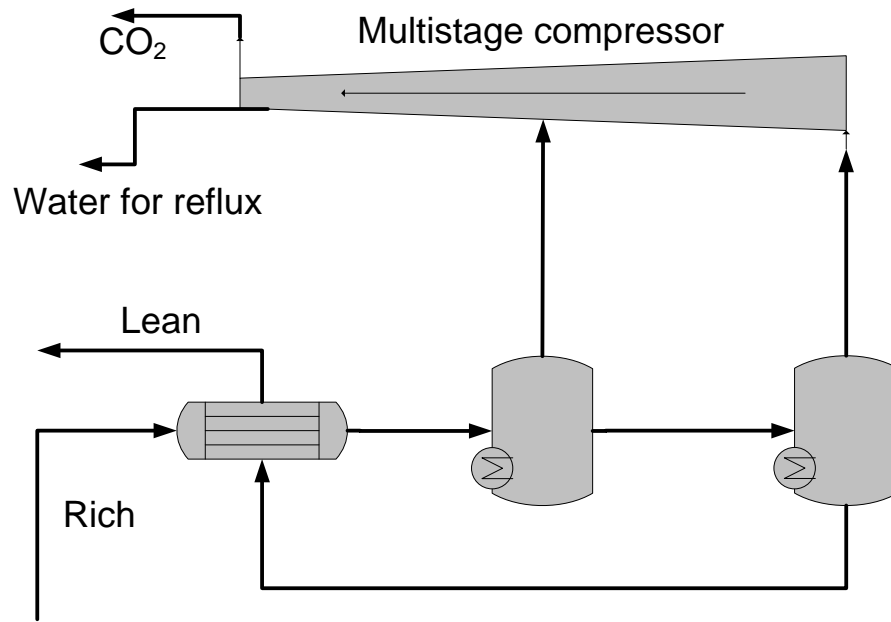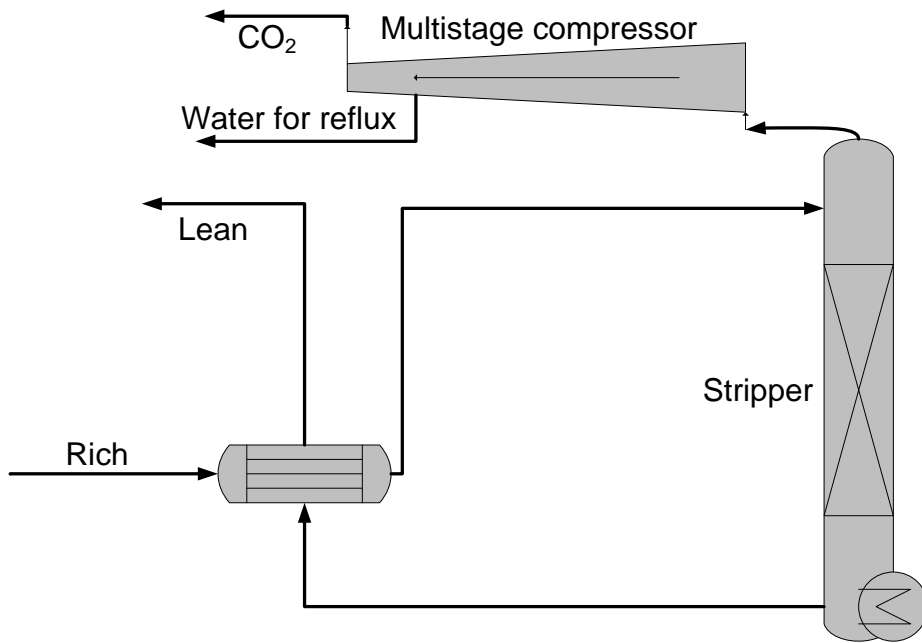

Figure 7: 1-Stage Flash

Figure 8: 2-Stage Flash
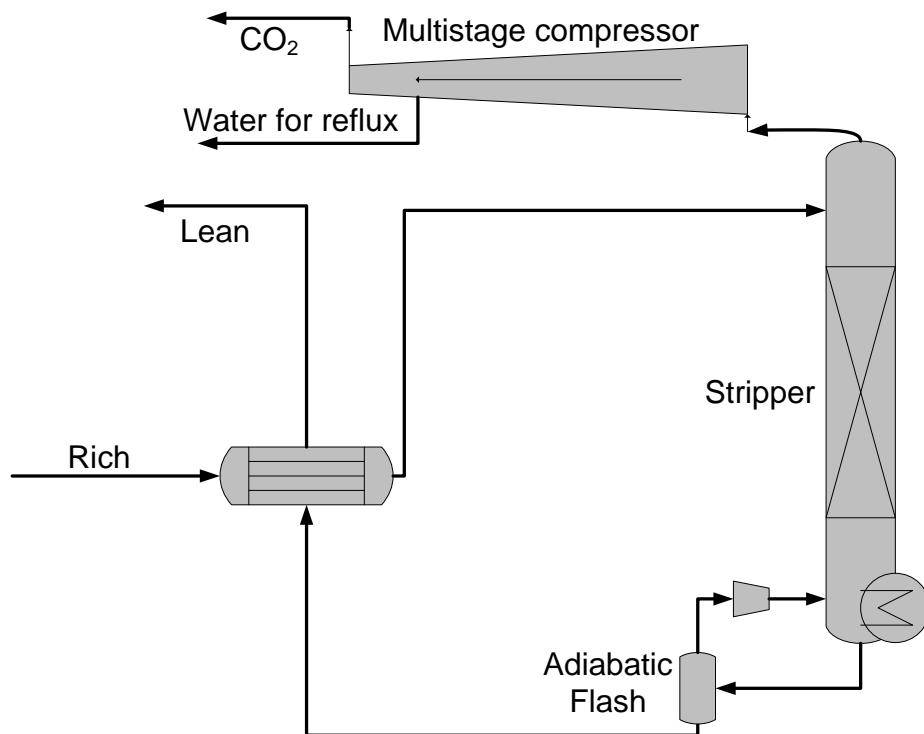

Figure 9: Simple Stripper

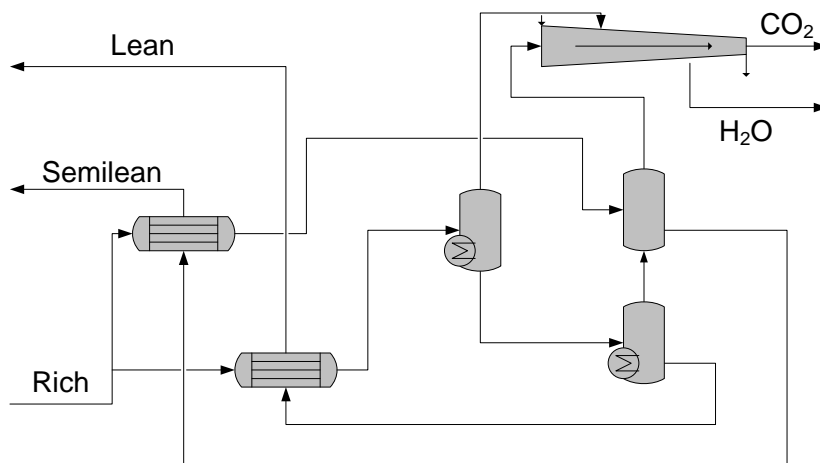**Figure 10: Stripper with Lean Adiabatic Flash**

Figure 11: Double Matrix Configuration with Equilibrium Flashes

The model for MEA developed by Hilliard (2008) works well for the 9 m solvent, so it was used for this analysis. The simulations were performed with as many variables held constant as possible. With this goal in mind, the stripped CO_2 was compressed to 15 MPa using 7 stages in all simulations. The rich pumps achieved the vessel pressure for a given configuration, and it also accounted for an additional 50 kPa for possible frictional losses as well as 250 kPa for gravitational losses if a column was used in exchange for a flash vessel. A constant rich loading

of 0.5 was used, which corresponds approximately to a CO_2 partial pressure of 5 kPa in the solvent. A 5 °C cold side approach was specified on all heat exchangers. A 10 °C approach on the steam reboilers was used for calculations of equivalent work. As in previous work, equivalent work was calculated as follows:

$$W_{eq} = \sum_{i=1}^{n_{reboilers}} 0.75 * Q_i \left(\frac{T_i + 10K - T_{sink}}{T_i + 10K}\right) + W_{pumps} + W_{comps} \tag{3}$$

where Q_i and T_i are the duty and temperature for reboiler i. The lean loading was optimized to minimize total equivalent work for each configuration. The equivalent work was evaluated for lean loadings ranging from 0.2 to 0.45. The optimum lean loadings were all above 0.35, but the performance was evaluated down to lean loadings of 0.2 because many industrial users prefer these low lean loadings to improve absorber performance.

This analysis considered only isothermal operation, with the exception of the configurations with adiabatic flashes. All configurations were evaluated using heater/reboiler temperatures of 110 °C, 120 °C, and 130 °C. 120 °C is considered to be the ceiling temperature for MEA due to thermal degradation issues at higher temperatures. However, 130 °C was included for completeness. To minimize the total number of graphs, Figure 12 below shows the performance of all six configurations using 120 °C as the reboiler temperature. There are two curves for the double matrix configuration with equilibrium flashes. One uses a split ratio of 20 : 80 between the low pressure and high pressure columns because this was found to be the optimum in much earlier work using 4.5 m K$^+$/4.5 m PZ. Following this analysis using the previous optimum split ratio, another case for 120 °C using this configuration was done while simultaneously optimizing the split ratio for each lean loading.
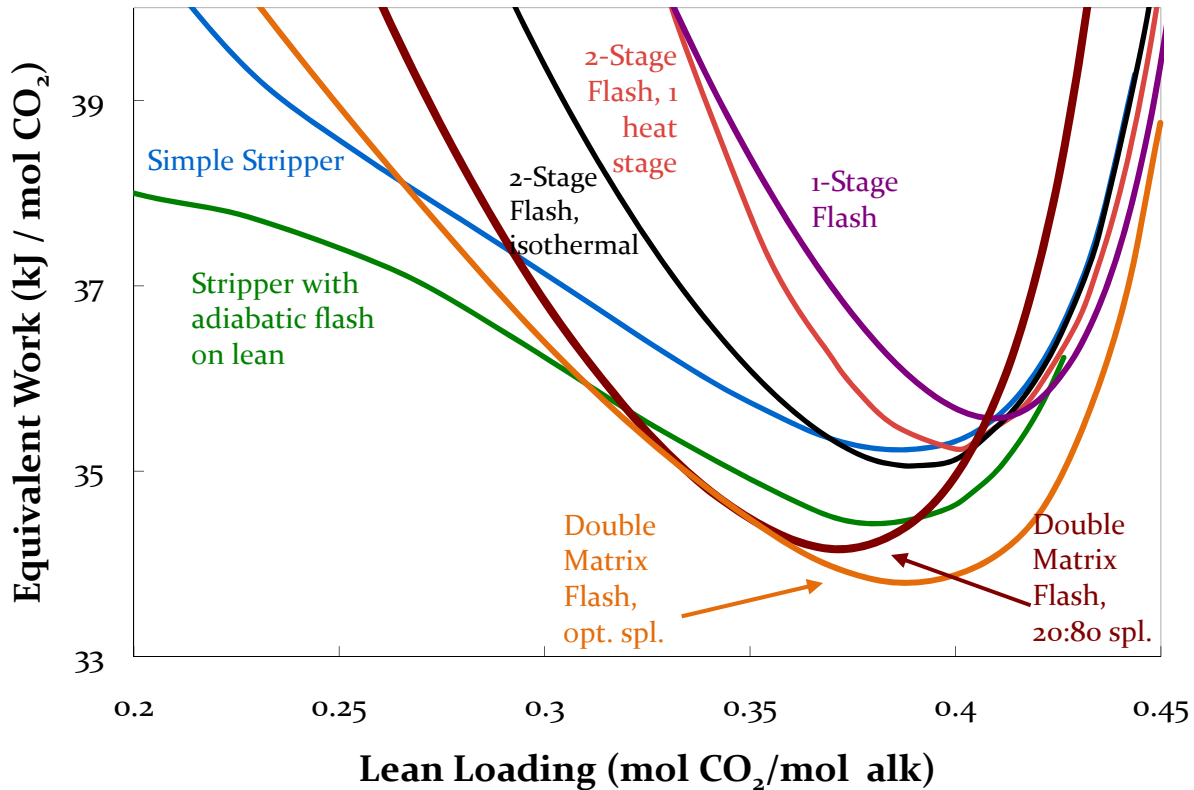
Figure 12: Equivalent work optimization for configurations of varying complexity, 9 m MEA, 120°C.

Through the evaluation of these configurations, the double matrix equilibrium flash configuration performed the best with an equivalent work of 33.8 kJ/mol CO_2 at an optimum lean loading of 0.39 using a split ratio of 7.5 : 92.5, whereas the work requirement was 34.2 kJ/mol CO_2 at an optimum loading of 0.37 using a split ratio of 20 : 80. The 2-stage isothermal flash configuration shows only minimal improvement over a simple stripper. The 2-stage flash configurations with only one heat stage demonstrated optimum performance roughly equivalent to the simple stripper, but with a slightly higher optimum loading. The placement of the heat stage for these configurations made minimal difference, but heating the first stage required slightly less energy because it was more isothermal over the case where the second stage was heated.

The configuration patented by Fluor, a stripper with an adiabatic flash on the lean solvent with vapor recompression, performed significantly better than the simple stripper, but was not as good as the double matrix. However, the two stripper configurations operate significantly more efficiently at very lean loadings compared to the configurations utilizing only equilibrium flashes. This result is a consequence of the packing having significant interfacial area for CO_2 stripping to take place. At low lean loadings where the CO_2 capacity of the solvent is high, packing removes the CO_2 more efficiently. The packing spreads a low mass transfer driving force across the height of the column instead of having single large driving forces in the

12

reboilers. For this reason, it is expected that applying packing to the flash configurations investigated will improve their performance at low lean loadings. It is uncertain whether their performance at the optimum lean loading will change significantly.

Conclusions

The property predictions by the June 2009 PZ model were investigated to evaluate the overall accuracy of the model for 8 m PZ. As documented in the previous quarter, the VLE and heat capacity predictions were very accurate. The volatility predictions were difficult to scrutinize because there are few data points from the lab. However, the Aspen Plus® predictions were systematically lower than the lab data, which may be accounted for when new data are collected with new FTIR software. Unlike these properties, the speciation and heat of absorption predictions were not adequate. The bicarbonate concentration seemed large, but no data are available for comparison with the solvent. The heat of absorption predictions were questionable for two reasons. First, the predictions did not approximate the magnitude of laboratory data collected at NTNU. However, the expected magnitude of the heat of absorption can be calculated using VLE data and the Gibbs-Helmholtz equation. The Aspen Plus® predictions and Gibbs-Helmholtz calculations both have values around 60–70 kJ/mol CO_2, whereas the laboratory data value is 20-30 kJ/mol CO_2 higher. The second concern with heat of absorption predictions in Aspen Plus® was whether the Gibbs-Helmholtz calculations are consistent with calorimetric results. Prior analysis with MEA demonstrated a slight difference between these two calculation methods, but the difference is severe for 8 m PZ.

The analysis of various stripper configurations with varying levels of complexity using 9 m MEA demonstrated a great benefit by using the double matrix setup. Only the configuration using equilibrium flashes in a double matrix arrangement has been evaluated thus far, but it had a 4.2% improvement over a simple stripper, with 35.3 kJ/mol CO_2 and 33.8 kJ/mol CO_2 for the simple stripper and double matrix, respectively. A significant portion of this work requirement is due to the compression of CO_2 to 150 atm and is unavoidable. A configuration developed by Fluor consisting of a simple stripper with an adiabatic flash on the lean stream also performed better than the simple stripper, but only reduced the equivalent work requirement to 34.4 kJ/mol CO_2. Other evaluated configurations which did not outperform the simple stripper included 1-stage and 2-stage flashes.

Future Work

Further improvement of the PZ model has been passed on to other members of the group with more direct access to laboratory data. The connection with AspenTech will be maintained to properly address the inconsistency in heat of absorption calculations using the Gibbs-Helmholtz method and calorimetric method.

The complexity analysis will be continued with 9 m MEA. The double matrix configuration with packing in place of any/all of the flashes will be addressed first. Other 2-stage configurations will also be analyzed, such as a stripper with a high-pressure preflash.

References

Freeman SA, Dugas RE, Van Wagener DH, Nguyen T, Rochelle GT. CO_2 capture with concentrated, aqueous piperazine. *GHGT-9*. Washington, DC: Elsevier, 2008.

Hilliard MD. *A Predictive Thermodynamic Model for an Aqueous Blend of Potassium Carbonate, Piperazine, and Monoethanolamine for Carbon Dioxide Capture from Flue Gas.* The University of Texas, Austin. Ph.D. Dissertation. 2008.

Oyenekan, Babatunde. *Modeling of Strippers for CO2 Capture by Aqueous Amines.* Ph.D. Dissertation, The University of Texas, Austin. Ph.D. Dissertation. 2007.

Rochelle GT et al. "CO_2 Capture by Aqueous Absorption, Third Quarterly Progress Report 2008." Luminant Carbon Management Program. The University of Texas, Austin. 2008.

Modeling CO$_2$ Absorption Using Aqueous Amines

Quarterly Report for July 1 – September 30, 2009

by Jorge M. Plaza

Supported by the Luminant Carbon Management Program

and the

Industrial Associates Program for CO$_2$ Capture by Aqueous Absorption

Department of Chemical Engineering

The University of Texas at Austin

October 9, 2009

Abstract

Work continued on the development of an absorber model for 8 m PZ. The thermodynamic model was updated by Van Wagener from version 02/06/09 to version 06/16/09. This update required re-regression of the density data. A density subroutine was implemented to calculate this property independent of speciation. However, the developed subroutine could not adequately represent the density data due to issues related to the average molecular weight. Density was re-regressed satisfactorily using the Clarke model for liquid molar volume for electrolyte solutions in Aspen Plus$^{®}$. The resulting parameters are presented in this report.

The behavior of the activity coefficient of CO$_2$ was corrected using the N$_2$O analogy with a correlation for Henry's constant presented in Cullinane (2005) for N$_2$O-water and regression work by Dugas (in progress) for N$_2$O-MEA. A linear relation for the activity of CO$_2$ and loading and temperature has been proposed. Previous work had shown a maximum value around a loading of 0.30. The activity coefficient was modified using the CO$_2$-ion local contribution parameters (τ) in the e-NRTL model. Resulting values are included in this report.

PZ Model Development

Physical Properties

Van Wagener (Rochelle et al., 2009b) re-regressed the PZ model to improve heat of absorption predictions and model convergence on the 02/06/09 version. This new version, 06/16/09, presented variations on the speciation that required revision of the previously fitted physical properties. Since the liquid viscosity is calculated using a FORTRAN subroutine based on loading, the changes in the thermodynamic model had no effect on this property. On the other hand, density was fit using the Clarke model for liquid molar volume for electrolyte solutions (Rochelle et al., 2009b) and required re-regression. A FORTRAN subroutine was created to calculate density independent of speciation. The form of the regressed equation uses the molar volume because that is the variable used in Aspen Plus$^{®}$. The proposed equation was as follows:

$$\frac{V_{sol}}{V_{H_2O}} = \ln\left[Ax_{CO_2} + Bx_{PZ} + C\frac{x_{CO_2}}{x_{PZ}} + D \right] \qquad (1)$$

Where V_{sol} is the molar volume in $cm^3/gmol$ and x is the weight fraction. Table 1 shows the obtained constants.

Table 1: Regression results for the constants for the molar volume correlation (equation 1)

Constant	A	B	C	D
Value	-1.9278	5.7465	0.6569	1.8554

The resulting correlation adequately fits the density data for 5 m, 7 m, 8 m, and 9 m PZ and from 0.20 to 0.46 mol CO_2/mol alkalinity (Rochelle et al., 2009b) as shown in Figure 1. However, when implemented in Aspen Plus® the correlation is no longer satisfactory (Figure 2).
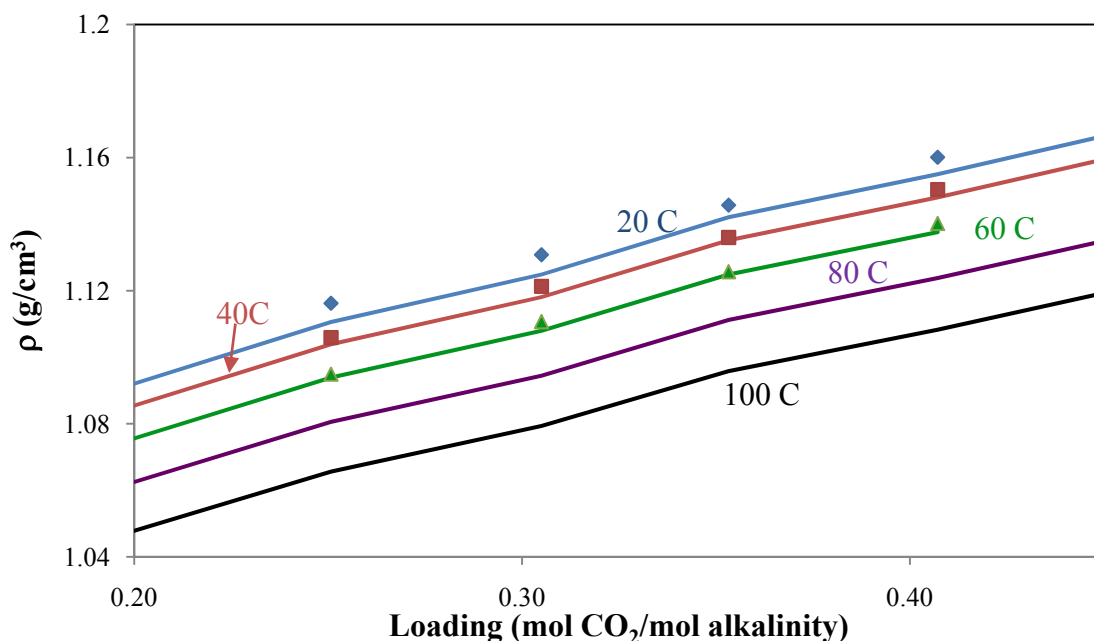
Figure 1: Density fit for 8 m PZ. Points by Freeman (Rochelle et al., 2009b). Lines using equation 1. Data for 80 °C and 100 °C are included to show extrapolation capacity of the correlation.
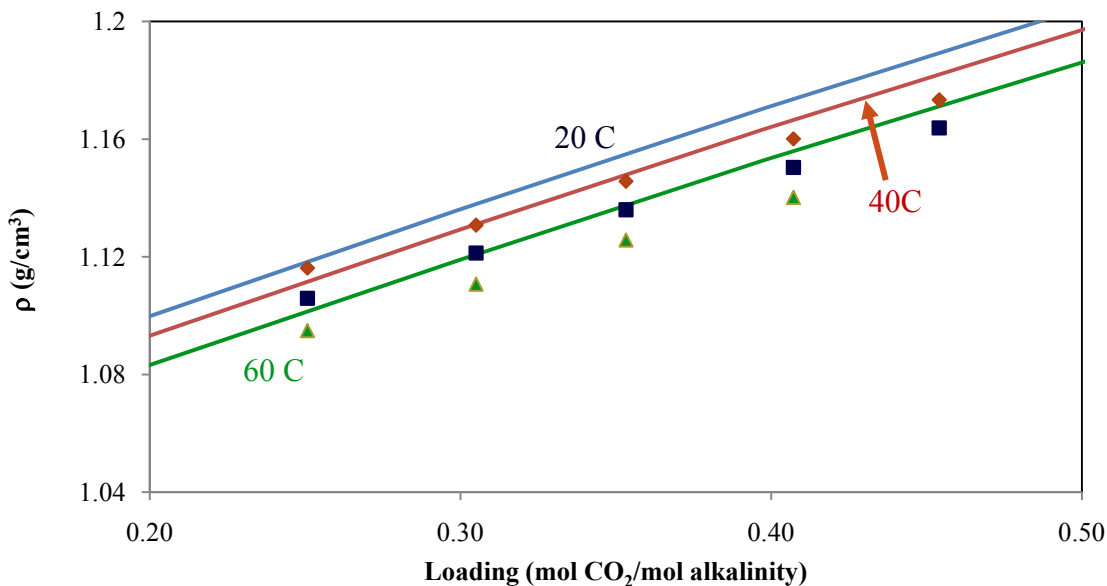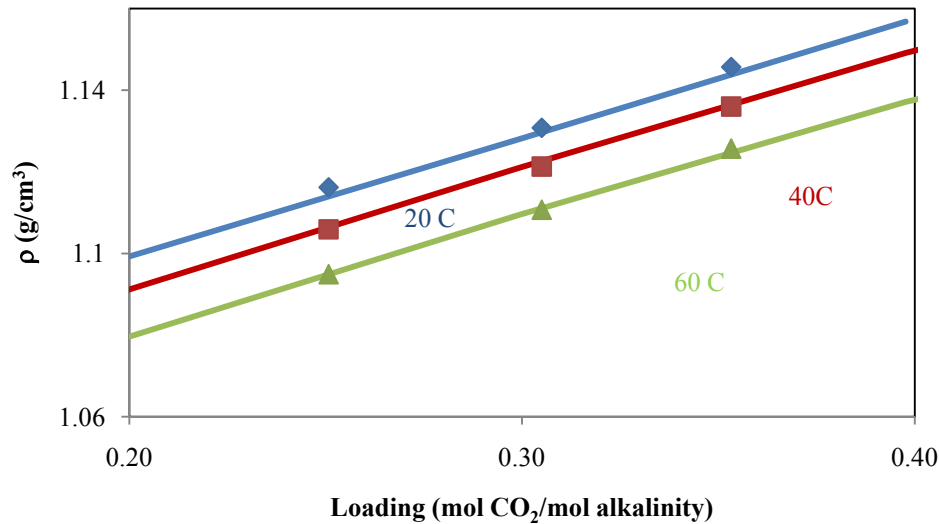
Figure 2: Density fit for 8 m PZ. Points by Freeman (Rochelle et al., 2009b). Lines generated in Aspen Plus® using a FORTRAN subroutine with equation 1.

The reason for these discrepancies seems to lie in the calculation of the average molecular weight. Since Aspen requires the molar volume to calculate the density, the experimental data is regressed using the average molecular weight (MW$_{ave}$) to convert to molar volume. The developed correlations are based on an average molecular weight calculated using the molar fractions of water, total piperazine, and CO_2. The average molecular weight in Aspen Plus® uses the true species thus the two values are different, as shown in Figure 3. These results demonstrate that it is not possible to decouple this calculation from the system speciation making the use of a FORTRAN subroutine to calculate density, pointless. Therefore, density was re-regressed using the Clarke model for liquid molar volume for electrolyte solutions as presented in a previous report (Rochelle et al., 2009c). The final model parameters are presented in Table 2 and the obtained fit is shown in Figure 4.
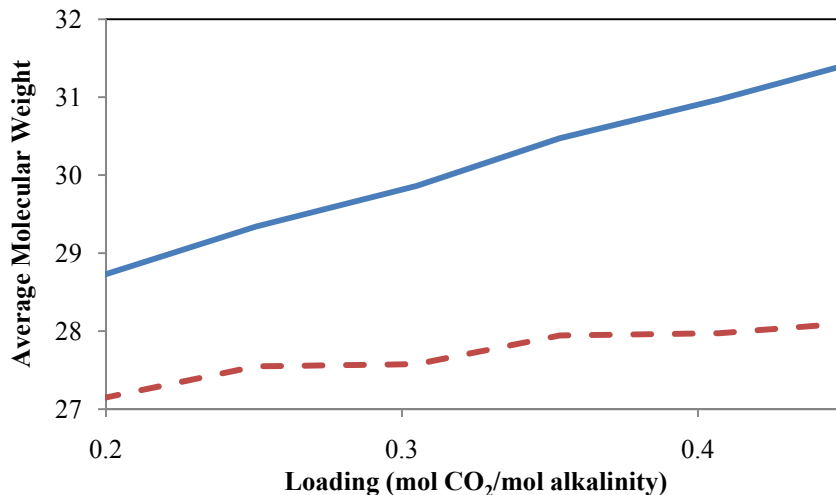
Figure 3: Average molecular weight change for 8 m PZ at 40 °C. (——)calculated using speciation in Aspen Plus®. (- -) calculated using total mole fraction of PZ, CO_2 and water.

3

Table 2: Regressed parameters for the density of PZ-CO₂-H₂O

Parameter	Component(s)	Value
Z_i^{RA} (RKTZRA)	PZ	0.2519
	CO_2	0.1144
V_{ca}^{∞} (VCA)	$PZH^+ - PZCOO^-$	0.1341
	$PZH^+ - PZ(COO^-)_2$	0.2418
	$PZH^+ - HCO_3^-$	0.2101
A_{ca} (ACA)	$PZH^+ - PZCOO^-$	0.2126
	$PZH^+ - HCO_3^-$	-0.5582

Figure 4: Density fit for 8 m PZ. Points by Freeman (Rochelle et al., 2009b). Lines generated in Aspen Plus® using the Clarke model for liquid molar volume for electrolyte solutions.

CO2 Activity Coefficient:

Previous work (Rochelle et al., 2009c) showed an unexpected maximum for the activity coefficient of CO_2 (γ_{CO2}) in 8 m PZ around a loading of 0.30. This variable is expected to be linear with respect to loading so work has been done to address this issue. Currently, there is no experimental data available for this system so the solubility of N_2O in water and MEA was used. The N_2O analogy was applied to calculate the activity coefficient of CO_2 in 8 m PZ. It assumes that since N_2O has a similar electrical configuration and the same molecular weight as CO_2, it behaves like CO_2 in reactive systems. This assumption implies that the ratio of solubilities for N_2O and CO_2 is constant for all systems so:

4

$$\frac{H_{CO_2}}{H_{N_2O}} = constant \tag{2}$$

Since CO_2 has fast reactions rates with amines it is not possible to measure its Henry's constant in the amine so the solubility of N_2O is used:

$$\left(\frac{H_{CO_2}}{H_{N_2O}}\right)_{AM} = \left(\frac{H_{CO_2}}{H_{N_2O}}\right)_{w} \tag{3}$$

where the sub index $_{AM}$ refers to the amine solvent and $_w$ to water.

Henry's constant for N_2O-water ($H_{N2O}{}^{w}$) was taken from Versteeg as reported in Cullinane (2005):

$$H_{N_2O}^{w} = 1.17x10^{-7} \; exp\left(\frac{2284}{T}\right) \tag{4}$$

where $H_{N2O}{}^{w}$ is in mol/m^3-Pa and T is the temperature in Kelvin.

The Henry's constant for N_2O-PZ ($H_{N2O}{}^{PZ}$) is not available for 8 m PZ so an equation regressed by Dugas for N_2O-MEA was used as an approximation:

$$\frac{1}{H_{N_2O}^{MEA}} = (4093 + 18.31x_{MEA} - 1115ldg + 294.7x_{MEA}ldg)exp\left(-1905\left(\frac{1}{T} - \frac{1}{298.15}\right)\right) \tag{5}$$

where $H_{N2O}{}^{MEA}$ is in Pa-m^3/mol, x_{MEA} is the amine weight fraction free of CO_2 and ldg is the loading of CO_2 (mol CO_2/mol alkalinity). This equation was used with the values for PZ.

The activity coefficient of CO_2 in PZ was then calculated using Henry's law:

$$P_{CO_2} = H_{CO_2}\gamma_{CO_2}^{*}x_{CO_2} \tag{6}$$

where $\gamma^{*}{}_{CO2}$ is the activity, x_{CO2} the mol fraction and P_{CO2} is the equilibrium pressure of CO_2.

Since the selected reference state is infinite dilution in water $\gamma^{*}{}_{CO2}$ approaches one. Henry's constant is then equal to:

$$H_{CO_2} = \frac{P_{CO_2}}{x_{CO_2}} \tag{7}$$

When calculating H_{CO2} from solubility data in the solvent the deviation from equation 7 can be assigned to the activity coefficient of CO_2 in the amine solution, thus:

$$\gamma_{CO_2}^{AM} = \frac{H_{CO_2}^{AM}}{H_{CO_2}^{w}} \tag{8}$$

where $\gamma^{AM}{}_{CO2}$ is the activity of CO_2 in the amine solvent. $H_{CO2}{}^{AM}$ is the apparent Henry's constant in the solvent and $H_{CO2}{}^{w}$ is Henry's constant in water. Using the N_2O analogy this equation becomes:

$$\gamma_{CO_2}^{PZ} = \frac{H_{N_2O}^{PZ}}{H_{N_2O}^{w}} \tag{9}$$

Figure 5 shows the resulting CO_2 activity coefficients in 8 m PZ for loadings from 0.1–0.5 and various temperatures.
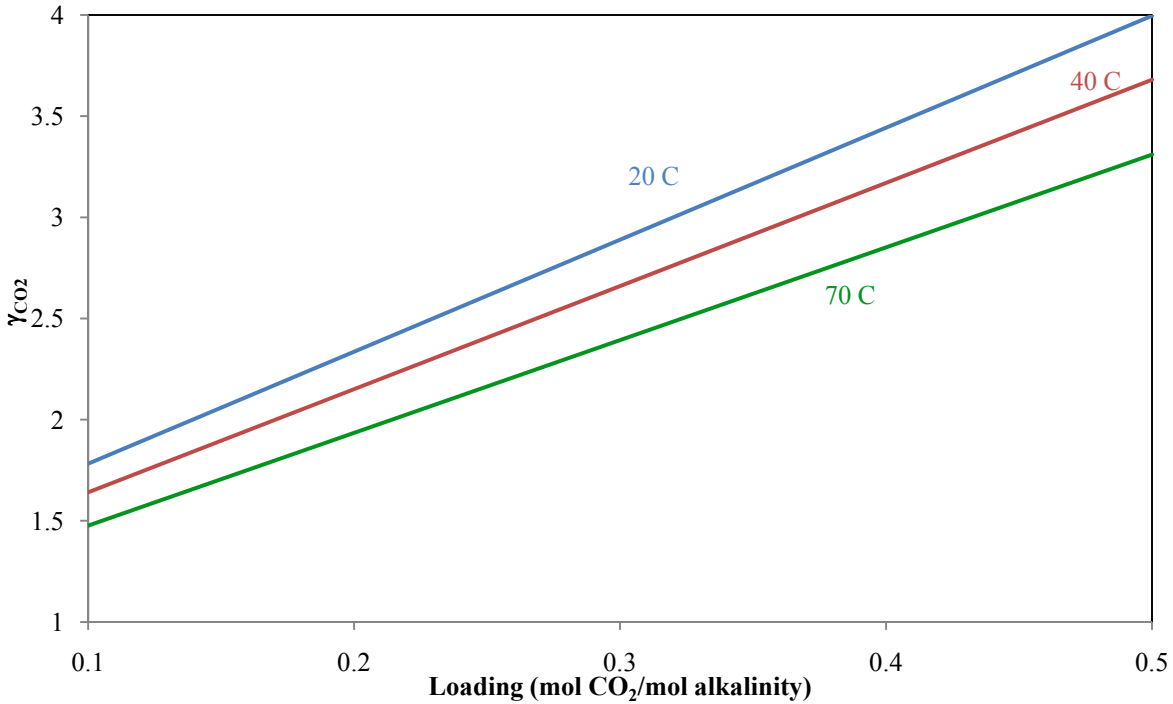
Figure 5: CO$_2$ Activity coefficients obtained using the N$_2$O analogy and data by Cullinane (2005) and Dugas (in progress)

The CO$_2$ activity coefficient was fit in Aspen Plus$^®$ with the local contribution parameters (τ) for CO$_2$- ion interaction used in calculating activity coefficients in the e-NRTL model. This had to be done as a trial and error in Aspen Plus$^®$ using the property analysis mode. Data at 40 ^{o}C and 70 ^{o}C and loadings of 0.2, 0.3, and 0.4 were fit using the A and B parameters of the τ:

$$\tau = A + \frac{B}{T} \qquad (10)$$

Table 3 shows the resulting values from the activity coefficient fit. Even though the activity coefficients at 40 ^{o}C and 70 ^{o}C were fit, there is an unexpected maximum in the temperature behavior (Figure 6) and convergence issues approaching a loading of 0.5. Additionally, the previously observed maximum with respect to loading can still be observed past 0.4 loading (Figure 7)

Table 3: τ parameters used to fit CO$_2$ activity coefficients in 8 m PZ at 40 ^{o}C and 70 ^{o}C

Parameter Pair	A (GMELCC-1)	B (GMELCD-1)
PZH$^+$,PZCOO$^-$/CO$_2$	23.5863	-8059.3067
CO$_2$/PZH$^+$,PZCOO$^-$	-659.1767	222078.6732
CO$_2$/PZH$^+$,HCO$_3^-$	28.9609	-6626.5411
PZH$^+$,HCO$_3^-$/CO$_2$	45.2129	-15223.1349
PZH$^+$, PZ(COO$^-$)$_2$/CO$_2$	55.3741	-17766.2939
CO$_2$/PZH$^+$, PZ(COO$^-$)$_2$	-3.0527	3617.7332

6
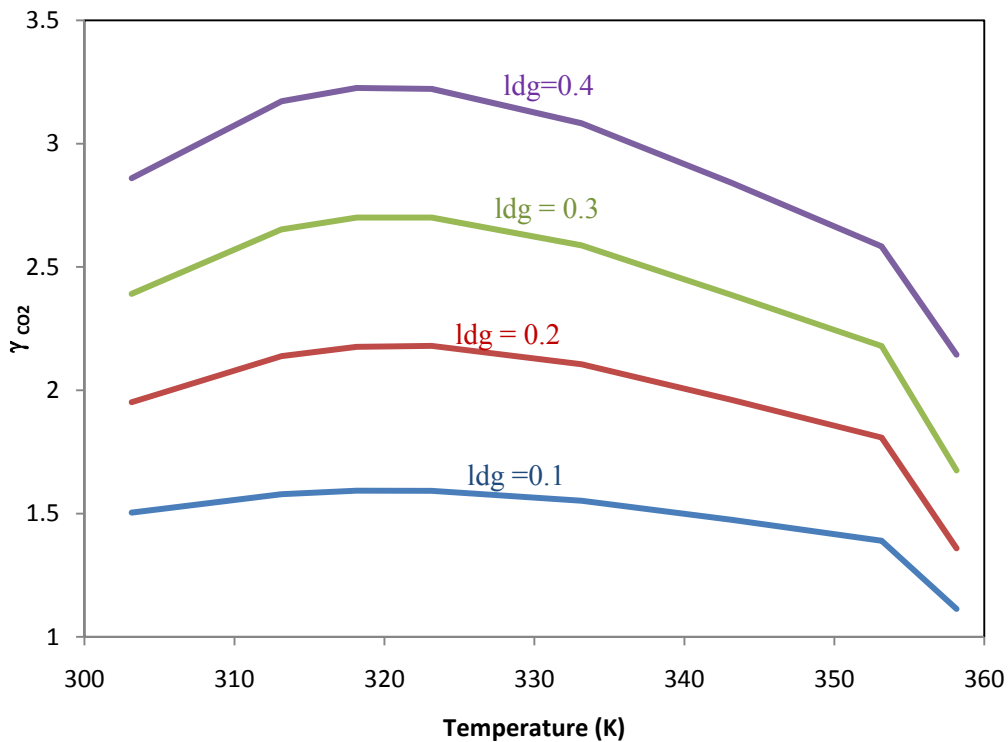
Figure 6: Change in activity coefficient of CO$_2$ with respect to temperature in 8 m PZ at various loadings predicted by Aspen Plus$^{\text{®}}$.
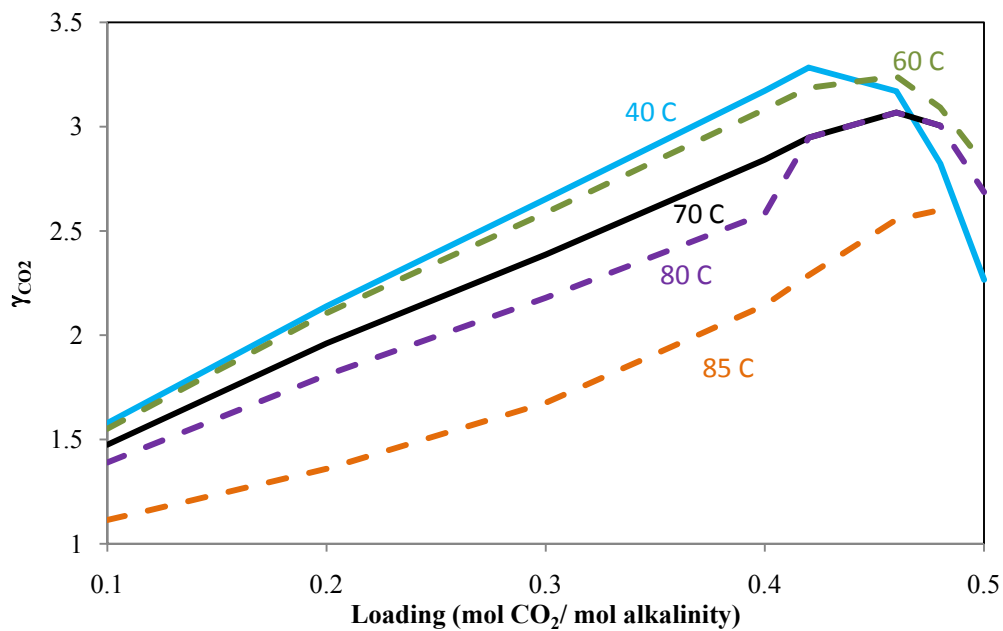
Figure 7: Change in activity coefficient of CO$_2$ with loading in 8 m PZ predicted in Aspen Plus$^{\text{®}}$. Solid lines for fitted conditions (40 $^{\text{o}}$C & 70 $^{\text{o}}$C)

The CO_2-ion local parameters were selected to change γ_{CO_2} because it was expected that due to the low concentration of CO_2 in solution their effect on the VLE would be negligible. Figure 8 shows the VLE obtained after introducing the new parameters. It is consistent with the values obtained experimentally. However, there are convergence issues above 90 $^{\circ}$C.
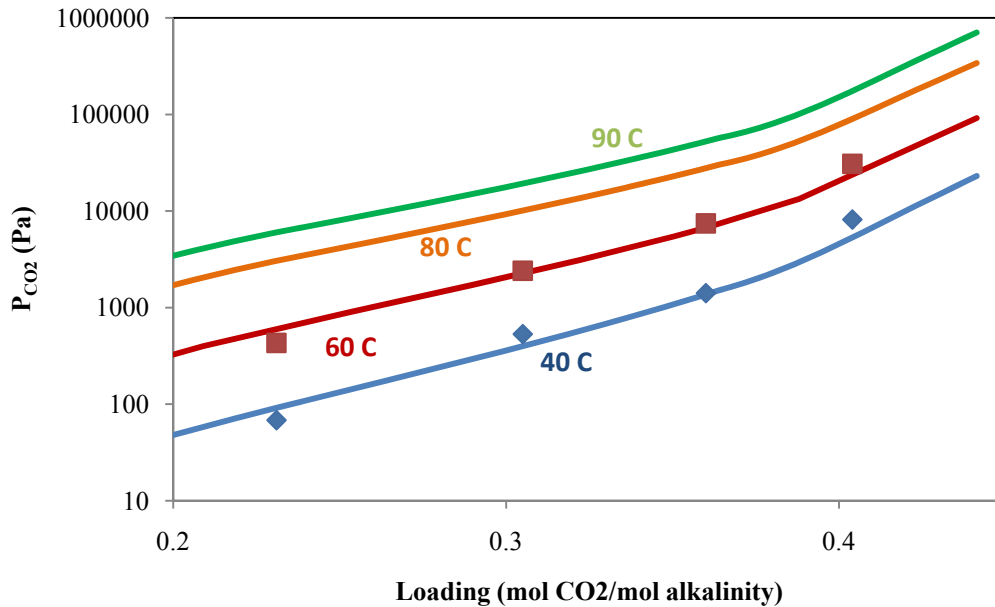
Figure 8: VLE verification for the Hilliard modified by Van Wagner version 06/16/09 (Rochelle et al., 2009c) with the modified CO_2 activity coefficients. Points by Dugas (Rochelle et al., 2009a). Solid lines in Aspen Plus®.

Conclusions

Physical Properties

It is not possible to set up a model for density independent of speciation using the proposed correlation and FORTRAN subroutine. Aspen Plus® uses the molar volume to generate density data and the conversion from molar volume to density requires the average molecular weight of the solution that depends on the speciation of the solution. However, the use of the Clarke model for liquid molar volume for electrolyte solutions proved adequate to model density although it requires re-regression of its parameters if the VLE is modified.

CO2 Activity Coefficient

The activity coefficient of CO_2 has been linearized for 8 m PZ and loadings between 0.1 and 0.42 (Figure 7). Above this range the activity coefficient behaves erratically. The temperature dependence shows a maximum for all studied loadings (Figure 6). Above 80 $^{\circ}$C an additional change of slope can be observed.

The expected loading operating range for the absorber and the available pilot plant data falls in the linearized activity coefficient region, so this fit is satisfactory. The temperature behavior will require further analysis due to the observed maximum.

The use of CO_2-ion τ parameters to modify the activity coefficient of CO_2 did not affect the VLE for CO_2-PZ. It was accurately represented with the modified parameters (Figure 8).

Further analysis is required to determine the applicability of this model at various amine concentrations since the regression work for γ_{CO2} was done at 8 m PZ.

Future Work

The modified thermodynamics will be used to create a wetted wall column (WWC) model in Aspen Plus$^®$ to extract kinetic constants for PZ from data generated by Dugas (Rochelle et al., 2009a). An absorber model will then be implemented and validated using data from the November 2008 campaign. Data reconciliation in Aspen Plus$^®$ will be used for this purpose. This new model will be used to evaluate absorber configurations.

References

Cullinane JT. *Thermodynamics and Kinetics of Aqueous Piperazine with Potassium Carbonate for Carbon Dioxide Absorption*. The University of Texas at Austin. Ph.D. Dissertation. 2005.

Dugas R. *Carbon Dioxide Absorption, Desorption and Diffusion in Aqueous Piperazine and MEA*. The University of Texas at Austin. Ph.D. Dissertation. In progress.

Rochelle GT et al. "CO_2 Capture by Aqueous Absorption, Fourth Quarterly Progress Report 2008". Luminant Carbon Management Program. The University of Texas at Austin. 2009a.

Rochelle GT et al. "CO_2 Capture by Aqueous Absorption, First Quarterly Progress Report 2009". Luminant Carbon Management Program. The University of Texas at Austin. 2009b.

Rochelle GT et al. "CO_2 Capture by Aqueous Absorption, Second Quarterly Progress Report 2009". Luminant Carbon Management Program. The University of Texas at Austin. 2009c.

Modeling Absorber/Stripper Performance with MDEA/PZ

Abstract

The goal of this study is to evaluate the performance of an absorber/stripper operation that utilizes the MDEA/PZ blended amine. Before analyzing unit operations and process configurations the thermodynamic framework for the blended amine must be satisfactorily constructed. The approach used in this study is first to construct separate MDEA and PZ models that can later be reconciled via cross parameters to accurately model the MDEA/PZ blended amine. Once the MDEA/PZ model has been completed it must be incorporated into separate absorber and stripper models similar to those developed by Van Wagener and Plaza. This study is currently in the process of developing the MDEA/PZ model based on thermodynamic data. The MDEA model has already been completed, but the PZ model is in need of some major corrections. The goal for the next quarter is to complete the MDEA/PZ thermodynamic model and begin constructing a rate-based model for the absorber.

Introduction

The removal of CO_2 from process gases using alkanolamine absorption/stripping has been extensively studied for several solvents and solvent blends. An advantage of using blends is that the addition of certain solvents can enhance the overall performance of the CO_2 removal system. A disadvantage of using blends is that they are very complex relative to a single solvent, thus making them much more difficult to model.

This study will focus on a blended amine solvent containing piperazine (PZ) and methyldiethanolamine (MDEA). Previous studies have shown that this particular blend has the potential to combine the high capacity of MDEA with the attractive kinetics of PZ (Bishnoi, 2000). These studies have supplied a rudimentary Aspen Plus® based model for an absorber with MDEA/PZ. The report also makes the recommendation that more kinetic and thermodynamic data must be acquired concerning the MDEA/PZ blend before the model can be significantly improved. Two researchers in the Rochelle lab have been acquiring this data, and I am in the process of incorporating it into the model. One of the major goals of this study will be to improve the supplied Aspen Plus® absorber model with up to date thermodynamic and kinetic

data. Another major goal of this study will be to make improvements to the MDEA and PZ thermodynamic models, which should simplify the construction of the blended amine model.

Methods and Discussion

This quarter's work dealt primarily with the MDEA and MDEA/PZ models. The MDEA model had already been regressed to include VLE, heat capacity, density, viscosity, and volatility data. The only improvement made to it this quarter was the inclusion of data for the activity coefficient of CO_2. Because Aspen Plus[®] cannot directly regress activity coefficients, an iterative method involving Microsoft Excel had to be employed. Tau parameters for key cation/anion pairs in CO_2 were adjusted until Aspen Plus[®] predicted values for the activity coefficient of CO_2 consistent with literature values (Weiland, 1994; Rinker, 1997). Figure 1 compares the experimental values (filled points) for the activity coefficient of CO_2 as a function of loading to the values predicted by the Aspen Plus[®] (lines) and Microsoft Excel (open points) regressions at temperatures of 25, 40, and 60 ^{o}C.
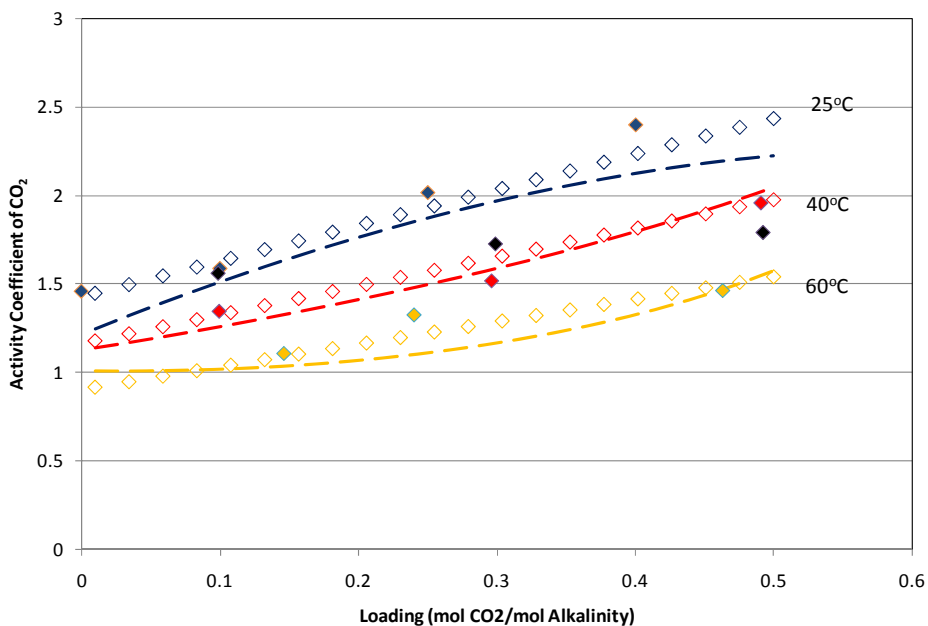
Figure 1: Activity Coefficient of CO_2 as a function of loading at temperatures of 25, 40, and 60 ^{o}C.

It should be noted that there was quite a bit of variation in the data at 25 ^{o}C. Both the blue and black points represent data at that temperature. Because of this variability, a Microsoft Excel regression was performed that expressed activity coefficient of CO_2 as a function of loading, temperature, and weight fraction of amine. Then, rather than attempting to fit the Aspen Plus[®] to the experimental points, it was fit to the Microsoft Excel regression. Over the loading range of interest (0.1 to 0.25) the percent difference between the Microsoft Excel and Aspen Plus[®] regressions was less than 10%. Table 1 contains the final values for the tau parameters used in this regression.

Table 1: Tau parameters used to fit the activity coefficient of CO_2

Parameter	Species	Value	Units
NRTL/1	CO_2/MDEA	2.5	N/A
NRTL/3	CO_2/MDEA	0.3	N/A
GMELCC	CO_2 ($MDEAH^+$/HCO_3^-)	15	N/A
GMELCC	($MDEAH^+$/HCO_3^-) CO_2	93.5	N/A
GMELCC	CO_2 ($MDEAH^+$/CO_3^{2-})	15	N/A
GMELCC	($MDEAH^+$/CO_3^{2-}) CO_2	-8	N/A
GMELCD	CO_2 ($MDEAH^+$/HCO_3^-)	0	^oC
GMELCD	($MDEAH^+$/HCO_3^-) CO_2	-30000	^oC
GMELCD	CO_2 ($MDEAH^+$/HCO_3^-)	0	^oC
GMELCD	($MDEAH^+$/HCO_3^-) CO_2	0	^oC

The only parameters regressed while constructing the MDEA/PZ model were the cross parameters (i.e. those that concern both MDEA and PZ). The ultimate goal of this exercise is to generate a model that will work for MDEA, PZ, and the blended system. Because it would be detrimental to this goal to alter parameters that had been set while constructing the single amine models, only the cross parameters were regressed. The first two sets of data incorporated into the model were the density and viscosity of the blended amine. Rather than using the Aspen Plus® default parameters for these two properties, Fortran subroutines were constructed to directly incorporate the data. The density subroutine used a polynomial expression to calculate density as a function of amine mole fraction, CO_2 mole fraction, and temperature in Kelvin. Equation 1 is the final result of the Microsoft Excel regression.

$$\rho_{Blend} = (1.3 - 0.00069T)\ln\left[0.19x_{CO2} + 1.45x_{AMINE} + 0.53\left(\frac{x_{CO2}}{x_{AMINE}}\right) + 2.39\right] \qquad (1)$$

The expression for the viscosity was also determined in Microsoft Excel and inserted directly into the Fortran subroutine, but it was expressed as a function of loading, temperature in Kelvin, weight fraction of amine, and the viscosity of water under similar conditions. Equations 2 through 4 constitute the expression entered into the subroutine.

$$\mu_{Blend} = \mu_{H2O}\exp\left(\frac{AA*BB*wt_{AMINE}}{T^2}\right) \qquad (2)$$

$$AA = (-0.014wt_{AMINE} + 0.042)T + (-0.001wt_{AMINE} + 0.0213) \qquad (3)$$

$$BB = ldg(3526wt_{AMINE}) + 1 \qquad (4)$$

Figures 2 and 3 compare the experimental data (open points), Microsoft Excel regressions (lines), and Aspen Plus® predictions (shaded points) for the density and viscosity data, respectively.
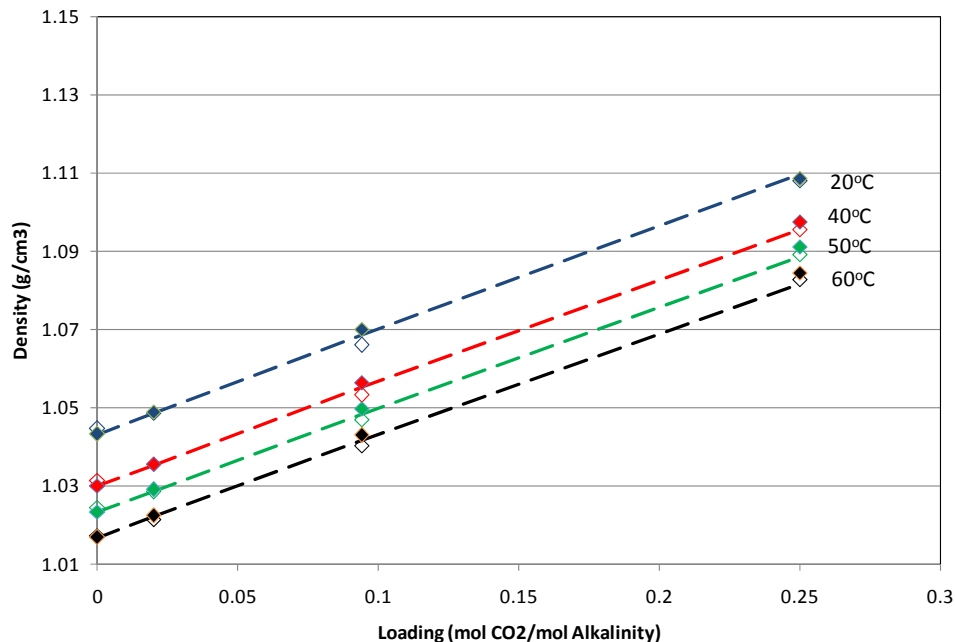
Figure 2: Density of 7 m/2 m MDEA/PZ blend as a function of loading at temperatures of 20, 40, 60, and 100 °C.
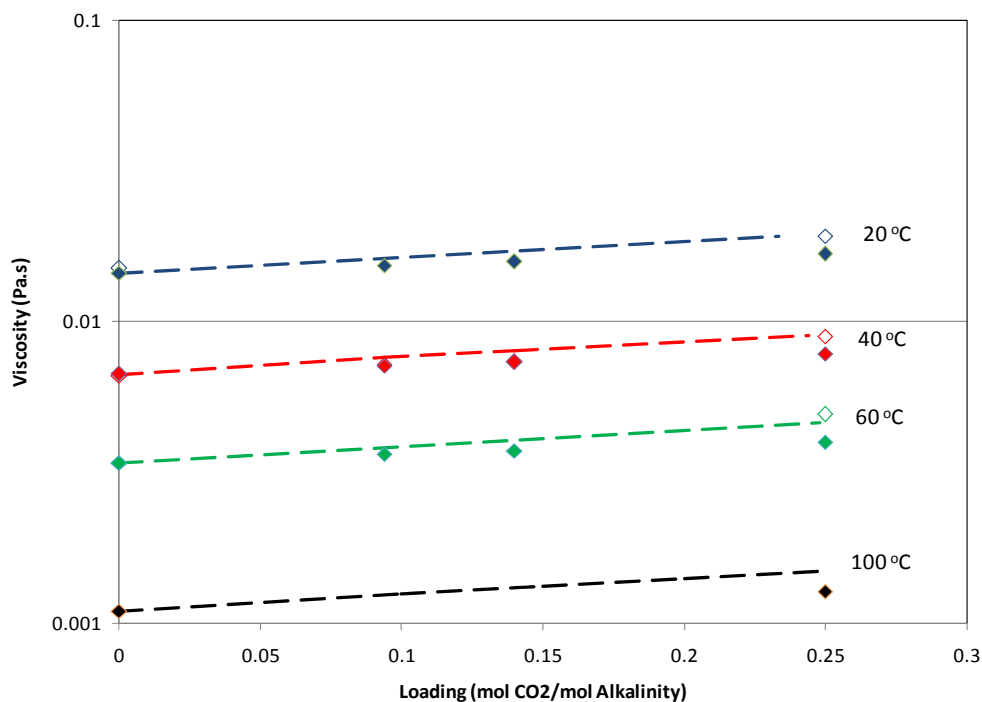

Figure 3: Viscosity of 7 m/2 m MDEA/PZ blend as a function of loading at temperatures of 20, 40, 60, and 100 °C.

Just as with the MDEA model, Aspen Plus® regressions were performed to incorporate the VLE and heat capacity data. Figures 4 and 5 compare the experimental data (open points) with Aspen Plus® predictions (lines) for the VLE and heat capacity data, respectively.
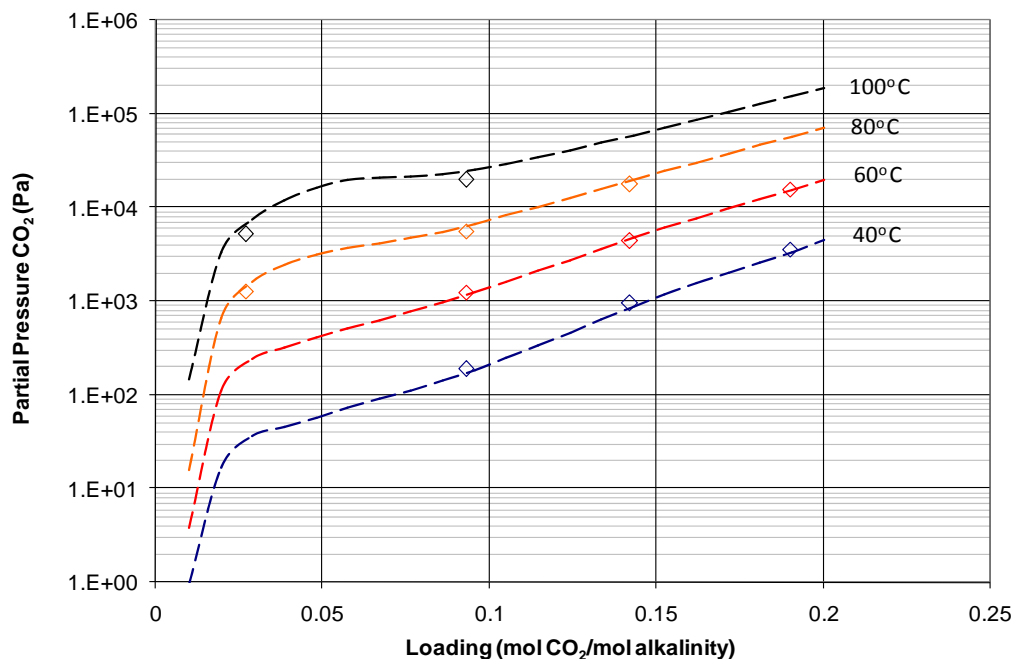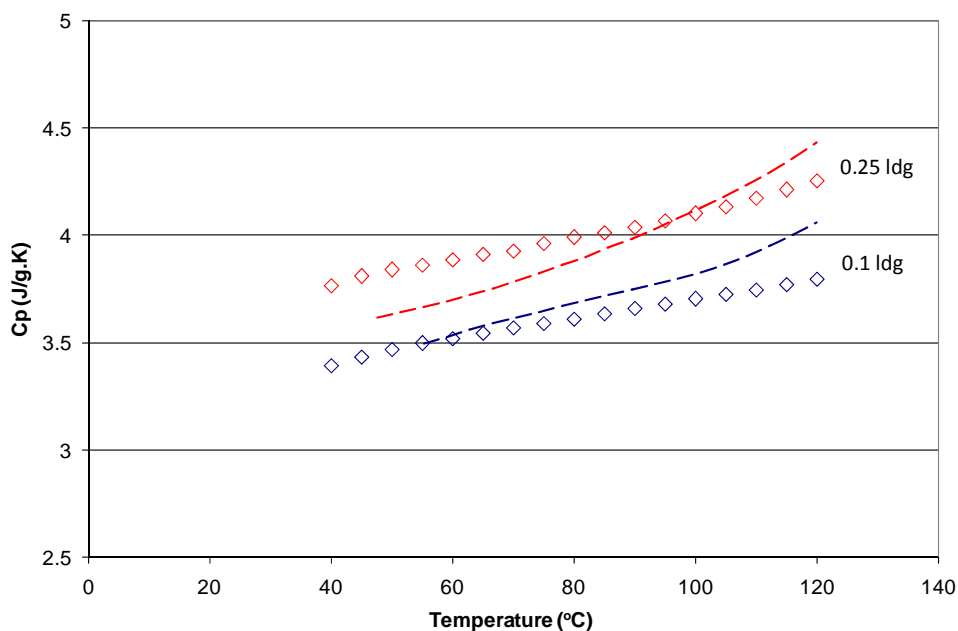
Figure 4: VLE for 7 m/2 m MDEA/PZ blend as a function of loading at temperatures of 40, 60, 80, and 100 °C.

Figure 5: Heat capacity of 7 m/2 m MDEA/PZ blend as a function of temperature at loadings of 0.1 and 0.25 moles CO_2 per mole of alkalinity.

As mentioned earlier, the only parameters used to regress this data were the cross parameters between the MDEA and PZ solvent systems. This includes the tau parameters for molecule-molecule interactions and the tau parameters for cation-anion interactions in the presence of a particular solvent.

Though the regression converged fairly easily, there are several issues with the thermodynamics that still need to be resolved. These issues primarily concern the MDEA and PZ models (not the blend), and they are discussed in much more detail in the Future Work section of this report.

Conclusions

Data for the activity coefficient of CO_2 in loaded MDEA solutions was successfully incorporated into Aspen Plus®, thus completing the MDEA model. Density and viscosity data for the MDEA/PZ blend were inserted directly into the model via Fortran subroutines. When cross parameters for the MDEA/PZ blend were regressed to fit the blended amine VLE and heat capacity data, the data easily converged. However, emerging problems in the PZ thermodynamic model necessitate a reevaluation of the approach to constructing the blended amine thermodynamic model.

Future Work

Before much progress can be made with the blended amine, the PZ thermodynamic model must be satisfactorily completed. Several problems with the PZ model have been documented by current and past researchers, and a couple of them must be resolved before continuing the MDEA/PZ model development. The problems of interest are amine volatility and the treatment of H^+PZCOO^-. In the past the amine volatility problem has been ignored due to its relatively insignificant impact on model operation. However, resolution of this problem is absolutely necessary if amine losses are ever going to be accounted for, and volatility data must be incorporated very early in the model development process. H^+PZCOO^- has always been treated as an ion with a charge of 10^{-5}, even though it is technically uncharged. This treatment has led to a sometimes problematic charge imbalance at high loadings, and Aspen Plus® always predicts that H^+PZCOO^- will have an activity coefficient of one. To remedy this H^+PZCOO^- will be treated as a Henry's component with an extraordinarily small Henry's constant, which will allow it to be treated as an ion with a net charge of zero in the aqueous phase. The goal for the next quarter will be to collaborate with other researchers in the lab to fix these problems in the PZ thermodynamic model and finally complete the construction of the MDEA/PZ thermodynamic model.

References

Bishnoi, Sanjay. *Carbon Dioxide Absorption and Solution Equilibrium in Piperazine Activated Methyldiethanolamine*. The University of Texas at Austin. Ph.D. Dissertation. 2000.

Weiland RH, Browning GJ. Physical Solubility of Carbon Dioxide in Aqueous Alkanolamines via Nitrous Oxide Analogy. *J Chem Eng Data.* 1994;39:817–822.

MDEA/PZ Degradation in Cycled Solvents

Quarterly Report for July 1 – September 30, 2009

by

Fred Closmann

Supported by the Luminant Carbon Management Program

and

Process Science and Technology Center

Department of Chemical Engineering

The University of Texas at Austin

October 19, 2009

Abstract

The integrated solvent cycling/degradation apparatus (ISDA) was modified in the third quarter to obtain accurate temperature and oxidation-reduction potential (ORP) measurements. Three cycling experiments were completed in the quarter. At conditions of 55 °C in the oxidative reactor and 120 °C in the thermal reactor, we measured a formate production rate of 0.6 mM/hr. When we reversed the formation of amides in samples from this same experiment, we observed a formate production rate of 0.98 mM/hr. When the same solvent was cycled at 55 °C in the oxidative reactor and thermal reactors, the formate production rate was 0.004 mM/hr. The measured amine loss rate at the 55/120 °C condition was ~61%/wk, which was over an order of magnitude greater than the rate (0–2.5%/wk) observed in thermal cylinder experiments conducted at 120 °C.

Using thermal cylinder experiments and LC-MS analytical detection equipment, we confirmed the presence of DEA degradation products expected in the presence of strong nucleophiles including piperazine (PZ) and methyl-PZ. The mass of those degradation products was 173.1 and 187.1, respectively, when DEA was reacted with PZ and methyl-PZ in CO_2 loaded samples degraded at 150+ °C.

Introduction

During the 3rd Quarter 2009, we completed modifications to the solvent cycling apparatus, including installation of electronic temperature measurement equipment, and the installation of oxidation-reduction potential (ORP) sensor loops at two locations in the system. In order to understand degradation pathways in the MDEA/PZ blend, as well as the characteristics of the solvent cycling system, we have conducted initial cycling studies (C-1, C-2, and C-3) using 7 m MDEA. Once the degradation of 7 m MDEA is understood, we will conduct further cycling studies using MDEA/PZ. We will be studying several solvents in the future, with priority placed on studying 7 m MDEA/2 m PZ.

We have utilized cation chromatography (IC) coupled to a mass spectrometre (MS), as well as an HPLC coupled to MS to identify degradation products and better understand thermal degradation pathways. These methods were used to analyze degraded solvents collected from previous experiments including Thermal No. 7, Thermal No. 8, and cycling experiment C-1. Additionally, three high temperature, short-term thermal degradation experiments were conducted to understand the degradation of DEA, the interactions between DEA (an MDEA degradation product) and other strong nucleophiles in degraded solvents including PZ and methyl-PZ. Key findings of those experiments (RPN-1, RPN-2, and RPN-3) are presented below.

At the end of the quarter, we sacrificed all samples from a thermal experiment (Thermal No. 9B) for cation analysis. This thermal degradation experiment utilized 7 m MDEA/2 m PZ treated with H_2SO_4 in sufficient quantity to neutralize 10% of total alkalinity. The solvent was not loaded with CO_2. Those data are not yet available, and will be presented in the next quarterly report.

Cycling/Integrated Solvent Degradation Apparatus

During the quarter, we completed the construction of the ISDA (solvent cycling), and tested temperature limits of the system using the MDEA/PZ blend. In testing, the system was simultaneously operated at 55 °C in the oxidative reactor and 129 °C in the thermal reactor. At those conditions and a nominal loading of 0.1 moles CO_2/mole alkalinity with the 7 m MDEA/2 m PZ blend, the pressurized section of the system (thermal reactor segment) required a back-pressure condition of >58 psig.

We installed two bimetal thermocouples, one inserted into the thermal reactor, and one into the oxidative reactor, such that accurate on-line electronic measurement of temperatures can be obtained. We will investigate the possibility that "hot spots" exist in the thermal reactor at internal metal surfaces (see discussion below). Another modification to the system is the installation of on-line measurement points for ORP at two locations; an ORP sensor (Hanna Instruments) designed for industrial use was purchasedfor this purpose. One ORP measurement bypass loop was installed just downstream of the positive displacement pump discharge, and a second loop was installed downstream of the counter-current cross-exchanger. The first location is expected to yield results indicative of an oxidizing condition, while the latter is expected to indicate reduced conditions when compared to the first. The purpose of these measurements is to understand whether an oxidizing condition prevails in solvents once they leave an absorber (oxidative reactor), and the extent to which a reduced condition exists at stripper conditions (thermal reactor).

After testing the system for safe operation, we completed three cycling experiments with 7 m MDEA at a loading of 0.1 moles CO_2/mole alkalinity (C-1, C-2, and C-3). A fourth experiment (C-4) was initiated but has not been completed yet. Table 1 lists the conditions of the experiments.

Table 1: MDEA and PZ Thermal Degradation Rates

Experiment	Solvent	Loading (moles CO_2/mole alk)	Additives	Conditions (T_{ox}/T_{th} °C)
C-1	7 m MDEA	0.1	None	55/120
C-2	7 m MDEA	0.1	None	55/55
C-3	7 m MDEA	0.1	0.4 mM Fe/0.1 mM Cr/0.05 mM Ni	55/55
C-4	7 m MDEA	0.1	0.4 mM Fe/0.1 mM Cr/0.05 mM Ni (Reduced stir rate in oxid reactor)	55/55

Cycling Experiment C-1

Sampling and analysis procedures for the cycling experiments followed the same protocols used for the low-gas and thermal cylinder experiments. A single sample of degraded amine was collected each day at the start of the cycling operation, but after ten minutes of low temperature circulation. A final sample was collected at the completion of operations. The duration of the experiment was eight days (~60 hours), with the system operated only during daytime; a daily start-up and shutdown procedure was utilized which entailed a one-hour warm-up and one hour warm-down to/from operational conditions. Samples were subjected to analyses for cations (amines) and anions (heat stable salts such as formate and glycolate). Each sample was hydrolyzed with 5N NaOH to reverse the formation of amides to heat stable salts which are measurable using anion chromatography (IC).

Figure 1 presents the concentration of total heat stable salts and MDEA measured in samples collected daily from C-1. Samples in this experiment only exhibited the heat stable salts formate and glycolate. After approximately 60 hours of operation, over 1,700 ppm formate (41 mM) and 940 ppm glycolate (13.2 mM) were produced in the cycling reactor. When the amides (formamide) were reverted to heat stable salts (formate) and measured with cation IC, we measured 3-351 ppm (78.6 mM) formate. After 60 hours of cycling operation, the MDEA concentration had decreased from approximately 6.35 m to 5 m, with an accompanying increase in heat stable salts. However, the concentrations of formate and glycolate only account for a fraction of the loss in MDEA.

MDEA Concentration vs. Heat Stable Salts Cycling: C-1
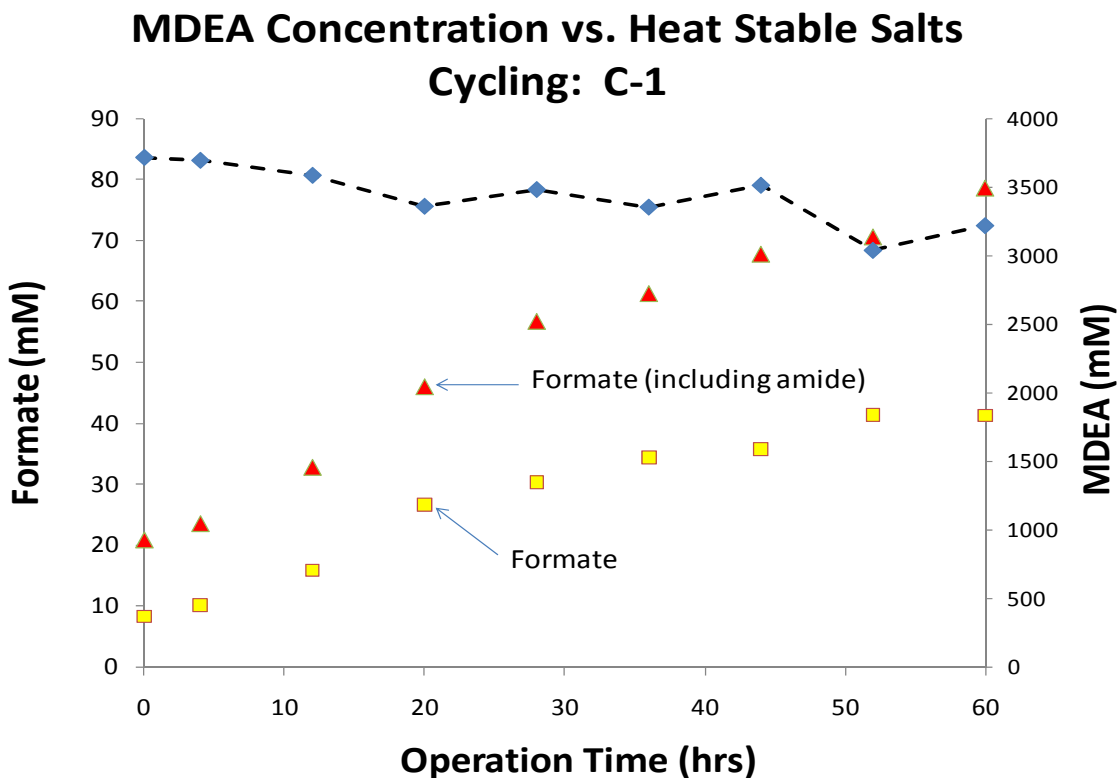
Figure 1: Cycling Experiment C-1, 7 m MDEA (55 °C/120 °C), α = 0.1

Experiment C-2 was conducted in the cycling apparatus at conditions of 55 °C in both the oxidative and thermal reactors operated simultaneously for approximately 64 hours. Figure 2 presents the formate concentrations from C-2. The data indicate that the amount of oxidative degradation resulting in production of formate is minimal, with approximately 0.15 mM formate measured at the end of the experiment. When amide formation was reversed through hydrolysis with 5N NaOH (not shown), the measured formate showed a lot of variability, with the highest amount detected at approximately 0.1 mM formate. Ignoring the last data point, the decrease in MDEA concentration in this experiment was minimal (6.7 m to ~6.2 m). This reduction is approximately half the measured reduction in C-1 experiment (6.4 m to ~5.5 m). Of note, the stirred section of the oxidative reactor is approximately 350 ml, and the entire system volume is approximately 2,400 ml; the oxidative reactor, therefore, comprises approximately 15% of the overall system volume.

We compared formate production in cycling experiments C-1 and C-2 with 7 m MDEA to measurements made in a low-gas experiment on the same solvent with a similar loading, but augmented with 1 mM Fe^{2+} (Figure 3). From this comparison, it is apparent that accelerated oxidation of MDEA is occurring when the thermal reactor is operated at 120+ °C (red squares), resulting in an order of magnitude greater concentration of formate. Further, in previous experiments with this solvent, the level of glycolate production was below detection using the methods we currently employ.
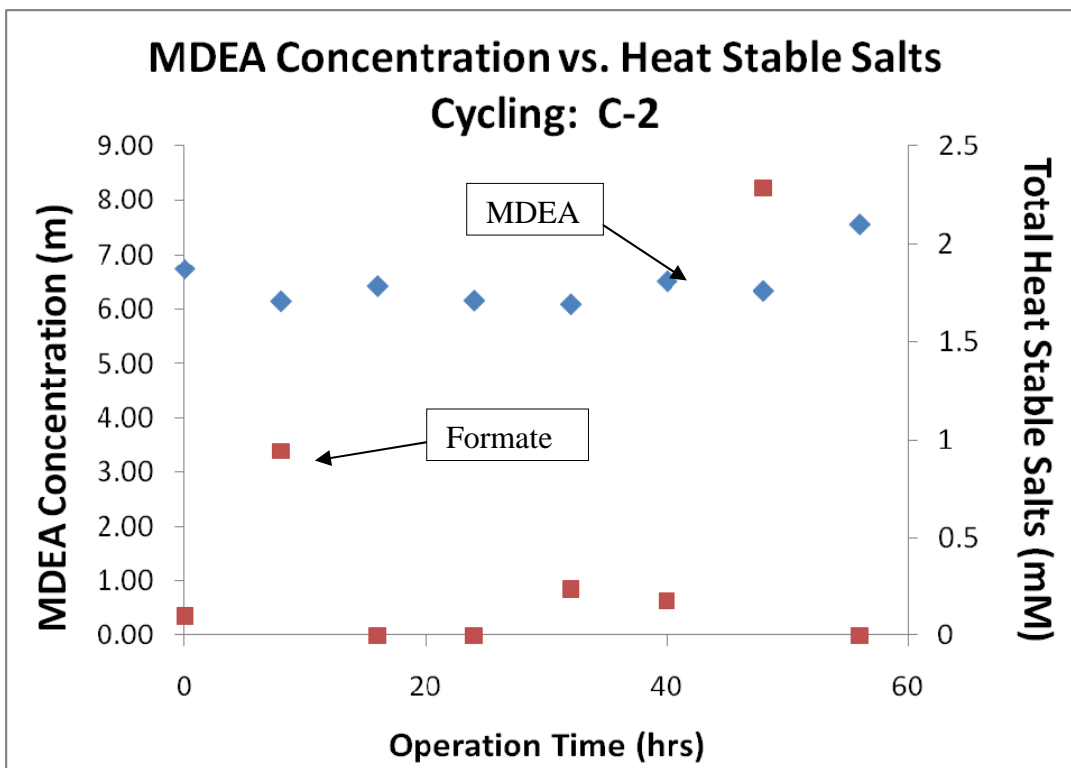
Figure 2: Cycling Experiment C-2, 7 m MDEA (55 °C/55 °C), α = 0.1
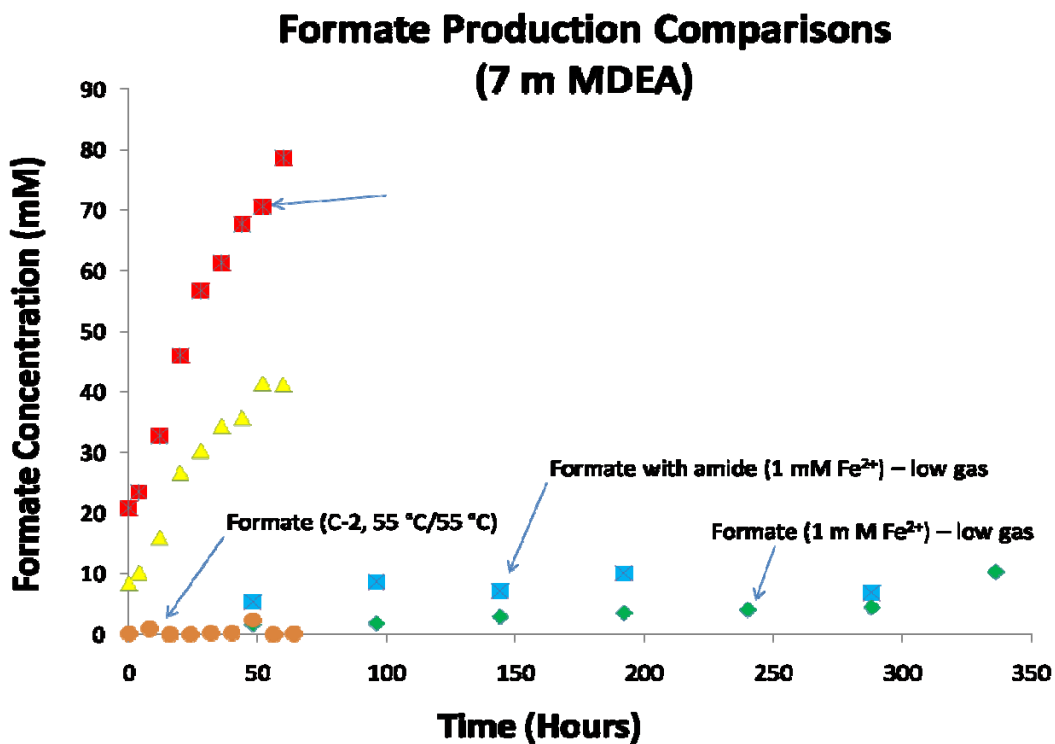
Figure 3: Formate Comparison: C-1, C-2, and Low-Gas Experiments, 7 m MDEA, α = 0.1

Figure 4 presents the concentration of MDEA from experiment C-1, and from experiments using thermal cylinders for degradation of 7 m MDEA at 120 and 135 °C. The rate of decrease in MDEA concentration in the cycling experiment was much greater than in the thermal cylinders maintained at 120 °C for up to 120 days (Thermal No. 3). From the thermal cylinders maintained at 135 °C for over 800 hours, the 7 m MDEA degraded much more rapidly over the initial 200-hour period, but leveled off. Table 2 lists % loss rates for MDEA from the above-described experiments to illustrate the differences in rates observed; the MDEA loss rate (61%/wk) was a full order of magnitude greater than that measured in the thermal cylinders at 120 and 135 °C.

We utilized LC-MS methods to assess the degradation products in degraded C-1 samples. We determined that diethanolamine (DEA) was prevalent in degraded samples after only twelve hours of cycling from 55 to 120 °C. Thereafter, DEA was present in degraded samples in this experiment. Other compounds were also present, but at lower levels due to smaller peak response. One of those compounds has been definitively identified as methylaminoethanol (MAE) with a mass of 75.1.
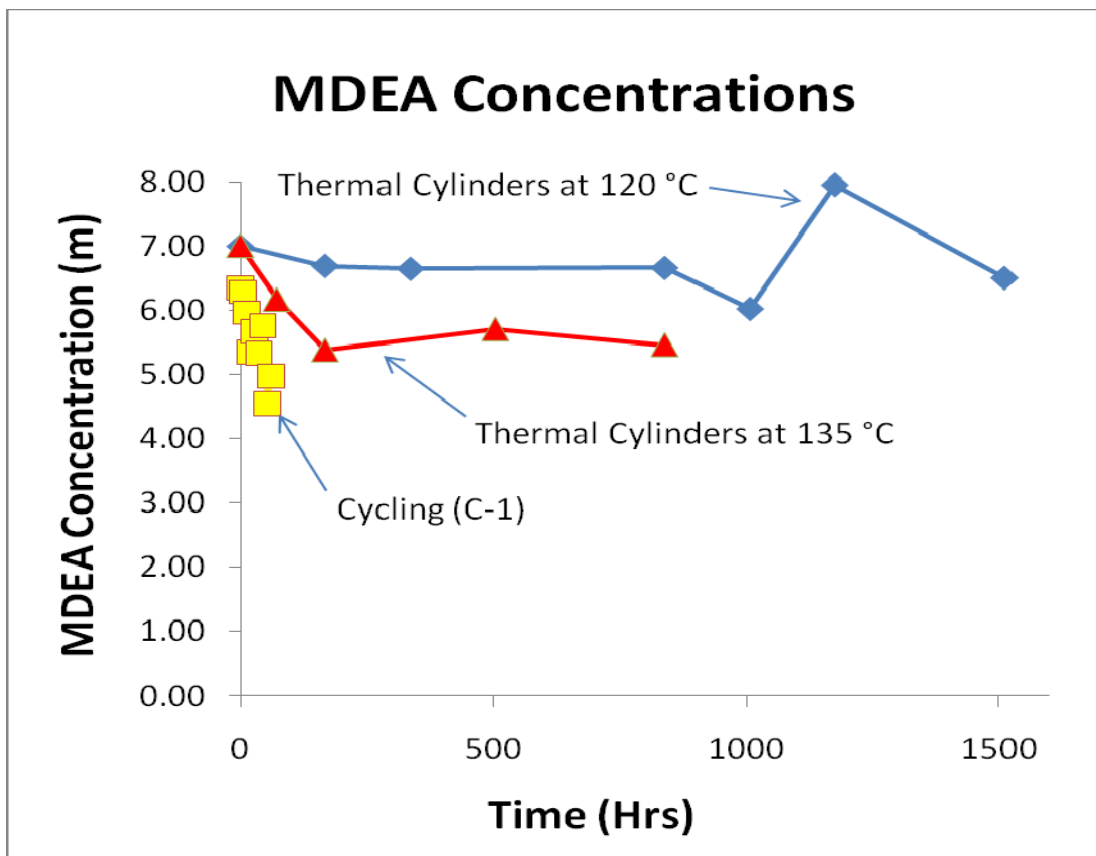
Figure 4: MDEA Comparison: Cycling (C-1) and Thermal Cylinders, 7 m MDEA, α = 0.1

Table 2: MDEA and PZ Thermal Degradation Rates

MDEA Loss Rate			
Experiment Type	Solvent	Temp (°C)	Loss (%/wk)
Cycling (C-1)	7 m MDEA	55/120	61
Thermal Cylinders	7 m MDEA	120 and 135	~0/23
Thermal Cylinders	7 m MDEA/2 m PZ	120 and 135	2.5/2.7

We currently believe that the design of the oxidative reactor (250 ml hold-up section) is resulting in the entrainment of undissolved gas bubbles in the inlet to the positive displacement pump which is located immediately upstream of the oxidative reactor hold-up section and cycles the fluids throughout the system. The entrained gas bubbles are likely 98% O_2 and 2% CO_2 and the result of surface interactions in the oxidative reactor. After becoming entrained, the bubbles gradually dissolve in the amine in the ¼-inch tubing, heat exchanger, preheater tubing, and thermal reactor until consumed in the oxidation reactions with MDEA and its degradation products. The entrained gas bubbles represent a source of dissolved oxygen as the solvent travels through the system in plug flow fashion and warms to the final temperature in the thermal reactor (120 °C). This oxygen source allows for greater oxidation of MDEA than is observed in the low-gas apparatus. It is possible that the MDEA thermal degradation products (including DEA, MAE, DMAE) are more easily oxidized to heat stable salts than MDEA, resulting in accelerated degradation and formate production over that observed in low-gas experiments. This effect is more pronounced in experiments using higher temperatures in the thermal reactor (e.g., C-1, 120 °C) because the oxidative degradation would be facilitated at gradually higher temperatures (up to 120 °C) than those existing in the low-gas experiments (55 °C). The effect of bubble entrainment is being tested through an experiment (C-4) utilizing a lower shaft rotation rate (~250 rpm vs. 1440 rpm) in the oxidative reactor. In preliminary experiments, we have determined that lowering the shaft rotation rate to less than 300 rpm in the oxidative reactor minimizes the amount of bubble entrainment in the amine solvent.

Pathway Assessments and Thermal Experiments

RPN-1, RPN-1, and RPN-3

Using IC-MS and LC-MS methods, DEA can be consistently detected in samples of MDEA/PZ when degraded in thermal cylinders and the cycling system. To better understand how the solvent blend thermally degrades, three short-term high temperature (135–175 °C) degradation experiments using Swagelok® thermal cylinders were conducted. Those experiments were specifically designed to determine how DEA interacts with other components of the degraded blend at high temperatures. The premise for these studies was the degradation pathway developed by Polderman (1956) wherein DEA, when in the presence of CO_2, will form a carbamate and subsequently cyclize to hydroxyethyl oxazolidone (HEOD). This compound will in turn react with a strong nucleophile yielding other products. We have observed methyl-PZ in degraded MDEA/PZ samples, making this compound one candidate for a strong nucleophile in the degraded blend.

Knowing that methyl-PZ and PZ will behave as strong nucleophiles in solution, we conducted RPN-1 and RPN-2 with these compounds. Figure 5 illustrates one possible pathway for the reactions which occur once MDEA degrades to DEA in the presence of PZ and one of its degradation products, methyl-PZ. We tested for this possible pathway in RPN-1 by reacting 1 m DEA with 1.5 m methyl-PZ loaded to 0.6 moles CO_2/mole alkalinity. Using LC-MS, we detected the presence of a compound with a mass of 187.1 after three days of degradation at 150 °C. This compound, depicted in Figure 5, is 2-[[2-(4-methyl-1-piperazinyl) ethyl]amino]ethanol is unavailable as a standard, preventing us from making a definitive identification of the compound detected in degraded RPN-1 samples with this mass.

Figure 6 depicts another possible pathway for the formation of degradation products once MDEA degrades to DEA. In RPN-2, we reacted 1 m DEA with 1.5 m PZ at a loading of 0.25 moles CO_2/mole alkalinity to test whether this pathway could be occurring. Using LC-MS, we detected a compound with a mass of 173.1 in a sample degraded at 150 °C for two days. This compound, named 2-[[2-(1-piperazinyl)ethyl]amino]ethanol, is currently unavailable as a standard, preventing us from making a definitive identification of the compound detected with the same mass. However, when using LC-MS, the compound detected with this mass provided the greatest response in terms of relative abundance at a retention time of ~22 minutes. In a sample degraded at 175 °C, we detected a compound with this mass after only 3.5 minutes.

In summary, we believe that DEA-carbamate cyclizes to HEOD, which is susceptible to attack at a C-N bond within the ringed structure, resulting in the opening of the structure and creation of triamines detected with masses of 187.1 and 173.1, respectively, in RPN-1 and RPN-2. Finally, RPN-3 was conducted with loaded 1 m DEA only to determine how this compound breaks down, and whether either of the degradation products with masses of 187.1 and 173.1 can be detected in this degraded solvent. Those results are unavailable at this time.
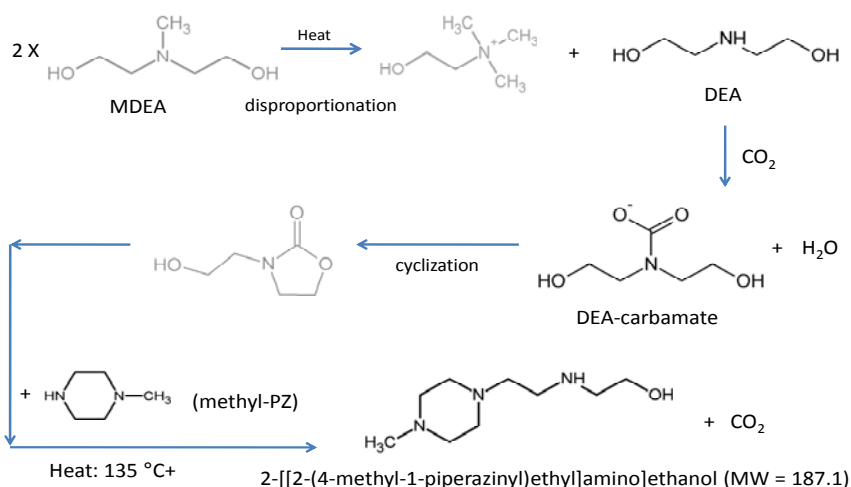
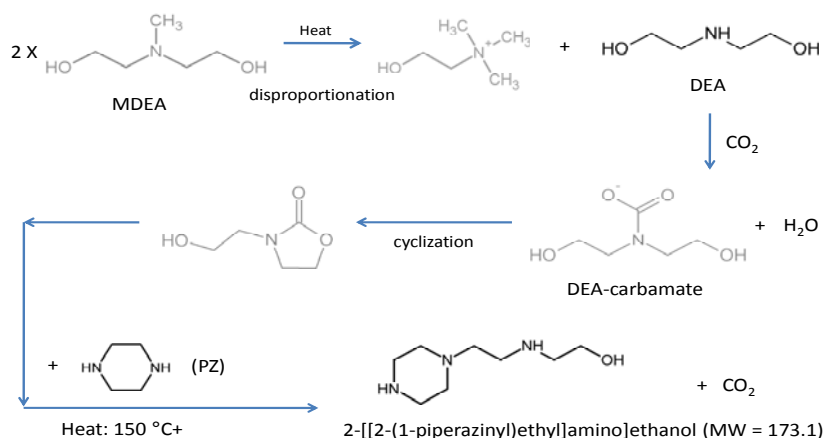**Figure 5: RPN-1: 1 m DEA/1.5 m methyl-PZ, α = 0.6 moles CO_2/mole alk**

Figure 6: RPN-2: 1 m DEA/1.5 m PZ, α = 0.25 moles CO₂/mole alk

Conclusions

The latest experimental work indicates that accelerated oxidative degradation is occurring in 7 m MDEA when cycled in ISDA. We observed amine loss rates of 61%/wk at cycling temperatures of 55/120 °C in experiment C-1. This loss rate is an order of magnitude or greater than the rates observed at 120 °C in degradation experiments in the thermal cylinders at the same temperature. Formate production was measured (C-1) at 0.59 mM/hr in the cycling apparatus when operated at 55 °C in the oxidative reactor and 120 °C in the thermal reactor. When we reversed the amide formation, we observed formate production at 0.98 mM/hr. These rates are also much greater than those observed in the low-gas experiment conducted at 55 °C with mM Fe^{2+}. Those rates were 0.024 and 0.026 mM/hr, respectively. When we operated the cycling system at 55 °C in both reactors, the formate production rate (0.004 mM/hr) was less than the rate observed in the low-gas system. The MDEA loss rate in the cycling system is an order of magnitude greater than that observed in our thermal cylinders maintained at 120 to 135 °C for comparable periods of time.

The current design of the cycling system allows for entrainment of undissolved bubbles at the inlet to the positive displacement pump, providing a source of dissolved oxygen downstream of the oxidative reactor as these bubbles dissolve into the amine. This dissolution effect leads to greater formate production, especially at higher thermal reactor temperatures.

We tested for possible degradation pathways in degraded MDEA/PZ blends in two experiments wherein we reacted DEA with PZ and methyl-PZ in loaded systems. We detected products with masses of 173.1 and 187.1, respectively. Both of these products were expected, based on the degradation of MDEA to DEA in loaded systems. The DEA was expected to subsequently cyclize and react with a strong nucleophile in solution (PZ and methyl-PZ).

9

Future Work

Future work will include the completion of cycling experiment C-4 which includes conditions of 55 °C in the oxidative and thermal reactors, but a reduced stir rate in the oxidative reactor to less than 300 rpm to test the effect of bubble entrainment on overall solvent degradation. We will also conduct a minimum of three more cycling experiments in the upcoming quarter with the cycling system. It is currently expected that those experiments will include one more experiment with 7 m MDEA at conditions of 55 °C in the oxidative reactor and 100 °C in the thermal reactor to test for accelerated degradation of the solvent. The stir rate of that experiment will be determined based on the results of C-4. We will then cycle the solvent PZ in the system to determine its resistance to degradation under the cycling environment.

All future experimental work will include the measurement of ORP at the two sensor loop locations installed in the third quarter; ORP data will be compared to understand whether solvents undergo a significant change in ORP when they pass from the oxidative reactor through the cross-exchanger and into the thermal reactor.

In parallel with cycling experiments, we will continue to analyze samples from RPN-1 through RPN-3 to assess the MDEA/PZ degradation pathway.

Finally, we recently initiated a thermal cylinder experiment (Thermal No. 11), which is a repeat of the Thermal No. 7 utilizing 7 m MDEA/2 m PZ to provide a greater body of thermal degradation data on this solvent and determine degradation rates over the range 120 to 150 °C.

My Ph.D. dissertation proposal was submitted to my committee in the third quarter and is attached to this quarterly report (Closmann, 2009).

References

Closmann, FC. "Degradation Mechanisms in MDEA/PZ Used for CO_2 Capture", Ph.D. Dissertation Proposal, The University of Texas at Austin, Department of Chemical Engineering, September 24, 2009.

Polderman, LD, Steele, AB. "Why Diethanolamine Breaks Down in Gas-Treating Service", *Oil & Gas J*. July 30, 1956. 206–214.

The University of Texas at Austin
Department of Chemical Engineering

Degradation Mechanisms in MDEA/PZ Used for CO$_2$ Capture

Research Proposal to PhD Committee

PhD. Committee:

Supervisor: Prof. Gary T. Rochelle
Prof. Grant Willson
Prof. John Ekerdt
Prof. Desmond Lawler
Dr. Steve Bedell (Dow Chemical Company)

Fred Closmann
9/24/09

Table of Contents

Problem Statement

The solvent blend methyldiethanolamine/piperazine (MDEA/PZ) is known to thermally degrade at 120+ °C. Understanding what chemical mechanisms lead to its degradation is complicated by the likelihood that secondary reactions between MDEA and PZ will occur in CO_2 loaded solvents once degradation is initiated. Another complicating factor in accurately assessing degradation characteristics is that in industrial applications solvents will be continuously cycled through oxidative and thermal degradation conditions, resulting in secondary effects thus far not adequately investigated. The degradation behavior of MDEA/PZ presents the need for the proposed investigative work in this document.

1.0 Description of the Problem

Alkanolamines have seen extensive use in the oil and gas industry for acid gas treatment for many years. Should global agreements and resulting cap and trade legislation (e.g., proposed legislation by Waxman and Markey, H.R. 2454, May 15, 2009) force the power generation industry to curtail CO_2 emissions in the future, the use of amines to scrub CO_2 from power plant flue gases would likely become a key tool in the effort to meet greenhouse gas emissions reduction requirements. The potential exists that a new generation of power plants incorporating flue gas CO_2 absorption/stripping systems will become the industry standard. The potential wide-spread use of this technology presents new challenges to the power generation industry looking for more reliable and cost-effective process designs.

Key performance considerations in the selection of an amine solvent for CO_2 capture purposes include CO_2 reaction rate, capture capacity, mass transfer characteristics, degradation resistance, corrosivity and foaming potential. The sum of these operational considerations determines how well a solvent will perform, but in practice, the screening and characterization of solvent degradation potential (oxidative and thermal) has emerged as a critical step in the early stages of solvent selection.
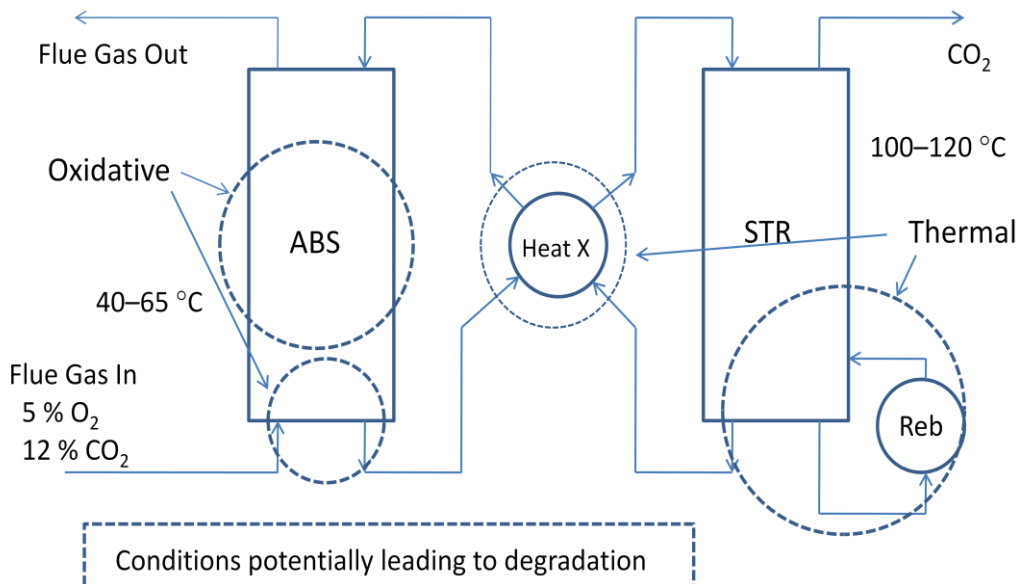

Figure 1: Absorber/Stripper System and Degradation Conditions

Predicting how a solvent will degrade in a system designed for CO_2 capture from flue gas streams requires an understanding of a typical absorber/stripper configuration. Figure 1 presents a process flow diagram for an absorber/stripper system intended for CO_2 removal from flue gas. Flue gas enters the absorber with approximately 7.5% O_2, 13.5% CO_2 and a temperature of 60 °C (Fayette Power Plant Unit 3, LCRA, June 2008). The flue gas is counter-currently contacted with a lean amine for CO_2 absorption in a reaction which is reversible. Absorber design generally includes a hold-up section sized for approximately five minutes of solvent retention time. After passing through a cross exchanger, the CO_2-rich amine enters a steam stripper for reversal of the CO_2 absorption process. Steam stripping increases the amine temperature to 120 °C or greater for desorption and removal of CO_2 for subsequent dehumidification and sequestration. Typical absorber operating conditions for MEA include a temperature of 55 to 60 °C with a potential temperature bulge of up to 74 °C (Kvamsdal, H. and G. Rochelle, 2008). The steam stripper (regenerator) would be operated at 1 atm and temperatures in the range of 100 to 120 °C (Aaron, D. and C. Tsouris, 2007).

It is anticipated that the prevailing degradation mechanism(s) in the absorber and absorber hold-up would follow oxidative pathways, with some oxidation of solvents continuing to occur in the cross-exchanger as dissolved and entrained O_2 is depleted. In contrast, it has been assumed that in the stripper, a high-temperature and oxygen-depleted environment would exist, resulting in chemical degradation processes including disproportionation and polymerization of carbamate structures (Rochelle et al., 2001); the latter mechanism occurs with amines which form carbamates (primary and secondary). We also anticipate that thermal degradation will occur in the rich amine as it is heated in the cross-exchanger before entering the steam stripper. The extent to which dissolved or entrained oxygen is carried over to the stripper resulting in an oxidative environment at higher temperatures has generally been assumed to be low. However, due to a general lack of pilot or full-scale data from flue gas CO_2 capture systems, the extent of entrainment or dissolution of O_2 in these applications is generally unknown; typical acid gas treatment feed gases in the oil and gas industry have less than 1% O_2 (Astarita et al., 1983).

One of the most commonly used alkanolamines in the acid gas treating industry is monoethanolamine (MEA); MEA is particularly effective for CO_2 removal due to its fast reaction with CO_2 and its formation of an MEA-carbamate. However, MEA is known to degrade in acid gas field applications. After studying degraded field samples of MEA, Polderman, et.al. (1955) reported that MEA breaks down at elevated temperatures to form 2-oxazolidone (HEOD) and 1-(2-hydroxyethyl)-2-imidazolidone (HEIA). Davis (PhD. Dissertation, 2009) reported that MEA thermally degrades with a rate constant of 0.021 wks^{-1} at 120 °C, and will preferentially degrade in blended amine systems. MEA will also degrade oxidatively to form heat stable salts including acetate, formate and glycolate, as reported by Rooney et al. (1998). Sexton found (PhD. Dissertation, 2009) that as much as 70 % MEA was lost after ten days when degraded oxidatively at 55 °C. The overall effect of this solvent degradation is to diminish CO_2 absorption capacity.

Because of other performance characteristics which limit their effectiveness for CO_2 capture, most amines provide a less-than ideal alternative for CO_2 capture in coal-fired power plant flue gas streams. One approach to solvent selection is the use of blends of those already in use (Appl et al., 1990) which utilize a tertiary amine such as MDEA promoted with a fast reacting diamine such as piperazine (PZ).

2

When combined at a ratio of 7 m (molal, or moles/kg water) of MDEA and 2 m PZ, the faster reacting PZ (k_{298} ~ 0.2 gmol/L vs. 0.02 - 0.2 gmol/L for MDEA) (Rochelle et al., 2001) ensures that the overall rate of reaction of CO_2 in the blend will be as good or better than in single amines already in use (i.e., MEA, MDEA, and DEA). The presence of MDEA at a concentration of 7 m improves capacity to absorb CO_2 by behaving as a sink for protons through formation of protonated MDEA ($MDEAH^+$).

Despite having performance advantages over non-blend solvents such as the industry standard monoethanolamine (MEA), the blend methyldiethanolamine/piperazine (MDEA/PZ) is known to thermally degrade at 120+ °C (Closmann, Quarterly Report, April 2009). Understanding what chemical mechanisms lead to its degradation is complicated by the likelihood that secondary reactions between MDEA and PZ will occur in CO_2-loaded solvents once degradation is initiated. The degradation behavior of MDEA/PZ presents the need for the proposed investigative work in this document.

2.0   Pertinent Literature

2.1   Thermal Degradation

The published amine thermal degradation work generally relies on batch experimentation using a single autoclave or multiple sample cylinders for rapid screening of multiple solvents, as in use at The University of Texas at Austin. The bulk of that work focused on MEA, but data relevant to the MDEA/PZ blend has been published. This section reviews the relevant work.

Polderman, et.al. (1955) studied MEA solutions from acid gas treatment systems to understand why most operations undergo a gradual loss in capture capacity. The authors reported the presence of degradation products including 2-oxazolidone and 1-(2-hydroxyethyl) imidazolidone (HEIA), and that the HEIA undergoes hydrolysis to N-(2-hydroxyethyl) ethylenediamine (HEEDA). The HEIA contributes no basicity or acid gas absorbing capacity, whereas the hydrolysis of the HEIA to HEEDA restores part of the lost alkalinity and acid gas absorption capacity.

Chakma and Meisen (1988) degraded MDEA in an autoclave for 144 hours at 180 °C and a CO_2 partial pressure of 2.59 MPa, and utilized gas chromatography/mass spectrometry (GC-MS) methods to identify degradation products. In doing so, they reported the presence of several compounds, most notably ethylene glycol, 2-(dimethylamino)ethanol (DMAE), 1,4-dimethylpiperazine, N-(hydroxyethyl)methylpiperazine (HMP), triethanolamine (TEA), and N,N-bis(hydroxyethyl)piperazine (BHEP). They also identified 3-(hydroxyethyl)-2-oxazolidone (HEOD) and N,N,N-tris-(hydroxyethyl)ethylenediamine (THEED) in degraded MDEA samples. Later, the same authors (1997) reported that MDEA will degrade at 200 °C to form several products including N,N-dimethylethanamine (DMEA), DMAE, diethanolamine (DEA) and BHEP. Using the same GC/MS techniques, Dawodu and Meisen (1996) reported the presence of many of the same compounds as well as methyl aminoethanol (MAE) which they termed a reactive intermediate in the thermal degradation of MDEA/MEA and MDEA/DEA blends.

Polderman and later Kennard and Meisen (April 1980) suggested that the mechanism for thermal degradation of DEA involved the formation of the oxazolidone of DEA (HEOD), and subsequent formation of BHEP (Figure 2).
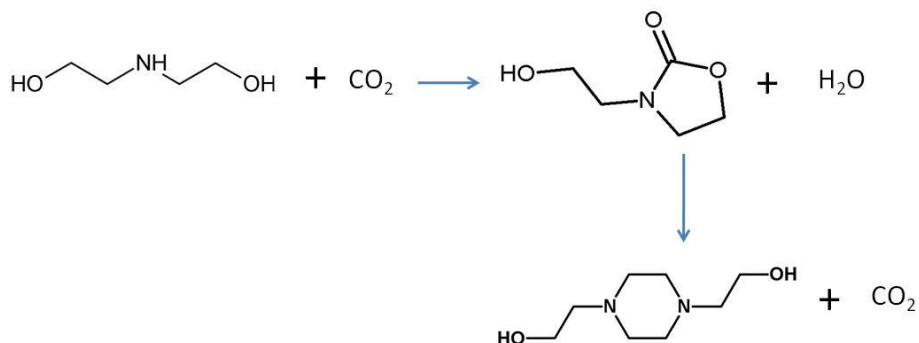

Figure 2: Degradation of DEA (Kennard & Meisen, 1980)

Their work was followed by that of Kim and Sartori (1984) wherein a kinetic model was derived based on degradation studies of CO_2 loaded solutions. The authors reported that the presence of CO_2 in aqueous DEA solutions was necessary to catalyze the degradation process. They reported a similar pathway for degradation of DEA involving the formation of HEOD, which degrades to THEED, then BHEP and other products.

Holub and Critchfield (1998) reported that when they analyzed acid gas field samples where DEA and MDEA had been in service, the primary degradation products they saw were the substituted ethylenediamines including THEED. In one case, they reported that approximately 25 % of the original DEA was converted to THEED in only six months of acid gas treatment operation. They also note that as in laboratory studies of the same solvents, they detect BHEP in field samples, but at far lower concentrations.

Using GC-MS, Lepaumier et al. (2009) reported that when they degraded DEA at 140 °C in a 100-ml stainless steel reactor for 15 days, the vast majority of degradation occurred due to ring closure which occurs after the DEA forms a carbamate. The DEA-carbamate will undergo ring closure to the oxazolidone structure easier than it will undergo an addition reaction. The authors also note that oxazolidones are very sensitive to nucleophilic reactions and react easily with another amine, resulting in addition products (dimers).

More recently, Bedell (Dow Chemical, February 2009) reported that when they thermally degraded the MDEA/PZ blend, they identified DMAE, DEA, TEA, methyl piperazine, and HMP. Bedell also reported that it is initially possible to close the carbon mass balance on the degraded solvent by accounting for the DMAE and TEA, but closing the balance becomes difficult as degradation proceeds further due to the evolution of CO_2.

2.2   Oxidative Degradation

In 1950, the Girdler Corporation (Kindrick et al.) reported a series of accelerated oxidative screening studies designed to determine the relative resistance of amines and amine blends to oxidative

degradation. Based on free amine concentration before and after oxidation, the authors reported that tertiary amines such as MDEA, as a group, are the most resistant to oxidation, whereas the primary amines (MEA) are the most susceptible to oxidation. The authors also reported that MEA degrades to form appreciable amounts of non-alkaline corrosive products.

In 1956, Hofmeyer et al. reported that up to 40 % of basicity loss in MEA can be attributed to oxidative deamination to form ammonia, with the remaining products being formic acid, a carbonyl compound and a high molecular weight polymer. Blachly and Ravner (1964) reported that when CO_2 free air was passed through 4N MEA at 131 °F (55 °C) for several days, no perceptible degradation occurred. However, the presence of just 1 % CO_2 resulted in almost instantaneous degradation, as evidenced by the generation of ammonia and peroxide. The authors also reported that N,N-diethanolglycine (VFS) can be used as an anti-oxidant to reduce the peroxide and prevent further degradation of MEA.

Rooney et al. (1998) studied the oxidative degradation of various amines including MDEA, MEA, DEA and DGA, and reported the presence of acetate, formate, and glycolate in each of these solvents after only 7 days. They also reported the presence of DEA in degraded MDEA solutions, but when the same experiments were conducted with a nitrogen blanket, no DEA was detected. The latter observation was noted as evidence of the role oxygen plays in the degradation of MDEA at elevated temperatures. The authors proposed pathways for the sequential oxidative degradation of MEA to end products including formic acid, acetic acid, and oxalic acid (Figure 3).
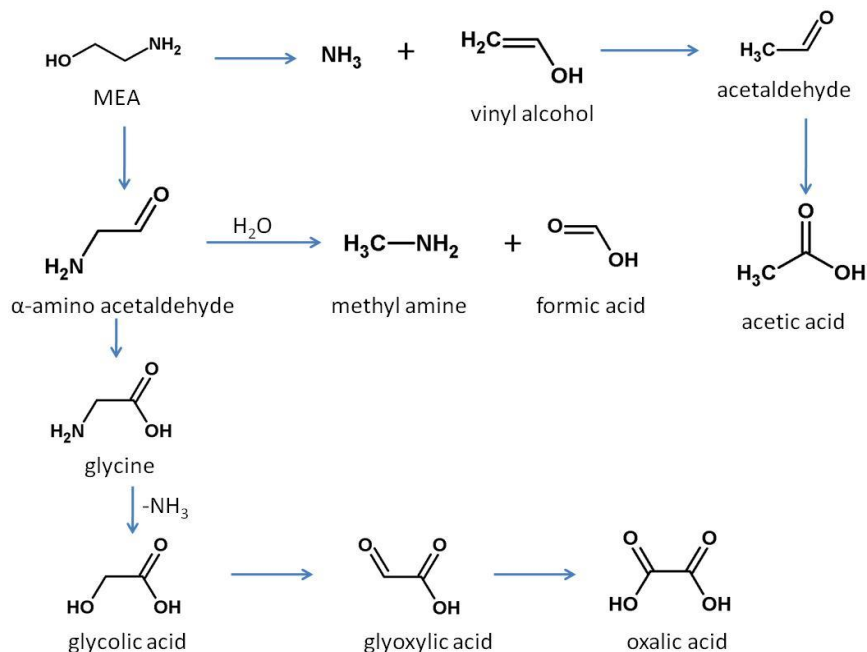
Figure 3: Oxidative Degradation of MEA (Rooney et al.)

Strazisar et al. (2003) attempted to develop a fundamental understanding of the degradation pathways associated with MEA by studying samples collected from the IMC Chemicals facility in Trona CA which uses MEA for scrubbing CO_2. Using GC methods, the authors analyzed process samples including

reclaimer bottoms to quantify degradation products. They reported that carbamate dimerization of MEA resulting in oxazolidone formation was not a significant pathway. The authors proposed that an alternate pathway wherein MEA reacts with acetic acid to form N-acetylethanolamine occurs. They also reported that the latter compound reacts with MEA to form an acetamide compound, which may then form a six-membered ring compound by internally eliminating water to form 1-hydroxyethyl-2-piperazinone or 4-hydroxyethyl-2-piperizinone.

We reported that CO_2 loaded solutions of 7 m MDEA/2 m PZ (~3.8 M MDEA/1.1 M PZ) with dissolved metals are fairly resistant to oxidative degradation at 55 °C (Closmann, Quarterly Report, January, 2009). For example, using our low gas apparatus on 7 m MDEA/2 m PZ with a loading of 0.30 moles CO_2/mole alkalinity and 1 mM Fe^{2+}, we measured a formate production rate of 0.011 mM/hr at 55 °C, with very little production of other heat stable salts. This rate is over an order of magnitude lower than that observed at the same conditions for MEA (0.39 mM/hr) (Sexton, 2009). Importantly, we also reported very little loss of total alkalinity and total MDEA or PZ concentrations in oxidatively degraded blend, whereas, at the same conditions, we see significant loss of 7 m MEA (Figure 4). Using the same experimental apparatus, Freeman (2008) attempted to oxidatively degrade 10 m PZ with various metals for catalyst, but reported a similarly low production of formate, and very little loss of PZ concentration as evidenced by alkalinity and IC measurement methods.
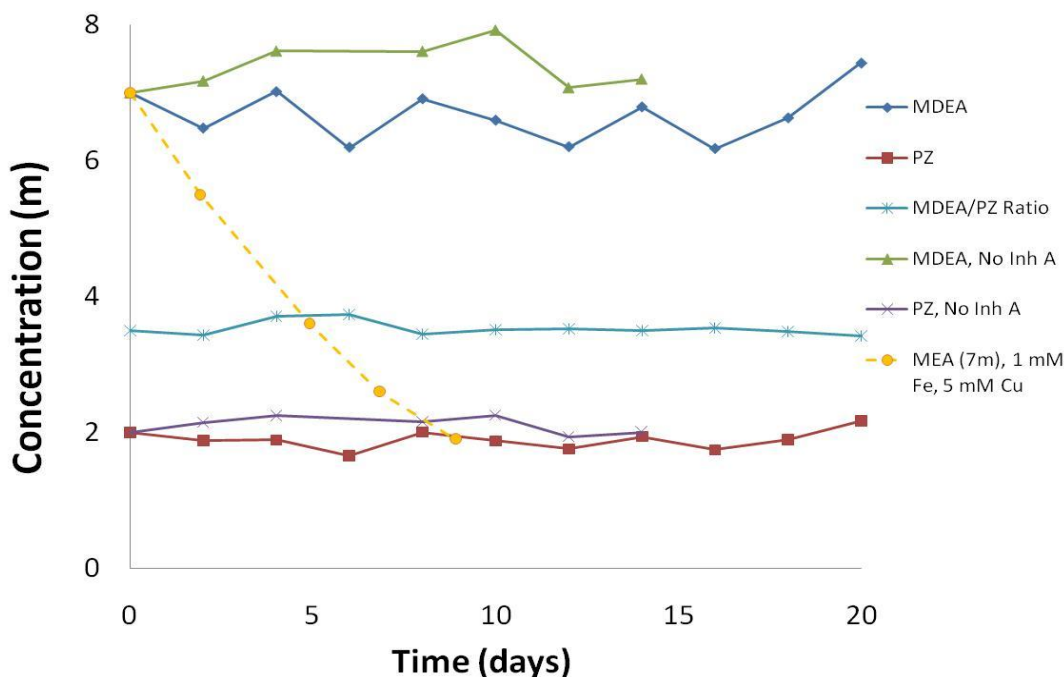
Figure 4: Oxidatively Degraded Solvents; 1 mM Fe^{2+}, 100 mM Inh A, 7 m MEA Data from Sexton (2008)

From MEA oxidative degradation studies, Sexton (2009) reported that the formation of heat stable salts can be followed by a reaction with MEA and the production of amides; formamide will be the product of a reaction between formic acid and MEA. Formamide can be converted back to formate through a simple hydrolysis step using 5N NaOH, and quantified through comparison of formate measured in

hydrolyzed versus unhydrolyzed samples. This hydrolysis step was performed on 7 m MDEA samples degraded in a solvent cycling apparatus (discussed below) for 60 hours, resulting in the production of as much as 37 mM formamide. When degraded in our low-gas apparatus, we observed no more than 7 mM formamide after 192 hours of degradation.

3.0   Objectives of Research

3.1   Degradation Mechanisms in MDEA/PZ (Primary Objective)

The primary objective of this research is to develop a fundamental understanding of the degradation mechanisms that occur in the MDEA/PZ blended solvent when used for CO_2 capture from flue gas feed streams. Emphasis will be placed on the MDEA/PZ blend because of its commercial use. Versions of this solvent are already in commercial use for acid gas treatment, and its performance benefits make its consideration as an alternative to MEA for CO_2 capture from flue gas attractive. We will seek to identify the degradation products of this solvent when used for CO_2 capture, and to understand the oxidative and thermal degradation mechanisms that simultaneously occur so that methods for preventing degradation can be developed. This may lead us to the specification of optimal operating conditions for this solvent.

As discussed above, MDEA is known to thermally degrade to DEA quite readily, with further degradation to other amine products well documented. Secondary reactions with PZ in the MDEA/PZ blend have been confirmed through detection of products such as methyl- and dimethyl-PZ. An understanding of the mechanisms leading to these secondary reactions is lacking. The subject research will seek to fill these data gaps.

The proposal scope will include similar degradation studies of one to two other blends with PZ, with 2-amino-2-methylpropanol (AMP) a likely candidate to replace MDEA in the blend. The purpose of this substitution is to investigate whether the hindered amine (AMP) initiates similar degradation processes in the blend, leading to secondary reactions with PZ and loss of both the AMP and PZ.

3.2   Investigating Effects of Solvent Cycling (Secondary Objective)

In addition to developing a basic understanding of the degradation mechanisms for the MDEA/PZ blend, this research will focus on the combined effects of oxidative and thermal degradation occurring in cycled solvents. To-date, the published data has typically been generated by performing batch experiments wherein the thermal and oxidative degradation effects are studied separately. The scope-of-work of my research will utilize an Integrated Solvent Degradation Apparatus (ISDA). ISDA continuously cycles a single charge of approximately 2.5 kg of solvent through oxidative and thermal degradation conditions in order to mimic the degradation environment of an absorber/stripper system. ISDA does not achieve CO_2 absorption and stripping as in a true absorber/stripper configuration. Instead, ISDA will cycle solvents at a preselected CO_2 loading, corresponding to either the rich or lean end of expected conditions.

Central to studies using ISDA is the need to understand why the rate of formation of heat stable salts in 7 m MDEA observed in Cycling Experiment C-1 was more than an order of magnitude greater than that

observed in oxidative experiments conducted with our low-gas apparatus. We will explore the potential that this observation was due to entrainment of O_2 in cycled solvents, thus allowing accelerated oxidative processes to occur in the thermal reactor at the higher temperature of 120 °C. The importance of this conclusion is that accelerated oxidation may occur in a stripper in flue gas applications where O_2 is present in the feed, thus requiring engineers to compensate for detrimental oxidative effects in CO_2 scrubber systems. This effect is in contrast to acid gas treatment applications where O_2 feed concentrations are typically less than 1 %. We will also investigate secondary reactions involving the oxidative degradation of thermal degradation products to heat stable salts (i.e., DEA degradation to formate).

4.0   Proposed Methods of Conducting Research

In the proposed research, emphasis will be placed on degrading solvents in a cycling environment wherein the solvents are alternately exposed to both oxidative and thermal degradation conditions in a single integrated apparatus (ISDA). The majority of the planned future work will utilize ISDA (described below). Other methods will also be utilized including: (1) thermal degradation in 10-ml 316 stainless steel sample cylinders at temperatures of 100 to 175 °C, and (2) oxidative degradation in a 400-ml low-gas reactor at atmospheric pressure and 55 °C. This section discusses each method of degrading solvents, and the analytical techniques we will use to analyze samples.

4.1   Thermal Degradation (Sample Cylinders)

Batch thermal degradation screening studies will be performed in sample cylinders constructed of 316 stainless steel tubing and Swagelok® compression fitting endcaps with a nominal volume of 10 ml. Each sample cylinder is charged with 8 to 10 ml of solvent, sealed, and placed in a forced convection oven at a preset temperature for a period of time. Cylinders are removed from the oven(s) over time and the solvent samples sacrificed for analysis.

Several sample cylinders are utilized for each experiment to provide several data points for each temperature and CO_2 loading. The sample cylinders allow us to rapidly screen solvents and degradation conditions, with multiple experiments possible at one time. The sample cylinder volume is adequate to allow a full suite of analyses including IC, IC/MS, HPLC, LC/MS, metals, TIC, and titrations. One limitation to the sample cylinders is the possibility that the amines are able to corrode the sample cylinders, despite being constructed of 316 stainless steel. Given this possibility, we will analyze for metals in degraded samples in all future experiments.

4.2   Oxidative Degradation (Low-Gas Reactor)

Rapid oxidative degradation screening will be achieved with a low-gas flow glass reactor with a nominal volume of 400 ml. The reactor is designed with a jacket to allow circulation of a temperature-controlled water bath in the reactor wall, thus maintaining solvent temperature at 53-55 °C. A gas mixture of 98 % O_2/2 % CO_2 is continuously pumped into the reactor headspace at a rate of 100 ml/min, forcing air out and limiting the driving force of CO_2 from solution to the atmosphere. The solvent is agitated with a stirring shaft and impeller operated at approximately 1440 rpm to induce rapid mixing and creation of a vortex. The operating conditions are designed to overcome mass transfer limitations associated with

dissolving O_2 into the solvent as degradation progresses. Solvents are degraded in the low-gas reactor for up to three weeks at a time, with samples collected daily for analysis.

The low-gas apparatus has the advantage of allowing rapid screening of the oxidative degradation potential of solvents while working with less than 0.5 L at a time. Using this method, we determined that 7 m MDEA/2 m PZ maintains nearly all of its MDEA and PZ concentration when degraded for three weeks at 55 °C with 1 mM Fe^{2+}. Under similar conditions (55 °C and 1 mM Fe^{2+}), we determined that 7 m MEA loses almost 70 % of its amine concentration and functionality (Sexton, 2009).

The low-gas apparatus has one significant limitation in that we have typically been unable to close the mass balance on oxidatively degraded solvents in past studies. Because the low-gas reactor is not a sealed vessel, the system experiences loss of gas-phase degradation products through the impeller shaft opening, thus preventing us from accounting for the evolution of volatile products such as ammonia and CO_2. This apparatus also requires that we maintain the water balance due to daily water losses of approximately 3 %; liquid loss is assumed to be 100 % water, and is accounted for through careful measurement of liquid level, and daily additions of make-up water. Another method employed to account for liquid loss entails the use of a non-volatile (inorganic) tracer such as sulfate.

4.3 Integrated Solvent Degradation Apparatus (ISDA)

The research described in this proposal places emphasis on the degradation of solvents in a cycling environment through use of the new degradation study tool ISDA (Figure 5). Its specifications are listed in Table 1. ISDA allows us to integrate the study of oxidative and thermal degradation of solvents in a single apparatus that mimics degradation conditions observed in an absorber/stripper configuration designed for CO_2 capture. Each batch of solvent is continuously cycled from the oxidative conditions that mirror an absorber to the thermal conditions prevalent in a stripper. It is anticipated that, when combined into a single experimental apparatus, the corresponding degradation processes will lead to secondary effects typically observed in field application samples. ISDA provides the possibility and flexibility to study degradation processes that occur in the field without having to rely on field samples from industrial operations.
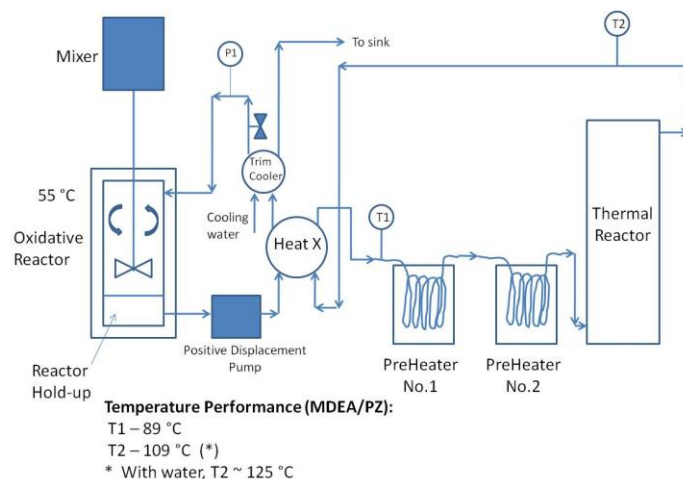
Figure 5: Integrated Solvent Degradation Apparatus (ISDA)

Table 1 - Integrated Solvent Degradation Apparatus (ISDA)			
Equipment	Type	Specifications	Manufacturer
Pump	Positive Displacement	50 - 5000 ml/min	Cole-Parmer
Cross Exchanger	Tube-in-tube	316 SS; 60 inch length	Exergy
Pre-Heaters	Coiled Tube/Oil Bath Immersion	316 SS Tubing, ~60 inch length	UT ChE Shop Fab
Trim Cooler	Tube-in-tube	316 SS; 18 inch length	Exergy
Oxidative Reactor	Flow-through Stirred Reactor	0.4 L Top Section, 0.25 L Bottom Section	Glass Fabrication (Welch)
Thermal Reactor	Tube-in-tube Reactor	316 SS; 0.9 L	UT ChE Shop Fab
Tubing	SS Tubing	316 SS	Swagelok®
Heat Baths	Water/Oil Circulation	2.25 kW	Lauda E200/E300

The oxidative reactor, which mimics conditions in an absorber, is a jacketed glass reactor with a top and bottom section. The top section has a nominal volume of 400 ml, while the bottom section, which mimics the absorber hold-up section, has a volume of approximately 250 ml providing hold-up retention times of 2 to 5 minutes, depending on solvent flow rate. The top section is agitated with an impeller shaft rotated at ~1,450 rpm to create a vortex on the liquid surface, thus ensuring the system is kinetically limited as opposed to mass transfer limited. We operate at a nominal flow rate of ~120 ml/min. The oxidative reactor is operated at atmospheric pressure and temperatures in the range of 53 to 55 °C.

CO_2-loaded amine is continuously pumped from the bottom section of the oxidative reactor through a positive displacement pump and into the shell side of a single-pass tube-in-tube cross-exchanger where it takes on heat from amine exiting the thermal reactor counter-currently. The amine is then passed through a series of two pre-heaters consisting of stainless steel coiled tubing immersed in Lauda oil baths operated at 110 and 132 °C, respectively. The amine exits the second pre-heater and enters the internal section of a thermal reactor, which is a stainless steel tube-in-tube heat exchanger with a nominal volume of 0.9 L. Dimethyl silicone oil is passed through the jacket side of the thermal reactor to impart heat to the amine; amine and jacket-side oil are operated in co-current fashion to ensure fully flooded operation of the thermal reactor. The amine then exits the thermal reactor and passes back through the inner tubing of the tube-in-tube cross-exchanger where it gives up heat to the amine passing on the shell side. The amine is then passed through the inner tube of a tube-in-tube trim cooler (heat exchanger) where it is cooled by tap water at ambient temperature passed through the shell side. Finally, the cooled amine is passed through a back-pressure valve (¼-inch metering valve) and returned to the oxidative reactor at a location just above the vortex liquid level at atmospheric pressure. All tubing is ¼-inch nominal size. Materials of construction include 316 stainless steel for all tubing, compression fittings, cross-exchanger, and thermal reactor, and PPS (polypropylene) for the pump head. The oxidative reactor is of glass construction.

4.4   Analytical Methods

Degraded samples are analyzed for a number of chemical parameters including: (1) total inorganic carbon (TIC) for CO_2 loading, (2) titration for alkalinity, (3) cation and anion chromatography for degradation product concentrations, (4) IC-MS and LC-MS to separate degradation compounds and determine their respective masses, (5) HPLC to separate and identify non-ionic degradation products, and (6) flame atomic absorption (AA) for individual metals. This section briefly discusses the analytical methods and how they will be used in my research.

Total Inorganic Carbon (TIC)

We measure CO_2 concentrations in prepared solutions and degraded samples using our TIC equipment which consists of a gas purge cell and Horiba infrared (IR) detector. Solvent samples are acidified in the gas purge cell with 30 wt % H_3PO_4 to convert all CO_2 species to gaseous CO_2, and nitrogen purge gas sweeps the sample to the IR detector. Carbon standards are injected for comparison and the CO_2 loading of a sample is calculated based on moles of CO_2 per mole of alkalinity. Data acquisition is achieved through a PC and PicoLog software connected to the IR detector.

Total Organic Carbon (TOC)

Total organic carbon (TOC) is measured in degraded samples using a Shimadzu 5050A TOC Analyzer (Kyoto, Japan). The analyzer measures TIC and total carbon of samples. The difference between these two measurements is TOC. In a similar fashion to that described above, TIC measurements involve liberating CO_2 species (aqueous CO_2, carbonate (CO_3^{2-}), bicarbonate (HCO_3^-) and amine carbamates) from solution as gaseous CO_2 with 25 wt % phosphoric acid (H_3PO_4). The CO_2 is carried by nitrogen gas to a non-dispersive infrared (NDIR) analyzer. For total carbon analysis, a slipstream of sample is metered and combusted over a platinum catalyst at 680 °C with ultra pure air. The CO_2 created by this combustion is carried to the NDIR detector for measurement of response. A 1000 ppm standard made of a mixture of sodium carbonate (Na_2CO_3) and sodium bicarbonate ($NaHCO_3$) in ultrapure water is used to calibrate instrument response. For TOC measurements, the Shimadzu has detection limit of four ppb and a range of up to 4000 ppm (Sexton, 2008).

Titration

Sample alkalinity of solvents is measured through acid titration with a Titrando auto titrator using 0.1N H_2SO_4. The results are used to determine the amount of amine functionality lost during degradation. Amine concentration and solution alkalinity are calculated based on the amount of acid needed to reach an equivalence point at a pH of 3.9.

Ion Chromatography (IC) – Cation and Anion

We utilize a Dionex ICS-2500 Ion Chromatography System (IC) with autosampler to quantify cations in degraded solutions (Dionex Corporation, Sunnyvale, CA). Our current separation method utilizes an IonPac CS17 analytical column (4 X 250 mm). The column is a sulfonated styrene divinyl benzene copolymer medium which can achieve separation of cations encountered in amine solvents when eluted

with a combination of ultrapure (deionized) water and methanesulfonic acid (MSA). The system is equipped with a Cationic Self-Generating Suppressor (CSRS) for anion suppression/removal prior to passing eluted material through the Dionex CD25 conductivity detector. Chromeleon proprietary software is used for all Dionex system controls and data acquisition.

A Dionex Dual RFIC ICS-3000 ion chromatograph is used for anion separation and quantification. The instrument is equipped with an RFIC EluGen KOH eluent generator; the method currently in use for anion separations utilizes a KOH gradient in ultrapure (deionized) water. Separations are achieved with an IonPac AS15 column (4X 250 mm) column which is a sulfonated styrene divinyl benzene copolymer medium. Separated samples are passed from the column through a 4-mm Anionic Self-Regenerating Suppressor (ASRS) device to remove cationic species. The system also utilizes two carbonate removal devices to remove excess carbonate species from samples (Continuously Regenerated Anion Trap Column or CR-ATC), and a conductivity detector for anion quantification. Chromeleon software on a PC is used to control the entire IC system, modify and launch sequences, and perform data acquisition.

Mass Spectrometry (MS) Coupled with IC and Liquid Chromatography

Degraded samples are also analyzed with a Dionex ICS-2000 RFIC Chromatography System coupled to a ThermoFinnigan TSQuantum mass spectrometer (MS) with an electrospray ionization detector. The Dionex system can be configured for cation IC or liquid chromatography (LC) mode coupled with the mass spectrometer (MS).

The TSQuantum consists of three basic components: (i) ion source, (ii) mass analyser, and (iii) ion detector. In the electrospray ionization, the liquid sample is electrostaticly sprayed through a needle held at high voltage, imparting a positive or negative charge to ions in the liquid. The ions are attracted to the entrance of the mass analyzer and emerge from a cone formed by the elongation of the solution at the needle tip. A counter-current dry gas evaporates the ionized liquid further, leaving ions which move closer together, eventually becoming small solvent-free ions that are passed through the mass analyzer and detected.

When coupled with the IC, which separates compounds in samples by cation activity, or LC which separates compounds in samples by polarity, the MS provides a spectrum of charge-to-mass ratios which is synchronized with the elution of the compounds from the respective column and detector, allowing determination of molecular weight of compounds aligned with elution time from the chromatograph. The utility of this combined analytical technique to the proposed work is that we can separate and detect cations or polar compounds in degraded amine samples, and assign molecular weights to peaks. In combination with knowledge about amine behavior (mono-amine vs. diamine functionality) and where these elute in IC, we can accurately determine the structure of degradation products with cationic behavior. For non-ionic species such as ureas, we see separation in elution times with the LC based on polarity, and assign mass in a similar fashion.

HPLC

The Dionex ICS-3000 modular Dual RFIC Ion Chromatography System contains an HPLC for analysis of degraded samples for non-ionic species. Our current separation method utilizes a gradient of methanol in ultrapure water to achieve separation of non-ionic species in an Atlantis T3 3µm column (4.6 X 150 mm) (Waters Corporation, Milford, MA). Samples are separated on the stationary phase column and passed through an evaporative light scattering detector (ELSD). The mobile phase entering the detector is nebulized with nitrogen to form aerosol droplets which then pass through a heated coil where the eluent is evaporated, leaving residual analyte. These analyte particles enter an optical chamber where they pass through a light beam which gets scattered. The magnitude of this scattered light is dependent on the size of the particle formed and is sensed by a photodiode. Suitability of a compound for detection with ELSD is generally dictated by vapour pressure (the lower the better); semi- and non-volatile species are more likely to be detected with ELSD than volatile species. In degraded amines, we expect that some urea compounds will be detectable with ELSD.

Atomic Absorption

We use a Perkin-Elmer atomic absorption (AA) spectrometer for metals analysis in degraded samples. The Perkin-Elmer AA spectrometer uses a flame to atomize liquid samples, and produce free analyte atoms from the samples; the source of energy for the free atom source is heat. The flame AA utilizes an air/acetylene flame. The sample is introduced as an aerosol into the flame by a nebulizer and spray chamber. A light beam source, either a cathode lamp (HCL) or an electrode-less discharge lamp (EDL), is aligned to pass light through the flame. The metals, which exist as ground state atoms, absorb energy in the form of light of a specific wavelength elevating them to an excited state. The amount of light energy absorbed at a given wavelength will increase as the number of atoms of the selected element in the light path increase. The relationship between the amount of light absorbed and the concentration of analytes present in standards is used to determine the concentration of the element in unknown samples. Each metal of interest requires a different light source emitting at a different wavelength. Measurements of metals concentrations are rapidly made in 10X dilution samples.

5.0 Data Analysis Methods

This research will generate amine degradation samples through several methods including ISDA, thermal degradation batch cylinders, and the low-gas oxidative degradation reactor. The analytical data from the instrumentation described above will be used for comparative analysis. We will compare the ISDA degradation data including identified degradation products from IC and MS methods to that collected using the other two experimental methods (Swagelok® sample cylinders and low-gas oxidative reactor). The following discussion articulates the basic analyses I will implement. Rates of degradation will be calculated, and relationships for how amine degradation is affected by temperature, CO_2-loading, and amine concentration will be derived through data regression.

5.1   Determination of Enhanced Degradation Effects in ISDA

At its most basic level, the data will be used to determine whether enhanced degradation effects are occurring when we continuously cycle the solvents over simple batch experiments. Analyses will include comparing degradation rates of known products (heat stable salts and cation products such as DEA), and assessing whether new products appear in ISDA samples. We will be able to use the data generated in past experiments (Thermal No.s 1-10 and OD-1 through OD-5) as a base of knowledge for how MDEA and MDEA/PZ degrade both thermally and oxidatively. Building on this data, cycling experiments will be designed for direct comparison at similar solvent concentrations (7m MDEA and the 7 m MDEA/2 m PZ blend), loadings (0.1 through 0.3 moles CO_2/mole alkalinity), and temperatures (oxidative degradation at 55 °C and thermal degradation at 120 °C).

5.2   Development of Thermal Degradation Mechanisms

We will seek to determine chemical degradation mechanisms in the MDEA/PZ blend through review of the time progression of degradation product appearance and concentration. For example, when we degrade MDEA, we start to form DEA after only four hours of operation in ISDA with concentrations of 55 and 120 °C in the oxidative and thermal reactors, respectively. The concentration increases with time for the duration of the experiment. In the presence of free CO_2, we can expect that DEA-carbamates will form, and lead to the formation of the oxazolidone and HEIA. In the presence of PZ, however, we expect that a set of competing reactions involving arm-switching will occur, as evidenced by the presence of N-methyl-PZ in thermal studies with batch cylinders. This work will strive to define the specific mechanisms that are occurring. Mechanisms have been postulated in Section 7.0.

5.3   Closure of Mass Balance

We will seek to close the carbon and nitrogen mass balances in degraded MDEA/PZ samples using IC, IC-MS, LC-MS and HPLC methods. When we degraded 7 m MDEA/2 m PZ using our sealed sample cylinders, we found that as much as 35 % of MDEA and over 90 % of PZ mass were lost after 42 days of degradation at 150 °C. Because total sample mass was not actually lost, we should be able to account for MDEA and PZ mass loss through identification of degradation products using the described analytical methods. IC-MS allows us to separate degradation products with cationic functionality (active nitrogen groups exhibiting alkalinity) and identify their mass. With the identification of the compounds exhibiting cation behavior in associated IC-MS analyses, we are only able to account for a fraction (<20 %) of the lost MDEA and PZ mass and alkalinity in this experiment. We will utilize LC-MS and HPLC to identify and quantify degradation products including non-ionic polar compounds such as ureas (HEIA) and dimers of urea.

6.0   Preliminary Data

Through experiments conducted to-date on 7 m MDEA, 8 m PZ, and the 7m MDEA/2 m PZ blend, we have developed a basic understanding of the degradation potential and behavior of these solvents. Experiments with the individual amines have been essential to understanding the more complex nature of the blend. The more important findings from my completed research are presented in this section.

6.1   Thermal Degradation

Figure 6 presents the concentrations of MDEA and PZ from a batch cylinder thermal degradation study conducted on 7 m MDEA/2 m PZ at a loading of 0.26 moles CO_2/moles alkalinity and temperatures of 135 and 150 °C. The concentration of PZ decreases to zero in less than 20 days at 150 °C, and less than 35 days at 135 °C. PZ losses are accompanied by apparent equimolar losses in MDEA concentration over the initial period of the experiment while PZ is being lost. At 135 °C, the MDEA loss rate slows after complete loss of PZ in the blend, with a distinct leveling out after 69 days in the study. However, at 150 °C, we see a continued loss in MDEA concentration, with determination of the longer term trend limited by lack of data past 69 days in the study.
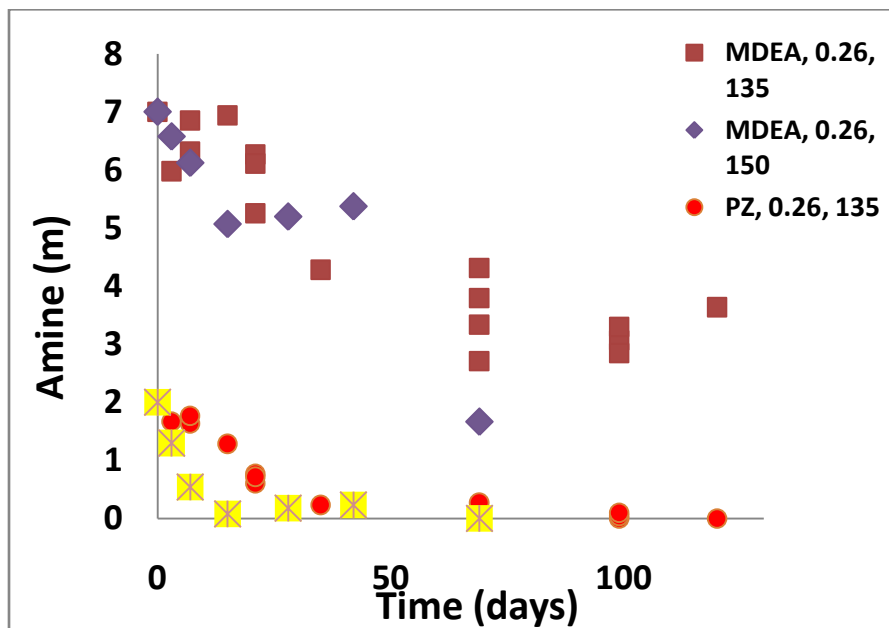
Figure 6: 7 m MDEA/2 m PZ Degradation (Thermal Cylinders)

Table 2 presents a summary table of thermal degradation rates measured in 7 m MDEA and 7 m MDEA/2 m PZ at nominal loadings of 0.1 and 0.2 moles CO_2/mole alkalinity. Using cation IC, we measured amine concentrations including undegraded solvent (MDEA and PZ) and degradation products. We estimated the concentration of diamine compounds appearing in degraded samples, calculated diamine appearance rates, and correlated PZ and MDEA loss rates with diamine appearance rates. Assuming PZ degrades in the blend to diamine products, the rates between PZ loss and diamine appearance generally matched. In general, the rates correlated well on an order of magnitude basis, with the exception of the higher loading (0.2 moles CO_2/mole alk), and at 150 °C. The most significant pattern arising from the data was an increase in the PZ loss rates from the blended solvent when the temperature was increased from 100 to 150 °C. Across the investigation temperature range, an increase in loading from 0.1 to 0.2 moles CO_2/moles alkalinity had little effect on the PZ loss rate, but a large effect on the MDEA loss rates, indicating that CO_2 played a role in MDEA loss. The mechanisms for loss of amine in the blend rely on a reaction with CO_2 to form either protonated MDEA or a DEA-carbamate (see Section 7.0), leading to further reactions. Hence, the observation that an increase in loading plays a

large role in amine degradation is consistent with assumptions about degradation mechanisms. Accounting for diamine production through cation analyses does not allow us to close the mass balance on degraded samples in the blend.

Solvent	Temp (°C)	Duration (Days)	MDEA Deg Rate (mmolality/day)		PZ Deg Rate (mmolality/day)		Diamine Appearance Rate (mmolality/day)	
			$\alpha = 0.1$	$\alpha = 0.2$	$\alpha = 0.1$	$\alpha = 0.2$	$\alpha = 0.1$	$\alpha = 0.2$
7m MDEA	100	63	6 ± 6	18 ± 52	NA	NA	NA	NA
	120	63	0.3 ± 11	31 ± 16	NA	NA	NA	NA
	135	69	55	53	NA	NA	NA	NA
7m MDEA	150	69	66	112	NA	NA	NA	NA
7m MDEA/2m PZ	100	54	3 ± 13	19 ± 4	2 ± 4	6 ± 1	1 ± 2	2 ± 2
	120	54	11 ± 11	7 ± 20	7 ± 3	9 ± 5	2 ± 2	5 ± 2
7m MDEA/2m PZ w/ 1 mM Fe^{2+}	100	42	NA	3 ± 13	NA	2 ± 5	NA	2 ± 3
	120	49	NA	18 ± 20	NA	11 ± 10	NA	12 ± 3
7m MDEA/2m PZ	135	28	8 ± 37	0 ± 20	30 ± 15	39 ± 11	44 ± 12	51 ± 8
7m MDEA/2m PZ*	150	28	8 ± 57	66 ± 21	79 ± 20	59 ± 25	NA	6 ± 15

Table 2 - Thermal Degradation Rates - Average MDEA/PZ Loss/Diamine Appearance Rates

Figure 7 of this proposal is a typical cation IC chromatogram for 7 m MDEA/2 m PZ loaded to 0.25 moles CO_2/mole alkalinity and degraded at 135 °C for 21 days. This sample was analyzed with an IC-MS, and the molecular weights of corresponding peaks are presented to illustrate the cation degradation products identified to-date. In this sample, we were able to account for four and possibly five (MW = 133.2 tentatively identified as diethanolethylamine) degradation products. With longer degradation time, this solvent degraded to yield additional unidentified peaks.
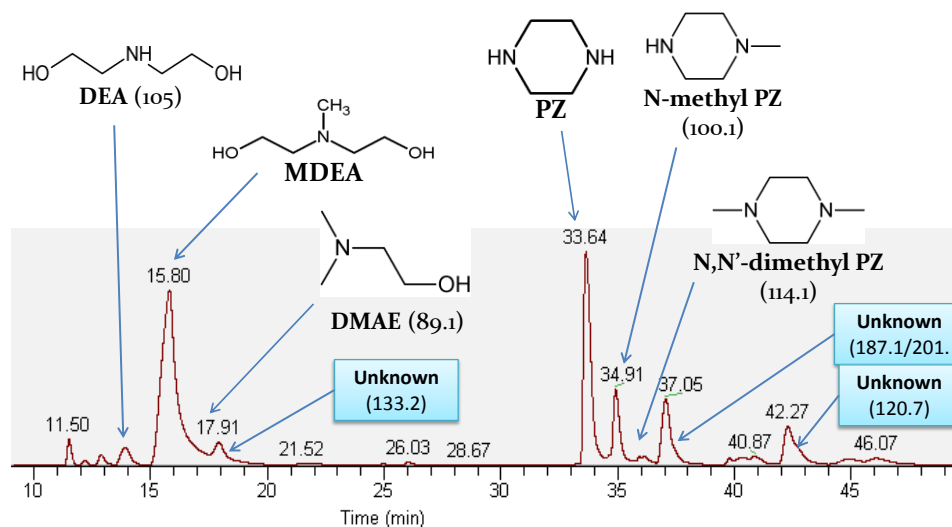
Figure 7: Cation Chromatogram/Mass Spectrum
7m MDEA/2m PZ, α = 0.25, T = 135 °C, 21 Days

16

Freeman (April 2009) reported that the cyclic amine PZ does not thermally degrade at temperatures up to 150 °C, despite forming a carbamate in CO_2 loaded solutions. However, I reported (Closmann, July 2009) that, when blended with MDEA at concentrations of 7 m MDEA/2 m PZ, both the MDEA and PZ are degraded, with complete PZ degradation within 30 days at 150 °C in batch cylinder degradation studies. We believe the MDEA undergoes thermal degradation to form DEA, which reacts with CO_2 to form DEA-carbamate. As demonstrated by Polderman, the DEA-carbamate will form an oxazolidone (HEOD), and in an analogous fashion to that reported by Davis (2009), will react with the strong nucleophile PZ to form a PZ derivative. We have been unable to identify the final PZ derivative(s) in degraded blends to-date. However, we have identified the compounds listed in Table 2 in MDEA/PZ blend studies using IC-MS. That list includes methyl piperazine, dimethyl piperazine, and 1-(2-aminoethyl)piperazine. We also detected compounds with molecular weights of 120.7, 127.6, 133.2, 169 and 187.2 at significant enough frequency and concentration to warrant further investigation.

In summary, our thermal degradation studies with the MDEA/PZ blend confirm the breakdown of MDEA to DEA and its degradation products. We also believe that PZ is acting as a strong nucleophile and reacting with these degradation products to form the PZ derivatives listed in Table 3. These findings are consistent with that of Davis (2009) who found that blends of MEA and another amine preferentially degraded the other amine over studies with the other amine alone, and with Lepaumier (2009) who reported that the oxazolidones are sensitive to nucleophilic reactions with other amines, which would include PZ.

Table 3 - Compounds Detected in Thermally Degraded MDEA/PZ				
Compound	Acronym	Intermediate/End Product*	Molecular Weight	Method
ethylenediamine	EDA	Intermediate	60.1	IC
methylaminoethanol	MAE	Intermediate	75.1	IC
dimethyl aminoethanol	DMAE	Intermediate	89.1	IC-MS, LC-MS
N-methyl piperazine	N-methyl PZ	Final	100.1	IC-MS
diethanolamine	DEA	intermediate	105.1	IC-MS, LC-MS
N,N'-dimethyl piperazine	2-methyl PZ	Final	114.2	IC-MS, LC-MS
N,N'-diethyl ethanolamine	-	Final	117.2	IC-MS
1-(2-aminoethyl)-piperazine	-	Final	129.2	IC
Diethanolethylamine	-	-	133.2	LC-MS
1-(2-hydroxyethyl)-4-methyl piperazine	HMP	Final	144.1	IC-MS, LC-MS
Dihydroxyethyl piperazine	BHEP	Final	174.1	LC-MS

   * Terminology provided in literature (Chakma & Meisen, 1997)

6.2   Oxidative Degradation and Cycling in ISDA

Figure 8 presents formate concentrations with time for oxidatively degraded 7 m MDEA from three studies. The first study was that conducted by Rooney et al. (1998). In 2008, we measured formate concentrations when we degraded the same solvent in our low-gas reactor. Most recently, we utilized ISDA to cycle and degrade the same solvent in Experiment C-1. We reported an order of magnitude greater production of formate and formamide (measured as formate) through cycling of the solvent in ISDA. Figure 9 presents the concentrations of MDEA, heat stable salts and amide (measured as formate in hydrolyzed samples) from that same cycling experiment. Note that losses in MDEA and production of heat stable salts and amides are not on the same order of magnitude. In fact, when we attempted to close the mass balance on degraded 7 m MDEA in experiment C-1, we were able to account for approximately 20 % of MDEA loss through estimates of DEA (cation IC), formate, gylcolate, formate and formamide concentration.

These data may indicate that thermal degradation products of MDEA are being oxidatively degraded to heat stable salts (formate), and/or the entrainment of gas bubbles (primarily O_2) is causing enhanced oxidative degradation to occur in the cross exchanger and thermal reactor in ISDA over that observed in our low-gas apparatus. These effects will be investigated in the proposed scope-of-work.
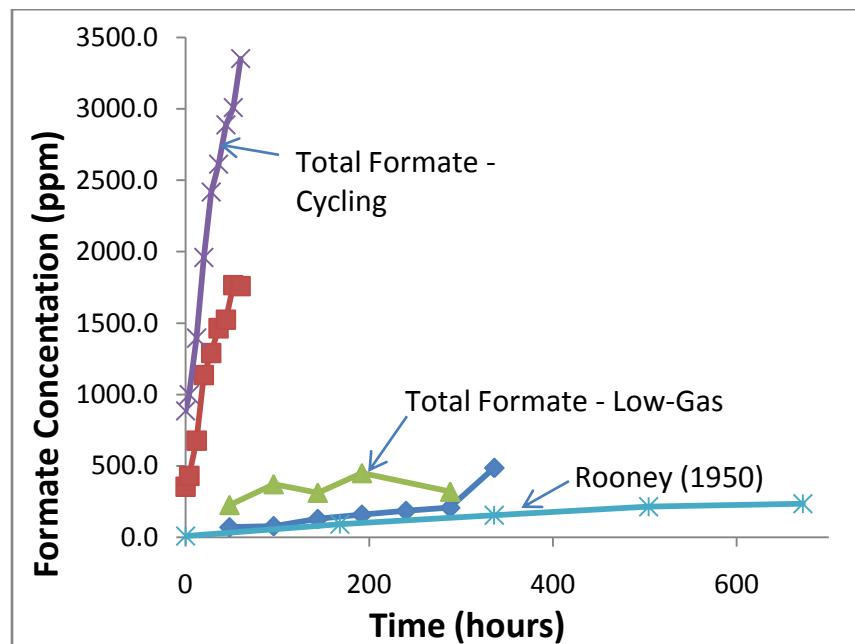
Figure 8: Formate Production in Oxidative Degradation of 7 m MDEA (Various Studies)

In order to understand whether corrosion played a role in the degradation of 7 m MDEA and the corresponding production of heat stable salts, we measured the concentration of iron, chromium and nickel in the daily samples from that experiment using flame AA. We found less than 5 ppm of iron at the very end of the experiment, but nickel and chromium were below detection.
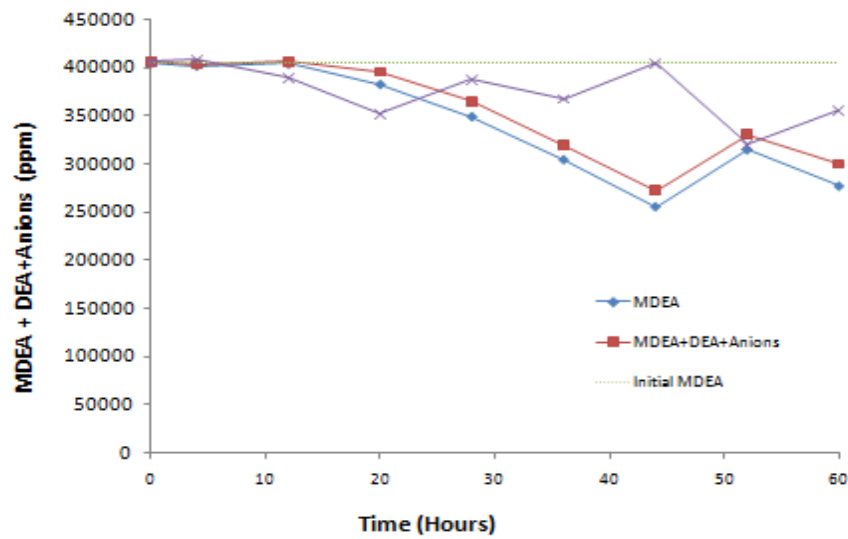
Figure 9: Degradation Products in 7 m MDEA (Cycling for 60 Hrs in ISDA)

7.0   Degradation Mechanisms

We have postulated thermal degradation mechanisms in the MDEA/PZ blend.   Three of those mechanisms are presented in this section. Using IC, IC-MS, LC-MS and HPLC methods with standards, we will continue the work of identifying products in degraded MDEA/PZ samples so that we can confirm these degradation mechanisms, and/or postulate new ones.

Currently published data indicate that, when MDEA/PZ is loaded with CO_2, the MDEA thermally degrades at temperatures of 120 °C and above to form DEA, MAE, DMAE and other products. This initial degradation step is followed by other reactions. DEA in particular, will form a DEA-carbamate in the presence of CO_2, and progress through the pathway first described by Polderman (1950) to form an oxazolidone and ethylenediamine compound.   In the presence of PZ, which will act as a strong nucleophile (pK~9.82), additional products such as 2-[[2-(1-piperazinyl)ethyl]amino]ethanol (MW=173) could be formed through attack of the carbon-oxygen bond at the ester-oxygen on the oxazolidone by free PZ (Figure 10). We believe that this reaction would be possible at loadings below the point at which all PZ reacts with CO_2 to form PZ-dicarbamate (i.e., < 4 /11 moles CO_2/moles total alkalinity). As of this time, we have not identified this compound using IC or other methods.
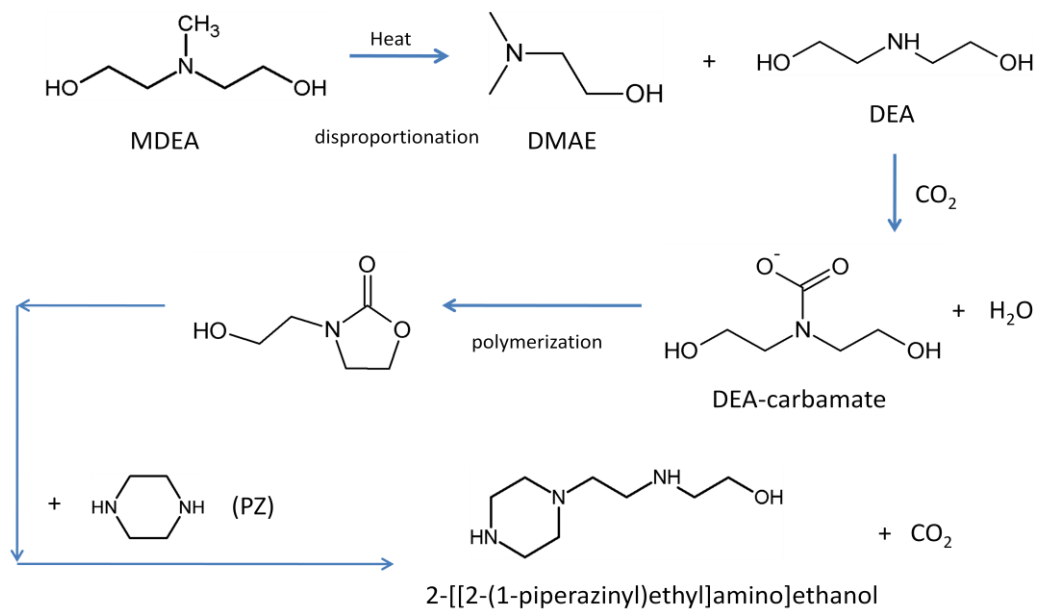
Figure 10: Thermal Degradation Mechanism – DEA-Carbamate Formation/PZ Nucleophile

Another proposed mechanism (Willson and Closmann, 2009) involves the protonation of MDEA (MDEAH+) in CO_2-loaded MDEA/PZ (Figure 11). MDEAH+ would be reactive and unstable, and in the presence of PZ, could undergo secondary reactions to form methyl-PZ and DEA, both of which have been observed in our degraded MDEA/PZ samples. From this point, the DEA would continue to degrade through the mechanism described above wherein the DEA-carbamate polymerizes then undergoes dehydration to form an oxazolidone. At this point, the mechanism described above would be possible, resulting in PZ derivatives.
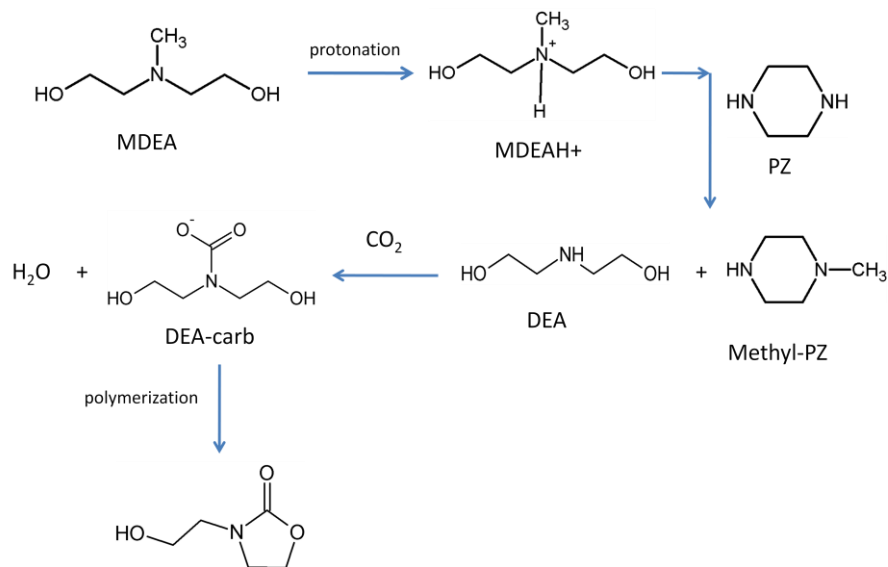
Figure 11: MDEA Protonation Pathway (Closmann/Willson, 2009)

A third mechanism we have considered (Figure 12) is similar to that presented in Figure 10 wherein MDEA degrades to DEA, forms the DEA-carbamate, and subsequently the oxazolidone (HEOD). The oxazolidone then reacts with N-methyl PZ which we have observed in thermally degraded samples. This reaction leads to the formation of the compound 2-[[2-(4-methyl-1-piperazinyl)ethyl]amino]ethanol with a molecular weight of 187.1. This compound will have an active nitrogen group and likely continue to react with DEA-carbamate and/or other strong nucleophiles in solution such as free PZ to form other compounds. We have observed a peak with a molecular weight of 187.1 through LC-MS analysis of samples of 7 m MDEA/2 m PZ thermally degraded for 3 to 15 days at 150 °C. Samples in this same series degraded for longer periods at 150 °C (69 days) do not exhibit this compound, possibly indicating their participation in additional reactions. Finally, this last mechanism is consistent with the protonation mechanism presented in Figure 11 which resulted in the production of both DEA and N-methyl PZ.

8.0   Planned Future Experiments

The proposed work is designed to fill data gaps and fulfill the research objectives reviewed in Section 3.0. Experiments will be sequenced to separate and understand the chemical degradation mechanisms occurring in the individual amines (MDEA and PZ) first, followed by developing that same understanding in the MDEA/PZ blend. For example, three cycling experiments utilizing ISDA for degradation of 7 m MDEA have been completed since July 2009. Each of these experiments has been designed to further our understanding of the degradation behavior of MDEA in the absence of PZ in the cycling environment created by ISDA (see Figure 8). After completion of MDEA experiments in ISDA, we will perform similar experiments with 2 m PZ. These experiments will be followed by a series of experiments in ISDA with 7 m MDEA/2 m PZ. In parallel with these experiments in ISDA, we will perform low-gas and thermal cylinder experiments on the same solvents as necessary to isolate oxidative and thermal degradation effects in these solvents. This overall sequence of experiments will provide the greatest opportunity to determine mechanisms in the blend.
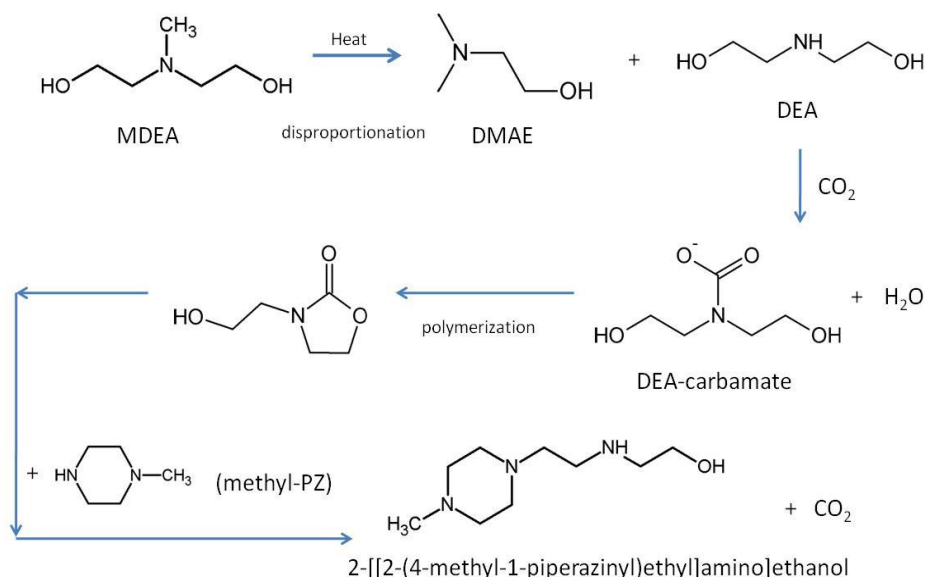
Figure 12: Thermal Degradation Mechanism – DEA-Carbamate Formation/N-methyl PZ Nucleophile

In an analogous fashion to the above-stated approach, we will investigate the degradation potential of a blend of the sterically hindered amine AMP with PZ.

I will utilize the analytical methods discussed in Section 4.0 on all degradation samples in order to achieve the research objectives stated in this proposal. Emphasis will be placed on utilizing IC-MS, LC-MS and HPLC to separate and identify degradation products in the experimental work. A significant amount of effort will be placed on refining our existing methods to learn more about the degradation processes with each experiment.

Typical cycling experiments require approximately ten to fifteen days to complete, and a one week turnaround period. Over the next 20 months, I anticipate completing a matrix of up to 18 experiments in ISDA to meet the research objectives. Thermal degradation experiments in Swagelok® cylinders will be conducted in parallel with cycling and low-gas experiments, allowing completion of all proposed experimental work in 20 months.

9.0   References

Aaron, Douglas and C. Tsouris, "Separation of CO_2 From Flue Gas: A Review", <u>Separation Science and Technology</u>, 40:1, 321 – 348, January 1, 2005.

Appl, M., U. Wagner, H.J. Henrici, K. Kuessner, K. Volkamer and E. Fuerst, "Removal of CO_2 and/or H_2S and/or COS from Gases Containing These Constituents", U.P. Office, USA, BASF GmbH: 9.

Astarita, Gianni and D. Savage and A. Bisio, <u>Gas Treating With Chemical Solvents</u>, J. Wiley & Sons, New York, 1983.

Bedell, Steve, Dow Chemical, personal communication, February 2009.

Blachly, C. H. and H. Ravner, "The Stabilization of Monoethanolamine Solutions for Submarine Carbon Dioxide Scrubbers", U.S. Naval Research Laboratory Report No. 0189, December 1964.

Chakma, Amitabha and A. Meisen, "Identification of Methyl Diethanolamine Degradation Products by Gas Chromatography and Gas Chromatography-Mass Spectrometry", <u>Journal of Chromatography</u>, 457, 287-297, 1988.

Chakma, Amitabha and A. Meisen, "Methyl Diethanolamine Degradation Mechanism and Kinetics", <u>The Canadian Journal of Chemical Engineering</u>, Volume 75, October 1997.

Closmann, Fred and Gary T. Rochelle, Quarterly Report for the Luminant Carbon Management Program, January 2009.

Closmann, Fred and Gary T. Rochelle, Quarterly Report for the Luminant Carbon Management Program, April 2009.

Closmann, Fred and Gary T. Rochelle, Quarterly Report for the Luminant Carbon Management Program, July 2009.

Davis, Jason, Ph.D. Dissertation, "Thermal Degradation of Aqueous Amines Used for Carbon Dioxide Capture", The University of Texas at Austin, August 2009.

Dawodu, Olukayode F., and A. Meisen, "Degradation of Alkanolamine Blends by Carbon Dioxide", The Canadian Journal of Chemical Engineering, Volume 74, December 1996.

Freeman, Stephanie and G. Rochelle, Quarterly Report for the Luminant Carbon Management Program, April 2009.

Hofmeyer, B.G., H.G. Scholten and W.G. Lloyd, "Contamination and Corrosion in Monoethanolamine Gas Treating Solutions", presentation to Symposium of American Chemical Society, Dallas, Texas, April 8-13, 1956.

Holub, Patrick E. and J.E. Critchfield, "Amine Degradation Chemistry in CO2 Service", presented at the Annual Laurance Reid Gas Conditioning Conference, Norman, OK, March 1-4, 1998.

Kennard, M.L. and A. Meisen, "Control DEA Degradation", Hydrocarbon Processing, 103-106, April 1980.

Kim, C.J., and G. Sartori, "Kinetics and Mechanism of Diethanolamine Degradation in Aqueous Solutions Containing Carbon Dioxide", International Journal of Chemical Kinetics, Vol. 16, 1257-1266, 1984.

Kindrick, R.C., A. Kenton and M.R. Arnold, "The Relative Resistance to Oxidation of Commercially Available Amines", The Girdler Corporation, Report No. T2.15-1-30, May 19, 1950.

Kvamsdal, Hanne and G. Rochelle, "Effects of the Temperature Bulge in CO_2 Absorption From Flue Gas by Aqueous Monoethanolamine", Ind. Eng. Chem. Res., 47 (3), 867-876, 2008.

Lepaumier, Helene, D. Picq and P.L. Carrette, "Degradation Study of new solvents for CO_2 capture in post-combustion, Energy Procedia, 1, 893-900, 2009.

Polderman, L.D., C.P. Dillon, and A.B. Steele, "Why M.E.A. Solution Breaks Down in Gas-Treating Service", The Oil and Gas Journal, May 16, 1955.

Rochelle, Gary T., Fayette Power Project Unit 3 Continuous Emissions Monitors (CEMS), June 2008, e-mail correspondence from LCRA, Sept. 17, 2008.

Rochelle, Gary T. and S. Bichnoi, S. Chi, H. Dang and J. Santos, "Research Needs for CO_2 Capture from Flue Gas by Aqueous Absorption/Stripping", Final Report for P.O. No. DE-AF26-99FT1029, U.S. Dept. of Energy, January 17, 2001.

Rooney, P.C., M.S. DuPart and T.R. Bacon, "Oxygen's role in alkanolamine degradation", Hydrocarbon Processing, 109-113, July 1998.

Sexton, Andrew, "Amine Oxidation in CO_2 Capture Processes", Ph.D. Dissertation, The University of Texas at Austin, December 2008.

Strazisar, Brian R., R.R. Anderson, and C.M. White, "Degradation Pathways for Monoethanolamine in a CO_2 Capture Facility", Energy & Fuels, Vol. 17, 1034-1039, 2003.

Oxidation and Thermal Degradation of Concentrated Piperazine

Abstract

Iron-catalyzed degradation of 8 m PZ is reduced with the addition of 100 mM Inhibitor A. PZ in the presence of iron loses 10% of the initial amine within 500 hours but A reduces this to effectively no loss. With 10 mM of A in the presence of stainless steel metals (Fe^{2+}, Cr^{3+}, Ni^{2+}), the loss of PZ was not reduced while fewer degradation products were produced

At 175 °C, 8 m PZ lost 71.5 and 73% over 15 weeks with 0.3 and 0.4 mol CO_2/mol alkalinity, respectively. This degradation produced large amounts of formate, total formate, and EDA. Total formate reached 560 and 690 mM while EDA reached 42 and 45 mM for the two loadings, respectively. The degradation in these experiments seen in the first 5 weeks matched the rate observed in previous experiments at this temperature. Despite the high rate of degradation observed in these two experiments, metal concentrations were low for Fe^{2+}, Cr^{3+}, and Ni^{2+}, all staying below 7 and 12 mM in the two experiments. Unique to these two experiments, Ni^{2+} was found in the highest concentration, not iron as is expected.

The behavior of 16 PZ derivatives was observed in the Cation IC-MS. Most of the amines, AcPZ, AEPZ, AMPZ, DFPZ, DMPZ, EDA, EPZ, FPZ, HEEDA, HEP, HEMP, MPZ, and TEDA, behaved as expected producing a single peak with the expected m/z ratio for that analyte. Doublet signals (m/z = 2*MW+1) were observed in 7 analytes as well. Three species, 2-Imidazolidone, 2-Methyl-2-Imidazoline, and 2,5-piperazindione, produced very weak signals without the expected m/z ratio. Cation IC-MS analysis of 11 oxidation and one thermal degradation sample was performed. In those where PZ degraded, namely OE2, OE4, and TE9, peaks of EDA and N-Formyl PZ were identified. Experiments with Inhibitor A both have the same unidentified peak that must be an adduct of A. ICP-OES will be used for metals analysis rather than AA because of ability to detect multiple metals in the same sample, reducing the volume of sample needed for analysis.

Introduction

Concentrated aqueous piperazine (PZ) is being investigated as a possible alternative to 30 wt % (or 7 m) MEA in absorber/stripper systems to remove CO_2 from coal-fired power plant flue gas. Preliminary investigations of PZ have shown numerous advantages over 7 m MEA (Freeman et al., 2009). PZ solutions have less oxidative and thermal degradation, as previously shown at concentrations of 5 and 8 m PZ (see previous quarterly reports). The kinetics of CO_2 absorption are faster in concentrated PZ (Cullinane and Rochelle, 2006; Dugas and Rochelle, 2009). The capacity of concentrated PZ is greater than that of MEA while the heat of absorption and volatilities are comparable (Freeman et al., 2009).

This quarter was focused on gathering experimental data in various areas related to the degradation of PZ. Four oxidation experiments were completed with iron and stainless steel-catalyzed degradation and the effect of Inhibitor A. Two thermal degradation experiments at 175 °C were completed and analyzed. Four new thermal experiments were started. Analysis of standards and experimental samples by Cation IC-MS was completed and analyzed. Finally, analyzing for metals concentration was done with both AA and ICP-OES and the results were compared.

Analytical Methods

Total Inorganic Carbon Analysis (TIC)

Quantification of CO_2 loading was performed using a total inorganic carbon analyzer. In this method, a sample is acidified with 30 wt % H_3PO_4 to release the CO_2 present in solution (Hilliard, 2008). The CO_2 is carried in the nitrogen carrier gas stream to the detector. PicoLog software was used to record the peaks produced from each sample. A calibration curve was prepared at the end of each analysis using a TIC standard mixture of K_2CO_3 and $KHCO_3$. The TIC method quantifies the CO_2, CO_3^{-2}, and HCO_3^- present in solution. These species are in equilibrium in the series of reactions shown below.

$$CO_3^{2-} + 2H^+ \leftrightarrow HCO_3^- + H^+ \leftrightarrow H_2CO_3 \leftrightarrow CO_2 + H_2O$$

Acidification of the sample shifts the equilibrium toward CO_2 which bubbles out of solution and is detected in the analyzer.

Acid pH Titration

Titration with 0.2 N H_2SO_4 was used to determine the concentration of amines in experimental samples. The automated Titrando apparatus (Metrohm AG, Herisau, Switzerland) was used for this method. A known mass of sample was diluted with water and the autotitration method was then used. The Titrando titrates the sample with acid while monitoring the pH. The equivalence points are recorded. The equivalence point around a pH of 3.9 corresponds to basic amine species in solution (Hilliard, 2008). The test is not sensitive to the type of amine, so if PZ has degraded to ethylenediamine (EDA), the titration test will detect the sum of contributions from the species.

Anion IC

The anion IC was used to determine the concentration of glycolate, acetate, formate, chloride, nitrite, sulfate, oxalate, and nitrate in experimental samples. A Dionex ICS-3000 instrument with AS15 IonPac column, 4-mm Anionic Self-Regenerating Suppressor (ASRS), carbonate removal device (CRD), and carbonate removal from eluent generation was used as previously described by Andrew Sexton using a linear KOH eluent concentration (Sexton, 2008). No major modifications have been made to the method in this quarter.

Cation IC

The cation IC was used to determine the concentration of PZ and ethylenediamine (EDA) in experimental samples. A Dionex ICS-2500 instrument with CS17 IonPac column with 4-mm Cationic Self-Regenerating Suppressor (CSRS) was used as previously described by Andrew Sexton with a linear increase of methanesulfonic acid (MSA) concentration in the eluent (Sexton, 2008). No major modifications have been made to the method in this quarter.

NaOH Treatment for Amides

An analytical test for the formation of amides was developed by Andrew Sexton and has been included in the results shown here. Experimental samples were treated with 5 N NaOH (in equal gravimetric amounts) and allowed to sit overnight. The anion IC analytical method was then used to quantify increases in the concentrations of analytes as compared to the original samples (Sexton, 2008). In most cases, the main increases were in the production of formate and oxalate following NaOH treatment.

The addition of strong base reverses the amide formation reaction that has occurred during the experiment. As an example, the formation of N-formylPZ is shown in Eq. 1 below:

$$\text{(PZ)} \qquad \text{(Formate)} \qquad \text{(N-formylPZ)} \tag{1}$$
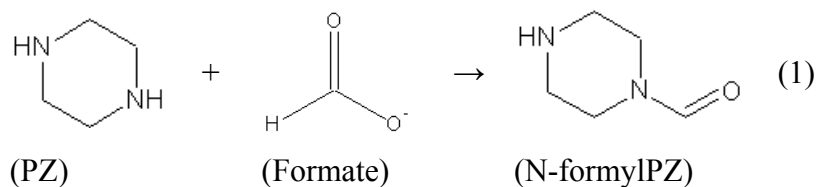
The addition of NaOH hydrolyzes the bond between the amine group and the carbon of the formyl group to reverse the reaction. In this way, the free formate created from reversing this reaction can be used to identify the formate bound as N-formylPZ. The same process can be used to identify the oxalate amine of PZ.

Inductively-Coupled Plasma Optical Emission Spectrometry (ICP-OES)

The concentration of multiple elements was measured using a Varian 710-ES Axial Inductively-Coupled Plasma Optical Emission Spectrometer (Varian Inc., Palo Alto, CA). The ICP-OES is effective for measuring the concentration of multiple analytes (heavy metals and other elements) simultaneously in a single dilution. The system is controlled through ICP Expert II Software. Samples are prepared by first making the desired dilution (10–1000X) and then adding 1% concentrated HNO_3. Each sample needs to be approximately 10 mL in volume and created in a plastic vial. An autosampler holds all the standards and samples to be run and each is pumped to the glass, concentric spray chamber, or nebulizer, where an argon stream nebulizes the sample and it is sent directly to the plasma flame. The molecules break down in the plasma into their

atoms and lose electrons, giving off optical wavelengths characteristic to each element. The emitted wavelengths are then sent to the solid state CCD detector. The plasma is created by electromagnetic induction, or time-varying magnetic fields, and creates energy that breaks down argon, the carrier or rarefield gas, into plasma. The plasma flame is stable and maintained at 7000 K.

For each element of interest, the four wavelengths with the highest intensity of absorption are measured and one argon wavelength as a background measurement. A separate calibration curve is made for each wavelength and the final concentration reported for each element is the average of the calibrated concentration of all four wavelengths. ICP-OES allows for quick analysis of multiple metals in solution which is especially useful for samples that corroded stainless steel (Fe, Cr, and Ni) or low gas flow experiments where multiple metals and tracers have been added (Fe, Cr, Ni, Cu, V, K, or Na).

Atomic Absorption Spectrophotometry (AA)

The concentration of individual heavy metals in solution has been measured using a Perkin Elmer 1100B flame atomic absorption spectrophotometer (AA). The AA uses a lamp producing a specific wavelength of light for each metal of interest. The AA also uses a flame fueled by acetylene with air added at either a rich or lean ratio. For iron and nickel, a lean (blue) flame is used that requires 2.5 L/min of acetylene with 8 L/min of air. Chromium requires a rich (yellow) flame with a higher acetylene-to-air ratio, so 4.0 L/min of acetylene was used. Samples analyzed for chromium also require the addition of 2% ammonium chloride (NH_4Cl) to suppress interference from iron and nickel. The AA atomizes the liquid sample and mixes it with fuel and air that is then sent to the flame. In the flame, the elements of interest are reduced to unexcited atoms which absorb the light at the characteristic wavelength of that metal. The absorbance of light is measured on the opposite end of the lamp to determine the amount of light absorbed by the analyte of interest. This is correlated to concentration using a set of known standards and a third order polynomial calibration curve.

Cation IC – Mass Spectrometry (MS)

Mass spectrometry (MS) with cation IC is used to help identify unknown peaks on cation IC chromatography or other unknown cations in solution. A thermal TSQ MS is attached to a Dionex ICS-2500 IC with an IonPac CS17 analytical column (4 x 250 mm), IonPac CG17 guard column (4 x 50 mm), Dionex AS-25 autosampler, and 4-mm CSRS is used as described above. The main modification is that the suppressor does not run in regeneration mode, the outlet analyte stream is sent to the MS and an additional water stream is added into the suppressor. After separation on the cation IC column, the sample stream enters the MS, which uses electrospray ionization (ESI) to ionize the molecules in solution. The ions then enter the mass analyzer of the MS which sorts ions based on their mass-to-charge ratio (m/z) using an electric field. The standard conditions used are a range of 50 to 300 m/z. There is a 2.2 minute delay in the resolution of the cation IC chromatogram and the MS spectrum that is taken into account when analyzing data.

4

Results and Discussion

Oxidative Degradation

An ongoing focus of this project is the oxidation of concentrated PZ solutions. The results listed in this section all relate to this topic and include a variety of work including low gas flow experiments, MS, and NMR work.

Reanalysis of OE9, OE10, OE11, and OE12 Samples

Last quarter, the results of four low gas flow experiments (OE9, OE10, OE11, and OE12) were reported. These experiments were blank experiments looking at PZ loss in the reactor without added metal catalysts and repeatability of the entire low gas flow procedure. OE9 and OE10 had an inlet gas with 98% N_2 and 2% CO_2 while OE11 and OE12 had 98% O_2 and 2% CO_2. These samples were reanalyzed on Anion and Cation IC because there were some discrepancies between the two pairs of experiments where the data should have been similar. After reanalyzing the data, it was found that the EDA data was incorrect in OE9 and OE11. In both experiments, the amount of EDA was less than first reported. The corrected data for OE9 and OE10 are shown in Figure 1. The new data for OE11 and OE12 are not shown because the EDA was just changed to zero, the other concentrations were not changed.
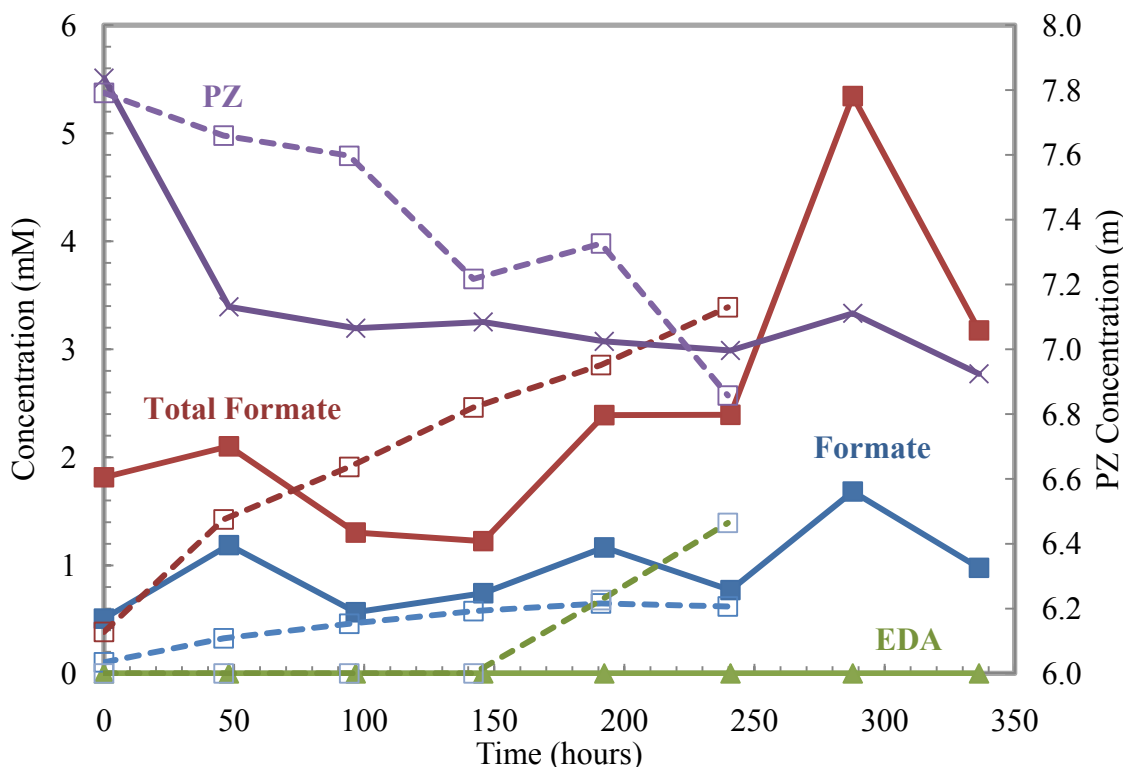
Figure 1: Comparison of OE9 and OE10 Concentration Profiles (Closed = OE9, Open = OE10)

EDA analysis is difficult because of the nature of cation IC analysis. A large dilution (5000 to 10000X) is required to get the PZ concentration low enough to detect with the conductivity detector. Since the amount of EDA is very small compared to the amount of PZ, at this low dilution the peak for EDA, if there is one, is very small. Manually trimming the peak can prove difficult because any small change in the area of the peak results in a large change in the concentration after the large dilution factor is applied.

New Oxidative Experiments

Four new oxidative experiments were completed this quarter. The important characteristics of these experiments are detailed in Table 1. The goal of these experiments was to obtain new baseline oxidation data for iron-catalyzed (OE13) and stainless steel-catalyzed (OE15) oxidation. The effect of Inhibitor A on these systems was also analyzed (OE14 and OE16) at the same time.

Table 1: Summary of Recent Oxidation Experiments

Expt	Solvent	Catalysts (mM)	Inhibitors (mM)	Length (hrs)
OE13	8 m PZ	$1.0\ Fe^{2+}$	-	523
OE14	8 m PZ	$1.0\ Fe^{2+}$	100 A	380
OE15	8 m PZ	$0.4\ Fe^{2+}, 0.1\ Cr^{3+}, 0.05\ Ni^{2+}$	-	427
OE16	8 m PZ	$0.4\ Fe^{2+}, 0.1\ Cr^{3+}, 0.05\ Ni^{2+}$	10 A	427

OE13 and OE14 were performed to establish a baseline degradation rate for iron-catalyzed degradation with and without Inhibitor A. The iron concentration for both experiments was 1.0 mM while 100 mM of A was used in OE14. The concentration profiles for PZ and the degradation for these experiments are shown in Figures 2 and 3 below. EDA concentrations were below detectable levels in both experiments. Overall, low concentrations of degradation products were produced, as with most PZ oxidation experiments, resulting in at most about 10 mM of anion degradation products.
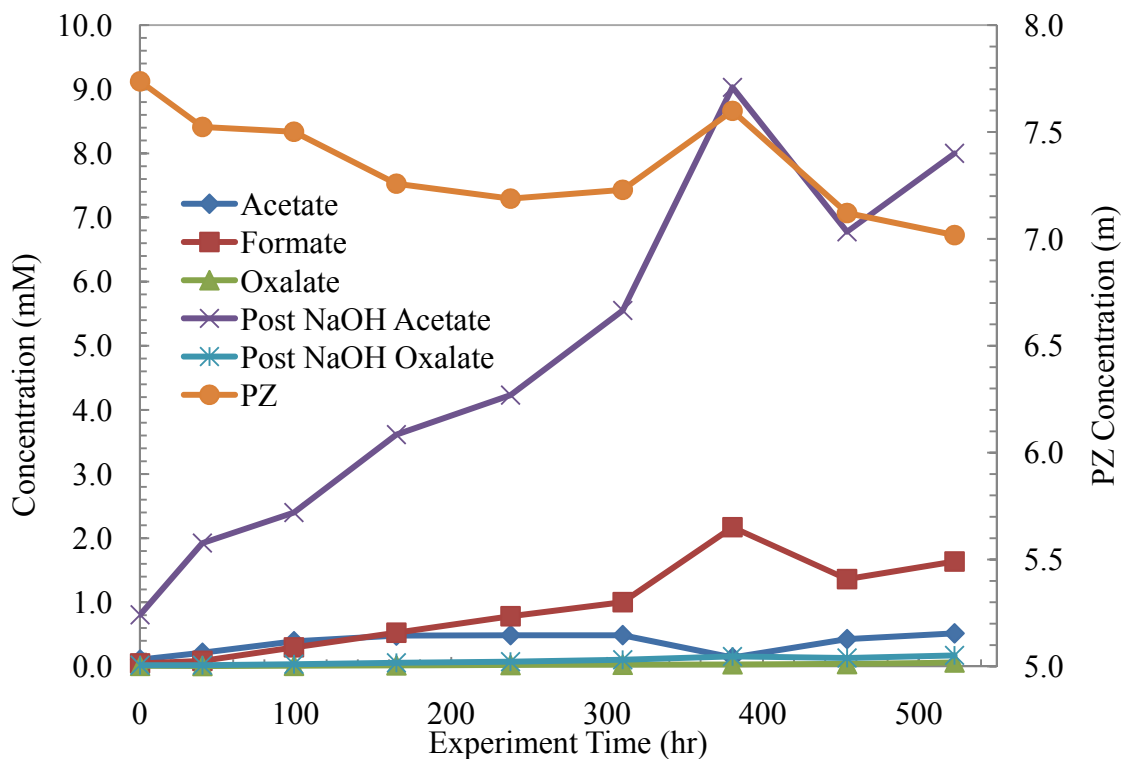
Figure 2: Concentration Profiles for PZ and Degradation Products for OE13 (8 m PZ, α=0.3, 55 °C, 1.0 mM Fe^{2+})
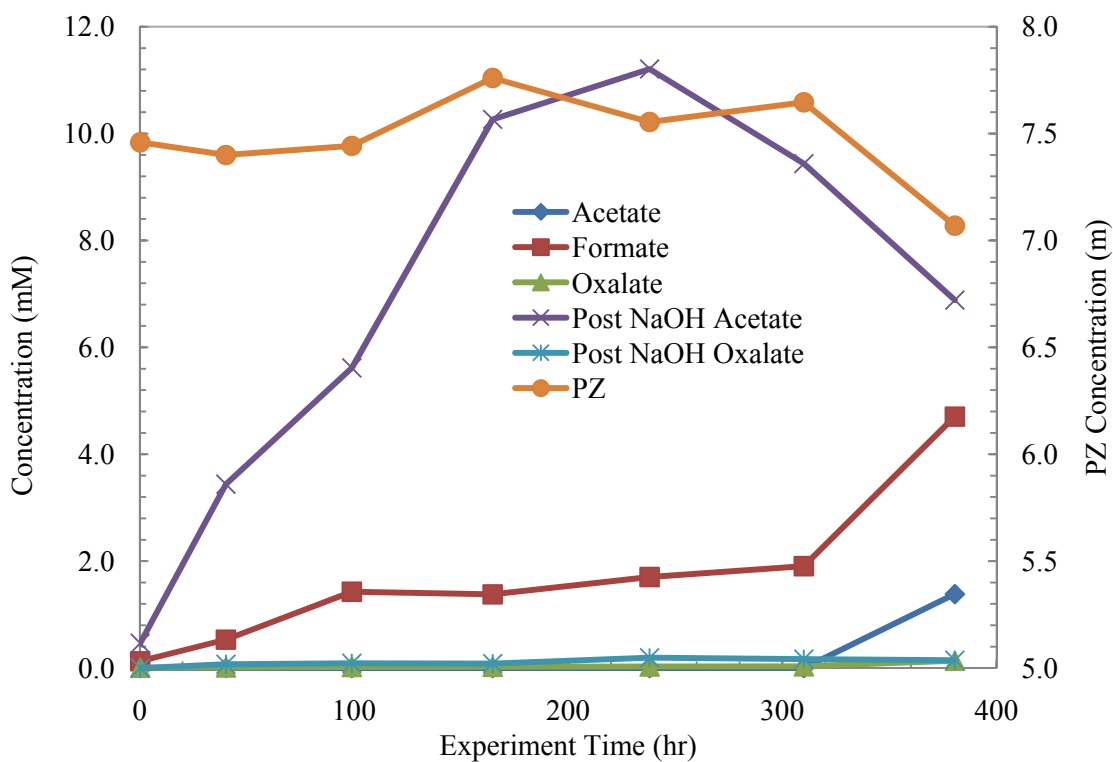
Figure 3: Concentration profiles for PZ and Degradation Products for OE14 (8 m PZ, α=0.3, 55 °C, 1.0 mM Fe^{2+}, 100 mM A)

One part of the analytical protocol was changed for these experiments. The NaOH treatment normally performed to determine the amine of amides in solution was modified to use more 5 N NaOH. The usual protocol calls for 1 g NaOH solution per 1 g sample while these samples were treated with 4 g NaOH solution per 1 g sample. This change was made based on the analysis of NMR data of OE5B that indicated that NaOH treated samples (using the original protocol) still have some protonated piperazine functionalities. It was believed that additional NaOH may be needed to fully basify the solution and convert all PZ species to PZ alone or PZ mono- or di-carbamate.

This new NaOH treatment changed the profile of amides produced. Surprisingly, this treatment removed any trace of formate in the treated samples. Any formate detected in the original sample was not found in the treated sample. Also, the level of acetate increased dramatically, reaching close to 10 mM in both experiments. Significantly increased levels of acetate after NaOH treatment have not been observed to date and this must be due to the change in the NaOH protocol. Possible N-acetyl amides include Acetamide and N-acetylpiperazine, shown below. N-acetylethylenediamine, would also be a possible species, but no EDA was found in these experiments. These species have not been confirmed, but are the most likely since PZ has the most prevalent amino groups for an amide formation reaction.
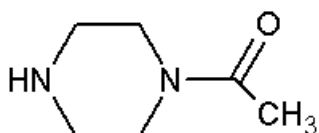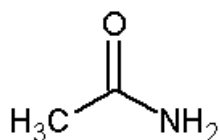
N-Acetylpiperazine   Acetamide

In these two experiments, it is also apparent that something went wrong at the time point of 380 hours. In both experiments, the data at this point deviate from the trends before it. In OE13, it is the data point third from the end and is the point where formate, total acetate, and PZ spike upward and acetate spikes downward. In OE14, this point is the final point were formate and acetate spike upward and PZ spikes downward.

OE15 and OE16 were performed to analyze the stainless steel-catalyzed degradation of 8 m PZ with and without Inhibitor A. Both experiments had 0.4 mM Fe^{2+}, 0.1 mM Cr^{2+}, 0.05 mM Ni^{2+} while OE16 had 10 mM of Inhibitor A. The concentration profiles of both experiments are shown in Figures 4 and 5 below. Overall, very little degradation was observed with the maximum degradation products found being up to 8 mM in total. No EDA was detected in either experiment.
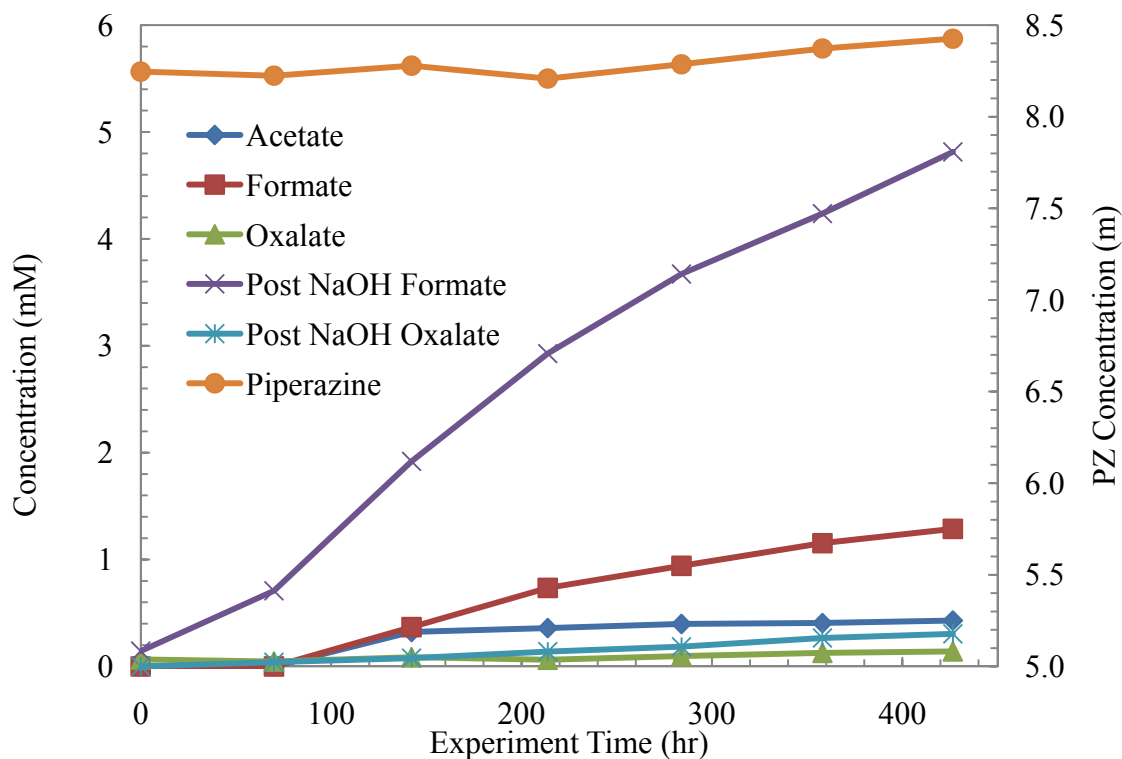
Figure 4: Concentration profiles for PZ and Degradation Products for OE15 (8 m PZ, α=0.3, 55 °C, 0.4 mM Fe^{2+}, 0.1 mM Cr^{3+}, 0.05 mM Ni^{2+})
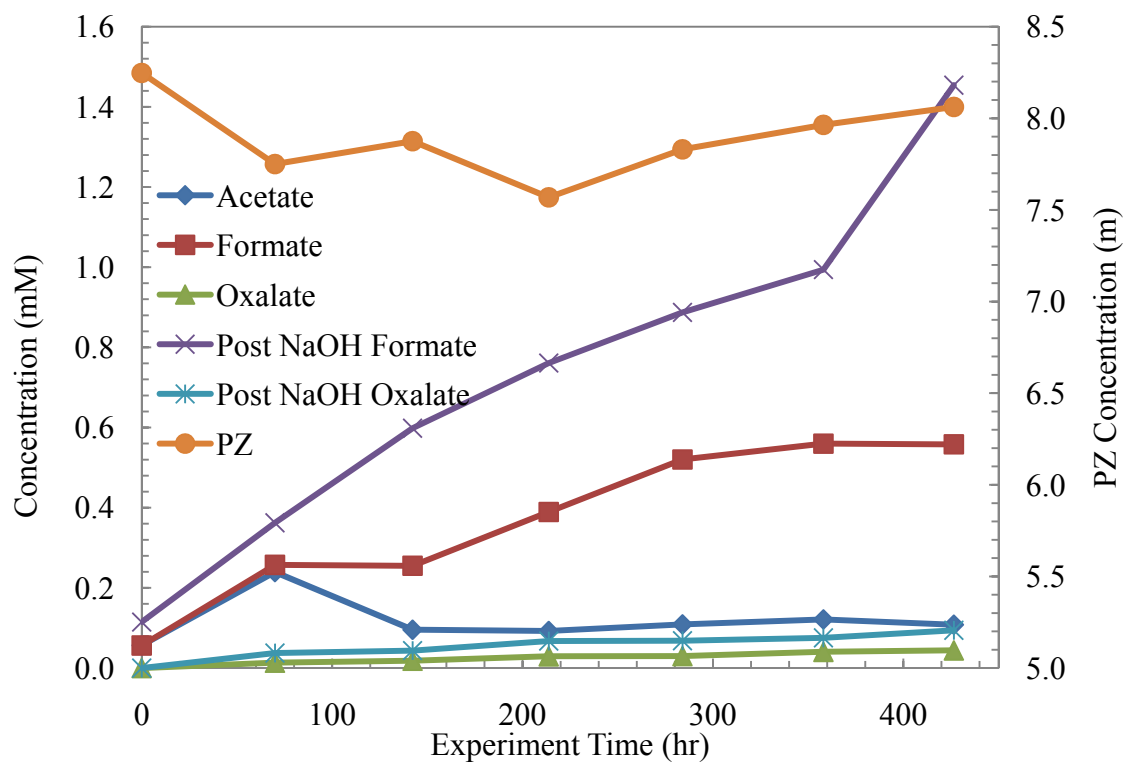
Figure 5: Concentration profiles for PZ and Degradation Products for OE16 (8 m PZ, α=0.3, 55 °C, 0.4 mM Fe^{2+}, 0.1 mM Cr^{3+}, 0.05 mM Ni^{2+}, 10 mM A)

9

A comparison between the two experiments demonstrates the effect of 10 mM of A. The PZ, formate, post-NaOH formate, and acetate concentrations are shown for both OE15 and OE16 in Figure 6 below.
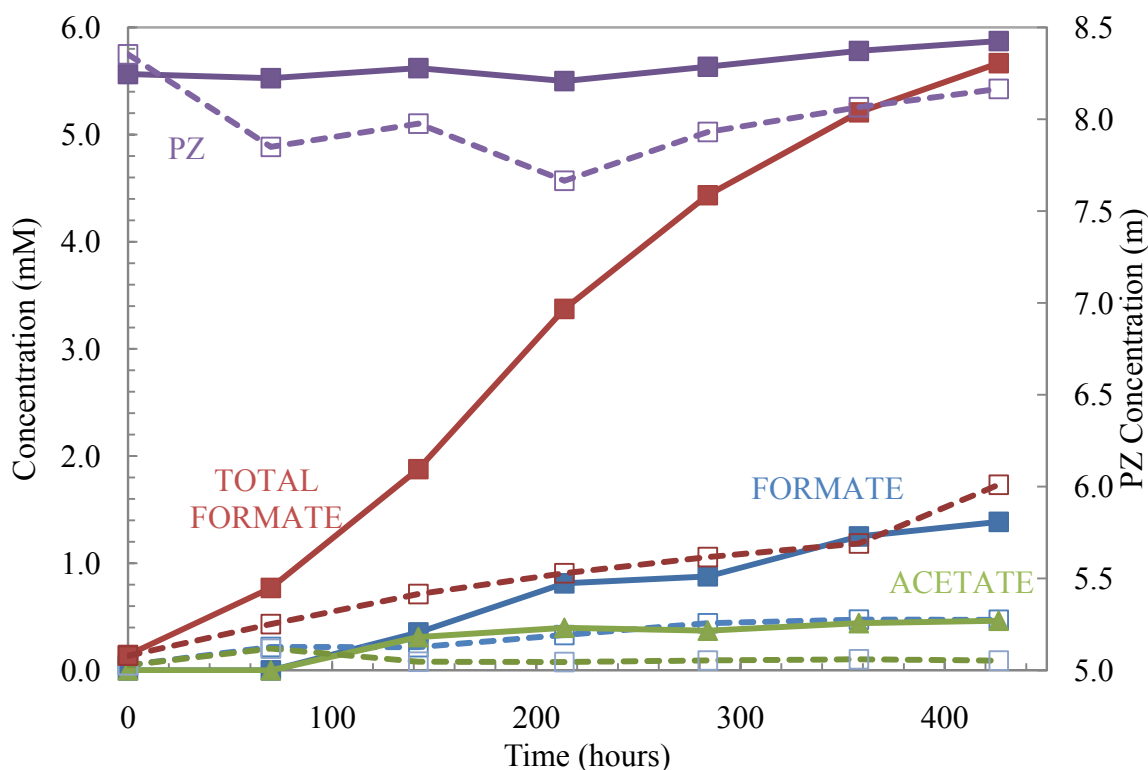
Figure 6: Comparison of OE15 and OE16 Concentration Profiles (Closed = OE15, Open =

There is not a very large difference between the two experiments. In OE15, more degradation products were formed, both formate and acetate, than OE16 but the levels overall are very low, only reaching 6 mM. For the PZ, the experiment without A (OE15) actually gained in concentration while the experiment with A went down and came back up to rest near the initial value. The PZ data itself are not conclusive since there was so little degradation that fluctuations in this data can easily occur due to water balance issues or small errors in the analytical procedure. At face value though, the effect was the opposite of what was expected where the A OE16)would reduce the loss of PZ. The degradation product data indicate that only 10 mM of A is enough to reduce the amount of formate and acetate produced during 450 hours of degradation.

Thermal Degradation

Two thermal degradation experiments ended this quarter (TE12 and TE13), four continued through the quarter (TE10, TE11, TE14 and TE15), and four new experiments were started (TE16, TE17, TE18, and TE19). A summary of the current and recently ended experiments is shown below in Table 2.

Table 2: Summary of Current Thermal Degradation Experiments

Expt	Solution	Loading (mol CO₂/mol alk)	Temperature (°C)	Duration (weeks)	Expected End Date
TE10	8 m PZ	0.3	135	72	Oct 2010
TE11	8 m PZ	0.4	135	72	Oct 2010
TE12	8 m PZ	0.3	175	12	Aug 2009
TE13	8 m PZ	0.4	175	12	Aug 2009
TE14	8 m PZ	0.3	150	30	Jan 2010
TE15	8 m PZ	0.4	150	30	Jan 2010
TE16		----------	Proprietary	----------	
TE17		----------	Proprietary	----------	
TE18	8 m PZ	0.3	175	6	Oct 2009
TE19	8 m PZ	0.4	175	6	Oct 2009

Experiments TE12 and TE13 were conducted to determine the behavior of 8 m PZ at 175 °C at two loadings, 0.3 and 0.4 mol/mol alkalinity. There was a greater amount of degradation found in both experiments, significantly more than at lower temperatures and in oxidation experiments. The concentration profiles for degradation products and PZ are shown below in Figures 7 and 8 for TE12 and TE13, respectively.
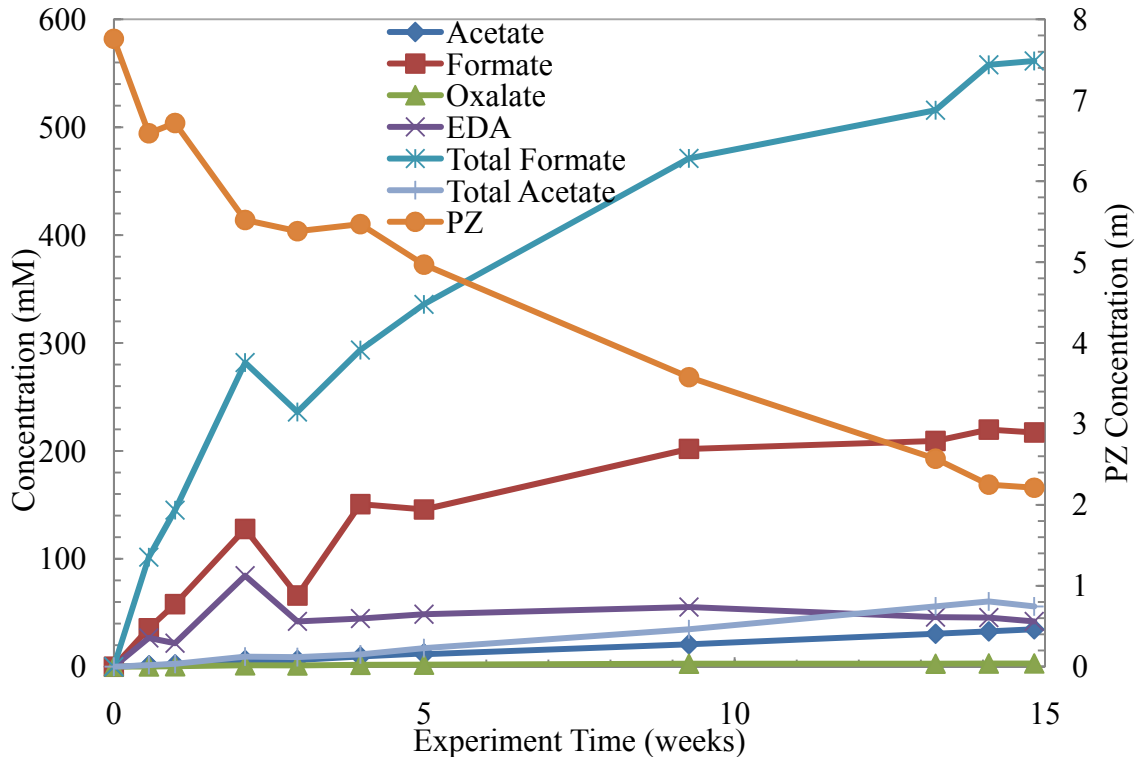
Figure 7: Concentration profiles for PZ and Degradation Products for TE12 (8 m PZ, α=0.3, 150 °C)
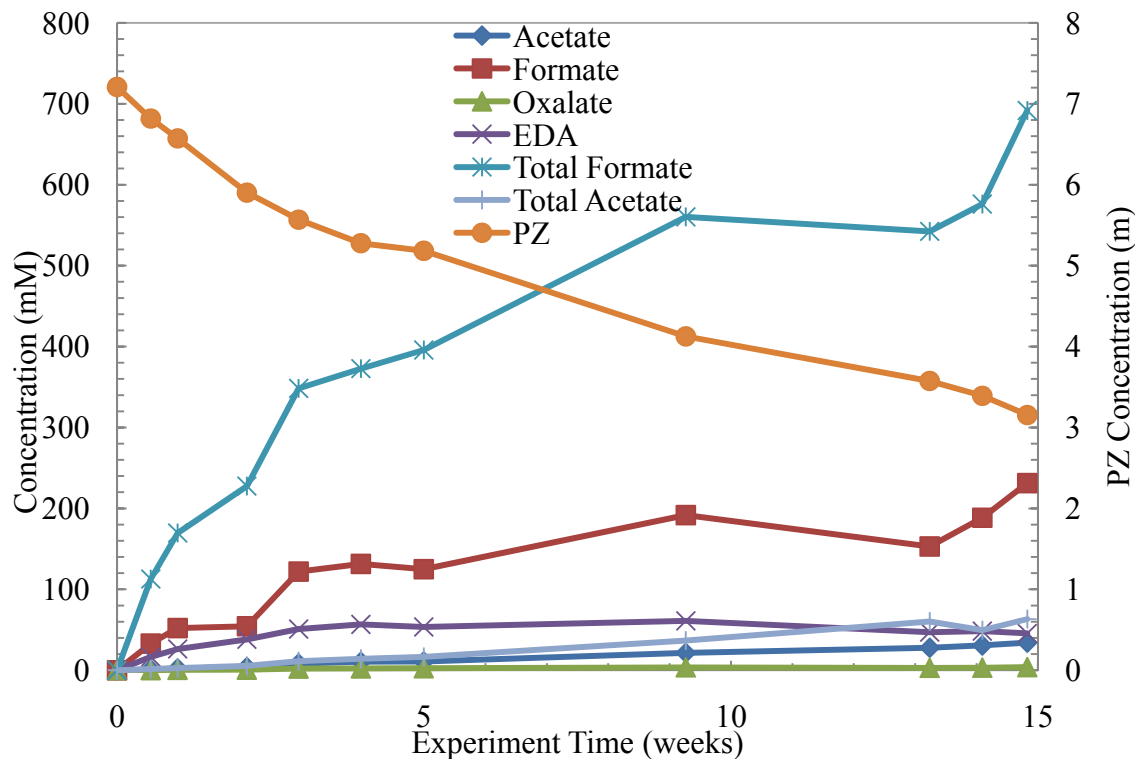
Figure 8: Concentration profiles for PZ and Degradation Products for TE13 (8 m PZ, α=0.4, 150 °C)

Overall, TE12 lost 71.5% of the initial PZ and TE13 lost 73% of the initial PZ. This is the most degradation observed to date in either oxidation or thermal degradation. The effect of loading on thermal degradation and the production of degradation products at this temperature appear to be minimal. Both experiments produced larger concentrations of formate, total formate, EDA, acetate, and total acetate. The loss of PZ in these experiments is similar to 4 previous short term experiments completed at 175 °C. TE5, TE5, TE6, and TE8 all looked at 8 m PZ with a loading of 0.3 mol/mol alkalinity at 175 °C. TE4 was a neat PZ solution while TE5, TE6, and TE8 each had a different additive. The additives for those three experiments, respectively, were: 0.1 mM Fe^{2+} + 5.0 mM Cu^{2+}, 0.1 mM Fe^{2+} + 5.0 mM Cu^{2+} + 100 mM A, and 0.1 mM Fe^{2+} + 0.6 mM Cr^{3+} + 0.1 mM Ni^{2+}. The loss of PZ as a fraction of the initial PZ is shown for these four experiments and the two recently completed long term 175 °C experiments, TE12 and TE13, in Figure 9 below.
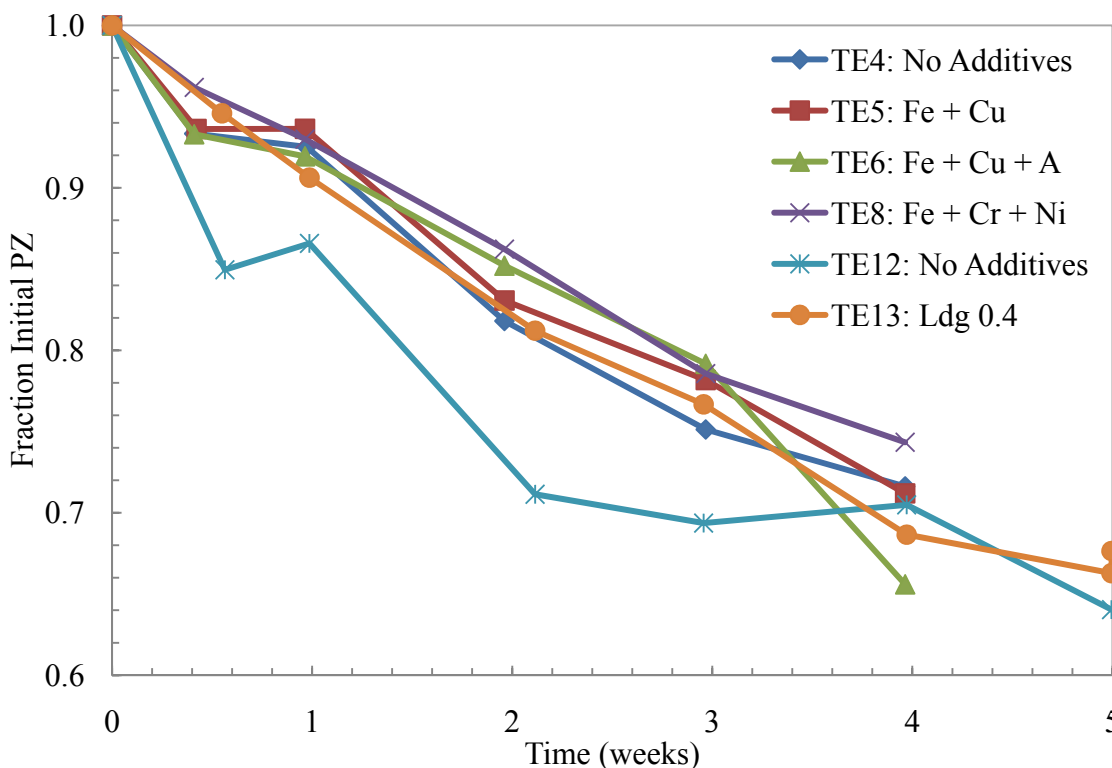
Figure 9: Comparison of PZ Loss of 8 m PZ at 175 °C (all α=0.3 mol/mol alkalinity, except TE13 which is α=0.4)

In the above figure, all six experiments track very similarly considering the various conditions. The first four experiments contained additives that did not affect the overall loss of PZ. This conclusion was reached with just analyzing these four experiments (Rochelle, 2008). The new data at 175 °C confirm earlier conclusions and match the overall loss of PZ observed. Unfortunately, the TE12 data at a loading of 0.3 mol/mol alkalinity doesn't match quite as close as the TE13 data that was at a loading of 0.4 mol/mol alkalinity. TE4 and TE12 are essentially repeats of each other, although the TE12 data extends to 15 weeks. All of TE4 through TE8 were at a loading of 0.3 mol/mol alkalinity, so the TE12 and TE13 results appear to be opposite of what was expected. The CO_2 loading appears, therefore, to have a minimal effect on overall PZ loss. This is not expected and contrary to the conclusions of Jason Davis' thesis. Davis saw a noticeable reduction in degradation at lower initial CO_2 loadings (Davis, 2009). To analyze PZ thermal degradation from another angle, the degradation experienced in TE12 is compared to that in OE2, an oxidation experiment with 10 m PZ and 4.0 mM Cu2+. Both of these experiments represent the most degradation observed with concentrated PZ via each pathway (temperature or oxygen). The loss of PZ and the concentration profiles for formate, total formate and EDA are shown below for the two experiments in Figure 10.
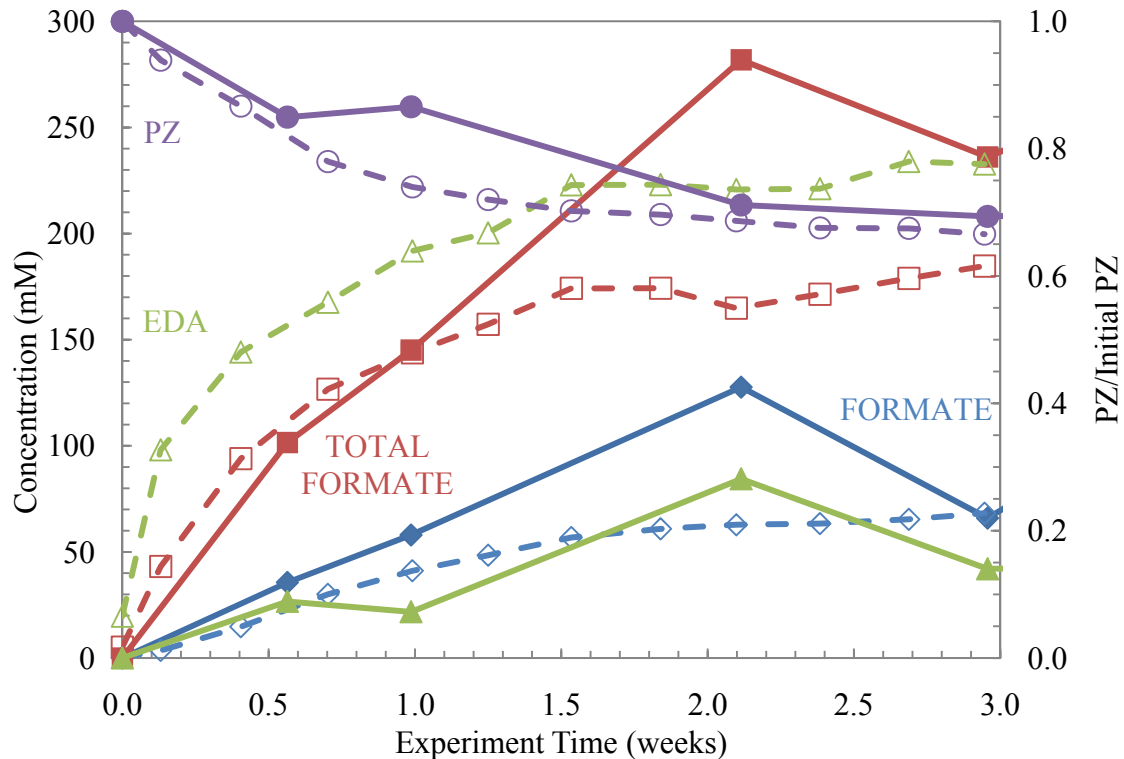
Figure 10: Comparison of Thermal Degradation and Oxidation of Concentrated PZ (Closed = Thermal Degradation at 175 °C, Open Points = Oxidation with 4.0 mM Cu²⁺)

The loss of PZ between these two experiments is very similar – about 30% of the initial amine after 3 weeks. Also, the concentration profiles for formate and total formate are surprisingly similar given the very different degradation conditions experienced in each experiment. The mechanisms for loss are assumed to be different between the two processes but I think this comparison is still interesting in that the same degradation is being done to PZ with both similar (formate) and different results (EDA). This points decisively to different mechanisms for degradation, as expected, but also allows a general comparison of how each process can contribute to overall solvent degradation in an industrial system.

Metals Analysis of Thermal Degradation Experiments

Last quarter, the concentration of metals in solution was first discussed and initial results were reported. Among those were data for 8 m PZ thermally degraded at 150 °C (TE9). At the time, AA was used to measure iron and nickel concentrations. Since then, the same samples have been reanalyzed with ICP-OES to include analysis for chromium. The difference between AA and ICP-OES is discussed below. The new concentrations for iron, chromium, and nickel are reported for TE9 in Figure 11 as measured by ICP-OES.
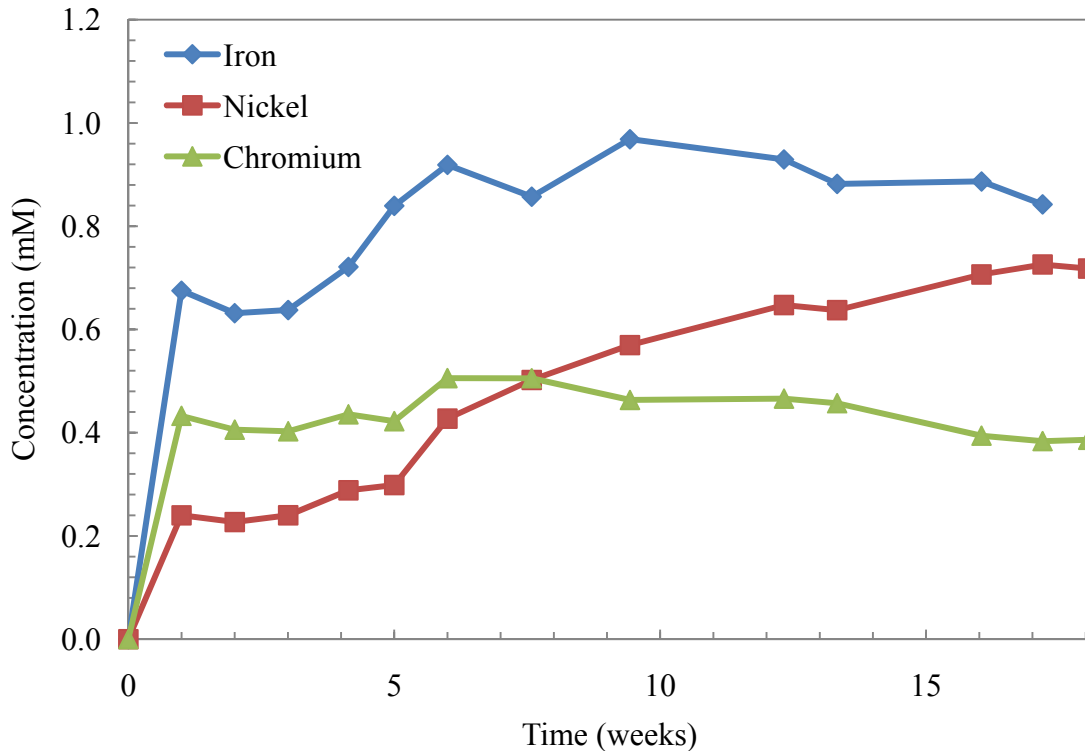
Figure 11: Concentration profiles for Iron, Chromium, and Nickel in TE9 (8 m PZ, α=0.3, 150 °C) Analyzed by ICP-OES

The iron and nickel concentrations are very similar to those reported last quarter from AA analysis. The concentration of iron at week 18 is 0.84 mM with ICP-OES and was reported as 0.9 mM last quarter with AA. The concentration of nickel at week 18 is 0.72 mM with ICP-OES and was reported as 0.7 mM last quarter with AA. The chromium concentration is lower than the iron, and starts lower than nickel but ends up larger at 18 weeks. Overall, the concentration of the three metals is very close with all of them only reaching a maximum concentration between 0.5 mM and 1.0 mM. These results reinforce the conclusions made last quarter that the amount of metal found in thermally degraded PZ samples is much lower than in 7 m MEA samples.

The concentration of stainless steel metals (iron, chromium, and nickel) was analyzed in both TE12 and TE13. Both of these experiments were 15 weeks in length and at 175 °C. At this high temperature, 71.5 and 73% of the PZ was lost in each experiment, respectively. The concentration profiles for iron, nickel, and chromium are shown below in Figures 12 and 13 for TE12 and TE13.
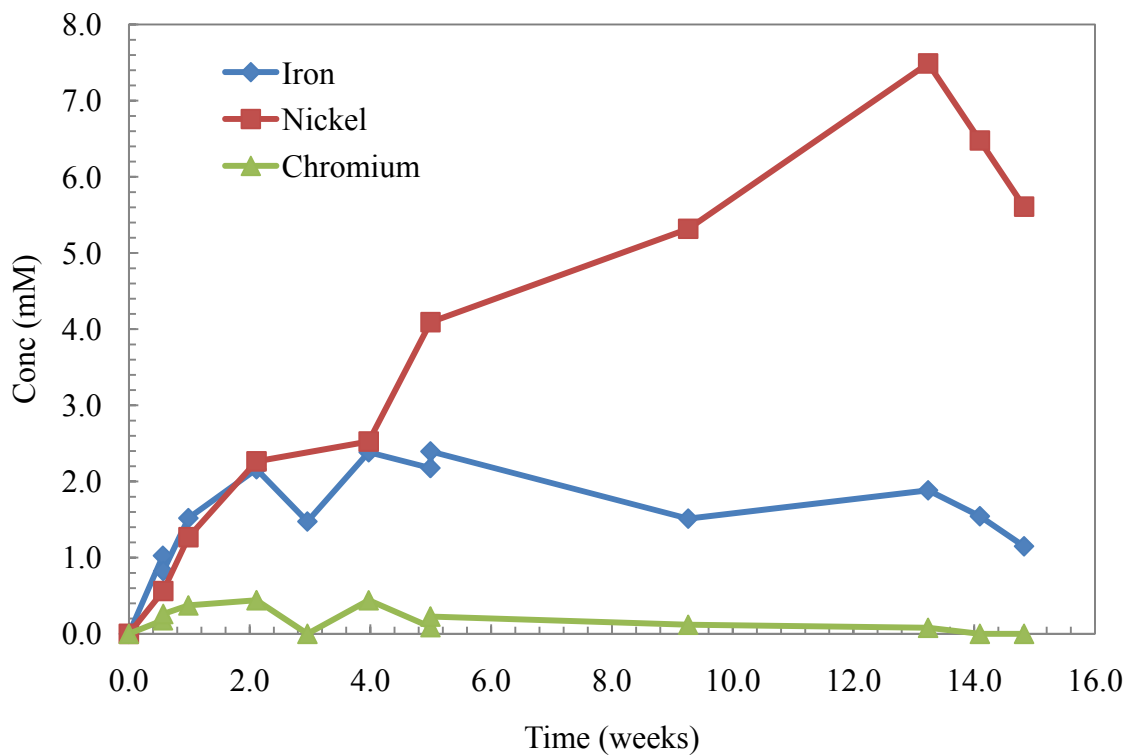
Figure 12: Concentration profiles for Iron, Chromium, and Nickel in TE12 (8 m PZ, α=0.3, 150 °C) Analyzed by ICP-OES
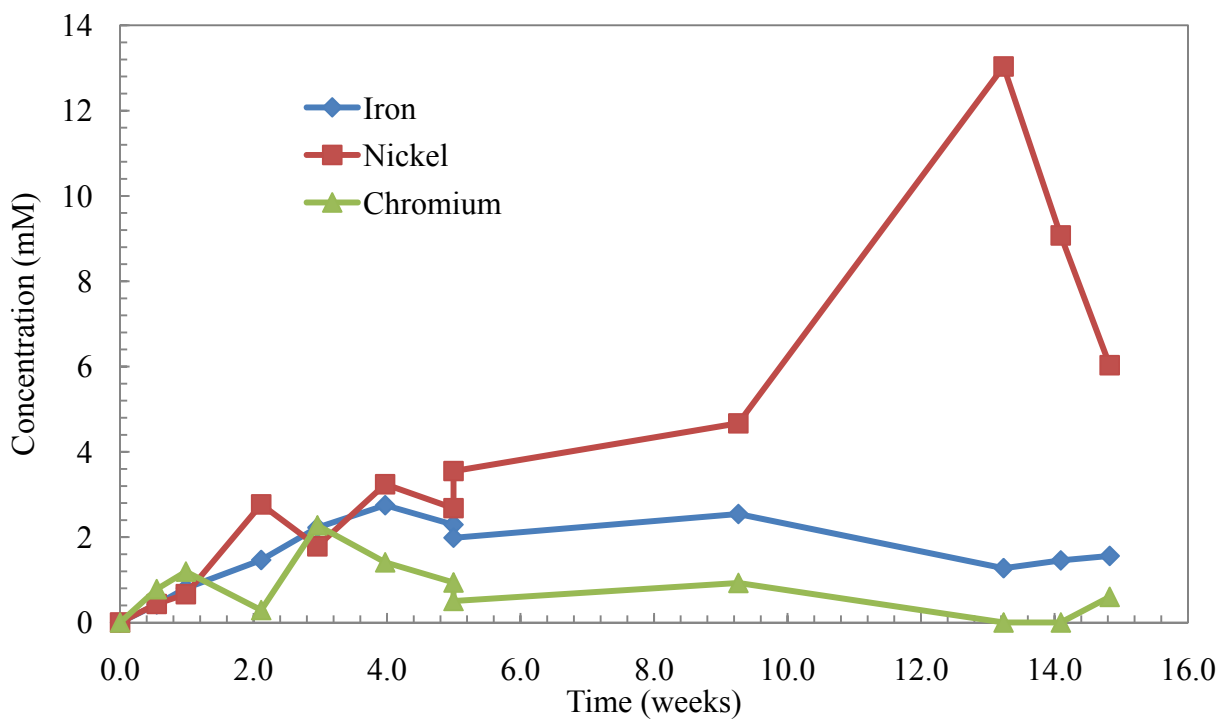
Figure 13: Concentration profiles for Iron, Chromium, and Nickel in TE13 (8 m PZ, α=0.4, 150 °C) Analyzed by ICP-OES

In both experiments, the metal present in the highest concetration was nickel. This was unexpected and contrary to previously presented results for TE9. The composition of 316 stainless steel is such that on a mass basis, the expected concentrations of iron, chromium, and nickel are 10:2.5:2. Given that they have very similar molecular weights, the trends in mM should follow. The results for TE9 made more sense in that at least iron was the most prevalent metal followed by chromium and nickel at similar concentrations. It is not clear at this point if the temperature alone caused such a high nickel concentration. Between TE9 and TE12, the only difference was an increase in temperature from 150 to 175 °C as both solutions were 8 m PZ with a loading of 0.3 mol/mol alkalinity.
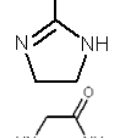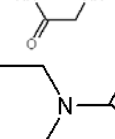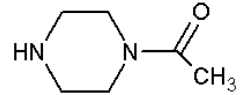
Mass Spectrometry (MS) for Identification of Unknown Compounds

Standards of PZ Derivatives

PZ derivatives that are suspected degradation products were analyzed this quarter using Cation IC-MS. IC-MS was used to identify where the compounds would show up on the chromatogram and what mass-to-charge (m/z) ratios would be shown for each compound. It is expected that each compound would acquire one proton making its m/z equal to the molecular weight plus one. However, it is possible that each molecule could behave differently than expected. For example, two molecules can attach to the same charge (m/z = 2*MW + 1) or a molecule can attach to potassium or sodium ion in the system (m/z = MW + 23 or 40).

The compounds tested are shown below in Table 3. The molecular weight and expected m/z for each compound is shown as well as its chemical structure. The Cation IC-MS chromatograms for a 1000 ppm solution of each species are shown in Figures 14 through 29. In each figure, the top panel is the total MS signal over the course of the chromatographic separation. The bottom panel is the Cation IC chromatogram total conductivity signal. The panels are aligned so that they correspond in time.

Table 3: Summary of PZ Derivatives Analyzed by Cation IC-MS

Compound	Abbr	MW (g/mol)	Expected m/z	Chemical Structure
2-Imidazolidone	-	86.1	87.1	
2-Methyl-2-imidazoline	-	84.1	85.1	
2,5-piperazindione	-	114.1	115.1	
N-Acetyl PZ	AcPZ	128.2	129.2	
N-(2-Aminoethyl) PZ	AEPZ	129.2	130.2	

Compound	Abbr	MW (g/mol)	Expected m/z	Chemical Structure
N-Amino-N'-Methyl-PZ	AMPZ	115.2	116.2	
N,N'-Diformyl PZ	DFPZ	142.2	143.2	
N,N'-Dimethyl PZ	DMPZ	114.2	115.2	
Ethylenediamine	EDA	60.1	61.1	
N-Ethyl PZ	EPZ	114.2	115.2	
N-Formyl PZ	FPZ	114.2	115.2	
N-(2-Hydroxyethyl) EDA	HEEDA	104.2	105.2	
N-Hydroxyethyl PZ	HEP	130.2	131.2	
N-(2-Hydroxyethyl)-N'-Methyl PZ	HEMP	144.2	145.2	
N-Methyl PZ	MPZ	100.2	101.2	
Triethylenediamine	TEDA	112.2	113.2	
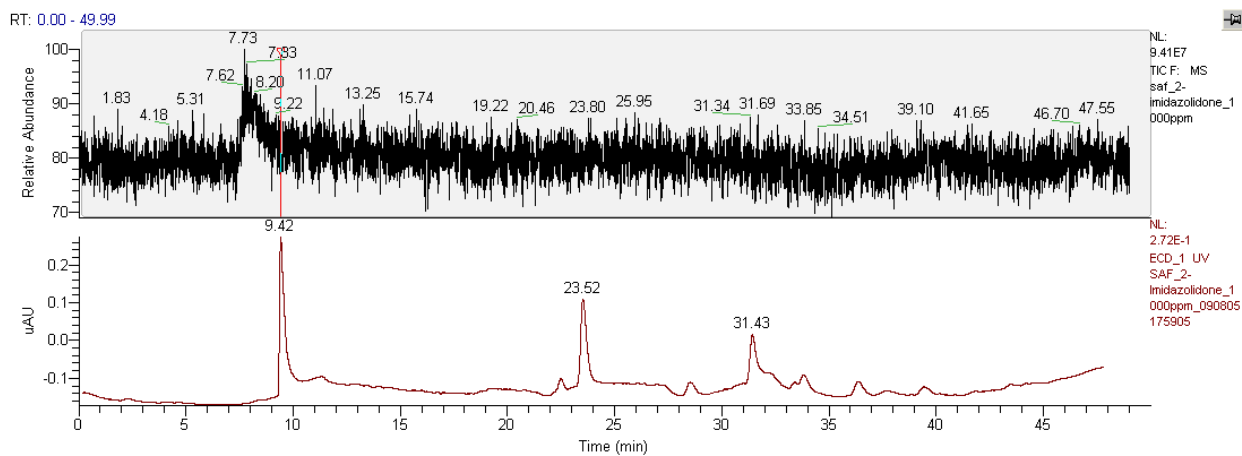
Figure 14: Cation IC-MS Chromatogram for 1000 ppm 2-Imidazolidone

18
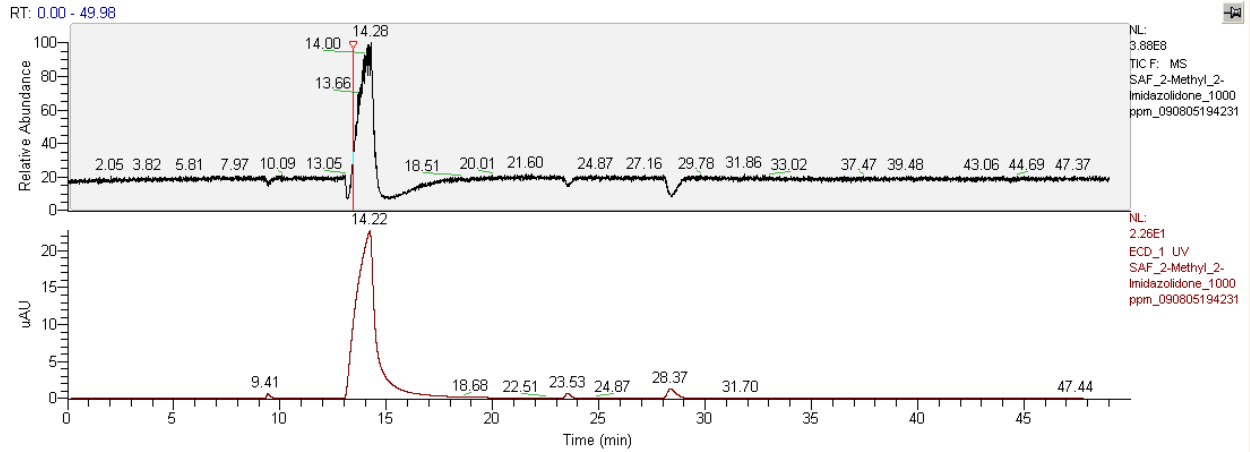
Figure 15: Cation IC-MS Chromatogram for 1000 ppm 2-Methyl-2-Imidazoline
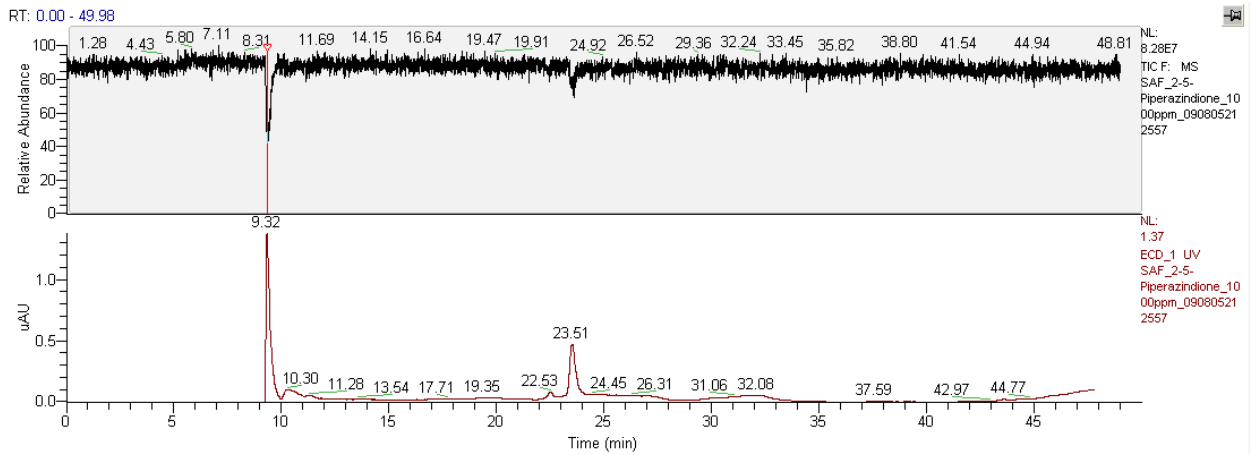
Figure 16: Cation IC-MS Chromatogram for 1000 ppm 2,5-Piperazindione
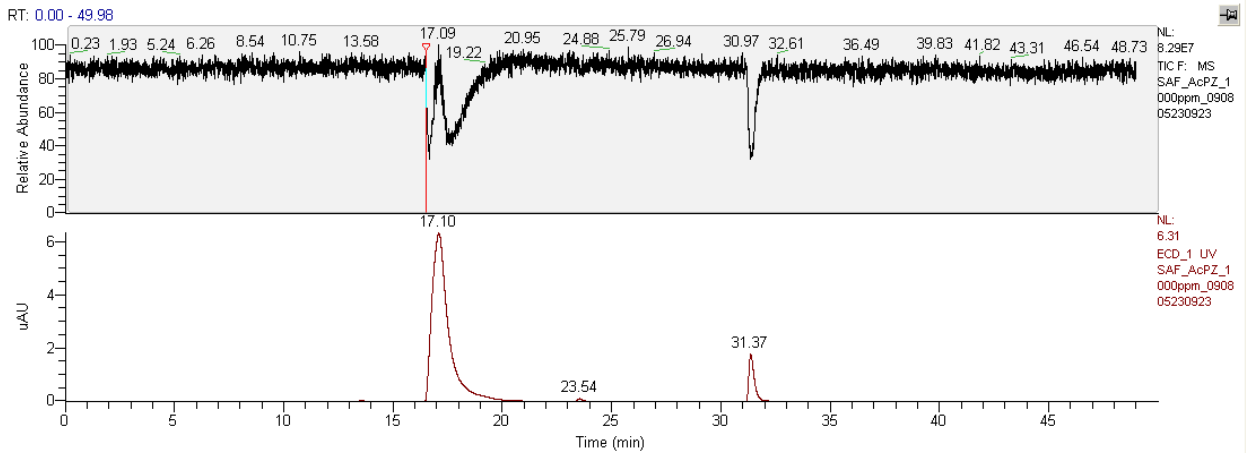
Figure 17: Cation IC-MS Chromatogram for 1000 ppm N-Acetyl PZ (AcPZ)
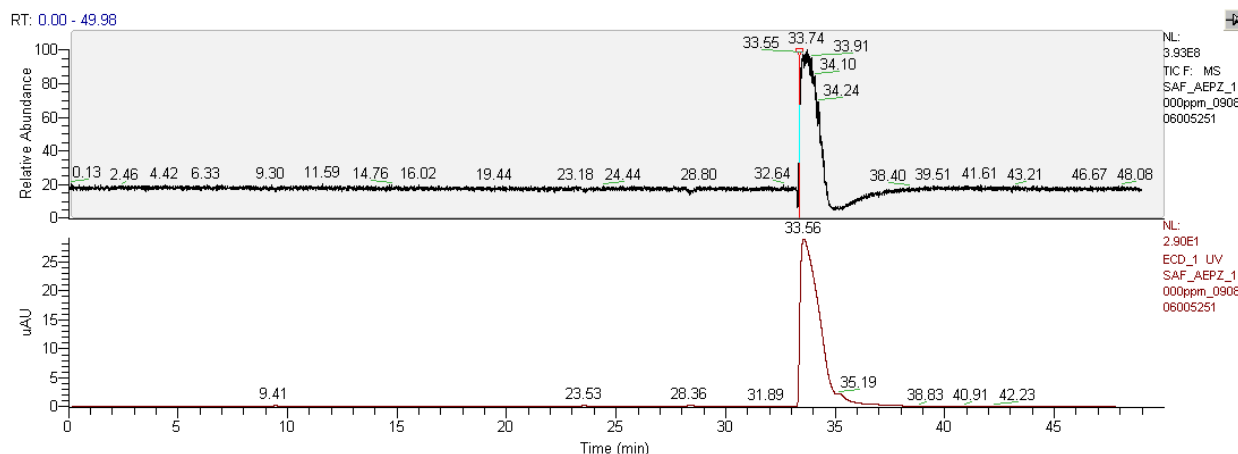
Figure 18: Cation IC-MS Chromatogram for 1000 ppm N-(2-Aminoethyl) PZ (AEPZ)
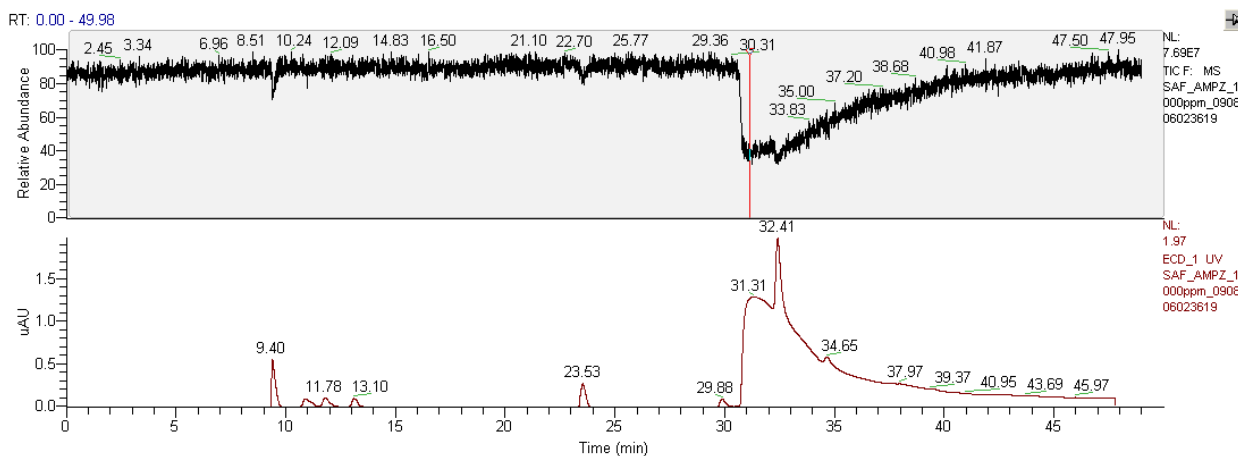
Figure 19: Cation IC-MS Chromatogram for 1000 ppm N-Amino-N'-methyl PZ (AMPZ)
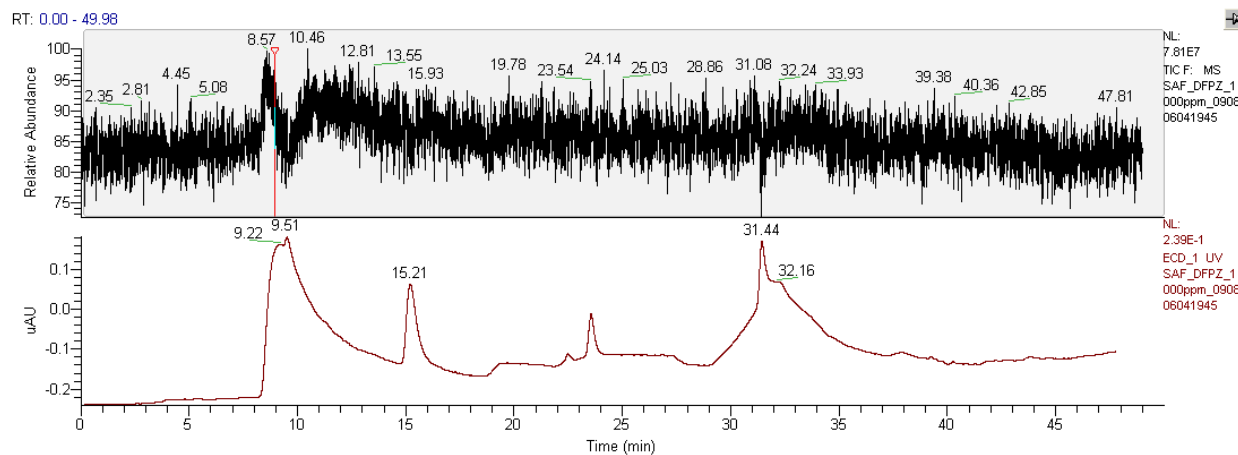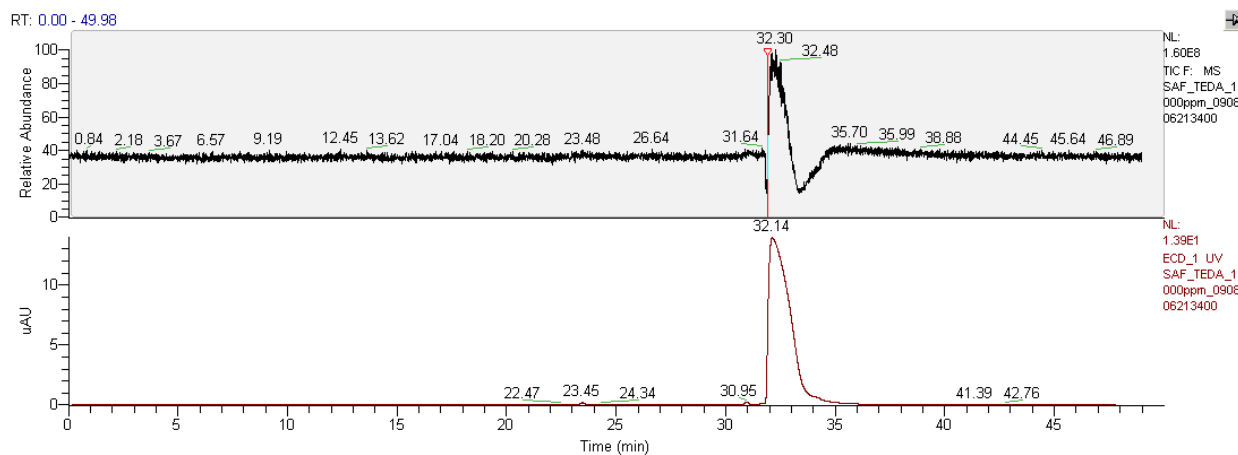

Figure 20: Cation IC-MS Chromatogram for 1000 ppm N,N'-Diformyl PZ (DFPZ)
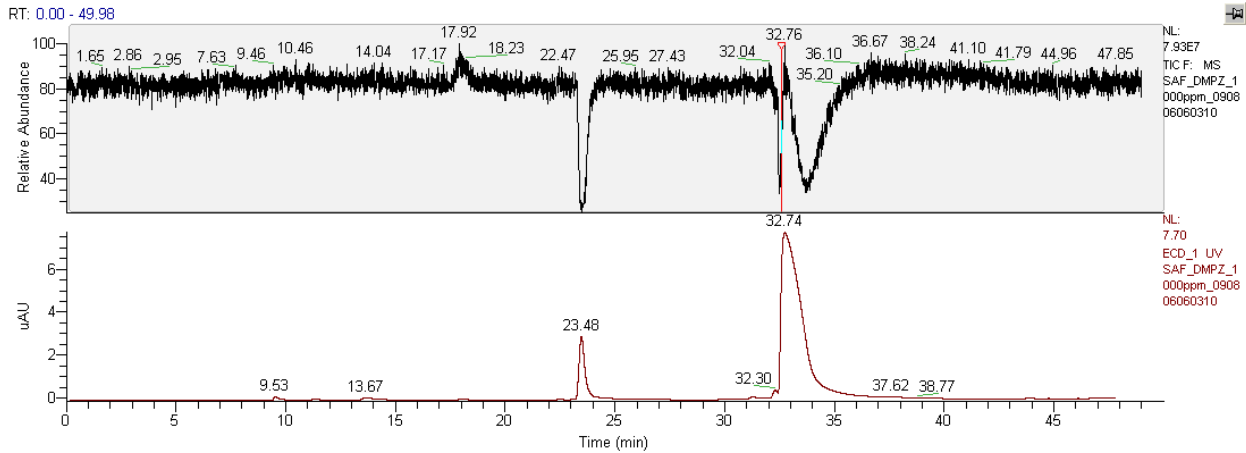
Figure 21: Cation IC-MS Chromatogram for 1000 ppm N,N'-Dimethyl PZ (DMPZ)
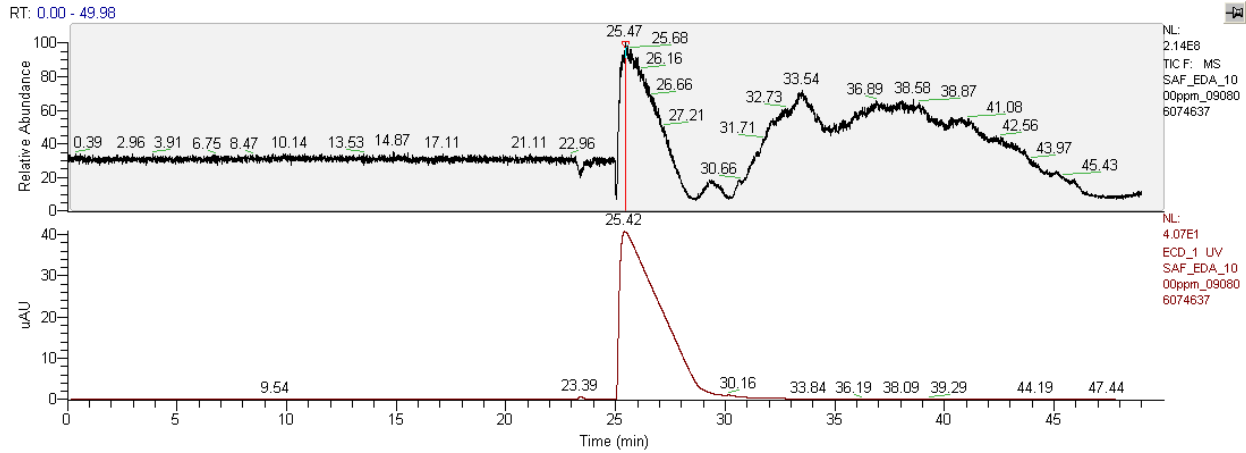
Figure 22: Cation IC-MS Chromatogram for 1000 ppm EDA
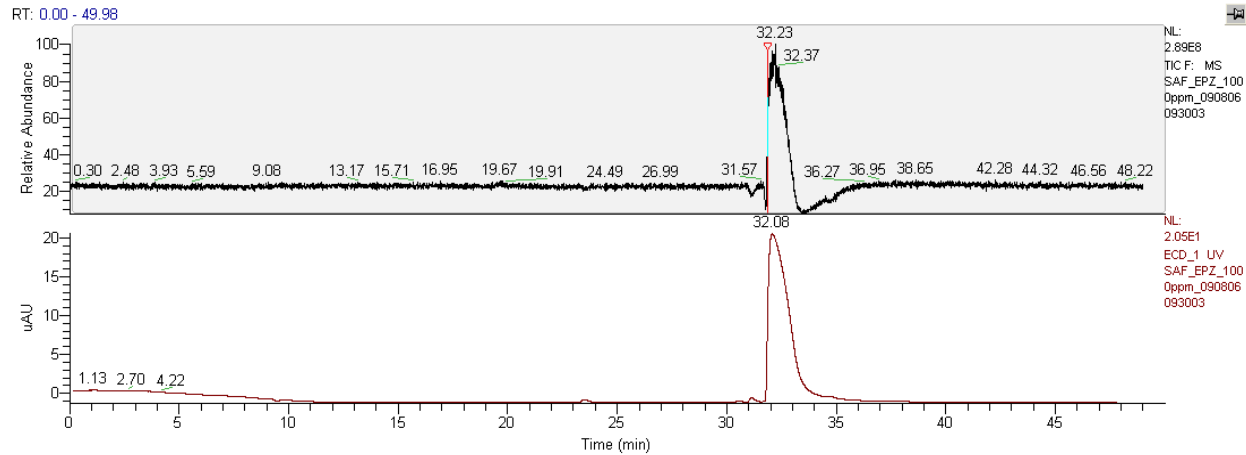
Figure 23: Cation IC-MS Chromatogram for 1000 ppm N-Ethyl PZ (EPZ)
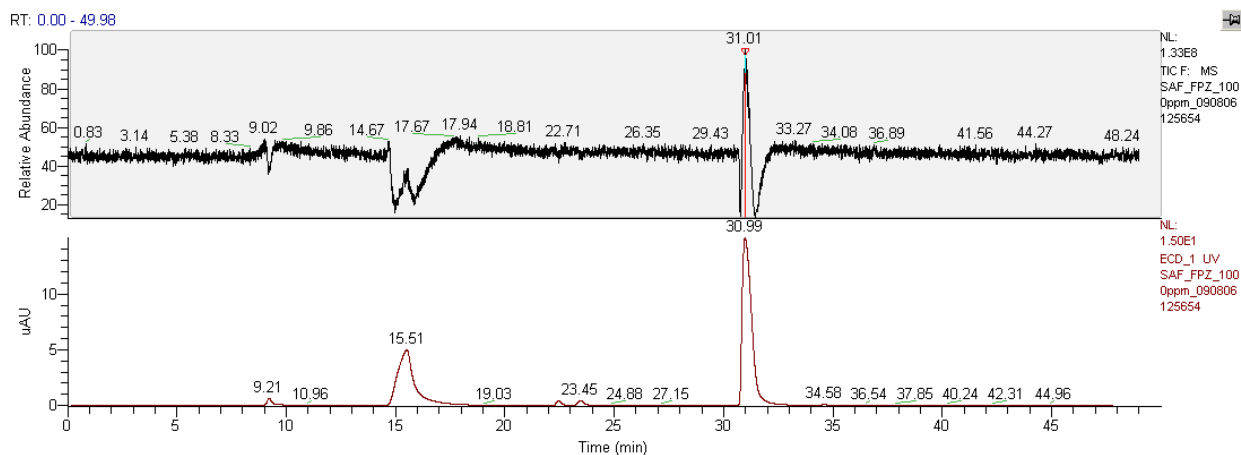
Figure 24: Cation IC-MS Chromatogram for 1000 ppm N-Formyl PZ (FPZ)
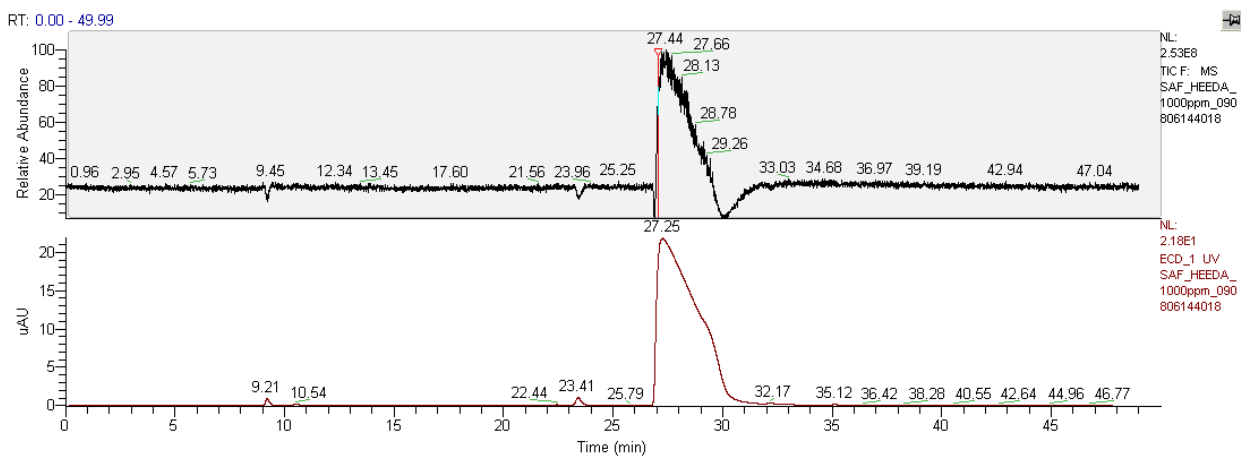
Figure 25: Cation IC-MS Chromatogram for 1000 ppm N-(2-Hydroxyethyl) EDA (HEEDA)
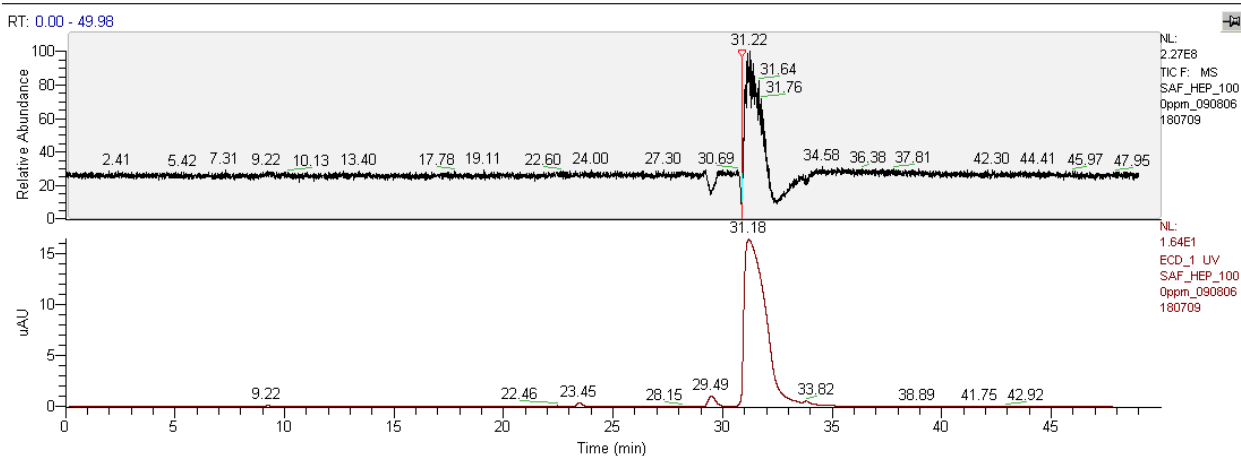
Figure 26: Cation IC-MS Chromatogram for 1000 ppm N-Hydroxylethyl PZ (HEP)
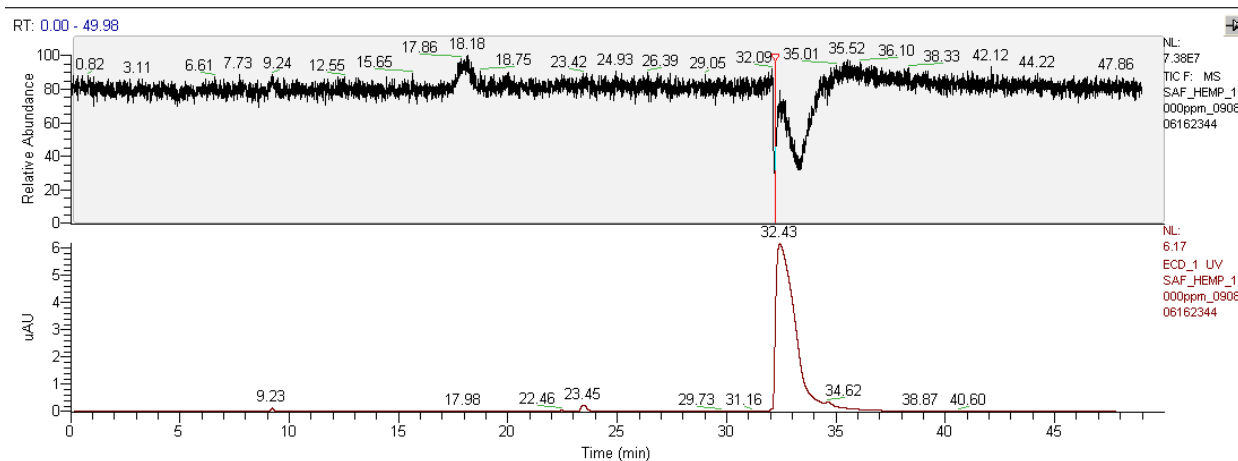
Figure 27: Cation IC-MS Chromatogram for 1000 ppm N-(2-Hydroxyethyl)-N'-Methyl PZ (HEMP)
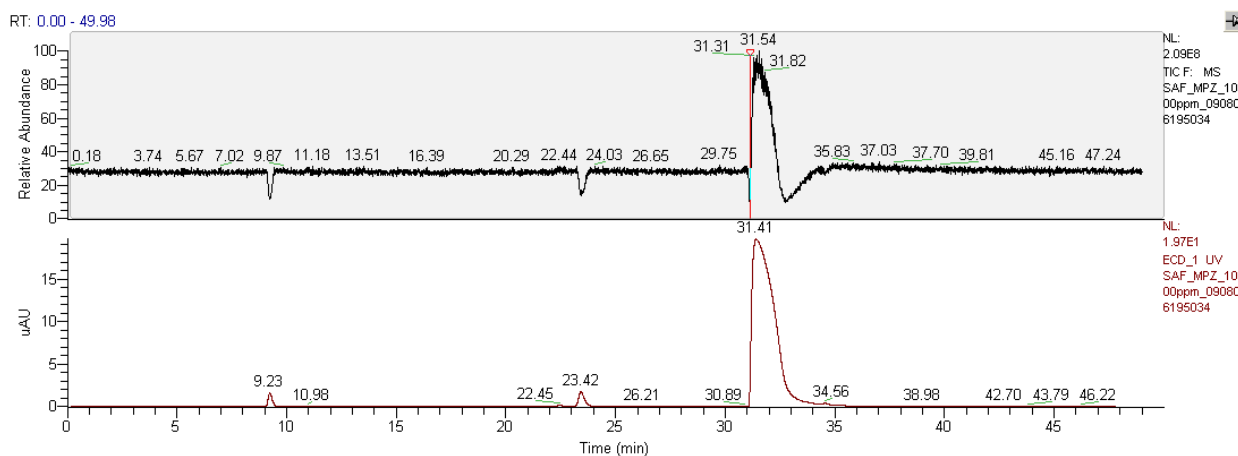
Figure 28: Cation IC-MS Chromatogram for 1000 ppm N-Methyl PZ (MPZ)

Figure 29: Cation IC-MS Chromatogram for 1000 ppm Triethylenediamine (TEDA)

23

Of the 16 derivatives analyzed by Cation IC-MS, 13 of the species, AcPZ, AEPZ, AMPZ, DFPZ, DMPZ, EDA, EPZ, FPZ, HEEDA, HEP, HEMP, MPZ, and TEDA, all gave clear chromatograms with good responses from the primary analyte. Each of these chromatograms had a primary peak that is significantly larger than any secondary peaks and contained the expected m/z value for the given compound. The retention times varied and a few, such as FPZ, had visible PZ contamination peaks.

A comparison of the analytes and their performance on Cation IC-MS is shown below in Table 4. For each analyte, the retention time of the main peak, any other m/z ratios found in that peak, and the maximum signal response of the main peak is shown. The other m/z ratios found in the main peak are indicated because 7 of the analytes formed doublets in the main peak (indicated by * in the table). Doublets occur when two analyte molecules attach to one charge, giving a m/z ratio that corresponds to 2*MW+1. Two analytes, DMPZ and EPZ, behaved differently as the main secondary m/z in the primary peak corresponded to 2*MW-1. It is not clear at this time how this m/z resulted or how the structure of DMPZ and EPZ led to this difference. Also, since all the analytes were 1000 ppm, the maximum response gives an indication of the response factor a particular analyte has for the Cation IC conductivity detector.

Table 4: Summary of PZ Derivative Cation IC-MS Results

Compound	Abbr	RT (min)	Also in Main Peak (m/z)	Maximum Response (uAU)	Notes
2-Imidazolidone		9.43	105.1	0.2	
2-Methyl-2-imidazoline		14.22	103.1, 205.1	23	**
2,5-piperazindione		9.32	77.0, 129.2	1.4	**
N-Acetyl PZ	AcPZ	17.10	257.2*	6	***
N-(2-Aminoethyl) PZ	AEPZ	33.56	130.1	28	
N-Amino-N'-Methyl-PZ	AMPZ	~31-32	114.1	2	
N,N'-Diformyl PZ	DFPZ	9.22	161.1	0.2	
N,N'-Dimethyl PZ	DMPZ	32.74	227.2*	8	
Ethylenediamine	EDA	25.42	121.1*	40	
N-Ethyl PZ	EPZ	32.08	227.2*	20	***
N-Formyl PZ	FPZ	15.51	229.1*, 87.1	15	***
N-(2-Hydroxyethyl) EDA	HEEDA	27.25	209.1*	22	
N-Hydroxyethyl PZ	HEP	31.18	129.1	16	
N-(2-Hydroxyethyl)-N'-Methyl PZ	HEMP	32.43	145.1, 287.1*	6	
N-Methyl PZ	MPZ	31.41	101.1, 119.1	16	
Triethylenediamine	TEDA	32.14	113.1, 225.2*	15	

* Secondary m/z found in peak is doublet of analyte
** Primary analyte is not in main peak. Details of main peak are still given.
*** PZ contamination is present at PZ RT of ~30.5 to 31 min

The results shown in Table 4 reveal important information on what PZ derivatives we can expect to see in future chromatograms of degraded PZ samples. First, the differences in maximum

response are very helpful. For the same concentration (1000 ppm), the responses vary from 0.2 to 40. This explains why EDA is one of the easiest degradation products to detect with Cation IC. EDA has a retention time separate from most of the other analytes and has a large response factor. Analytes that have small response factors (2-Imidazolidone, AMPZ, and DFPZ) are not likely to be detected in experimental samples unless their concentrations are very high. The retention times also indicate that quite a few analytes overlap and elude at similar times, making it very difficult to distinguish between the two (or more) analytes. Two sets of three analytes, DFPZ, 2,5-piperazindione, and 2-imidazolidone and HEP, AMPZ, and MPZ, elude within 0.2 minutes of each other. EDA and HEEDA are within 0.2 minutes of each other and both are within1.8 minutes of PZ. Finally, EPZ, HEMP, and DMPZ are all within 0.6 minutes of each other.

MS Analysis of Experimental Samples

The final samples of multiple experiments were also analyzed by Cation IC-MS this quarter. Only the final samples were analyzed to observe any possible degradation products not already analyzed for on the standard Cation IC and Anion IC analysis done at the end of the experiment. The Cation IC-MS chromatograms for OE1 through OE10 and TE9 are shown below in Figures 30 through 41. The chromatographs are displayed in the same way as the PZ derivatives panels above (Figures 14 through 29): the top panel is the total MS signal while the bottom panel is the Cation IC chromatogram total conductivity signal.   The panels are aligned so that they correspond in time. In each of these chromatographs, peaks that are known to correspond to a particular species are indicated. They all contain PZ, the primary peak at ~30.5 mins. Other peaks positively identified include EDA, N-Formyl PZ, MEA, and MDEA. Other peaks with well established m/z values are shown and tentative identifications of peaks are indicated with a question mark.
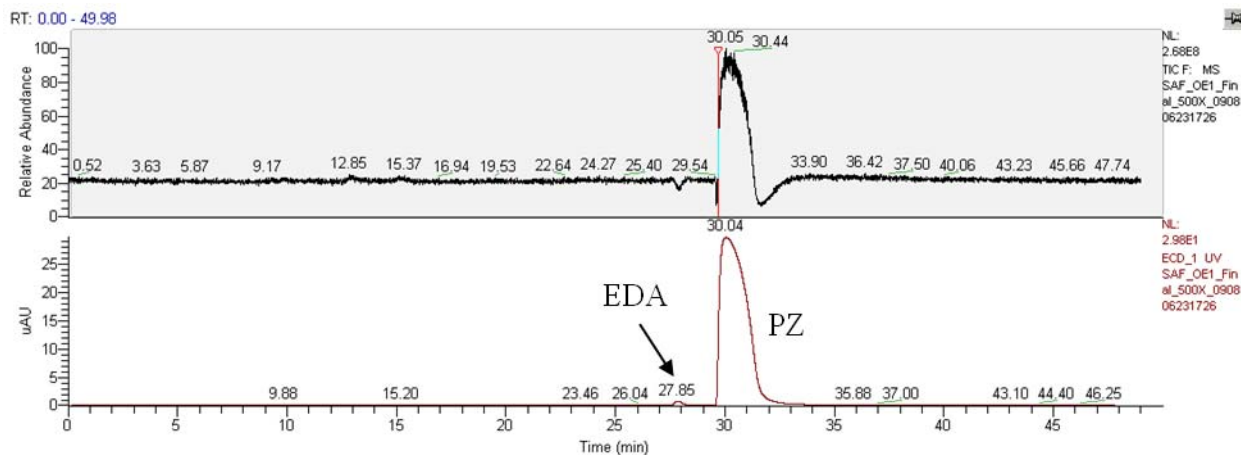

Figure 30: Cation IC-MS Chromatogram for the Final Sample of OE1 (10 m PZ, 55 °C, 2% CO_2, 0.26 mM Fe^{2+}, 0.65 mM Cr^{3+}, 0.26 mM Ni^{2+})
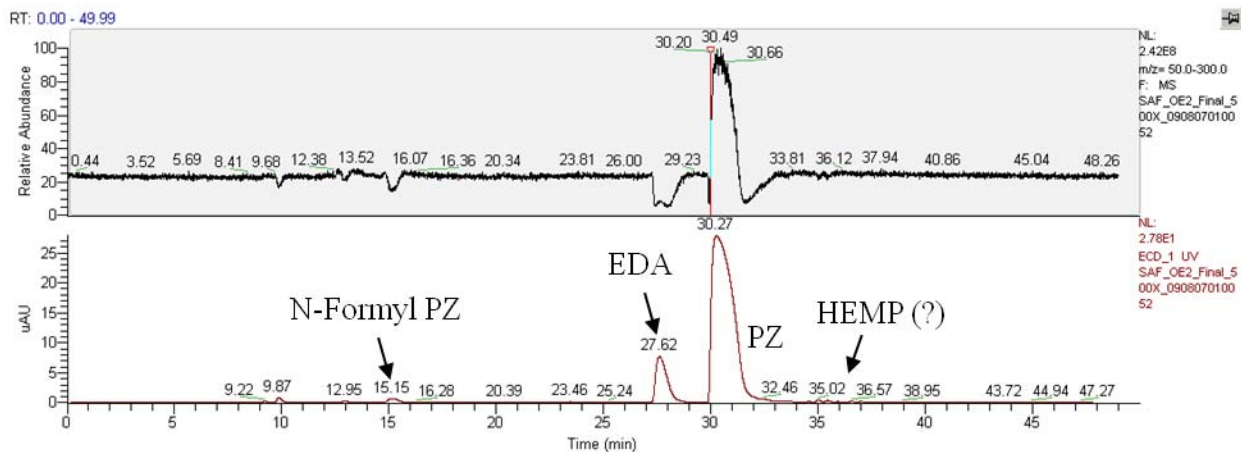
Figure 31: Cation IC-MS Chromatogram for the Final Sample of OE2 (10 m PZ, 55 °C, 2% CO_2, 4.0 mM Cu^{2+})
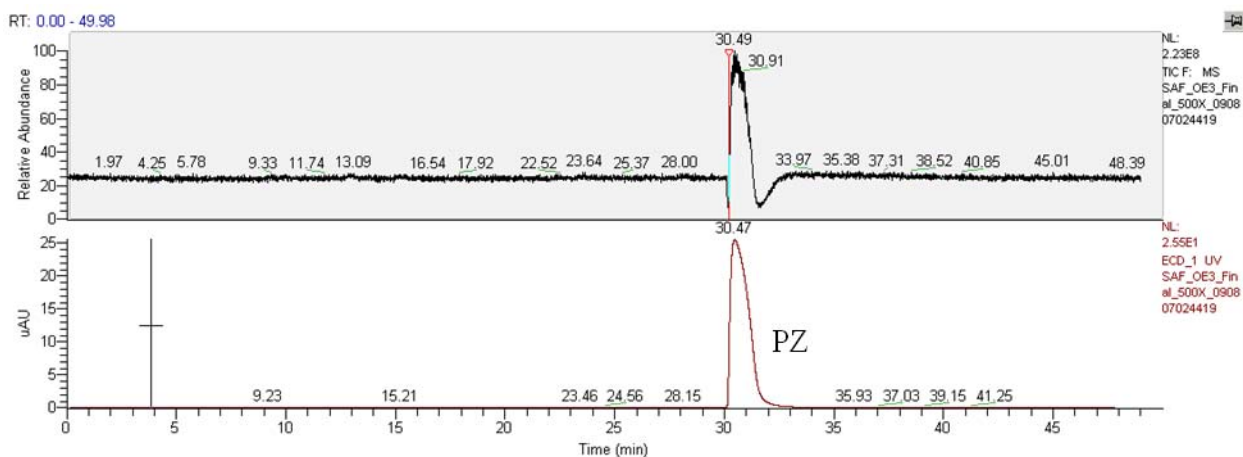

Figure 32: Cation IC-MS Chromatogram for the Final Sample of OE3 (8 m PZ, 55 °C, 2% CO_2, 0.1 mM Fe^{2+}, 0.1 mM V^{5+})
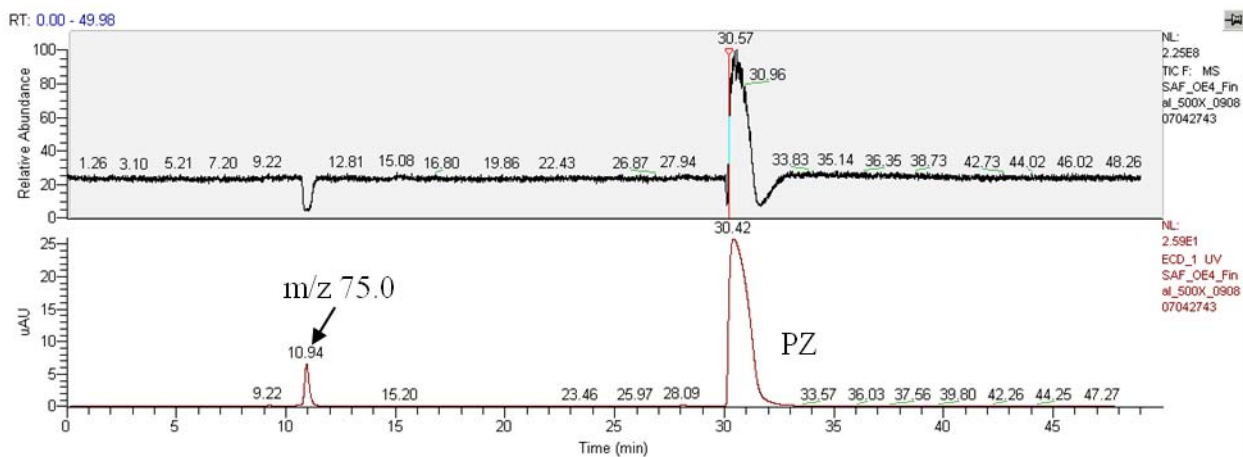

Figure 33: Cation IC-MS Chromatogram for the Final Sample of OE4 (8 m PZ, 55 °C, 2% CO_2, 5.0 mM Cu^{2+}, 0.1 mM Fe^{2+}, 100 mM Inhibitor A)
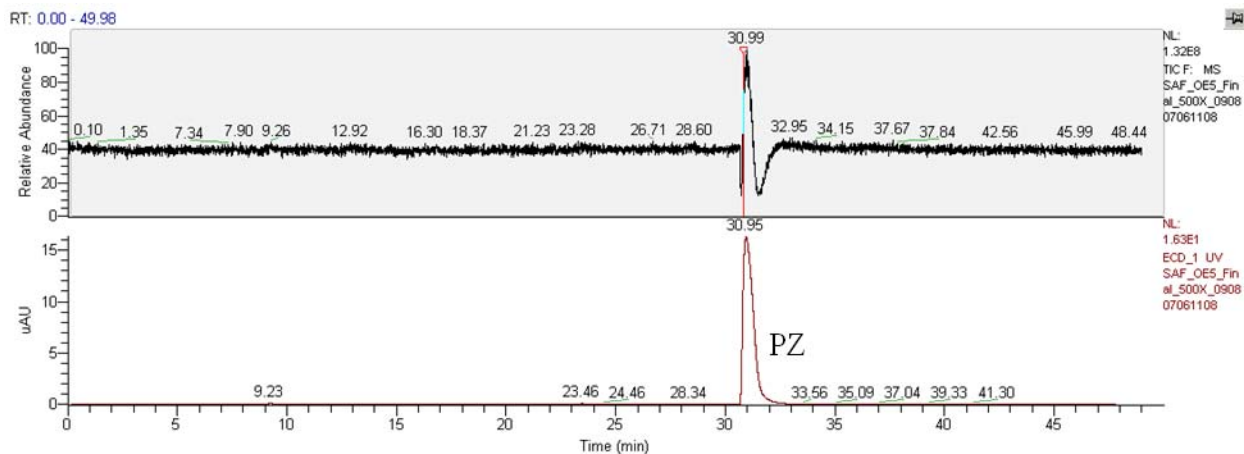
Figure 34: Cation IC-MS Chromatogram for the Final Sample of OE5B (8 m PZ, 55 °C, 2% CO$_2$, 1.0 mM Fe^{2+})
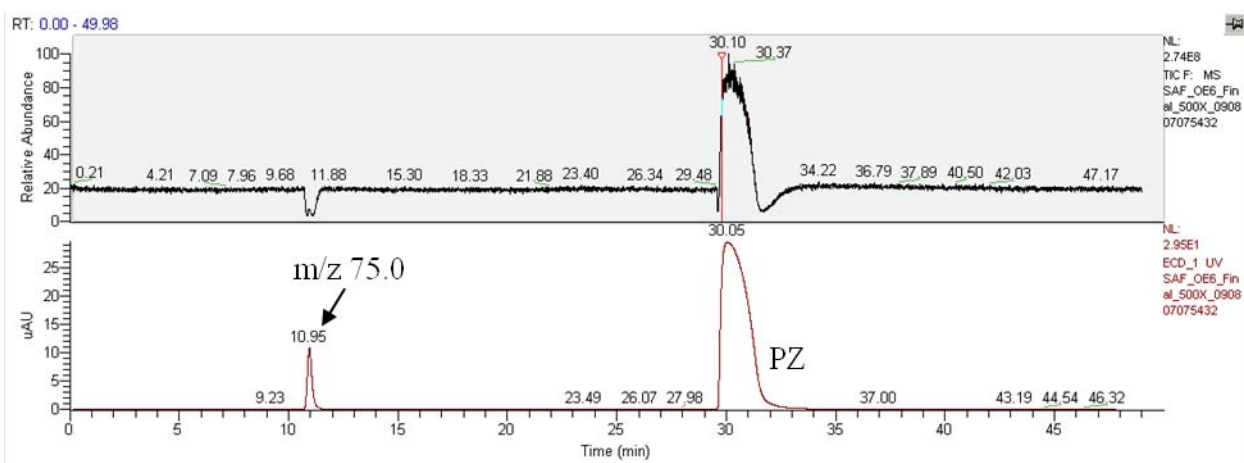
Figure 35: Cation IC-MS Chromatogram for the Final Sample of OE6B (8 m PZ, 55 °C, 2% CO$_2$, 1.0 mM Fe^{2+}, 100 mM Inhibitor A)
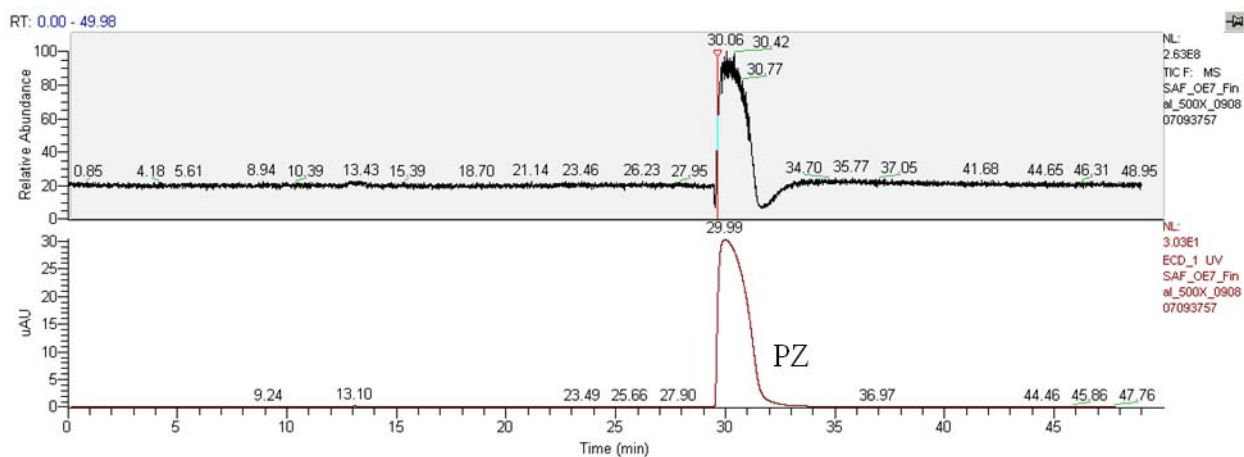

Figure 36: Cation IC-MS Chromatogram for the Final Sample of OE7 (8 m PZ, 55 °C, 2% CO$_2$, 1.0 mM Fe^{2+}, 20 mM Inhibitor B)
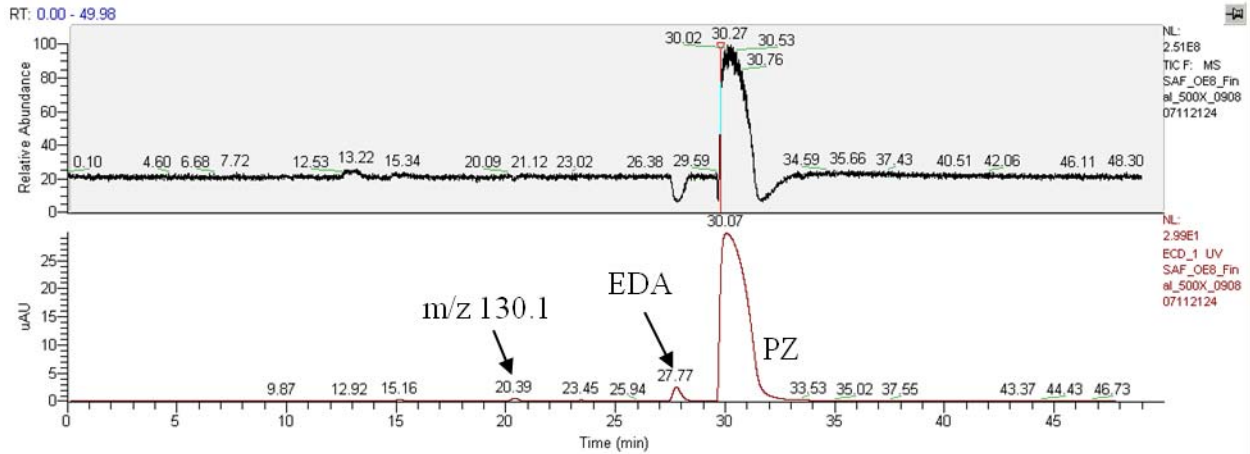
Figure 37: Cation IC-MS Chromatogram for the Final Sample of OE8 (8 m PZ, 55 °C, 2% CO$_2$, 1.0 mM Fe^{2+}, 30 mM EDTA)
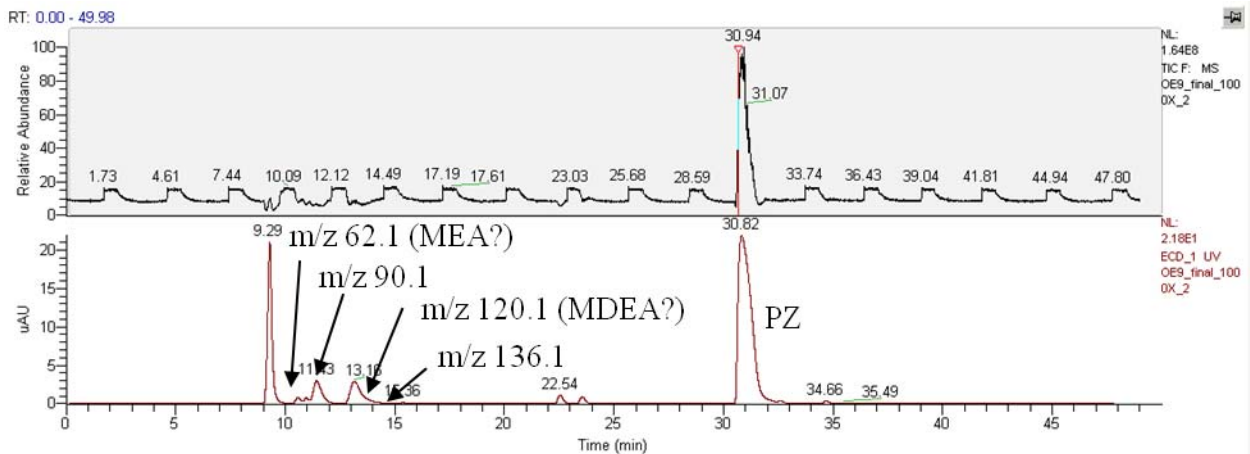

Figure 38: Cation IC-MS Chromatogram for the Final Sample of OE9 (8 m PZ, 55 °C, 2% CO$_2$ in N$_2$)
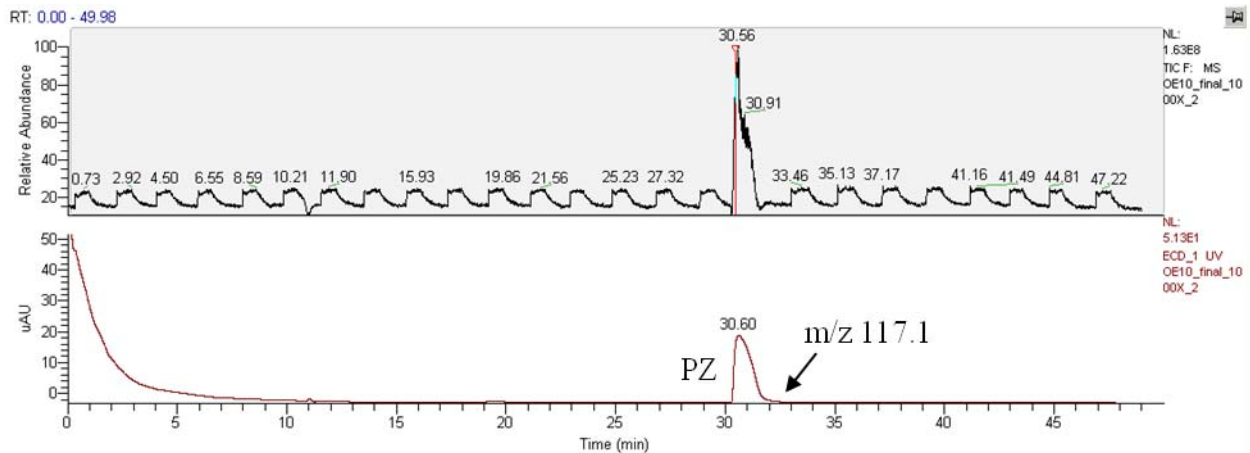

Figure 39: Cation IC-MS Chromatogram for the Final Sample of OE10 (8 m PZ, 55 °C, 2% CO$_2$ in N$_2$)
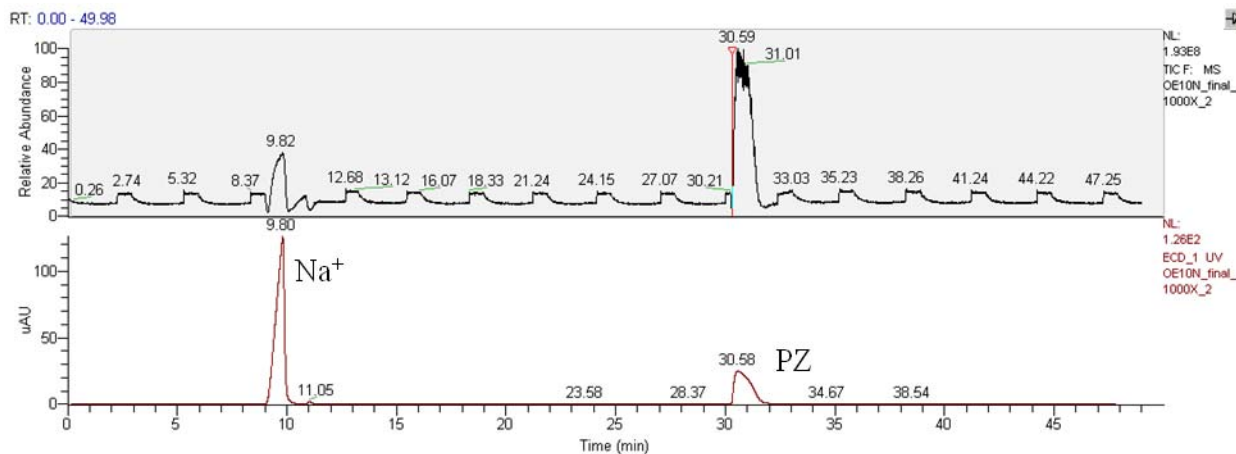
Figure 40: Cation IC-MS Chromatogram for the Final Sample of OE10 Treated with 5N NaOH (8 m PZ, 55 °C, 2% CO_2 in N_2)
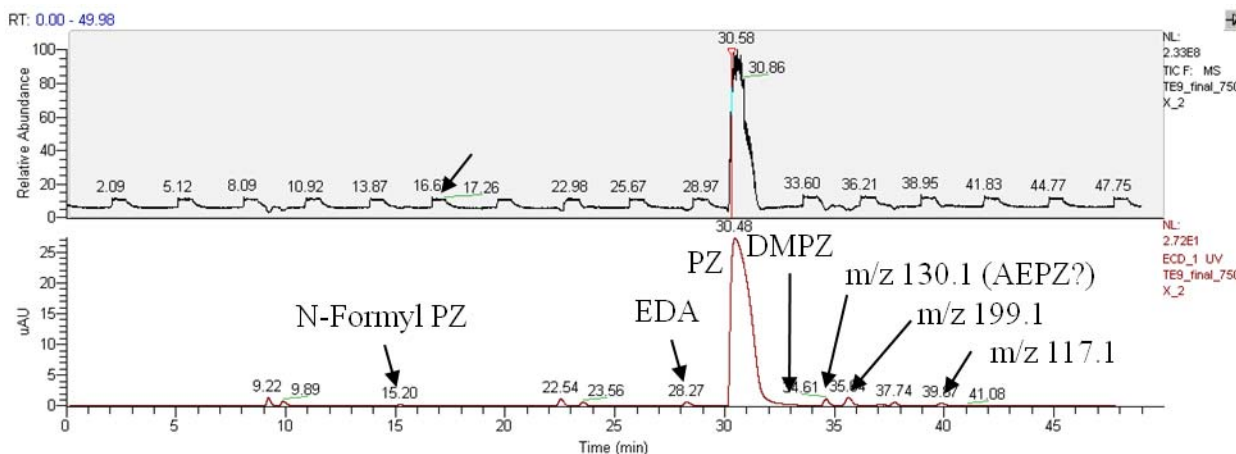

Figure 41: Cation IC-MS Chromatogram for the Final Sample of TE9 (8 m PZ, α=0.3 mol/mol alkalinity, 150 °C)

A few peaks in the final OE9 sample (Figure 39) have been identified as MEA and MDEA. This sample was analyzed in a run with other people's samples. The retention time and m/z are consistent with MEA and MDEA contamination and are not believed to be actual degradation products. The only two experiments with Inhibitor A have an unidentified peak at a retention time of 10.9 with a m/z of 75.0. This molecule has not been specifically identified yet, but must relate to the A in solution.

Trace Metals Analysis – AA vs. ICP-OES

The concentration of metals in nearly all of my experimental solutions is important. For oxidation experiments, metals are added as catalysts while metals in thermal degradation experiments are the result of corrosion. In either case, a reliable method for determining the concentration of important metals is crucial and must be accurate, fast, and require a small volume of sample. To this end, a comparison was made this quarter between two methods,

Flame Atomic Absorption Spectrophotometry (AA) and Inductively-Coupled Plasma Optical Emission Spectrometry (ICP-OES), for determining metals concentration.

In Flame AA, a single element is measured at a time with an element specific lamp. A calibration is performed each time samples are run to ensure accuracy. Lamps are available for all the metals we are interested in but interferences do occur. The measurement is manual and requires acetylene and air as the fuel for the flame. In ICP-OES, high temperature plasma creates emissions of light from elements of interest. Multiple elements (as many as desired) are measured from one sample and multiple wavelengths for each are determined simultaneously. There is a convenient autosampler that draws the desired sample and the system requires argon as the carrier gas.

To compare these methods, the same four samples were run under a variety of conditions. The five samples were 7 m MEA thermally degraded at 150 °C for 4 weeks. The AA analysis had four different solvents as the diluents: water, ammonium chloride (NH_4Cl), hydrochloric acid (HCl), and both NH_4Cl and HCl. The standard procedure for AA is acidification of the sample with a strong acid (HCl or HNO_3) to increase the solubility of the metals for analysis. This was not originally done to the samples so the difference this acidification made was assessed. Also, the Perkin Elmer AA Cookbook suggested the use of NH_4Cl to reduce interference between chromium and iron. The use of NH_4Cl and NH_4Cl with acid were used to dilute the samples to see how metals concentrations would be affected. The figures below show the comparison between the four AA solvents and the ICP-OES method using the standard protocol for iron (Figure 42), chromium (Figure 43), and nickel (Figure 44).
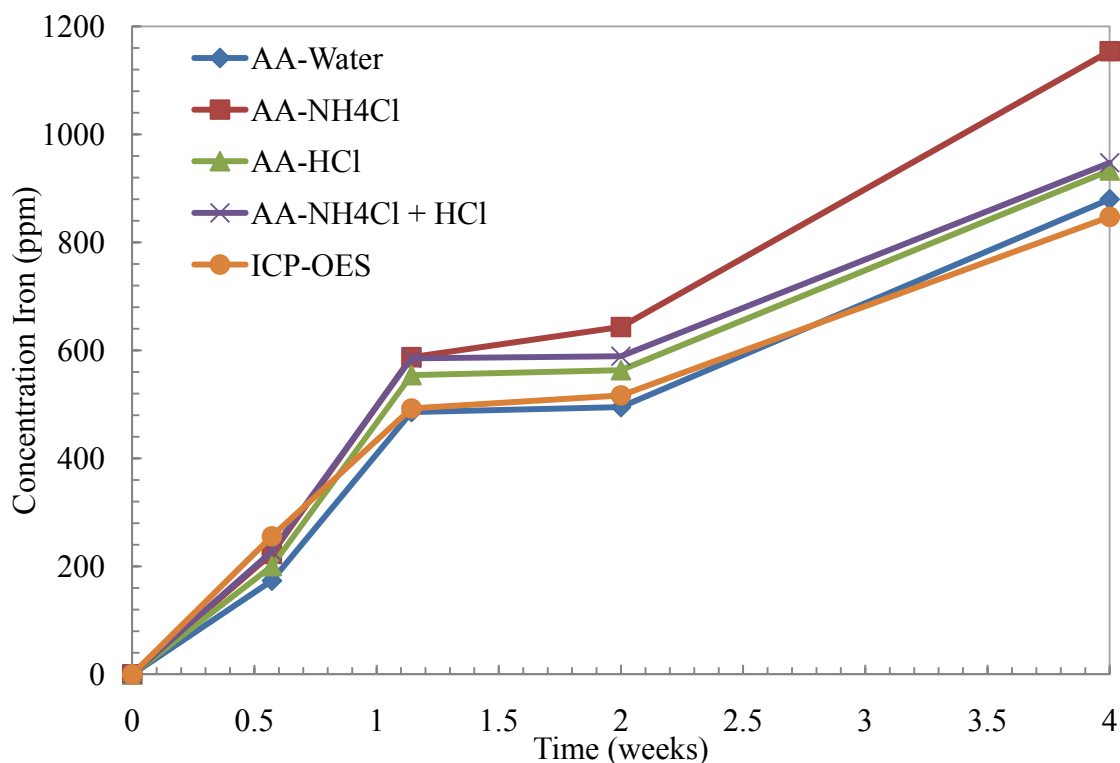

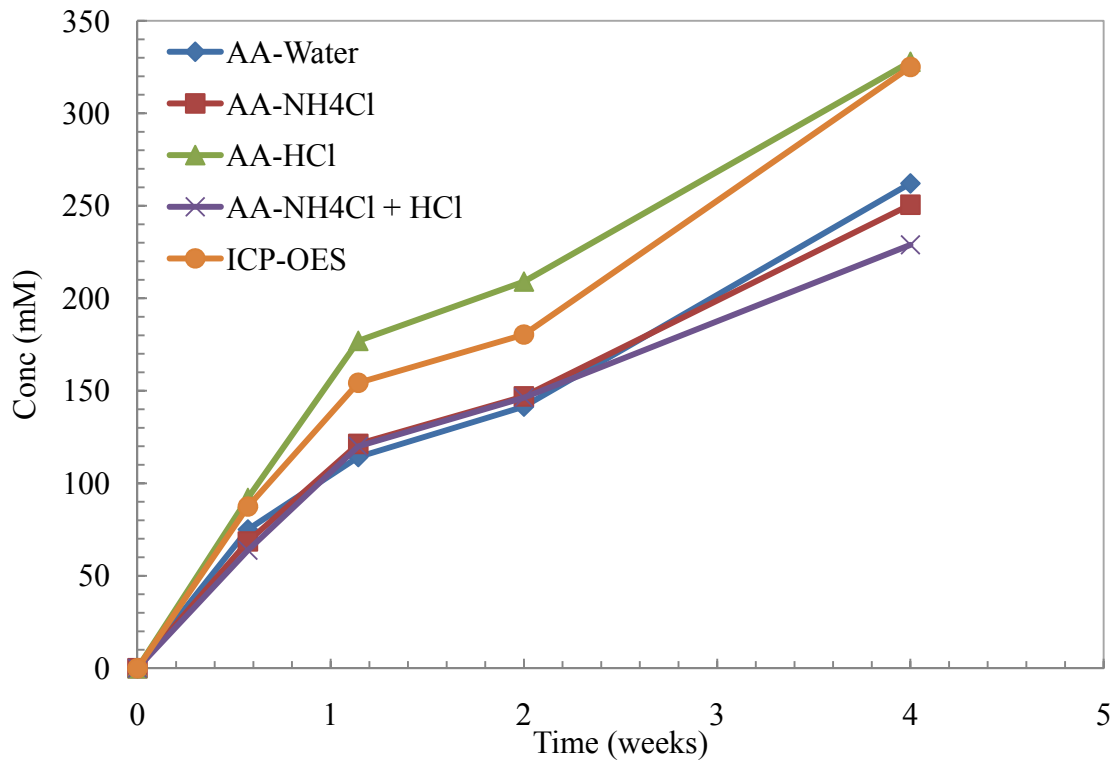**Figure 42: Iron Concentration for 7 m MEA at 150 °C measured by AA and ICP-OES**

Figure 43: Chromium Concentration for 7 m MEA at 150 °C measured by AA and ICP-OES
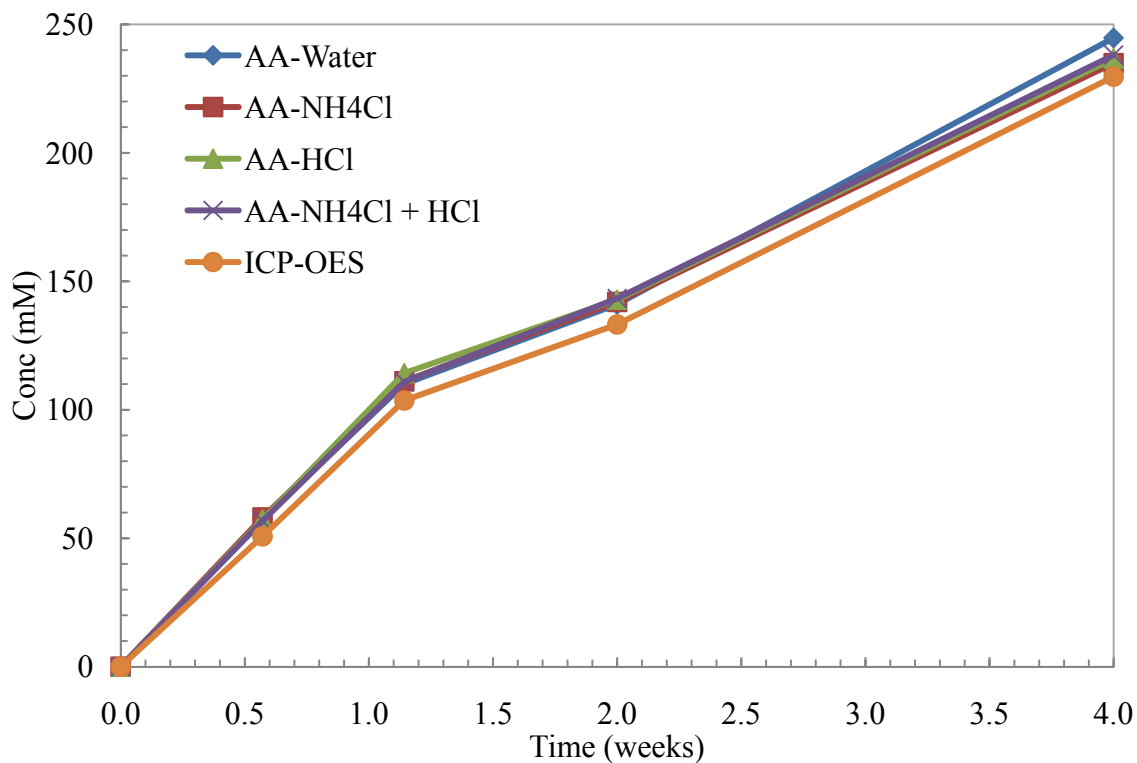

Figure 44: Nickel Concentration for 7 m MEA at 150 °C measured by AA and ICP-OES

For iron, the five methods measured the concentration to be 952 ± 120 ppm. The largest difference in concentration was 302 ppm between the NH_4Cl method and the ICP-OES. For chromium, the predicted concentration was 279 ± 45.0 ppm. The spread of data at 4 weeks was at most 77.2 ppm between the HCl and the NH_4Cl + HCl treatments. There was very little difference observed between the five methods for the nickel measurement as the concentration was predicted to be 237 ± 5.46 ppm. In fact, the four AA methods produced nearly identical results while the ICP-OES method measured slightly lower concentrations throughout. The spread of data at 4 weeks for nickel was only 15.1 ppm. Unfortunately, the iron results showed the least consistency and iron is generally the most important of the three metals because of its known catalytic effect on amines. This large spread is also a function of the high concentration in these samples due to significant corrosion caused by MEA.

Another set of data has been analyzed by both AA and ICP-OES but only for iron and nickel. As mentioned above in the thermal degradation section, TE9 was analyzed for these metals last quarter and the samples were subsequently reanalyzed this quarter using ICP-OES. Figure 45 below shows the comparison between the two sets of data.
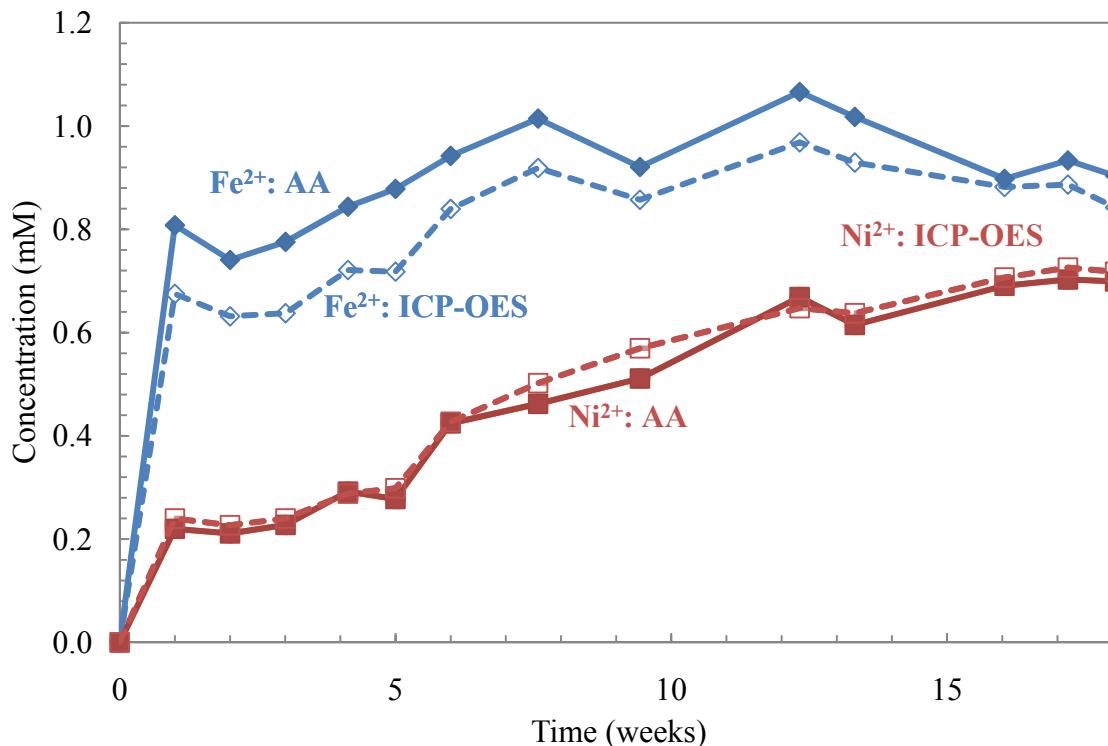

Figure 45: Iron (blue, top) and Nickel (red, bottom) Concentration for 8 m PZ at 150 °C (TE9) measured by AA (Closed Points) and ICP-OES (Open)

As with the MEA data in Figures 42 and 44, the iron and nickel concentrations overall are very similar with both methods. The nickel is especially close, with the data essentially overlapping. With the iron, the AA concentrations are slightly higher although the biggest difference between the two sets of data is 0.16 mM at 5 weeks. This matches the MEA data where the AA found larger concentrations of iron.

I will use the ICP-OES method for all future corrosion and metals work. Although finding slightly lower iron concentration in the test samples compared to AA, the ease of sample handling and ability to do multi-element analysis are very important positives. The reason for larger iron concentrations in AA is not clear at this point and I am not able to conclude if the ICP-OES underestimates or the AA overestimates the true value. Future work may need to analyze additional metals such as copper, vanadium, or manganese so the ability to quickly analyze any number of metals (1 to 10) in one solution is very advantageous. Additionally, using a computer and autosampler to automate calibration and sampling handling is an important time saver.

Conclusions

Iron-catalyzed degradation of 8 m PZ is reduced with the addition of 100 mM A. With only 10 mM of A, stainless steel-catalyzed PZ degradation was not significantly affected while the production of degradation products was reduced. The loss of PZ is so small in the presence of stainless steel metals that any improvement from 10 mM A was difficult to determine considering the experimental and analytical error.

At 175 °C, 8 m PZ significantly degraded losing 71.5 and 73% over 15 weeks for solutions with loadings of 0.3 and 0.4 mol/mol alkalinity, respectively. This degradation produced large amounts of formate, total formate, and EDA as well. Total formate reached 560 and 690 mM while EDA reached 42 and 45 mM for the two loadings, respectively. The degradation in these experiments seen in the first 5 weeks matched the rate observed in previous experiments at this temperature. Despite the high rate of degradation observed in these two experiments, metals concentrations were low for iron, nickel, and chromium, all staying below 7 and 12 mM in the two experiments. Unique to these two experiments, nickel was found in the highest concentration, not iron as was expected.

The behavior of 16 PZ derivatives was observed in the Cation IC-MS. Most of the amines, AcPZ, AEPZ, AMPZ, DFPZ, DMPZ, EDA, EPZ, FPZ, HEEDA, HEP, HEMP, MPZ, and TEDA, behaved as expected, producing a single peak with the expected m/z ratio for that analyte. Doublet signals (m/z = 2*MW+1) were observed in 7 analytes. Three species, 2-Imidazolidone, 2-Methyl-2-Imidazoline, and 2,5-piperazindione, produced very weak signals without the expected m/z ratio.

Cation IC-MS analysis of 11 oxidation and one thermal degradation sample was performed. The results were not enlightening as most of the experiments experienced very little PZ degradation. In those where PZ degraded, namely OE2, OE4, and TE9, peaks of EDA and N-Formyl PZ were identified. Experiments with Inhibitor A both have the same unidentified peak that must be an adduct of A.

ICP-OES and AA are both effective and efficient ways to measure aqueous metals in experimentally degraded solutions. ICP-OES will be used from now on because of its ability to detect multiple metals in the same sample, reducing the volume of sample needed for analysis.

Future Work

The final quarter of 2009 will focus on work relating to identifying degradation products of PZ. Work with the Cation IC-MS and LC-MS is making progress overall and appears promising to help identify degradation products that can fill in the mass balance gaps.

The main focus on the oxidation of PZ will be in testing the new oxidation reactor. The glass reactor was finished this quarter and most of the major pieces are in place. Testing will begin in the early portion of the next quarter with, it is hoped, two or three experiments completed before the end of 2010.

Thermal degradation experiments will continue to be sampled periodically throughout the end of this year with most current experiments finishing in the first quarter of 2010.

References

Cullinane JT, Rochelle GT. "Kinetics of carbon dioxide absorption into aqueous potassium carbonate and piperazine". *I&ECR.* 2006;45(8):2531–2545.

Davis J. 2009. *Thermal Degradation of Aqueous Amines Used for Carbon Dioxide Capture*. The University of Texas at Austin. Ph.D. Dissertation. 2006.

Dugas R, Rochelle GT. "Absorption and desorption rates of carbon dioxide with monoethanolamine and piperazine". *Energy Proc*. 2009;1(1):1163–1169

Freeman SA, Dugas R, VanWagener D, Nguyen T, Rochelle GT. "Carbon dioxide capture with concentrated, aqueous piperazine". *IJGGC*. In Press.

Hilliard MD. *A Predictive Thermodynamic Model for an Aqueous Blend of Potassium Carbonate, Piperazine, and Monoethanolamine for Carbon Dioxide Capture from Flue Gas*. The University of Texas at Austin. Ph.D. Dissertation. 2008.

Rochelle GT. CO_2 Capture by Aqueous Absorption, First Quarterly Progress Report 2008. Luminant Carbon Management Program. The University of Texas at Austin. 2008.

Sexton AJ. *Amine Oxidation in CO_2 Capture Processes*. The University of Texas at Austin. Ph.D. Dissertation. 2008.

Evaluation of Ethylenediamine and
Thermal degradation of 2-Piperidineethanol

Abstract

The density of 8 m and 12 m ethylenediamine (EDA) with different CO_2 loading was measured. The solution density has a linear relationship with CO_2 concentration in the solutions (mol CO_2/kg solution).

8 m EDA samples which had been degraded for 8 weeks in thermal degradation experiment were measured by atomic absorption. 8 m EDA is more corrosive than MEA and piperazine (PZ).

Heat capacity of 12 m EDA was measured. With less water in the solution, the heat capacity of loaded 12 m EDA is lower than both 8 m PZ and 7 m MEA.

Thermal degradation experiments of 2-Piperidineethanol (2-PE) were performed at 120–150 ^{o}C. Thermal degradation of 2-PE is slower than that of MEA, but 2-PE polymerized in the thermal degradation process.

Introduction

CO_2 absorption in ethylenediamine (EDA) was studied by several authors since 1955. Jensen and Christensen (1955) reported that CO_2 reacts with EDA to produce both monocarbamate and dicarbamate. Trass and Weiland (1971) measured CO_2 solubility and tested 1.6～4.2M EDA in a pilot plant. Sharma (1965) , Sada (1977) , Hikita et al. (1977) and Li et al. (2007) obtained similar rate constants for CO_2 absorption into EDA solution with different experiment methods. Based on this previous work, EDA reacts at a faster rate with CO_2 than MEA at low amine concentration (< 2 M) with low CO_2 loading (< 0.1). At 298K, second order rate constant is 15.1 m^3 $mol^{-1}s^{-1}$ for EDA, and 7.6 m^3 $mol^{-1}s^{-1}$ for MEA (Sharma, 1965).

Thermal degradation, oxidative degradation, foaminess, volatility, and reaction rate of CO_2 were tested for EDA solution. 8 m EDA with 0.4 loading showed a similar thermal degradation rate with 7 m MEA with 0.4 loading at 135 ^{o}C. The degradation rate decreases significantly as temperature decreases. 90% EDA remained after 16 weeks at 100 ^{o}C. The oxidative degradation rate is also similar to MEA. Inhibitor A can protect EDA from oxidation effectively in the environment with 1 mM Fe^{2+}. Oxidative degradation rate is reduced 80% with A. Although the absorption rate of CO_2 into EDA is less than 50% of that of 7 m MEA with rich loading, the

working capacity of 12 m EDA is more than 1.5 times that of 7 m MEA. EDA shows similar foaminess with MEA. Its reasonable price also makes EDA an attractive alternative solvent for CO_2 capture.

2-Piperidineethanol (2-PE) was screened in the wetted wall column by Chen (Rochelle et al., 2009). Although the CO_2 absorption rate for 8 m 2-PE is a little slower than for MEA, 2-PE showed a CO_2 working capacity 2.6 times that of 7 m MEA. 2-PE may be a promising amine if its degradation rate is slow.

Experimental Methods

Density was measured using a Mettler-Toledo DE40 densitometer (Mettler-Toledo, Inc, Columbus, Ohio, USA). It measures density by vibrating the glass u-tube inside the meter at a certain frequency. Calibration is performed with air and degassed-deionized (DDI) water at each temperature that measurements are taken. The accuracy is 0.0001 g/cm^3 (Mettler Toledo US, 2009). Liquid samples are pumped into the measurement u-tube and pumped out after the measurement is completed. The u-tube is cleaned with DI water and acetone after each sample (Freeman, 2009).

Atomic absorption analysis was carried out using a Perkin Elmer 1100B flame atomic absorption spectrophotometer. The device was operated using acetylene as a fuel source and air as the oxidant at 2.5 and 8 L/min, respectively (Rochelle et al., 2009).

The heat capacity determination was performed in accordance with ASTM E 1269-05 (Hilliard, 2008). A 304 stainless steel pan is filled to capacity with 60 μL of solution before being sealed with its lid and O-ring. A vapor headspace of roughly 5–15% in volume is estimated to exist in the sealed unit. The sample pan is then placed against an empty reference pan inside a Differential Scanning Calorimeter (DSC) to measure the difference in the amounts of heat absorbed by the two pans. This heat differential is subsequently used to determine the heat capacity of the solution. A more detailed description can be found in the first quarterly report of 2009.

Thermal degradation experiments were performed as detailed in the Davis dissertation (2009). 2-PE was sealed in 10 mL stainless steel bombs. All the bombs were put in a forced convection oven at 120 ^{o}C to 150 ^{o}C for different times.

Analytical Methods

Cation IC: A Dionex ICS-2500 Ion Chromatography System with CS17 IonPac column with CSRS 4 mm self-regenerating suppressor was used to determine concentrations of EDA and the cationic species in degraded solutions. The system and analytical method are the same as described by Davis (2009). All the samples were diluted about 10,000 times for cation analysis.

IC/MS: A Thermal TSQ mass spectrometer coupled with a Dionex-2500 IC was used for mass determination of ionic products in 2-PE degraded sample. The programming method is also documented by Davis (2009).

TIC: The concentration of carbon dioxide in the solution was measured using the Total Inorganic Carbon Analyzer. CO_2 loading of solutions can be calculated from the result of TIC.

Acid pH Titration: Metrohm 835 Titrando with an 801 stirrer was used to determine the total concentration of amines in the solution. The analytical method is the same as described by Freeman (2009)

Material

Table 1: Chemical Reagent Specifications

Reagent	CAS#	Supplier	Molecular Weight	Assay %	Lot #
Ethylenediamine	107-15-3	Strem Chemicals	60.10	99	A4879029(v)
2- Piperidineethanol	1484-84-0	ACROS Organics	129.2	95	A0262351

Results

All the experiment data are listed below.

Table 2: Density of 8 m EDA

CO_2 loading (mol CO_2 / equiv EDA)	Density (g/cm^3)				
	20 ^{o}C	30 ^{o}C	40 ^{o}C	50 ^{o}C	60 ^{o}C
0.47	1.178	1.1732	1.1682	1.1631	1.158
0.43	1.1619	1.1567	1.152	1.1471	1.142
0.40	1.1455	1.1408	1.1356	1.1307	1.1255
0.35	1.1287	1.124	1.1188	1.1138	1.1085
0.30	1.1111	1.1065	1.1013	1.0961	1.0908
0.21	1.0748	1.0702	1.0647	1.0594	1.0538
0			0.9852		0.9722

Table 3: Density of 12 m EDA

CO_2 loading (mol CO_2 / equiv EDA)	Density (g/cm^3)				
	20 ^{o}C	30 ^{o}C	40 ^{o}C	50 ^{o}C	60 ^{o}C
0.48	1.2135	1.2086	1.2034	1.1983	1.1932
0.43	1.1976	1.1928	1.1876	1.1825	1.1775
0.38	1.1776	1.1728	1.1674	1.1623	1.1571
0.33	1.1581	1.1531	1.1478	1.1426	1.1374
0.29	1.1374	1.1324	1.1269	1.1217	1.1163
0.20	1.0938	1.0885	1.0827	1.0771	1.0712
0			0.9848		0.97

Table 4: Metal concentration, 8 m EDA,0.4 loading, 8 weeks thermal degradation

T (^{o}C)	Metal concentration (mM)		
	Fe	Ni	Cr
100	25	5	4
120	26	7	5
135	54[1]	12	7

[Fe] in the solution is out of calibration range. This number is estimated according to the calibration curve.

Table 5: Heat capacity (J/ (g*K)) of 12 m EDA

T (^{o}C)	α=0	α=0.35	α=0.4	α=0.45
40	3.72	2.87	2.78	2.75
45	3.76	2.89	2.81	2.79
50	3.79	2.91	2.84	2.82

55	3.83	2.94	2.87	2.84
60	3.85	2.96	2.89	2.85
65	3.89	2.98	2.91	2.88
70	3.91	3.00	2.93	2.90
75	3.94	3.02	2.95	2.92
80	3.97	3.04	2.97	2.95
85	3.99	3.06	3.00	2.98
90	4.01	3.08	3.02	3.01
95	4.03	3.10	3.05	3.04
100	4.05	3.13	3.07	3.07
105	4.07	3.15	3.10	3.11
110	4.08	3.17	3.13	3.15
115	4.08	3.19	3.17	3.19
120	4.08	3.22	3.20	3.24

Where α is the CO_2 loading in mol CO_2/equivalent EDA

Table 6: 2-PE concentration (M) in thermal degradation experiment

Solution	T (°C)	Time (week)				
		0	1	2	4	8
8 m 0.4 loading	150	3.6	2.5	2.1*	1.7*	
	135	3.6		3.0	2.7*	2.4*
	120	3.6			3.2	3.1
7 m 0.6 loading	135	3.3		2.6	2.4*	2.1*
7 m 0.4 loading	135	3.3		2.8	2.5*	

* There was colloidal suspension in the sample.

The specific gravity of partially loaded 8 m and 12 m EDA is given in Figure 1. The density of solution was divided by density of water at the same temperature. Normalized density of EDA solution is not a strong function of amine concentration, and can be predicted only by CO_2 concentration. Therefore, CO_2 concentration can be inferred from on-line measurements of solution density in this range of EDA concentration. In the operation loading range, the density of 12 m EDA is between 1.15 and 1.2 g/cm^3, which is similar to that of 8 m PZ.

Metal concentration in thermally degraded EDA samples was measured by atomic absorption. Thermally degraded samples were treated with HNO_3 to dissolve the metal in the solution and then introduced into the AA spectrophotometer. Corrosivity of EDA increases with temperature. Typical metal concentration data of MEA (Voice, 2009), PZ (Freeman, 2009), and EDA are compared in Figure 2. Metal concentrations in the EDA sample are much higher than those in PZ, and similar to those of MEA. The corrosion rate of 316L stainless steel will be about $5*10^{-6}$ m/y when EDA solution is used between 100 °C and 120 °C.
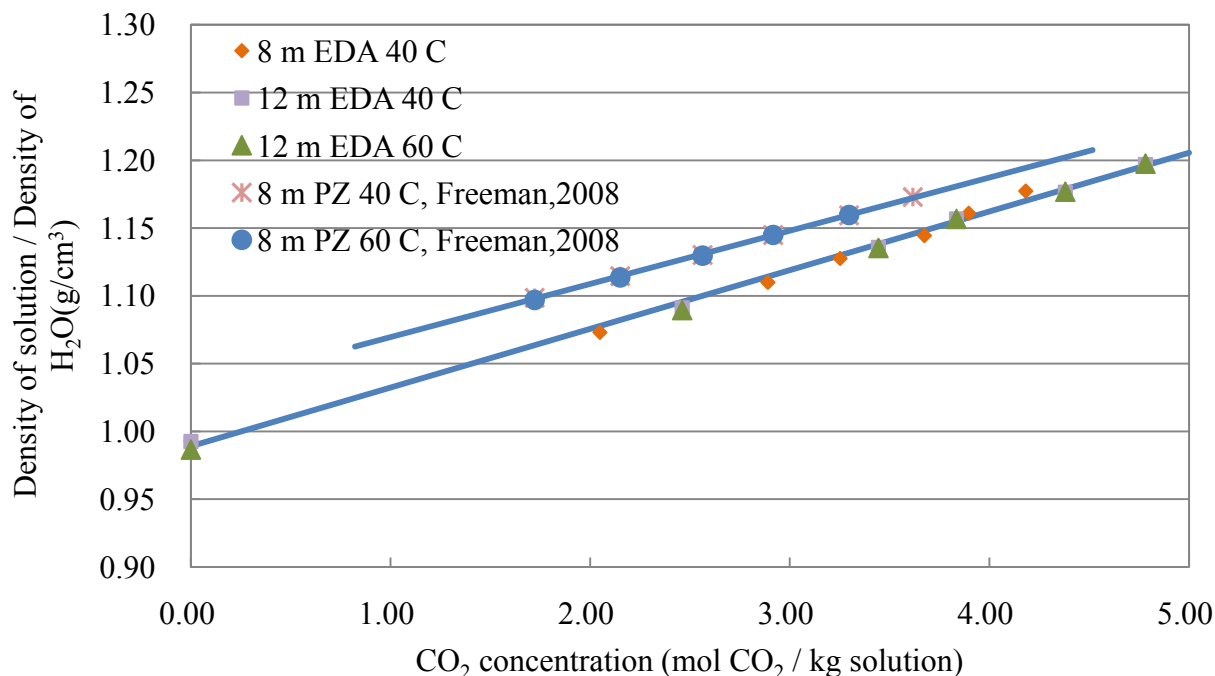
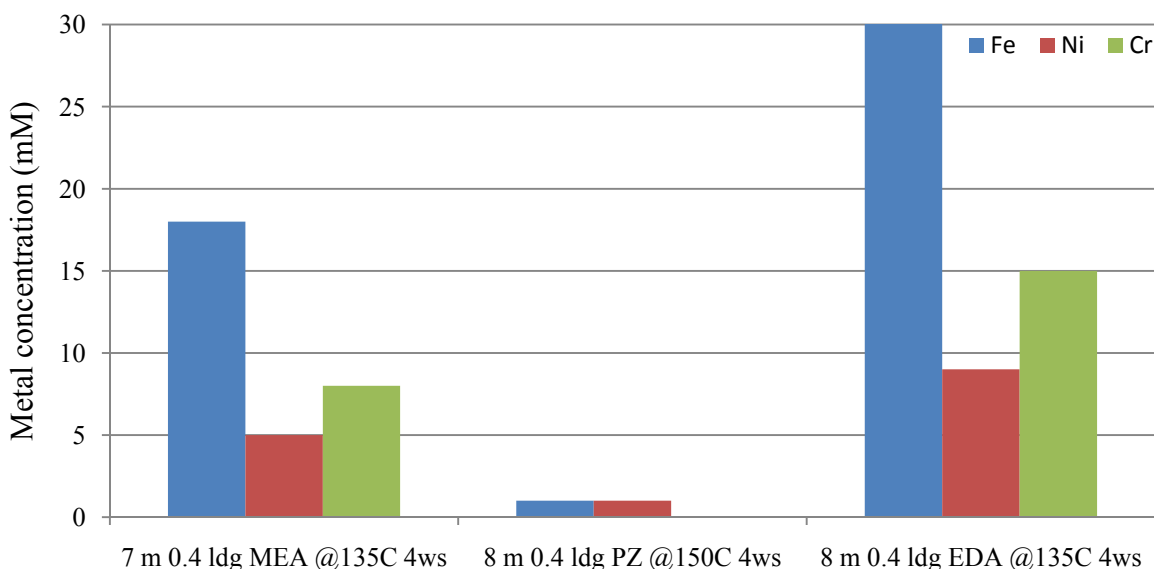**Figure 1: Density of EDA solution**

Figure 2: Corrosivity of MEA, PZ, and EDA thermally degraded sample, 8 weeks

The heat capacity of 12 m EDA was measured. Raw data of loaded sample are plotted in Figure 3. C_p is also reported on a CO_2 free basis ($J/(g_{H2O+EDA}*K)$) in Figure 4. At temperatures lower than 90 ^{o}C, the heat capacity of EDA solution increases as CO_2 loading decreases. Meanwhile, the apparent C_p increase rate with temperature is higher with higher CO_2 loading. The same phenomenon was also observed on concentrated PZ solution. The apparent partial heat capacity of total CO_2 in loaded solution is negigible. H2O and CO_2 vaporized into the headspace of the cell and required more heat at higher temperature. More CO_2 vaporized at higher loading, which makes the apparent C_p of higher loading solutions increase faster than lower loading solutions.

The C_p of loaded 12 m EDA is lower than that of 8 m PZ and 7 m MEA due to higher CO_2

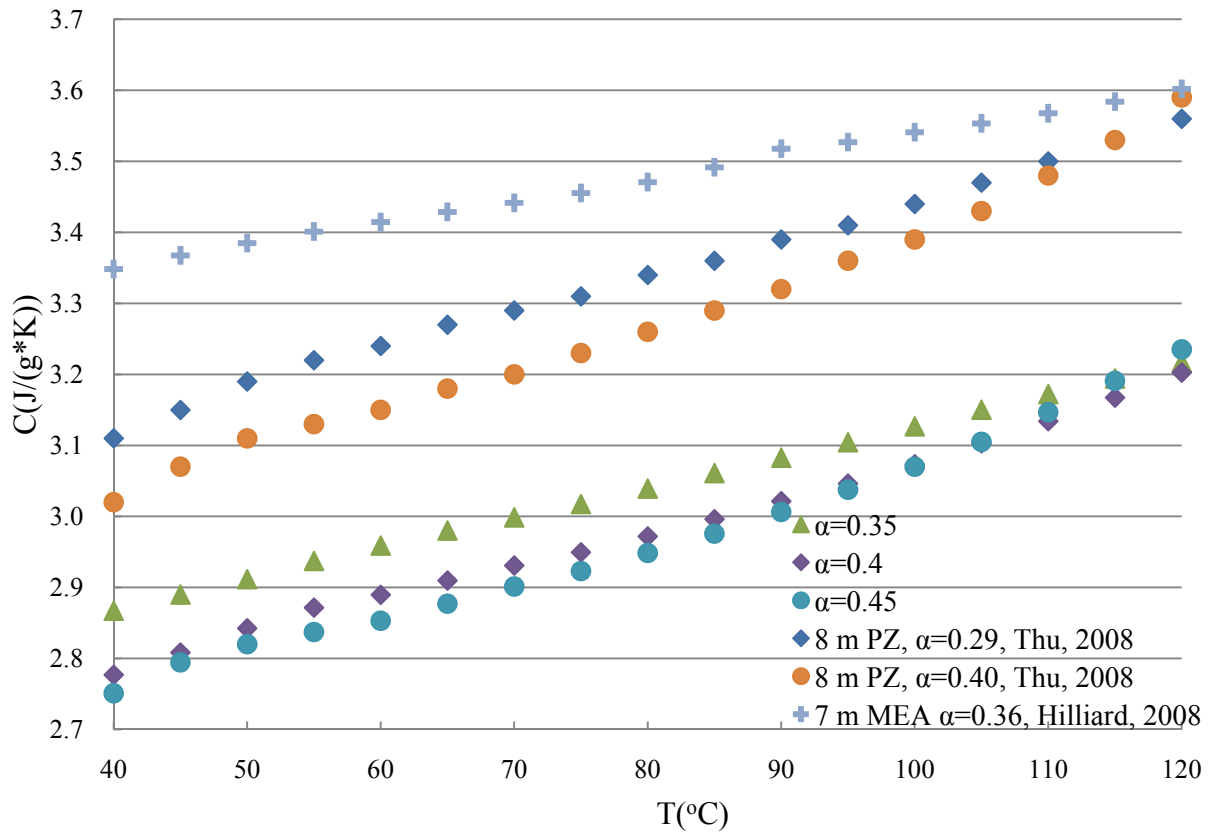content. Higher amine concentration and higher loading can help to reduce the sensible heat requirment.

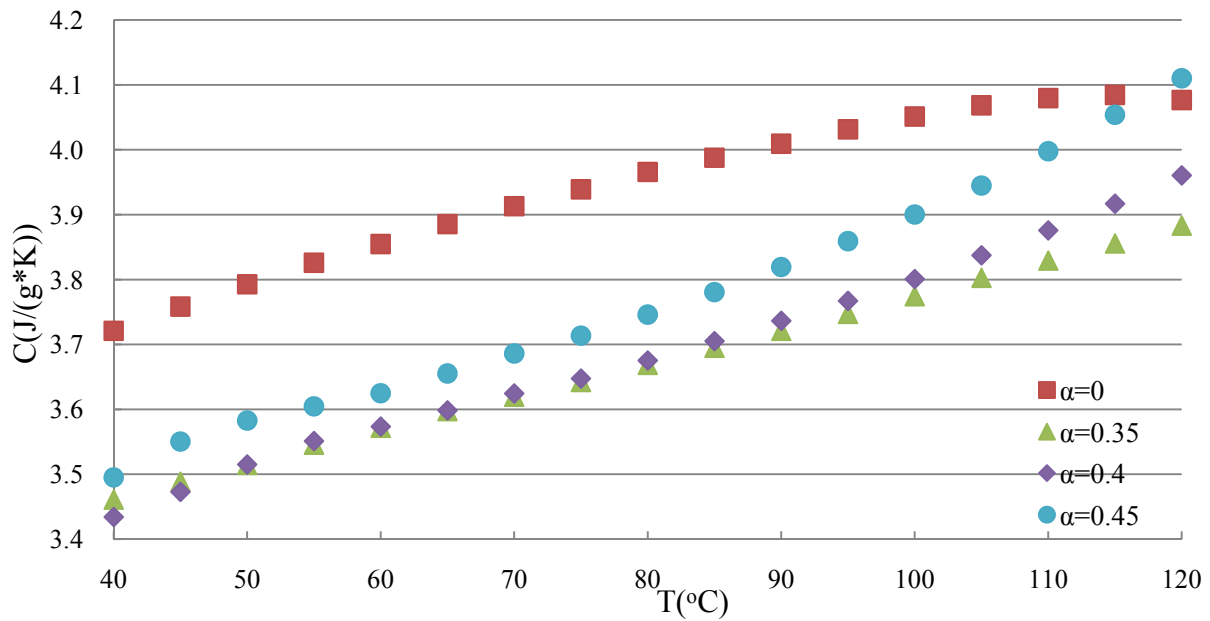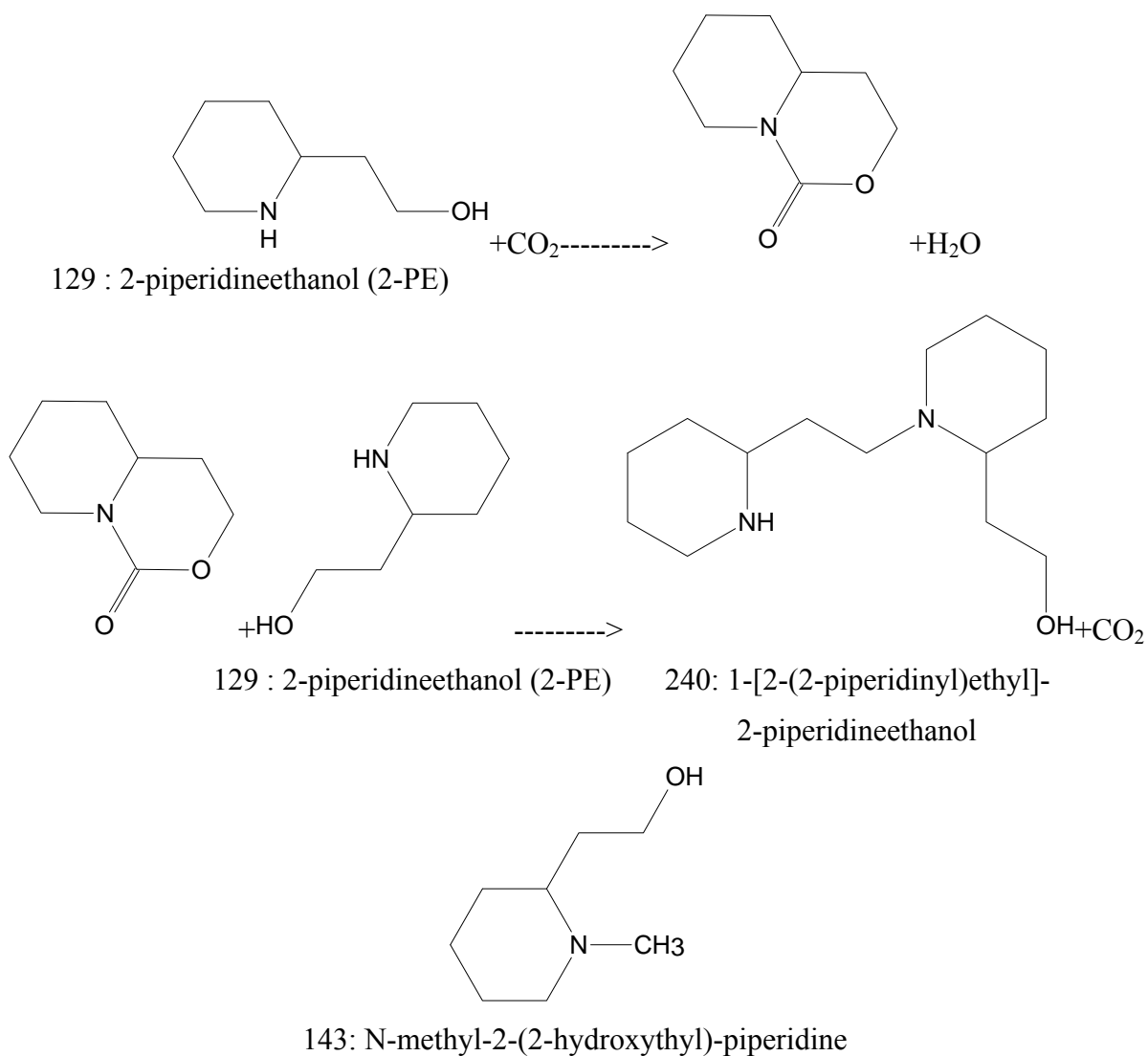**Figure 3: Apparent heat capacity of 12 m EDA, MEA, and PZ**

Figure 4: C_p of 12 m EDA plotted on a CO_2-free basis

Figure 5 is a typical cation chromatogram of a thermally degraded 2-PE sample. This chromatogram has been smoothed by subtracting out the response of a blank. The main contents in the sample are labeled by the molecular weight from IC/MS. 129 stands for 2-PE. The retention time of 2-PE is about double that of MEA. This may be due to the larger molecular weight. 143 is presumed to be N-methyl-2-(2-hydroxyethyl)-piperidine, one of the expected side products in the 2-PE production process (Meagher, 2000). It also appears in the chromatogram of the fresh solution, but does not grow in the degraded samples. 240 is the main degradation product which can be seen from cation IC. Compared with the degradation products of 2-piperidine methanol (2PD) (Davis, 2009), 240 is probably the dimer of 2-PE, 1-[2-(2-piperidinyl) ethyl]-2-piperidineethanol. The retention time of this species is longer than that of diamine with smaller molecular weight. The structures of these molecules and probable reaction paths are shown below. 99 and 210 are the products that appeared in heavily degraded samples. These two molecules are still not identified.
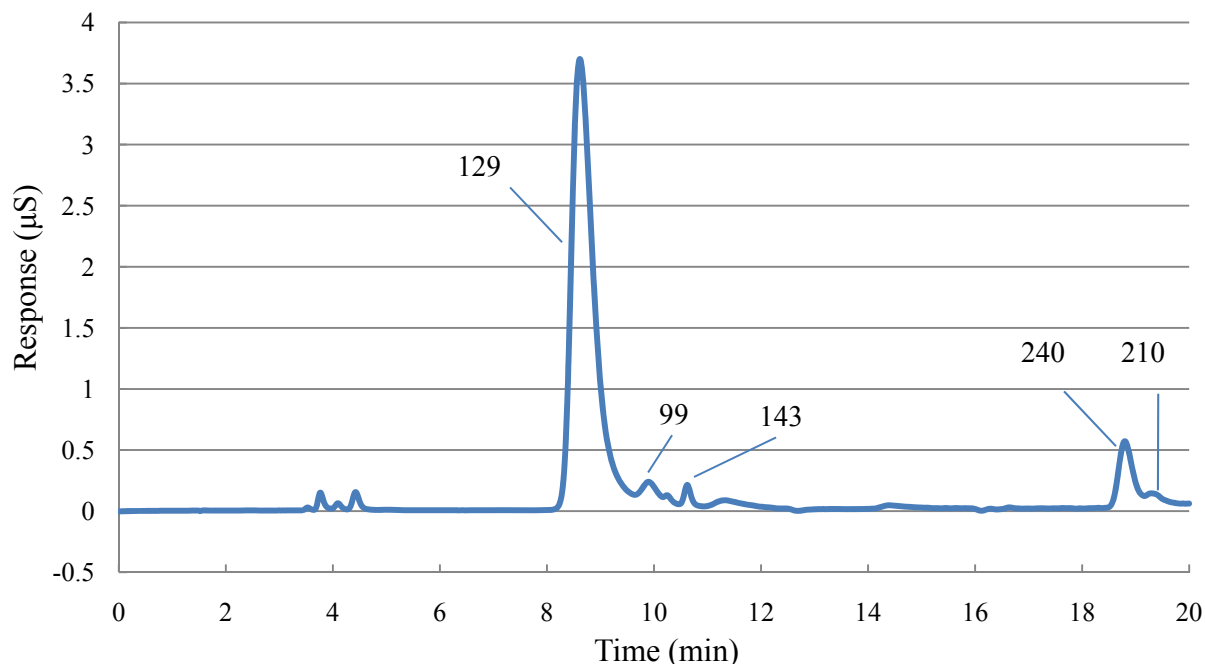

129 : 2-piperidineethanol (2-PE) $+CO_2$---------> $+H_2O$

129 : 2-piperidineethanol (2-PE)   ---------> 240: 1-[2-(2-piperidinyl)ethyl]-2-piperidineethanol $+CO_2$

143: N-methyl-2-(2-hydroxythyl)-piperidine

Figure 5: Cation chromatogram of thermally degraded 2-PE, α=0.4, T=135 $^{\mathrm{o}}$C, t=8 weeks

Figure 6 shows 2-PE remaining in thermal degradation experiment. 2-PE loss is significant in thermal degradation at 135 $^{\mathrm{o}}$C and 150 $^{\mathrm{o}}$C, but the degradation rate is slower than MEA and EDA. About 24% 2-PE was lost after 4 weeks at 135 $^{\mathrm{o}}$C. This value for MEA is 37% (Davis, 2009). However, colloidal suspension appeared in the thermally degraded 2-PE samples at 135 $^{\mathrm{o}}$C and 150 $^{\mathrm{o}}$C. The colloidal suspension blocked the thermal bombs when samples were poured into vials and stayed on the top of clear solutions. Clear solutions at the bottom were sampled, diluted, and analyzed in cation IC. The dimer of 2-PE is the main product on cation IC. Other 2-PE molecules can go on to combine with the dimer 2-PE. The colloidal suspension may be a polymerization product of 2-PE.

Piperazine has a foaming problem after degradation although it degraded insignificantly (Rochelle et al., 2008). 2-PE is a cyclic compound like PZ. The degradation product of 2-PE may also cause the foaming problem.
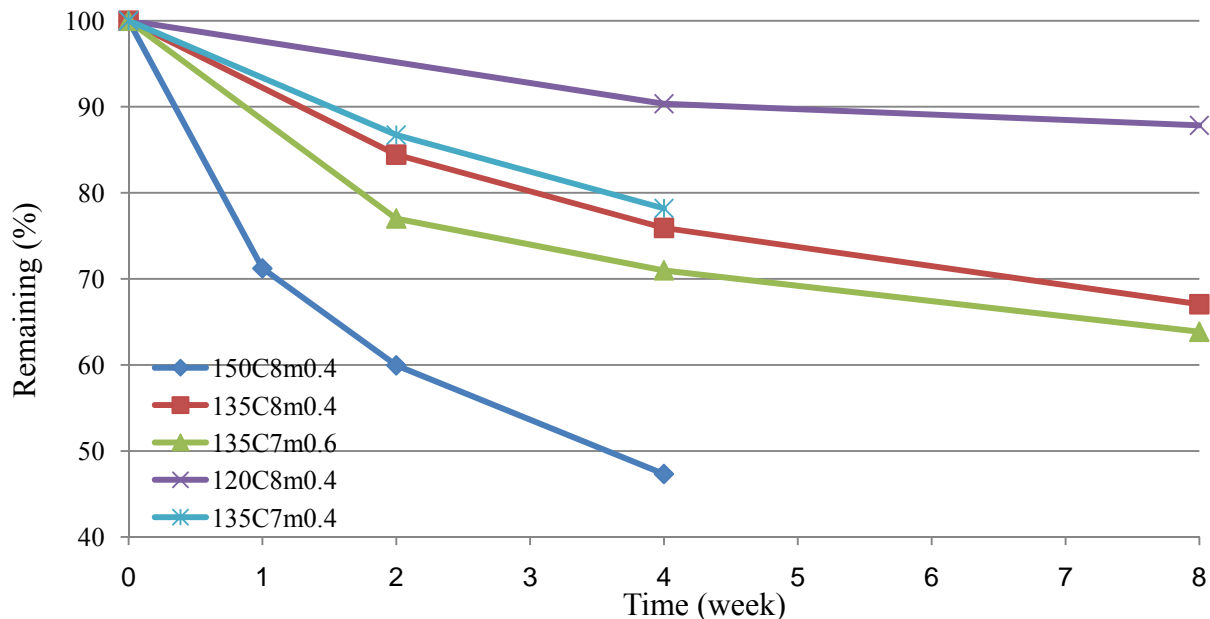
Figure 6: 2-PE remaining in thermal degradation experiment

Conclusions

Normalized density of EDA solution is not a strong function of amine concentration, and can be predicted only using CO_2 concentration.

Metal concentrations in EDA samples are much higher than those in PZ and about twice those of MEA. EDA may have a corrosivity problem.

The C_p of loaded 12 m EDA is lower than that of 8 m PZ and 7 m MEA. High amine concentration with high loading helps to reduce the sensible heat requirement.

8 m 2-PE thermally degrades slower than 7 m MEA and EDA, but much more significantly than PZ. Dimer of 2-PE is the main thermal degradation product. There is colloidal suspension in thermally degraded 2-PE samples.

Future Work

A new series of thermal degradation experiments is being performed. The tested amine is 1,2-Diaminopropane, which has one more methyl group than EDA. This new amine will be compared with EDA.

References

Davis J. *Thermal Degradation of Amines Used in Carbon Dioxide Removal Applications*. The University of Texas at Austin. Ph.D. Dissertation. 2009.

Freeman S et al. "Carbon dioxide capture with concentrated, aqueous piperazine" *Energy Procedia*. 2009;1:1489–1496.

Hikita H, Asai S, Ishikawa H, Honda M. "The kinetics of reactions of carbon dioxide with monoisopropanolamine, diglycolamine and ethylenediamine by a rapid mixing method." *Chem Eng J*. 1977;14:27–30.

Jensen A, Christensen R. "Studies on Carbamates XI the Carbamate of Ethylenediamine." *Acta Chem Scand*. 1955;9(3):486–492.

Li J. Henni A, Tontiwachwuthikul P. "Reaction kinetics of CO_2 in aqueous ethylenediamine,

ethyl ethanolamine, and diethyl monoethanolamine solutions in the temperature range of 298–313K, using the stopped-flow technique." *Ind Eng Chem Res.* 2007;46:4426–4434.

Meagher, Timothy P. "Processes for preparing 2-piperidineethanol compounds" PCT Int. Appl. (2000), WO 2000012476 A1 20000309.

Rochelle GT et al. "CO_2 Capture by Aqueous Absorption, First Quarterly Progress Report 2009." Luminant Carbon Management Program. The University of Texas at Austin. 2009a.

Rochelle GT et al. "CO_2 Capture by Aqueous Absorption, First Quarterly Progress Report 2009." Luminant Carbon Management Program. The University of Texas at Austin. 2009b.

Sada E, Kumazawa H, Butt MA. "Absorption of carbon dioxide into aqueous solutions of ethylenediamine: Effect of interfacial turbulence." *Chem Eng J.* 1977;13:213–217.

Sada E, Kumazawa H, Han ZQ. "Kinetics of Reaction between carbon dioxide and ethylenediamine in non-aqueous solvents." *Chem Eng J.* 1985;31:109–115.

Sharma MM. "Kinetics of reactions of carbonyl sulphide and carbon dioxide with amines and catalysis by Brönsted bases of the hydrolysis of COS." *Trans Faraday Soc.* 1965;6:681–688.

Trass O, Weiland RH. "Absorption of carbon dioxide in ethylenediamine solutions II. Pilot Plant Study of Absorption and Regeneration". *Can J Chem Eng.* 1971;49:773–781.

Weiland RH, Trass O. "Absorption of carbon dioxide in ethylenediamine solutions I. Absorption kinetics and equilibrium." *Can J Chem Eng.* 1971;49:767–772.

Degradation of Amine Solvents for Carbon Capture

Abstract

The degradation of MEA was carried out in two successive steps to represent absorber and stripper conditions. Amine loss was 17.4% after 13 days at 135 ^{o}C, before being transferred to the oxygen environment at 55 ^{o}C. Degradation in this environment was initially 1.8%/week, but dropped off steeply to 0.3%/week by the third week. These rates were consistent with previous thermal (Davis, 2009) and oxidative (Sexton, 2008) degradation work.

The reaction of monoethanolamine (MEA) with formate to form N-formyl-ethanolamine was studied at temperatures of 55–130 ^{o}C. The activation energy of this reaction was determined to be 48±6 kJ/mol

Samples from an industrial CO_2 capture process were analyzed for heat stable salts (HSS). The lean solution contained 11 mM of total HSS (glycolate and formate were the highest, with 6 and 3 mM, respectively). The reclaimer waste contained 326 mM of HSS and their respective amide derivatives (N-carboxyl-ethanolamine). Formate and N-formyl-ethanolamine were found at concentrations of 64 mM and 170 mM, respectively.

Dissolved chromium was found to catalyze oxidation of MEA in the high gas flow apparatus. Degradation occurred at an average rate of 0.48mmol/kg/hr and was unaffected by Cr concentration (0.01–1 mM). Equimolar addition of EDTA reduced the degradation rate by 50%.

The thermal degradation rate of 7 m MEA was the same in the presence of formate and formamide as in the neat solution. The loss of MEA was consistent with Davis' data for thermal degradation of MEA.

Introduction

Solvent degradation is a serious problem for many carbon capture systems employing amine absorption/stripping technology. It can contribute to loss of capacity and corrosion, which increase operating costs and reduce the life of the plant. Degradation can be divided into two main categories: oxidative degradation, which occurs primarily in the absorber packing and sump (due to the presence of oxygen), and thermal degradation, which occurs primarily in the stripper, cross exchanger and reboiler (due to elevated temperature).

The oxidative degradation mechanism for MEA is not fully understood, although several pathways have been proposed (Petryaev et al., 1984; Chi and Rochelle, 2002). Oxidative degradation is understood to occur in the presence of dissolved metals (Blachly and Ravner, 1965), and contribute to the formation of heat stable salts (HSS) in solution (Rooney, 1998) and ammonia (Goff, 2005). Oxidative degradation has also been shown to lead to the formation of the N-carboxyl-ethanolamine derivatives of these HSS (Sexton, 2008). The HSS and amide derivatives should exist in equilibrium with one another, although it is unclear where this equilibrium lies or which species is the primary degradation product (equation 1).

$$OH\text{-}CH_2\text{-}CH_2\text{-}NH_2 + \text{-}OOC\text{-}R \leftrightarrow OH\text{-}CH_2\text{-}CH_2\text{-}NH\text{-}OC\text{-}R \qquad (1)$$

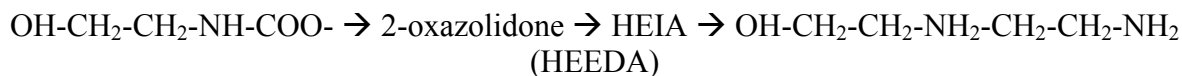R = H (formate)
R = CH_3 (acetate)
R = COO- (oxalate)
R = CH_2-OH (glycolate)
R = CO-NH-CH_2-CH_2-OH (N-oxamyl-ethanolamine)

Factors which enhance oxidative degradation include:
- High temperature
- High oxygen mass transfer
- High solvent concentration
- High metals concentrations

Thermal degradation occurs by a polymerization pathway, which has been thoroughly studied. In the proposed mechanism, MEA carbamate attacks itself to form the cyclic, five-membered 2-oxazolidone by dehydrolysis of the carboxyl group. This intermediate can in turn react to form 1-(2-hydroxyethyl)-2-imidazolidone (HEIA), another cyclic molecule. HEIA can be hydrolyzed to N-(2-hydroxyethyl)-ethylenediamine (HEEDA), a dimer of MEA, and CO_2 (Polderman, 1955).

$$OH\text{-}CH_2\text{-}CH_2\text{-}NH\text{-}COO\text{-} \rightarrow 2\text{-}oxazolidone \rightarrow HEIA \rightarrow OH\text{-}CH_2\text{-}CH_2\text{-}NH_2\text{-}CH_2\text{-}CH_2\text{-}NH_2$$
$$(HEEDA)$$

HEEDA can go on to react by the same mechanism to form trimer and quatromer degradation products. Many of these products have been identified in thermally degraded samples by LCMS and ICMS. In addition, this polymerization pathway has been shown to occur only at temperatures above 100 ^{o}C, and is significant only above 120 ^{o}C (Davis, 2009).

Factors which enhance thermal degradation include:

- High loading
- High temperature
- High solvent concentration

Analytical Methods

Amide reversal

Anion chromatography was used to quantify heat stable salts formed during oxidative degradation. This method can also be used to quantify amides (presumed to be of the form N-carboxyl-MEA). Degraded samples were treated 2:1 (v/v) with a solution of 5 N sodium hydroxide and allowed to react for 24 hours. This hydrolizes the amide, converting it to the corresponding carboxylate anion, which can be detected by anion chromatography.

$$OH\text{-}CH_2\text{-}CH_2\text{-}NH\text{-}OC\text{-}R + NaOH(xs) \rightarrow OH\text{-}CH_2\text{-}CH_2\text{-}NH_2 + \text{-}OOC\text{-}R$$
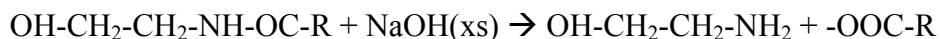
Carboxylate/N-Carboxyl-MEA Equilibrium

The equilibrium of MEA and carboxylate degradation products was studied by reacting MEA with the carboxylic acid at various temperatures. The reaction was carried out in a make-shift reactor comprised of ½-inch stainless steel (SS-316L) tubing cut to 10 cm lengths and capped. The stainless steel tubes were then placed in either a convection oven or a water bath. The contents of the tube remained sealed during exposure to high temperature. In this work, all variables except temperature were kept constant. The solution was 7 m MEA at 0.2 loading, with 0.1mols of formate (added as formic acid) per mol of MEA. The reaction was assumed to be of the form:

$$\frac{c_A - c_{A,eq}}{c_{A,i} - c_{A,eq}} = \exp\left(-ktc_{A,eq}\right)$$

$$\ln(k) = a + b/T$$

c_A = Concentration of species A
$c_{A,eq}$ = Equilibrium concentration of species A
$c_{A,i}$ = Initial concentration of species A
k = Temperature dependent reaction rate constant
t = Time

Single-Cycle Experiment

In the single-cycle experiment, an amine was degraded thermally for a sufficient period of time to achieve significant thermal degradation (10–20% amine loss). The degraded amine was then placed in a reactor (low gas flow system) and degraded oxidatively in 98% oxygen and 2% CO_2 at 55 ^{o}C. The purpose of this experiment was to determine the fate of thermal degradation products when they are cycled back to the stripper, and study any other synergies that exist between the two degradation regimes. Samples were taken prior to thermal degradation, after 13 days of thermal degradation, and at regular intervals over 25 days of oxidative degradation.

LCMS and HPLC

An analytical method for identifying unknown degradation products by LCMS was developed this quarter. The instrument employed is a reverse phase liquid chromatogram, which uses a water-methanol-acetonitrile mobile phase and a C-18 stationary phase. The program ramps the methanol concentration from 2%v. to 100%v.

The HPLC and LCMS instruments both use essentially the same method. The key difference is that the HPLC uses an evaporative light scattering detector, while the LCMS has a UV detector. The machine detects the absorbance at 3 wavelengths (230, 254, and 280nm) as well as the total UV absorbance.

The mass spectrometer program was developed by Jason Davis (2009). The program will register any mass between 50 and 300 Daltons, and has a resolution of 0.7 Daltons.

Previous Analytical Methods

Table 1: Summary of Previous Analytical Methods for Degradation

Method	Analyte (s)
Total inorganic carbon (by phosphoric acid release)	Dissolved carbon dioxide
Cation chromatography	Amines (ethanolamine, ethylene diamine, piperazine, etc.)
	Thermal degradation products (MEA-oxazolidone, MEA-urea)
Anion chromatography	Organic carboxylic acids (Formate, oxalate, glycolate, acetate)
	Amides (Formamide, oxalamide, glycolamide, acetamide)
	Inorganic salts (Nitrates, nitrites, sulfates, chloride)
Cation chromatography mass spectroscopy	Unknown cation degradation products
Titration	Total alkalinity $\approx$ amine concentration, exact for unloaded neat solns
High pressure liquid chromatography	Hydroxyethyl imidazole, N-formyl-ethanolamine (MEA-formamide), 1-(2-hydroxyethyl)-2-imidazolidone (HEIA)
Fourier transform infrared (FTIR) analyzer	Gas phase degradation products (ammonia, N_2O, NO_x)
	Gas phase inerts (water, carbon dioxide)
	Other gas phase components (including not limited to methane, ethylene, formaldehyde, acetaldehyde, methanol, methylamine)

Previous Experimental Methods

The low gas flow reactor was used for conducting oxidative degradation experiments. In this system, 350 mL of amine solution was loaded into a glass jacketed reactor. The reactor was heated to 55 ^{o}C and stirred at 1450RPM. Oxygen (98%) and carbon dioxide (2%) were fed to the head space in the reactor at a rate of 100 mL/min. The gas exits around the gap where the agitator passes through the stopper.

The high gas flow reactor is similar to the low gas system in that the temperature, solution volume, and agitation rate are all the same. However, the gas rate and makeup are different—they are 6.5LPM and 20.5% oxygen. In addition, the HGF system is connected to an FTIR analyzer for continuous gas-phase analysis.

Results

Analysis of a Pilot Plant Solution

A solution of aqueous ethanolamine from a carbon dioxide absorption/stripping process was analyzed for amine content, loading, and HSS concentrations. The reported conditions of the process are given in Table 2 below.

Table 2: Relevant Pilot Plant Process Conditions

Stripper Bottom Temperature (^{o}C)	86.1
Rich Amine Temperature (^{o}C)	52.2
Solvent Rate (LPM)	2760
Solvent Inventory (L)	68040
MEA Concentration (wt %)	16

MEA concentration of the lean solution leaving the stripper and the reclaimer bottoms (waste) were analyzed by cation chromatography. The calibration curve is shown below.
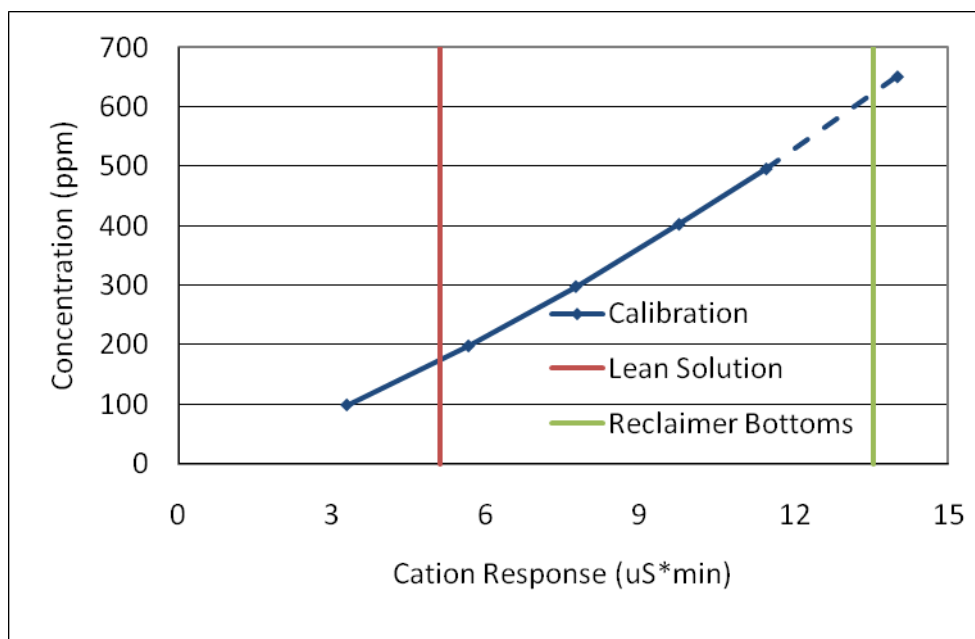

Figure 1: Calibration of MEA on Cation Chromatography

Table 3: Cation Analysis of a Field Sample

Sample Name	Area (uS*min)	Concentration (ppm)
100 ppm	3.287	98.9
200 ppm	5.653	198.2
300 ppm	7.743	297.9
400 ppm	9.751	402.6
500 ppm	11.447	495.9
Lean	5.084	173.7
Reclaimer Waste	13.535	621.5

Total inorganic carbon was assessed by elution of carbon dioxide by treatment with phosphoric acid. The calibration curve for this method is shown below.
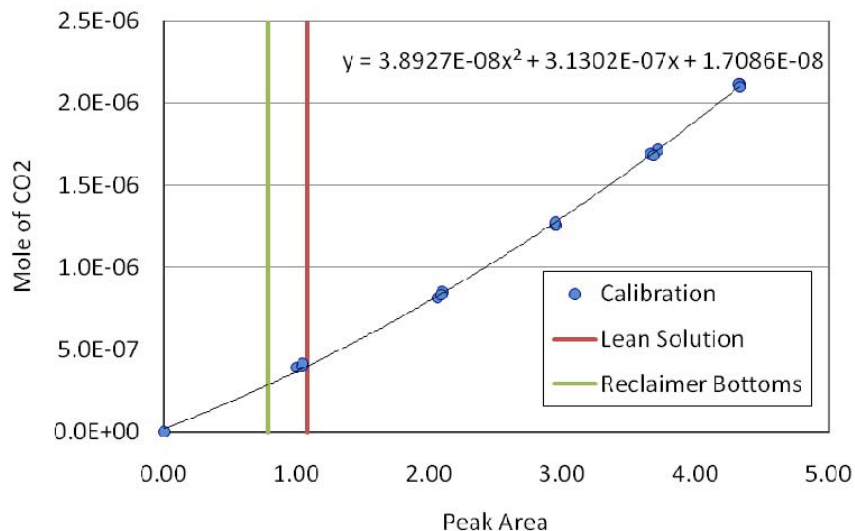

Figure 2: Calibration Curve for Total Inorganic Carbon

The solution was also analyzed via titration with sulfuric acid. The endpoint volume of sulfuric acid was used to determine the weight fraction of MEA in the sample. The cation chromatography analysis is more accurate because it involves direct analysis of the component of interest, whereas other acids or bases in solution can interfere with the titration analysis.

Table 4: Field Sample Lean Solution Composition by Weight

Component	Lean Solution (wt. frac)	Reclaimer Waste
CO_2	0.0930	0.0148
MEA	0.1737	0.6215
Water	0.7333	0.3637
MEA by titration	0.1470	0.6031

Concentrations of all heat stable salts in the lean solution were very low: formate, formamide, and glycolate were the only salts present in significant quantities. The reclaimer waste, however, contained high concentrations of several degradation products, most prominently formate and formamide.
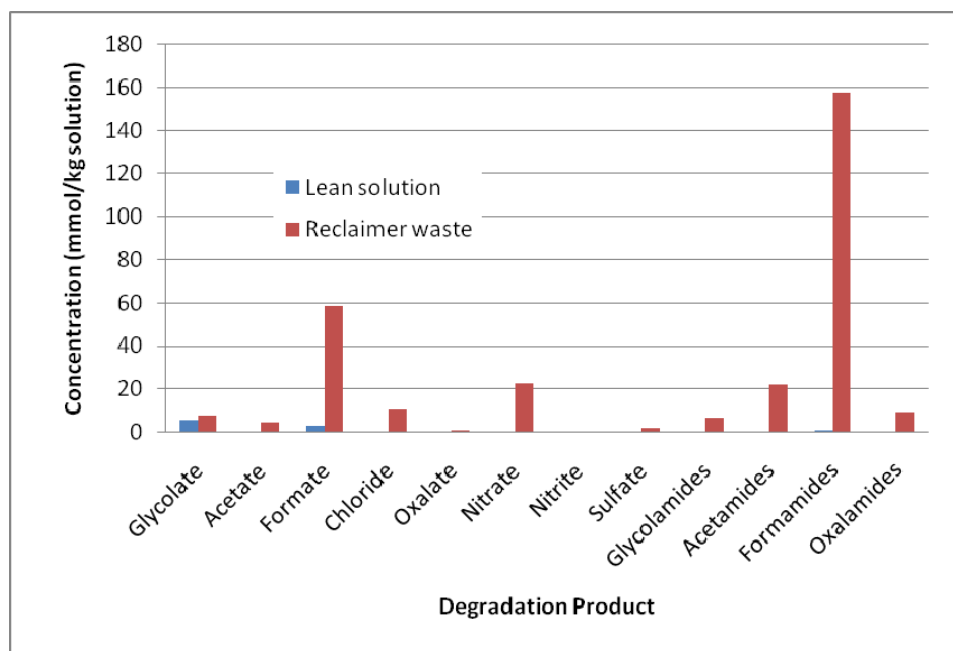
Figure 3: Heat Stable Salt Concentrations in Field Sample
Table 5: HSS in Field Sample (mmol/kg solution)

	Lean	Reclaimer
Glycolate	5.83	7.59
Acetate	0.00	4.72
Formate	2.86	58.61
Chloride	0.32	10.36
Oxalate	0.39	1.03
Nitrate	0.42	22.77
Nitrite	0.10	0.19
Sulfate	0.08	1.96
Glycolamides	0.00	6.68
Acetamides	0.00	21.86
Formamides	0.79	157.51
Oxalamides	0.02	9.46

Single Cycle Experiment

Results are presented from an experiment where MEA was thermally degraded for 13 days at 135 °C. MEA loss occurred at a rate comparable to that in Sexton's experiments. The rate of oxidative degradation of the thermally degraded solution was found to be more than that of neat solution with 1 mM Fe added, but less than that of experiments conducted by Sexton in the presence of Cr and Ni or Cu and Fe. Analysis of metals in solution by atomic absorption found 23 mM Fe, 4.8 mM Cr, and 6.9 mM Ni. Neat MEA was degraded in the presence of these metals ("High Metals") in an attempt to separate the effects of thermal degradation on oxidative degradation from that of the catalyst concentration. Significant quantities of metals were observed to precipitate in this solution. The degradation rate of the high metals experiment was

less than that of the single cycle experiment. This suggests that some of the MEA loss is due to a synergistic effect of thermal degradation.

Table 6: Single Cycle Experiment Operating Conditions

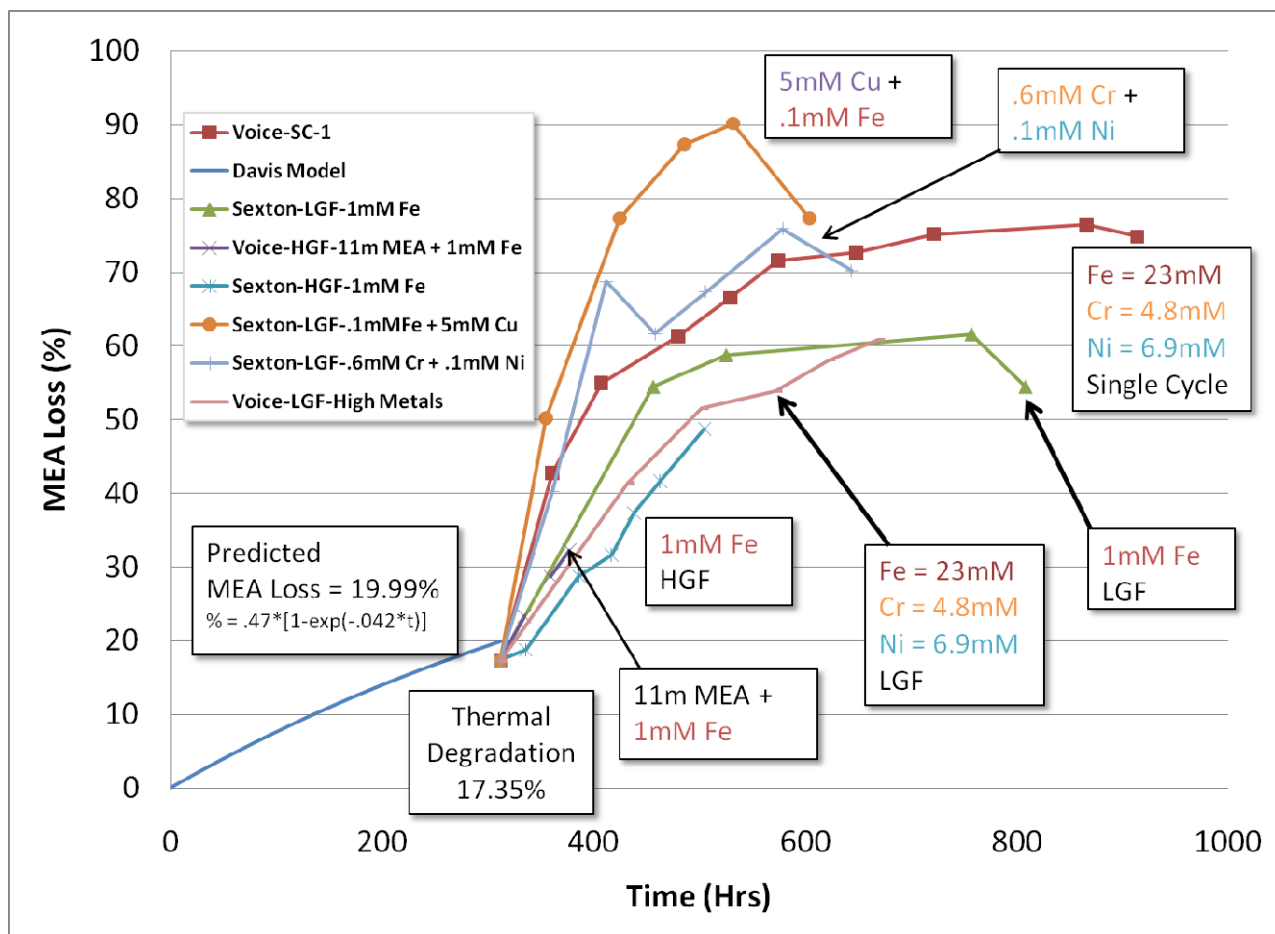|	Thermal Degradation	Oxidative Degradation
Temperature	135 ^oC	55 ^oC
CO_2	0.4 loading	2% CO_2 in 98% O_2
Time	13 Days	25 Days
Apparatus	10 ml SS316 Cylinder	LGF Apparatus
Solution	7 m MEA	Thermally degraded MEA

Figure 4: Comparison of Low Gas Flow Experiments with Single-cycle (SC-1) Experiment

Table 7: MEA Oxidative Degradation Comparison

Voice-Single Cycle-7/09		Sexton-LGF-4/08		Sexton-LGF-7/08		Sexton-LGF-9/07	
Fe = 23 mM Cr = 4.8 mM Ni = 6.9 mM		Cr = 0.6 mM Ni = 0.1 mM		Fe = 0.1 mM Cu = 5 mM		Fe = 1 mM	
Time (Days)	Amine Loss (%)	Time (Days)	Amine Loss (%)	Time (Days)	Amine Loss (%)	Time (Days)	Amine Loss (%)

13.00	17.35	0.00	0.00	0.00	0.00	0	0.00
15.04	42.78	0.92	2.86	1.79	32.86	6.00	37.14
16.98	55.00	1.88	8.57	4.71	60.00	8.88	41.43
20.00	61.31	3.83	12.86	7.25	70.00	18.54	44.29
22.06	66.53	6.42	20.00	9.17	72.86	20.67	37.14
23.94	71.55			12.17	60.00		
27.02	72.67						
30.07	75.17						
36.08	76.44						
38.09	74.84						

Table 8: Thermal Degradation Estimate

Time (hrs)	Predicted Amine Loss (%) % Loss = .474*(1-e$^{-.0422*t}$)
0	0.00
10	0.83
35	2.83
70	5.48
100	7.63
140	10.33
190	13.45
250	16.84
312	19.99

Values are estimated from data in Davis, 2009 for
7 m MEA/0.4 loading/135 $^\circ$C

Samples from SC-1 were hydrolyzed and analyzed for HSS by anion chromatography. The result is displayed below along with data from a previous 7 m MEA/1 mM Fe low gas flow experiment (Sexton, 2008). The data show that production of formamide from the thermally degraded solution is significantly higher than in Sexton's experiment with 1 mM Fe. Production of oxalamide was also higher, although production of nitrite was significantly lower.
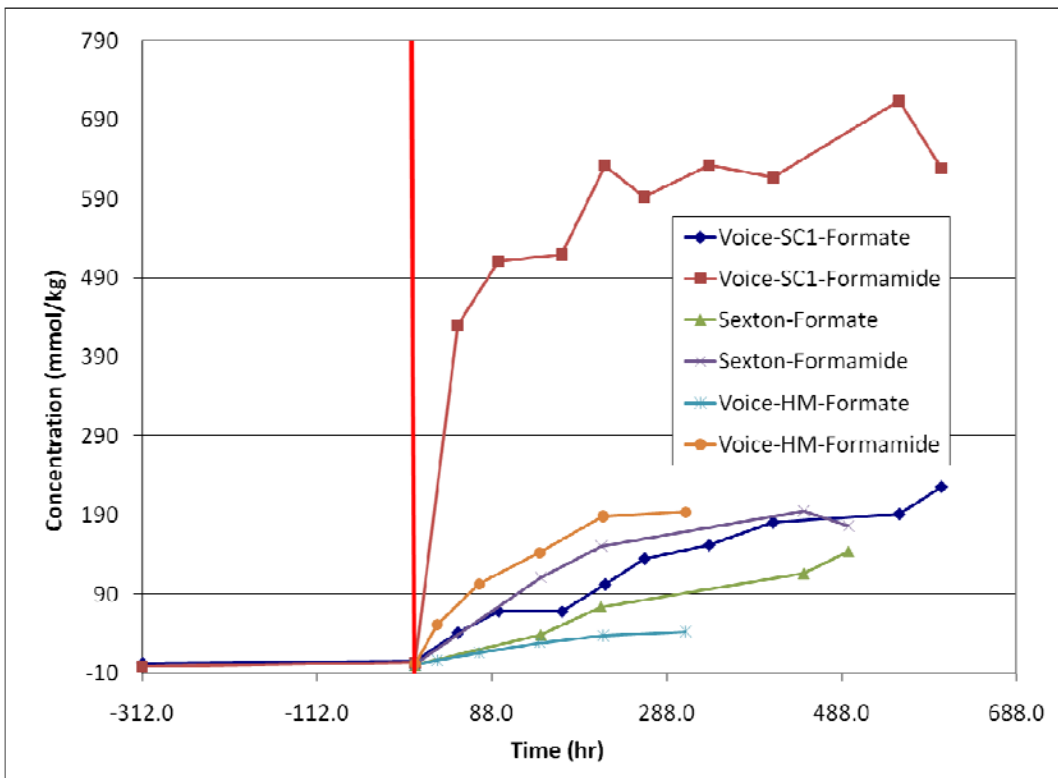
Figure 5: Production of Formate and Formamide in MEA solution in the LGF reactor at 55 °C following thermal degradation
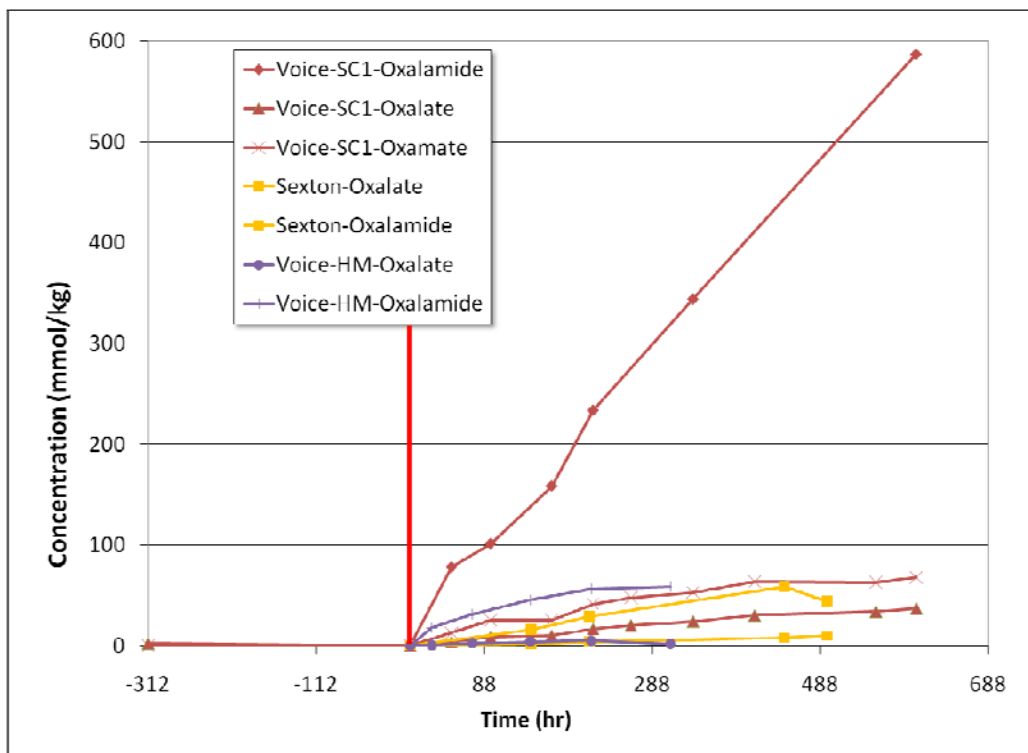

Figure 6: Production of Oxalate, Oxamate, and Oxamide in MEA solution in the LGF reactor at 55 °C following thermal degradation
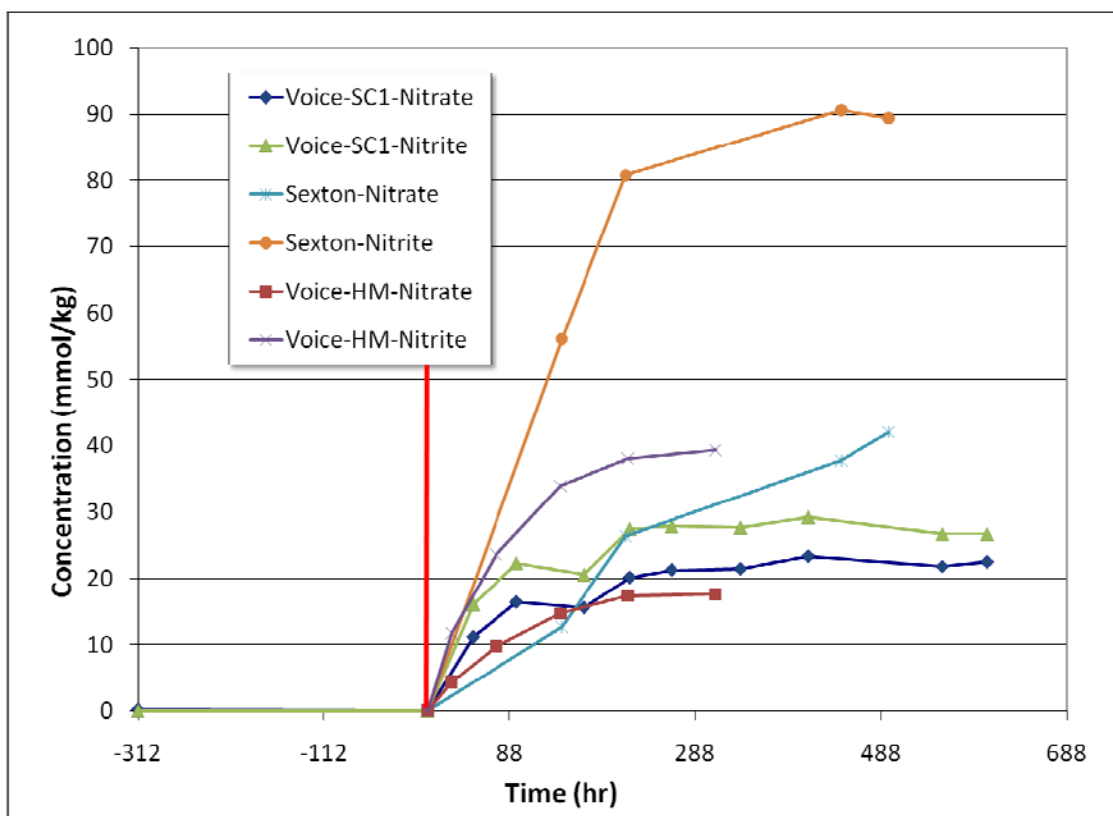
**Figure 7: Production of Nitrate and Nitrite in MEA solution in the
LGF reactor at 55 °C following thermal degradation**

Table 9: Production of Heat Stable Salts in thermally degraded 7 m MEA in LGF

Time (hrs)	Formamide (mmol/kg)	Formate (mmol/kg)	Oxalate (mmol/kg)	Oxamate (mmol/kg)	Oxalamide (mmol/kg)	Nitrate (mmol/kg)	Nitrite (mmol/kg)
-312.0	0	2	2	0	0	0	0
0.0	3	5	0	0	0	0	0
48.9	430	41	4	13	78	11	16
95.5	511	68	9	25	101	16	22
168.1	519	68	10	26	158	16	21
217.5	632	102	17	41	234	20	27
262.5	593	134	20	48		21	28
336.4	632	152	24	53	344	21	28
409.7	617	180	30	63		23	29
553.9	714	191	34	63		22	27
602.1	629	225	37	68	587	22	27

Table 10: Production of Heat Stable Salts in LGF with 22 mM Fe, 4.8 mM Cr, 6.9 mM Ni

Time	Formate	Formamide	Oxalate	Oxalamide	Nitrate	Nitrite
0.00	0	2	0	0	0	0
25.55	6	51	1	18	4	12

11

73.55	16	103	2	31	10	24
142.68	28	142	4	45	15	34
215.22	37	188	5	56	17	38
309.63	43	194	2	59	18	39

Table 11: 7 m MEA/1 mM Fe – LGF Experiment (Sexton, 2008)

Time (hrs)	Formamide	Formate	Oxalate	Oxalamide	Nitrate	Nitrite
0	1.26	0.44	0	0	0	0
144	110.99	38.44	1.65	16.2	12.66	56.12
213	150.82	73.69	3.98	29.14	26.36	80.76
445	195.5	115.8	7.94	58.62	37.76	90.59
496	176.19	143.57	10.06	44.34	42.03	89.39

Carboxylate/N-Carboxyl-MEA Equilibrium

Stainless steel reactors with 10 mL volume were used to react formic acid with ethanolamine at various temperatures. Formamide concentrations were evaluated by sodium hydroxide hydrolysis. The reaction is observed to reach equilibrium faster at higher temperatures. Data from four temperatures were used to calculate the activation energy of the reaction as 48±6kJ/mol.
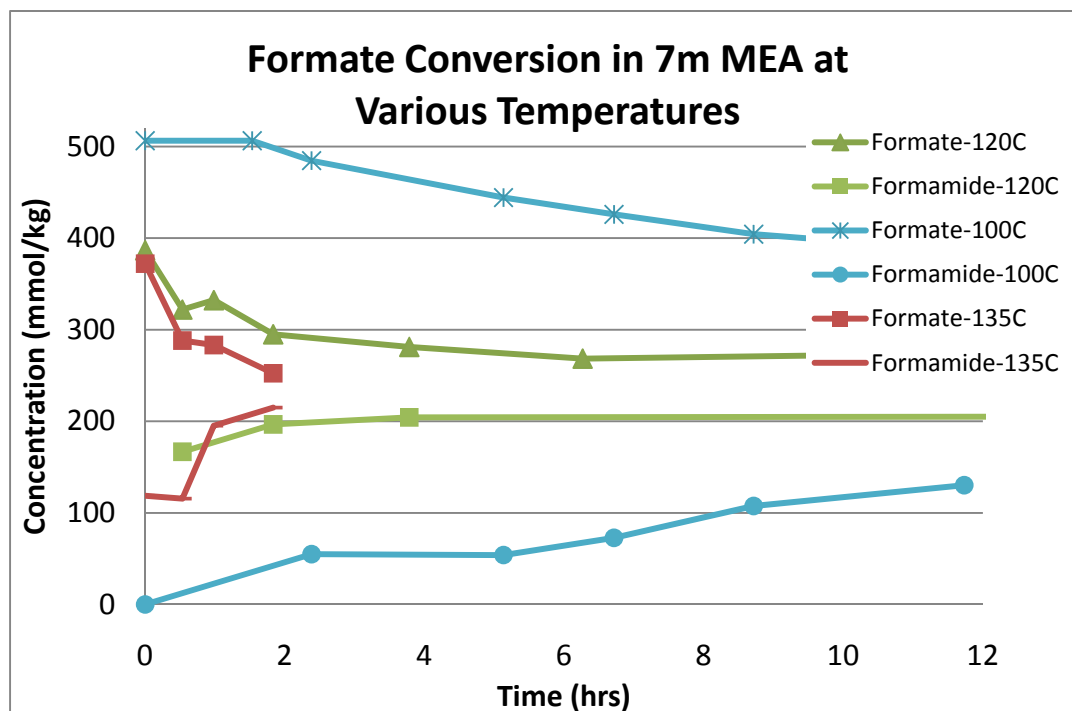

Figure 8: Conversion of Formate to Formamide at Different Temperatures

Table 12: Conversion of Formate to Formamide in 10 mL Stainless Steel Reactors at 55 and 100 °C

55 °C			100 °C		
Time (hours)	Formate	Formamide	Time (hours)	Formate	Formamide
0.00	666	85	0	506	0
25.55	656	196	1.53	506	
73.55	648	191	2.38	485	55
142.68	609	242	5.13	444	54
215.22	545	307	6.72	426	73
309.63	518	328	8.72	404	108
			11.73	386	130
120 °C			135 °C		
Time (hrs)	Formate	Formamide	Time (hrs)	Formate	Formamide
0	387		0.00	372	119
0.53	322	166	0.53	288	116
0.98	332		0.98	283	195
1.83	295	196	1.83	252	215
3.78	281	204			
6.27	268.4				
24.3	286.6	206			

Oxidative Degradation Catalyzed by Cr

MEA was degraded in the presence of 0.01–1 mM Cr in the high gas flow apparatus. The reactor is semi-batch: dry air and 2% CO_2 flow continuously through the batch of MEA. Water is fed directly to the reactor to make up water removed by the dry gas. Some evaporation and condensation occurs when the flow rates do not match, which results in a corresponding change in volatility. An equimolar addition of EDTA reduced the ammonia rate by 50%. Further addition of EDTA did not affect the NH_3 rate.
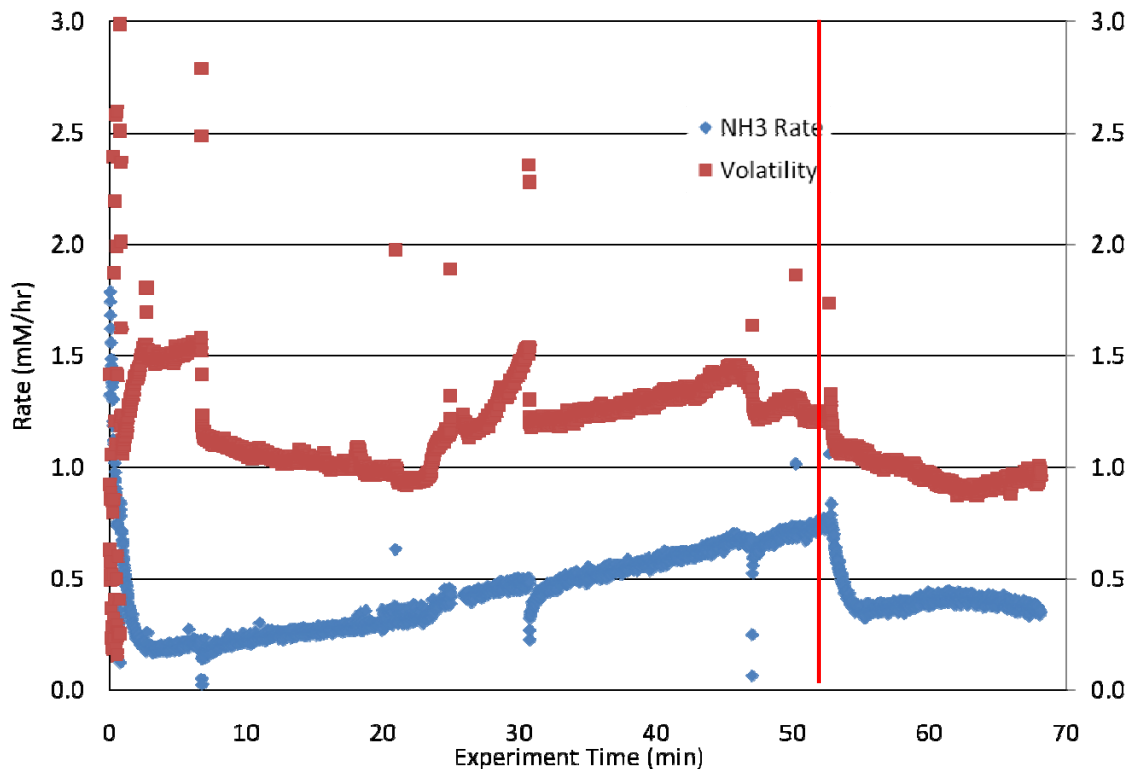
Figure 9: NH₃ and MEA production from 7 m MEA with Cr and EDTA in the High Gas Flow System. The red line indicates addition of equimolar EDTA.
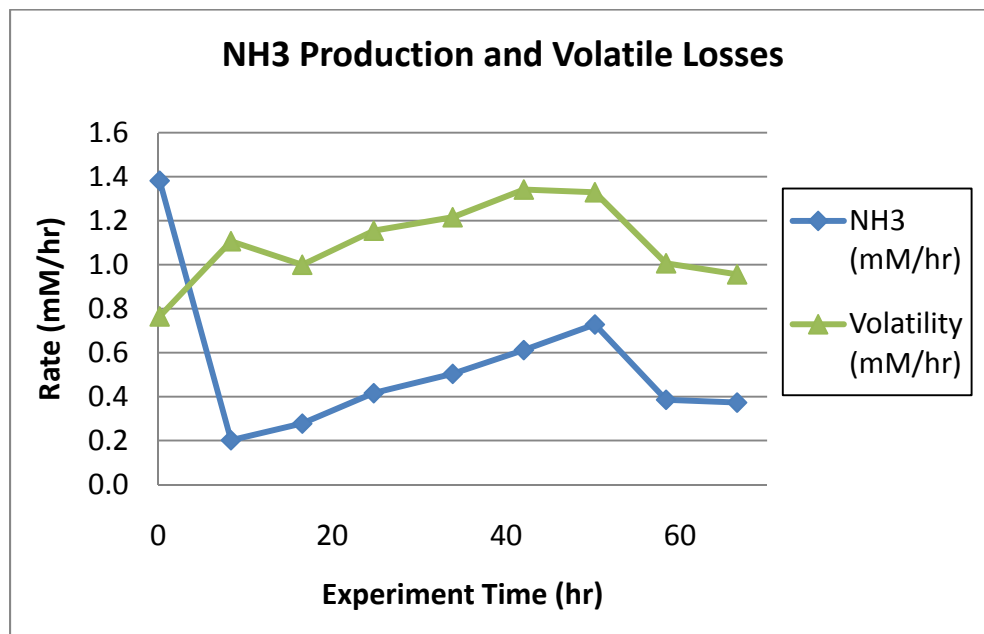

Figure 10: Selected data from Cr/EDTA experiment

14

Table 13: Selected Data from FTIR Gas Phase Analysis of MEA Degradation

Time (hr)	NH_3 (mM/hr)	Cum NH_3 (mM)	Volatility (mM/hr)	Cum Volatility (mM)
0.16	1.382	1.559	0.765	1.518
8.36	0.202	3.819	1.107	12.655
16.56	0.277	5.835	0.999	21.243
24.77	0.416	8.466	1.154	29.468
33.85	0.503	12.933	1.216	42.029
42.03	0.612	17.45	1.342	52.533
50.21	0.728	22.807	1.329	63.625
58.39	0.386	27.009	1.006	72.745
67.66	0.366	30.696	0.954	80.912

Formate Consumption in the HGF

Formate is converted to formamide in the presence of Inhibitor A in the HGF. The consumption of formate may match formamide production, although there is significant scatter in the data. MEA consumption is significantly greater than formamide production, and is higher than expected when formamide production, volatility, and degradation are considered.
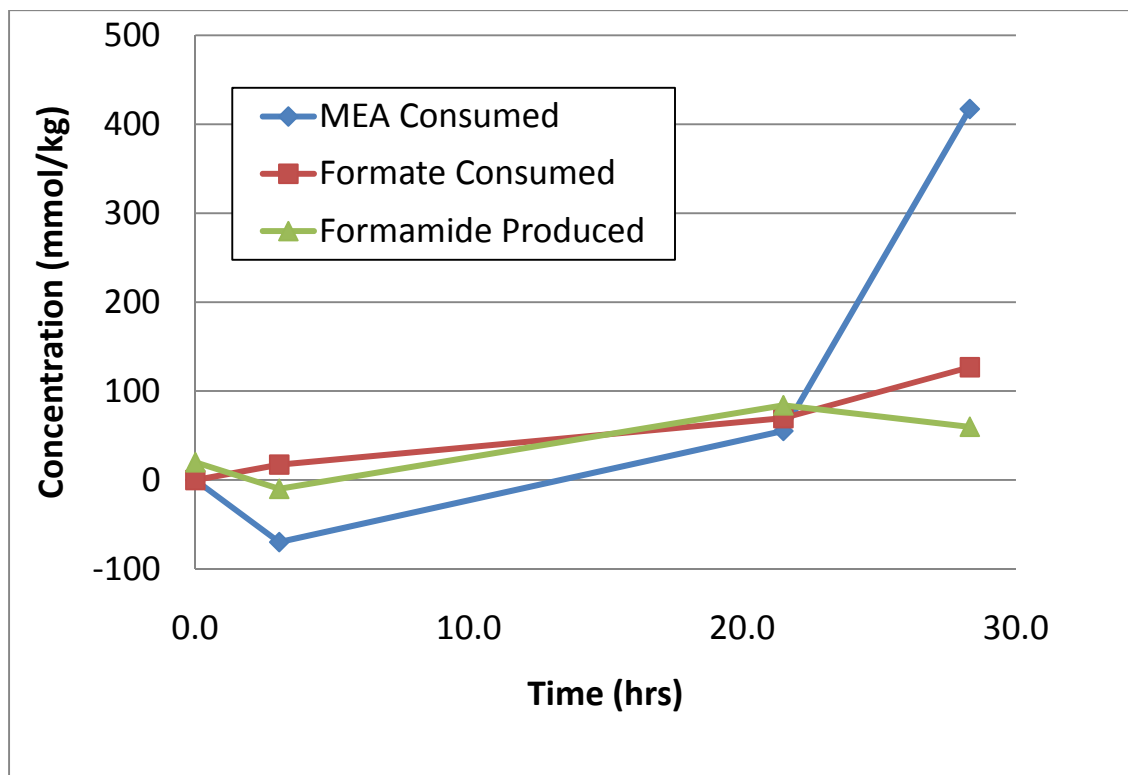

Figure 11: Formate Conversion in 7 m MEA/0.4ldg/0.1molCOO⁻/mol MEA

15

Table 14: Formate Conversion in 7 m MEA/0.4ldg/0.1molCOO⁻/mol MEA

Time	MEA Consumed	Formate Consumed	Formamide Produced
0.0	0	0	20
3.1	-70	17	-10
21.5	55	70	84
28.3	417	127	60

Thermal Degradation in the Presence of Additives

All four solutions appear to match Davis' experimental data for thermal degradation of 7 m MEA at 0.4 loading. There is no clear dependence of thermal degradation on formic acid or formaldehyde additives
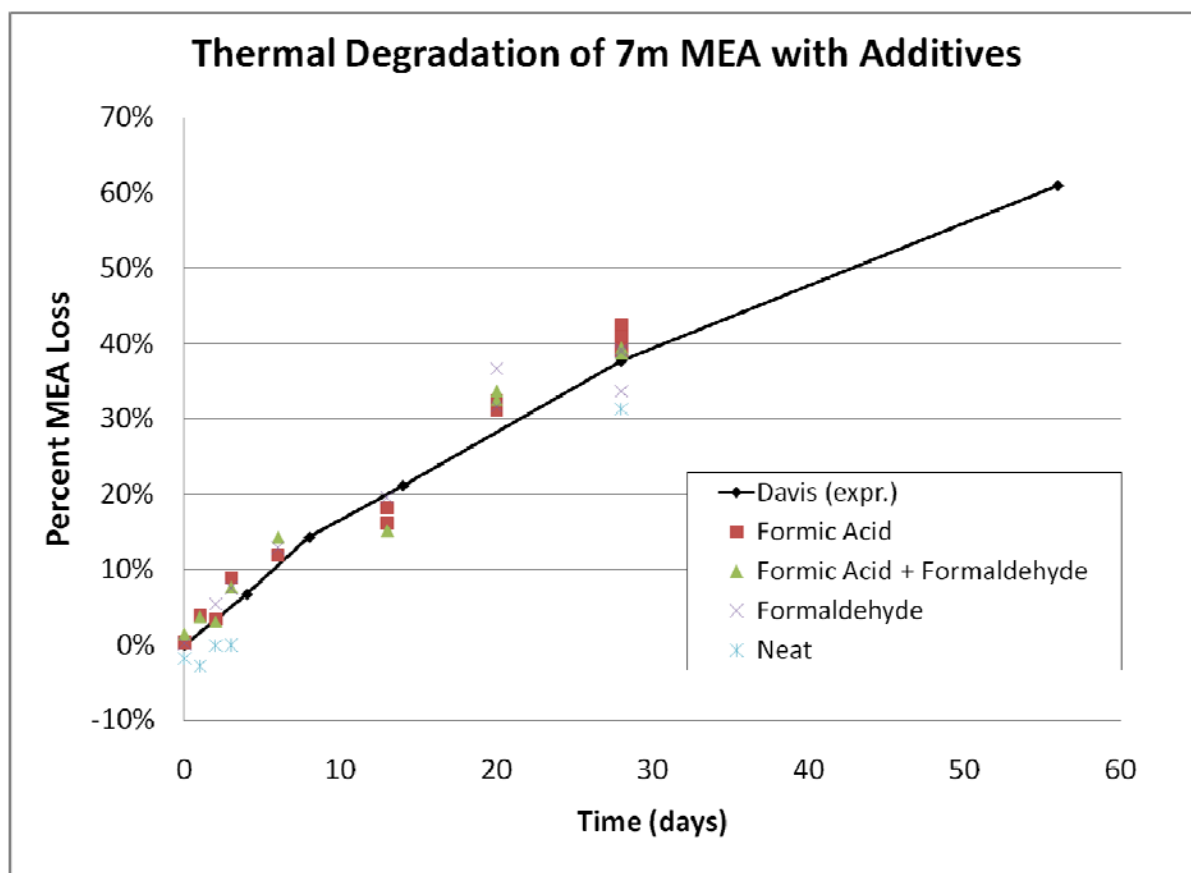
Figure 12: Metals in Thermally Degraded 7 m MEA/0.4ldg/135 °C with additives
Table 15: Metals in Thermally Degraded 7 m MEA/0.4ldg/135 °C with additives

Time (Days)	% MEA Loss				
	Davis, 7 m MEA, 0.4 ldg	Neat 7 m MEA, 0.4ldg	Formic acid	Formaldehyde	Formic acid and formaldehyde
0	0	-0.018	0.003	0.002	0.014
1		-0.028	0.039		0.037
2		-0.001	0.034	0.054	0.030

16

3		0.000	0.089	0.076	0.076
4	0.067143				
6			0.119	0.129	0.143
8	0.142857				
13			0.161	0.195	0.152
13			0.182	0.317	
14	0.211429				
20			0.311	0.367	0.325
20			0.324		0.337
28	0.377143	0.313	0.424	0.392	0.388
28			0.392	0.337	0.394
28			0.409	0.389	
56	0.61				

Iron concentrations in thermally degraded solutions are scattered, although a general trend emerges. Concentrations as high as 1000ppm are observed in some solutions. The amount of iron in the different samples does not appear to be a function of the additives.
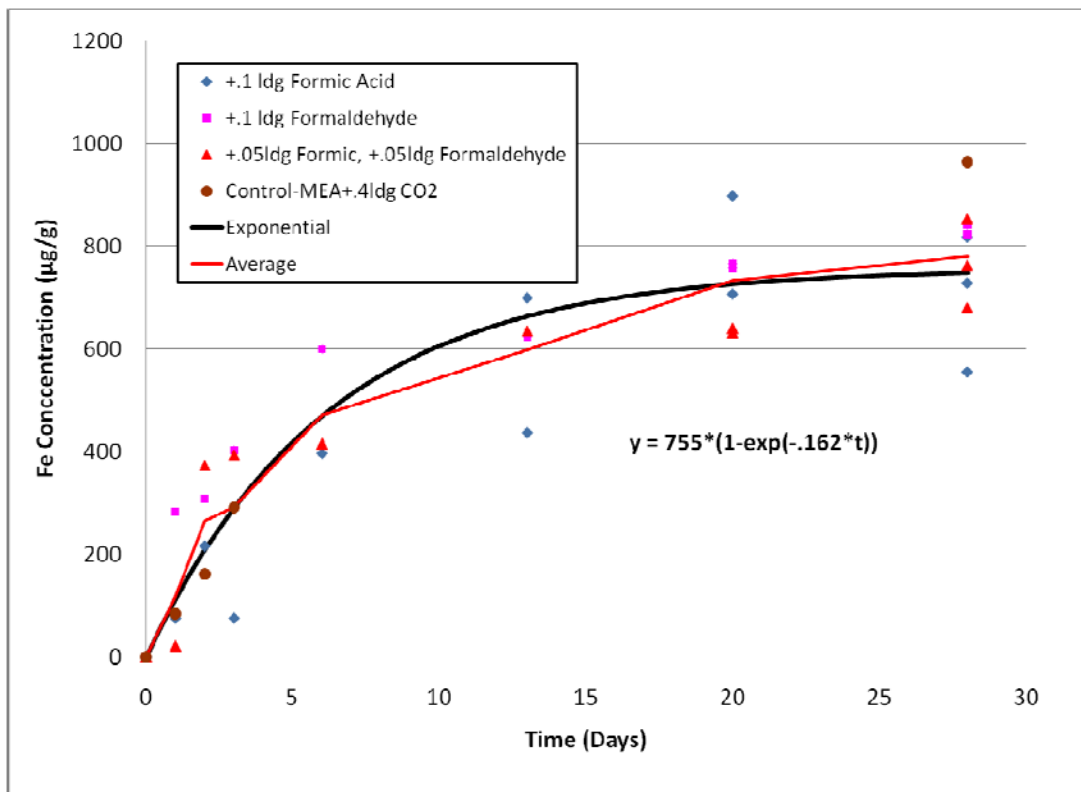

Figure 13: Iron in Thermally Degraded 7 m MEA with Various Additives at 135 ^{o}C /0.4ldg

Table 16: Iron in Thermally Degraded 7 m MEA with Various Additives at 135 ^{o}C /0.4ldg

Time (Days)	Neat 7m MEA, .4ldg	Formic acid	Formaldehyde	Formic acid and formaldehyde
0	0	0	0.0006	0.0006
1	0.0464	0.0422		0.0122

17

2	0.0808	0.1006	0.1204	0.1422
3	0.1226		0.1268	0.1466
4		0.0422		
6		0.1472	0.1486	0.1512
8				
13		0.1974	0.1832	0.1884
13		0.1554	0.1866	0.1878
14				
20		0.1984	0.2062	0.1892
20		0.2216		0.2166
28	0.2288	0.2124	0.205	0.1948
28		0.1762	0.2152	0.2056
28		0.2012	0.213	

A solution of 43.8 wt % proline was prepared. The solution was cooled from 55 $^{\circ}$C, and was observed to be soluble down to 4 $^{\circ}$C.

Table 17: Preparation of Aqueous Potassium Proline Solution

	Masses Added	Molar Concentration (mol/kg)	Weight %	Analysis	Notes
Proline	4.4175 g	3.806	43.8%	41.6%	10.12–12.8 molal*
Potassium Carbonate	2.663 g	2.2945	26.4%	TIC not analyzed	1.004 mol K+/ mol proline;
Water	3.0 mL	2.5849	29.8%		0.502 mol CO_2/mol proline

*Depending on speciation $2H^+ + CO_3^{2-} \rightarrow H_2O + CO_2$ and whether the gravimetric or titration amine concentration is used

Future Work

The liquid chromatography method requires further refinement. Future work will involve identifying unknown peaks, improving the resolution of early peaks, and achieving better detection. Unknown peaks will be qualified by injecting pure components and use of LCMS; better separation can be achieved by modifying the eluent gradient ramp and flow rate; detection may be improved by tuning the ELSD settings or using a different detector.

A method was developed for evaluating activity coefficients of CO_2 using FTIR. This method was convenient to develop due to experience working with the high gas flow reactor system, which will be used to take this measurement. Under the proposed method, the glass jacketed reactor will be charged with the amine solution of interest. CO_2 will then be sparged into the system; the reactor gas will be analyzed by FTIR. When the CO_2 concentration in the gas stream

stabilizes, N_2O will be sparged into the system, until the N_2O concentration in the reactor gas stabilizes. The equilibrium liquid phase N_2O can be determined by integrating the difference between N_2O observed in the gas phase during loading and the concentration at equilibrium.

Conversion of formate to MEA-formamide may be catalyzed by dissolved metals. Future experiments will explore this effect through the addition of $FeSO_4$ to MEA/formate solutions in glass reactors.

The field sample described in this report requires further analysis. Future analysis by LCMS and ICMS will be used to determine the existence, or lack thereof, of known and unknown degradation products. Samples from other pilot plants will be acquired for purposes of comparison.

Future degradation work will focus on repeating the results of SC-1 and identification of unknown peaks observed in this experiment. Additional amines will be tested in the HGF system to confirm the production of NH_3 or other gas phase oxidative degradation products (such as short chain alkylamines, NO_x, and N_2O. Finally, the viability of proline and other amino acids will be investigated through oxidative and thermal degradation screening.

References

Blachly CH, Ravner H. "Stabilization of Monoethanolamine Solutions in Carbon Dioxide Scrubbers". *J Chem Eng Data.* 1966**;**11(3):401–403.

Davis J. *Thermal Degradation of Amines Used in CO_2 Removal Applications*. The University of Texas at Austin. Ph.D. Dissertation. 2009.

Goff, G. *Oxidative Degradation of Aqueous Monoethanolamine in CO_2 Capture Processes: Iron and Copper Catalysis, Inhibition, and O_2 Mass Transfer.* The University of Texas at Austin. Ph.D. Dissertation. 2005.

Rochelle GT et al. *CO_2 Capture by Aqueous Absorption, First Quarterly Progress Report 2009.* Luminant Carbon Management Program. The University of Texas at Austin. 2008.

Rochelle GT et al. *CO_2 Capture by Aqueous Absorption, Fourth Quarterly Progress Report 2008.* Luminant Carbon Management Program. The University of Texas at Austin. 2008.

Rooney PC, DuPart MS, Bacon TR. "Oxygen's Role in Alkanolamine Degradation". *Hydroc Proc, Int. Ed.* 1998;77(7):109–113.

Sexton A. *Amine Oxidation in CO_2 Capture Processes*. The University of Texas at Austin. Ph.D. Dissertation. 2008.

Dynamic Modeling and Control of CO_2 Absorption/Stripping with 7 M MEA

Abstract

This work presents the dynamic behavior of the amine absorption/stripping system in response to the changes in the capture or steam cycles operating conditions. This dynamic simulation was run in a flow sheet of Aspen Custom Modeler® (ACM®) by integrating the dynamic models of the absorber and the stripper and including simplified steady state models of the cross heat exchangers, the lean solvent cooler, and pumps.

The dynamic results demonstrate that, in the absence of any control system, the CO_2 capture reaches steady state in less than 30 minutes smoothly after making a step change in the steam rate and flue gas rate. However the CO_2 capture continues to vary slowly because no control action is bringing the water content back to balance.

Regulating the temperature of lean solvent recycling to the absorber is presented as an alternative strategy to control the water balance, but it is not proposed as an instantaneous control action.

In addition, controlling the levels in the inventories in an acceptable range is indicated as a mandatory control action. It should be considered for amine systems to make sure that thermal and oxidative degradation and liquid/vapor separation criteria will always being satisfied.

Introduction

Several studies have been done on optimizing the absorber performance, minimizing energy requirement for solvent regeneration and CO_2 compression. However, almost all of them are based on steady state simulations. There is little work on understanding the dynamics and operability of post-combustion capture with varying load. Previous work was limited to modeling the absorber or stripper columns and has not addressed any effective strategies for regulatory control purposes or wide range operation for the whole system. In this work, the dynamic model of amine absorption/stripping process is expanded into an ACM® flow sheet and dynamic responses to small changes in reboiler steam rate and inlet flue gas rate are presented in the following sections of this report.

Discussion

The dynamic model of the absorber and stripper which has been developed is connected in a flow sheet of ACM® framework. The integrated model includes simplified steady state models of lean and rich solution pumps, the cross heat exchanger, and the lean solvent cooler. The dynamic behavior of the system was evaluated separately in response to a couple of possible changes in the plant: a step change in the reboiler steam rate and a step change in the flue gas rate as a result of any change in the boiler load.

In the current integrated model, it is assumed that the steam cycle can provide an almost constant pressure at the extraction point for the steam used for solvent regeneration, even though the boiler load or extracted steam rate changes. This assumption might be valid when we investigate the dynamics and control of the capture from a regulatory control point of view. Nevertheless, the assumption is likely to be incorrect when we have a big change in the capture and power cycle operating conditions. Therefore, we need to include IP/LP crossover pressure as a function of extracted steam rate and boiler for future studies on dynamics and control of the capture over a wide range of operation.

We have a plan to compare the dynamics and control performances of the capture using 7 M MEA running at different lean loadings: high, low, and medium (around critical L/G). In the first case study being discussed in this report, the capture is running at a high lean loading of 0.44. The pressure at the top of the stripper is kept constant at 270 kPa. The steady state design of the cross heat exchanger and reboiler are based on 5 °C, and 10 °C temperature approaches, respectively. The absorber contains 10 m of Mellapak 250Y packing and the stripper contains 3 m of the same packing. Both columns are sized based on 80% flood.

Dynamics of open loop system

The simulation was run for two cases separately. In the first case, the steam valve opening was reduced within 5% at 0.01 hr in order to understand the dynamic behavior of the whole plant in response to the steam rate change and steam temperature in the absence of any control loop. As already mentioned, we assumed that upstream of the steam valve, the pressure of steam extracted from the steam turbines remains constant when the steam rate varies. In the second case, a -5% step change was made for flue gas at 0.01 hr to study the dynamic behavior in response to the flue gas flow disturbance from the boiler side.

When the steam valve closes, the pressure drop across the valve increases instantly and with constant upstream pressure, and the steam side temperature of the reboiler initially drops fast (Figure 1). Afterwards it decreases slowly as the steam rate moves to the asymptote. However, in the solvent side of the reboiler, one-minute hold-up time is considered in the initial point, which results in the temperature dropping more slowly than in the steam side (Figure 2).
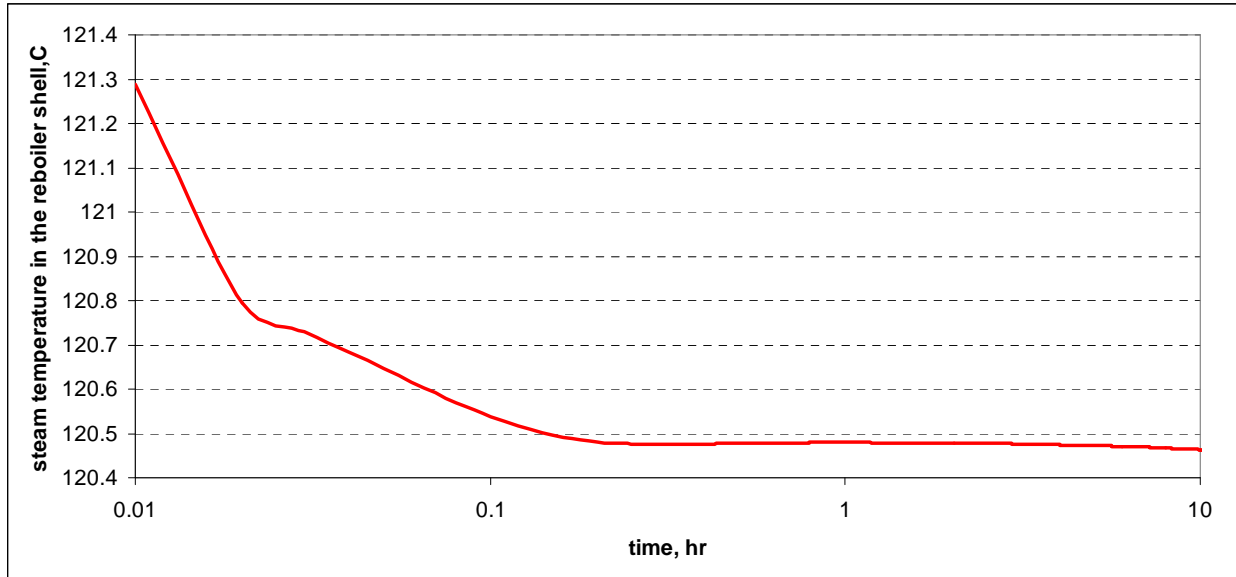
Figure 1: The response of the steam side temperature of the reboiler to a 5% closing of the steam valve

The steam rate, which is affected by temperature driving force in the reboiler, indicates an initial inverse response due to the different time constants associated with the temperature in both sides (Figure 3).

In this system, no control loop is designed to control the liquid level in the absorber and the stripper. With a change in the steam rate or flue gas flow rate, an increased liquid hold-up is expected in one column, and a decreased liquid hold-up in the other one, because the amount of liquid in the system remains almost constant, and varies only slightly due to the change in CO_2 hold-up and water content.

Figures 4 and 5 indicate the response of the liquid level in the stripper and the absorber sumps respectively for each case. In the first case, as the steam rate decreases, the liquid is accumulated in the stripper because of the lower rate of vaporization. The liquid level tends to increase in the stripper and decrease in the absorber before reaching steady state in around one hour. As shown in figures 4 and 5, the levels tend to reach to a steady state at first, but eventually never become constant. The system shows this kind of unstable behavior whenever something is changing in the plant, because there is no control on the amount of water leaving the absorber. This unbalanced water content condition could result in losing water from the solvent or bringing up water in the solvent continuously and causing the amine concentration to vary over time.

Because the accumulation or elimination of water from the system is not an immediate effect but a long-term effect, an instant automatic control action for balancing the water in the system may not be necessary. It can be controlled manually by adding or removing water every week if a significant loss or accumulation of water is observed. The amine concentration control is also a long-term control; it may be controlled once a day by regulating the injection of amine.

Comparing the liquid level responses in the absorber and the stripper sumps in figures 4 and 5, the necessity of controlling the levels in an acceptable range becomes remarkable. If we do not consider any control action for balancing the liquid levels among the columns or added inventories, a small change in the steam rate or flue gas rate or any other possible disturbance

3

can cause some process or safety problems. For instance, an increase in the liquid hold-up can cause the packing or sump to flood and make the column inefficient. On the other hand, decreasing liquid hold-up can result in less than minimum hold-up for liquid/vapor separation in the sump and/or enough time for mass/heat transfer on the packing. For our system, it is more likely to have a tight control for levels, as we need to meet the criteria of minimizing oxidative and thermal degradation.
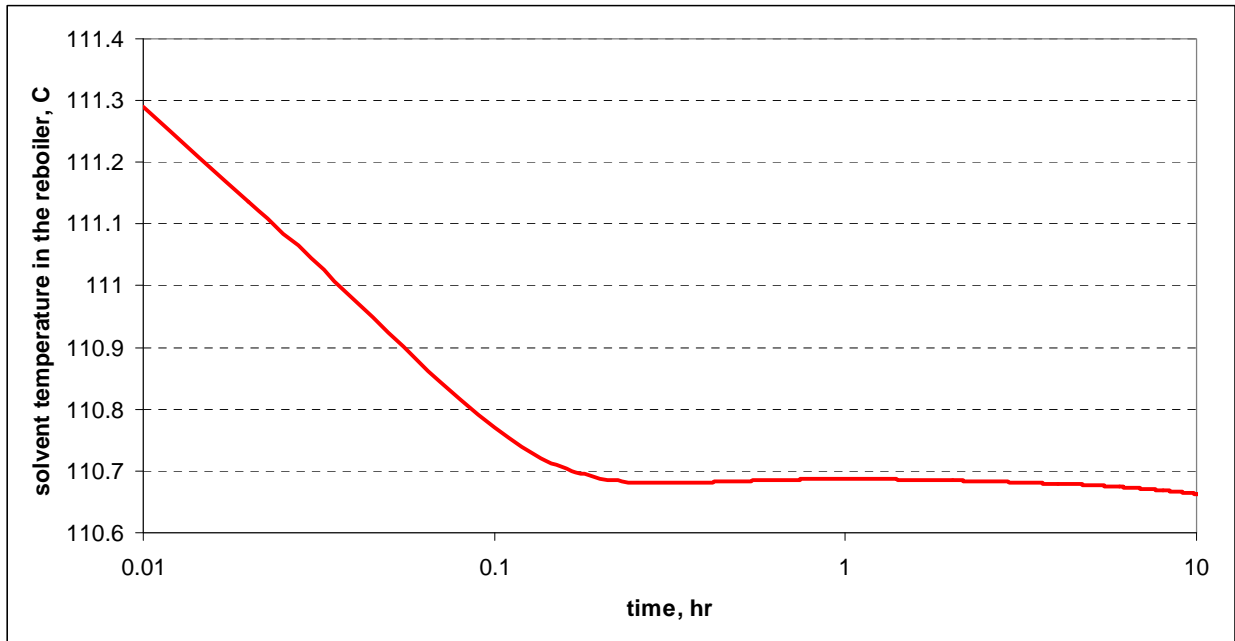

Figure 2: The response of the solvent side temperature in the reboiler to a 5% closing of the steam valve
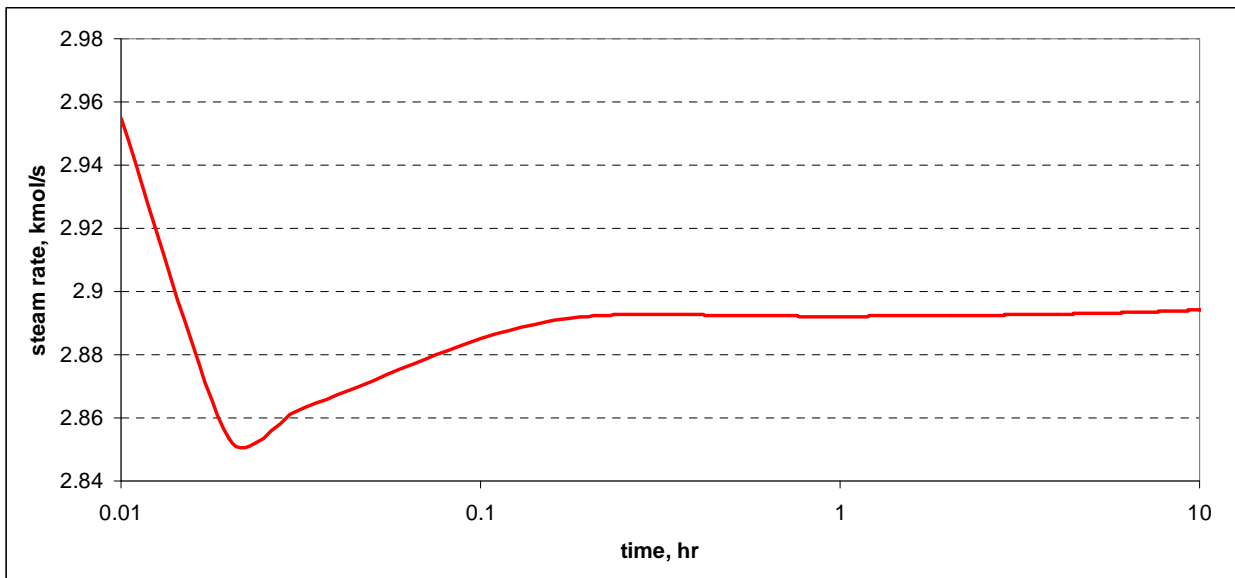
Figure 3: Steam rate response to a 5% closing of the steam valve
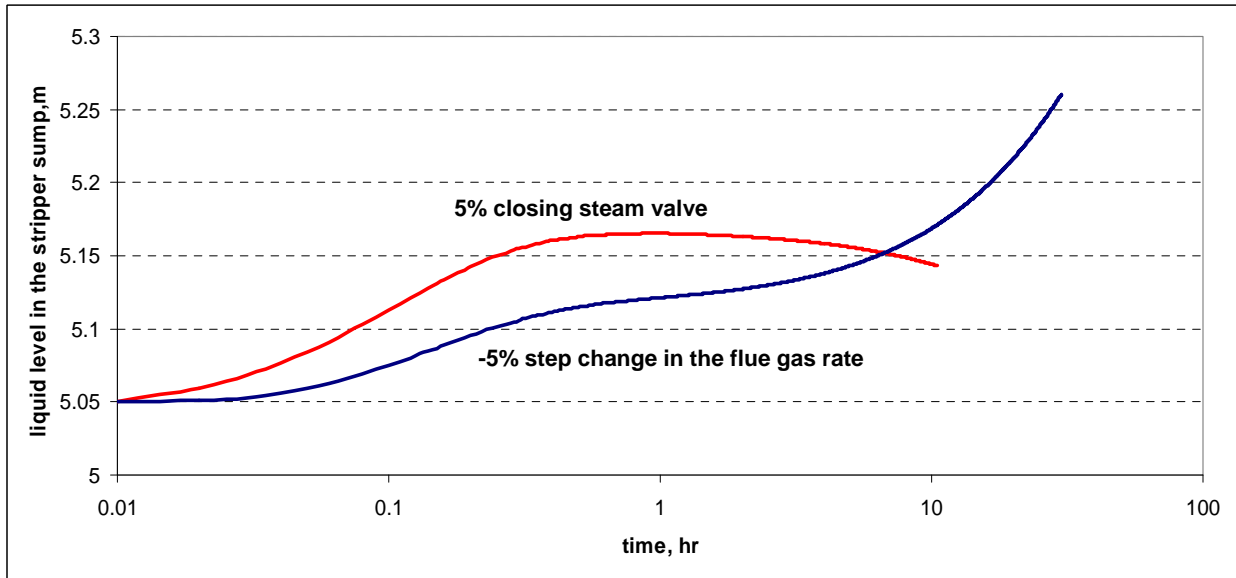
Figure 4: The dynamic response of the liquid level in the stripper sump
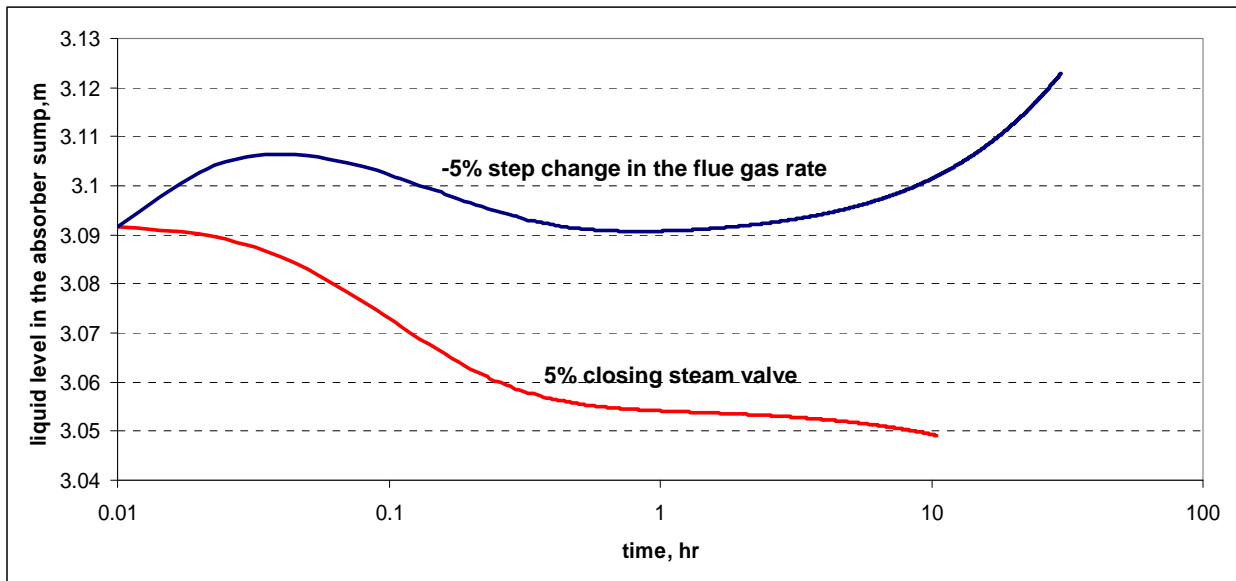
Figure 5: The dynamic response of liquid level in the absorber sump

The dynamic response of the liquid level on the packing of the stripper indicates two time constants, which are different by an order of magnitude. (Figure 6)

The initial rapid drop of the liquid hold-up over about 1 minute could have resulted from a sudden decrease in the vapor rate. The second response intending to reach the second asymptote in about 20 minutes might be the result of combination of dynamics of cooling the solution in the reboiler and changing the solvent circulation rate.

Figure 6: The dynamic response of liquid level on the packing in the stripper

Stabilizing the plant by lean solution temperature control

As already discussed, if the amine system is exposed to a disturbance, the amount of water gets out of balance and the plant does not remain constant at the new steady state, but its process variables continuously change. Because the changes are not rapid, we think it is not necessary to implement an instant control action to bring the w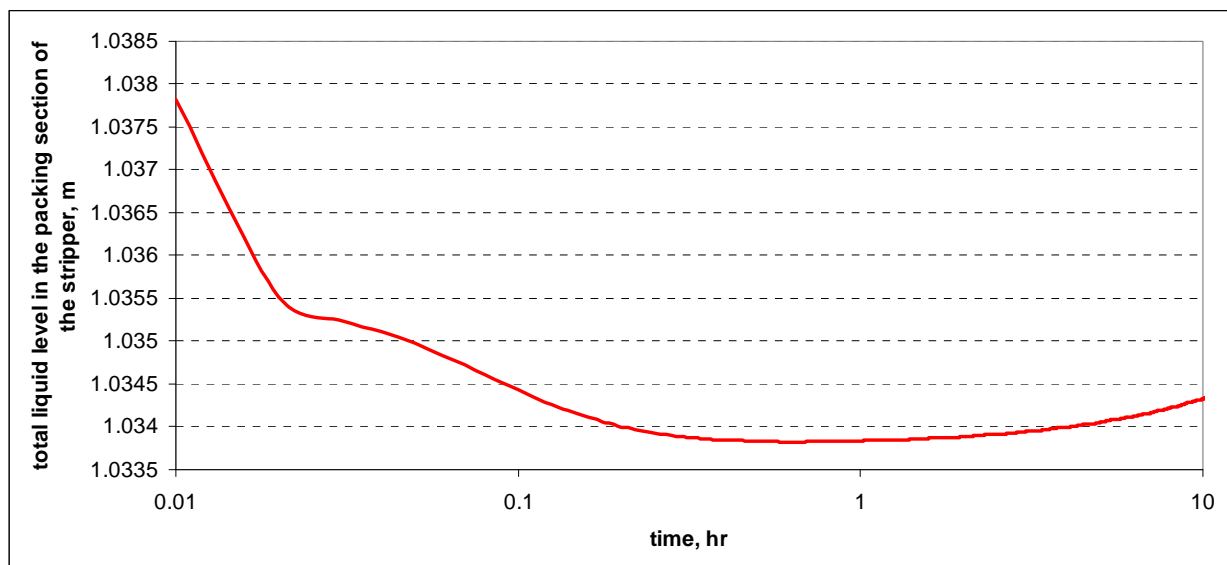ater in balance. However, if instant control over the water balance is required, it can be done by controlling the temperature of the lean solution entering the absorber by regulating the cooling water flow rate.

This control strategy was simulated with our current dynamic model by measuring and controlling solvent flow rate using a PI control to calculate the required outlet cooler temperature (set point of temperature control loop). The dynamic responses show that this strategy is able to stabilize the plant, but it creates oscillatory responses. Comparing the CO_2 removal response to step changes in steam valve position and flue gas rate with and without controlling the lean solvent temperature shows that an open loop system produces faster and smoother dynamic behavior. (Figures 7 and 8)

As demonstrated in Figure 8, in the closed loop system the CO_2 removal reaches steady state in about 2 hours and because of oscillatory behavior during the transition time we will lose the capture performance.

6
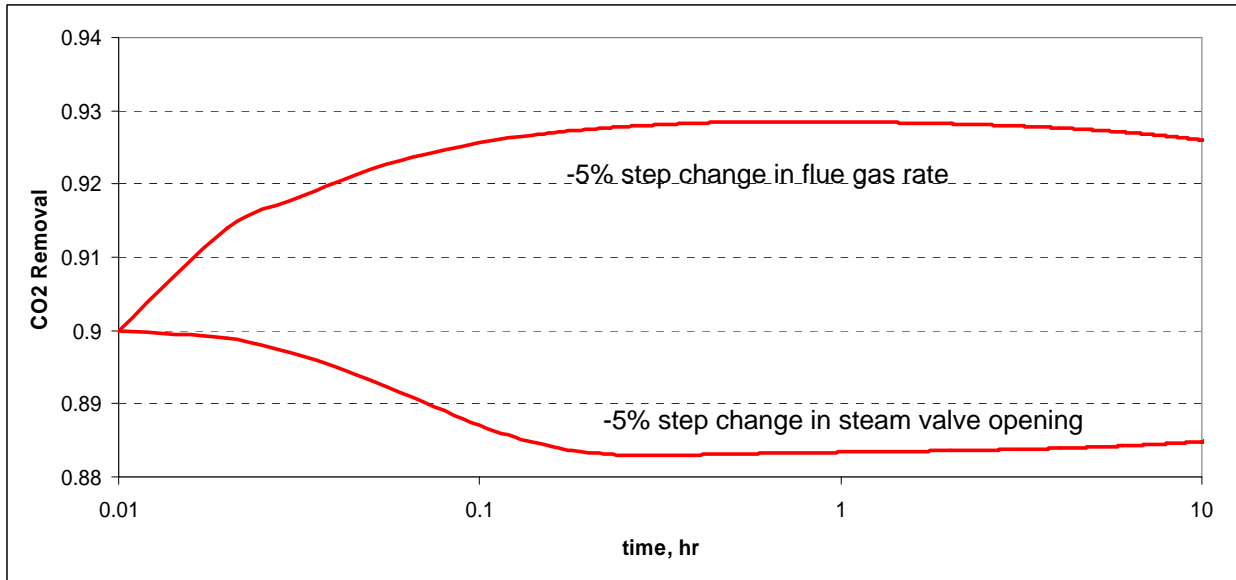
Figure 7: CO₂ removal responses in the open loop system
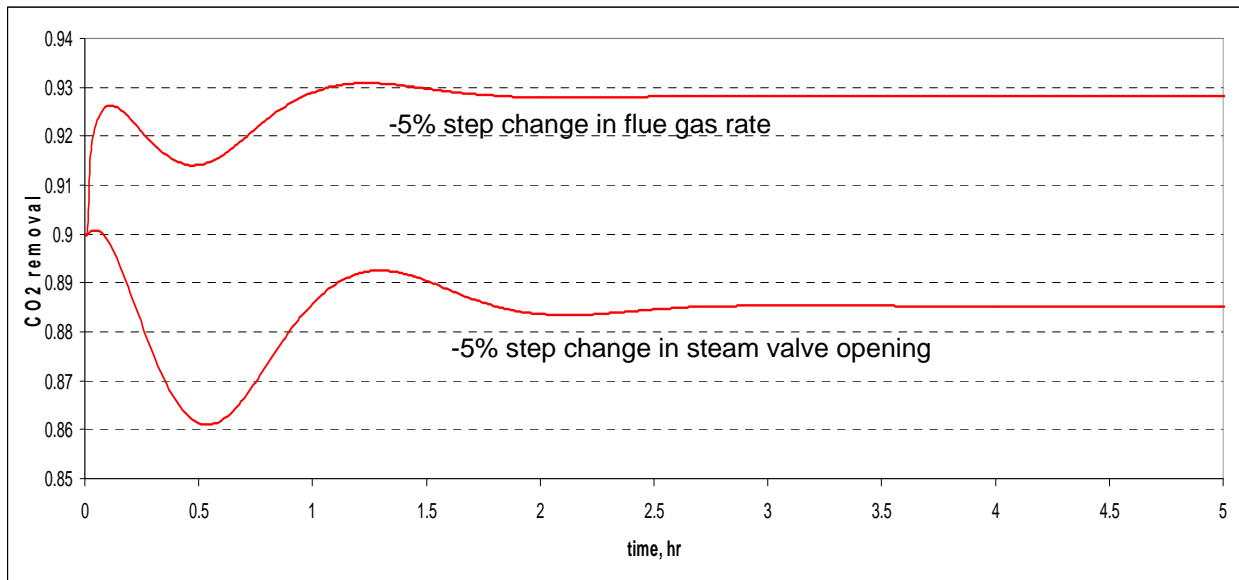

Figure 8: CO₂ removal responses in the presence of lean solvent temperature control loop

Conclusions

Dynamic simulation of the integrated absorption/stripping process was performed in ACM®. The dynamic behavior of the plant was evaluated in response to two possible disturbances in the system: a step change in the steam rate, and a step change in the flue gas rate.

Dynamic results demonstrated that, in the absence of any control loop, the system gets to steady state in less than half an hour smoothly but it continues to vary slowly because the water content becomes out of balance in response to any possible change in the plant. We can control the water balance in the absorber by controlling the temperature of solvent recycling to the absorber, however an immediate control turns out not to be necessary as it just makes the system responses oscillatory and leads in losing CO_2 capture efficiency during the transition time.

As expected, dynamic responses of liquid hold-ups in the inventories show the necessity of controlling the levels in an acceptable range to balance the hold-ups and meet the thermal and oxidative degradation and liquid/vapor separation criteria.

Future Work

In this work, we assumed that the pressure of steam extracted from the crossover point of IP/LP turbines is always constant and it does not change when the steam rate or boiler load changes. We also assumed the pressure at the top of the stripper is constant.

In future, we will include a realistic steam pressure performance as a function of steam rate and boiler load in order to investigate the influence of power plant steam cycle on the design and operation of capture and the possibility and benefits of running the stripper at variable pressure.

In addition, the ratio control strategy which was proposed by Ziaii et al., (2008) as an alternative strategy will be implemented in the simulation in order to keep the capture at the optimum condition (minimum equivalent work).

References

Ziaii S, Cohen SM, Rochelle GT, T. F. Edgar TF, Webber ME, "Dynamic operation of amine scrubbing in response to electricity demand and pricing". In *9th International Conference on Greenhouse Gas Control Technologies*, Elsevier: Washington D.C., 2008.

Electric Grid-Level Implications

of Flexible CO$_2$ Capture Operation

Abstract

A first-order model of hourly electric grid dispatch and pricing has been adapted in order to investigate the implications of flexible carbon dioxide (CO$_2$) capture over a multi-year time frame with annually varying fuel prices, CO$_2$ prices, electricity demand, and power plant fleet. Preliminary analysis of the Electric Reliability Council of Texas (ERCOT) electric grid over a 21-year period with six natural gas and CO$_2$ price path combinations shows that coal-fired plants continue to be dispatched at base load regardless of the availability of CO$_2$ capture unless natural gas prices are low and CO$_2$ prices are high. Operation of flexible CO$_2$ capture in response to demand-induced electricity price variations depends on complex interactions of fuel and CO$_2$ prices, operating costs, and the current power plant fleet. When the emissions cost penalty of partial-load CO$_2$ capture is only a few dollars per megawatt-hour, flexibility can be used for modest operating profit improvements, but these improvements could be offset by any operating cost penalty for using a flexible system. However, by eliminating the need for new capacity to replace output lost to full-load CO$_2$ capture, flexibility can greatly improve the net present value of a CO$_2$ capture investment.

The same dispatch and market model has also been expanded for use in a comparative study of flexible CO$_2$ capture in the United Kingdom (UK) and ERCOT electric grids. The two grids are similar in market structure and size, but differences in capacity mix, demand variations, and fuel markets will likely produce diverging behaviors of flexible CO$_2$ capture systems.

Background and Introduction to Flexible CO$_2$ Capture

Flexible operation of a post-combustion amine absorption and stripping system could allow plant operators to recover some or all of the energy required for carbon dioxide (CO$_2$) capture and increase power output under appropriate electricity market conditions. Flexible operation would consist of redirecting some or all of the steam being used for solvent regeneration back to the power cycle, thereby reducing the need for energy to compress CO$_2$.

Operating the energy intensive components of the amine absorption/stripping process at partial- or zero-load could allow the plant operator to choose the CO$_2$ capture operating point that

provides the most economical combination of cost and output under current electricity market conditions. For instance, it may be profitable to operate CO_2 capture at partial- or zero-load when electricity prices are high if additional electricity sales offset any increase in CO_2 emissions costs under a CO_2 regulatory framework (Ziaii, Cohen et al., 2008).

In addition, operating CO_2 capture at zero-load during annual peak electricity demand can eliminate the need to spend billions of dollars to replace generation capacity lost when CO_2 capture operates at full-load (Cohen, Rochelle et al., 2008).

There are two basic concepts for flexible CO_2 capture with an amine absorption/stripping system. This report will focus on the concept shown in Figure 1, where the steam and rich solvent flow rates to the stripper are reduced equally and simultaneously during partial- or zero-load operation (Ziaii, Cohen et al., 2008). At partial-load, rich solvent that is not sent to the stripper is recycled to the absorber, so CO_2 removal rates in the absorber will decrease as solvent becomes saturated with CO_2. Zero-load could involve recirculating all solvent through the absorber, or the CO_2 capture system could be bypassed completely. This design's primary disadvantage is increased CO_2 emissions at partial- or zero-load, which would incur additional CO_2 costs under a CO_2 regulatory regime.
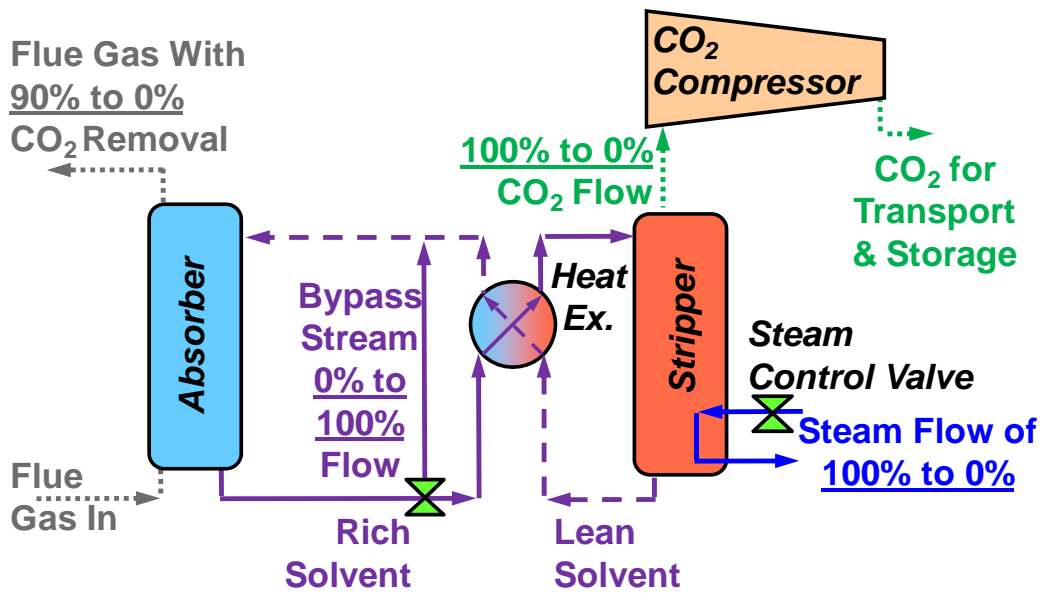
Figure 1: Simultaneously reducing steam and rich solvent flow to the stripper allows increased output but at the expense of additional CO_2 emissions.

The other concept for flexible CO_2 capture involves using large scale solvent storage tanks to allow continued CO_2 absorption when stripping and compression systems operate at partial- or zero-load. This concept is described in detail in the 2nd Quarterly Report of 2009 and will not be discussed further in this report (Rochelle et al., 2009b).

Investment Life Analysis Using a Dynamic ERCOT Model

A primary research activity this quarter was utilizing the analysis methodology first described in the 4th Quarterly Report of 2008 to investigate the performance, economic, and environmental

implications of flexible CO_2 capture over an investment lifetime using a dynamic electric grid modeling framework (Rochelle et al., 2009a). Typically, complexity and calculation time make electric grid-level models unsuitable for analysis periods that span several years, but the first-order nature of my electricity dispatch and market model allows calculations to be made rapidly enough to allow multi-year analysis. The dynamic model makes dispatch calculations in hourly time intervals that can subsequently be aggregated into annual and lifetime performance measures as well as annual cash flows for use in a discounted cash flow analysis. Consideration of several natural gas and CO_2 price paths provides insight into electric grid and CO_2 capture operation under several market outlook scenarios.

Methodology

Brief Description of the Dynamic ERCOT Dispatch Model

The electric grid-level has been described in detail in several other reports and publications, so I will only discuss it briefly here (Cohen, 2009). The deterministic model operates in a MATLAB environment and compares electric grid scenarios with and without flexible and inflexible CO_2 capture systems. The model can be used for any electricity system with the proper input data, but the Electric Reliability Council of Texas (ERCOT) electric grid has been the primary case study due to data availability.

In each hour, the model calculates the marginal generation costs of each facility in the electric grid, creates a cost-ordered power plant dispatch order, chooses the least expensive plants available to meet the current electricity demand, and sets the electricity price for that hour equal to the marginal costs of the most expensive plant dispatched in that hour. Marginal generation costs at each facility include any applicable fuel, CO_2, and operation and maintenance costs as well as any additional costs associated with CO_2 capture. Marginal costs for plants with CO_2 capture account for changes in plant efficiency and CO_2 emissions rate as well as costs associated with solvent makeup, solvent reclaiming, reclaimer waste disposal, additional water use, transport and storage, and additional maintenance, labor, and administration.

Costs and electricity prices in each hour are used to find profits, and the total generation of each plant can be used to calculate its CO_2 emissions. The rule-based dispatch algorithm does not account for sophisticated plant- and grid-level constraints such as transmission congestion and ramp rates, but it successfully approximates a competitive market for electricity in order to provide insight into the role of flexible and inflexible CO_2 capture facilities in the electric grid under varying market conditions.

Scenarios Considered

As in previous work, the model considers the following scenarios.

BAU: Business as Usual – No CO_2 Capture

The business as usual scenario does not allow for any CO_2 capture facilities.

CCS Base: Inflexible CO_2 Capture

For the base case CO_2 capture scenario, CO_2 capture systems must be operated at 100% load continuously throughout the year.

FLEX Op Costs: Flexible CO_2 Capture Option

In this flexible scenario, plants with CO_2 capture choose the operating condition (20% or 100% load) that has the lowest marginal cost of electricity production.

FLEX Profit: *Flexible CO_2 Capture Option*

In every hour, each plant with CO_2 capture calculates its hourly profits for two scenarios: if all plants with CO_2 capture operate at (A) 100% load or (B) 20% load. If profits are greater for a particular plant for Option A, that plant will operate capture at 100% load; otherwise, it will operate at 20% load.

Utilizing the Dispatch Model for Investment Life Analysis

In order to adapt the model to efficiently calculate plant dispatch over an investment lifetime, the model reads an input file with long-term projections of coal, natural gas, and CO_2 prices and automatically cycles through each year in the investment life, exporting annual results summaries after each year of calculations. Electricity demand and the ERCOT fleet of power plants may change throughout the investment life, so the model also imports electricity demand and power plant information that are specific to the current calculation year.

Once annual calculations are made for all years, lifetime trends and totals are determined, and annual operating profits are included in a discounted cash flow analysis that accounts for capital costs, capital depreciation, and profit taxes. Using National Energy Technology Lab (NETL) guidelines, the investment life is 20 years starting in 2012, the first year when CO_2 prices would exist in the U.S. under recent proposed legislation such as the Lieberman-Warner or Waxman-Markey climate bills (NETL, 2005; USEIA, 2008; USEIA, 2009). The cash flow analysis uses a NETL recommended discount rate of 10.3%, capital depreciation under a 20-year Modified Accelerated Cost Recovery System (MACRS) half-year convention, and a 38% profit tax (NETL, 2005). Since the half-year convention is used, depreciation takes place in 21 different calendar years, so the analysis considers a 21-year period. Rather than attempt to replicate an all-inclusive cash flow analysis like that performed in an engineering design study, the cash flow analysis in this study is meant to demonstrate broad economic tradeoffs across the coal-based fleet under no-capture, inflexible capture, and flexible capture scenarios.

Capital costs used in the cash flow analysis are \$221 per kilowatt (kW) for any required sulfur dioxide (SO_2) removal systems and \$908/kW for CO_2 capture systems (USNETL, 2007). Because the need for new capacity to replace any output permanently lost to CO_2 capture, its plant type, and how it may be accounted for is unclear, the sensitivity of the cash flow analysis to replacement capacity cost is investigated.

Representation of CO_2 Capture Systems

Among current plants, eight are chosen to be considered for CO_2 capture based on their operating costs with CO_2 capture, capital costs of CO_2 capture systems, and capital costs of any required SO_2 removal systems that must be installed to prevent solvent degradation (Davidson, 2007). In addition, any new coal-fired plants installed after 2006 utilize CO_2 capture in the *CCS Base* and flexible CO_2 capture scenarios. This quantity of CO_2 capture retrofits would reduce coal fleet emissions by more than 50% if CO_2 capture systems operate continuously at 100% load, even if all coal-fired plants remain base load facilities.

As in previous work, any flexible CO_2 capture systems may operate at 20% or 100% load, and any CO_2 not captured at 20% load is assumed to be vented to the atmosphere. CO_2 capture

performance at these load points is shown in Table 1 below. System response time is not incorporated explicitly in the model, but it is assumed that results from one-hour calculation intervals will approximate those found using the 1–2 hour response time found in process modeling results (Ziaii, Cohen et al., 2008).

Table 1: Energy performance of CO_2 capture is similar at 20% and 100% load, but CO_2 removal is much lower at 20% load.

Parameter	20% Load	100% Load
CO_2 Capture Energy Requirement (MWh/tCO_2)[1]	0.281	0.269
CO_2 Removal (%)	18	90

Annual Demand Growth

ERCOT electricity demand growth is based on the ERCOT 2008 long-term energy forecast of 1.79% growth per year (ERCOT, 2008). Using historical data as a reference, there will then be 342 million MWh of electricity demand in 2012 and 488 million MWh in 2032.

Changes to the ERCOT Power Plant Fleet

The Environmental Protection Agency's (EPA) eGRID power plant database is used for performance parameters of all plants installed through 2004 (USEPA, 2007). To represent the ERCOT plant fleet through 2031, additional power plants are added based on installations since 2004 and planned installations through 2018 from reports by the Public Utilities Commission of Texas (PUC) and the Texas Water Development Board (TWDB) (King, Duncan et al., 2008; ERCOT, 2008). Performance parameters of any new plants are assumed to be similar to those of typical plants of the same type.

Figure 2 displays the resulting estimate of the ERCOT fleet through 2032 in terms of installed capacity in gigawatts (GW)[2]. There are several coal-fired plant installations planned through 2013, three of which are Integrated Gasification Combined Cycle (IGCC) facilities. Three new petroleum coke-fired plants are also included in the coal-fired capacity category since these plants have similar performance characteristics to coal-based plants. Since wind turbines are typically built on a relatively short-term planning horizon, there are currently no planned wind turbine installations after 2012. Though obvious regulatory and economic hurdles remain, Texas's existing nuclear power plants are scheduled for a capacity doubling in 2015, and two new nuclear plants are scheduled to come online in 2018. Some additional natural gas-fired facilities are also to be installed through 2014. The current planning horizon does not extend past 2018, but new natural gas-fired capacity is added in 2029–2032 so that there is enough capacity available to meet peak demand. Natural gas is chosen for this new capacity in an attempt to minimize the potential effect on coal-fired generation, which is the main focus of this study.

---

[1] MWh – megawatt-hour, tCO_2 – metric ton of CO_2

[2] Installed capacity is the product of the plant's rated capacity (maximum output under design conditions) and an availability factor, which accounts for the average amount of time throughout a year that the plant is not available due to a planned or unplanned outage.
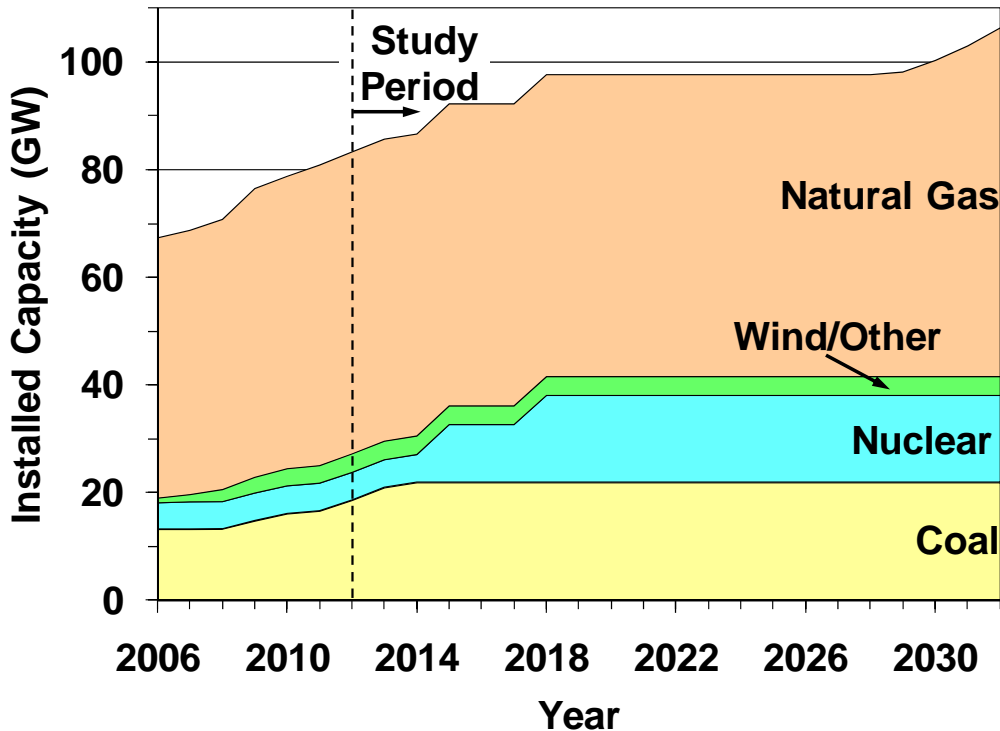
Figure 2: Publicly released planning reports estimate the installed capacity of each power plant type in the ERCOT grid through 2032 (USEPA, 2007; King, Duncan et al., 2008; ERCOT, 2008)

Fuel and CO$_2$ Price Paths

Two natural gas price paths and three CO$_2$ price paths are analyzed, for six different price path combinations. Since coal prices are expected to be significantly less volatile than natural gas and CO$_2$ prices, coal prices are kept constant throughout all calculations, and results shown below use a coal price of $1.45 per million British thermal units (MMBTU).

The chosen price paths, shown in Figure 3, are not meant to be predictive; they are chosen primarily to demonstrate a broad a range of plant and electric grid behaviors. The High Natural Gas price path is characterized by a linear increase from $5/MMBTU to $15.5/MMBTU, where the Inverted Natural Gas price path symbolizes a dramatic long-term transition in the natural gas market where prices increase rapidly from $5/MMBTU then fall to below $9/MMBTU in 2032. The Low CO$_2$ path is identical to the CO$_2$ price path in the Core case of the Energy Information Administration's (EIA) analysis of the Lieberman-Warner Climate Bill, the most recent proposed U.S. climate legislation when this analysis began (USEIA, 2008). The High CO$_2$ price path is meant to create an electricity market where coal-fired power plants have a clear advantage in operating economics if CO$_2$ capture is available. The "best FLEX" CO$_2$ price path is intended to establish a CO$_2$ price where, when combined with the High Natural Gas price path, creates electricity market conditions such that operating economics at coal-fired power plants are better with flexible CO$_2$ capture than with inflexible CO$_2$ capture or no CO$_2$ capture at all. This price path was estimated using previous analysis of flexible CO$_2$ capture under different fuel price

combinations (Cohen, Fyffe et al., 2009). The success of the "best FLEX" CO_2 path in finding the best economic conditions for flexible CO_2 capture will be evaluated in the results.
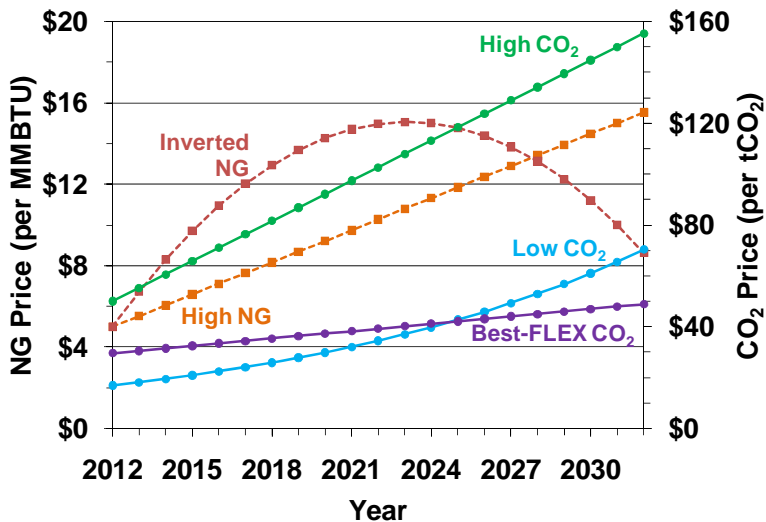

Figure 3: Two natural gas and three CO_2 price paths are investigated in the analysis.

Preliminary Results

This section contains some preliminary results from the investment life analysis in order to provide a general overview of the types of outputs available. These data incorporate a large overestimate of the additional maintenance costs of CO_2 capture flexibility and a slightly lower than desired coal price. Final results will integrate changes to these parameters and will be submitted to the American Society of Mechanical Engineers (ASME) 4th Annual Conference on Energy Sustainability, to be held May 2010 in Phoenix, Arizona.

Generation and Utilization of Flexible CO_2 Capture

The long-term analysis can be used to investigate trends in generation by plant type over the years. As an example, Figure 5 displays annual generation by plant type for the *BAU* (no CO_2 capture) and *CCS Base* (inflexible CO_2 capture) scenarios with the inverted natural gas and high CO_2 price paths. Initially, low natural gas prices depress coal-fired generation; however, rising gas prices and new nuclear capacity dramatically decrease natural gas-based generation that only recovers throughout the years because no new plants are built. When natural gas prices begin to decline, gas-fired plants start to displace higher cost coal-fired facilities in the dispatch order, causing coal-based generation to decrease in the latter years of the study.

From 2013–2029, there is more coal-based generation in *BAU* than *CCS Base* due to the energy requirement of CO_2 capture. Despite high CO_2 prices, high natural gas prices allow coal-fired generators to remain at base load even without CO_2 emissions controls. However, when natural gas prices fall while CO_2 prices are high, CO_2 capture systems allow more coal-based electricity to remain economical. In both scenarios, generation from new nuclear installations primarily displaces natural gas-based electricity but also replaces some generation from the most expensive coal-based facilities.
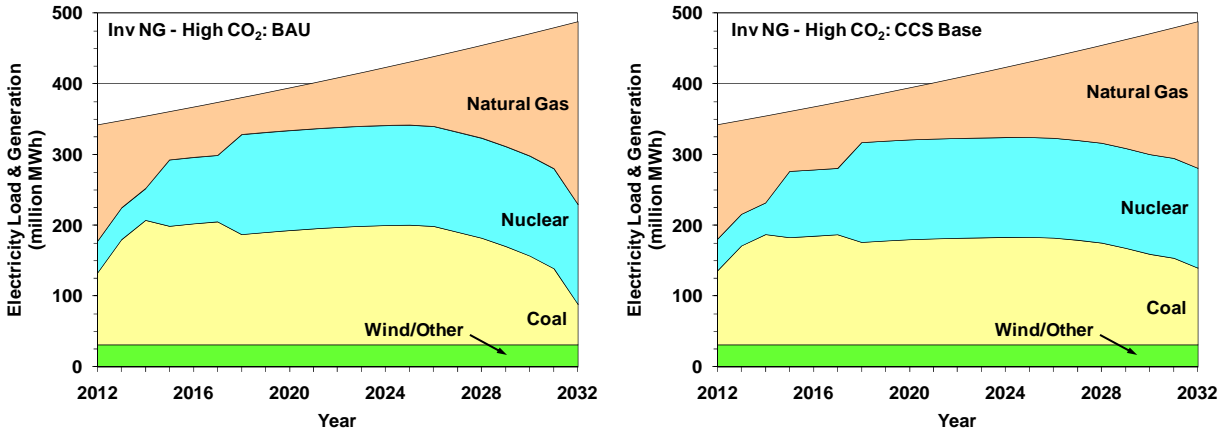
7

Figure 4: Under the inverted natural gas and high CO$_2$ price paths, there is a much larger decline in coal-fired generation when natural gas prices are low if CO$_2$ capture is unavailable (*BAU*).

Figure 5 provides some initial insight into the operation of flexible CO$_2$ capture plants in each scenario. The figure displays the percent of time throughout each year that flexible CO$_2$ capture facilities, when operating, operate at 100% load in the *FLEX Profit* scenario.

Flexible plants operate continuously at 100% load throughout investment life when both natural gas and CO$_2$ prices are high. Even though high natural gas prices greatly increase electricity prices, the large increase in emissions costs at 20% load is not justified.

In contrast, when CO$_2$ prices are low and natural gas prices high, generation costs are only a few $/MWh greater at 20% load, so high electricity prices often justify the additional emissions costs, and in early years it is sometimes more economical to operate at 100% load to withhold output and drive electricity prices higher.

When gas prices are high and CO$_2$ prices follow the "best FLEX" path, operating costs are almost always lower at 100% load CO$_2$ capture, but there is still a significant portion of the time when emissions costs are offset by additional electricity sales. Since demand and natural gas prices rise faster than CO$_2$ prices, this behavior becomes more frequent in the later years. The utilization of flexibility across the 21-year time period demonstrates success in choosing the CO$_2$ price path to promote consistent utilization of flexible CO$_2$ capture.

Trends are more complex for the inverted gas and "best FLEX" price path combination. Rapidly rising gas prices and relatively low CO$_2$ prices in earlier years justify 20% load operation, though the effects are damped by new nuclear installs in 2015 and 2018, which lower average electricity costs by providing inexpensive base load generation. Once natural gas prices begin to fall, additional electricity sales at CO$_2$ capture 20% load become less valuable relative to the extra CO$_2$ emissions costs, so that by 2032, flexible CO$_2$ capture facilities operate continuously at 100% load.

These data demonstrate that the operation of a flexible CO$_2$ capture system will be a complex function of fuel and CO$_2$ prices, operating costs, and the current power plant fleet. These types of effects cannot be captured with a traditional cash flow analysis.
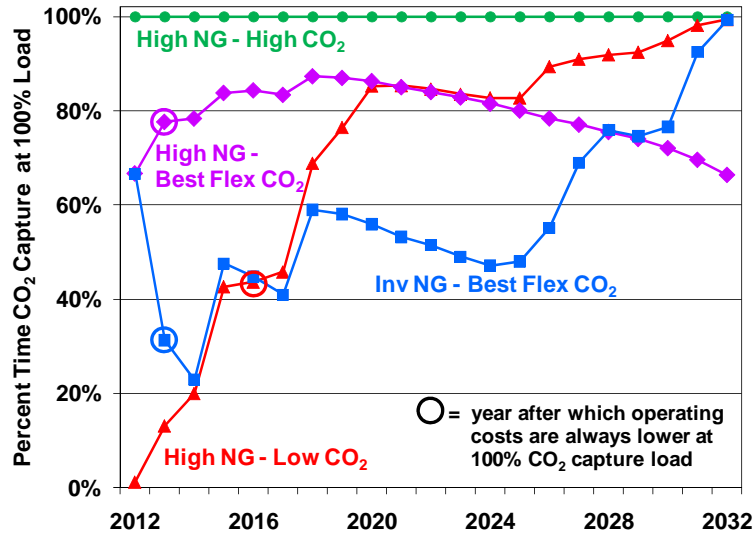
8

Figure 5: The percent of time in each year that flexible CO$_2$ capture facilities in the *FLEX Profit* scenario operate at 100% load differs widely between scenarios. Also shown are the years after which operating costs are always lower when CO$_2$ capture is at 100% load.

Data for calculated CO$_2$ emissions will not be discussed in depth here. Across all six fuel price scenarios, *CCS Base* has 40% lower lifetime CO$_2$ emissions than *BAU* on average, *FLEX Op Costs* has 37%, and *FLEX Op Costs* 33%.

Economics

Under all price path combinations, electricity prices are still usually set by natural gas-fired facilities, so price trends over time generally follow changes in fuel and CO$_2$ emissions costs at natural gas-based plants. For each combination of natural gas and CO$_2$ price paths, electricity prices only differ by a few \$/MWh among the four scenarios. One break in these trends is that new nuclear capacity additions in 2015 and 2018 slow or reverse the increase in electricity prices by adding a large quantity of inexpensive base load generation.

Figure 6 displays the cumulative annual operating profits across the coal-fired power plants being considered for CO$_2$ capture in the *BAU*, *CCS Base*, and *FLEX Profit* scenarios under two price path combinations. Both cases have high natural gas prices, but the left panel considers the high CO$_2$ price path whereas data in the right panel are for the low CO$_2$ path. The difference in CO$_2$ price paths has a major effect on operating profits in all scenarios, and trends depend on whether CO$_2$ capture is available. Aside from years when new nuclear installations depress electricity prices, operating profits monotonically increase. When CO$_2$ prices are high, profits are much lower in *BAU* even though plants are still dispatched primarily at base load, because CO$_2$ capture is not available to mitigate CO$_2$ emissions costs. However, when CO$_2$ prices are lower, plants earn greater operating profits without CO$_2$ capture in the first few years, and *BAU* profits remain much closer to those in CO$_2$ capture scenarios throughout the investment life. Profits are greater in the CO$_2$ capture scenarios with high CO$_2$ prices because higher CO$_2$ prices add emissions costs to natural gas-fired facilities that typically set electricity prices.

With high gas and high CO$_2$ prices, flexibility is not utilized in the *FLEX Profit* scenario, so operating profits remain lower than *CCS Base* because the model assumes an additional

maintenance cost of flexibility that increases marginal costs at flexible plants by approximately $5/MWh. This additional cost is thought to be a large overestimate, especially in a scenario where no cycling of the CO_2 capture system occurs, so finalized results will incorporate a much more reasonable value. Even though flexibility is utilized in all years with the high gas, low CO_2 price paths in the *FLEX Profit* scenario, the additional cost of flexibility prevents operating profits from exceeding those of the inflexible CO_2 capture scenario.
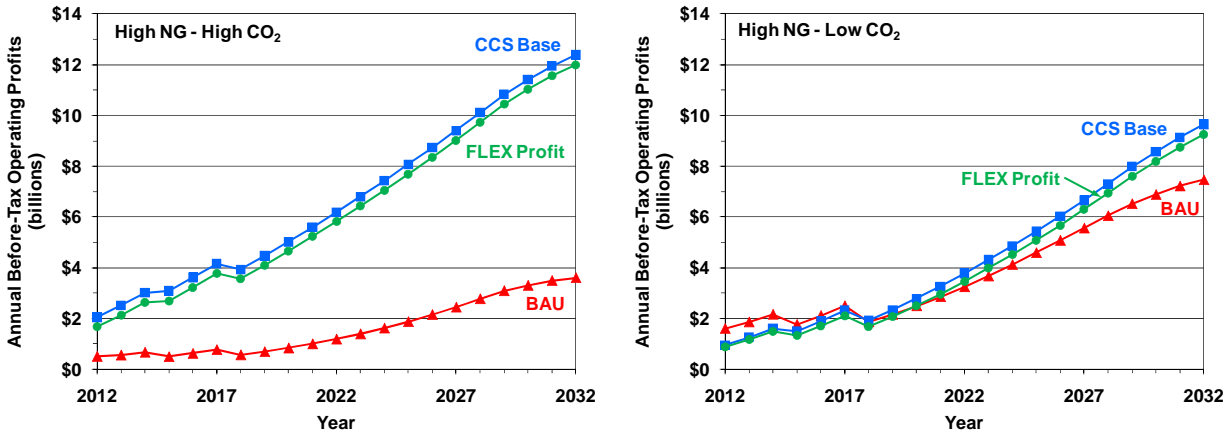

Figure 6: Cumulative annual before-tax operating profits in each year at plants being considered for CO_2 capture depend largely on natural gas and CO_2 price trends.

Sample results of the cash flow analysis are shown in Figure 7, which displays the cumulative net present value (NPV) across all plants being considered for CO_2 capture in the *BAU*, *CCS Base*, and *FLEX Profit* scenarios under each price path combination. In *BAU*, there are no capital costs. There are capital costs for CO_2 capture and some SO_2 removal systems in both CO_2 capture scenarios, but the energy requirement for 100% load CO_2 capture must be replaced in *CCS Base* whereas *FLEX Profit* only requires replacement capacity for 20% load CO_2 capture. The operator of a CO_2 capture system may not actually pay for any capacity to replace the energy required for CO_2 capture, and it is unclear how replacement capacity costs would be accounted for and how much they would be. The replacement capacity cost used to create Figure 7 is $3,000/kW to represent the approximate cost of new coal-fired facility with CO_2 capture, but it must be emphasized that replacement capacity costs in this analysis are meant primarily to display the system-level costs rather than a cost to a particular plant operator (USNETL, 2007).

NPV is greater in *BAU* when CO_2 prices are low because there are no capital costs. However, with high CO_2 prices, the operating profit benefit of having CO_2 capture outweighs any required capital costs. Though operating profits are greater in *CCS Base*, the additional capital cost of replacement capacity reduces the NPV below that of *FLEX Profit*, and NPV is even negative when gas prices are high and CO_2 prices are low.

A final display of results from the cash flow analysis will demonstrate the sensitivity of NPV to the capital cost of replacing any capacity permanently lost to CO_2 capture energy requirements. If the cost of replacement capacity is assumed to be lower or not accounted for at all, there will be less discrepancy in NPV between *CCS Base* and *FLEX Profit*, and relative operating profits will dominate the NPV calculation.
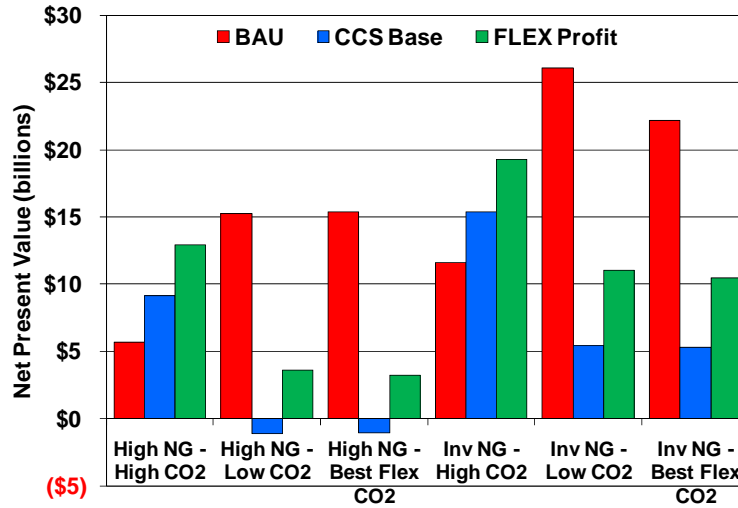
Figure 7: Cumulative net present value across all plants being considered for CO_2 capture is shown for *BAU*, *CCS Base*, and *FLEX Profit* for each fuel price path combination when replacement capacity costs are assumed to be $3,000/kW.

Preliminary Conclusions

The dynamic grid-level modeling methodology has been successfully adapted to investigate flexible CO_2 capture over multi-year periods with annually varying fuel prices, CO_2 prices, electricity demand, and power plant fleet. Preliminary investigation of the ERCOT electric grid over a 21-year period demonstrates that coal-fired power plants, regardless of the availability of CO_2 capture, continue to be dispatched at base load under a wide range of fuel and CO_2 price paths. However, the operating profits at coal-fired plants will suffer greatly if CO_2 prices are high and CO_2 capture is not utilized, and natural gas-based generators will displace some coal-fired facilities without CO_2 capture if natural gas prices are low while CO_2 prices are high. Since coal usually remains a base load fuel, natural gas-fired facilities remain the primary determinants of electricity price, so their fuel and CO_2 costs are the primary influence on electricity price trends.

The operation of a flexible CO_2 capture system will be a complex function of fuel and CO_2 prices, operating costs, and the current power plant fleet, but flexibility in response to demand-driven electricity price variations is most often utilized when there is a relatively small emissions cost penalty for reduced CO_2 capture load. Flexible CO_2 capture used in this manner may be able to achieve modest improvements in operating profits, but these benefits could be offset if there is a significant operating cost penalty for using a flexible system. Though flexible CO_2 capture may have limited value in energy markets, ancillary service markets may provide another opportunity for flexible CO_2 capture to improve upon the overall economics of CCS. Regardless, by eliminating the need for new capacity to replace output lost to CO_2 capture energy requirements, flexible operation greatly improves the net present value of an investment if replacement capacity costs are accounted for.

Comparing and Contrasting the Implications of Flexibility in the ERCOT and United Kingdom Electric Grids

Another primary task this quarter was continuing the collaboration with Hannah Chalmers of the Imperial College of London to compare and contrast flexible CO_2 capture in the ERCOT and United Kingdom (UK) electric grids. This analysis will include a qualitative assessment of the two electric grids along with quantitative analysis using my electricity dispatch model. The study is a work in progress, so I will describe the motivation and current status of the quantitative analysis before discussing the next steps in the collaborative effort. Preliminary results will be presented at the International Energy Agency Greenhouse Gas Research and Development Programme (IEA-GHG)/Imperial College Workshop on Operating Flexibility of Power Plants with CCS in London on November 10–11.

Motivation

The collaboration was initiated because Hannah and I have complementary focuses and knowledge on flexible CO_2 capture, especially in our geographical regions of interest (Chalmers, Chen et al., 2006; Chalmers, Lucquiaud et al., 2009). We thought it valuable to advance the study of flexible CO_2 capture by investigating regional differences in the implications of flexible post-combustion systems through comparative case studies of the ERCOT and UK electric grids.

Both electric grids operate in competitive markets for electricity, meaning that the previously described dispatch and electricity market model provides a suitable first-order approximation of least-cost dispatch and electricity prices. Other than internationally traded electricity across the England-France interconnector, both electric grids are mostly self-contained "island" electricity systems (MacLeay, Harris et al., 2008). Though Texas is not geographically separated from other U.S. electric grids, ERCOT functions as its own interconnect entirely within Texas, and its power is not generally synchronized with the eastern or western North American interconnects (ERCOT, 2007). Unlike ERCOT, the UK electricity system currently incorporates a market for CO_2, where CO_2 allowance prices are passed through to power plant operating costs. U.S. legislators have been moving towards similar carbon legislation, but no CO_2 price presently exists in the ERCOT market.

The two electric grids are also somewhat similar in size. ERCOT had 72,820 MW of installed capacity as of May 2008, where the UK had 84,880 MW of rated capacity if all power producers are accounted for. Total electricity consumption in 2007 was 307 TWh in ERCOT and 373 TWh in the UK. Excluding onsite use of electricity and pumping load at pumped storage hydroelectric facilities in the UK, the peak 2007 electricity demand was 62.2 GW in ERCOT and 61.9 GW in the UK (ERCOT, 2007; MacLeay, Harris et al., 2008; Nationalgrid, 2009).

While total capacity and generation are similar, Figure 8 Figure 8 shows differences in the capacity of each power plant type in ERCOT and the UK. ERCOT has a much greater percentage of gas-fired capacity due to a large number of older gas-fired boilers, whereas the UK has greater percentages of nuclear-, coal-, and non-coal/natural gas-based thermal generation[3]. Neither grid has a large capacity percentage of renewable sources, but renewable capacity in

---

[3] Natural gas-fired capacity in ERCOT includes natural gas combined-cycle (NGCC), natural gas-fired boilers, and open-cycle gas turbines. The UK does not have a significant quantity of natural gas-fired boiler capacity, and its open-cycle gas turbines are included in the "Non-Coal Boilers, Gas Turbines, Oil Engines" category because the data do not separate gas turbines from oil engines.

ERCOT is primarily wind turbines, whereas hydroelectric power dominates UK renewables. Not evident on these graphs is that natural gas-fired combined heat and power facilities are much more prevalent in the UK. These plants are typically designed to supply heat load instead of electric load, meaning that they may operate at maximum output even if their generation costs may not justify maximum output dispatch in the electricity market.

Though there are major differences in capacity mix, overall generation by plant type is relatively similar. Though ERCOT has a much greater percent capacity of natural gas-fired plants, nearly half of this capacity is made up of infrequently used natural gas-fired boilers. Since natural gas is usually much more expensive than coal in ERCOT, coal-fired plants are typically base load generation, so their percent energy production is much greater percentage than their capacity percentage. In contrast, seasonal fuel price variations in the UK typically allow coal-fired generators to operate at base load in the winter when natural gas demand and price is greater due to heating loads, and falling natural gas prices allow the UK's NGCC plants to replace coal-fired power plants at base load in the summer.
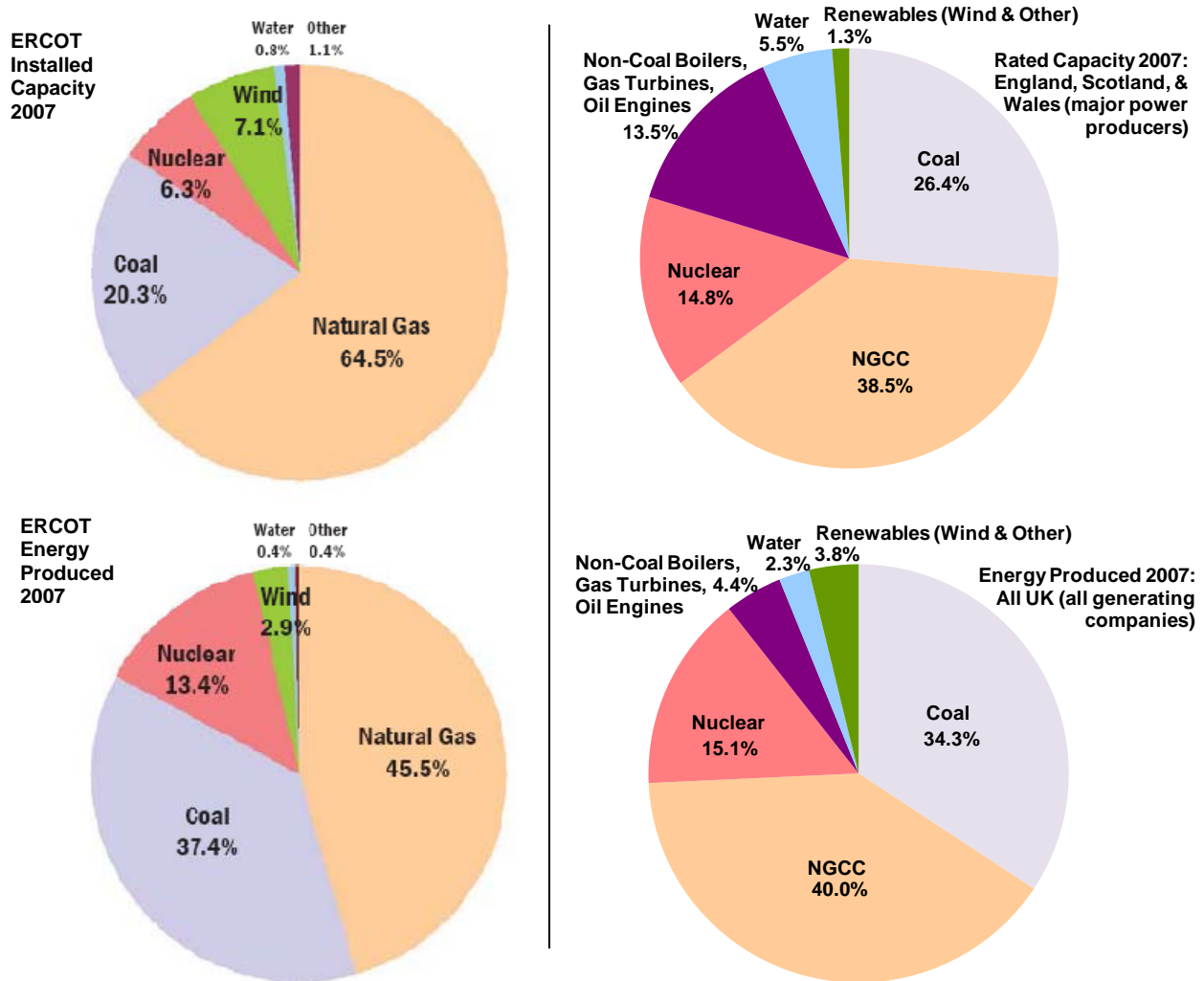

Figure 8: ERCOT has a much larger percent of natural gas-based capacity, but the percent contribution of different plant types to energy production is relatively similar between ERCOT and the UK (ERCOT, 2007; MacLeay, Harris et al., 2008).

Previous work has shown the impact of fuel prices on flexible CO_2 capture operation, and this study will investigate how two realistic combinations of fuel price and generation fleet affect how plants are dispatched and the role that flexible and inflexible CO_2 capture plants will have in the electricity system. Though total annual electricity demand in each grid is similar, differences in diurnal and seasonal demand variations will likely create discrepancies in aggregate electric grid behavior.

Methodology

The two grids will be compared as configured in 2006, using actual 2006 fuel prices and a range of CO_2 prices, so that output will be similar to that presented in earlier work (Ziaii, Cohen et al., 2008; Cohen, Fyffe et al., 2009). Average annual fuel prices will likely be used, but the analysis may also consider seasonal variations of natural gas prices in the UK. The year 2006 is chosen due to data availability and to remain consistent with prior work.

Model Changes and Additions

The modeling framework will remain the same as that described above, but additional features have been added to account for major differences in the UK grid. Unlike ERCOT, the UK grid has a significant capacity contribution by hydroelectric plants, oil-fired facilities, and gas-fired combined heat and power (CHP) plants. Therefore, appropriate parameters and plant cost calculations for these three plant types were incorporated into the model so that these plants could be dispatched correctly. In the model, oil-fired facilities are categorized along with a few small gas-fired piston engine driven generators in a "miscellaneous peaking plant" category. However, all of these plants are given characteristics of the oil-fired boilers that dominate the category.

Gas-fired CHP plants are approximated as always following a constant heat load, so the model's dispatch algorithm is modified to assure that gas-fired CHP facilities always produce their full output capacity regardless of their placement in a cost-sorted dispatch order.

The same four scenarios for flexible, inflexible, and no CO_2 capture are analyzed (*BAU*, *CCS Base*, *FLEX Op Costs*, *FLEX Profit*). Flexible CO_2 capture plants may again choose between 20% and 100% load, and the same eight current coal-fired power plants are considered for CO_2 capture in ERCOT.

Input Parameters

Electricity demand data are the same for ERCOT as in previous work. Since the model now considers three additional power plant types, ERCOT power plant data are modified so the model separates these plants from the more general categories used in past analysis.

Since the power plants on the Scottish Isles do not appear to interact with other plants in the UK electricity market, they are not included in this study (MacLeay, Harris et al., 2008). Since the modeling framework is not currently designed to accommodate dispatch and operation of pumped storage hydroelectric facilities, pumped storage facilities are not included in the analysis, and electricity demand data that are used exclude load from pumped storage pumping (Nationalgrid, 2009). If model validation reveals that pumping inefficiencies significantly damage the accuracy of results, demand data could be modified to account for average pumping energy loss.

UK hourly electricity demand data are readily available, as is a list of power plants and their rated capacities. However, there is no UK equivalent to the EPA's eGRID database, so other power plant performance parameters had to be estimated. Average availability of each plant type is estimated using data in reports by Redpoint Energy, the IEA, and the UK Department for Business Enterprise & Regulatory Reform (BERR) (IEA and NEA, 2005; Neuhoff, Skillings et al., 2008; MacLeay, Harris et al., 2008). Availabilities of coal-, natural gas-, and oil-fired plants are taken directly from the reports, and availability factor is assumed equal to the load factor in the 2008 Digest of UK Energy Statistics (DUKES, 2008) for wind, hydroelectric, and nuclear-based generators. Generation costs of wind-, hydro-, and nuclear-powered facilities are kept at a constant value for all plants in both electric grids. Heat rates and CO_2 emissions rates are used to calculate costs at fossil fuel-based plants. Currently, the data set uses a uniform distribution of heat rates and CO_2 emissions rates for each plant type that is calculated using average plant performance from DUKES 2008 and the National Atmospheric Emissions Inventory (NAEI) along with the distribution of plant performance from EPA's eGRID database (NAEI, 2009). The final set of UK power plant performance parameters may instead match the shape of the distribution of plant performance values from the eGRID database.

There is a wide variety of uncertain parameters required to perform this analysis, so sensitivity studies will be undertaken for parameters that are suspected to have a major effect on results.

Next Steps

Once all base case power plant performance and economic parameters, fuel prices, and a test range of CO_2 prices are finalized, a fraction of the UK coal-fired fleet will be chosen to be considered for CO_2 capture. Only the Longannet plant is expected to be a serious candidate for retrofitting, but in order to allow comparison with ERCOT results, enough coal-fired plants will be chosen to achieve a CO_2 emissions reduction of approximately 50% across the coal-based fleet if CO_2 capture operates continuously at full-load.

The model and inputs will then be validated with historical 2006 data. After making any appropriate adjustments, the full range of CO_2 prices will be considered along with any sensitivity studies that appear relevant to one or both grids.

Future Work

First-Order Analysis of Using Solar Energy for Solvent Stripping

One new research topic I will begin this semester is an initial analysis of the feasibility and tradeoffs involved in using solar thermal energy for solvent stripping during daytime hours. I will investigate different types of solar thermal technology, evaluate their compatibility with post-combustion amine absorption and stripping systems, and examine their performance, economic, and environmental tradeoffs. Previous analysis by David Van Wagener will provide insight into stripper configurations conducive to solar stripping, and I will use these results in an analysis of the plant- and electric grid-level impacts of solar stripping.

Analyzing Several Replacement Capacity Scenarios and Partial/Zero-Load Points

As another extension on previous work with electric grid dispatch modeling, I plan to investigate inflexible CO_2 capture scenarios with various types of capacity used to replace output lost to CO_2 capture energy and compare these replacement capacity scenarios with flexible CO_2 capture

cases. Where previous calculations have been limited to a 20% partial-load point for the CO_2 capture system (Ziaii, Cohen et al., 2008), I hope to study several other partial-load points such as 0% load with and without a residual energy penalty.

Continuation of Solvent Storage Optimization

After completing the other tasks mentioned above, I intend to extend the solvent storage optimization analysis to incorporate electricity price seasonality as well as a finite system response time required to transition from storage mode to regeneration mode. I may also include a more detailed representation of power plant economics as well as consider the possibility of partial-load boiler operation in conjunction with flexible CO_2 capture.

Acknowledgements

References

King C, Duncan I *et al*. Water Demand Projections for Power Generation in Texas. *Bureau of Economic Geology*. Austin, TX. 2008.

Chalmers H, Chen C *et al*. Initial Evaluation of Carbon Capture Plant Flexibility. *8th International Conference on Greenhouse Gas Control Technologies*. Trondheim, Norway, Elsevier Ltd. 2006.

Chalmers H, Lucquiaud M *et al*. "Flexible Operation of Coal Fired Power Plants with Postcombustion Capture of Carbon Dioxide". *J Environ Eng*. June 2009.

Cohen SM, Fyffe J *et al*. "The Effect of Fossil Fuel Prices on Flexible CO_2 Capture Operation". *ASME 3rd International Conference on Energy Sustainability*. San Francisco, CA. 2009.

Cohen SM. *The Implications of Flexible CO_2 Capture on the ERCOT Electric Grid*. The University of Texas at Austin. M.S. Thesis. 2009;154.

Cohen SM, Rochelle GT *et al*. "Turning CO_2 Capture On & Off in Response to Electric Grid Demand: A Baseline Analysis of Emissions and Economics". *ASME 2nd International Conference on Energy Sustainability*. Jacksonville. 2008.

Davidson RM. "Post-combustion carbon capture from coal fired plants – solvent scrubbing". *IEA Clean Coal Centre*. 2007.

ERCOT. 2007 Annual Report. 2007.

ERCOT. 2008 Capacity, Demand, Reserves Report. *2008_Capacity_Demand_Reserves_Report_FINAL.xls*. Taylor, TX. 2008.

ERCOT. "Long-Term Hourly Demand Energy Forecast". *ERCOT 2008 Planning*. 2008.

IEA and NEA. Projected Costs of Generating Electricity: 2005 Update. *OECD*. Paris, France. 2005.

Neuhoff K, Skillings S *et al*. "Implementation of EU 2020 Renewable Target in the UK Electricity Sector: Renewable Support Schemes". *Redpoint Energy Ltd*. 2008.

MacLeay I, Harris K *et al*. "Digest of United Kingdom Energy Statistics 2008". *Department for Business Enterprise & Regulatory Reform*. 2008.

NAEI. National Atmospheric Emissions Inventory Emission Factors Database. *http://www.naei.org.uk/emissions/*. 2009.

Nationalgrid. Demand Data. *http://www.nationalgrid.com/uk/Electricity/Data/Demand+Data/*. 2009.

NETL. Carbon Capture and Sequestration Systems Analysis Guidelines. USDOE. 2005.

Rochelle GT *et al*. CO_2 Capture by Aqueous Absorption, Fourth Quarterly Progress Report 2008. *Luminant Carbon Management Program.* The University of Texas, Austin. 2009a.

Rochelle GT *et al*. CO_2 Capture by Aqueous Absorption, Second Quarterly Progress Report 2009. *Luminant Carbon Management Program.* The University of Texas, Austin. 2009b.

Ziaii S, Cohen SM, *et al*. "Dynamic operation of amine scrubbing in response to electricity demand and pricing". *9th International Conference on Greenhouse Gas Technologies*. Washington, DC, Elsevier. 2008.

USEIA. Energy Market and Economic Impacts of S. 2191, the Lieberman-Warner Climate Security Act of 2007. *Office of Integrated Analysis and Forecasting, USDOE.* Washington, DC. 2008.

USEIA. Energy Market and Economic Impacts of H.R. 2454, the American Clean Energy and Security Act of 2009. *Office of Integrated Analysis and Forecasting, USDOE.* Washington, DC. 2009.

USEPA. Emissions & Generation Resource Integrated Database (eGRID). *eGRID2006_Version_2_1*. 2007.

USNETL. Cost and Performance Baseline for Fossil Energy Plants. *Bituminous Coal and Natural Gas to Electricity*. J. M. Klara. 2007;1.

Measurement of Packing Effective Area and

Mass Transfer Coefficient

Quarterly Report for July 1 – September 30, 2009

Chao Wang

Supported by the Luminant Carbon Management Program,

Industrial Associates Program for CO_2 Capture by Aqueous Absorption,

and the Process Science and Technology Center

Department of Chemical Engineering

The University of Texas at Austin

October 6, 2009

Abstract

Packings are widely used in distillation, stripping, and scrubbing processes because of their relatively low pressure drop, good mass transfer efficiency, and ease of installation. Packings are also are also being investigated for the post combustion carbon capture process for these reasons. Research continues to focus on development of high performance packing, especially on minimizing pressure drop, maximizing mass transfer efficiency, and minimizing costs. The design of packed absorbers for carbon dioxide capture will require the reliable measurement and accurate prediction of the effective area, gas and liquid film mass transfer coefficient. A variety of experimental methods for measuring effective area, gas and liquid film mass transfer coefficient k_La have been reported. Consistent measurements of these important design parameters will be tried this summer and will continue in the fall.

Absorption of CO_2 with NaOH is applied to measure the effective area of packings. Atmospheric carbon dioxide is used as gas phase and 0.1 M NaOH is used as liquid phase. The effective area can then be determined by the measured overall volumetric gas phase mass transfer coefficient ($K_{og}a$, Henry's constant, carbon dioxide diffusivity, free OH concentration and the predicted reaction rate constant. These measurements have been obtained on a wide variety of random and structured packings by the UT/SRP. In recent years, Robert Tsai has obtained additional gas/liquid contact area data by adjusting the surface tension and viscosity of the system.

The absorption of SO_2 into NaOH solution will be used to measure the gas phase film volumetric mass transfer coefficient. Sulfur dioxide (SO_2), blended with ambient air at a composition of approximately 80 ppm, will be absorbed by 0.1 M NaOH solution. The gas phase film mass transfer coefficient may be determined from the measured gas phase volumetric mass transfer coefficient (k_ga) and the previously measured gas/liquid contact area (a).

The stripping of toluene from water with air is applied to measure the liquid phase volumetric mass transfer coefficient (k_La). Ambient air is used to strip soluble toluene from water. The

liquid phase mass transfer coefficient can be determined from the measured liquid phase volumetric mass transfer coefficient and the previously measured gas/liquid contact area.

In this quarter, a new SO_2 analyzer has been installed and incorporated into the UT/SRP air/water pilot plant and DeltaV control system. The SO_2 analyzer underwent testing and troubleshooting separately. In addition, a gas chromatographic system was set up to allow measurements of ppm levels of toluene in water. The analytical system has also been checked out and trouble-shooted. Three structured packings will be studied in the upcoming quarter: Raschig-Jaeger RSP250, Sulzer Mellapak 2X, and Koch-Glitsch Flexipac 1.6Y HC. These packings were obtained during this quarter.

Introduction

This quarterly report is focused on the experimental methods of measurement of effective area a_e, gas-side volumetric mass transfer coefficient k_Ga, and liquid-side volumetric mass transfer coefficient k_La.

We plan to measure the liquid phase volumetric mass transfer coefficient, k_Ga, by absorbing SO_2 into 0.1 M NaOH solution. The reaction is instantaneous and the mass transfer process is controlled by the gas phase. Thus the overall mass transfer coefficient K_G can be replaced by gas phase film mass transfer coefficient k_G. This experiment can be combined with the effective area experiment as long as the gas and liquid flow rates are set at the same level. The gas phase mass transfer coefficient can be calculated by the equation:

$$k_G = \frac{u_G \ln(\frac{y_{SO2in}}{y_{SO2out}})}{ZRTa_e} \tag{1}$$

The SO_2 inlet and outlet concentration will be measured using a Thermo Scientific Pulsed Fluorescence SO_2 analyzer. The range is set to 0–100 ppm. The inlet SO_2 is a mixture of SO_2 stream coming out of 2% SO_2 cylinder and atmosphere air.

The inlet SO_2 concentration is set to around 80 ppm to make sure it is in the range of the SO_2 analyzer. This is done by controlling the valve connected to the SO_2 cylinder. The outlet SO_2 concentration should be around 1–2 ppm if 4 feet of packing is used.

The stripping of toluene from water with air is applied for the measurement of the liquid phase mass transfer coefficient. Ambient air is used to strip soluble toluene from water. As a result of the high Henry's constant, the mass transfer resistance is controlled by the liquid phase. The gas flow rates and liquid flow rates are set at the same value with the effective area measurement to make the 3 experiments consistent. The liquid phase mass transfer coefficient can be calculated by the equation:

$$k_L = \frac{u_L}{Za_e}\ln(c_{LA1}/c_{LA2}) \tag{2}$$

Toluene concentration is measured using a HP 5890A Gas Chromatograph (GC). The GC can detect toluene concentration from more than 1,000 ppm to 1 ppm. In the planned experiment, the inlet toluene concentration is set to equilibrium solubility of toluene in water, which is around 600 ppm depending on the temperature. The outlet toluene concentration can be measured down to less than 1 ppm if 4 feet of packing is used. Since 1 ppm is close to the pinch

of the detector, we will concentrate the outlet sample by 10 times and then measure the concentrated sample. The real outlet sample concentration is the number we get from the GC divided by 10.

Experimental Methods

Measurement of hydraulic performance

The packing characteristics will be measured along with the mass transfer experiments. The goal of the hydraulic experiment is to determine how the pressure drop and holdup vary with liquid and gas flow rates. For example, Figure 1 shows the relationship of fractional liquid holdup with gas and liquid flow rates. The gas flow rate is expressed by F-factor, which is the square root of gas density multiplied by superficial gas velocity.
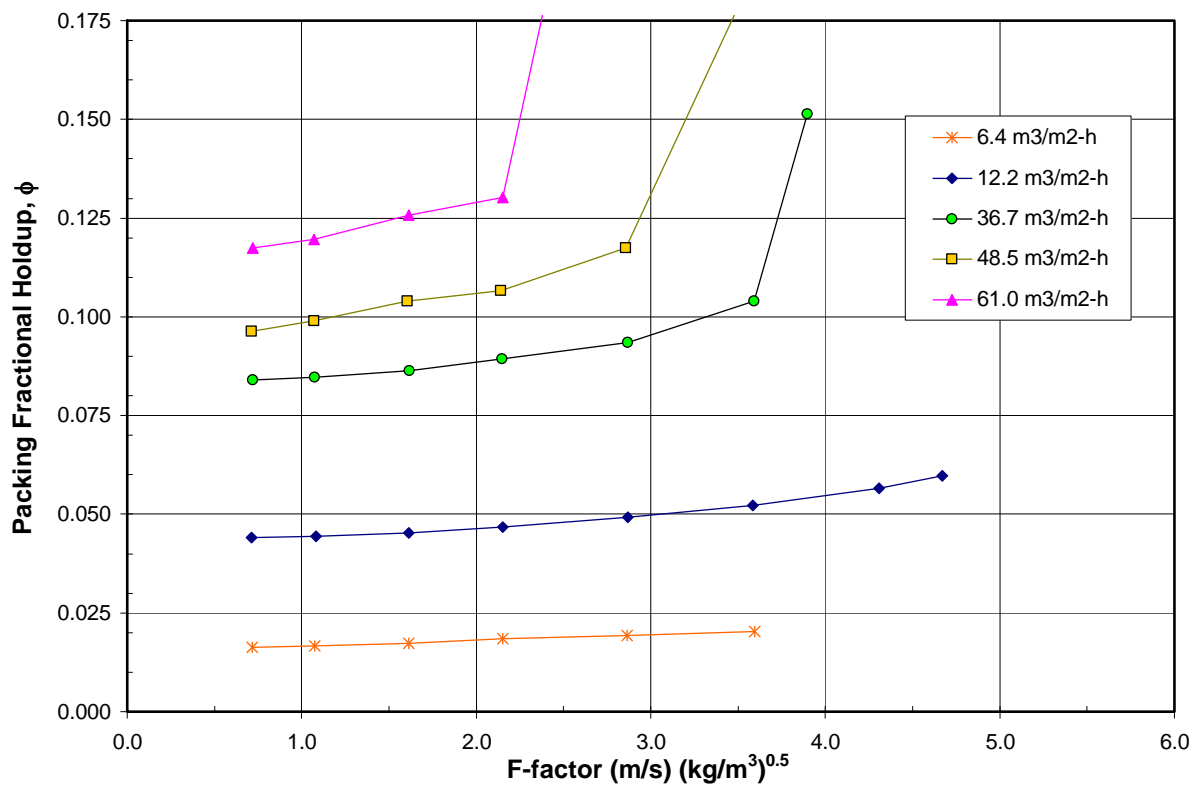
Figure 1: Hydraulic performance of Sulzer MellapakPlus 252Y

The y-axis is packing fractional liquid holdup which is the total liquid holdup divided by the volume of the packing. The x-axis is the F-factor. As expected, the fractional liquid holdup increases with liquid load. In the non-loading region, liquid holdup is relatively independent of gas flow rate. In the loading region, liquid holdup increases sharply with gas rate.
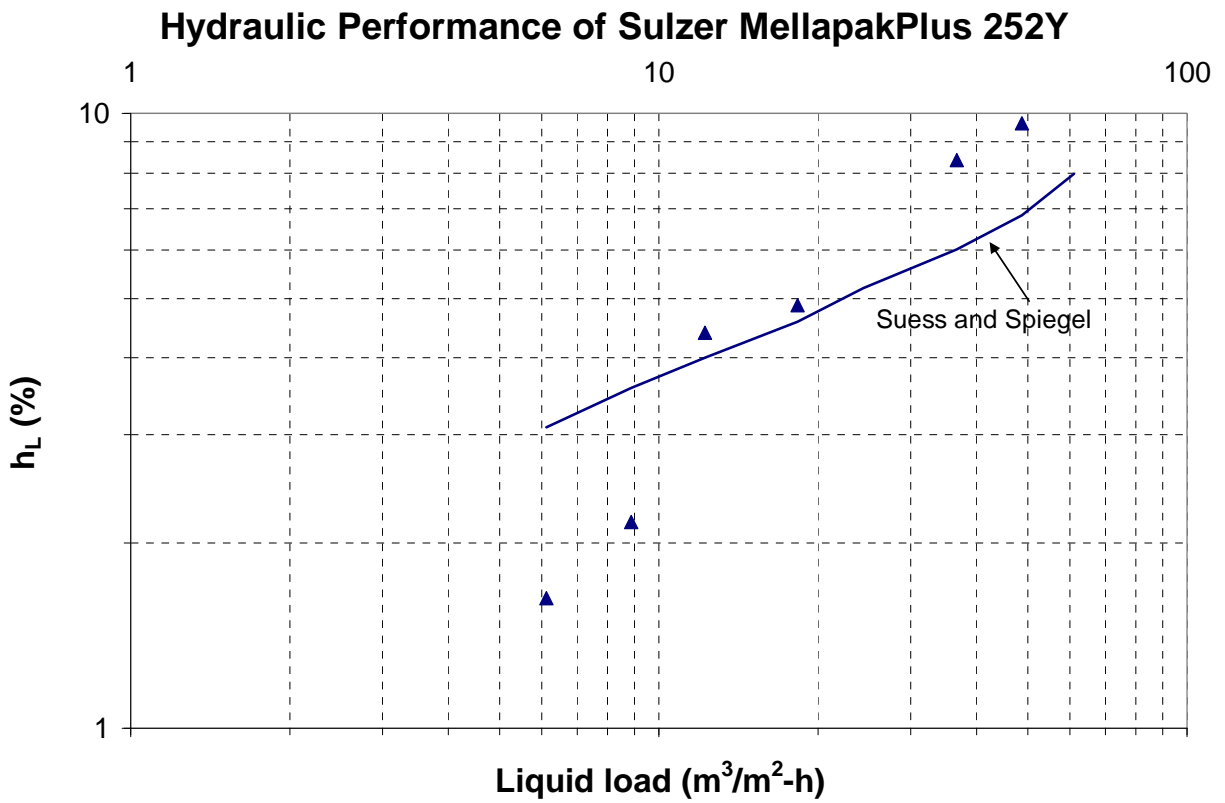
Figure 2: hold-up vs. liquid load

The relationship of liquid holdup and liquid velocity is given by Figure 2. The experimental data are compared with the model of Suess and Spiegel. From Figure 2, the holdup increases almost linearly with liquid load. The Suess and Spiegel holdup model does not compare favorably with these data. The agreement is better at higher liquid loads.
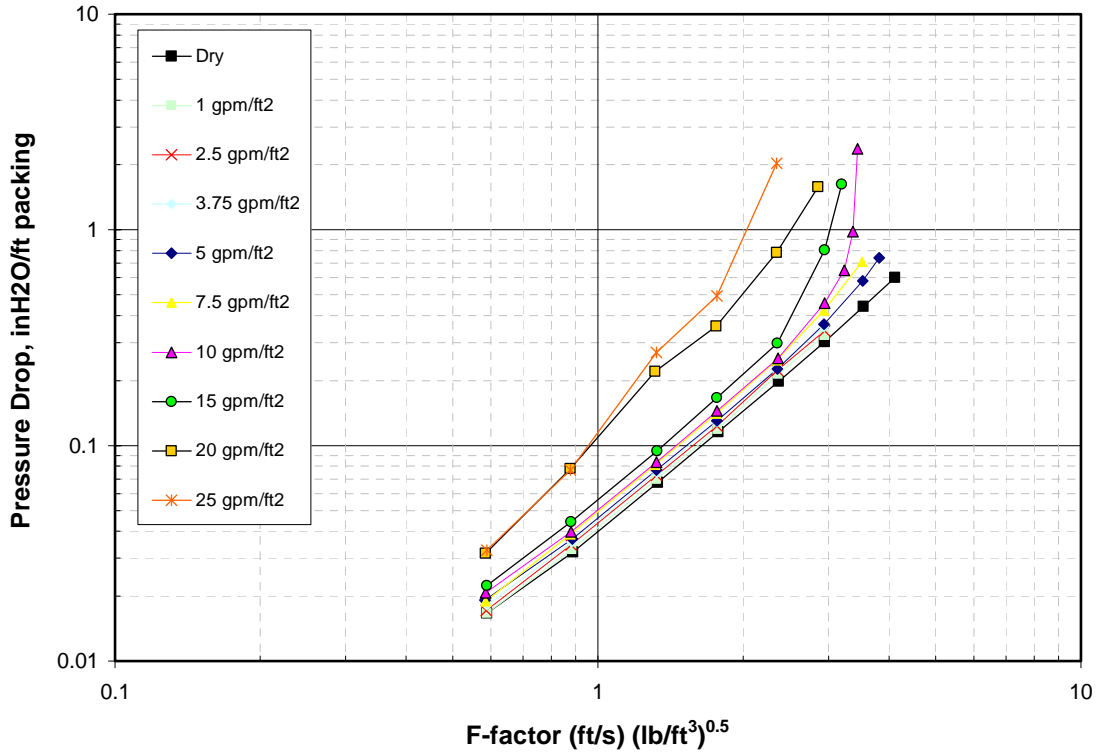
Hydraulic Performance of Sulzer MellapakPlus 252Y

Figure 3: Pressure drop vs. F-factor and liquid load

An example of the packing pressure drop and flooding characteristics is shown in Figure 3. These data are based on the Mellapak 252Y obtained by Bob Tsai. From the figure, we can see that pressure drop increases most with F-factor with an exponent of 1.8–2.0 at low liquid loads. The pressure drop increases with liquid flow rate as expected.

Measurement of effective area

Absorption of CO_2 in air with 0.1 M NaOH solution is used for the measurement of effective gas/liquid contact areas and has been discussed in earlier quarterly reports by myself and Bob Tsai. The effective area could be calculated from the following equation. Typical data are shown in Figure 4.

$$a_e = \frac{u_G \ln(\frac{y_{CO2in}}{y_{CO2out}})}{ZK_GRT} \approx \frac{u_G \ln(\frac{y_{CO2in}}{y_{CO2out}})}{Zk_g'RT} \tag{3}$$
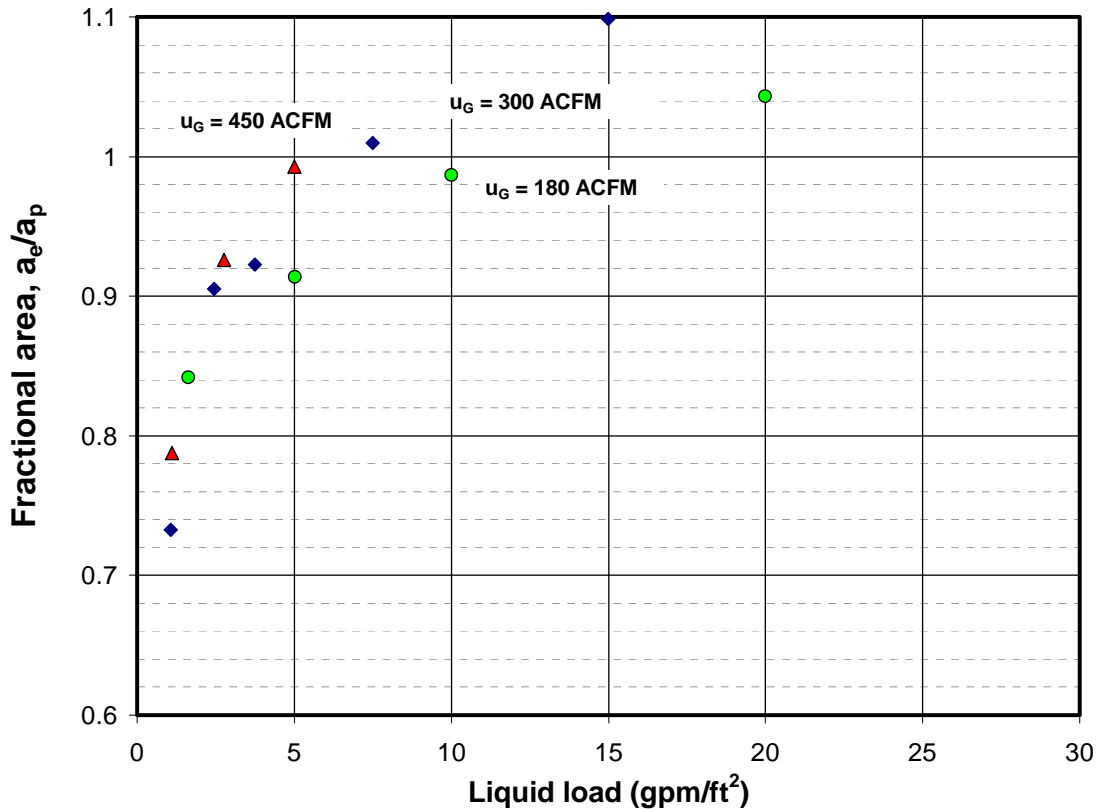
Figure 4: Fraction area vs liquid load, gas load. Packing =MellapakPlus 252Y. Data obtained by Bob Tsai.

While packing hydraulic and gas/liquid contact area data will be obtained as discussed above, this work will include new measurements of gas film and liquid film mass transfer coefficients.

Measurement of gas side mass transfer coefficient

The absorption of SO_2 with 0.1 N NaOH solution will be used for the measurement of gas film mass transfer coefficient. The feed SO_2 concentration will be controlled to around 80 ppm by mixing 2% SO_2 in cylinder with air. The initial NaOH concentration is 0.1 M. In my last quarterly report varying experimental systems for measuring gas film mass transfer coefficients were discussed. Among these systems, the SO_2/NaOH system has advantages. SO_2 is similar to CO_2 and can be absorbed with 0.1 M NaOH solution. The absorption mechanism is an instantaneous reaction where equilibrium is easy to reach. The SO_2 concentration can be readily determined with a commercial and highly accurate SO_2 analyzer.

The reaction is:

$$SO_2 + 2OH^- \rightarrow SO_3^{2-}$$

It is an irreversible instantaneous reaction. The mass transfer resistance in the liquid phase is negligible compared with the resistance in the gas phase. Thus, the liquid side mass transfer resistance can be ignored. The overall volumetric mass transfer coefficient can be assumed equal to the volumetric gas film mass transfer coefficient. The volumetric gas side mass transfer coefficient could be measured by the following equation (Sharma, 1966):

6

$$k_G a = \frac{u_G \ln(\frac{y_{SO2in}}{y_{SO2out}})}{ZRT} \qquad (4)$$

Where u_G is the superficial gas velocity, y_{SO2in} and y_{SO2out} is the concentration of SO_2 in the gas phase at the inlet and outlet of the column. The SO_2 concentration is measured by Thermo 43i SO_2 analyzer which has a range of 0–100ppm and can reach as low as 0.5 ppb. The inlet SO_2 concentration is adjusted to around 80 ppm by mixing 2% SO_2 from the cylinder with air. The outlet SO_2 concentration could be around 10 ppb with 10 feet of packings. From our previous measurement of effective area, the k_G value could be calculated by:

$$k_G = \frac{k_G a}{a_e} \qquad (5)$$

Therefore, the k_G value can be obtained from direct measurement.

These experiments will be combined with the effective area measurements to refine the determination of the effective area and also used to determine k_g. The inlet air will be spiked with SO_2 and both the SO_2 concentration and the CO_2 concentration should be measured. The gas and liquid flow rates for both experiments are identical. Both experiments will use 0.1 N NaOH solution. The concentration of OH⁻ is calculated by:

$$[OH^-]_{remaining} = [OH^-]_{initial} - 2[CO_3^{2-}] - 2[SO_3^{2-}] \qquad (6)$$

The concentration of carbonate is calculated from the FTIC analysis:

$$\left[CO_3^{2-}\right] = \frac{x \ grams C}{10^6 \ grams \ so\ln} \times \frac{1 mol C}{12.011 gC} \times \frac{1g}{1mL} \times \frac{1000mL}{1L} = \frac{x \ ppm C}{(1000)(12.011)}$$

x ppm C could be read from the standard curve.

The concentration of sulfite is calculated from the material balance of S:

$$[SO_3^{2-}] = \frac{P}{RT} G * (y_{SO2in} - y_{SO2out}) * t \qquad (7)$$

Where G is the gas flow rate, t is the time for each run.

The inlet and outlet SO_2 concentrations will be measured with a Thermo Scientific SO_2 analyzer model 43i. Prior to running these experiments, a calibration of the SO_2 analyzer will be performed. Pure nitrogen is used as zero gas and 91.6 ppm SO_2 balanced with nitrogen is used as span gas.
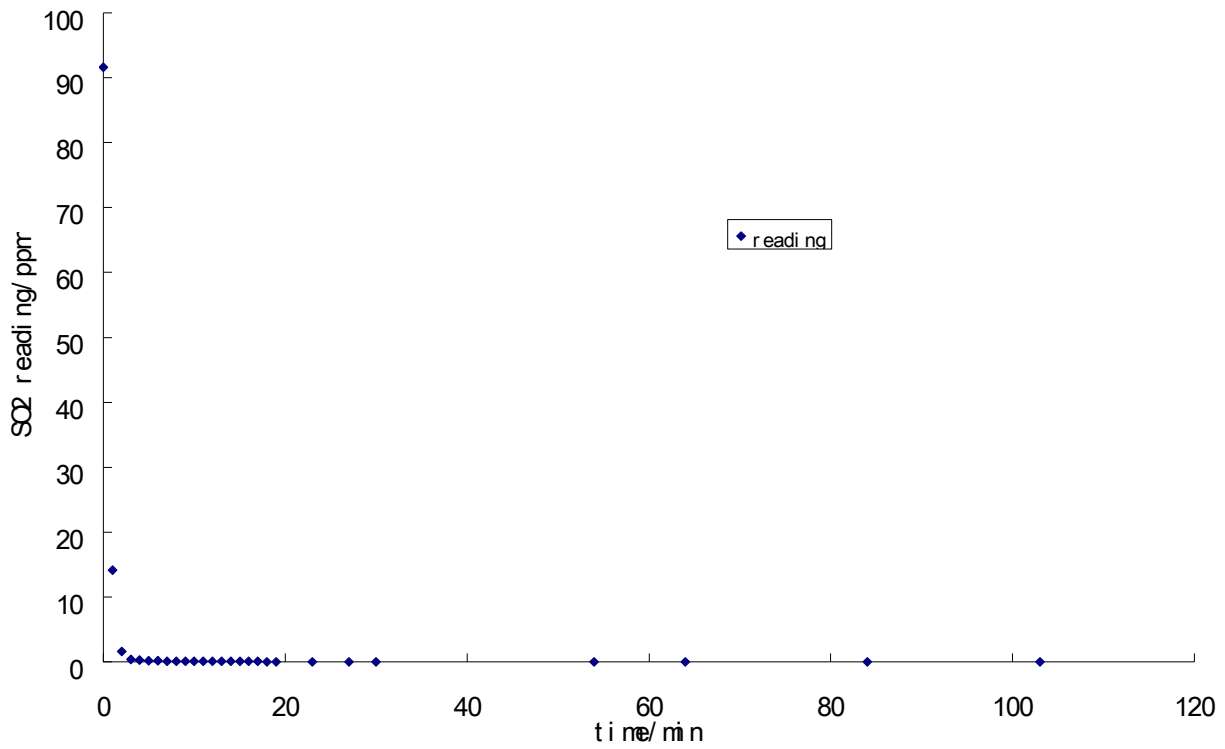
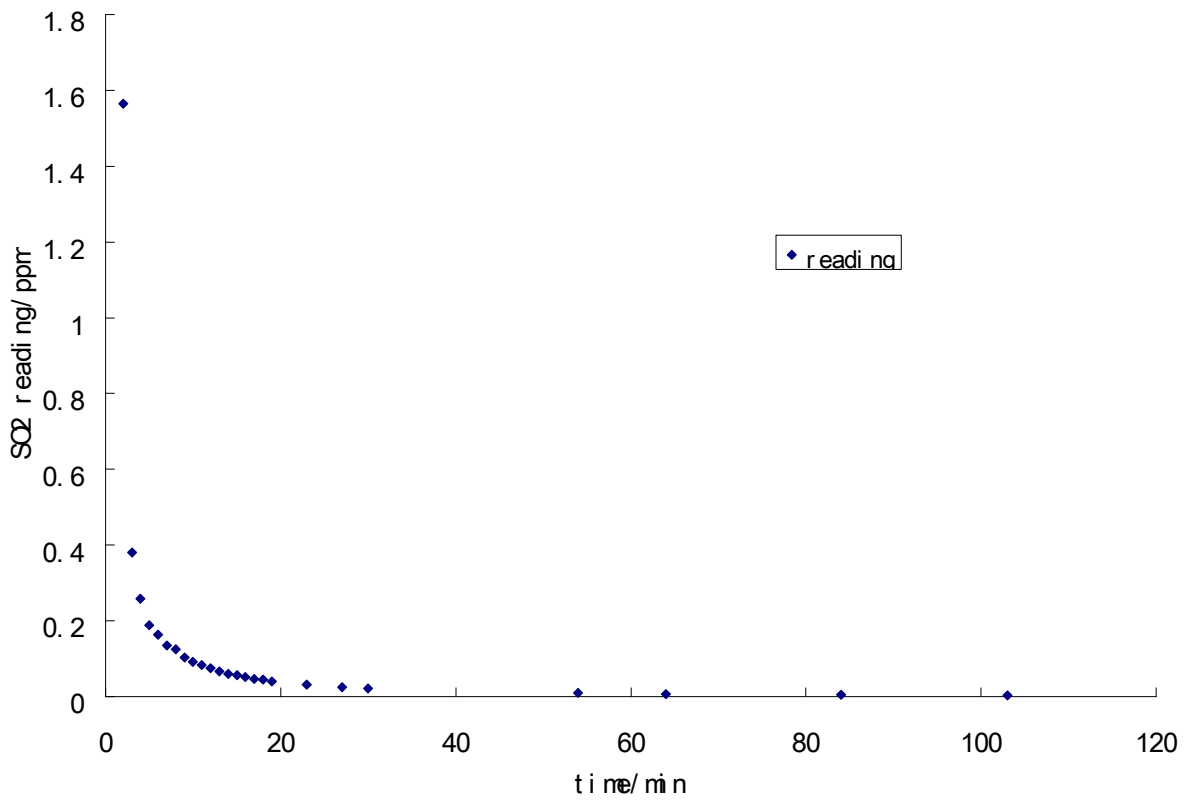**Figure 5: SO₂ reading vs time for Thermo SO₂ analyzer at total range**

Figure 6: SO₂ reading vs time for Thermo SO₂ analyzer at low range

Figure 5 shows the SO$_2$ concentration read by the Thermo SO$_2$ analyzer against time, while figure 6 shows the same data at maximum range 0 to 2 ppm during the calibration process. From the figure the reading is very fast from 90 to less than 10 ppm. Response time is less than 5 minutes for this range. However, the device response is much slower when the reading drops below 2 ppm. It requires 10 minutes for the reading down to 0.1 ppm and 30 minutes for the reading down to 0.02 ppm.

Recommendation:

(1) Four feet of packing is proposed so the outlet SO$_2$ concentration is greater than 2 ppm.

(2) Another reason for the low response time could be that SO$_2$ absorbed in the pipe wall or SO$_2$ dissolved in water which remains in the pipe which makes it difficult to purge SO$_2$. One solution is to use N$_2$ to purge SO$_2$ from the sample line when switched from the inlet to the outlet concentration mode.

3) Remove flow restrictor within the analyzer to increase purge flow.

Currently, we plan to adopt methods 1-3 and use 4 feet of packing.

Measurement of liquid side mass transfer coefficient

The stripping of toluene from water using air is adopted for the measurement of liquid film mass transfer coefficient. According to the 2-film theory (Basmadjian, 2004):

$$\frac{1}{K_x a} = \frac{1}{k_x a} + \frac{1}{m k_y a} \tag{8}$$

where K$_x$ is the overall mass transfer coefficient, k$_x$ is the liquid film mass transfer coefficient; k$_y$ is the gas film mass transfer coefficient; m is the slope of equilibrium curve. If we choose a system with a large m, the liquid side mass transfer resistance will be much larger than the gas side mass transfer resistance. Therefore we can assume the overall liquid phase mass transfer coefficient equals liquid film mass transfer coefficient. Thus, we can measure the liquid film volumetric mass transfer coefficient from the overall liquid phase volumetric mass transfer coefficient.

An air/Toluene/water system is an example of such a test system. The Henry's constant of toluene in water is 353.1 atm/mol fraction (Chapoy, 2008) and the solubility is 542 ppm (Carl, 1990) in room temperature and atmosphere. m equals Henry's constant times activity coefficient divided by total pressure. In this system, m is large enough to ignore the gas side resistance. The system used is water saturated with toluene; samples are taken from the inlet and the outlet of the column and analyzed in a GC. The gas flow rate is 180, 300, and 450 CFM and liquid flow rate is 1–25 gpm/ft^2. The liquid film volumetric mass transfer coefficient can be measured by the following equation(Linek, 1984):

$$k_L a = \frac{u_L}{Z} \ln(c_{LA1} / c_{LA2}) \tag{9}$$

Where u$_L$ is the superficial liquid velocity, Z is the packing height and c$_{LA1}$ and c$_{LA2}$ is the liquid phase toluene concentration at the inlet and outlet of the column. Since we have the value of the effective area from our previous experiment, we can calculate the k$_L$ by:

$$k_L = \frac{k_L a}{a_e} \qquad (10)$$

An HP 5890A Gas Chromatograph will be used to measure inlet and outlet toluene concentrations. A capillary GC column for C6 through C12 is used. 0.5 ml hexane is used to extract toluene from 0.5 ml sample since water is not allowed for the column. A calibration for the GC has been made and a standard curve for toluene obtained.
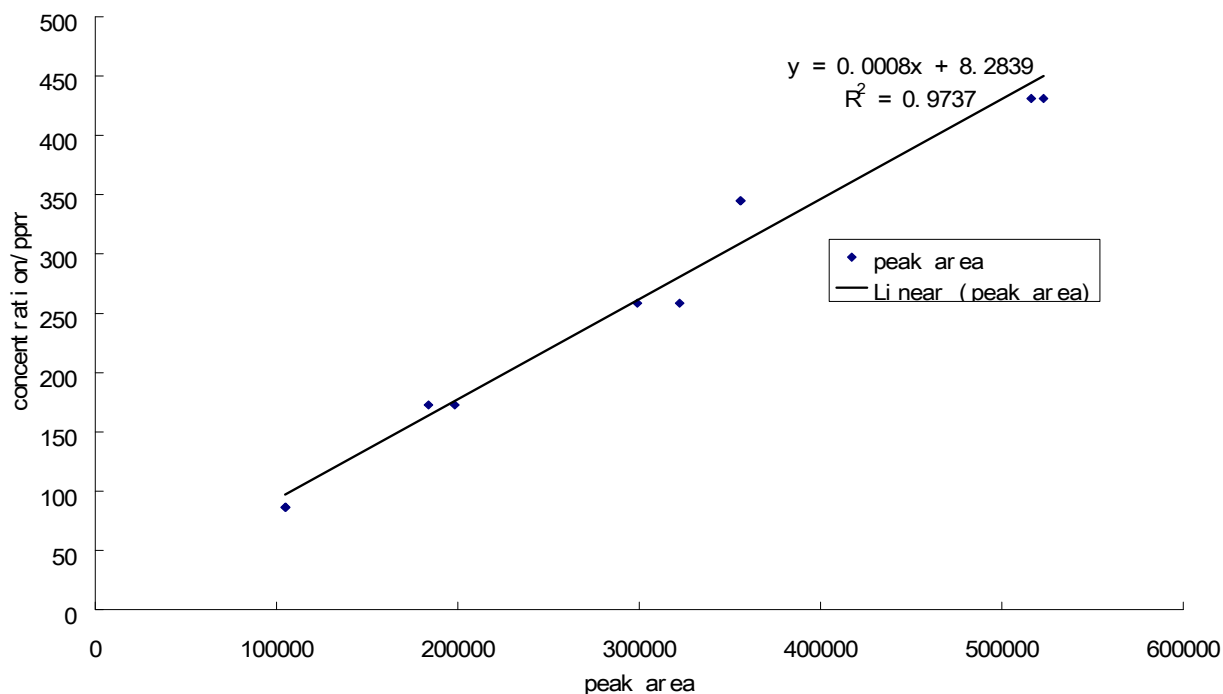

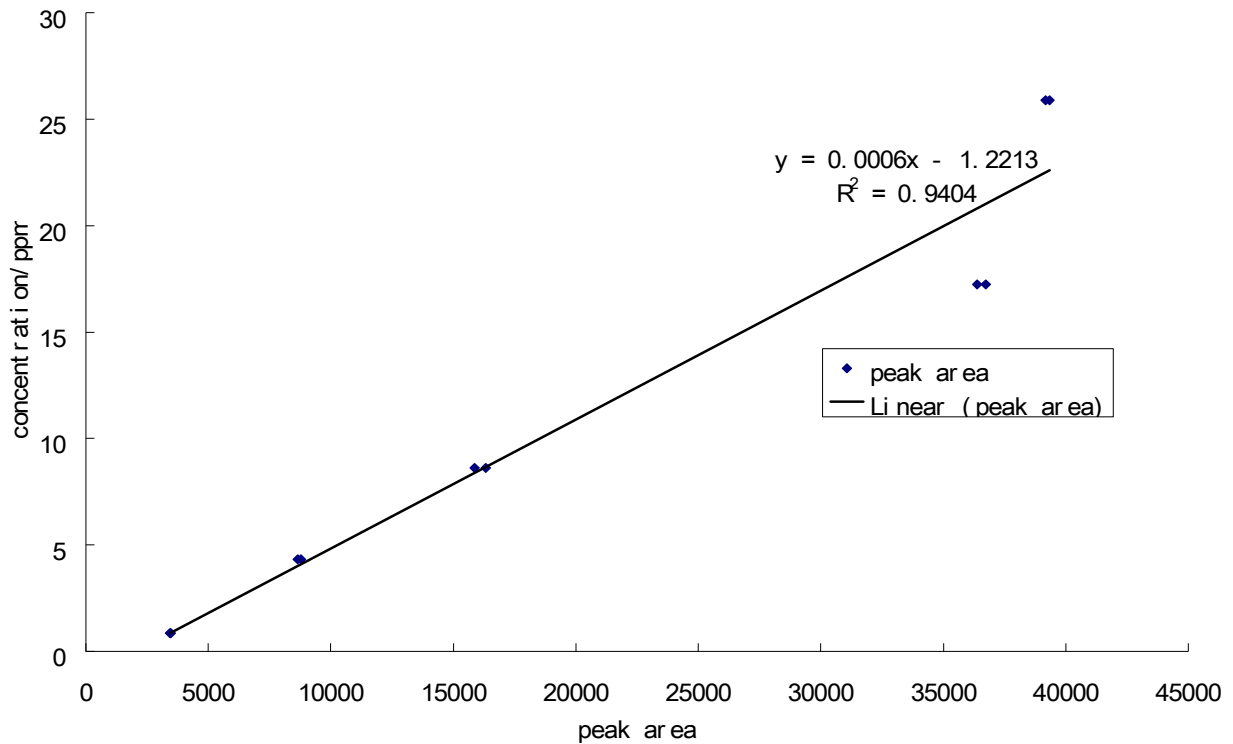**Figure 7: Standard curve for toluene in water. (concentration vs. peak area, range:0-500 ppm)**

Figure 8: Standard curve for toluene in water. (concentration vs. peak area,range:0-30 ppm)

Figure 7 is the curve for the whole range and Figure 8 provides the low toluene range representing the expected outlet composition. Two different correlations will be utilized to determine the toluene concentration from the peak areas. Measurement of $k_L a$ will begin in October.

Future Work

We are planning to complete the measurement of effective area ae, gas film mass transfer coefficient $k_G a$ and liquid film mass transfer coefficient $k_L a$ for Raschig RSP 250 by October. Our next plan is to complete similar measurements of the Mellapak 2X and Flexipac 1.6 Y HC structured packings by December. We will switch to random packings in early 2009.

References

Schultes M, Chambers S, "How To Surpass Conventional and High Capacity Structured Packings with Raschig Super-Pak". *AIChE Spring National Meeting,* 23-27 April, 2006.

Olujic Z, Seibert AF, Kaibel B, Jansen H, Rietfort, T, Zich E. "Performance of a New High Capacity Structured Packing", *AIChE Spring National Meeting,* 22-26 April, 2001.

Hausch G, Nieuwoudt I, Sommerfeldt RA. Advances in styrene fractionation with InTALOX packed tower systems: Part 2-FLEXIPAC HC Structured Packing. *AIChE Spring Natl. Meet. Conf. Proc. 2005*, 1813.

Bishnoi S. *Carbon Dioxide Absorption and Solution Equilibrium in Piperazine-Activated Methyldiethanolamine.* University of Texas at Austin. Ph.D. Dissertation. 2000.

Rocha JA, Bravo JL, Fair JR. "Distillation Columns Containing Structured Packings: A Comprehensive Model for Their Performance. 2. Mass-Transfer Model". *Ind Eng Chem Res.* 1996;35(5):1660.

Tsai R, Schultheiss P et al. "Influence of Surface Tension on Effective Packing Area". *Ind Eng Chem Res.* 2008;47:1253–1260.

Barrett PVL. "Gas absorption on a sieve plate".Ph.D. Dissertation, University of Cambridge, Cambridge, England, 1966.

Danckwerts PV. *Gas-Liquid Reactions*. McGraw-Hill: New York, 1970.

Pohorecki R, Moniuk W. "Kinetics of Reaction between Carbon Dioxide and Hydroxyl Ions in Aqueous Electrolyte Solutions". *Chem Eng Sci.* 1988;43(7):1677.

Basmadjian D. *Mass transfer: principles and applications.* CRC Press: Boca Raton, Fl, 2004.

Chapoy A, Haghighi H, Tohidi B. "Development of a Henry's constant correlation and solubility measurements of n-pentane, i-pentane, cyclopentane, n-hexane, and toluene in water". *J Chem Thermodynamics.* 2008;40:1030–1037.

Carl LY, Haur-Chung Y. "Water solubility data for organic compounds". *Pollution Engineering.* 1990;22(10):79–75.

Linek V, Petericek P. "Effective interfacial area and liquid side mass transfer coefficients in aborption columns packed with hydrophilised and untreated plastic packings". *Chem Eng Res Des.* 1984;62:13–21.

Rocha JA, Bravo JL, Fair JR. "Distillation columns containing structured packings: A comprehensive model for their performance. 2. Mass-Transfer model". *Ind Eng Chem Res.* 1996;35:1660–1667.

Pilot Plant Testing of Advanced Process Concepts using Concentrated Piperazine

Abstract

Pilot plant testing of 8 m piperazine (PZ) in a two-stage heated flash is planned for the spring of 2010. Substantial modifications to the existing pilot plant at SRP will be needed. The process flow diagrams (PFD) and piping and instrument diagrams (P&ID) were updated. The high pressure pump, cross-exchanger, two pressure vessels, and two steam heaters were designed and ordered. Three-dimensional models of the skid equipment are being developed and will be used to design the layout of the skid structure and process piping. A list of process instrumentation and control valves was developed and quotes were obtained.

Introduction

The concept of concentrated (8 m) PZ with high temperature stripping in a two-stage heated flash is ready for pilot plant testing. The concept is described by Freeman et al. (2009). A successful three-week campaign with a simple stripper was completed in the SRP pilot plant in the Fall of 2008. A campaign is proposed for the SRP pilot plant in the spring of 2010. This campaign will require substantial equipment modifications for the high temperature stripping. A portable skid will be constructed, consisting of a cross-exchanger, two shell and tube heat-exchangers, two gas-liquid separators, and a high pressure pump. The skid will be designed to fit inside an ocean shipping container and ultimately be shipped to a site for field validation with real flue gas. Absorber intercooling will also be added to SRP pilot plant and will consist of a pump and a heat-exchanger. This system will be operated for three weeks with 8 m PZ to determine mass transfer, heat transfer, and energy performance at the SRP site. At the completion of the campaign, additional modifications to the high temperature two-stage flash skid will be made and it will be shipped out for field testing.

1

Pilot Plant Modifications

Two-Stage Flash Equipment Design

The two-stage heated flash process will be designed to be mounted on a portable skid that will enable it to be transported for field testing. Equipment size was specified based on a nominal liquid flow rate of 15 gpm. The skid will consist of a high pressure pump, high pressure cross-exchanger, two steam heaters, and two gas-liquid separators. To accommodate field testing, the skid will be design to fit inside a standard 20 ft ocean shipping container. The dimensions for the inside length, door width, and door height are 19'4", 7'8", and 7'6", respectively.

Piping and Instrumentation Diagram

The piping and instrumentation diagram (P&ID) for the skid was updated (Figure 1). Pipe lines sized for the gas and liquid were added. The liquid lines will be 2 inches and the majority of the gas and steam lines will be 1.5 inches. The inlet and outlet nozzle dimensions for the six major pieces of equipment have been finalized and reducers were added to reflect the line size changes.

Temperature controllers for the steam flows to the high and low pressure heaters were added. The liquid level control valve downstream of the low pressure flash vessel was relocated to the outlet of the hot-stream on the cross-exchanger. The lean solvent will not flash across the control valve at the new location. An additional flowmeter was added downstream of the high pressure pump to measure liquid flow. The liquid flow measurement will be used to control the variable speed drive of the high pressure pump to match the inlet flow rate to the skid.

The filters upstream of the cross-exchanger cold and hot inlets were eliminated. Instead, activated carbon will be used to filter a slipstream of the liquid to remove precipitated oxides in the 0.1 to 10 micron range. A second bag filter downstream of the activated carbon will remove particle fines. An orifice plate will be sized to filter a slipstream of approximately 10%.
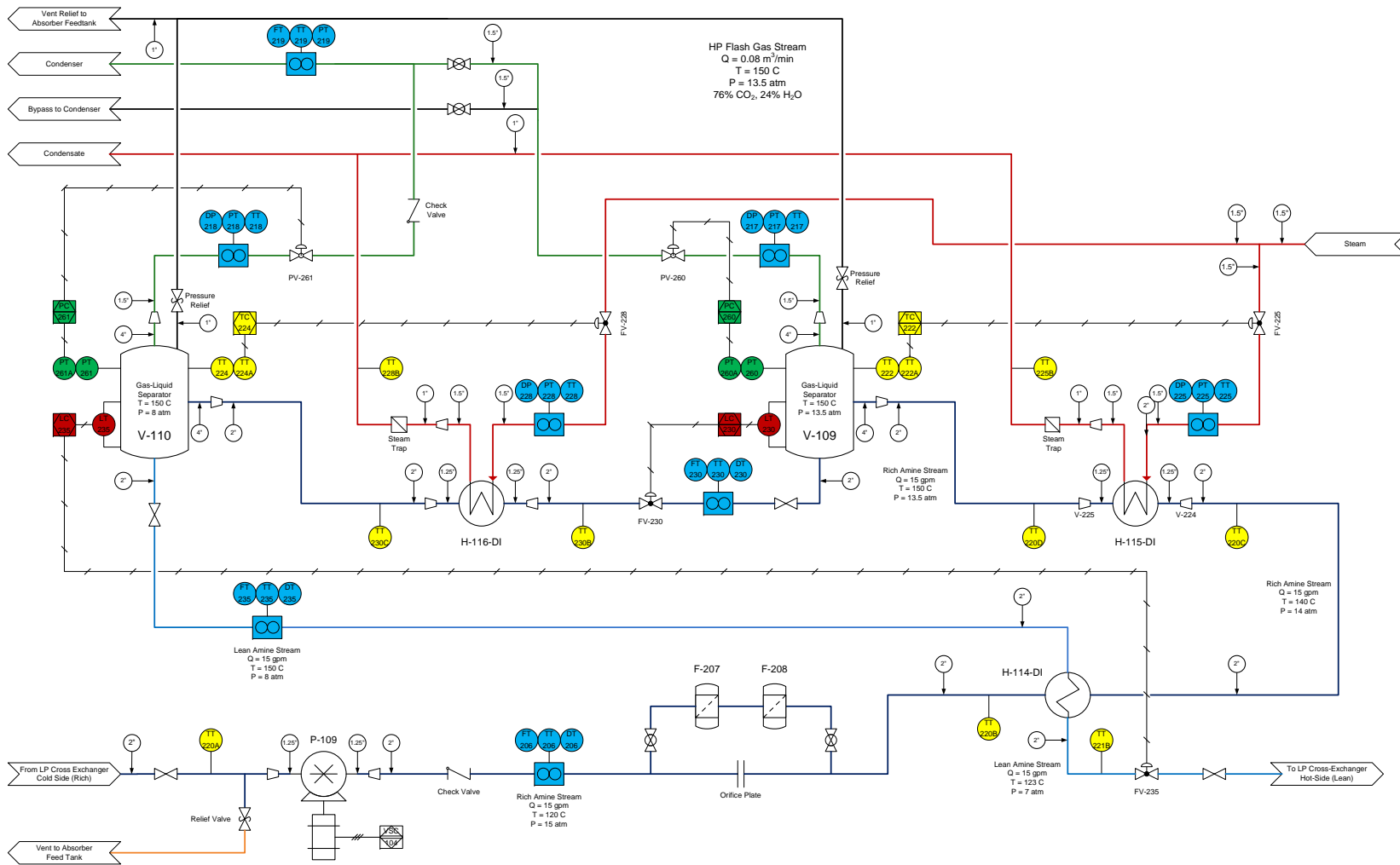
Figure 1: Piping and instrument diagram for two-stage flash system mounted on skid

High Pressure Pump

The Grundfos multi-stage centrifugal pump was ordered and has been procured. The pump specifications are listed in the table below.

Table 1: High pressure pump specification

Model	Grundfos CRNE5-24
Flow	20 GPM @ 250 psig
Matl. of Const.	316 Stainless Steel
Power	7.5 HP / 480V
Motor	TEFC
Controller	Variable Speed
Mechanical Seal	Kalrez

High Pressure Cross-Exchanger

Specifications for the high pressure cross-exchanger were further refined. The new cross-exchanger will be installed downstream of the existing low-pressure Alfa Laval TL10 cross-exchanger. It is anticipated that the solvent will begin flashing at approximately 133 °C. Therefore, the cross-exchanger was redesigned to be single-pass instead of the original multi-pass design to prevent the flashed vapor from being trapped inside the exchanger.

Due to the flashing limitation, the size and cost of the cross-exchanger increased dramatically in order to retain the same heat transfer requirement. The exchanger was designed to heat the rich solvent from 105 to 140 °C. The heat duty was calculated to be approximately 490,000 Btu/hr at 15 gpm and a rich loading of 0.4 mol CO_2/total alkalinity.

The final cross-exchanger specifications are shown in Table 2. The exchanger was ordered and has been delivered to the facilities at SRP. The final drawing is shown in Figure 2.

Table 2: High pressure cross-exchanger specification

Vendor.	Alfa Laval
Model	M6-MFD
Flow	15 GPM
Heat Exchanged	490.6 kBTU/hr
LMTD	15.5 °F
Heat Transfer Area	217.0 ft^2
No. of plates	146
No. of passes	1
Matl. of Const.	316 Stainless Steel
Gasket Matl.	EPDMP
Design Pressure	250 psi
Design Temperature	320 °F

FRAME PLATE (FIXED)

23.62"
37.01"
26.2"
5.91"
13.00"
5.51"
S1 S2 S4 S3
23.62"
RECOMMENDED FREE SPACE FOR OPENING AND CLOSING

PRESSURE PLATE (MOVABLE)
SECTION A-A

1.57"
511 mm
37.4"
47.2"
1.5"
M24
THIS SPACE SHOULD BE KEPT FREE FROM FIXED INSTALLATIONS
A A

0.39"
13.00"
11.42"
2.761.18"
1.57"
43.9"
HOLES Ø28 FOR M20 OR M24 FOUNDATION BOLTS
1.57"
2.17"
1.0"
0.39"

ASME 300
SPECIAL LOOSE FLANGE
S3
S1,S2,S3,S4
5/8"-11UNC
4.05"
Stub end supplied by customer.
3.46"
1.38"
ØB
FLANGE: W = 4.17" H = 5.35"

REMARKS:	SIDE1	SIDE2
DESIGN PRESSURE	250 psi	250 psi
TEST PRESSURE	325 psi	325 psi
MAX TEMPERATURE	320 °F	320 °F
MIN TEMPERATURE	32 °F	32 °F
MAWP	250 psi	250 psi
MDMT	-20 °F	

GASKET	EPDMP CLIP-ON
PLATE MATERIAL	ALLOY 316
PLATE THICKNESS	0.50 mm
HEATING SURFACE	217 ft²
PLATE GROUPING	1*73H/1*72H
WEIGHT WITH WATER	852 lb
NET WEIGHT	717 lb

ALL DIMENSIONS IN INCHES   REV 0 - GENERATE DWG   REV 1 - CHANGE FROM 150# TO 300# CONNECTIONS

SIDE	MEDIA	INLET	TEMP.	OUTLET	TEMP.	FLOW RATE		
1	Lean Solvent UT	S4	302.1 °F	S3	231.8 °F	8223 lb/h		
2	RS 2 points	S2	221.0 °F	S1	284.0 °F	8590 lb/h		

TOTAL LENGTH	46.1"	LIQUID VOL.
TOTAL WIDTH	13"	
TOTAL HEIGHT	37"	
PRESSURE DROP		
0.04241 psi		1.11 ft³
0.8976 psi		1.1 ft³

SUPPLIER	REF. 27462-10	TAG: L/R INTERCHANGER	PLATE HEAT EXCHANGER	Alfa Laval
AGENT / REF. / 743109			M6-MFD	
CUSTOMER NAME / REF. NO. University of Texas At Austin / 2010A01110				SERIAL NO. 30111-99541
SIGN. STR		RISKCATEGORY N/A	ASME	DATE 2009-09-23	REV NO. 1

Figure 2: Final drawing for cross-exchanger

Steam Heaters

Two shell and tube steam heaters were designed and ordered from Ketema LP, a subsidiary of Alfa Laval. The heat exchangers were designed assuming 120 psia steam and will be used to heat the rich solvent to 150 °C, one for each stage in the high temperature stripping process. The heat duty for the high and low pressure steam heaters was calculated to be 200,000 Btu/hr and 150,000 Btu/hr, respectively. The exchanger specifications are listed in the tables below and the final drawings are shown.

Table 3: High pressure steam heater specification

Vendor.	Ketema LP
Size	4 x 54 inch
Type	BEU, Horiz
Process Flow	15 gpm
Heat Exchanged	205 kBTU/hr
LMTD	47.5 °F
Heat Transfer Area	14.36 ft^2
No. of passes (Tube)	2
Matl. of Const.	316 Stainless Steel

Table 4: Low pressure steam heater specification

Vendor.	Ketema LP
Size	4 x 42 inch
Type	BEU, Horiz
Process Flow	15 gpm
Heat Exchanged	153 kBTU/hr
LMTD	44.2 °F
Heat Transfer Area	11.22 ft^2
No. of passes (Tube)	2
Matl. of Const.	316 Stainless Steel
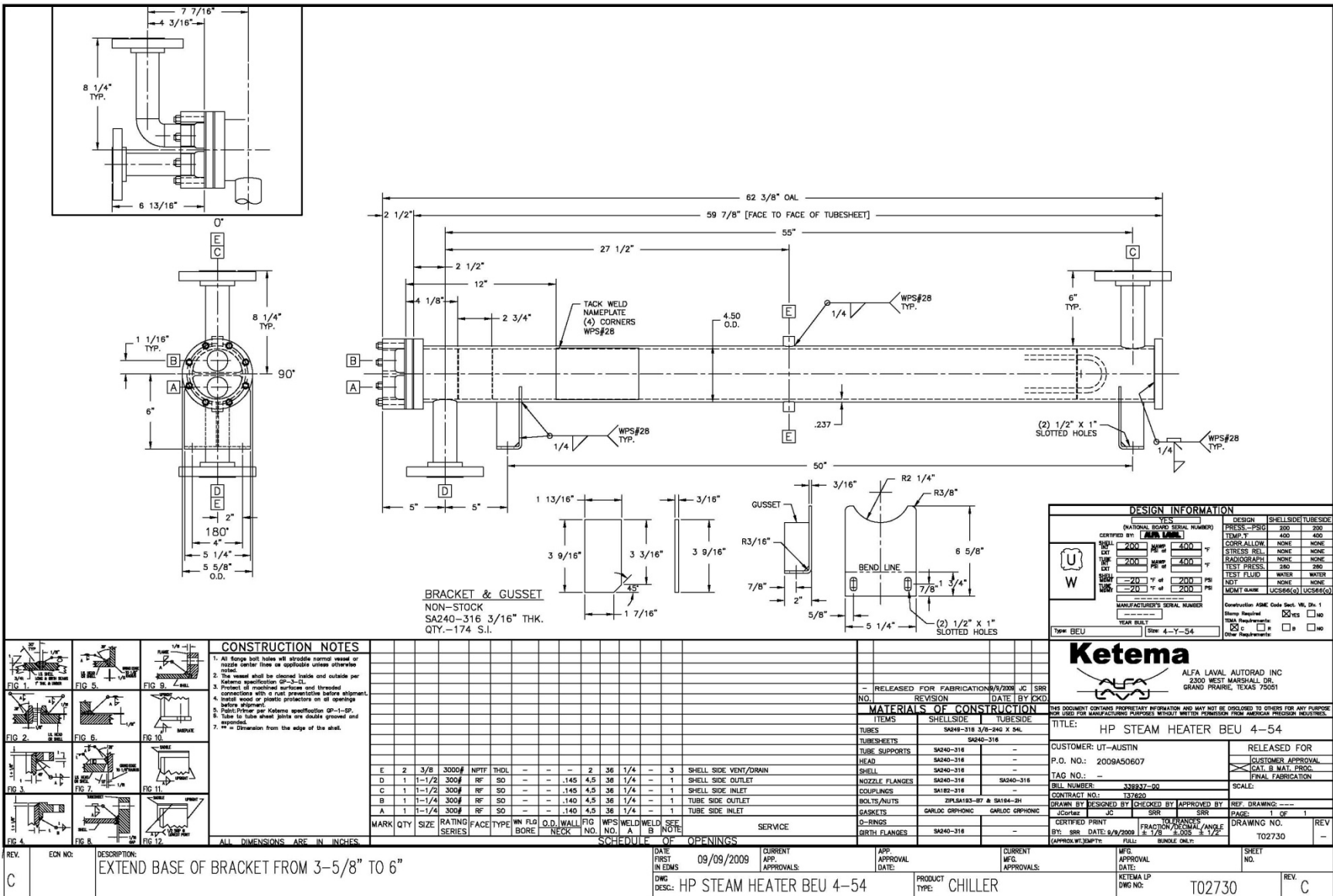
Figure 3: Final drawing for high pressure steam heater
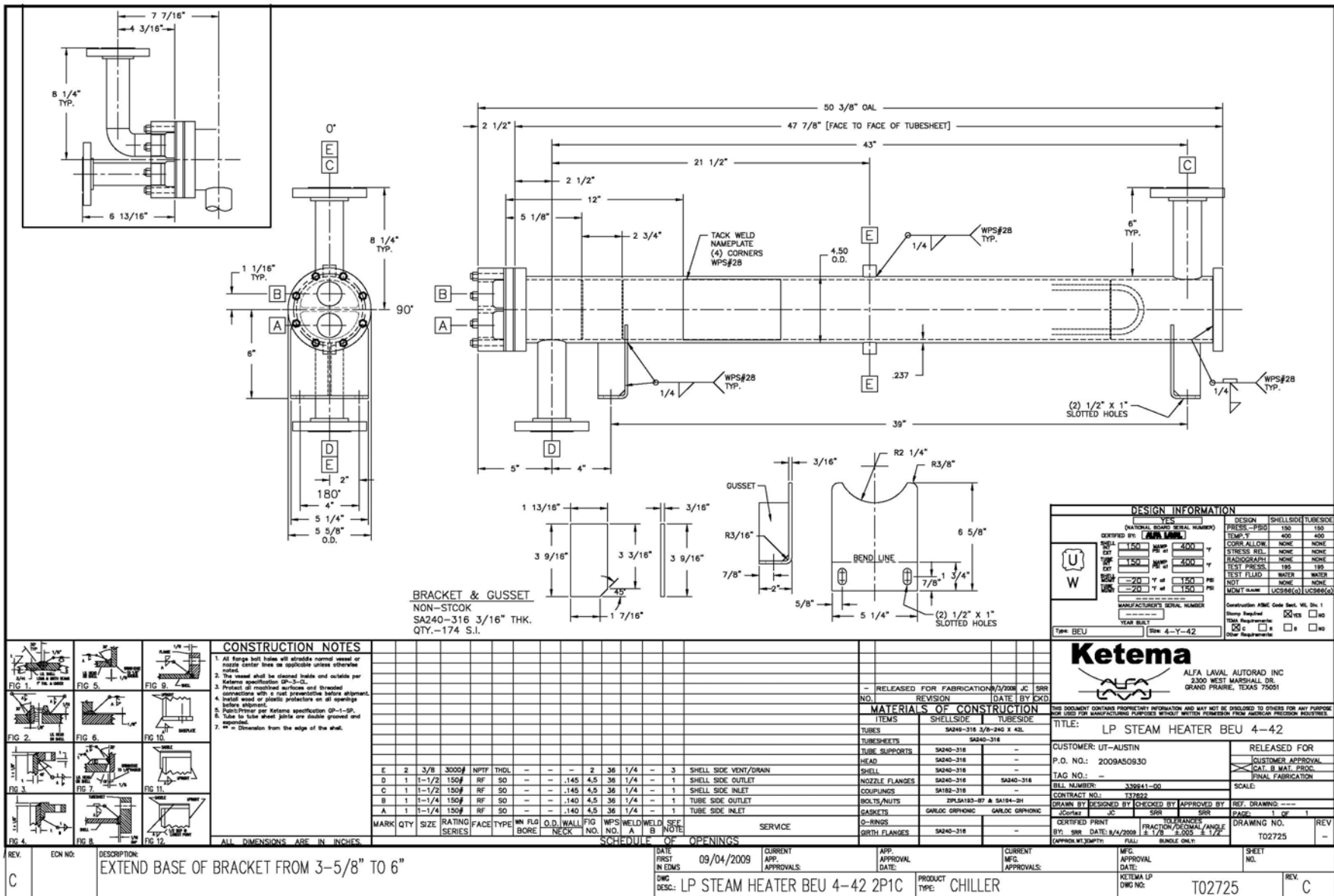
Figure 4: Final drawing for low pressure steam heater

Gas-Liquid Separator

Two gas-liquid separator vessels were designed and have been ordered. The vessels are designed to separate the gas and liquid downstream of each steam heater. At 15 gpm, the vessels will have a liquid hold time of approximately one minute. The high pressure vessel was designed to operate at 150 °C and 13.5 atm. The outer diameter of the vessel will be 18 inches. The inlet nozzle will be tangential to the vessel and will be a 4-inch nozzle. The 2-inch nozzles on the body vessel will be used to measure liquid level in the tank. A vortex breaker will be installed at the outlet of the liquid drain, which will be 2 inches.

A 6-inch mist eliminator pad will be installed above the inlet. An 18-inch flange will bolt the top head to the body of the vessel. The majority of the vessel will be manufactured using 304 stainless steel. Carbon steel will be used on legs, lifting lugs, and the 18-inch flange. On the vessel head, the gas outlet will be 4 inches and the 1-inch nozzle will be used for installation of the relief valve. The thickness of the vessel wall will be 0.25 inches. The flanges will be 300# class.

The low pressure vessel has the same dimensional design as the high pressure vessel, but is rated for 150 °C and 8 atm. The flanges will be 150# class and the wall thickness of the vessel will be 0.19 inches. The final drawings for the two vessels are shown below. Both vessels will be fabricated according to ASME standards by Central Fabricators Incorporated in Ohio.

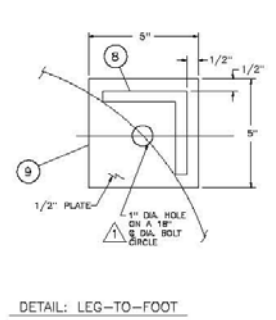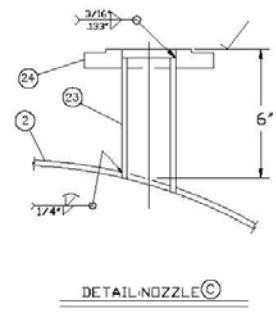**Table 5: Gas-liquid separator dimensional and material specifications**

Vendor.	Central Fabricators
Outer diameter	18 in
Total height	67 in
Inlet nozzle	4 in
Outlet gas nozzle	4 in
Outlet liquid nozzle	2 in
Mist eliminator	6 in
Matl of const.	304 SS

Table 6: High and low pressure gas-liquid separator specifications

	High Pressure	Low Pressure
Operating temp.	150 °C	150 °C
Operating pres.	13.5 atm	8 atm
Wall thickness	0.25 in	0.19 in
Flange class	300	150

Figure 5: Final drawing for high pressure gas-liquid separator

Figure 6: Final drawing for high pressure gas-liquid separator – close-up details

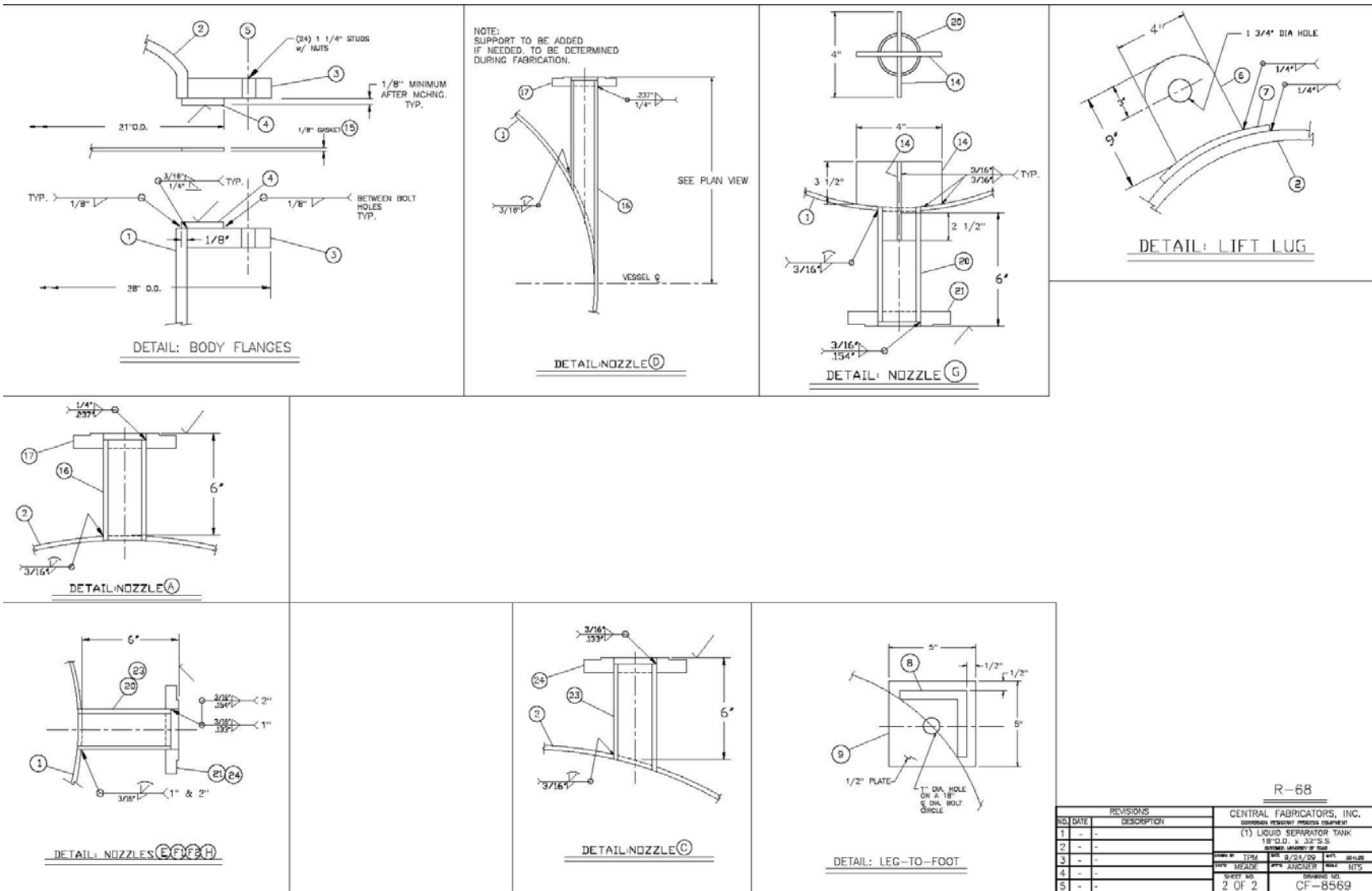**Figure 7: Final drawing for low-pressure gas-liquid separator**

Figure 8: Final drawing for low pressure gas-liquid separator – close-up details

Process Instrumentation

One unique feature of the skid is that it will incorporate the latest wireless technology from Emerson Process. Currently, wireless temperature and pressure measurements are the two main products that are commercially available. However, in-depth evaluation of the existing wireless technology found that the technology to send and receive discrete I/O to Micromotion® Coriolis flowmeters, integral orifice flowmeters, and control valves does not currently exist. A work-around solution to this problem was proposed, but was deemed too cumbersome. Further exploration by our contacts at Emerson will be conducted to determine if the THUM adapter can be customized to fit our process control and instrumentation needs.

Three F100 Micromotion® flowmeters will be used to measure the liquid flow downstream of the high pressure pump and the outlet liquid stream of each gas-liquid separator. Three Rosemount 3051 SFP integral orifice flowmeters will measure the gas outlet of each gas-liquid separator and the combined gas flowrate of the two separators. Integral orifice flowmeters will also be used to measure the steam flow rate downstream of the control valve. Baumann 24000SVF stainless steel control valves will be used to control the pressure in the gas-liquid separators, regulate the steam flow to the steam heaters and maintain the liquid level in the gas-liquid separator vessels. RTDs will be used to take temperature measurements and the Rosemount 3051 pressure transmitter will be used to measure pressure. The default option will be to use hard-wired Foundation Fieldbus devices if the wireless/THUM adapter options do not work.

Major Process Equipment Cost

The total cost of the process equipment that has been ordered so far is listed in the table below, which includes the high pressure pump, cross-exchanger, two steam heaters, and the two gas-liquid pressure vessels. More than half of the process equipment cost was allocated on the pressure vessels. The cost of the cross-exchanger was also high because of the single pass design. It is proposed that future designs incorporate a large multiple-pass plate and frame exchanger that would be used to recover heat up to the temperature and pressure before the solvent flashes and a small single-pass plate and frame exchanger would be used downstream for the final heat recovery. This would eliminate the need for a large single pass plate and frame exchanger and reduce capital costs.

Table 7: Major process equipment costs

Item	Cost
Grundfos pump	$8000
Cross-exchanger	$12,500
HP steam heater	$4200
LP steam heater	$3900
HP gas-liquid separator	$16,600
LP gas-liquid separator	$14,600
Total	**$60,000**

Absorber Intercooling Design

It has been proposed that a fiberglass reinforced plastic (FRP) plate and frame heat exchanger be used as the absorber intercooler. Additional investigation will need to be conducted to determine the detailed specifications and limitations of the FRP exchanger.

Three-Dimensional Skid Design and Layout

Three-dimensional models have been developed for the major components of the skid and will be used to design the layout and skid structure. In addition, 3D models were developed for the Micromotion® flow meters, control valves, gates valves, check valves, and orifice flowmeters. The 3-D drawings were made using Google Sketchup version 7.1.

Figures 9 and 10 illustrate the relative size of each process equipment on a 6 ft x 9 ft footprint. Please note that the drawing layout in the figures do not reflect the final design of the skid structure and equipment layout. Figure 11 shows the 3-D drawings for the Micromotion® flowmeter, Baumann control valve, gate valve and check valve. The skid structure will be broken up into two sections, which can be bolted together and reassembled. This will allow each skid to be easily moved by a fork lift.

Pilot Plant Schedule

Pilot plant tests using 8 m PZ and the two-stage high temperature stripping process are planned for Spring 2010. Activities will include the design, layout, and construction of the skid mounted two-stage flash system and installation of absorber intercooling system. The pilot plant will be operated for three weeks. The proposed schedule for the planned pilot plant campaign is shown in the table below.

Table 8: Pilot plant schedule for 2009-2010

October	Equipment and instrument procurement
November	Begin equipment installation and skid construction
December	Complete equipment installation
January	Begin pilot plant campaign
February	Complete campaign

After the completion of testing at SRP, long term testing of concentrated PZ with real flue gas is planned. The system will be operated for 3 to 6 months at a coal-fired facility. Some possible locations include the Wilsonville pilot plant constructed by Southern Co. and also the Tarong pilot unit being constructed by CSIRO in Australia.
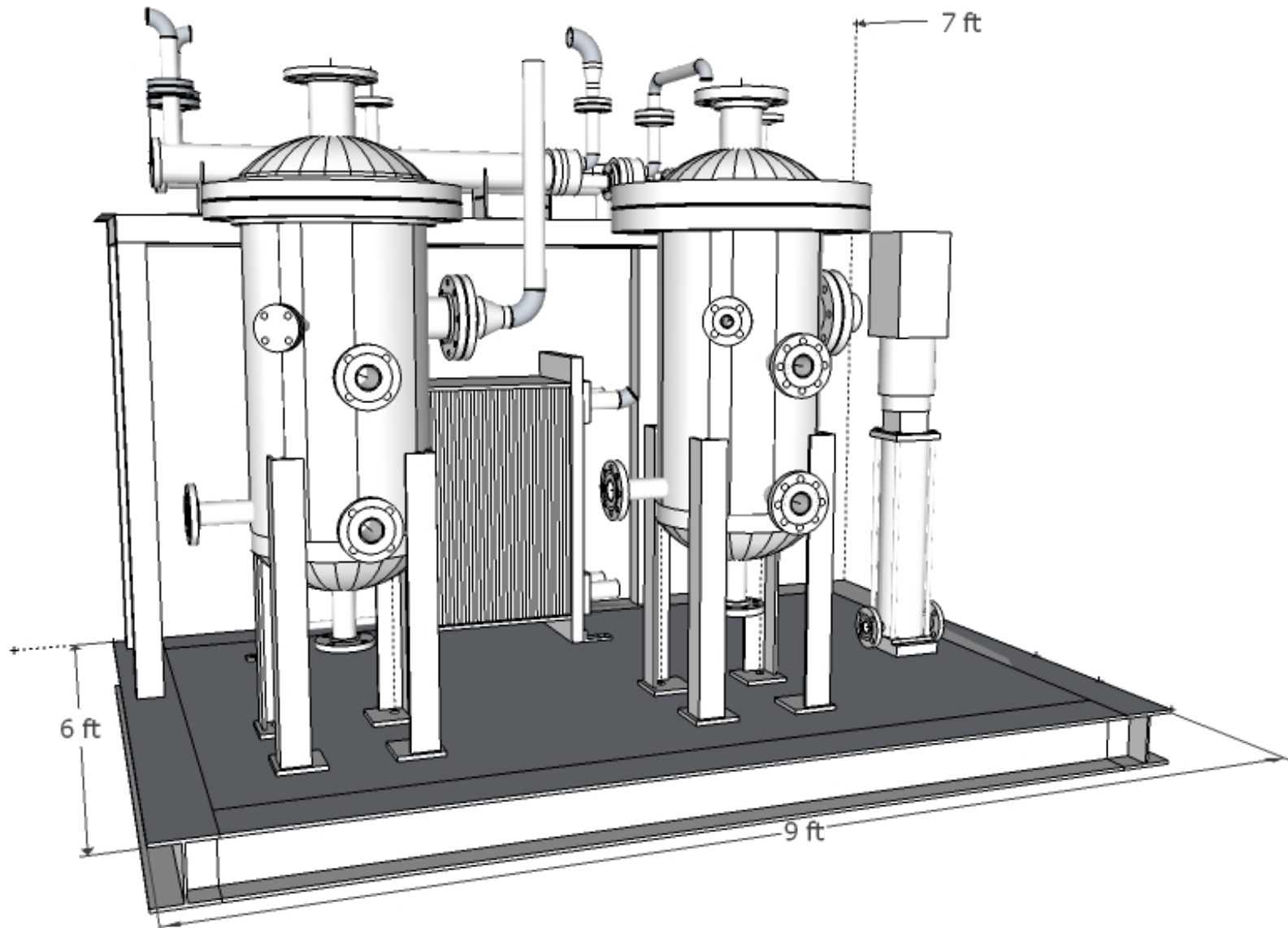
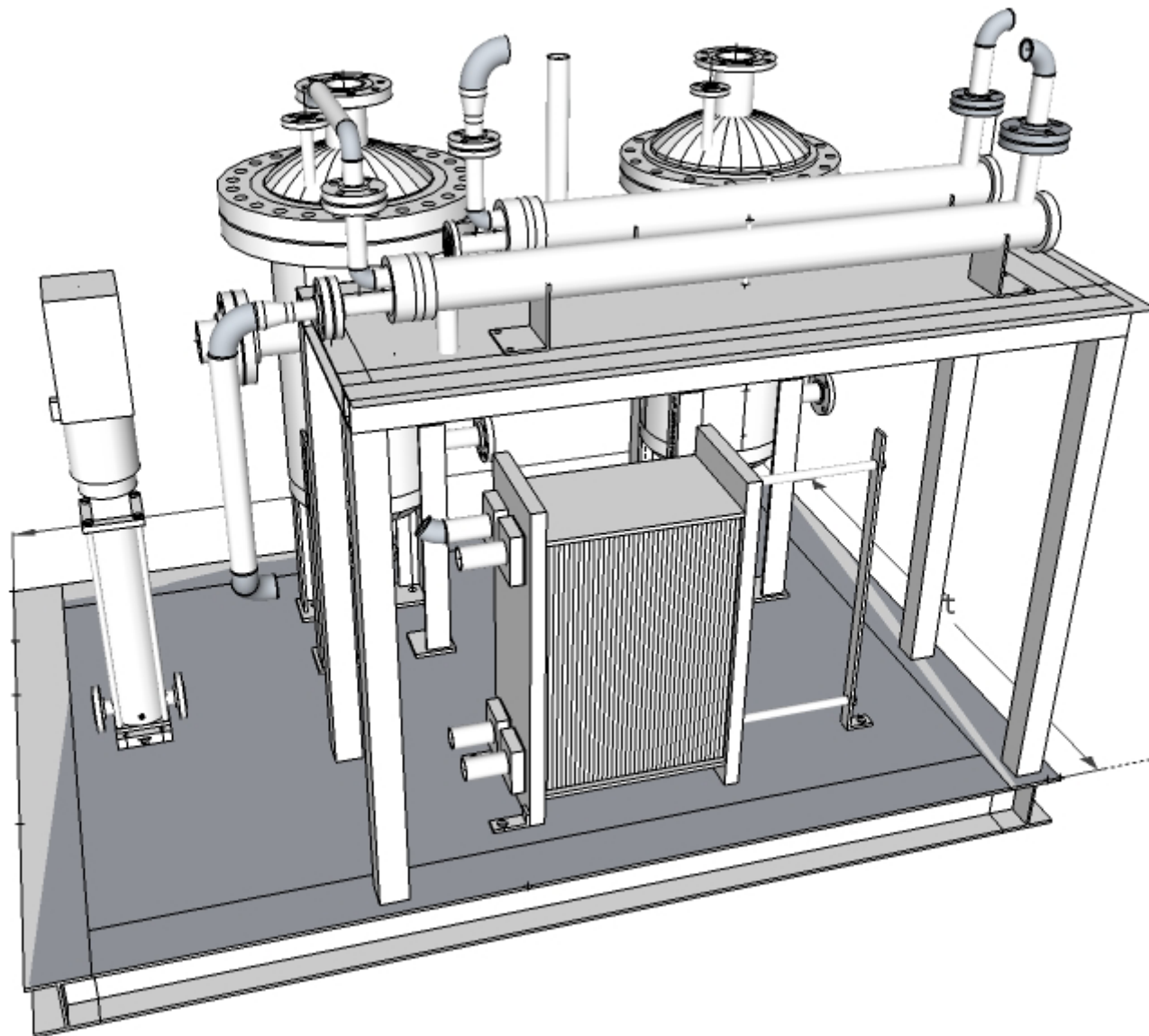**Figure 9: Three-dimensional view of major process equipment on 6 ft x 9 ft footprint**

7 ft

6 ft

9 ft

Figure 10: Three-dimensional view of major process equipment on 6 ft x 9 ft footprint from opposite side
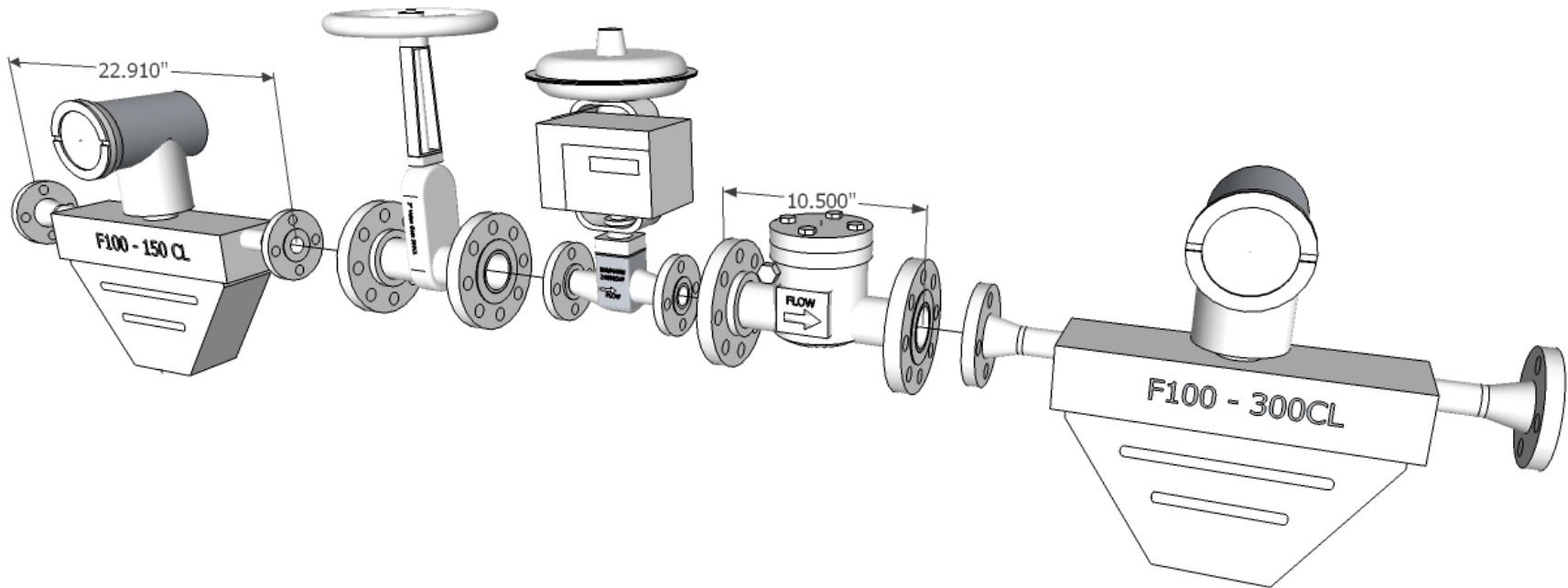
Figure 11: Three-dimensional view of Micromotion® flowmeters, control valve, gate valve, and check valve

Future Work

The skid design and layout needs to be completed in the 3-D model. The 3-D model will be used to bid on the fabrication of the skid support structure and for the welding of the piping. The availability of the wireless technology for the skid process instrumentation needs to be determined so that an instrumentation route can be proposed.

References

Freeman SA, Dugas R, Van Wagener D, Nguyen T, and Rochelle GT. "Carbon dioxide capture with concentrated, aqueous piperazine". submitted to IJGGC.

Nitrosamine Formation in CO$_2$ Capture Plant

Abstract

The purpose of this work is to investigate nitrosamine formation in CO$_2$ capture plants from coal-fired power plant flue gas.

Nitrosamines are important, because of their carcinogenic effect on animals and humans. Almost all studies related to nitrosamines have been done in acidic conditions which are compatible with in vivo conditions.

The project is going to determine whether nitrosation reagents are present in the system, and, if there are sufficient nitrosation compounds, what is the possibility of nitrosamine formation in a basic medium, because amine solutions in CO$_2$ capture plants have alkaline and basic properties.

The specific objectives of this work will be:
- Develop an appropriate method for measuring and detecting nitrosamine to monitor nitrosamine production reaction in CO$_2$ capture plants.
- Qualify the nitrite sources in CO$_2$ capture plants: flue gas, absorber, and stripper.
- Determine nitrite and amine reaction rates to qualify nitrosamine formation in basic solution.
- Analyze amine oxidation and thermal degradation products and their effects on amine and nitrite reaction to examine if they are nitrosamine formation catalysts or inhibitors.
- Investigate piperazine behavior in reaction with nitrites and nitrosopiperazine inhibition methods.

Introduction

During this quarter I have done a literature review and prepared a future work plan. Nitrosamines are produced from the reaction between nitrites and secondary amines. Nitrosamines are a group of undesired industrial and environmental pollutants, many of which are carcinogenic, mutagenic, and teratogenic. Figure 1 shows the Lethal Dose (LD50) of different component on rats.
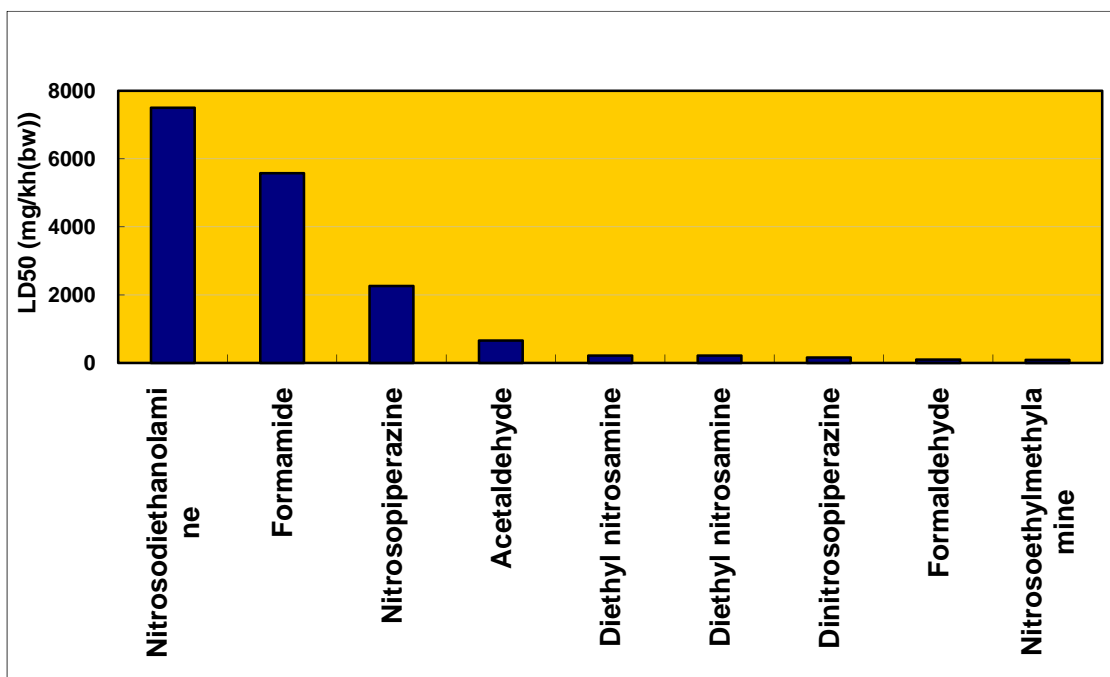
Figure 1: LD50 for nitroso-compounds and some other common products in environment (MSDS)

Nitrosamines can cause cancers in wide variety of animal species including humans. Since the discovery of the carcinogenicity of nitrosodimethylamine (NDMA) by Magee and Barnes (1956), much attention has been paid to the formation and characteristic carcinogenicity of several kinds of nitrosamines (Mizgireuv et al., 2004; Fukushima et al., 2005; Tanaka et al., 1988; Anderson et al., 1992). It has been demonstrated that tertiary and quaternary amines react with nitrite to form N-nitrosamines under acidic conditions (Fiddler et al., 1972; Lijinsky et al., 1972; Smith and Loeppky, 1967). Investigations about the rate and kinetics of nitrosamine formation from amines and nitrous acid have been done in several studies (Russell et al., 1961; Kalatzis and Ridd, 1966; Lovejoy and Vosper, 1968; Mirvish et al., 1972; Jones et al., 1973; Cachaza et al.,1978; Challis and Outram, 1982; Kirsch et al., 2003; Masuda et al., 2000; Choi et al., 2003; Zhao et al., 2006; Winter et al., 2007; Andrzejewski et al., 2008)

There are broad studies on nitrosamines formation in acidic conditions, but in basic and alkaline solutions few projects have been done. Keefer and Roller (1973) conducted some experiments on N-nitrosation by nitrite ion in neutral and basic medium. They found that formaldehyde and chloral catalyzed the conversion of different secondary amines to nitrosamine in the pH range 6.4–11. The nitrosamine formation from secondary amines and nitrites has been studied by in resting cells of Escherichia Coli B, (Kunisaki and Hayashi, 1979). They used dimethylamine and piperidine in pH from 6 to 9. Casado et al. (1984) investigated the nitrite ion as a nitrosating reagent in the nitrosation of morpholine and diethylamine in the presence of formaldehyde. They described the kinetics of nitrosation in the presence of formaldehyde at pH values from 6.5 to 8.2 and from 6.9 to 8.7, respectively.

Many years later basic media again attracted researchers. Mitch and Sedlak (2002) studied the formation of nitrosodimethylamine from dimethylamine during chlorination. They conducted a

series of experiments in the pH range of 6 to 9 and showed that the formation of nitrosodimethylamine during chlorination may involve the slow formation of 1, 1-dimethylhydrazine by the reaction of monochloramine and dimethylamine followed by its rapid oxidation to nitrosodimethylamine and other products including dimethylcyanamide and dimethylformamide. Lv et al. (2009) presented a theoretical investigation of nitrosodimethylamine formation from dimethylamine nitrosation which catalyzed by carbonyl compounds.

Studies have been done to find ways to nitrosamine inhibition. Archer and Wishnok, (1975) studied the effect of ascorbate on the formation of nitrosomorpholine. Depending on whether oxygen was present in the system, the formation of nitrosomorpholine was completely inhibited. Cannon (1985) recorded a patent that is directed to the inhibition of nitrosamines in dinitroaniline herbicides by the incorporation of an additional compound of an alkali metal or ammonium bisulfate with an aldehyde or ketone.

In 1996, Blazard et al. recorded a patent that mentioned a method of inhibiting the formation of nitrosamines and nitrites during the preparation and storage of amine oxides. They presented a composition of bicarbonates, carbonates, and phosphonates at alkaline pH to inhibit nitrosamine formation in preparation of different kinds of amine oxides. Itoh et al. (1999), considered the effect of oxygen on the reaction of secondary amines with nitric oxide. They showed that dinitrogen trioxide formed in the presence of NO nitrosate aromatic secondary amines in a catalytic manner.

Previous Research Results

Nitrosamines are important, because of their carcinogenic effect on animals and humans. Therefore almost all studies related to the nitrosamines have been done in acidic conditions which are compatible with in vivo conditions. But amines are used in natural gas refineries to remove H_2S and CO_2 from sour gas and also in CO_2 capture plants to remove CO_2 from industrial flue gas, especially coal-fired power plants. Nitrogen compounds exist in plants from different sources, input flue gas, oxidative degradation, and thermal degradation, so there is a possibility of formation of nitrosamine ifwhile nitrosation reagent is present in the system. Nitrites and secondary amines react and produce nitrosamine in acidic pH, but in CO_2 capture plants, pH is going to be in the basic range. Studies show that nitrosamine formation in basic medium is not a concern, but some products can catalyze the reaction in basic medium, such as chloral and formaldehyde. Experiments show that oxidative amine degradation products contain glycolate, acetate, formate, nitrite, nitrate, oxalate, aldehyde, N-formyl amides, N-oxyl amides, ethylenediamine, ethylenediamine amides, (Sexton, 2008; Freeman, 2009). Keefer and Roller (1973) demonstrated that formaldehyde can catalyze nitrosodimethylamine formation in alkaline solution. This research proposed to provide some experiments to consider each component in absorber and stripper at a CO_2 capture plant whether they are a catalyst to nitrosamine formation or an inhibitor. There follows a few investigations which have been done in a high pH range.

Using alkaline formaldehyde solution caused nitrosation of secondary amines in basic medium. When Keefer and Roller (1973) conducted experiment with 0.13 M pyrrolidine and 4.0 M sodium nitrite in the presence of 13 M formaldehyde and 0.1 M sodium hydroxide, they found a yield of 46% nitrosamine formation compare to the reaction without formaldehyde. Figure 2 shows the yield of nitrosodimethylamine formation after 17 hours at 24°C respect to pH in the reaction of 0.05 M dimethylamine, 0.2 M sodium nitrite, and 0.05 M formaldehyde.
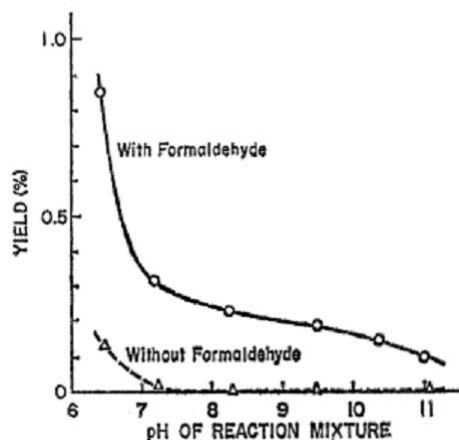
Figure 2: The effect of formaldehyde on nitrosodimethylamine formation at high pH (Keefer and Roller, 1973)

There is a pH optimum value in the study that has been done (Kunisaiki and Hayashi, 1978), Figure 3. Their reactions were carried out in a basic medium between 6 to 9 that was adjusted by 0.1 M of sodium dihydrogen phosphate, and they used a E. coli B containing protein to form nitrosodimethylamine from 0.25 M dimethylamine and 0.1 M nitrite.
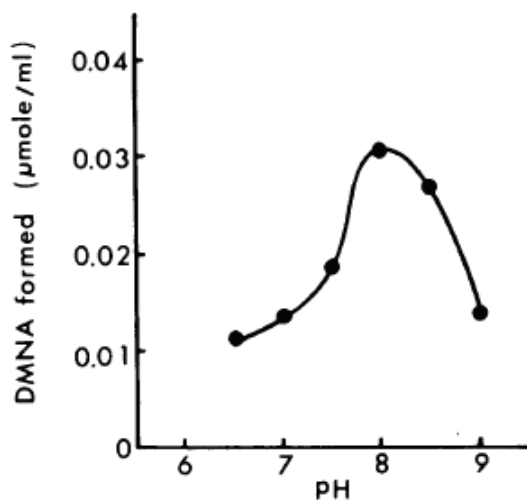

Figure 3: The effect of pH on nitrosodimethylamine in E. Coli B condition, (Kunisaiki and Hayashi, 1978)

Lv et al., (2009) presented a theoretical investigation of the mechanistic path of the reactions of dimethylamine with nitrite anion catalyzed by carbonyl compounds. A comparison of energy barriers of nucleophilic addition reaction and the electrophilic substitution reaction indicated that the order of the catalytic activity was obtained as formaldehyde > chloral > acetaldehyde > acetone.

This research program will focus on the possibility of nitrosamine formation in reaction between nitrite and amines which are used in CO_2 capture by alkanolamine absorption/stripping. There

4

have been no studies to date that consider nitrosamine formation in CO_2 capture plants which may emit to the environment.

Research Plan

This research program will consist of the following steps. First, analytical methods to detect and monitor nitrosamine formation will be investigated and validated. Next, reactions in the liquid and gas phases in the absorber and stripper sections of a CO_2 capture plant at operating conditions will be measured with rich reagents and field samples. Then, reaction catalysts and inhibitors will be examined. Finally, it will be established if nitrosamine is likely to be formed during the CO_2 capture process, and if so how best to inhibit or destroy it.

Task 1:

The purpose of this section is to describe and develop the analytical methods that are available for detecting, measuring, and monitoring nitrosamines, especially nitrosopiperazine. The methodology for nitrosopiperazine analysis includes several steps: sample collection, extraction, detection, measuring, and determination of nitrosopiperazine.

Methods have been reported for the determination of nitrosamines in biological fluids. A spectrophotometric method was reported by Ziebarth et al. (1975). Gas liquid chromatographic (GLC) methods, using nitrogen-specific flame ionization detection (Sander et al., 1975), or thermal energy (Osterdah and Bellander, 1983), were also reported. Because these chromatographic methods offer a high degree of specificity, sample clean-up and the instrument limitations prevent their use in routine clinical studies, and there is still a need for an alternative for the chromatographic methods. Voltammetry was a promising substitute regarding sensitivity, efficiency, and simplicity (Belal et al., 2000). Walash et al., (2001) described a reversed-phase HPLC method using UV detection to measure low concentrations of N, N-dinitrosopiperazine in gastric juice.

This research will develop a method to detect dinitrosopiperazine using a combination of mass spectrophotometry and HPLC in non-biological conditions and in both liquid and gas phases.

Task 2:

During this step, the nitrite ion sources as nitrosation reagent will be qualified in different areas of CO_2 capture plants: flue gas, absorber, and stripper. The flue gas composition will be analyzed because of the presence of nitrogen oxides which can react with water and produce nitrous acid that is one of the nitrosating reagents. The amine oxidative and thermal degradation products in the absorber and stripper will be analyzed and the kinetics of reaction between nitrite and amine will be investigated to determine the rate of nitrosamine formation in high pH. Several studies have been done on nitrosamine formation in acidic conditions but the proposed condition for this project is a high pH and basic medium.

Task 3:

One of the most important considerations in this project is the effect of the degradation products which are present in absorber and stripper on amine nitrosation. Freeman (2008) predicted the existence of aldehyde in amine oxidative products. Keefer and Roller (1973) showed that using alkaline formaldehyde solution caused nitrosation of secondary amines in basic medium.

Therefore this research will conduct investigation on all amine degradation products including glycolate, acetate, formate, and oxalate to see if they catalyze or inhibit the formation of nitrosamine.

Task 4:

Finally the project will give an overall conclusion about nitrosamine formation in CO_2 capture plants using a blend of aqueous potassium carbonate and piperazine which make a basic medium. The final report will present nitrosopiperazine formation inhibitors and catalysts even inside the system or by appropriate additives.

All experiments will be conducted in duplicate and in a fume hood or glove box to avoid nitrosamine spilling in the lab environment. Reactions will be done in glass flask with three necks and the temperature will be maintained using water bath.

Research Management

The schedule of this three-year (12 quarters) timed project is as follows:

Task	Season											
	1	2	3	4	5	6	7	8	9	10	11	12
Analytical method to detect and measure nitrosamine	▓	▓										
Qualifying nitrosamine formation reagent in CO_2 capture plant and appropriate reactions in liquid and gas phase			▓	▓	▓	▓	▓	▓	▓			
The effect of amine degradation products on nitrosamine formation						▓	▓	▓	▓	▓	▓	
Overall conclusion about nitrosopiperazine and final report				▓				▓			▓	▓

References

Anderson JD Austern MH. "Measurement of Z' couplings at future hadron colliders through decays to τ leptons." *Phys Rev*. 1992;6:290–302.

Andrzejewski P, Kaspprzyk-Horden B, Nawrocki J. "N-nitrosodimethylamine (NDMA) formation during ozonation of dimethylamine-containing waters." *Water Res*. 20089;42:863–870.

Archer MC, Wishnok JS. "Quantitative Aspects of Human Exposure to Nitrosamines." *Food Cosmet Toxicol*. 1975;15:233.

Belal F, Walash MI, Ibrahim F, Hefnawy M, Eid M. "Voltammetric determination of N,N′-dinitrosopiperazine in simulated gastric juice." *Il Farmaco*. 2000;55(11-12):694-699.

Blezard M, Jones GR. "Nitrosamine inhibition." United States Patent Application No. 5,223,644; 1993.

Cachaza JM, Casado J, Castro A, Lopez MA. "Kinetic studies on the formation of nitrosamines I." J. Cancer Res Clinical Onc. 1978;91(3).

Cannon WN. (Cumberland, IN). Application Number: 06/495273. Patent 4501608, 1985.

Challis BC, and Outram JR. "The chemistry of nitroso-compounds. Part 17. Formation of N-nitrosamines in solution from dissolved nitric oxide in the presence of hydriodic acid or metal iodides." *Chem Soc, Perkin Trans*.,1982;2:693–699.

Choi Y, Kang J, Park JHY, Lee Y, Choi J, Kang Y. "Polyphenolic flavonoids differ in their antiapoptotic efficacy in hydrogen peroxide-treated human vascular endothelial cells." J. Nutr. 2003;133:985–991.

Freeman SA. "Carbon dioxide capture with concentrated, aqueous piperazine." *GHGT-9*, Washington D.C. 2008.

Freeman SA. "Carbon dioxide capture with concentrated, aqueous piperazine." *GHGT-9*, Washington D.C. 2008.

Fukushima N, Edegger B, Muthukumar VN, Gros G. "Evaluation of matrix elements in partially projected wave functions." *Phys. Rev*. 2005; 2;144505-14.(Is this page range correct? Seems very high.)

Jones K ,Bailoar JC, Emeleus HJ, Nyholm RE. "In comprehensive inorganic chemistry." Pergamon, 1973;2:323–356. (Is this an article or a book?)

Kalatzis E, Ridd JH. "Nitrosation, diazotisation, and deamination. Part XII. The kinetics of N-nitrosation of N-methylaniline." *J Chem Soc B*, 1966;2325–2328.

Keefer LK, Roller PP. "N-Nitrosation by Nitrite Ion in Neutral and Basic Medium." *Science*, 1973;181:1245–47.

Kirsch M, Fuchs A, De Groot H. "Regiospecific Nitrosation of N-terminal-blocked Tryptophan derivatives by N_2O_3 at Physiological pH." JBC Papers in Press, 2003. (Is this a book? Need full citation.)

Kirsch M, Korth H, Sustmann AR, De Groot H. "Carbon Dioxide but Not Bicarbonate Inhibits N-Nitrosation of Secondary Amines" Evidence for Amine Carbamates as Protecting Entities". *Chem Res Toxic*. 2000;13(6):451–461.Kunisaki N, Hayashi M."Formation of N-Nitrosamines from Secondary Amines and Nitrite by Resting Cells of Escherichia coli B." APPLIED AND ENVIRONMENTAL MICROBIOLOGY, 1978;37(2):279–282. (Why is this title capitalized?)

Lijinsky W, Conrad E, Van de Bogart R. "Nitrosamines formed by drug/nitrite interactions." *Nature* (Lond.), 1972; 239:165–167.

Lovejoy DJ, Vosper AJ. " Dinitrogen trioxide. Part VI. The reactions of dinitrogen trioxide with primary and secondary amines." *J. Chem. Soc. A*, 1968;2325-2328.(Need full citation.)

Lv Cl, Liu YD, Zhong RG. "Theoretical investigation of N-Nitrosodimethylamine formation from Dimethylamine nitrosation catalyzed by carbonyl compounds." *J. Phy. Chem. A.*, 2009; 113(4):713-718.

Magee PA, Barnes JM. "Toxic liver injury. metabolism of dimethylnitrosamine." *Biochem J*. 1956;64:676-682. (need correct title)

Masuda M., Mower HF., Pignatelli B., Celan M., Friesen MD., Nishino H., and Ohshima H. " Formation of N-nitrosamines and N-nitramines by the reaction of secondary amines with (need full citation)

Mirvish S, Wallcave L ,Eagen M, and P." Ascorbate-Nitrite Reaction: Possible Means of Blocking the Formation of Carcinogenic N-Nitroso Compounds." *Science*, 1972;177(4043);65-68.

Mitch WA., Sedlak DL."Factors controlling nitrosamine formation during wastewater chlorination." *Water Supply,* 2002;3:191–198.

Mizgireuv I, Majorova IG., Gorodinskaya VM " Carcinogenic effect of N-nitrosodimethylamine on diploid and triploid zebrafish." *Toxicol Pathol*; 2004;32:514–518.

Osterdahl BG, ellander B"Determination of n-mononitrosopiperazine and n,n′-dinitrosopiperazine in human urine, gastric juice and blood." *J. Chromatogr*. 1983;278:71. (Is the second author's name correct?

peroxynitrite and other reactive nitrogen species: comparison with nitrotyrosine formation." Chem. Res. Toxicol.,2000;13;301–308. (need full citation)

Russelles D., Onalod R., and Exvan PE. "A mechanism for the reaction of diethylamine with nitric oxide." Chem. Soc., Perkin Trans.,196;53; 4337-39.

Sander J., LaBar J., Ladenstein M., and Schweinsberg F,." N-nitroso Compounds in the Environment." IARC,1975; p. 123.

Sexton A. Amine Oxidation in CO2 Capture Processes. The University of Texas at Austin. Ph.D. Dissertation. 2008.

Smith AS., Loeppky RN. " Nitrosative Cleavage of Tertiary Amines." J. Am. Chem. Soc., 1967; 89 (5);1147–1157.

Tanaka H., Ando A., Ogura K., Ide S., Iida M., Oho K., Ozaki S., Iwamura K., Yamazaki A., Nakamura M., Maekawa T., Terumichi Y., and Tanaka S.. " Electron cyclotron current drive at the second harmonic in the WT-3 tokamak." Phys. Rev. 1988;60;1033-1036.

Walash ML., Belal F.,Ibrahim F., Hefnawy M., and Eid M. " LC determination of dinitrosopiperazine in simulated gastric juice." Journal of Pharmaceutical and Biomedical Analysis,2001;26(5-6);1003-1008.

Winter JW., Paterson S., Scobie G." Nitrosamine Generation From Ingested Nitrate Via Nitric Oxide in Subjects With and Without Gastroesophageal Reflux." Gastroenterology,2007;133;164-174.

Zhao Y., Boyd J., Hrudey SE., and Li X. " Characterization of new nitrosamines in drinking water using liquid chromatography tandem mass spectrometry." Environ. Sci. Technol.,2006;40; 7636–7641.

Ziebarth D.,Bogovski P., and Walker AE." N–nitroso Compounds in the Environment." IARC, 1975; p. 137.

Degradation of aqueous piperazine in carbon dioxide capture

Stephanie A. Freeman, Jason Davis, Gary T. Rochelle*

Abstract:

Concentrated, aqueous piperazine (PZ) is a novel solvent for carbon dioxide (CO_2) capture by absorption/stripping. One of the major advantages of PZ is its resistance to thermal degradation and oxidation.

8 m PZ is 23 to 70 times more resistant to thermal degradation at 135 and 150 °C than 7 m monoethanolamine (MEA). After 18 weeks at 150 °C, only 6.3% of the initial PZ was degraded, about 0.4%/week. PZ was the most resistant amine tested, with the other screened amines shown in order of decreasing resistance: 7 m 2-amino-2-methyl-1-propanol, 7 m diglycolamine ®, 7 m N-(2-hydroxyethyl)piperazine, 7 m methyldiethanolamine/2 m PZ, 8 m ethylenediamine, 7 m MEA, and 7 m diethylenetriamine. Thermal resistance allows the use of higher temperatures and pressures in the stripper, potentially leading to overall energy savings of the stripper.

Concentrated PZ solutions demonstrate resistance to oxidation compared to 7 m MEA solutions. Experiments investigating metal-catalyzed oxidation found that PZ solutions were 3 to 5 times more resistant to oxidation than MEA. Catalysts tested were 1.0 mM iron (II), 4.0 to 5.0 mM copper (II), and a combination of stainless steel metals (iron (II), nickel (II), and chromium (III)). Inhibitor A reduced PZ degradation catalyzed by iron (II) and copper (II).

1

1. Introduction

Amine-based absorption/stripping with aqueous amines offers a competitive approach for capturing carbon dioxide (CO_2) from coal-fired power plant flue gas. This technology relies on an effective amine solvent to capture CO_2 from the gas stream and release a concentrated CO_2 stream using temperature swing absorption/desorption.   Due to the nature of the absorption/stripping process, an ideal amine must have a high affinity for reacting with CO_2, beneficial physical properties such as physical solubility and viscosity, and stability at a variety of temperatures.

Monoethanolamine (MEA) is considered the baseline solvent for this application (Aaron and Tsouris, 2005; Hilliard, 2008). Examples of other solvents investigated include potassium carbonate (KCO_3)/piperazine (PZ), methyldiethanolamine (MDEA)/PZ, and 2-amino-2-methyl-1-propanol (AMP) (Bishnoi, 2000; Cullinane and Rochelle, 2004; Hilliard, 2008). PZ has been used in blended systems as a promoter to increase the rate of absorption of CO_2 in systems with attractive solvent characteristics, but low absorption rates. New data have allowed stable, concentrated PZ solutions to be created and used effectively for CO_2 absorption with fast kinetic rates, high absorption capacity, and beneficial solvent properties (Freeman et al., 2009).

Recent research has demonstrated the importance of thermal degradation and oxidation of solvents in absorption/stripping systems (Davis, 2009a; Sexton, 2008). Solvent degradation contributes significantly to a plant's operating cost through solvent make-up costs and reduced capture capacity. The behavior of MEA at high temperatures has recently been well explained as well as the economic impacts of this degradation (Davis, 2009b). Fundamental studies on the thermal degradation of common alkanolamines MEA, diethanolamine (DEA), MDEA, AMP, and blends between them have been conducted previously (Chakma and Meisen, 1987; Davis, 2009b; Dawodu and Meisen, 1996; Reza and Trejo, 2006). Lower concentration PZ systems have been identified as having resistance to thermal degradation but concentrated systems have not yet been studied (Davis, 2009a).

Amine oxidation is understood to be catalyzed by metals, especially iron (II), copper (II), chromium (III), and nickel (II) (Fe^{2+}, Cu^{2+}, Cr^{3+}, and Ni^{2+}) (Girdler Corporation, 1950; Blachly and Ravner, 1964; Blachly and Ravner, 1966; Chi and Rochelle, 2002). The oxidation of MEA, MDEA, and MEA blended systems both alone and in the presence of metals has been studied extensively previously (Goff and Rochelle, 2004; Goff and Rochelle, 2006; Rooney et al., 1998; Sexton, 2008). The oxidation of low concentration PZ and MEA/PZ has also been investigated recently with the results showing promise for the use of PZ solvents in CO_2 capture (Sexton, 2008).

This paper demonstrates the improved resistance to both thermal degradation and oxidation of concentrated, aqueous PZ. Although degradation has been studied to some extent in low concentration PZ, this work focuses on concentrated PZ systems and confirms earlier conclusions regarding the resistance of concentrated PZ to degradation.

2. Materials and methods

2.1 Solution preparation, CO_2 concentration, and amine concentration

Aqueous PZ solutions were created as described previously by melting PZ hexahydrate (99%, Alfa Aesar, Ward Hill, MA) in water and gravimetrically sparging CO_2 (99.5%, Matheson Tri Gas, Basking Ridge, NJ) to achieve the desired CO_2 concentration (Freeman et al., 2009; Hilliard, 2008).

The concentration of CO_2 was determined by total inorganic carbon (TIC) analysis, as described previously (Hilliard, 2008). The diluted sample was acidified with 30 wt % phosphoric acid (pure, Thermo Fisher Scientific, Waltham, MA) to release aqueous CO_2, carbamate, and bicarbonate species as gaseous CO_2. A nitrogen stream carried the CO_2 to an infrared analyzer which registered a change in voltage (Horiba Instruments Inc., Spring, TX). The resulting voltage peaks were integrated and correlated to CO_2 concentrations using a 1000 ppm inorganic carbon standard made from a mixture of potassium carbonate and potassium bicarbonate (Ricca Chemical, Pequannock, NJ). CO_2 concentration is reported as loading using the symbol "α" in moles CO_2 per mole alkalinity.

PZ concentration was determined using sulfuric acid titration, as described previously using a Titrando automatic titrator (Metrohm, Riverview, FL) (Hilliard, 2008). A 300X diluted sample was titrated with 0.1 N H_2SO_4 (Thermo Fisher Scientific) and the acid needed to reach the equivalence point near pH 3.9 was used to calculate the total PZ concentration. Additional equivalence points seen prior to pH 3.9 were not used in the analysis. Amine concentrations are reported using units of molality (m, moles amine per kg water).

2.2 Thermal degradation – thermal cylinders

Thermal sample cylinders were constructed from $^1/_2$-inch 316 stainless steel tubing with two Swagelok® end caps (The Swagelok Company, Solon, OH). Cylinder dimensions provided an area-to-volume ratio of 315 m^2/m^3. Cylinders were filled with 10 mL of amine solution, sealed, and placed in forced convention ovens maintained at the experimental temperature. Individual cylinders were removed from the ovens at each sampling point and the contents were analyzed for degradation products, remaining amine, and CO_2 loading. Amine losses are reported as the percent of amine lost compared to the initial amine concentration as analyzed using cation chromatography (Davis, 2009a; Freeman et al., 2009).

2.3 Oxidative degradation – low gas flow apparatus

Oxidative degradation experiments were performed in an agitated reactor with a saturated mixture of 98% O_2 (Matheson Tri Gas) and 2%CO_2 fed into the headspace at 100 mL/min (Sexton, 2008). The reactor was a 500-mL jacketed reactor filled with 350 mL of solvent. The jacket contained circulated water maintained at 55 °C. The reactor was agitated at 1400 rpm to increase the mass transfer of oxygen into the solution. The reactor was operated continuously for three to five weeks, depending on the experiment. Liquid samples were taken every two days and water was added to maintain the water balance on the reactor contents. The liquid samples

were analyzed for PZ, CO_2 loading, and degradation.

2.4 Cation ion chromatography (IC)

Cation IC was used to identify and quantify positively charged ions in solution. A Dionex ICS-2500 Ion Chromatography System with AS25 autosampler was used (Dionex Corporation, Sunnyvale, CA). The eluent contained varying concentrations of methanesulfonic acid (MSA) in analytical grade water. Separation occurred in an IonPac CG17 guard column (4 x 50 mm) and IonPac CS17 analytical column (4 x 250 mm). Both columns contained ethylvinylbenzene cross-linked with 55% divinylbenzene resin as the primary separation medium. The system contained a 4-mm Cationic Self-Regenerating Suppressor (CSRS) to remove anionic species before cationic species are detected with a conductivity cell. Chromeleon software on the attached computer analyzed the conductivity output and controls the entire system. The cation IC was used to quantify potassium, ethylenediamine (EDA), MEA, PZ, MDEA, and numerous other amines.

2.5 Anion IC

Anion IC was used to identify and quantify low molecular weight, negatively charged ions in solution. A Dionex ICS-3000 modular Dual Reagent Free IC (RFIC) system with AS40 autosampler was used (Dionex Corporation). The eluent contained varying concentrations of potassium hydroxide in analytical grade water. Separation occurred in an IonPac AG15 guard column (4 x 50 mm) and IonPac AS15 analytical column (4 x 250 mm). Both columns contain ethylvinylbenzene cross-linked with 55% divinylbenzene resin affixed with quaternary ammonium groups as the primary separation medium. The system contains a 4-mm Anionic Self-Regenerating Suppressor (ASRS) to remove cationic species before anionic species are detected with a conductivity cell. Two carbonate removal devices are in place to remove excess carbonate species from the samples (Continuously Regenerated Anion Trap Column – CR-ATC) and the analytical grade water (Carbonate Removal Device – CRD). Chromeleon software on the attached computer analyzes the conductivity output and controls the entire system. The anion IC is used to quantify glycolate, acetate, formate, chloride, nitrite, sulfate, oxalate, and nitrate. Experimental samples were treated with 5 N sodium hydroxide (1 g to 1 g sample) to reverse any amide formation. These samples were analyzed for anion concentration where the increase in concentration over the original samples represents the amine concentration (i.e. formyl or oxalyl compounds).

3. Results
3.1 Thermal degradation of PZ

Thermal degradation of PZ was investigated at temperatures slightly above normal stripper operating conditions (135 °C) and much higher than normal stripper temperatures (150 and 175 °C). Degradation of PZ and production of degradation products were tracked during the course of experiments ranging up to 18 weeks in length.

For degradation at 150 °C, the concentration profile for PZ and that of the three most abundant degradation products, ethylenediamine (EDA), formate, and formyl amides, are shown in Figure 1. For this experiment, multiple thermal cylinders were taken out of the oven at 6 weeks. The error bars in Figure 1 represent the standard deviation of the experimental procedure, sampling, and analysis process between three cylinders. Over 18 weeks, the PZ concentration decreased by 8.0% or 0.4 % per week. EDA and formate were produced in nearly equimolar amounts, both reaching around 20 mM after 18 weeks. The other primary degradation product was formamide, or the amount of formate produced from sodium hydroxide treatment of the sample. This quantity represents the concentration of total formamide species, either formamide itself, N-formyl PZ, N-formyl EDA, or others, that are produced through the basic treatment. The total concentration of degradation products that have been identified represents less than half of the piperazine that was lost, so there remains a substantial concentration of unidentified or unquantified degradation products.
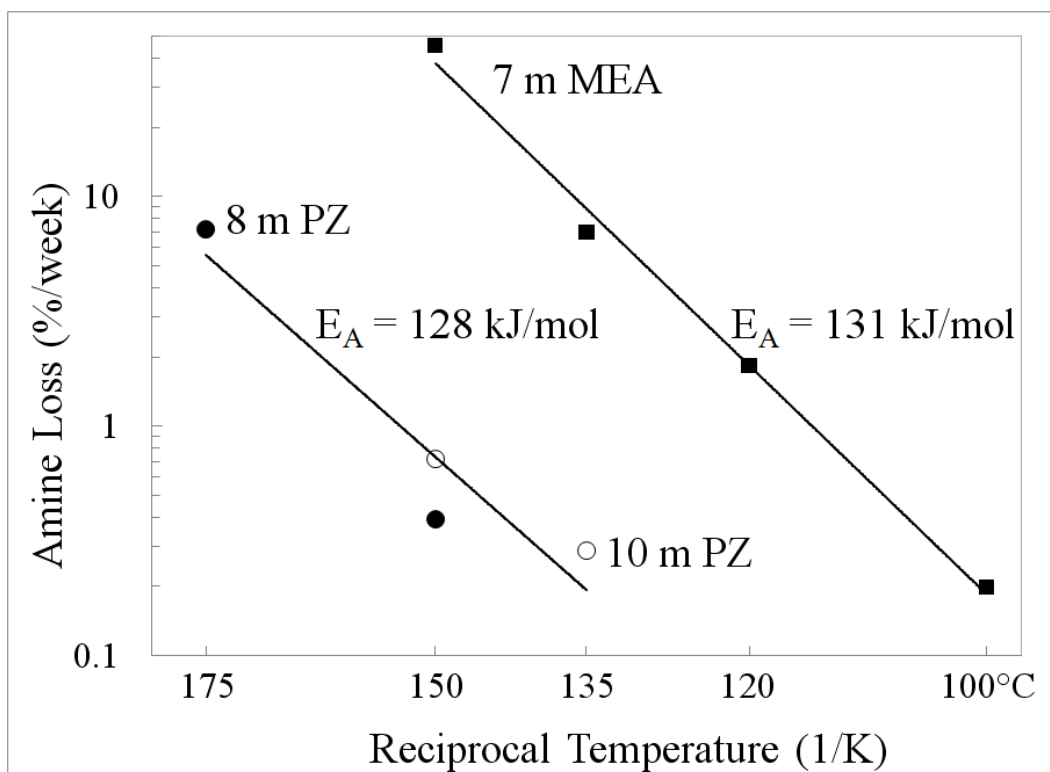
Figure 1: Concentration profiles for PZ degraded at 150 °C for 18 weeks. Curves shown are PZ (●), EDA (○), Formate (■), and Formyl Amides (□).

3.2 Comparison of thermal degradation

The thermal degradation of monoethanolamine (MEA) has been studied extensively by Davis along with screening of alternative amines and amine blends (Davis, 2009a). To compare the thermal degradation behavior of PZ to other common amines, the thermal degradation rate is reported as amine loss. This analysis looks only at changes in the amine itself, not the

5

production of any degradation products. This loss is normalized by the length of time of each experiment as the experiments varied from 4 to 18 weeks in length. The degradation rate at 135 °C is compared in Table 1 for a number of amines. It should be noted that previous literature on MDEA degradation has used the acronym HEP for N,N'-bis(2-hydroxyethyl) piperazine) (Yanicki and Trebble, 2006) which is usually referred to as BHEP (Chakma and Meisen, 1997).

Table 1: Thermal Degradation Rates at 135 °C with a loading of 0.4 mole CO_2/mole alkalinity

[Amine] (m)	Solvent	Amine Loss (%/week)
10	PZ	0.3
7	2-amino-2-methyl-1-propanol (AMP)	2.3
7	Diglycolamine® (DGA)	2.3
7	N-(2-hydroxyethyl) piperazine (HEP)	3.3
7/2	Methyldiethanolamine (MDEA)/PZ	3.7
8	Ethylenediamine (EDA)	4.0
7	MEA	9.3
7	Diethylenetriamine (DETA)	23.5

The degradation rates shown in Table 1 demonstrate the enhanced resistance of concentrated PZ to high temperature degradation. PZ has the lowest degradation rate followed by AMP and DGA which lose over seven times as much amine per week. MEA has the second highest degradation rate at 9.3%/week, 31 times that of PZ. DETA was found to have the greatest rate of thermal degradation at 23.5%/week, 78 times that of concentrated PZ.

To further compare 7 m MEA and concentrated PZ, the amine loss rate for each is plotted against reciprocal temperature (Figure 2). The x-axis is labeled with degree Celsius for reference, but the plot is made from inverse Kelvin. The data in Figure 2 are at nominal lean loading, which is 0.3 mole CO_2/mole alkalinity for PZ and 0.4 mole CO_2/mole alkalinity for MEA.

Data for 8 and 10 m PZ are both included in Figure 2 because of the similarity of the concentration and data. Each data set is indicated by a separate shape but the trend line uses all four data points. The trend line on each graph is an Arrhenius relationship between the logarithm of the amine loss against the reciprocal temperature. This relationship is shown in Equation 1 as the rate of amine loss in percent per week, k, in terms of the temperature in Kelvin, T, a pre-exponential factor, A, the activation energy for degradation, E_A, and the universal gas constant, R.

$$\ln k = \ln A - \frac{E_A}{RT}$$
(1)
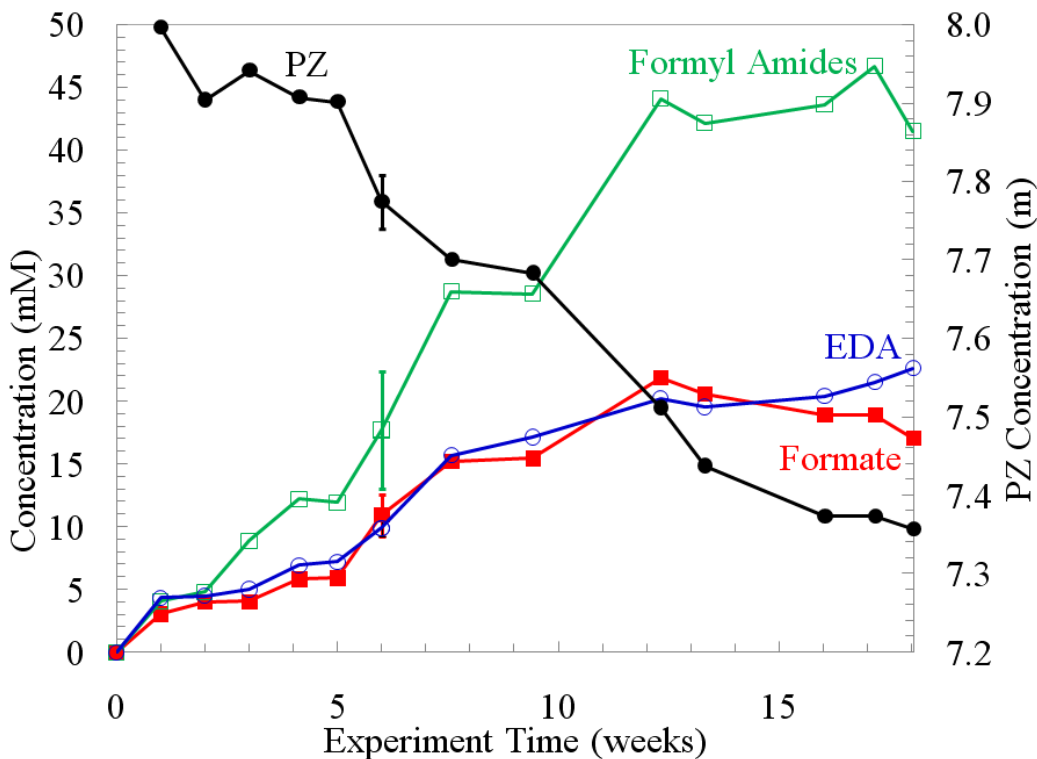
Figure 2: Amine Loss of Concentrated PZ and 7 m MEA from 100 to 175 °C. Data shown are for 8 m PZ (●), 10 m PZ (○), and 7 m MEA (■)

The trend lines in Figure 2 are power law regressions that take the form of Equation 3. The activation energy, E_A, for thermal degradation can be predicted using these trend lines for either solvent system. The predicted E_A values are shown in Figure 2. The lines appear parallel and the activation energies reflect this observation. The activation energy for 7 m MEA is 134 kJ per mole, only slightly higher than the 127 kJ per mole for concentrated PZ. Previous work on the development of a kinetic model for MEA thermal degradation predicted activation energies for the six dominant MEA thermal degradation reactions ranging from 131 to 143 kJ/mol (Davis, 2009a). The average of these activation energies was 137 kJ/mole, in good agreement with the Arrhenius prediction from Figure 2.

The figure demonstrates the enhanced thermal resistance of concentrated PZ over 7 m MEA. At 135 and 150 °C where the experimental data overlaps, the loss of PZ is 23 to 70 times less than MEA. Data at temperatures below 135 °C were not collected for PZ due to the length of time needed to observe degradation. In an opposite thread, MEA degradation was not tested above 150 °C because over 62% was lost after 2 weeks at 150 °C.

Predictions for the optimum stripper operating conditions for 7 m MEA systems have been performed by Davis based on the kinetic model mentioned above (Davis, 2009a). The optimum based on balance of energy costs for steam stripping and solvent replacement was found to be a stripper pressure of 3.5 atm and temperature of 122 °C. This high pressure stripper configuration is not likely to be used in industrial designs, but provides a set of conditions at

7

which to compare thermal degradation. At this temperature, there is an MEA loss of approximately two percent of the amine per week due only to thermal degradation. Assuming PZ is twice the cost of MEA, an acceptable PZ thermal degradation rate may be predicted as one percent per week. Using Figure 2 as a simple way to estimate acceptable solvent loss, a stripper temperature of around 150 °C or higher is predicted for concentrated PZ systems, allowing one percent loss per week. Further system modeling of concentrated PZ systems will illuminate the optimum operating conditions for PZ-based absorption/stripping systems.

3.3 Oxidation of concentrated PZ

The oxidation of concentrated PZ was investigated using the low gas flow apparatus. Aqueous metals were added to the reactors prior to the start of agitation and gas flow. Metal concentrations were selected to represent expected values with carbon steel construction (moderate levels of Fe^{2+}), and stainless steel construction (low levels of Fe^{2+}, Cr^{3+}, and Ni^{2+}), or if a copper-based corrosion inhibitor was used (high levels of Cu^{2+}). To better gauge the significance of the PZ oxidation results, data obtained on the same apparatus for 7 m MEA were used as a direct comparison of oxidation (Sexton, 2009).

In systems constructed of carbon steel, any corrosion will likely lead to aqueous iron species present in the amine solution. To simulate the effects of iron-catalyzed degradation, 8 m PZ was oxidized in the presence of 1.0 mM Fe^{2+}. The PZ loss throughout the experiment is compared in Figure 3 to a similar experiment with 7 m MEA and 1.0 mM Fe^{2+}. In the absence of any other metal catalyst or inhibitor, 8 m PZ loses 8.0% of the original amine after 450 hours. In the same time, 44.3% of the 7 m MEA is lost. PZ is 5.5 times more resistant to iron-catalyzed degradation than the comparable MEA system.

Stainless steel will more likely be used as the material of construction for absorber/stripper systems due to its enhanced resistivity to corrosion. If any corrosion does occur, low concentrations of iron, chromium, and nickel can exist as aqueous species in the amine solutions. To simulate the catalytic effect for oxidation of iron, chromium, and nickel, 10 m PZ was oxidized in the presence of 0.26 mM Fe^{2+}, 0.65 mM Cr^{3+}, and 0.26 mM Ni^{2+}. The amine loss for this experiment is shown in Figure 4 along with a comparable 7 m MEA experiment. The MEA experiment contained a slightly different mix of metals, 0.6 mM Cr^{2+} and 0.1 mM Ni^{2+}. After 350 hours, only 8.4% of the original PZ was degraded compared to 51.4% of the MEA. The resistance of PZ to oxidation via stainless steel metal-catalyzed degradation is clear as 6.1 times less amine was lost compared to MEA. It is predicted that the inclusion of Fe^{2+} in the MEA experiment would have only enhanced the amount of amine lost and increased the relative resistance of PZ to oxidation.
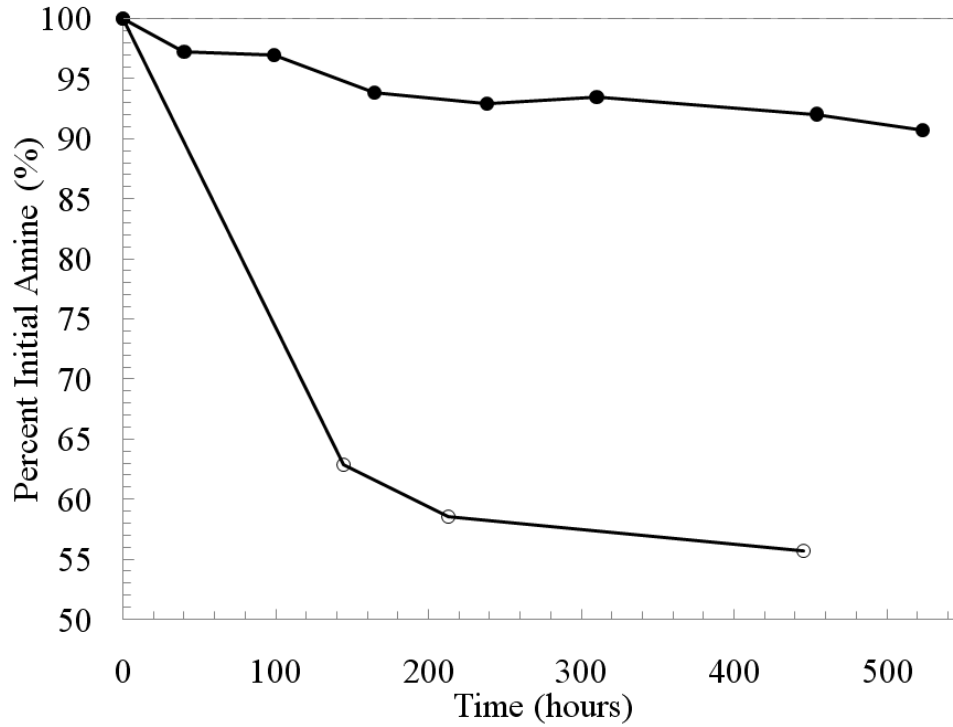
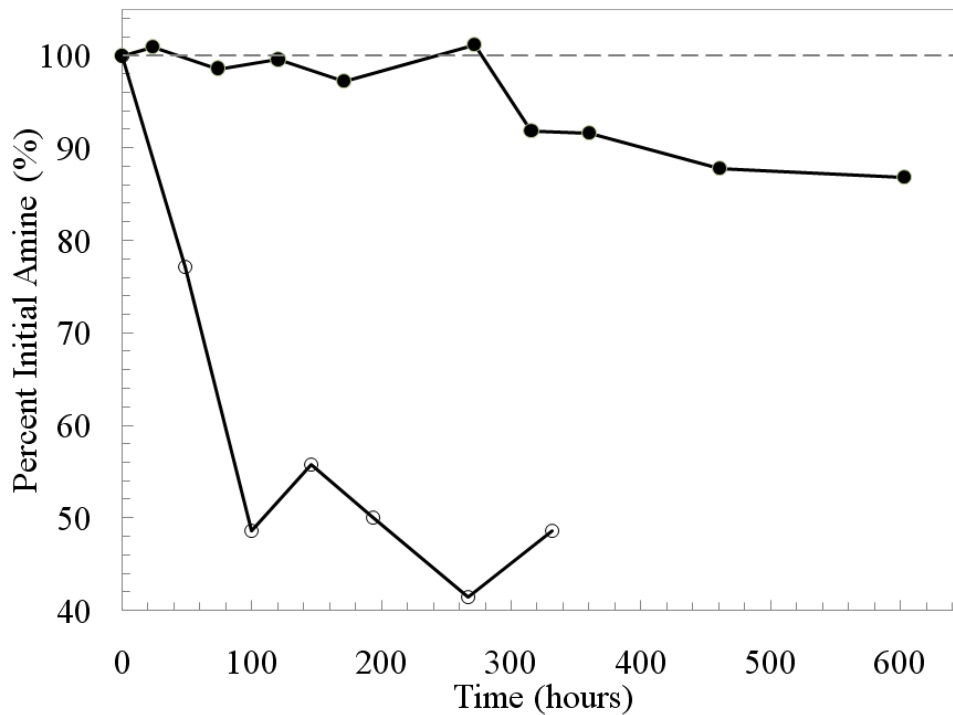Figure 3: Effect of iron on oxidation – comparison of amine loss for 8 m PZ (●) and 7 m MEA (○) each with 1.0 mM Fe^{2+}

Figure 4: Effect of stainless steel metals – comparison of amine loss for 8 m PZ with 0.26 mM Fe^{2+}, 0.65 mM Cr^{2+}, and 0.26 mM Ni^{2+} (●) and 7 m MEA with 0.6 mM Cr^{3+} and 0.1 mM Ni^{2+} (○)

9

Copper salts have been used as a corrosion inhibitor in industrial gas treating systems and are also a well known catalyst for amine degradation. To determine the extent of copper-catalyzed oxidation, 10 m PZ was degraded in the presence of 4.0 mM Cu^{2+}. The amine loss for this experiment is shown in Figure 5 with a comparable 7 m MEA experiment. This MEA experiment contained 1.0 mM Fe^{2+} and 5 mM Cu^{2+}. Although the metals concentrations are not exactly the same, the effect of copper on amine oxidation is clearly demonstrated. After 220 hours, 28% of the PZ had been degraded while 72.9% of the MEA was degraded. PZ oxidation is highly catalyzed by Cu^{2+} in solution. Even though PZ showed 2.6 times less degradation than 7 m MEA, the 28% degradation observed was nearly four times more than both iron- and stainless steel metal-catalyzed oxidation. PZ demonstrated resistance to copper degradation but the large amount of degradation that occurred indicates that a copper-based corrosion inhibitor is not recommended for use with concentrated PZ systems.
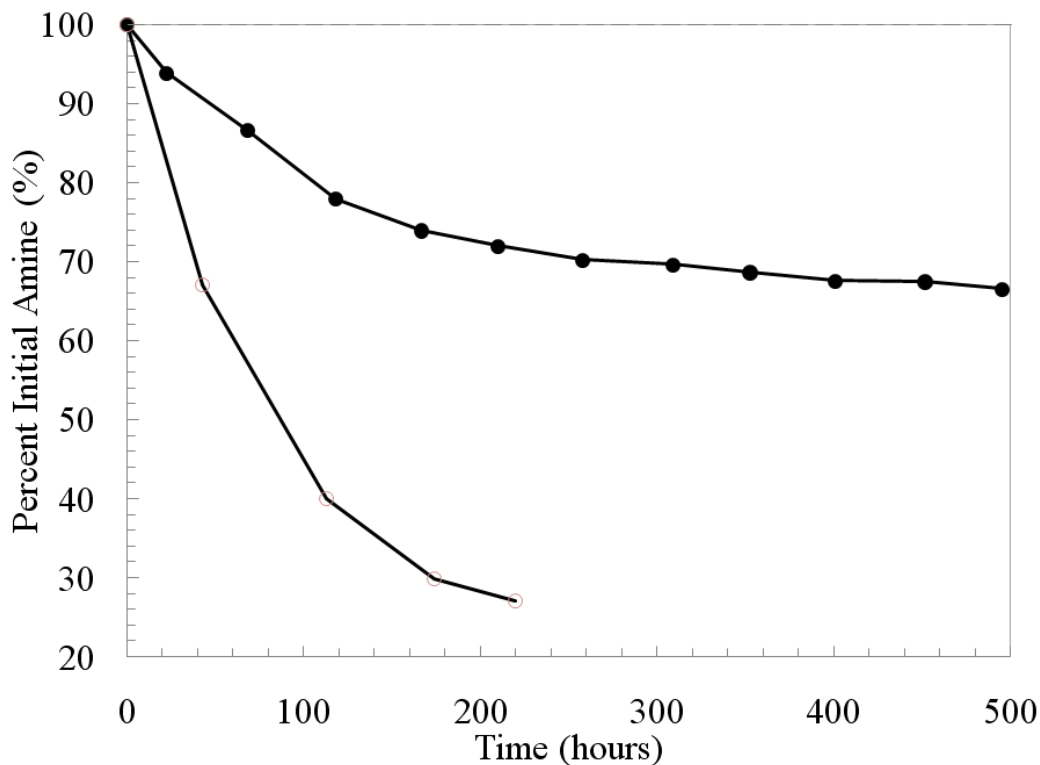
Figure 5: Effect of copper on oxidation – comparison of amine loss for 8 m PZ with 4 mM Cu^{2+} (●) and 7 m MEA with 5.0 mM Cu^{2+} and 1 mM Fe^{2+} (○)

The efficacy of Inhibitor A to inhibit metal-catalyzed oxidation was tested with 8 m PZ. Inhibitor A has been proven to be effective at impeding both iron and copper degradation in other amines such as MEA and 7 m MEA/2 m PZ blends (Goff and Rochelle, 2006; Sexton, 2008). Sexton (2006) also demonstrated that Inhibitor A reduced the production of degradation products for 2.5 and 5 m PZ. Experiments were conducted in the low gas flow apparatus as described above. To investigate iron-catalyzed oxidation, 8 m PZ was degraded in the presence

of 1 mM Fe^{2+} and 100 mM Inhibitor A and compared to the experiment with 1 mM Fe^{2+}. For copper-catalyzed oxidation, 8 m PZ was degraded in the presence of 5 mM Cu^{2+}, 1 mM Fe^{2+}, and 100 mM Inhibitor A and compared with an experiment with 4 mM Cu^{2+}. The results are shown in Figure 6 as the amount of PZ remaining during the experiments.

As demonstrated in Figure 6, Inhibitor A is effective at inhibiting both iron- and copper-catalyzed PZ oxidation. Despite iron causing low levels of oxidation in PZ solutions, as discussed before, Inhibitor A decreases the amount of oxidation further. In the system examined with 1 mM Fe^{2+} and 100 mM Inhibitor A, almost no degradation was seen as the concentration actually slightly increased during the course of the experiment. This increase demonstrates the experimental error due to the water balance in the reactor changing during the experiment and the cumulative error involved in the analytical process. The baseline iron-catalyzed oxidation with 1 mM Fe^{2+} is 10% loss after 500 hours and Inhibitor A essentially reduces this to zero loss.

For copper-catalyzed degradation, Inhibitor A significantly reduces the loss of PZ to levels observed in iron-catalyzed experiments. After 500 hours, PZ loss is reduced by two-thirds as 34% was lost in the copper-catalyzed experiment compared to 11% when Inhibitor A was present.
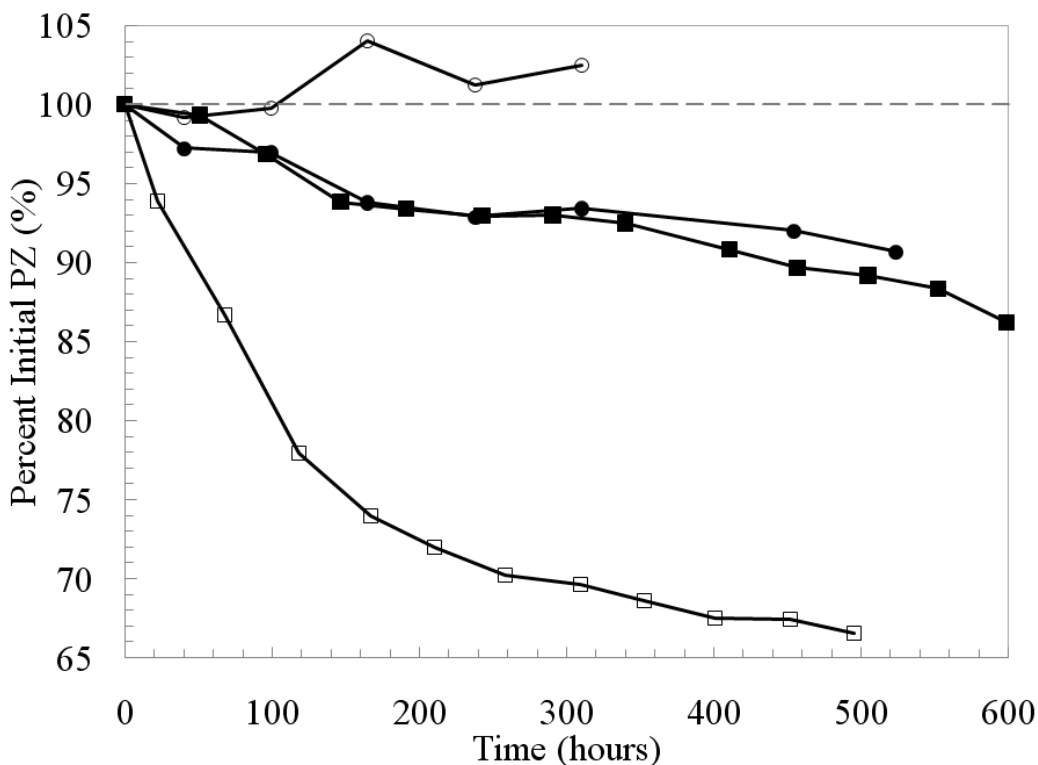
Figure 6: Effect of Inhibitor A on iron- and copper-catalyzed PZ degradation – data are shown for 1.0 mM Fe^{2+} (●), 1.0 mM Fe^{2+} and Inhibitor A (○), 4.0 mM Cu^{2+} (■), and 5.0 mM Cu^{2+} + 1.0 mM Fe^{2+} + 100 mM Inhibitor A (□).

4. Conclusions

Concentrated, aqueous solutions of PZ have shown promise for improved solvent performance in absorption/stripping systems used for CO_2 capture. Solutions of 8 m PZ demonstrate substantial thermal resistance over 7 m MEA. At temperatures of 135 and 150 °C, well above currently used stripper temperatures, PZ has 23 to 70 times less degradation than MEA. PZ also fares better than common solvents tested for CO_2 absorption solvents such as AMP, DGA, DETA, and MDEA.

Concentrated PZ solutions also demonstrate resistance to oxidation in the presence of metals. In the presence of 1 mM Fe^{2+}, a well known oxidation catalyst, concentrated PZ is 5.5 times more resistant to oxidation than 7 m MEA after 450 hours. In the presence of stainless steel metals, Fe^{2+}, Cr^{3+}, and Ni^{2+}, 8 m PZ is 6.1 times more resistant than 7 m MEA after 350 hours. Finally, in the presence of copper 8 m PZ is 2.6 times more resistant to oxidation than MEA after 220 hours. Copper catalyzed the most degradation in concentrated PZ systems, but the overall oxidation observed for metal-catalyzed degradation was up to 6.1 times less than comparable MEA systems.

Inhibitor A is effective at reducing iron- and copper-catalyzed degradation by up to 66% in concentrated PZ. In the presence of Fe^{2+}, 100 mM of Inhibitor A reduced the iron-catalyzed degradation to essentially zero. In the presence of Cu^{2+}, 100 mM of Inhibitor A reduced the copper-catalyzed degradation by 67%.

5. Acknowledgements

6. References

Aaron, D., Tsouris, C., 2005. Separation of CO_2 from flue gas: A review. Separation Science and Technology 40(1-3), 321-348.

Bishnoi, S., 2000. Carbon Dioxide Absorption and Solution Equilibrium in Piperazine Activated Methyldiethanolamine. Doctoral dissertation, The University of Texas at Austin, Austin, TX.

Blachly, C.H., Ravner, H., 1964. The Stabilization of Monoethanolamine Solutions for Sumbarine Carbon Dioxide Scrubbers. AD609888, NRL-6189; US Naval Research Laboratory: Washington D.C.

Blachly, C.H., Ravner, H., 1966. Stabilization of Monoethanolamine Solutions in Carbon Dioxide Scrubbers. Journal of Chemical and Engineering Data 11(3), 401-403.

Chakma, A., Meisen, A., 1987. Degradation of Aqueous DEA Solutions in a Heat-Transfer Tube. Canadian Journal of Chemical Engineering 65(2), 264-273.

Chakma, A., Meisen, A., 1997. Methyl-diethanolamine degradation - Mechanism and kinetics. Canadian Journal of Chemical Engineering 75(5), 861-871.

Chi, S., Rochelle, G.T., 2002. Oxidative degradation of monoethanolamine. Industrial & Engineering Chemistry Research 41(17), 4178-4186.

Cullinane, J.T., Rochelle, G.T., 2004. Carbon dioxide absorption with aqueous potassium carbonate promoted by piperazine. Chemical Engineering Science 59(17), 3619-3630.

Davis, J., 2009a. Thermal Degradation of Aqueous Amines Used for Carbon Dioxide Capture. Doctoral Dissertation, The University of Texas at Austin, Austin, TX.

Davis, J., 2009b. Thermal degradation of monoethanolamine at stripper conditions. Energy Procedia 1(1), 327-333.

Dawodu, O.F., Meisen, A., 1996. Degradation of alkanolamine blends by carbon dioxide. Canadian Journal of Chemical Engineering 74(6), 960-966.

Freeman, S.A., Dugas, R., VanWagener, D., Nguyen, T., Rochelle, G.T., 2009. Carbon dioxide capture with concentrated, aqueous piperazine. International Journal of Greenhouse Gas Control In Print.

Girdler Corporation, 1950. Carbon Dioxide Absorbents. Contract No. 50023. Girdler Corporation, Gas Processing Division: Louisville, KY, June 1 1950.

Goff, G.S., Rochelle, G.T., 2004. Monoethanolamine degradation: O_2 mass transfer effects under CO_2 capture conditions. Industrial & Engineering Chemistry Research 43(20), 6400-6408.

Goff, G.S., Rochelle, G.T., 2006. Oxidation inhibitors for copper and iron catalyzed degradation of monoethanolamine in CO_2 capture processes. Industrial & Engineering Chemistry Research 45(8), 2513-2521.

Hilliard, M.D., 2008. A Predictive Thermodynamic Model for an Aqueous Blend of Potassium Carbonate, Piperazine, and Monoethanolamine for Carbon Dioxide Capture from Flue Gas. Doctoral dissertation, The University of Texas at Austin, Austin, TX.

Reza, J., Trejo, A., 2006. Degradation of aqueous solutions of alkanolamine blends at high temperature, under the presence of CO2 and H2S. Chemical Engineering Communications 193(1), 129-138.

Rooney, P.C., DuPart, M.S., Bacon, T.R., 1998. Oxygen's role in alkanolamine degradation. Hydrocarbon Processing 77(7), 109-113.

Sexton, A., 2008. Amine Oxidation in CO_2 Capture Processes. Doctoral dissertation, The University of Texas at Austin, Austin, TX.

Sexton, A.J., 2009. Catalysts and Inhibitors for Oxidative Degradation of Monoethanolamine International Journal of Greenhouse Gas Control (in print).

Yanicki, G., Trebble, M.A., 2006. Experimental measurements of foaming tendencies in aqueous gas sweetening solutions containing MDEA over a temperature range of 297-358 K and a pressure range of 101-500 kPa. Chemical Engineering Communications 193(10), 1151-1163.

Corresponding Author: Gary Rochelle,

Corresponding Author's Institution: Univ. of Texas

First Author: Gary T Rochelle, Ph.D.

Order of Authors: Gary T Rochelle, Ph.D.; Gary Rochelle; Thu Nguyen, M.S.

Abstract: Amine volatility is a key screening criterion for amines to be used in CO2 capture. Volatility
directly affects the amount of amine fugitive emission which poses an environmental concern;
additionally, it dictates the financial costs associated with sizing a water wash tower and replenishing
spent amine. This paper reports measured amine volatility. The volatility of 7 m MEA
(monoethanolamine), 8 m PZ (piperazine), 7 m MDEA (n-methyldiethanolamine)/2 m PZ (piperazine)
blend, 12 m EDA (ethylenediamine), and 5 m AMP (2-amino-2-methyl-1-propanol) was measured at
40 ºC-60 ºC and lean and rich loadings giving CO2 partial pressures of 0.5 kPa and 5 kPa. The amine
concentrations were chosen to maximize CO2 capture capacity at acceptable viscosity. While the
temperature behavior of these amines varies from one to another (depending on whether the heat of
solution for a given system is exothermic or endothermic), the behavior with respect to loading is
consistent with intuition as the presence of CO2 serves to reduce amine volatility in every case. At the
lean loading condition (where volatility is of greatest interest), the amines are ranked as follows in
order of increasing volatility: 7 m MDEA/2 m PZ (7/6 ppm), 12 m EDA (9 ppm), 8 m PZ (14 ppm), 7 m
MEA (28 ppm), 5 m AMP (112 ppm). The heats of solutions for these systems are also estimated from
the data using Gibbs-Helmholtz relations. These values range from ~10-40 kJ/mol of amine with 5 m
AMP being the minimum and 12 m EDA being the maximum. The estimated heats of solution are
generally smaller for systems that are most volatile.

1

Title: Amine Volatility in CO$_2$ Capture

Corresponding Author:

Gary T. Rochelle

Department of Chemical Engineering

The University of Texas at Austin

1 University Station   Mail Code: C0400

Austin, TX 78712-0231

Phone: 512-471-7230

Fax: 512-471-7060

gtr@che.utexas.edu

Amine Volatility in CO$_2$ Capture

Thu Nguyen[a], Marcus Hilliard[b], Gary T. Rochelle[a]

[a]Department of Chemical Engineering, The University of Texas at Austin

[b]The Dow Chemical Company

Abstract: Amine volatility is a key screening criterion for amines to be used in CO$_2$ capture. Volatility directly affects the amount of amine fugitive emission which poses an environmental concern; additionally, it dictates the financial costs associated with sizing a water wash tower and replenishing spent amine. This paper reports measured amine volatility. The volatility of 7 m MEA (monoethanolamine), 8 m PZ (piperazine), 7 m MDEA (n-methyldiethanolamine)/2 m PZ (piperazine) blend, 12 m EDA (ethylenediamine), and 5 m AMP (2-amino-2-methyl-1-propanol) was measured at 40 ℃–60 ℃ and lean and rich loadings giving CO$_2$ partial pressures of 0.5 kPa and 5 kPa. The amine concentrations were chosen to maximize CO$_2$ capture capacity at acceptable viscosity. While the temperature behavior of these amines varies from one to another (depending on whether the heat of solution for a given system is exothermic or endothermic), the behavior with respect to loading is consistent with intuition as the presence of CO$_2$ serves to reduce amine volatility in every case. At the lean loading condition (where volatility is of greatest interest), the amines are ranked as follows in order of increasing volatility: 7 m MDEA/2 m PZ (7/6 ppm), 12 m EDA (9 ppm), 8 m

PZ (14 ppm), 7 m MEA (28 ppm), 5 m AMP (112 ppm). The heats of solutions for these systems are also estimated from the data using Gibbs-Helmholtz relations. These values range from ~10–40 kJ/mol of amine with 5 m AMP being the minimum and 12 m EDA being the maximum. The estimated heats of solution are generally smaller for systems that are most volatile.

Keywords:

Amine Volatility; CO_2 Capture; VLE; monoethanolamine; piperazine; n-methyldiethanolamine; ethylenediamine; 2-amino-2-methyl-1-propanol

1. Introduction

Absorption/stripping with aqueous amine will be an important technology for CO_2 capture from fossil fuel combustion. Monoethanolamine (30 wt %, 7 m MEA) is the baseline solvent for this application. Alternative amines may provide better energy performance because of greater CO_2 capacity, faster rate of CO_2 absorption, or greater heat of CO_2 absorption. To minimize environmental impact and makeup cost, these new amines must also have low rates of thermal and oxidative degradation and an acceptable amine volatility.

Aqueous amine absorbers will probably be designed to operate near 40 ℃ at atmospheric pressure. Cleaned flue gas leaving the absorber will tend to be in equilibrium with lean amine solution at 40 ℃. Most systems will add a water wash tower to minimize the loss of amine to the stack.

Amine losses up the stack may be environmentally significant. The amine can participate in atmospheric reactions to produce ozone and other toxic compounds. The make-up cost of amine lost up the stack will be economically significant, especially with more expensive amines. Higher amine volatility will also increase the capital cost of the water wash system.

While there are several publications on the VLE of binary MEA-H_2O system, only a few directly measured MEA volatility, more specifically the vapor phase mole fraction of MEA. Lenard et al. (1990) measured the gas phase composition of MEA in binary aqueous solution (343K and 363K) using gas chromatography. These data were represented using a three parameter Redlich-Kister expansion. Cai et al. (1996) measured isobaric VLE at 101.3 kPa and 66 kPa (373K–443K) using the standard curve of refraction index versus mole fraction of the binary mixture at 20 ºC. The liquid phase activity coefficients were calculated with the UNIFAC group contribution model as published by Larsen et al. (1987). These data are in the high temperature range, and therefore are considered outside the scope of our low temperature application. At temperatures relevant to absorption-stripping, McLees et al. (2006) directly measured the volatility of MEA in a binary system (3.5 m, 7.0 m, 23.8 m MEA) as well as in blends having piperazine (PZ) as a promoter. PZ volatility was also measured for 0.9 m, 1.8 m, 2.5 m, and 3.6 m PZ. The data were obtained with hot gas FTIR (Fourier Transform Infrared Spectroscopy). Efforts were made to model the experimental data in terms of binary interaction parameters by utilizing the NRTL model within Aspen Plus[®].

There have been other thermodynamic measurements of MEA-H_2O. Touhara et al. (1982) measured the total pressure of this system at 298K and 308K. Nath and Bender (1983) measured total pressure for pure substances as well as binary and ternary mixtures of alcohols, alkanolamines, and water from 60–95 $^{\circ}$C in a vapor-recycle equilibrium cell. Specifically, the MEA-H_2O system was studied at 60, 78, and 91.7 $^{\circ}$C. Activity coefficients for each system were calculated using the Wilson and UNIQUAC equations and were seen to have negative deviations from an ideal solution.

This paper reports measured amine volatility of 7 m MEA (monoethanolamine), 8 m PZ (piperazine), 7 m MDEA (n-methyldiethanolamine)/2 m PZ blend, 12 m EDA (ethylenediamine), and 5 m AMP (2-amino-2-methyl-1-propanol). The experimental data is obtained from FTIR spectroscopy for both unloaded and nominal lean and rich CO_2 systems. Volatility is of greatest interest at the top of the absorber at 40 ºC and nominal lean loading.

2. Materials & Methods

2.1. Solution Preparation

Approximately 500–520 g of solution was prepared for each experiment. Solutions were prepared by dissolving pure, analytical-grade amine in water to achieve the desired molality (m, moles amine/kg water). High concentrations of PZ were heated to dissolve anhydrous solid PZ in water. The solutions were loaded with CO_2 by sparging CO_2 in a glass cylinder on a balance to provide a gravimetric CO_2 loading. The chemical suppliers

and purity grades were: MEA (Acros Organics 99%), PZ (Alfa Aesar 99%), MDEA (Acros Organics 99+%), EDA (Strem Chemicals 99%), AMP (Acros Organics 99%).

2.2. CO_2 Loading

The CO_2 concentration was determined by Total Inorganic Carbon (TIC) analysis (Hilliard, 2008). The samples were diluted in H_2O and injected into 30 wt % H_3PO_4 to release CO_2. The CO_2 was carried by N_2 to an infrared detector. The resulting voltage peak was integrated and calibrated with a 1000 ppm inorganic carbon standard made from a mixture of potassium carbonate and potassium bicarbonate (Ricca Chemical, Pequannock, NJ).

2.3. Amine Concentration

The amine concentration was determined by acid titration (Hilliard, 2008) with an automatic Titrando series titrator with automatic equivalence point detection. A 300X diluted sample was titrated with 0.1 N H_2SO_4 to a pH of 2.4. The amount of acid needed to reach the equivalence point at a pH of 3.9 was used to calculate the total amine concentration.

2.4. Amine Volatility Measurement

Amine volatility was measured in a stirred reactor coupled with a hot gas FTIR analyzer (Fourier Transform Infrared Spectroscopy, Temet Gasmet Dx-4000) as shown in Figure 1.

(Figure 1. Amine Volatility Experimental Setup)

The 1L glass reactor was agitated at 350 rpm. Temperature in the reactor was controlled by circulating dimethylsilicone oil. The reactor was insulated with thick

aluminum insulation material. Vapor from the headspace of the reactor, primarily 5–10 L/min. nitrogen, was circulated by a heated sample pump to the FTIR through a heated Teflon line. Both the line and analyzer were maintained at 180 ºC to prevent possible condensation or adsorption of amine. The FTIR measured amine, CO_2, and water concentration in the gas. After the gas passed through the FTIR, it was returned to the reactor through a heated line maintained ~55 ºC hotter than the reactor. It was determined that the 55 ºC difference was sufficient to ensure that the return gas does not upset the solution that is in equilibrium with the gas inside the reactor, and to prevent potential heat loss at the bottom of the reactor.

3. Theory

Amine volatility is quantified by an apparent activity coefficient (γ_{amine}) as defined by the modified Raoult's law.

$$\gamma_{amine} = P_{amine} / [x_{amine} * P^{°}_{amine}] \tag{1}$$

γ_{amine} is the apparent activity coefficient of the amine

P_{amine} is the partial pressure of the amine in the gas

x_{amine} is the liquid phase mole fraction of the amine

P^{o}_{amine} is the vapor pressure of the amine at a given temperature

 The reference value for γ_{amine} is 1 which is the case of a solution having ideal species interaction. Note that the activity coefficients presented in this paper are apparent values, instead of being actual values, as they are computed using x_{amine} that are not the true liquid phase mole fractions of free amine present in solution. The liquid composition of

the amine in this case assumes total amine concentration in the presence of total CO_2 unspeciated.

The heat of amine solution, and similarly, the heat of amine vaporization (or desorption from solution), are calculated by the Gibbs-Helmholtz relations.

$$d (\ln P_{amine}) / d (1/T) = -\Delta H_{vaporization} / R \qquad (2)$$

$$d (\ln \gamma_{amine}) / d (1/T) = -\Delta H_{solution} / R \qquad (3)$$

4. Results

Tables 1 through 5 give the measured values of equilibrium partial pressures for CO_2 (P_{CO2}) and the respective amine (P_{amine}). The amine concentration is given in molality, m (moles amine/kg water). The apparent activity coefficient (γ_{amine}) is calculated from the nominal mole fraction of the total amine. The loading is always defined as moles CO_2/equivalent of amine.

(Table 1. 3.5 m, 7.0 m, 11.0 m MEA Volatility (Hilliard, 2008))

(Table 2. 2 m, 5 m, 8 m PZ Volatility)

(Table 3. 7 m MDEA / 2 m PZ Blend Volatility)

(Table 4. 8 m and 12 m EDA Volatility)

(Table 5. 5 m AMP Volatility)

5. Discussion

Figure 2 shows MEA partial pressure for 7 m and 11 m MEA at 40 ºC and 60 ºC.

(Figure 2.   MEA Partial Pressure)

As expected, MEA partial pressure increases with amine concentration and temperature. The amine partial pressure decreases linearly with loading because free MEA is converted to MEA carbamate and protonated MEA. The stoichiometry of the MEA reaction with CO_2 to produce carbamate would suggest that the volatility should approach zero at a loading of 0.5. In practice there is some free MEA at 0.5 to 0.6 loading because some of the CO_2 reacts to make bicarbonate and protonated MEA at the higher loading.

Figure 3 gives the MEA results as an apparent activity coefficient for MEA at 40 ºC and 60 ºC. The apparent activity coefficient, γ, is defined as the measured amine partial pressure divided by the total amine mole fraction and the vapor pressure of liquid amine at the measured temperature. The vapor pressure of liquid MEA is given by (DIPPR):

$$P^o_{MEA} \text{ (Pa)} = \exp[92.6 + (-1.04 \times 10^4 / T) - (9.47 \ln T) + (1.9 \times 10^{-18} T^6)] \tag{4}$$

(Figure 3. Apparent Activity Coefficient of MEA (Vapor Pressure of Liquid MEA from   Eq. 4))

All of the results representing different MEA concentrations (3.5 m, 7.0 m, 11.0 m) collapse onto individual lines representing only the effect of temperature. Furthermore, the effect of temperature has also been greatly reduced by normalizing by the vapor pressure of liquid MEA. The apparent activity coefficient of MEA decreases slightly with temperature with an apparent excess enthalpy of ~33 kJ/mol.

The volatility of 8 m PZ is shown in Figure 4 as the calculated apparent activity coefficient.

(Figure 4. Apparent Activity Coefficient of 8 m PZ (Vapor Pressure of Liquid PZ given in Eq. 5))

The vapor pressure of liquid PZ is given as (DIPPR):

$$P^o_{PZ} \text{ (Pa)} = \exp[70.5 - (7914.5/T) - (6.65 \ln T) + (5.2 \times 10^{-18} T^6)] \tag{5}$$

While the above equation is meant to be applied to liquid PZ from 380K–638K, which is outside the operating temperature range of the absorber, it has been extrapolated to lower temperature conditions relevant to our application. The result of this extrapolation has been unproblematic and consistent with higher temperature data.

The apparent PZ activity coefficient in 8 m PZ also decreases with loading, as free PZ is converted by reaction with CO_2 to other nonvolatile species. The apparent PZ activity coefficient is somewhat greater at 60 ℃ than at 40 ℃, exhibiting endothermic behavior. In subsequent plots, it can be seen that the temperature behavior for lower concentrations of PZ (5 m and 2 m) is different from 8 m due to unique and complex speciation occurring at each concentration. At lean conditions of the absorber (40 ℃, lean loading 0.3, $P_{CO2} \sim 0.5$ kPa), 8 m PZ volatility is ~ 21.4 ppm.

With 5 m PZ (Figure 5) there is little effect of temperature on the apparent activity coefficient.

(**Figure 5. Apparent Activity Coefficient of PZ in 5 m PZ**)

With 2 m PZ (Figure 6) there is a reversed effect of temperature on the apparent activity coefficient.

(**Figure 6. Apparent Activity Coefficient of PZ in 2 m PZ**)

In this case, the apparent PZ activity coefficient is greater at 40 ℃ than at 60 ℃ which indicates an exothermic behavior. In summary, as PZ concentration is lowered from 8 m to 5 m and then to 2 m, the solution transitions from being endothermic to exothermic as indicated by the temperature behavior of the apparent PZ activity coefficient in each case. This is possibly due to different speciation effects occurring at

each concentration. At zero loading, however, the apparent PZ activity coefficient is always higher for 60 ℃ than for 40 ℃ due to the lack of speciation from the CO_2 reactions.

The volatility of PZ in 7 m MDEA (methyldiethanolamine)/2 m PZ blend is presented in Figure 7.

(Figure 7. Apparent Activity Coefficient of PZ in 7 m MDEA/2 m PZ)

7 m MDEA/2 m PZ shows temperature and loading effects similar to those of MEA. The apparent PZ activity coefficient of the blend decreases with loading as there is less free amine present in solution in the presence of greater CO_2 at higher loading. PZ in this blend shows an endothermic behavior with the apparent PZ activity coefficient being greater at 60 ℃ than at 40 ℃. At the operating condition of interest, PZ volatility for this blend is roughly 6 ppm which is much less than that of 7 m MEA and 8 m PZ.

Figure 8 shows the volatility of MDEA in the 7 m MDEA/2 m PZ blend. The vapor pressure of MDEA is calculated from the following (DIPPR):

$$P^o_{MDEA} \text{ (Pa)} = \exp[253.1 - (18378/T) - (33.9 \ln T) + 2.3 \times 10^{-5} T^2] \qquad (6)$$

(Figure 8. Apparent Activity Coefficient of MDEA in 7 m MDEA/2 m PZ Blend)

Unlike PZ, MDEA in the 7 m MDEA/2 m PZ blend does not show a very strong dependence on loading as the apparent MDEA activity coefficient remains rather constant throughout the loading range shown. This behavior is due to CO_2 reacting more preferentially with PZ than with MDEA in the blend, and thereby MDEA volatility stays roughly constant. Again the temperature behavior is endothermic. The volatility of MDEA for this blend is about 6.9 ppm at the relevant operating condition.

Figure 9 presents ethylenediamine (EDA) volatility for 8 m EDA and 12 m EDA at 40 ºC and 60 ºC. The vapor pressure of EDA is given as (DIPPR):

$$P^o_{EDA} \text{ (Pa)} = \exp[73.5 - (7572.7 / T) - (7.14 \ln T) + (1.21 \times 10^{-17} T^6)] \qquad (7)$$

(Figure 9. Apparent Activity Coefficient of EDA in 8 m and 12 m EDA)

The apparent EDA activity coefficient is greater at higher temperature than at lower temperature which is again an indication of endothermic behavior. As loading is increased, EDA volatility decreases as has been seen with all the other amines. At the operating condition of interest, 12 m EDA volatility is approximately 14.1 ppm.

Figure 10 shows 5 m AMP (2-amino-2-methyl-1-propanol) volatility. The vapor pressure of AMP is provided from the following (Pappa et al., 2006):

$$P^o_{AMP} \text{ (kPa)} = \exp[15.155 - (3472.6 / (T - 107.32))] \qquad (8)$$

While the above equation is applicable to liquid AMP from 373K–464K, it has been extrapolated for use at lower temperatures relevant to our application (~340K) without any discontinuity or inconsistency (Pappa et al., 2006).

(Figure 10. Apparent Activity Coefficient of AMP in 5 m AMP)

The apparent activity coefficient of 5 m AMP displays an endothermic temperature behavior. Volatility for this solution is seen to decrease with CO_2 loading as has been seen with other amines. At 40ºC and a nominal lean loading of 0.3, 5 m AMP volatility is 97 ppm, greater than any of the amines studied.

The following graph summarizes the volatility of all the systems in terms of amine partial pressure as a function of CO_2 partial pressure at 40ºC.

(Figure 11. Amine Volatility Comparison)

The least volatile system observed is 7 m MDEA/2m PZ as indicated by low MDEA partial pressure (PZ partial pressure for the blend is relatively low as well). The system with the next highest volatility is 12 m EDA. However, unloaded 12 m EDA has the greatest volatility of all the systems. 8 m PZ is seen to have comparable volatility to the baseline 7 m MEA solvent. 5 m AMP is the most volatile system at the P_{CO2} of interest, 100 to 500 Pa at 40 ℃.

6. Conclusions

Table 6 ranks the amine systems in order of increasing volatility. It also tabulates estimated values of the amine heats of solution (the amount of heat given off as the amine comes into solution with water and CO_2) and the heats of vaporization (the amount of heat it takes to desorb the amine from the solution). Calculations of these quantities are done per the Gibb's-Helmholtz relations as presented in the Theory section.

(Table 6. Summary of Amine Volatility)

These amine systems are all ranked at the nominal lean loading that corresponds to a CO_2 partial pressure of approximately 500 Pa at 40 ℃. In order of increasing volatility, 7 m MDEA/2 m PZ is the least volatile system, followed by 12 m EDA, 8 m PZ, baseline 7 m MEA, and 5 m AMP. It appears that the less volatile systems have higher heats of solution. There is no apparent correlation between amine volatility and the amine heat of vaporization.

7. Acknowledgement

8. References

Cai, Z., Xie, R., Wu, Z., 1996 Binary Isobaric Vapor-Liquid Equilibria of Ethanolamines + Water. J. Chem. Eng. Data. 41, 1101−1103.

DIPPR 801: Thermophysical Property Database for Pure Chemical Compounds.

Hilliard, M., 2008. A Predictive Thermodynamic Model for an Aqueous Blend of Potassium Carbonate, Piperazine, and Monoethanolamine for Carbon Dioxide Capture from Flue Gas. Ph.D. Dissertation, The University of Texas at Austin.

Larsen, B.L.; Rasmussen, P., Fredenslund, A., 1987. A Modified UNIFAC Group Contribution Model for Prediction of Phase Equilibria and Heats of Mixing. Ind. Eng. Chem. Res. 26, 2274−2286.

Lenard, J., Rousseau, R., Teja, A., 1990. Vapor-Liquid Equilibria for Mixtures of 2-aminoethanol + water. AIChE Symposium Series. 86.

McLees, J.A., 2006. Vapor-Liquid Equilibrium of Monoethanolamine/Piperazine/Water at 35−70 °C. M.S.E. Thesis, The University of Texas at Austin.

Nath, A., Bender, E., 1983. Isothermal Vapor-Liquid Equilibria of Binary and Ternary Mixtures Containing Alcohol, Alkanolamine, and Water with a NewStatic Device. J. Chem. Eng. Data. 26, 370−375.

Pappa, G., Anastasi, C., Voutsas, E., 2006. Measurement and thermodynamic modeling of the phase equilibrium of aqueous 2-amino-2-methyl-1-propanol solutions. Fluid Phase Equil. 243, 193−197.

15

Touhara, H., Okazaki, S.; Okino, F., Tanaka, H., Ikari, K., Nakanishi, K., 1982. Thermodynamic Properties of Aqueous Mixtures of Hydrophilic Compounds 2-Aminoethanol and its Methyl Derivatives. J. Chem. Thermodynamics. 14, 145–156.

Figure 1. Amine Volatility Experimental Setup

Figure 2.   MEA Partial Pressure

Figure 3. Apparent Activity Coefficient of MEA (Vapor Pressure of Liquid MEA from Eq. 4)

Figure 4.   Apparent Activity Coefficient of 8 m PZ (Vapor Pressure of Liquid PZ given in Eq. 5)

Figure 5. Apparent Activity Coefficient of PZ in 5 m PZ

Figure 6. Apparent Activity Coefficient of PZ in 2 m PZ

Figure 7. Apparent Activity Coefficient of PZ in 7 m MDEA/2 m PZ

Figure 8. Apparent Activity Coefficient of MDEA in 7 m MDEA/2 m PZ Blend

Figure 9. Apparent Activity Coefficient of EDA in 8 m and 12 m EDA

Figure 10. Apparent Activity Coefficient of AMP in 5 m AMP

Figure 11. Amine Volatility Comparison

5-10 L/min.

Picolog for T & P reactor

1L vessel

180°C

constant T

Oil Bath

FTIR

Gasmet
180°C

350 rpm

Dimethylsilicone oil

$T_{reactor}$ + 55°C

Figure showing P_{amine} (Pa) versus P_{CO2} (Pa) at 40°C for 5 m AMP, 7 m MEA, 8 m PZ, 12 m EDA, and 7 m MDEA/2 m PZ.
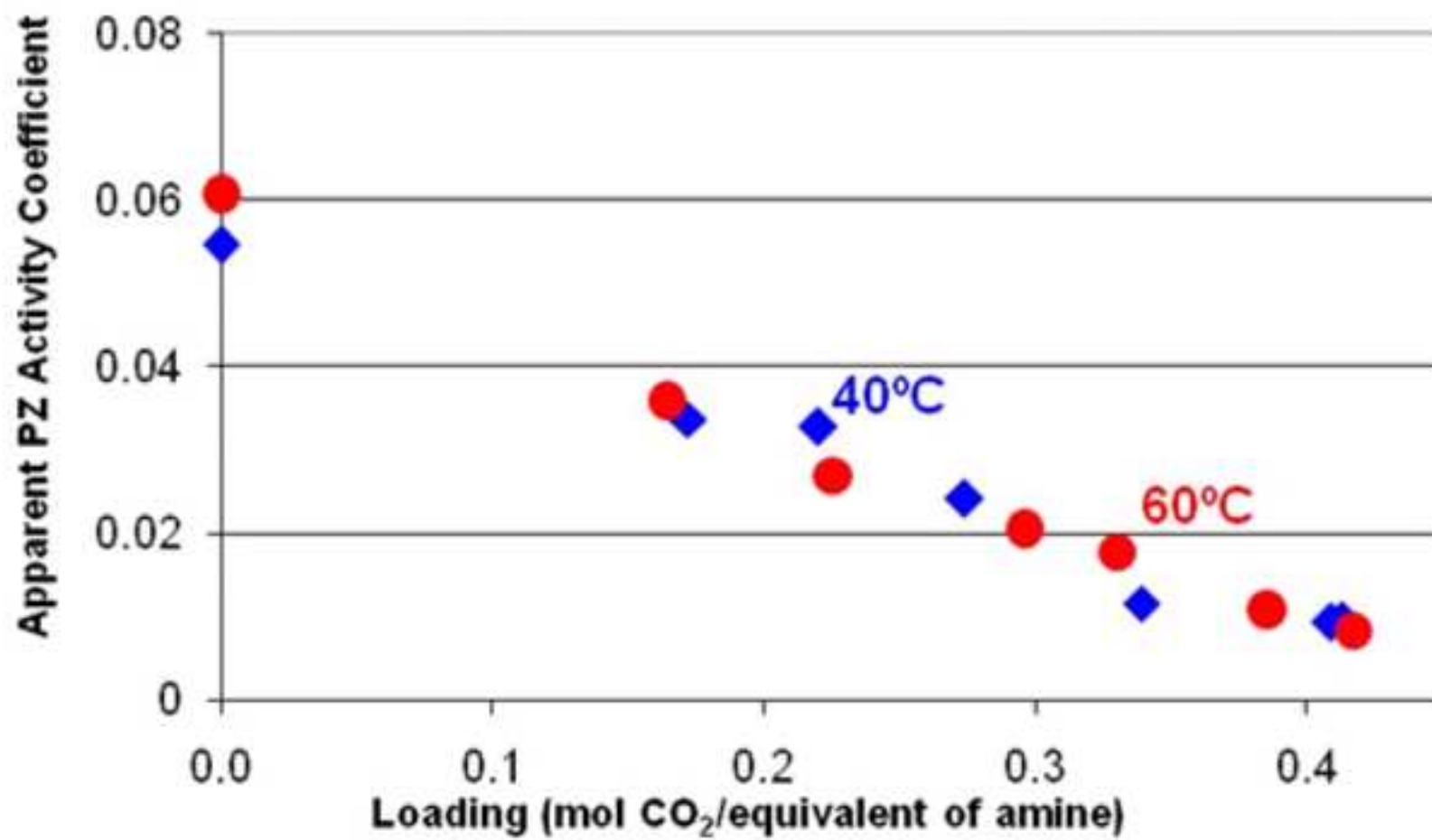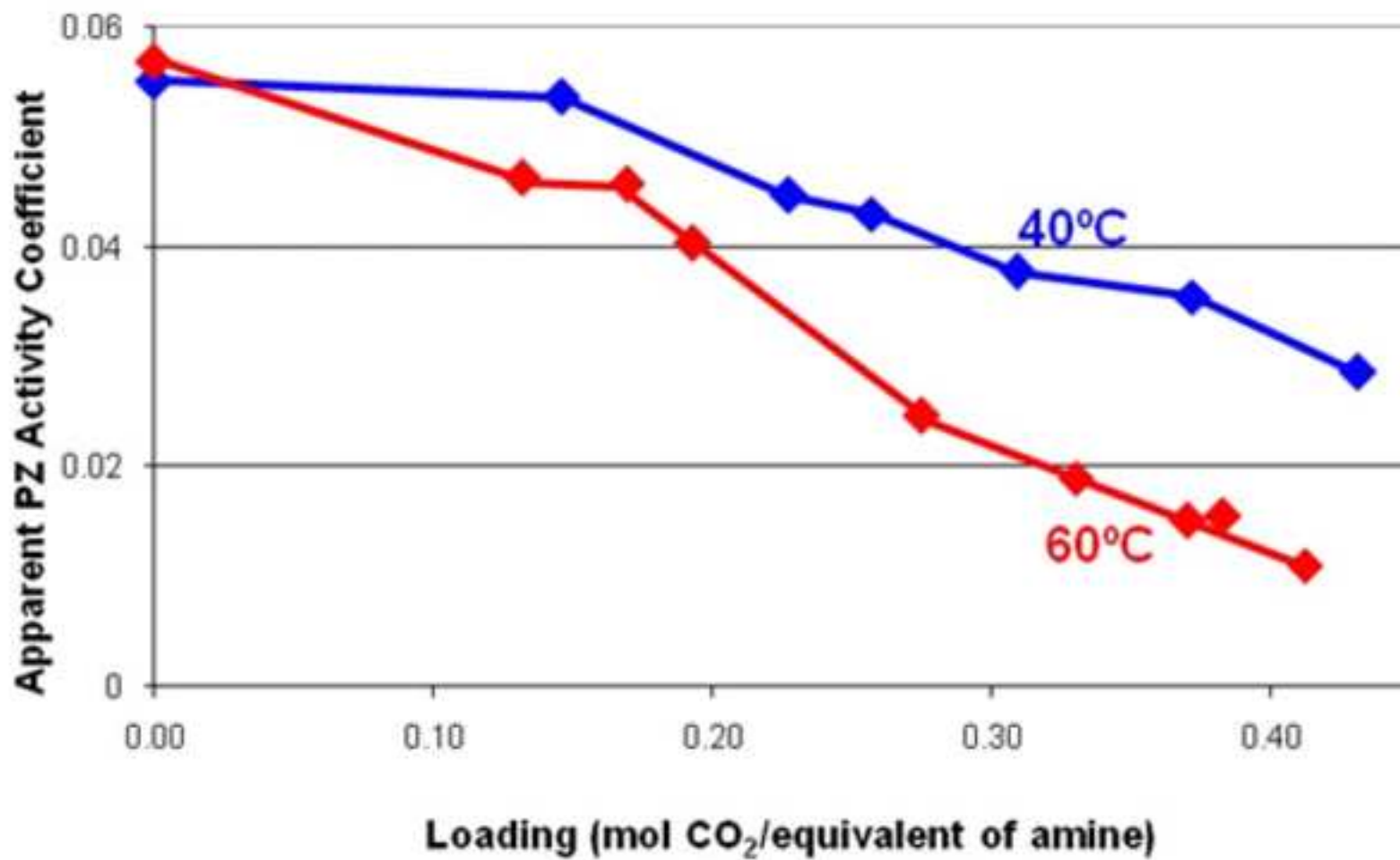
Table 1. 3.5 m, 7.0 m, 11.0 m MEA Volatility (Hilliard, 2008)

MEA (m)	T (C)	Loading	P_{CO2} (Pa)	P_{MEA} (Pa)	γ_{MEA}
3.50	60.0	0	0	13.2	0.338
3.57	59.9	0.16	21.2	11.0	0.279
3.63	60.1	0.22	78	9.26	0.232
3.53	60.0	0.31	244	7.20	0.186
3.57	60.0	0.38	794	5.08	0.130
3.55	59.9	0.48	4320	3.23	0.084
3.54	60.0	0.5	14800	2.19	0.057
3.50	40.0	0	0	4.19	0.436
3.53	40.0	0.12	5.6	3.91	0.407
3.46	40.0	0.21	14	3.41	0.363
3.51	39.9	0.3	36.2	2.81	0.297
3.54	40.1	0.37	116	2.24	0.236
3.57	40.0	0.47	879	1.68	0.176
3.49	40.0	0.55	8560	0.98	0.106
7.00	40.0	0	0	10.0	0.551
6.88	40.0	0.15	5.7	6.58	0.375
6.98	40.0	0.17	7.2	6.36	0.358
6.95	40.1	0.16	6.6	6.36	0.359
6.85	40.0	0.19	9.9	6.45	0.370
6.97	40.1	0.19	10	6.23	0.352
6.93	40.4	0.27	22.4	5.11	0.293
7.06	40.0	0.23	14.6	5.63	0.316
7.08	40.1	0.25	19.1	5.53	0.310
7.10	40.0	0.27	23.1	5.16	0.289
7.12	39.9	0.36	96.6	3.55	0.201
7.05	40.0	0.35	72.1	4.23	0.241
7.06	39.9	0.39	120	3.62	0.207
7.05	39.9	0.39	113	3.38	0.193
7.05	40.0	0.4	128	3.5	0.200
7.58	40.1	0.38	131	3.32	0.178
7.00	39.9	0.47	574	2.7	0.157
7.11	40.0	0.59	28300	1.46	0.085
7.06	40.0	0.48	883	2.47	0.142
7.17	40.0	0.46	750	2.66	0.151
7.06	40.0	0.5	1870	1.99	0.115
7.11	39.9	0.49	1100	1.93	0.111
7.06	40.0	0.52	3030	1.72	0.100
7.06	39.9	0.33	48.5	4.58	0.260
7.04	39.9	0.35	66.2	4.23	0.241
7.00	60.0	0	0	27.1	0.367
7.00	59.9	0.11	19.4	21.5	0.295
7.08	60.0	0.19	58.9	18.6	0.255
7.07	60.0	0.29	209	14.1	0.196
7.03	59.9	0.39	763	10	0.141
7.14	59.8	0.49	4860	4.94	0.069

7.17	60.1	0.54	25800	3.16	0.045
7.38	59.9	0.57	50200	2.88	0.040
11.00	40.0	0	0	12	0.448
11.00	40.0	0.12	5.1	10.4	0.395
10.75	40.0	0.2	10.8	8.42	0.331
10.90	39.9	0.3	29.5	6.03	0.238
11.28	40.1	0.37	104	4.39	0.171
11.06	40.0	0.49	1620	1.98	0.079
11.12	40.0	0.55	22300	0.95	0.038
11.00	60.0	0	0	40.2	0.369
11.21	60.0	0.14	15.5	36.09	0.333
11.17	60.0	0.23	73.1	28.38	0.267
11.12	60.0	0.29	199	22.52	0.215
11.36	60.0	0.42	847	14.3	0.137
11.32	59.9	0.46	6980	6.55	0.063
10.98	60.0	0.5	26500	4.16	0.041

Table 2. 2 m, 5 m, 8 m PZ Volatility

8 m PZ

T (C)	Loading	P_{CO2} (Pa)	P_{PZ} (Pa)	γ_{PZ}
40	0.28	513	2.14	0.016
40	0.38	6501	1.07	0.008
60	0	0	34.18	0.079
60	0.28	4930	16.31	0.040
60	0.38	30621	7.39	0.019

5 m PZ (Hilliard, 2008)

T (C)	Loading	P_{CO2} (Pa)	P_{PZ} (Pa)	γ_{PZ}
40	0	0	5.12	0.055
40	0.17	28.7	3.12	0.034
40	0.22	60.5	2.88	0.031
40	0.27	211	2.2	0.024
40	0.34	798	1.03	0.011
40	0.41	5710	0.82	0.009
40	0.41	6990	0.86	0.009
60	0	0	17.2	0.061
60	0.16	137	10.2	0.036
60	0.23	365	7.45	0.026
60	0.3	1290	5.59	0.020
60	0.33	3310	4.86	0.017
60	0.39	18300	2.86	0.010
60	0.42	51400	2.23	0.008

2 m PZ (Hilliard, 2008)

T (C)	Loading	P_{CO2} (Pa)	P_{PZ} (Pa)	γ_{PZ}
40	0	0	2.17	0.055
40	0.15	21.5	2.12	0.054
40	0.23	106	1.8	0.046
40	0.26	184	1.68	0.043
40	0.31	526	1.49	0.038
40	0.37	1950	1.38	0.036
40	0.43	10100	1.09	0.028
60	0	0	6.78	0.057
60	0.13	92.4	5.55	0.047
60	0.19	296	4.8	0.040
60	0.28	1400	2.93	0.025
60	0.33	3950	2.24	0.019
60	0.37	9910	1.77	0.015
60	0.41	24700	1.28	0.011
60	0.17	142	5.13	0.043
60	0.38	13700	1.87	0.016

Table 3. 7 m MDEA / 2 m PZ Blend Volatility

T (C)	Loading	P_{CO2} (Pa)	P_{MDEA} (Pa)	P_{PZ} (Pa)	γ_{MDEA}	γ_{PZ}
40	0.00	0	0.81	2.04	1.78	0.058
40	0.10	399	0.69	0.59	1.55	0.017
40	0.19	2581	0.60	0.09	1.37	0.003
60	0.00	0	7.37	12.37	2.90	0.116
60	0.10	2967	6.53	4.80	2.61	0.046
60	0.19	18640	6.48	2.47	2.63	0.024

Table 4. 8 m and 12 m EDA Volatility

EDA (m)	T (C)	Loading	P_{CO2} (Pa)	P_{EDA} (Pa)	γ_{EDA}
8	40	0.00	0	24.1	4.7E-02
8	40	0.41	248	0.93	1.8E-03
8	40	0.49	4090	0.46	9.2E-04
8	60	0.00	0.0	166	1.2E-01
8	60	0.41	2696	6.19	4.4E-03
8	60	0.49	25054	2.90	2.1E-03
12	40	0.00	0	57.0	7.9E-02
12	40	0.42	204	1.41	2.0E-03
12	40	0.50	10748	0.16	2.3E-04
12	60	0.00	0	430	2.1E-01
12	60	0.42	2420	8.64	4.4E-03
12	60	0.50	32960	1.20	6.2E-04

Figure

Table 5. 5 m AMP Volatility

T (C)	Loading	P_{CO2} (Pa)	P_{AMP} (Pa)	γ_{AMP}
40	0	0	14.2	0.99
40	0.3	1091	9.84	0.68
40	0.55	7768	4.57	0.33
60	0	0	64.3	1.01
60	0.3	6816	55.5	0.86
60	0.55	30818	26.4	0.42

Figure

Table 6. Summary of Amine Volatility

Solution	Ldg (mol CO_2/mol tot alk)	Volatility (ppm)	ΔH_{sol} (kJ/mol)	ΔH_{vap} (kJ/mol)
7m MDEA/2m PZ	0.12	7 / 6	23 / 43	100 / 112
12m EDA	0.44	9	40	82
8m PZ	0.31	14	35	108
7m MEA	0.45	28	33	55
5m AMP	0.25	112	10	75

Absorber Intercooling in CO_2 Absorption by Piperazine Promoted Potassium Carbonate

Jorge M. Plaza, Eric Chen, and Gary T. Rochelle

Department of Chemical Engineering, The University of Texas at Austin, 1 University Station, Mail Code C0400, Austin, TX 78712-0231, USA

Intercooling was evaluated as a process option in CO_2 absorption by piperazine (PZ) promoted potassium carbonate. The system performance with 4.5 m K^+/4.5 m PZ was simulated by a model in Aspen Plus$^®$ RateSep^{TM}. The absorber was evaluated for use with a double matrix stripper by optimizing the position of the semilean feed and intercooling stages to maximize CO_2 removal. Additionally, a simple absorber system was modeled to observe the effect of intercooling on systems with variable CO_2 lean loading. Intercooling increases CO_2 removal by as much as 10% with the double matrix configuration. With a simple absorber, the effectiveness of intercooling depends on solvent rate. Near a critical liquid/gas ratio (L/G) there is a large improvement with intercooling. This is related to the position of the temperature bulge. An approximation is proposed to estimate the critical L/G where intercooling may maximize removal.

Introduction

Carbon dioxide capture and sequestration is a major option to reduce greenhouse gases and address global climate change. Chemical absorption is the most attractive technology to reduce CO_2 emissions from coal fired plants.

Intercooling is a common strategy to increase the performance of absorption systems. Jackson and Sherwood[1] showed that intercooling increased absorption up to 37% and even higher during the winter in refinery gas absorbers for absorption of C_4^+ from cracking coil gas. Linhoff[2] reports the use of intercooling in a refinery with vapor recovery by an absorption oil. Sobel[3] introduces the use of a computational method for absorbers which routinely include a feature for modeling intercooling. A number of authors have shown that absorber intercooling can be effective with CO_2 capture by amines (Thompson & King[4], Chang & Shih[5], Tobiesen at al.[6] and Freguia & Rochelle[7]). Patents have also been filed with more complex intercooling configurations to increase absorber performance[8-10].

Intercooling is especially useful for systems where the heat of absorption (i.e. heat of solution and/or reaction) results in an increase in temperature of the solvent affecting the vapor pressure of the dissolved species. Kvamsdal and Rochelle[11] observed this behavior for the absorption of carbon dioxide from flue gas by aqueous monoethanolamine (MEA). They studied absorber parameters such as liquid/gas ratio (L/G), height of packing, and flue gas composition and its effect on the appearance of a temperature bulge

in the absorber. Chen[12] observed similar behavior for systems using piperazine (PZ) promoted potassium carbonate (K^+). He developed a rate-based absorber model for the mentioned system. The model was originally generated from work carried out by Cullinane[13] and later translated into Aspen Plus® by Hillard[14]. Chen used the Data Regression System® in Aspen Plus® to simultaneously regress equilibrium constants and interaction parameters to predict equilibrium and speciation.

This work uses the tools developed by Chen to analyze a system using a 4.5 m K^+/4.5 m PZ solvent. Different absorber configurations were studied to evaluate the effect of intercooling on absorber performance.

Vapor-Liquid Equilibrium (VLE) and Kinetics Model

The K^+/PZ solvent was introduced by Cullinane[13] as an alternative to the widely used MEA. MEA has a high capacity and a fast rate of CO_2 absorption. According to Cullinane, the K^+/PZ solvent has a higher CO_2 capacity than MEA because PZ is a diamine and potassium carbonate increases the absorption capacity. Furthermore, the rate of absorption was increased due to the presence of two amine groups in PZ, the high pK_a, and the large quantity of carbonate/bicarbonate. He reported a CO_2 absorption rate 1.5 to 3 times faster than with 30 wt % MEA.

Cullinane[13] measured the thermodynamics and kinetics of potassium carbonate, piperazine, and carbon dioxide using a wetted wall column and developed a rigorous thermodynamic model in FORTRAN using the electrolyte non-random two-liquid (e-NRTL) theory. The model predicted vapor-liquid equilibrium (VLE) and speciation for the H_2O-K_2CO_3-PZ-CO_2 system. The equilibrium constants and interaction parameters were regressed using experimental data and input into the FORTRAN model. Additionally, a rigorous kinetic model was developed that determined the rate constants and diffusion coefficients based on experimental data.

Cullinane conducted experiments with 0.45–3.6 m PZ and 0–3.1 m potassium carbonate at 25–110 °C. The absorption rate of CO_2 was determined using the eddy diffusivity model developed by Bishnoi and Rochelle[15] and rate constants were regressed from the experimental data using the model. The reaction of CO_2 with piperazine was modeled with a termolecular, base-catalyzed mechanism.

The following amine reactions were used in the Cullinane[13] model.

$$PZ + CO_2 + \begin{cases} OH^- \xleftrightarrow{k_{PZ-OH^-}} PZCOO^- + H_2O \\ H_2O \xleftrightarrow{k_{PZ-H_2O}} PZCOO^- + H_3O \\ PZ \xleftrightarrow{k_{PZ-PZ}} PZCOO^- + PZH^+ \\ CO_3^{2-} \xleftrightarrow{k_{PZ-CO_3^{2-}}} PZCOO^- + HCO_3^- \\ PZCOO - \xleftrightarrow{k_{PZ-PZCOO^-}} PZCOO^- + H^+ PZCOO^- \end{cases} \quad (1)$$

$$PZCOO^- + CO_2 + \begin{cases} H_2O \xleftrightarrow{k_{PZCOO^- - H_2O}} PZ(COO^-)_2 + H_3O \\ PZ \xleftrightarrow{k_{PZCOO^- - PZ}} PZ(COO^-)_2 + PZH^+ \\ CO_3^{2-} \xleftrightarrow{k_{PZCOO^- - CO_3^{2-}}} PZ(COO^-)_2 + HCO_3^- \\ PZCOO- \xleftrightarrow{k_{PZCOO^- - PZCOO^-}} PZ(COO^-)_2 + H^+PZCOO^- \end{cases} \quad (2)$$
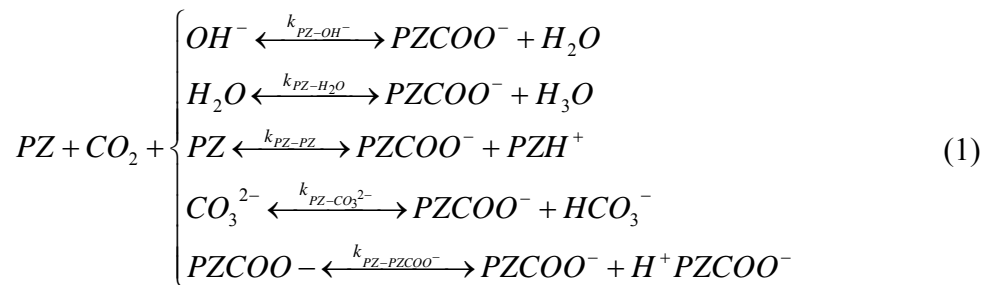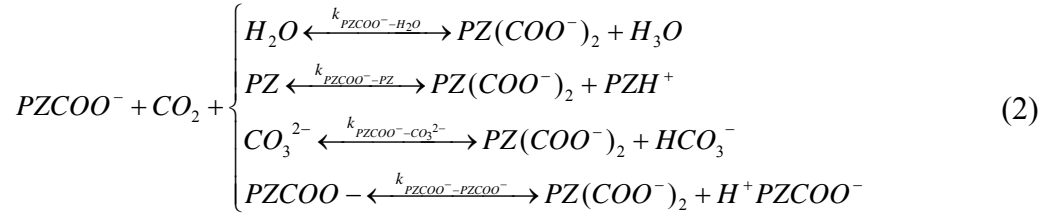
All of the buffering reactions were considered to be in equilibrium and reversible rate expressions for CO_2 with PZ and $PZCOO^-$ were developed. The catalysis of the formation of bicarbonate ion by hydroxide, piperazine, and piperazine carbamate was also included in the Cullinane model. The reactions to form bicarbonate ion were included to properly model equilibrium in the boundary layer and do not affect the CO_2 absorption rate. The three reversible reactions are:

$$CO_2 + OH^- \xleftrightarrow{k_{OH^-}} HCO_3^- \quad (3)$$

$$PZ + CO_2 + H_2O \xleftrightarrow{k_{PZ}} PZH^+ + HCO_3^- \quad (4)$$

$$PZCOO^- + CO_2 + H_2O \xleftrightarrow{k_{PZCOO^-}} H^+PZCOO^- + HCO_3^- \quad (5)$$
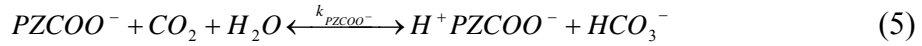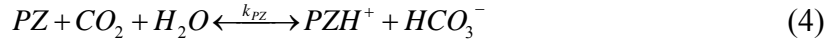
Hilliard[14] developed a VLE model in Aspen Plus® using the thermodynamic data by Cullinane and the Data Regression System® (DRS) to simultaneously regress the interaction parameters and equilibrium constants to be used in the built-in electrolyte-NRTL model.

Later, Chen[12] developed a rate-based model using Aspen Plus® RateSep™. It incorporates the Hilliard VLE model to predict equilibrium and speciation, and the rate constants developed by Cullinane to predict kinetics. The model calculates heat and mass transfer using Onda[16] and the Chilton-Colburn Analogy and physical properties using correlations specified by the user within the Aspen Plus® framework.

Initial absorber modeling by Chen predicted an unexpected temperature profile indicating that the heat of absorption for CO_2 was not being correctly predicted by Aspen Plus®. This was in part due to the fact that the simultaneous regression of the interactions parameters by Hilliard did not incorporate heat capacity data for the K_2CO_3-PZ-CO_2-H_2O system. Therefore, the temperature dependence of the regressed binary interaction and enthalpy parameters may not have been adequately captured.

The heat of absorption calculated by Aspen Plus® is derived from an enthalpy balance using the heats of formation, heat capacities, and heats of vaporization of the various species. The heats of formation of the piperazine species (PZH^+, $PZCOO^-$, $PZ(COO^-)_2$, and H^+PZCOO^-) were adjusted to provide the same heat of CO_2 absorption as that predicted from equilibrium constants used in the chemistry model. The heats of formation (liquid) at 298.15K were calculated using the parameters from the equilibrium constants and the Van't Hoff equation. The equilibrium equations and results obtained for the four piperazine species can be found in Chen[12].

Since the Hilliard VLE model does not contain heat capacity parameters for the PZ species (PZH^+, $PZCOO^-$, $PZ(COO^-)_2$, H^+PZCOO^-) regressed entropy reference values for the four PZ species were used to calculate heat capacities. Multi-parameter heat capacity correlations were developed using the equilibrium constants. Aspen Plus® does not account for the existence of net-neutrally charged zwitterions which were included in the Hillard K^+/PZ VLE model. The H^+PZCOO^- ion was given a net charge of 0 and was thus treated as a molecule. This created a number of issues such as the skewed predictions of the heats of absorption. Therefore, the charge for the H^+PZCOO^- ion was changed to 0.0001.

The equilibrium constants were activity-based while the rate constants developed by Cullinane used concentration-based units. Therefore, Chen implemented activity-based kinetics within the model, taking advantage of the fact that the new version of RateSep™ has the capability to handle activities, in terms of mole gamma, using the power law kinetic expression:

$$r = k \left(\frac{T}{T_o} \right)^n \exp^{\left(\frac{-E}{R} \left(\frac{1}{T} - \frac{1}{T_o} \right) \right)} \prod (x_i \gamma_i)^{\alpha_i} \tag{6}$$

where k is the pre-exponential factor (independent of temperature), n is the temperature exponent, E is the activation energy, T_o is the reference temperature (298.15K), x_i is the fraction of reactant species i, γ_i is the activity coefficient, and α_i is the reaction order for the species.

A simple algebraic manipulation was performed using the following equation:

$$k_a = \frac{k_c [PZ][CO_2][b]}{(x_{PZ} \gamma_{PZ})(x_{CO_2} \gamma_{CO_2})(x_b \gamma_b)(total\ mol/L)} \tag{7}$$

where k_a is the activity-based rate constant, k_c is the concentration-based rate constant, [b] is the concentration of species b in units of mol/L, and x_b is the mole fraction and γ_b is the activity coefficient. The last term in the denominator represents the total molar concentration per liter of solvent and will be specific for a particular solvent composition and loading. Therefore, a representative total molar concentration was selected and assumed to be constant across the column.

Kinetics developed by Cullinane contain a correction for ionic strength. However, in Aspen Plus®, this correction cannot be directly implemented. Therefore, a representative ionic strength at 50°C and 0.5 loading (mol CO_2/total alkalinity) was selected over the temperature and loading range of this study (the calculated ionic strength varied less than 5%)

Chen[12] reported results for the forward and reverse activity-based rate parameters for piperazine, piperazine carbamate, and bicarbonate reactions as input into Aspen Plus® RateSep™ for systems with 5 m K^+/2.5 m PZ, 6.4 m K^+/1.6 m PZ. The power law constants for the 4.5 m K^+/4.5 m PZ, were calculated using the methodology used by Chen and are presented in Tables 1 to 3.

Table 1: Activity-Based Rate Parameters for formation of PZCOO⁻ in 4.5m K⁺/4.5m PZ

b*	Forward			Reverse		
	$k \times 10^{10}$	E (kJ/kmol)	n	k	E (kJ/kmol)	n
OH^-	28.11	-67,847	34.75	2.12×10^{-2}	246,966	-38.02
H_2O	0.0127	-42,414	23.48	2.93×10^{12}	160,611	-26.81
PZ	3.25	-155,841	53.66	6.12×10^2	325,276	-66.41
CO_3^{-2}	17.64	-105,880	53.25	3.42×10^3	200,502	-32.53
$PZCOO^-$	10.40	-51,821	28.72	6.12×10^2	325,276	-66.41

*b corresponds to $PZ + CO_2 + b \leftrightarrow PZCOO^- + bH^+$

Table 2: Activity-Based Rate Parameters formation of $PZ(COO^-)_2$ in 4.5m K⁺/4.5m PZ

b*	Forward			Reverse		
	$k \times 10^{12}$	E (kJ/kmol)	n	k	E (kJ/kmol)	n
H_2O	0.0039	61,606	-1.46	2.22×10^{13}	78,135	-1.46
PZ	2.02	-51,821	28.72	9.45×10^3	242,800	-41.06
CO_3^{-2}	5.39	-1,860	28.31	2.59×10^4	118,027	-7.18
$PZCOO^-$	0.0065	52,199	3.78	2.07×10^4	116,084	3.78

*b corresponds to $PZCOO^- + CO_2 + b \leftrightarrow PZ(COO^-)_2 + bH^+$

Table 3: Activity-Based Rate Parameters for the formation of HCO_3^- in 4.5m K⁺/4.5m PZ

a*	b*	Forward			Reverse		
		$k \times 10^{12}$	E (kJ/kmol)	n	k	E (kJ/kmol)	n
--	OH^-	5.28×10^{-6}	54,758	5.24	2.18×10^{-3}	66,014	19.54
H_2O	PZ	2.27×10^{-8}	-30,856	24.15	2.35	146,702	-8.85
H_2O	$PZCOO^-$	1.04×10^{-8}	73,163	-0.79	7.39	19,986	35.99

*a, b correspond to $a + CO_2 + b \leftrightarrow HCO_3^- + bH^+$. ($OH^-$ does not form bH^+)

Absorber Modeling

The absorber was simulated with a rate-based model accounting for mass transfer resistance and reaction kinetics. Kinetics, in the liquid film, were calculated by discretizing it into 5 segments with a ratio of ten for the first 4 segments starting at 0.0001 and a value of 0.4 for the segment closest to the bulk liquid. Electrolyte thermodynamics were also considered. This approach required a full characterization of mass and heat transfer, hydrodynamics, vapor-liquid equilibrium, and physical properties of the entire system. This model was set up in Aspen Plus® using RateSep™. The previously obtained activity-based kinetics were introduced along with the VLE model generated by Hilliard[14]. Packing interfacial area was calculated using the built-in correlation in Aspen by Onda[16]

The developed model was used to evaluate the effect of solvent loading and intercooling on the performance of the absorber. The absorber was modeled with 15 m of packing divided into 30 calculation stages. Table 4 shows the absorber design specifications. Table 5 shows the conditions of the gas feed stream.

Table 4: Absorber design conditions for most modeling cases

Variable	Value
Diameter (m)	9.8
Height (m)	15.0
Packing Characteristics	
Type	CMR
Vendor	MTL
Material	Metal
Dimension	NO-2P
Liquid hold up (%)	5

Figure 1: Double Matrix Stripper Configuration

Table 5: Flue gas conditions used for simulation cases

Variable	Value
Flow (kmol/s)	5.4879
Temperature (^oC)	40.0
Pressure (kPa)	111.33
Mol fraction	
H_2O	0.0670
CO_2	0.1270
N_2	0.7569
O_2	0.0491

The Double Matrix System.

Oyenekan[17] proposed a stripper configuration for the regeneration of the solvent for the absorption of CO_2 that reduces the temperature change across the stripper by using a multipressure system (see Figure 1). The rich solution from the absorber is split into two streams: one goes to a higher pressure stripper while the other goes to a lower pressure stripper. This configuration generates two return streams to the absorber (lean and semilean). Depending on the operating condition these streams will be at higher or lower loading and their flow will also vary.

Van Wagener[18], based on the work by Oyenekan, modeled the double matrix configuration using the 4.5 m K^+/4.5 m PZ solvent. Results from this analysis provided an optimum loading (moles of CO_2/moles of alkalinity) of 0.4012 for the lean stream and 0.4598 for the semilean stream. The flow split between the streams was 0.1850(mol semilean/mol lean). These values correspond to 0.5 kPa partial pressure of CO_2 in the lean stream at 40 ^{o}C. These data were used to set up an absorber optimization to maximize CO_2 removal using a fixed packing height and varying the position of the semilean feed and an additional intercooling point. Figure 2 summarizes the conditions used for this analysis.

Figure 3 demonstrates optimization of the case using a semilean feed without intercooling. The position of the semilean feed was adjusted to maximize CO_2 removal. Removal is not very sensitive to the feed position, but an optimum is found 30% from the top. Figure 4 gives the resulting liquid temperature and CO_2 rate profile.

Figure 2: Absorber modeling conditions for 4.5 m/4.5 m K^+/PZ

Figure 3: CO_2 removal with semilean feed with no intercooling for the 4.5 m/4.5 m K^+/ PZ system. 0.5 kPa CO_2 lean solvent, 15 m packing.

Figure 4: Temperature and CO_2 absorption rate profiles for absorber with semilean feed at 0.30 column height; no intercooling. Solvent 4.5m/4.5 m K^+/ PZ. 0.5 kPa CO_2 lean solvent. 15 m packing.

Intercooling was defined to achieve 40 °C at the selected stage, which should be feasible with cooling water. When intercooling was used at the same point as the semilean feed, the optimum semilean feed position changed from the upper half of the column to the lower third. (See Figures 5 and 6.)

Figure 7 shows the profiles obtained with an additional intercooling stage. The semilean feed with intercooling was simultaneously optimized along with the additional intercooling point. The optimum locations for the semilean and the additional intercooling were found at 0.63 and 0.87 of the column height, respectively.

Figure 5: CO_2 removal with intercooled semilean feed for 4.5m/4.5 m K^+/PZ. 0.5 kPa CO_2 lean solvent. 15 m packing.

Figure 6: Temperature and CO_2 rate profiles for absorber with semilean feed and intercooling at 0.70 column height. Solvent 4.5m/4.5 m K^+/PZ. 0.5 kPa CO_2 lean solvent.

Figure 7: Temperature and CO_2 rate profiles for absorber with intercooled semilean feed at 0.63 and intercooling at 0.87 column height. Solvent 4.5m/4.5 m K^+/PZ. 0.5 kPa CO_2 lean solvent.

Van Wagener reported conditions for the stripper using a higher loading lean solvent corresponding to 0.7 kPa CO_2 partial pressure. The lean solvent loading was 0.4208, the semilean loading was 0.4743 and the split was 0.1453. An analysis analogous to the 0.5 kPa loading was conducted, obtaining similar results. A summary of the results for the various operating conditions modeled is presented in Table 6. A single intercooling at the point of the semilean feed is very effective. Additional intercooling provides only marginal improvement.

Table 6: CO_2 removal results for K^+/PZ absorber configurations

CO_2 Pressure in lean Solvent @ 40°C	0.5 kPa	0.7 kPa
Intercooling	**CO_2 Removal (%)**	
None	81.4	71.6
Single with semilean feed	91.3	82.9
Double	92.8	84.2

Effect of Intercooling on solvent capacity and rich loading

The lean solvent loading was varied to determine its effect on solvent capacity and rich loading for a simple absorber system with a single feed while maintaining removal at 90%. Solvent capacity is defined as the kmol of CO_2 removed per kg lean solvent feed.

Intercooling was set up in a similar matter to the previous analysis. It was placed in the middle of the column and at the optimum point (minimum amount of solvent for the level of lean loading). The flue gas and absorber specifications are the same as in Tables 4 and 5 but packing height was increased to 20 m. Figure 8 shows the effect of lean loading in solvent capacity Figure 9 presents the corresponding change in rich loading

In both figures the optimum curve and the $Z/Z_{Total} = 0.5$ curve overlap along the studied range. Thus, the position of the intercooling stage is not critical with 20 m of packing.

Figures 10 and 11 show that intercooling at high loading lean feed is not very beneficial because there is a limited temperature increase (7 °C) in the absorber. The higher solvent flow needed at high lean loading buffers any temperature increase due to reaction. The heat is absorbed by the increased solvent flow. Thus, mass transfer is not limited by the increase of temperature.

On the other hand, lean loading solvent feeds (Figures 12 and 13) show a large increase in solvent temperature towards the top of the column. The low CO_2 content in the solvent offers an initial high driving force that allows for increased reaction rates at the top of the column causing a noticeable temperature increase. The lower solvent rates are not capable of absorbing all the generated heat and there is a top of column temperature bulge (around 70 °C). As temperature increases the equilibrium becomes a limiting factor, yet most of the CO_2 has already been absorbed so the bottom of the column does not react much. Figure 13 shows that the use of intercooling does not provide a considerable benefit in performance. The CO_2 rate profile obtained without intercooling (Figure 12) differs little from the former.

However, absorbers operating at conditions within the loading bracket 0.27 to 0.40 mol CO_2/mol alkalinity benefit from intercooling. The temperature bulge is located near the center of the column and limits mass transfer rates. By adding intercooling it is possible to boost this phenomenon thanks to a lowering of the temperature of the bulge and of the column in general. (See Figures 14 and 15) This bracket is defined as the critical L/G region.

Looking at the behavior of the rich loading with respect to lean loading (Figure 9), intercooling proves especially beneficial between in the critical L/G (0.27–0.40 mol CO_2/mol alkalinity) for stripper performance. The higher loading from the absorber allows for lower energy consumption in the stripper.

Figure 8: Change in solvent capacity vs. lean loading. 4.5 m K⁺/4.5 m PZ. 90% CO_2 removal with 20 m of CMR#2 packing.

Figure 9: Variation of rich loading with lean loading. 4.5 m K⁺/4.5 m PZ. 90% CO_2 removal with 20 m of CMR#2 packing.

Figure 10: Temperature and CO_2 rate profiles for absorber. 4.5 m K⁺/4.5 m PZ with a lean loading of 0.44.

Figure 11: Temperature and CO_2 rate profiles for absorber with intercooling at 0.50 column height. 4.5 m K⁺/4.5 m PZ with a lean loading of 0.44.

Figure 12: Temperature and CO_2 rate profiles for absorber. 4.5 m K⁺/4.5 m PZ with a lean loading of 0.21.

Figure 13: Temperature and CO₂ rate profiles for absorber with intercooling at 0.50 column height. 4.5m/4.5 m K⁺/PZ with a lean loading of 0.21.

Figure 14: Temperature and CO₂ rate profiles for absorber. 4.5m/4.5 m K⁺/PZ with a lean loading of 0.315.

Figure 15: Temperature and CO₂ rate profiles for absorber with intercooling at 0.50 column height. 4.5m/4.5 m K⁺/PZ with a lean loading of 0.315.

Determining the critical Liquid-Gas ratio (L/G)$_c$

The benefit of using intercooling is maximized when the selected operating conditions cause the temperature bulge to coincide with a mass transfer pinch. This relates to the capacity of the gas and the liquid to carry heat out of the column. At the critical L/G the heat generated by the absorption of CO_2 is removed evenly between the liquid and the gas producing a temperature bulge towards the middle of the column.

In order to determine the critical L/G it is useful to set up global mass and energy balances and balances between the top of the column and the location of the temperature bulge. The global energy balance can be written as follows:

$$L_{in}H_{in}^L + G_{in}H_{in}^G = L_{out}H_{out}^L + G_{out}H_{out}^G \qquad (8)$$

where: L and G are the liquid and gas flow rates respectively (moles/s);
   H is the enthalpy of the stream;
   ^{L,G} are superscripts for gas and liquid properties;
   $_{in, out}$ label inlet and outlet streams around the absorber.

Likewise, an energy balance around the top of the absorber and the location of the temperature bulge results in the following equality:

$$L_{in}H_{in}^L + G_bH_b^G = L_bH_b^L + G_{out}H_{out}^G \qquad (9)$$

where $_b$ stands for conditions at the temperature bulge location.

The following approximations and assumptions will be made to determine (L/G)$_c$ based on engineering criteria and observations from the presented modeling cases:

- In the global energy balance enthalpies are determined using the inlet liquid temperature (T_{in}^L) as reference temperature (T_o). This eliminates the inlet liquid term from equation 8.
- The energy contribution due to CO_2 absorption and vaporization of water is included in the outlet gas enthalpy as follows:

$$G_{out} H_{out}^G = G_{out} Cp_{out}^G (T_{out}^G - T_o) + \left(n_{out}^{CO_2(g)} - n_{in}^{CO_2(g)}\right) h_{abs}\big|_{T_o} + \left(n_{out}^{H_2O(g)} - n_{in}^{H_2O(g)}\right) h_{vap}\big|_{T_o} \tag{10}$$

where: n is the flow rate (moles/s) of ^{CO2} or ^{H2O} respectively in the gas;

   T_o is the reference temperature;

   $h_{abs}\big|_{To}$ is the CO_2 heat of absorption at T_o;

   $h_{vap}\big|_{To}$ is the heat of vaporization of water at T_o;

   Cp_{out}^G is the heat capacity of the gas at outlet conditions.

- Replacing equation 10 in the global energy balance and including the expressions for outlet liquid and inlet gas enthalpy results in:

$$G_{out} Cp_{out}^G (T_{out}^G - T_{in}^L) + \left(n_{out}^{CO_2(g)} - n_{in}^{CO_2(g)}\right) h_{abs}\big|_{T_{in}^L} + \left(n_{out}^{H_2O(g)} - n_{in}^{H_2O(g)}\right) h_{vap}\big|_{T_{in}^L} +$$
$$L_{out} Cp_{out}^L (T_{out}^L - T_{in}^L) = G_{in} Cp_{in}^G (T_{in}^G - T_{in}^L) \tag{11}$$

where: Cp_{out}^L, is the heat capacity of the liquid at outlet conditions;

   Cp_{in}^G is the heat capacity of the gas at inlet conditions.

- We have observed from simulations that the maximum temperature at the bulge is approximately equal to the temperature that the gas would have if all of the heat of absorption were carried out with the gas. The global energy balance (equation 11) for a system in which all the heat leaves with the gas out the top of the absorber ($T_{out}^L = T_{in}^L$) is reduced to:

$$G_{out} Cp_{out}^G (T_{out}^G - T_o) + \left(n_{out}^{CO_2(g)} - n_{in}^{CO_2(g)}\right) h_{abs}\big|_{T_o} + \left(n_{out}^{H_2O(g)} - n_{in}^{H_2O(g)}\right) h_{vap}\big|_{T_o} = 0 \tag{12}$$

The right side of equation 12 is set to zero because for all of the cases the inlet liquid temperature was set equal to the gas inlet temperature (40 ^{o}C)

- By defining a desired removal (R) the outlet gas water content is calculated. Assuming that the outlet gas leaves in equilibrium with the inlet solvent it is possible to determine the outlet temperature using equations of state or steam tables. This value is used as an approximation to the bulge temperature (T_b):

$$\left(\frac{n_{out}^{H_2O}}{G_{out}}\right) \frac{P_{Total}}{x_{in}^{H_2O}} = \frac{y_{out}^{H_2O}}{x_{in}^{H_2O}} P_{Total} = P_{sat}^{H_2O} = f(T) \tag{13}$$

Here the outlet gas flow (G_{out}) is calculated using the inlet gas composition and taking into account the outlet water content and the removed carbon dioxide. x_{in}^{H2O} is the mole fraction of water in the inlet solvent.

- If in equation 9 the reference temperature (T_o) is set to the bulge temperature (T_b) the resulting energy balance is:

$$L_{in} Cp_{in}^L (T_{in}^L - T_b) + \left(n_{out}^{CO_2(g)} - n_b^{CO_2(g)} \right) h_{abs}\big|_{T_b} + \left(n_{out}^{H_2O(g)} - n_b^{H_2O(g)} \right) h_{vap}\big|_{T_b} =$$
$$G_{out} Cp_{out}^G (T_{out}^G - T_b) \tag{14}$$

- The change in liquid flow rate across the column is neglected and the gas flow rate is defined as:

$$G = G^i + n^{CO_2(g)} + n^{H_2O(g)} \tag{15}$$

Here G^i, represents the inert species present in the gas stream: oxygen and nitrogen

- Introducing equation 15 into equation 14 and after some manipulation:

$$\left(\frac{L}{G_i}\right)_c = \left(1 + (1-R)Y_{in}^{CO_2} + Y_{out}^{H_2O}\right)\left(\frac{Cp_{out}^G}{Cp_{in}^L}\right) + \frac{\left(Y_b^{CO_2} - (1-R)Y_{in}^{CO_2}\right)h_{abs}\big|_{T_b} + \left(Y_{out}^{H_2O} - Y_b^{H_2O}\right)h_{vap}\big|_{T_b}}{Cp_{in}^L (T_{in}^L - T_b)} \tag{16}$$

where: $(L/G)_c^i$ is the critical ratio of liquid to inert gas species;
Y^{H2O}, Y^{CO2} are the fractions of water and carbon dioxide respectively to inert species in the gas stream (n^{CO2}/G^i, n^{H2O}/Gi).
- The outlet gas water content can be calculated using an equilibrium relation:

$$y_{out}^{H_2O} = x_{in}^{H_2O} P_{sat}^{H_2O} (T_{in}^L) \tag{17}$$

where: y_{out}^{H2O}, x_{in}^{H2O} are mole fractions of water in the gas and liquid;
P_{sat}^{H2O} is the vapor pressure of water at the inlet liquid temperature (T_{in}^L).

- The CO_2 content at the temperature bulge is approximated based on results for simulations at various removals. Figure 16 gives total CO_2 removal as a function of the removal obtained at the bulge. Results fit the following equation depending only on the desired final removal:

$$R_b = 1.4728R - 0.7038 \tag{18}$$

where R_b is the removal at the bulge. Equation 18 fits the data adequately independent of the packing height used.

Figure 16: CO₂ removal at the bulge as a function of total removal. Points are simulation results. All cases with 10 m packing height. For 90% removal two additional points are included at 20 m and 5 m of packing.

It is worth noticing that equation 16 is independent of the height of packing and was generated from simple energy and heat balances. Its validation was done at constant removal (R) varying the height of packing, and at constant packing height but variable removal (Table 7).

The proposed approximation gives a relatively good estimate of the critical L/G (less than 10% deviation) for all cases except at 60% removal. As for the temperature bulge, it is adequately predicted with a maximum deviation of 4 $^\circ$C.

Table 7: Temperature bulge and critical L/G predictions. Variable packing and removal.

Packing Height (m)	CO₂ Removal (%)		$(L/G)_c$		T_b ($^\circ$C)		y_{out}^{H2O}		T_{out}^{G} ($^\circ$C)	
	Total	Below Bulge	Aspen	Approx.	Aspen	Approx	Aspen	Approx	Aspen	Approx.
5	90	61.9	3.9	4.0	69	68	0.09	0.06	46	40
10	90	63.8	4.1	4.0	72	68	0.10	0.06	46	40
20	90	61.2	4.1	4.0	72	68	0.09	0.06	46	40
10	80	47.0	3.8	4.1	69	66	0.10	0.06	48	40
10	60	18.1	3.5	4.5	61	62	0.09	0.06	47	40

Conclusions

Absorber intercooling increases CO₂ removal by as much as 10% in the double matrix example. Adequate positioning of the intercooled semilean feed and the additional intercooling assures the best possible performance of the column in this configuration

In simple absorbers where the temperature of the solvent is increased by heat of absorption, as with the K^+/PZ system, intercooling appears beneficial if the temperature bulge is located towards the middle of the column and coincides with a mass transfer pinch (critical L/G). In this case it will allow for higher absorption by reducing the magnitude of the bulge temperature and increasing solvent capacity by as much as 45%. Additionally, intercooling will offer a benefit in energy consumption in the stripper because of the richer feed from the absorber. However, for systems with low L/G where the bulge is located towards the top of the column and away from the mass transfer pinch, intercooling will offer limited improvement. In the same way, with high L/G the temperature bulge is small and its location matches the pinch at the bottom of the column, so intercooling will also offer very limited enhancement. In both cases intercooling may prove to be impractical because of capital costs required for its implementation.

An approximation of the critical L/G for the absorption of CO_2 has been developed. It requires knowledge of the heat of absorption of the solvent and approximate values for the heat capacities of the gas and the liquid. Its accuracy is strongly dependent on the estimation of the CO_2 content at the temperature bulge. For the expected operating removal (>80%) it is capable of calculating $(L/G)_C$ with less than 10% error for the K^+/PZ system. The temperature bulge can also be predicted to 4 ^{o}C.

This approximation also gives some insight into the possible behavior of the critical L/G with different solvents. A solvent with a heat of absorption 30% lower than the studied K^+/PZ will result in a 15% lower critical L/G. Similarly, a solvent with a heat of absorption 30% higher will result in a 15% higher critical L/G.

The developed approximation may prove to be a valuable tool when optimizing lean loading operation since it gives an idea of conditions to avoid where intercooling is not an option, without running any simulation models.

References

1.   Jackson, R. M.; Sherwood, T. K., Performance of Refinery Gas Absorbers with and without Intercoolers. *American Institute of Chemical Engineers Transactions* **1941,** 37, 959-978.
2.   Linhoff, H. R., Intercoolers used in absorber at vapor-recovery plants. *National Petroleum News* **1930,** 22, (20).
3.   Sobel, B. A., Iterative processes: a relaxation operator and its application to the the computation of absorber columns. *American Chemical Society, Division of Petroleum Chemistry* **1968,** 13, (3), 5.
4.   Thompson, R. E.; King, C. J., Energy conservation in regenerated chemical absorption processes. *Chemical Engineering and Processing* **1987,** 21, (3), 14.
5.   Chang, H.; Shih, C. M., Simulation and optimization for power plant flue gas CO2 absorption-stripping systems. *Separation Science and Technology* **2005,** 40, (4), 877-909.
6.   Tobiesen, F. A.; Svendsen, H. F.; Mejdell, T., Modeling of blast furnace CO2 capture using amine absorbents. *Industrial & Engineering Chemistry Research* **2007,** 46, (23), 7811-7819.
7.   Freguia, S.; Rochelle, G. T., Modeling of CO2 capture by aqueous monoethanolamine. *AIChE Journal* **2003,** 49, (7), 1676-1686.
8.   Mark, S. Purification and Separation of Gaseous Mixtures. 1934.
9.   Geleff, S. Method and Device for Recovery of Thermal Energy from an Exothermic Carbon Dioxide Absorption Process 10.04.2003, 2003.
10.   Reddy, S.; Scherffius, J.; Gilmartin, J.; Freguia, S. Split Flow Process and Apparatus. 2006.
11.   Kvamsdal, H. M.; Rochelle, G. T., Effects of the temperature bulge in CO2 absorption from flue gas by aqueous monoethanolamine. *Industrial & Engineering Chemistry Research* **2008,** 47, (3), 867-875.

12.   Chen, E. Carbon Dioxide Absorption into Piperazine Promoted Potassium Carbonate using Structured Packing. Ph.D. Dissertation, The University of Texas at Austin, Austin, Texas, 2007.

13.   Cullinane, J. T. Thermodynamics and Kinetics of Aqueous Piperazine with Potassium Carbonate for Carbon Dioxide Absorption. Ph.D. Dissertation, The University of Texas at Austin, Austin, Texas, 2005.

14.   Hilliard, M. Thermodynamics of Aqueous Piperazine/Potassium Carbonate/Carbon Dioxide Characterized by the Electrolyte NRT Model within Aspen Plus[®]. Masters, The University of Texas at Austin, Austin, Texas, 2005.

15.   Bishnoi, S.; Rochelle, G. T., Absorption of carbon dioxide in aqueous piperazine/methyldiethanolamine. *Aiche Journal* **2002,** 48, (12), 2788-2799.

16.   Onda, K., H. Takeuchi, et al. , Mass transfer coefficients between gas and liquid phases in packed columns. *Journal of Chemical Engineering of Japan* **1968,** 1 (1), 6.

17.   Oyenekan, B. A.; Rochelle, G. T., Alternative stripper configurations for CO2 capture by aqueous amines. *Aiche Journal* **2007,** 53, (12), 3144-3154.

18.   Rochelle, G.; Seibert, F.; Closmann, F.; Cullinane, J. T.; Davis, J.; Goff, G.; Hilliard, M.; McLees, J.; Plaza, J. M.; Sexton, A.; Van Wagener, D.; Xu, Q.; Veawab, A.; Nainar, M. *CO$_2$ Capture by Absorption with Potassium Carbonate*; DE-FC26-02NT41440; DOE: 2007.

Concentrated Piperazine
A new standard solvent

by
Gary T. Rochelle
gtr@che.utexas.edu
Luminant Carbon Management Program
Department of Chemical Engineering
The University of Texas at Austin
September 30, 2010

Why 8 m (40 wt% Piperazine?

- 10-20% less energy than 30 wt% MEA
  - 2 x CO_2 mass transfer rate
  - 1.8 x capacity
  - High P (6 – 15 atm) Stripper, stable to 150°C
- Oxidatively stable, esp. with Inhibitor A
- Less volatile than 7 m MEA
- Soluble at 0^oC at operating loading
- Good Opportunities for Reclaiming

Roadmap

- Energy Properties
- Solvent Management
- Pilot Plant

Energy Properties

- Chemistry – 2 active amines per molecule
- Viscosity & Solubility allow 8 m PZ when loaded
- CO_2 solubility
  - Capacity – 0.84 moles/kg solvent
  - Heat of Desorption – 76 kJ/mole
- Thermal Stability to 150°C
- 2-stage heated flash reduces energy 15%

Solubility Envelope for PZ
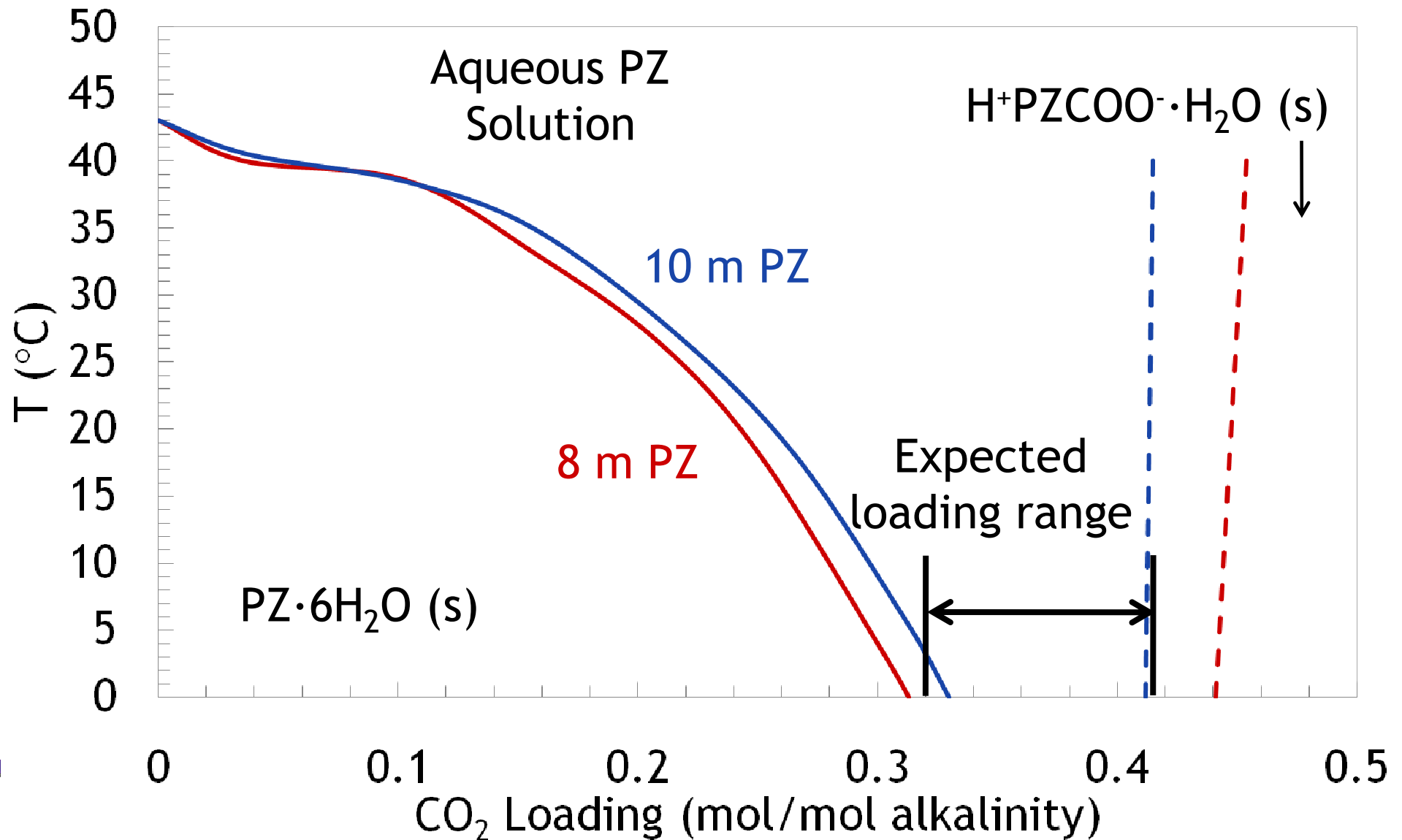
CO_2 solubility in Aqueous PZ

ΔH_{CO2}

160°C

120

80

40

0.84 mol CO_2/kg solvent
(0.48 for MEA)

P_{CO2} (bar)

ΔH_{abs} (kJ/mol)

CO2 loading (moles/equiv PZ)
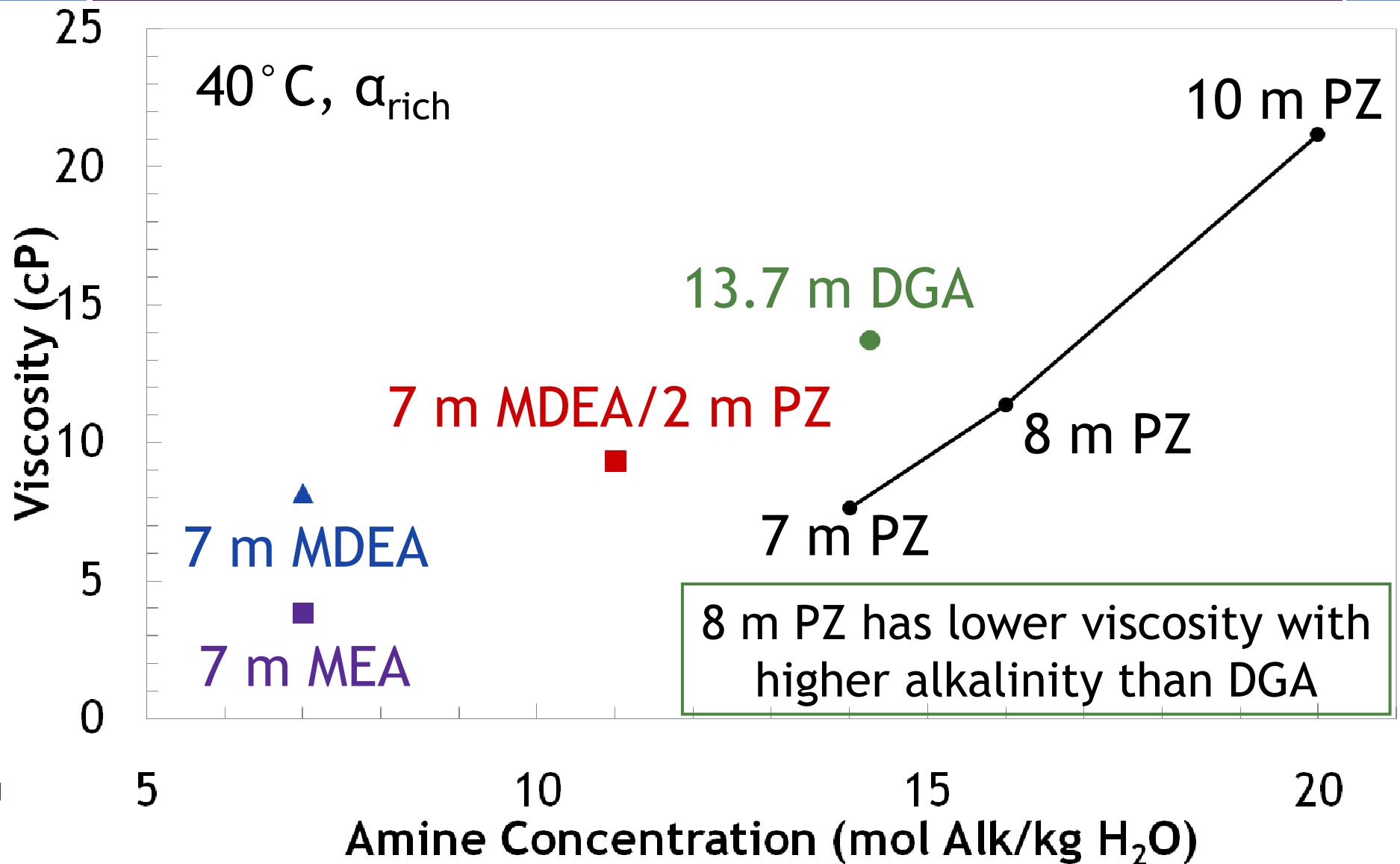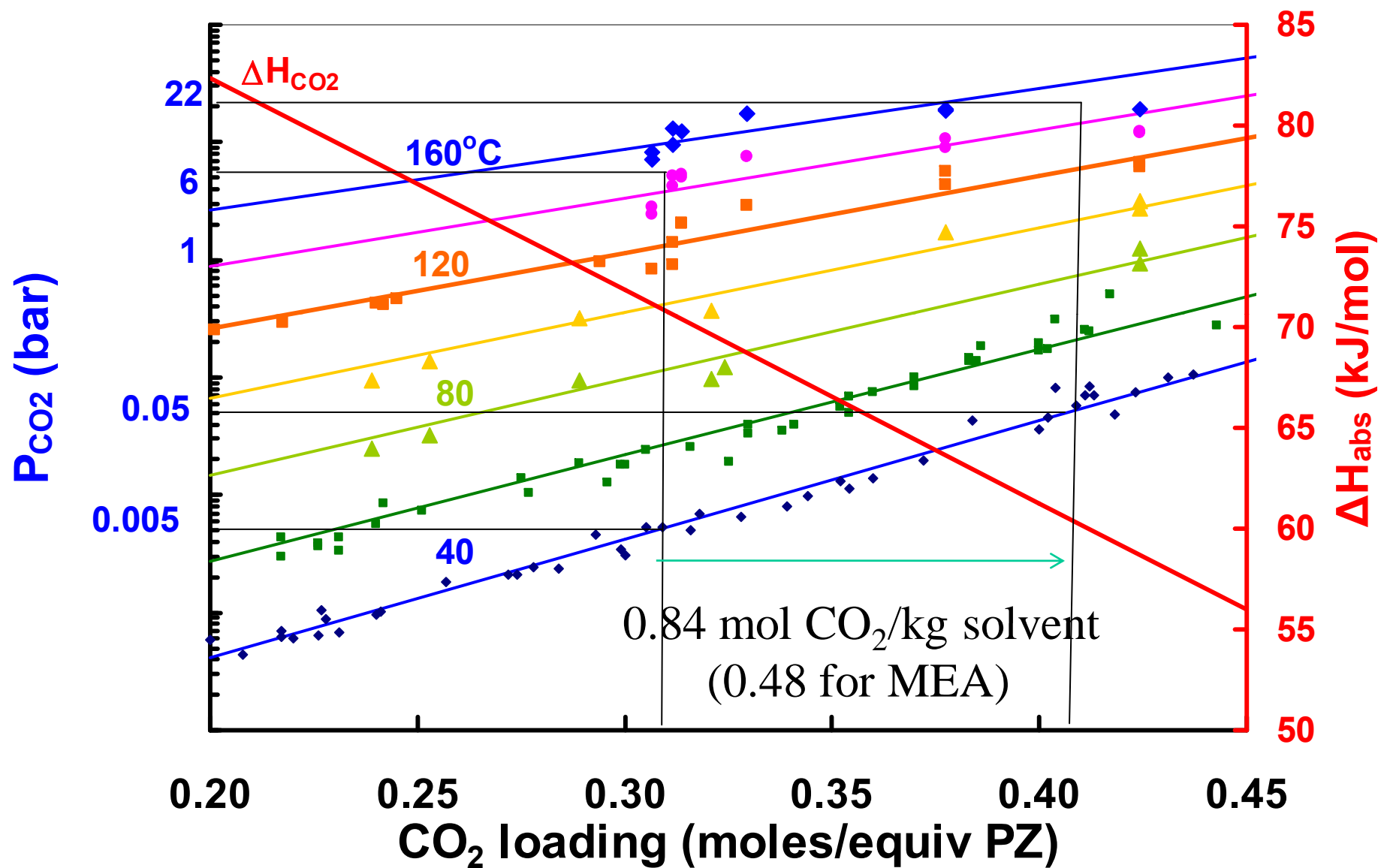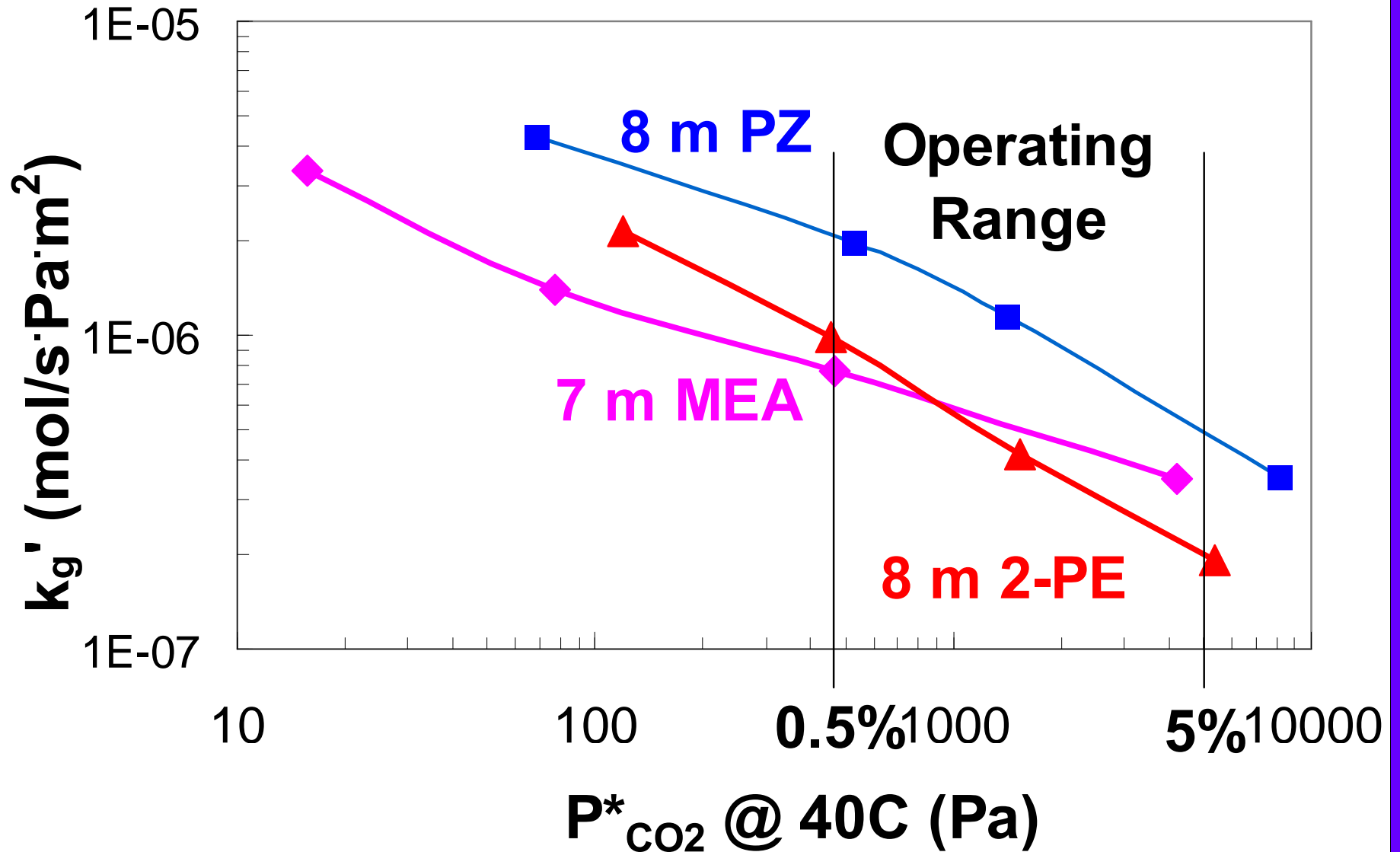
Thermal Degradation at Rich Loading
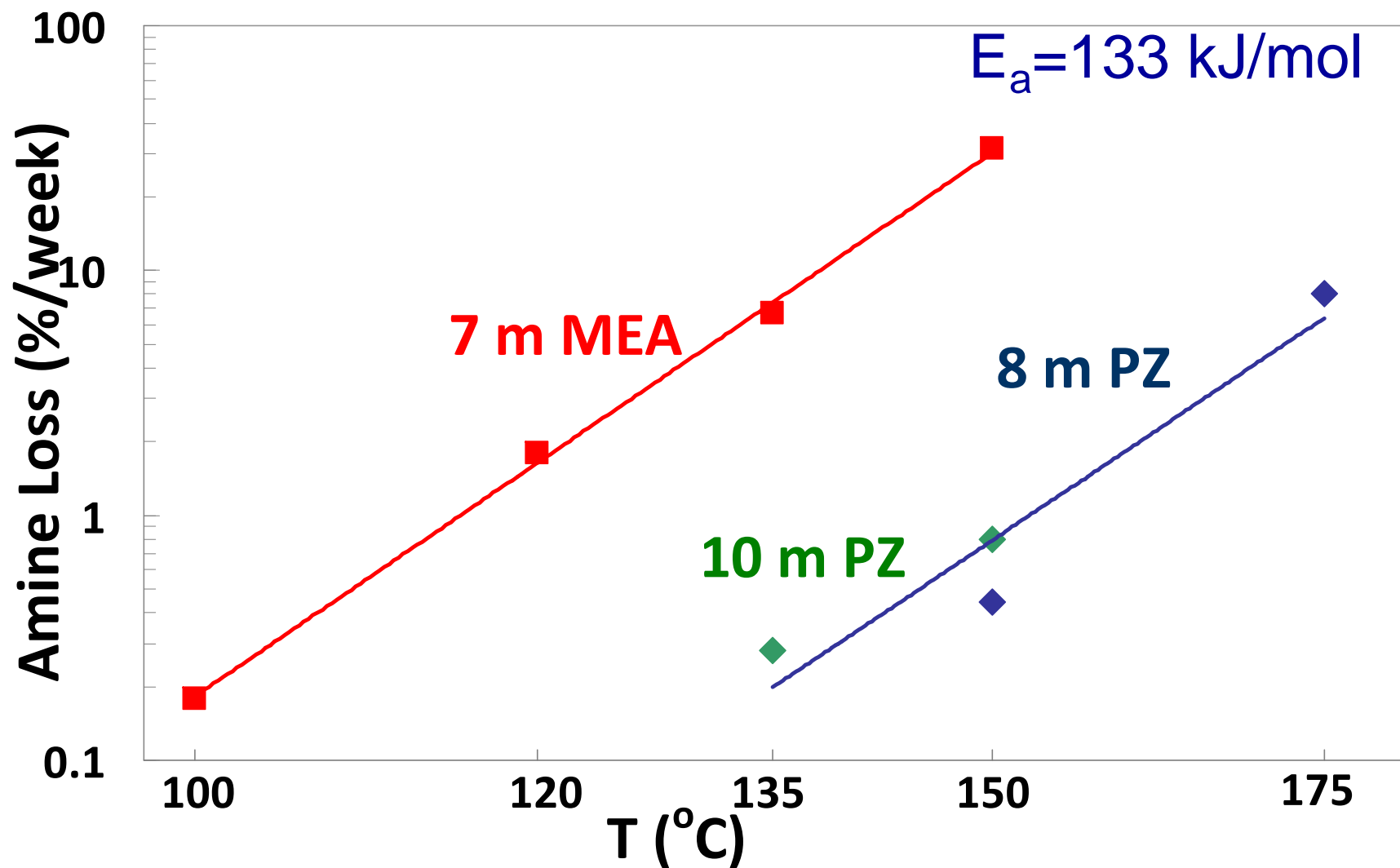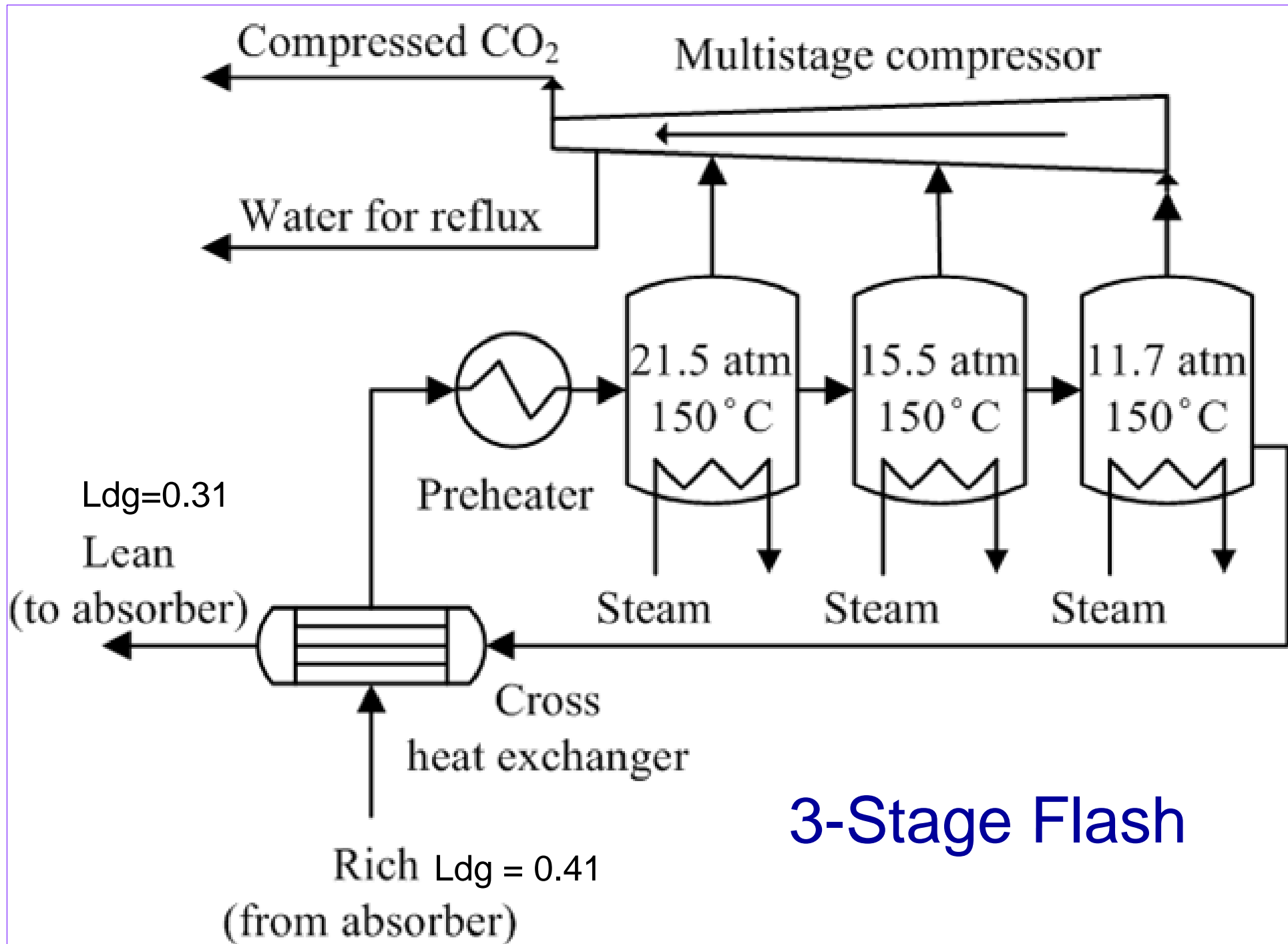
3-Stage Flash

Stripping 8 m PZ
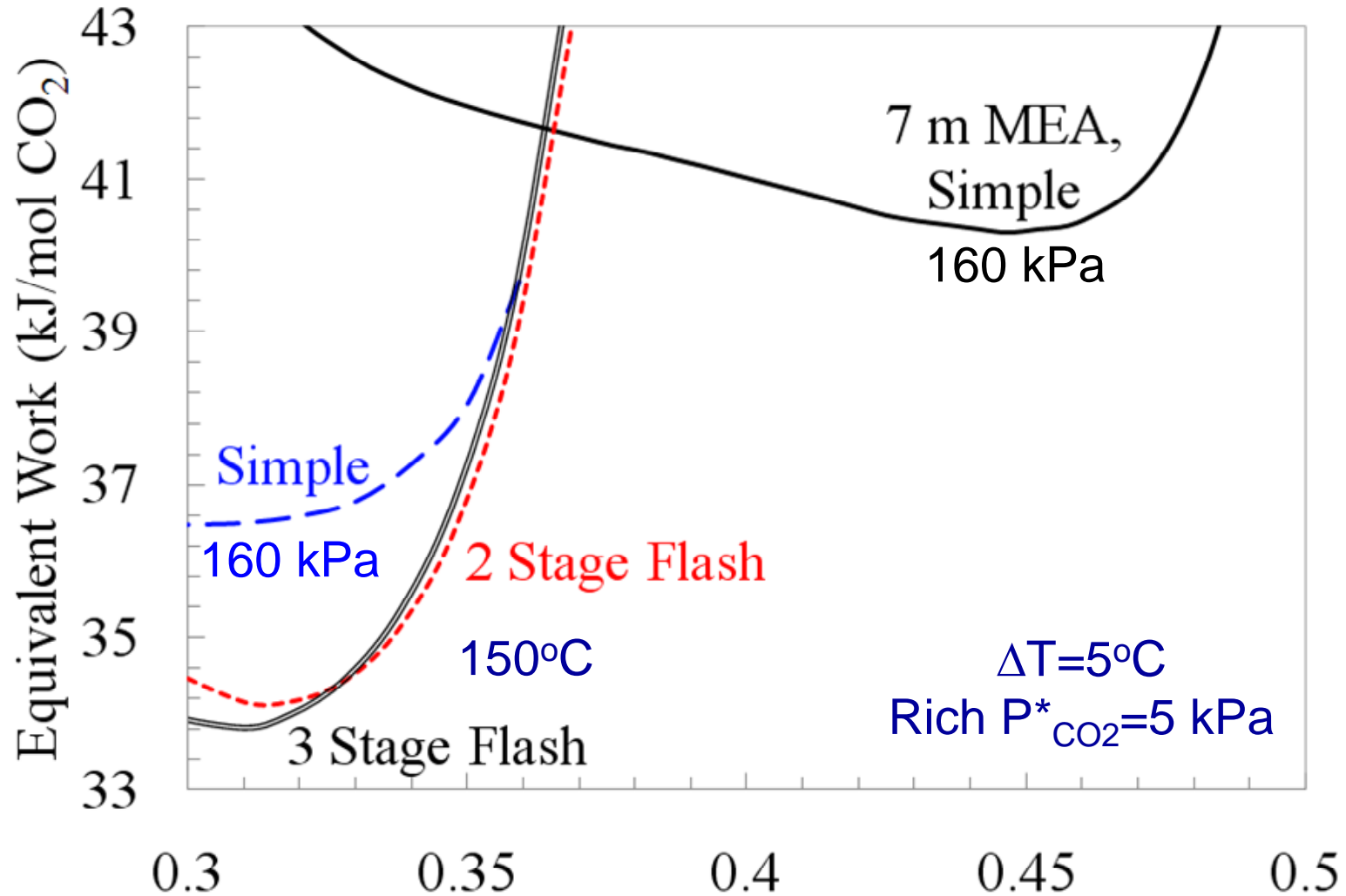
$$W_{eq} = \left[\sum 0.75 \cdot Q_{reb} \left(\frac{T_{reb} + 10K - T_{sink}}{T_{reb} + 10K} \right) \right] + W_{pump/comp}$$

Solvent Management

- Volatility <20 ppm at lean conditions
  - Air Impacts minimized by Water Wash
- Oxidation 3 x less than MEA
  - Eliminated by inhibitor A
- 316 SS resistant to corrosion
- Piperazine easily reclaimed by existing options

SS316 corrosion in thermal degradation experiments

7 m MEA, 135°C
(6.7% loss/wk)
Fe & Ni

8 m PZ, 150°C
(0.4% loss/wk)
Fe & Ni

Concentation (mM)

Time (weeks)

(Voice 2009)
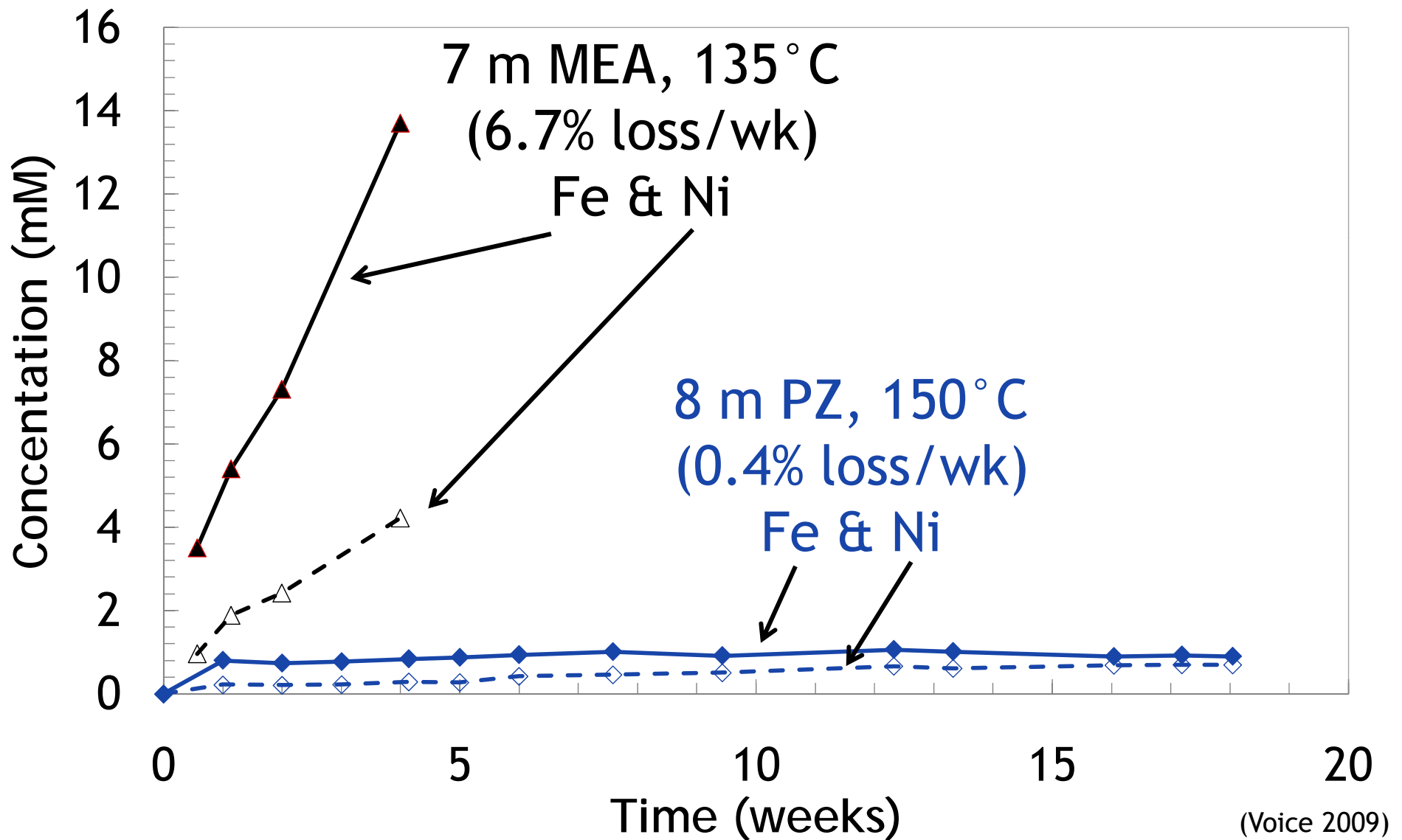
Reclaiming concepts

- Traditional Thermal or distillation Reclaiming
  - Atm or vacuum
  - PZ more volatile than MEA
  - PZ thermally stable
- Inhibitor A recovered from conc soln by supplier
- Ion Exchange or electrodialysis as with MEA
- K_2SO_4 crystallization with addition of KOH
  - 0.17 m sulfate solubility

Pilot Plant

- Results in 0.1 MW with air/CO_2
    - Mass Transfer Rate
    - Energy
- Plans for 0.1 MW with high P 2-stage flash

Selected Pilot Plant Runs, 8 m PZ
20 ft Mellapak 2X, 200m^2/m^3

Gas (acfm)	Liq (gpm)	P_{STRP} (psia)	Rem (%)	Lean Ldg	Rich Ldg
350	18	51	93.2	0.27	0.34
350	15	20	93.4	0.25	0.33
350	18	20	79.3	0.30	0.36
350	15	60	76.1	0.31	0.36

Loading = mol CO_2/Total Alkalinity

Wetted wall kg′ & Pilot plant K_G
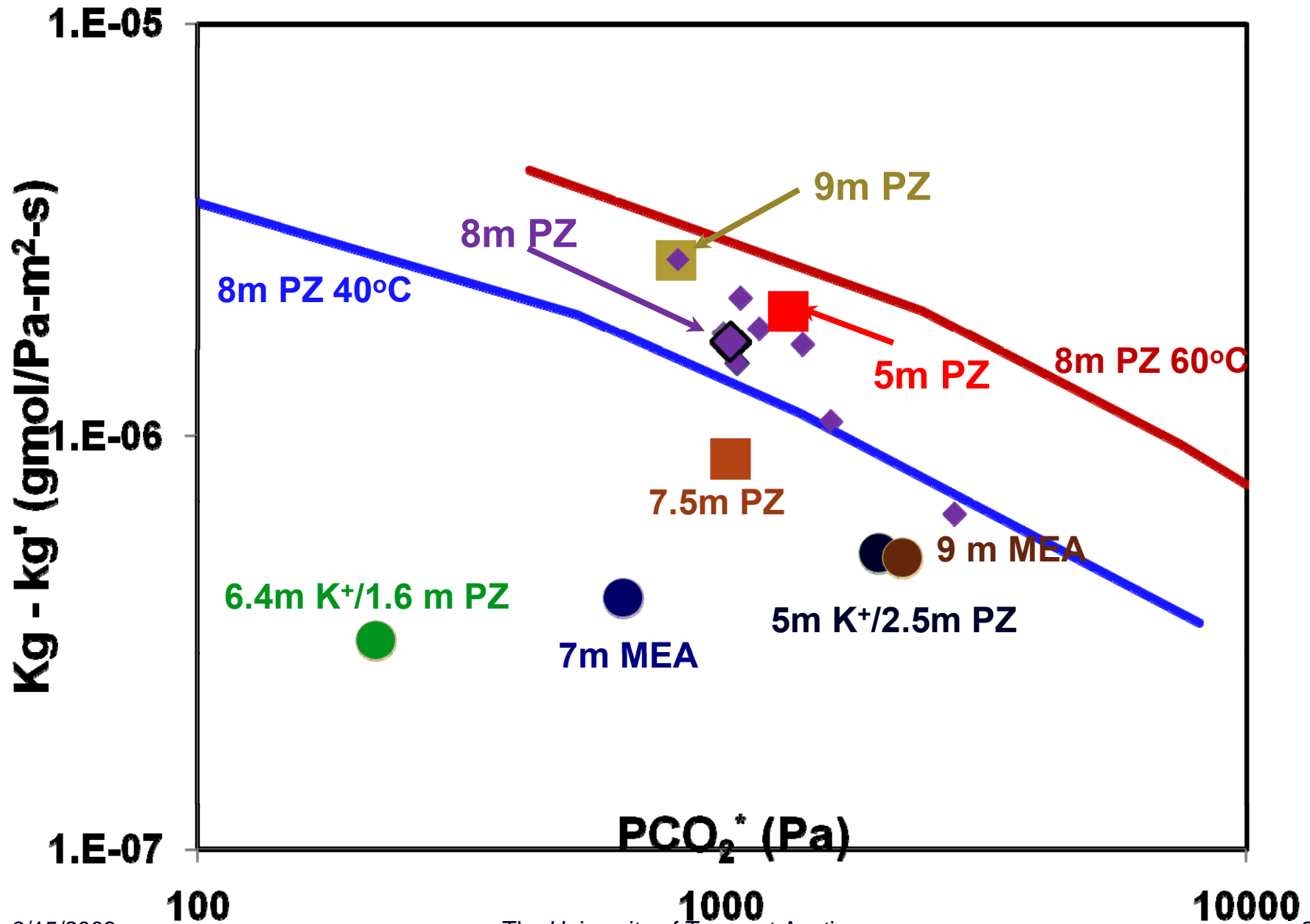
Stripper Performance
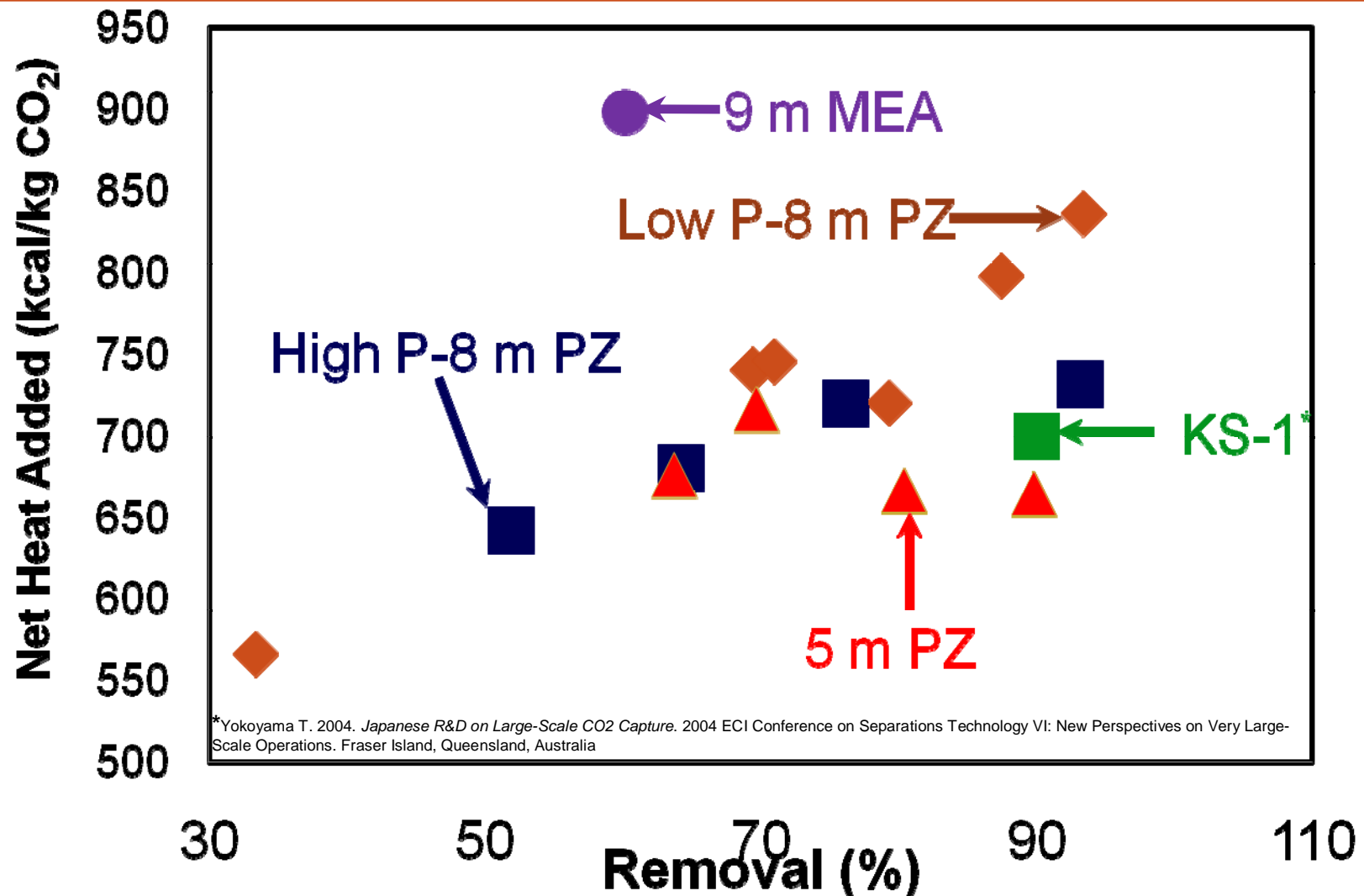
Conclusions

- 10-20% less energy than 30 wt% MEA
  - Double the CO_2 mass transfer rate
  - 1.8 x capacity
  - High P (6 – 15 atm) Stripper, stable to 150°C
- Oxidatively stable, esp. with Inhibitor A
- Less volatile than 7 m MEA
- Soluble at 0°C at operating loading
- Good Opportunities for Reclaiming

Accurate Screening of Candidate Solvents by the Wetted Wall Column

Xi Chen, Ross Dugas, Fred Closmann,
Shan Zhou, Gary T. Rochelle

The University of Texas at Austin

Outline

- Background
  - Research needs
  - Literature review
- Apparatus
  - Wetted Wall Column (WWC)
- Results:
  - CO_2 solubility, CO_2 capacity, Heat of absorption
  - Absorption/Desorption Rates
- Conclusions

Research Needs

- Previous amine capacity & kinetics studies:
  - Low amine concentration (< 3 M)
  - Zero or very lean CO_2 loading
  - Narrow temperature range (25~60 ^{o}C)
- Typical industrial conditions for CO_2 capture
  - Absorber: 40-60 ^{o}C
  - Stripper: 80-120 ^{o}C
  - 12% CO_2 in flue gas at 1atm and 90% removal: CO_2-loaded amine solvent ($P^*_{CO2,lean}$=0.5 kPa and $P^*_{CO2,rich}$=5 kPa)
- Previous amine screening efforts
  - Simple gas sparging: Absorption rate affected by solution property (density, viscosity & surface tension etc.)
  - CO_2 capacity for industrial conditions not available

Why WWC for Screening?

- More representative of commercial packing than laminar jet or stirred cell.

- More accurate VLE and mass transfer rate in loaded solution.

- Adequate for design of absorber and stripper.

Previous work with WWC

Literature	Solvents	[Amine]$_{max}$ (molality)
Dugas 2009	MEA/PZ	13
Cullinane 2005	K$^+$/ PZ	4
Al-Juaied 2004	DGA / Morpholine	18
Bishnoi 2000	MDEA/PZ	8
Pacheco 1998	MDEA/ DGA	12
Mashewa 1995	MDEA/DEA	9

Scope of this work

		Conc. (m)	Viscosity@ 40°C& $P^*_{CO_2}$ =5kPa (cP)
Primary Amines	Ethanolamine (MEA)	7	2.5
	Ethylenediamine (EDA)	12	14
	Diglycolamine® (DGA®)	10	n/a
Piperazine & derivatives	Piperazine (PZ)	8	10
	N-(2-hydroxyethyl)piperazine(HEP)	7.7	17
	1-(2-Aminoethyl)piperazine (AEP)	6	23
Hindered Amines	2-amino-2-methyl-1-propanol (AMP)	4.8	4
	2-piperidineethanol (2-PE)	8	24
Promoted Tertiary Amine	Methyldiethanolamine (MDEA)/ Piperazine (PZ)	7/2	8

Wetted Wall Column
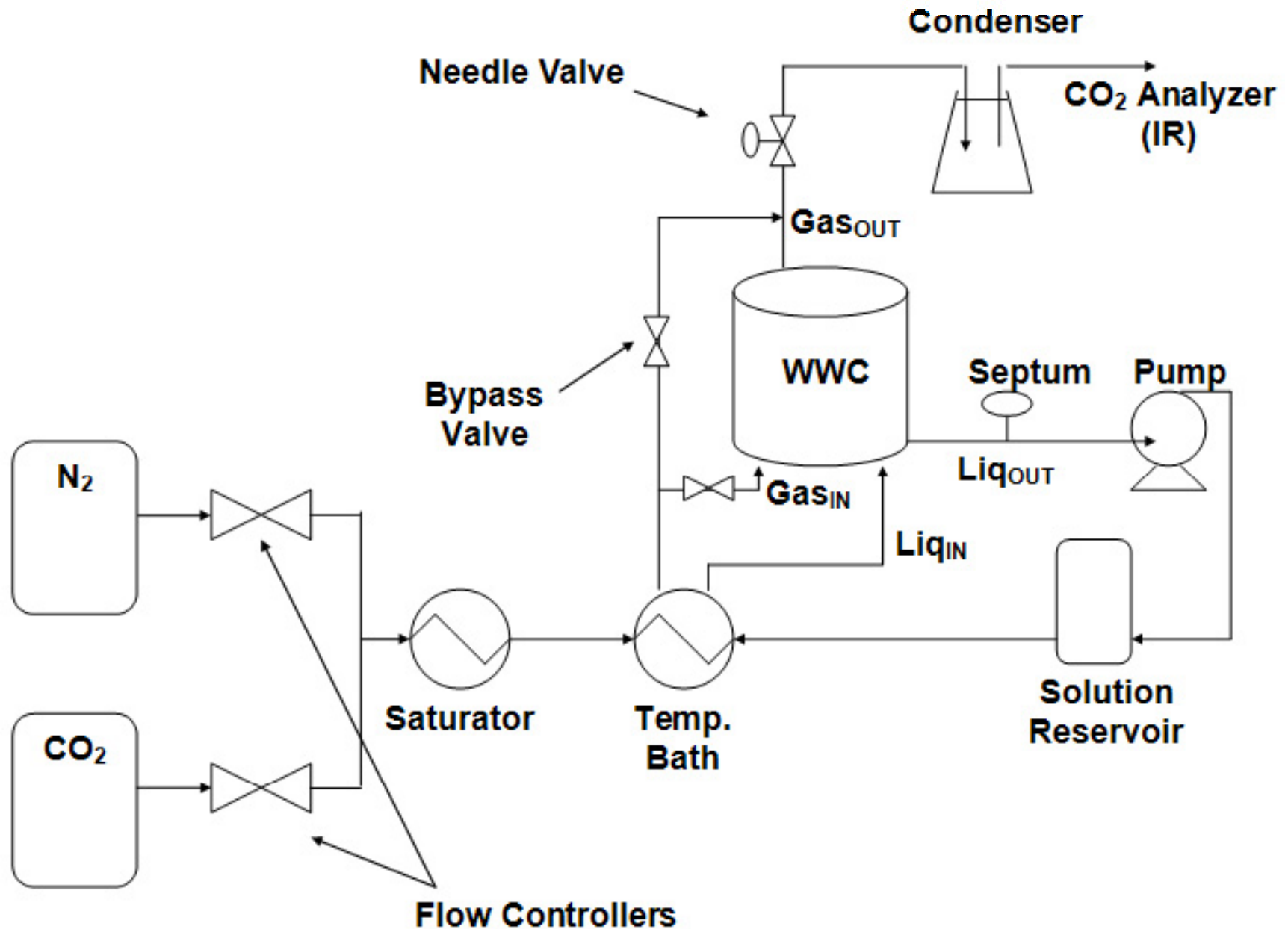
$$R_1 = \frac{1}{k_g} \qquad R_2 = \frac{H_{CO_2}}{Ek_l^0} \qquad R_3 = \frac{1}{k_{l,PROD}^0} \frac{\partial P_{CO_2}^*}{\partial [CO_2]_T}$$
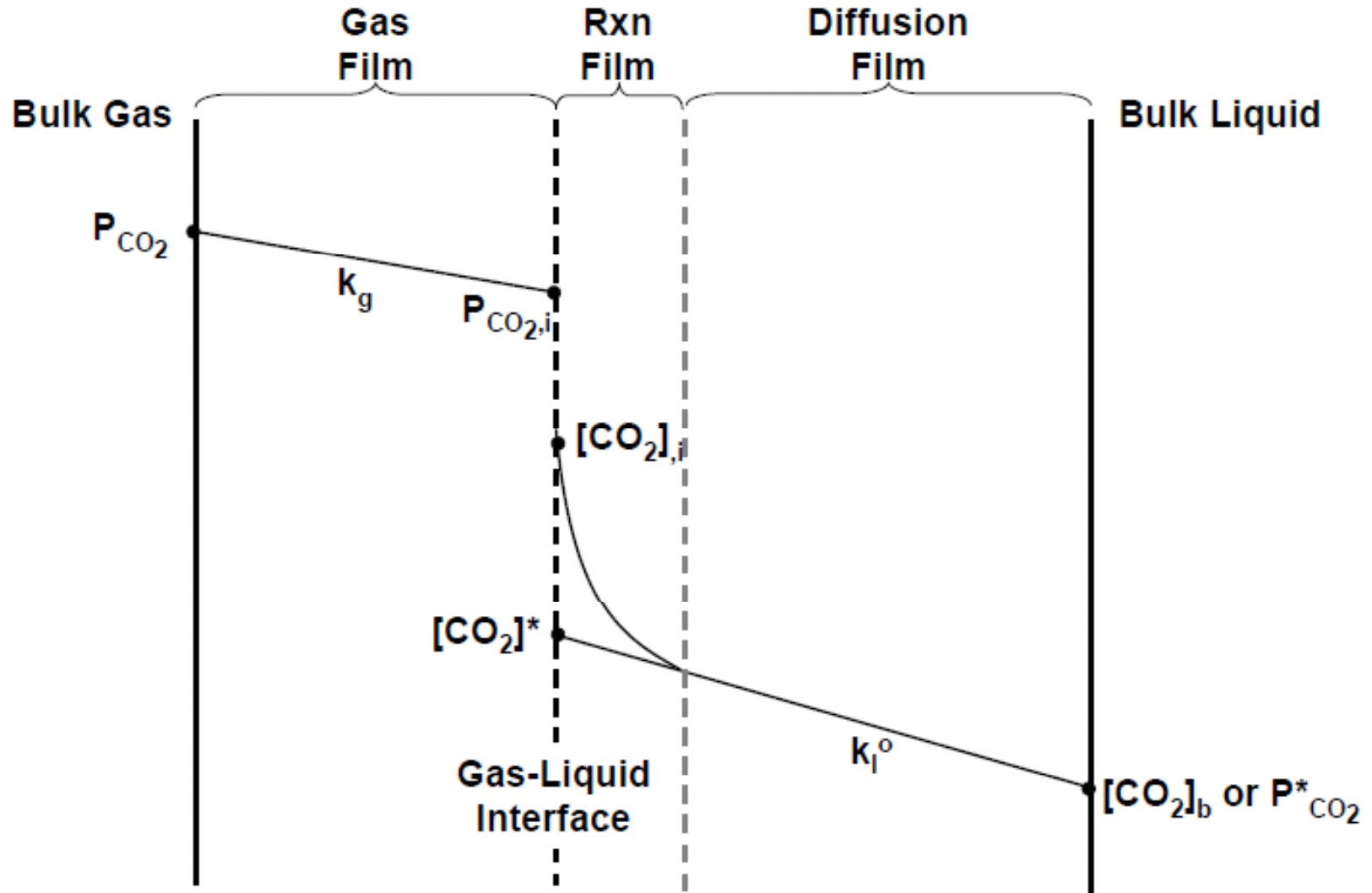
$$\frac{1}{K_G} = \frac{1}{k_g} + \frac{H_{CO_2}}{Ek_l^0} + \frac{1}{k_{l,PROD}^0} \frac{\partial P_{CO_2}^*}{\partial [CO_2]_T} = \frac{1}{k_g} + \frac{1}{k_g'}$$

$$N_{CO_2} = K_g(P_{CO_2,g} - P_{CO_2,l})$$

$$= k_g'(P_{CO_2,i} - P_{CO_2,l})$$

$$\Rightarrow k_g' = \frac{N_{CO_2}}{P_{CO_2,i} - P_{CO_2,l}}$$

$$\approx \frac{\sqrt{D_{CO_2} k_2 [Am]_b}}{H_{CO_2}}$$
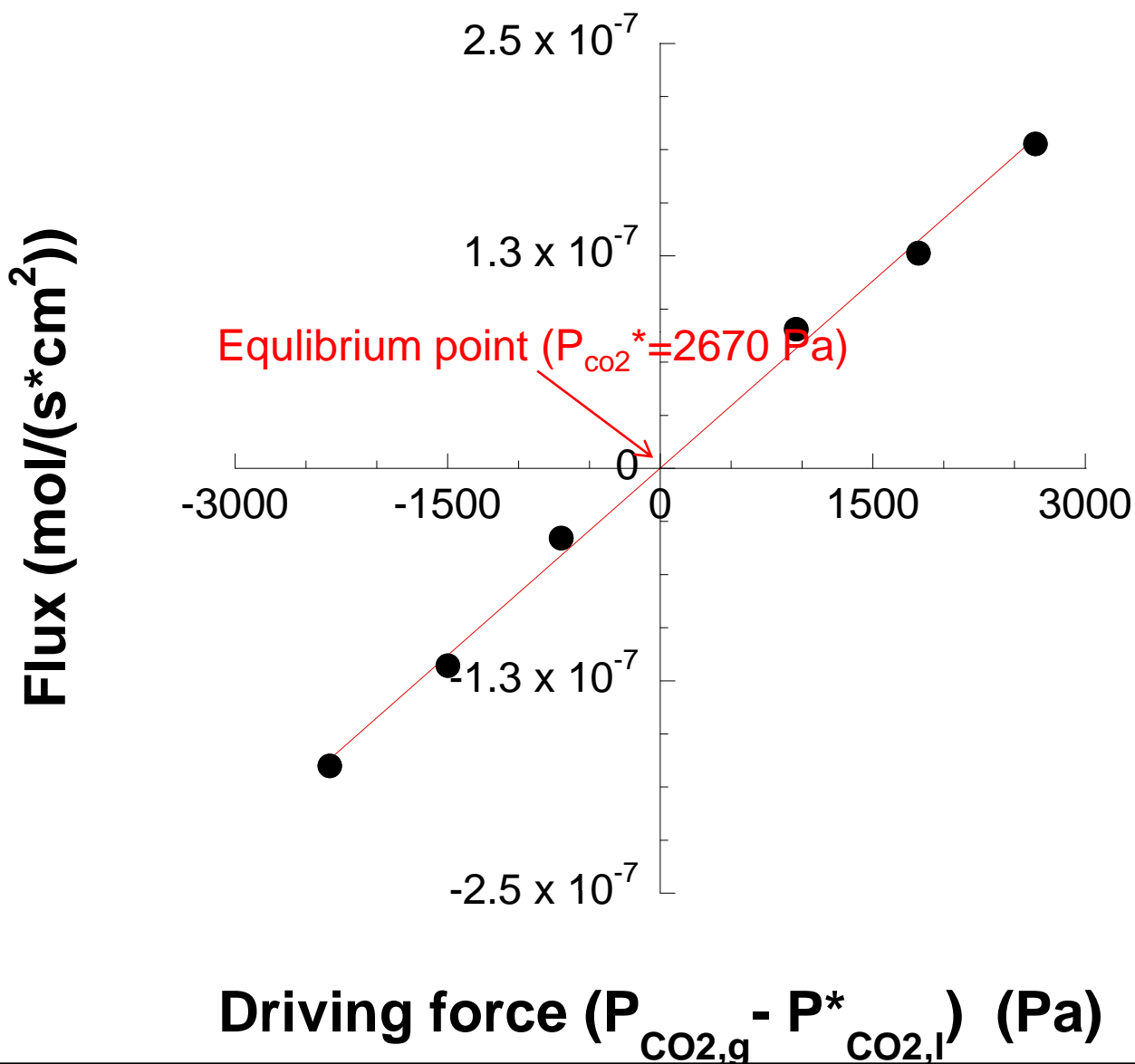
PIPERAZINE DERIVATIVES

CO$_2$ Solubility 7.7m HEP

$$\ln P = a + b/T + c \cdot \alpha + d \cdot \alpha/T + e \cdot \alpha^2$$

100 °C

80 °C

60 °C

40 °C

P* (kPa)

CO$_2$ Loading (mol/mol alkalinity)

Capacity=0.68 mol CO$_2$/kg (H$_2$O+HEP)

6m AEP

$$\Delta H_{abs} = -R \frac{d(\ln P)}{d(1/T)}$$

100 °C

80 °C

60 °C

40 °C

0.66
mol CO$_2$
/kg Solv.

P* (kPa)

5kPa
0.5kPa

Heat of absorption (kJ/mol)

CO$_2$ Loading (mol/mol alkalinity)
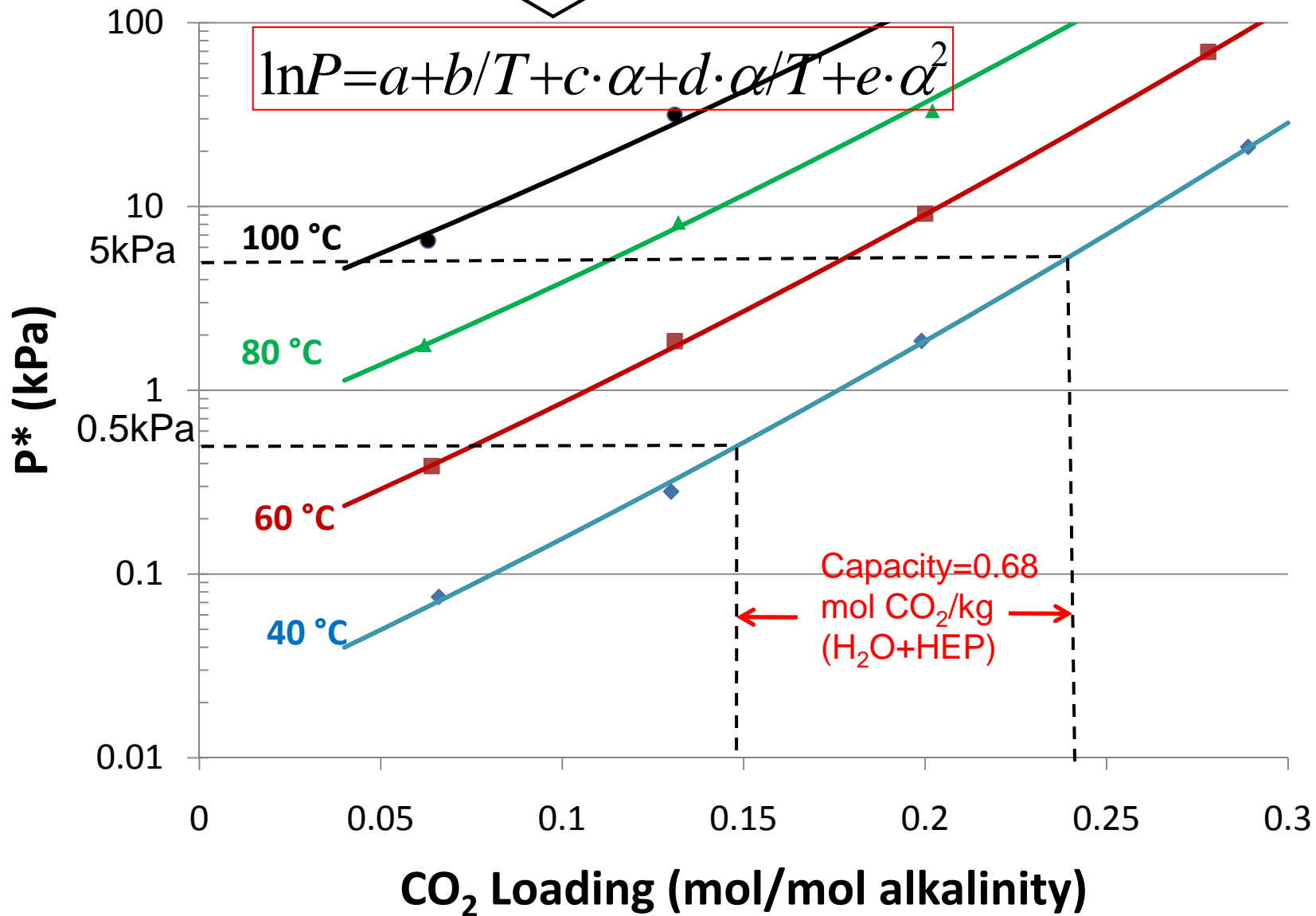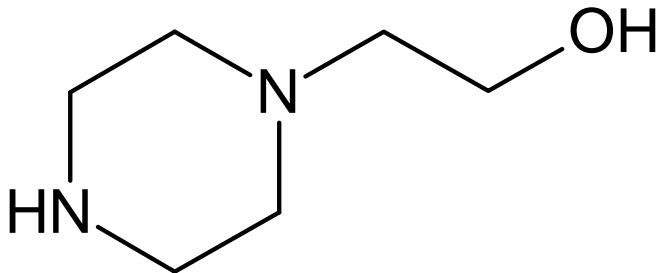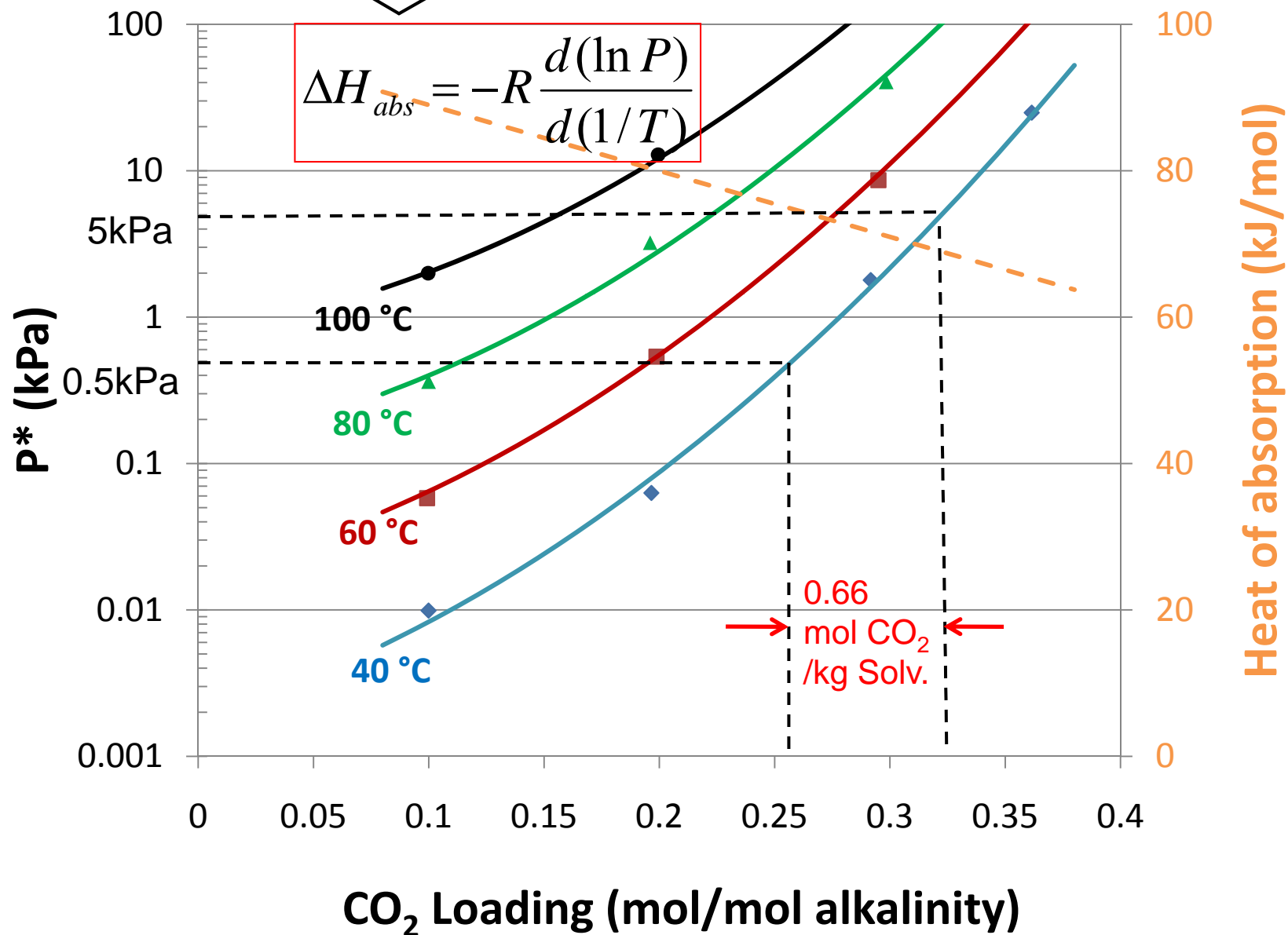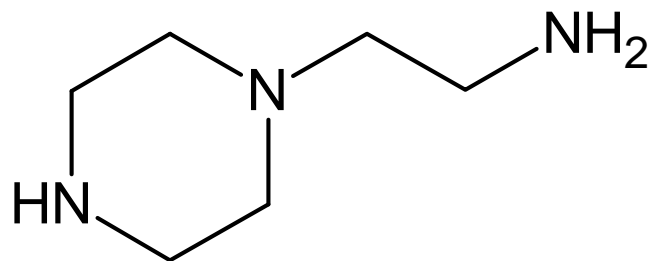
HINDERED AMINE
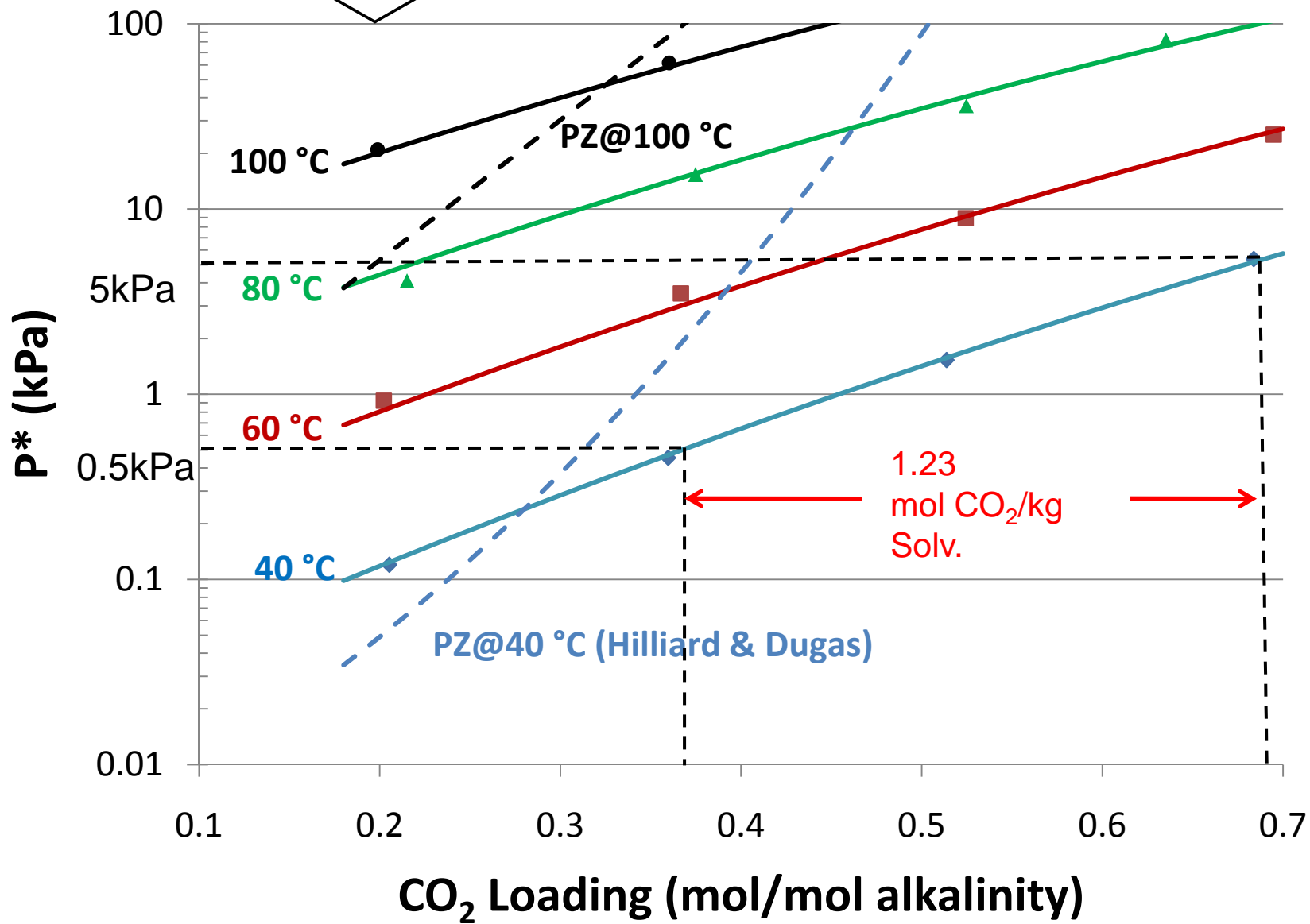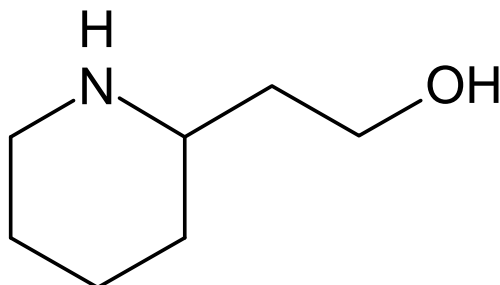
PRIMARY AMINE
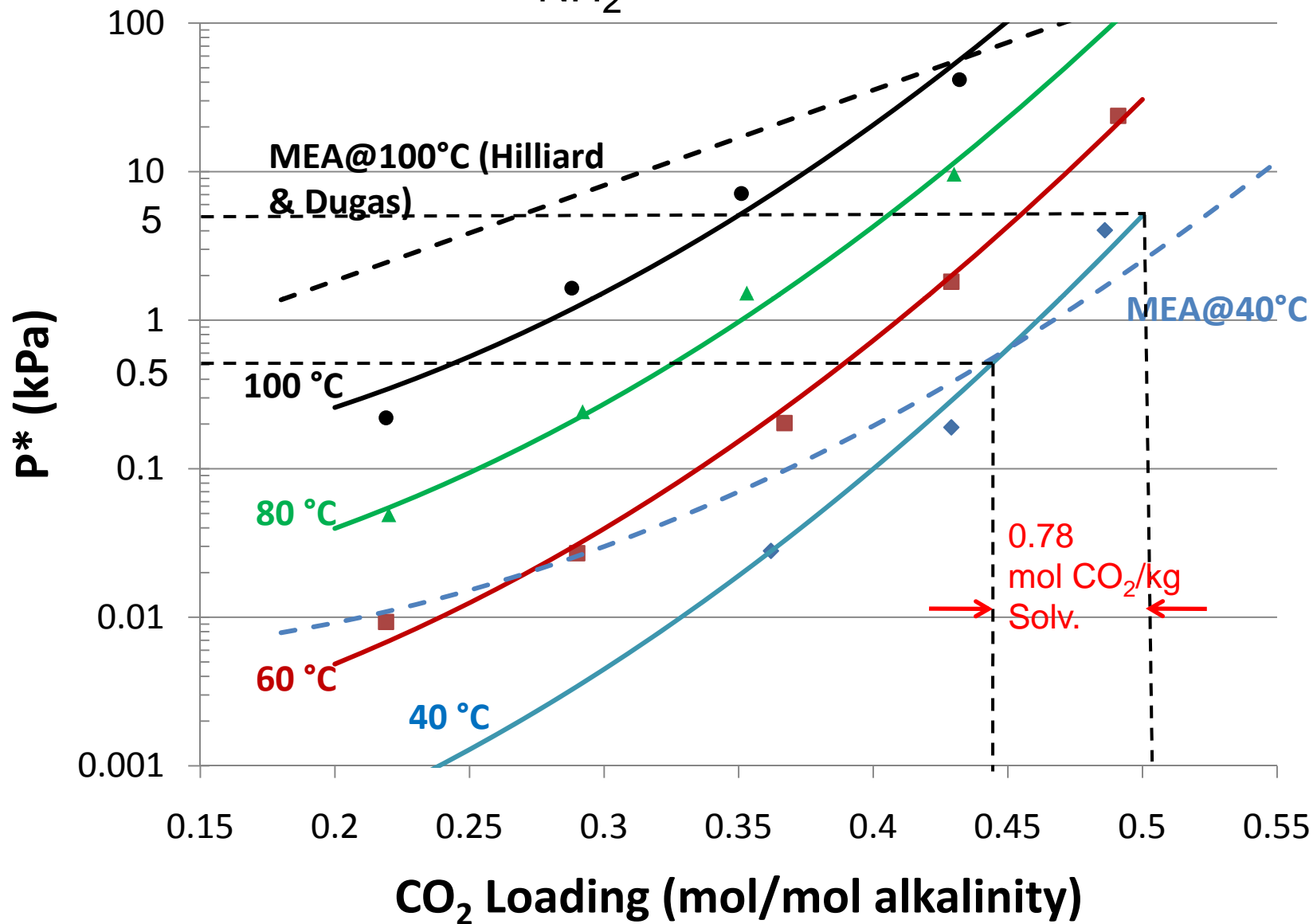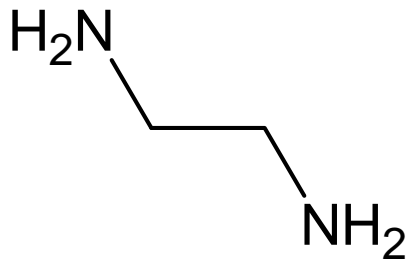
PROMOTED TERTIARY AMINE

7m MDEA/2m PZ
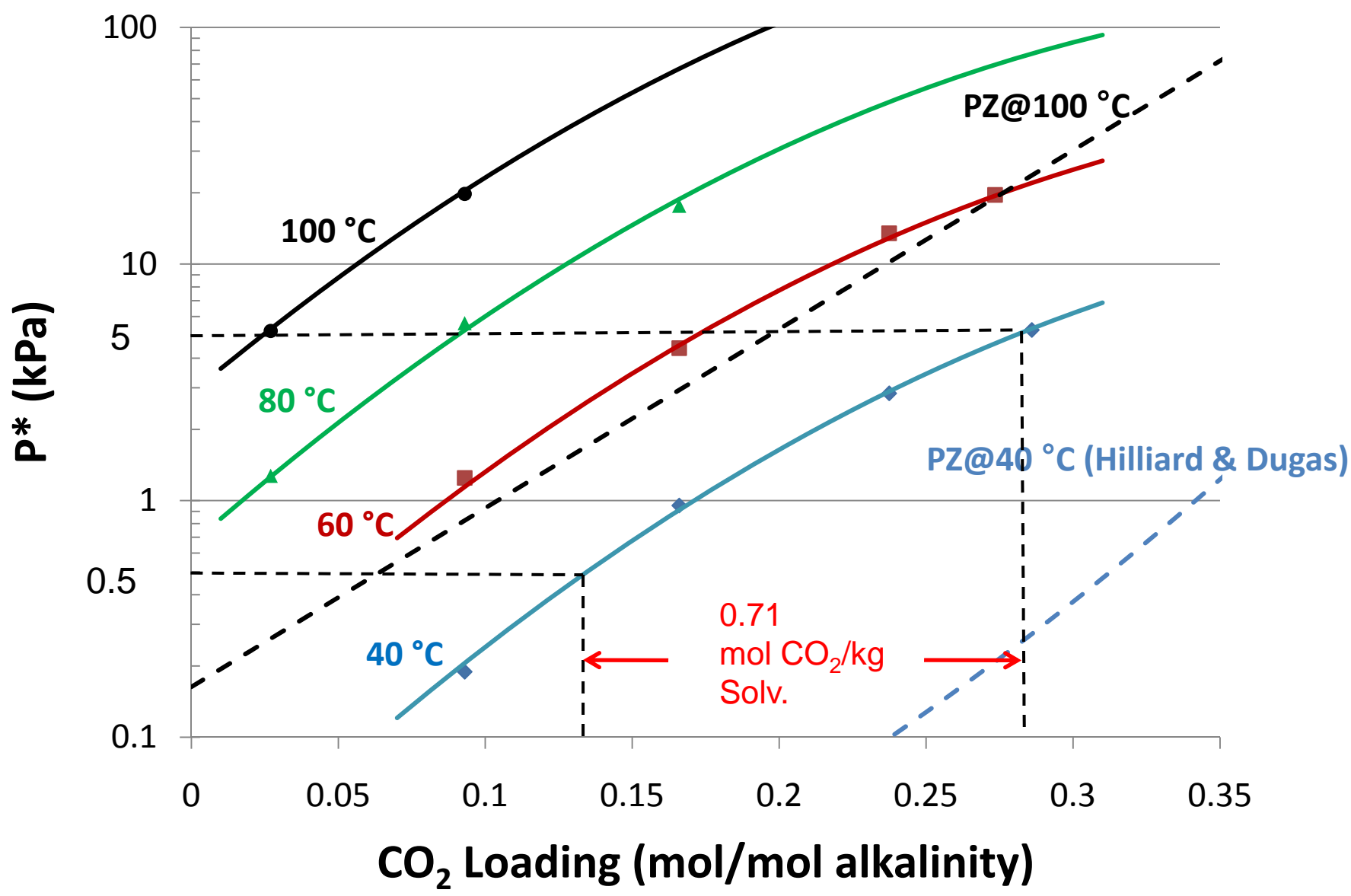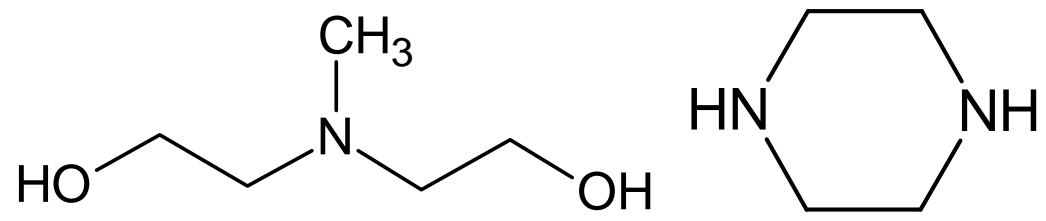
CO₂ Capacity for 5kPa Rich Solution

Enthalpy of CO_2 Absorption

$$k_g' \approx \frac{\sqrt{k_2[Am]D_{CO2}}}{H_{CO2}}$$

k_g' (mol/s·Pa·m²)

40°C
60°C
80°C
100°C

P*$_{CO2}$ @ 40C (kPa)

Filled Points – 2, 5, 8, 12 m PZ

Empty Points – 7, 9, 11, 13 m MEA

(by Ross Dugas)
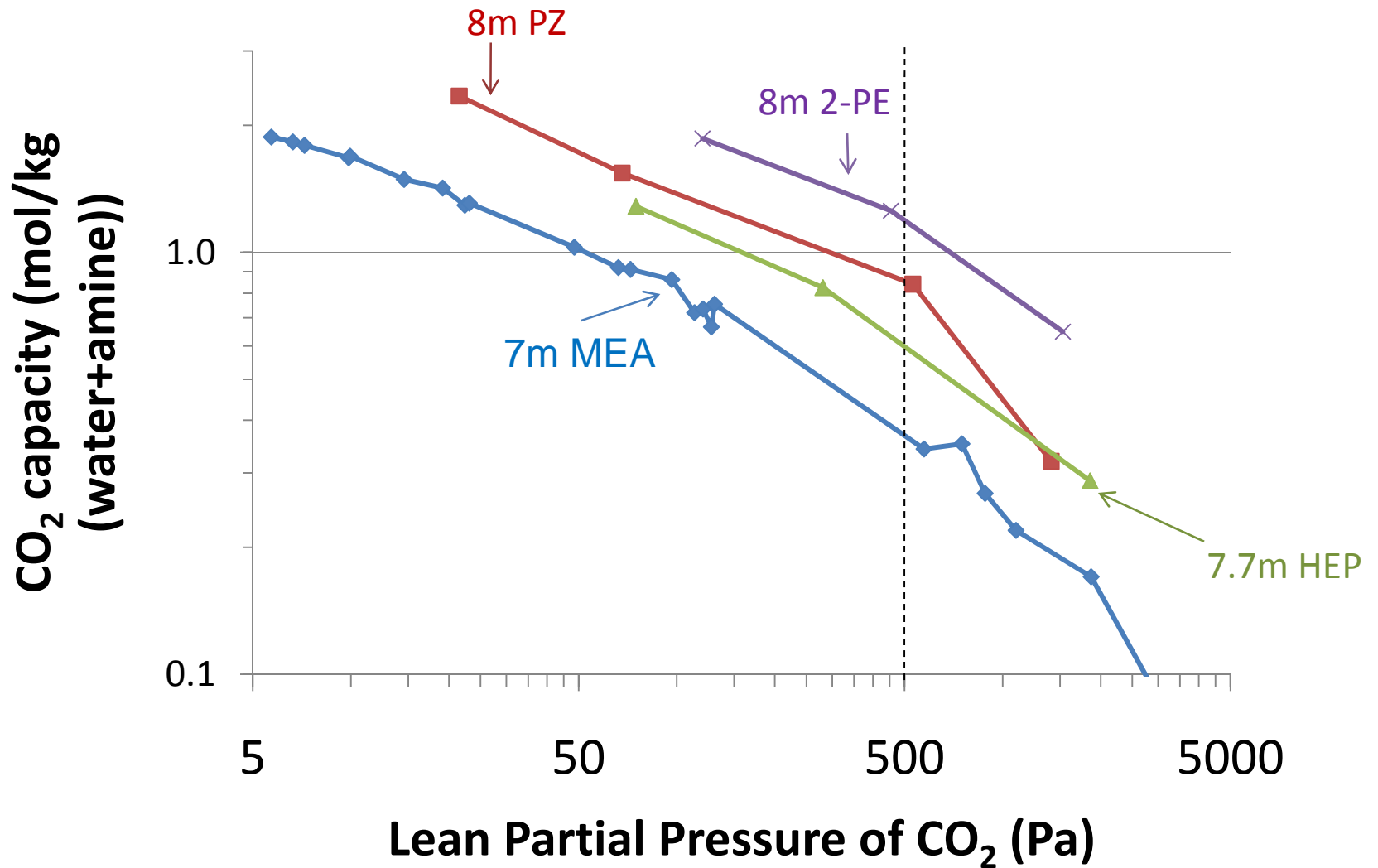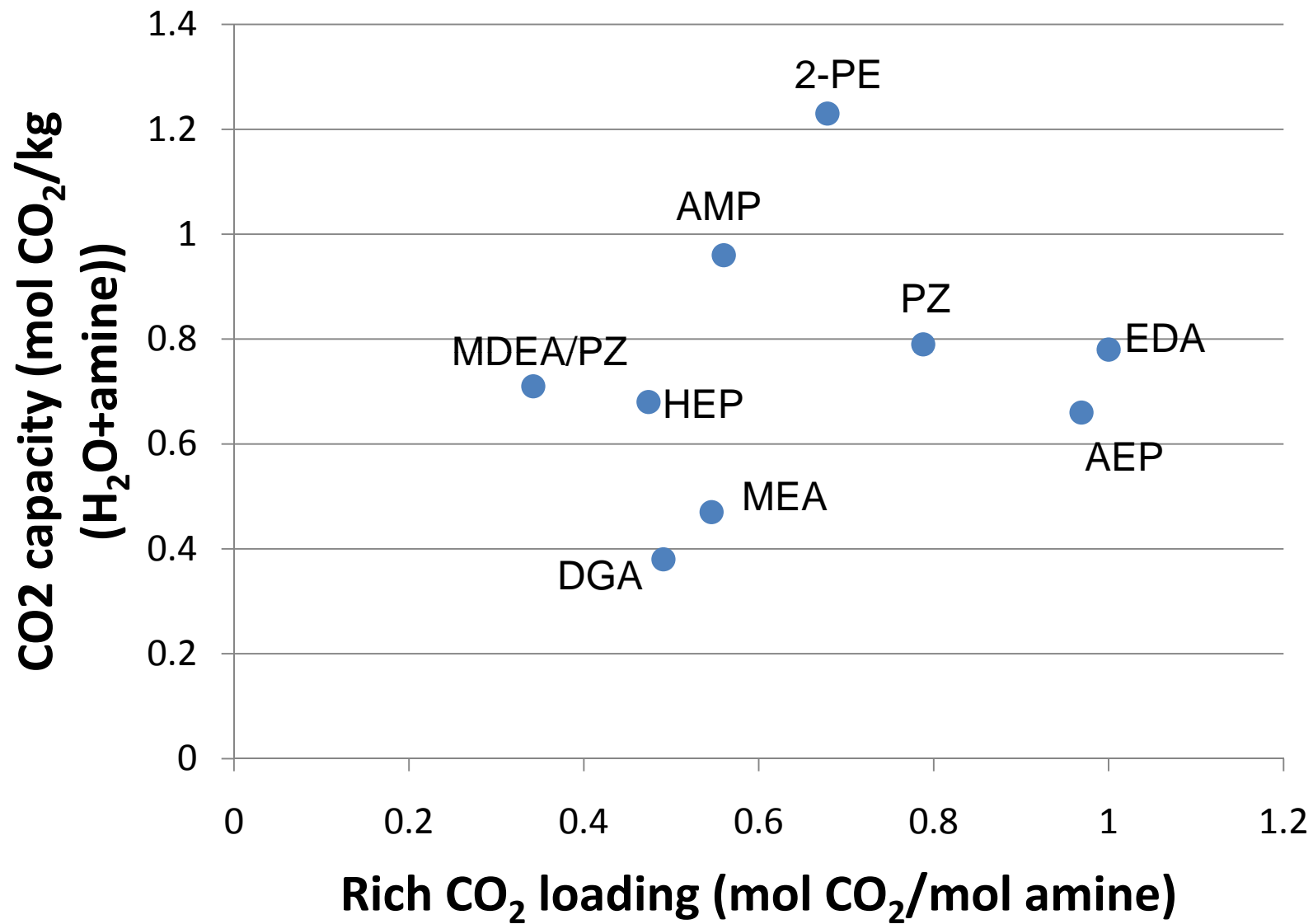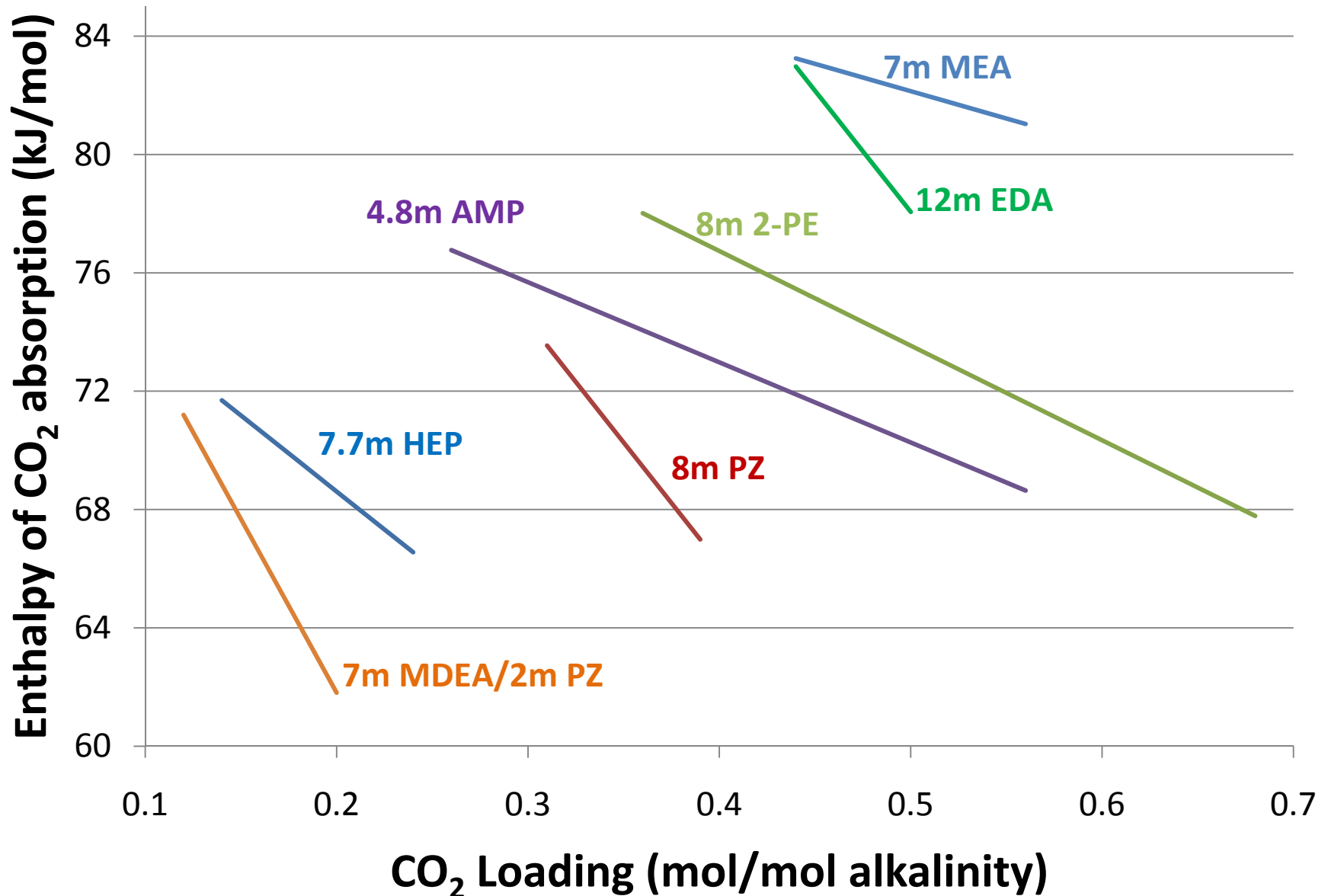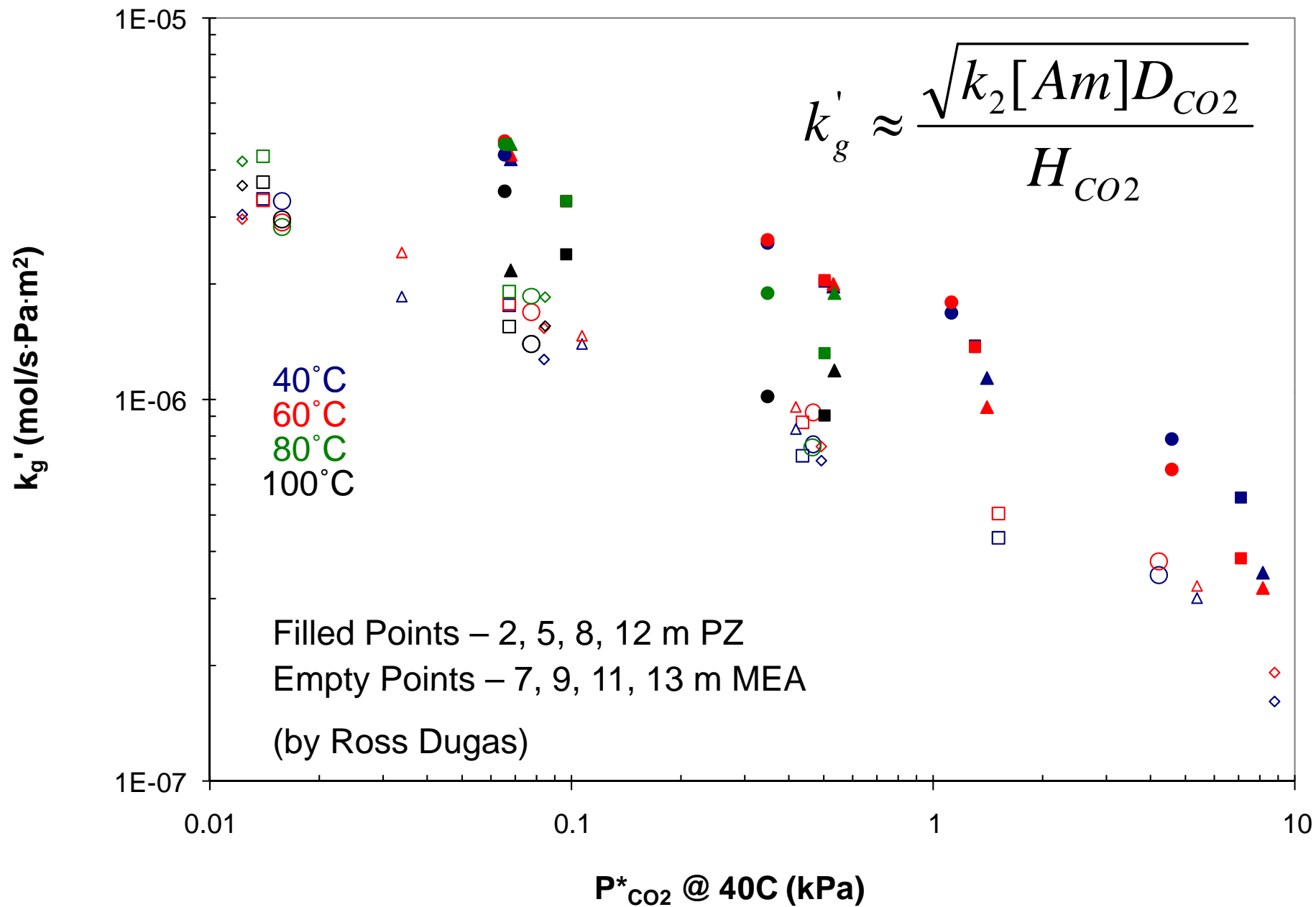
Absorption/Desorption rates for 7.7m HEP

$$k_g^{'} = \frac{N_{CO_2}}{P_{CO_2,i} - P_{CO_2,b}}$$

8 m PZ@40°C

7 m MEA@40°C

HEP@100°C

HEP@80°C

OH

HEP@40°C

HEP@60°C

HN

$k_g^{'}$ (mol/s·Pa·m²)

P*$_{CO2}$ @ 40C (kPa)

5E-06

5E-07

5E-08

0.01

0.1

1

10

8m 2-PE

12m EDA

k_g' (mol/s·Pa·m²) vs. $P^*_{CO_2}$ @ 40C (kPa)

8 m PZ@40°C

7 m MEA@40°C

80°C

100°C

40°C

60°C

H_2N

NH_2
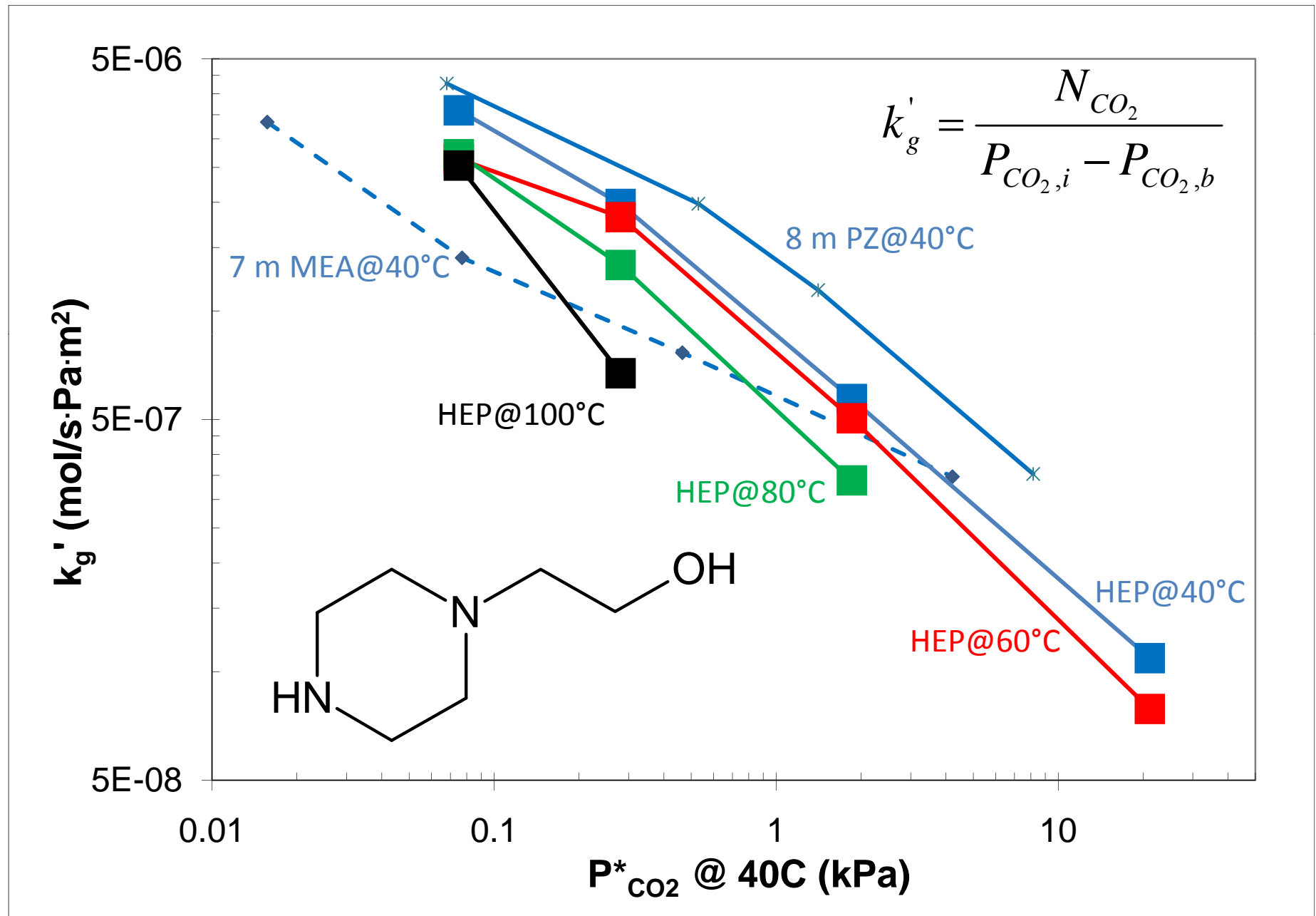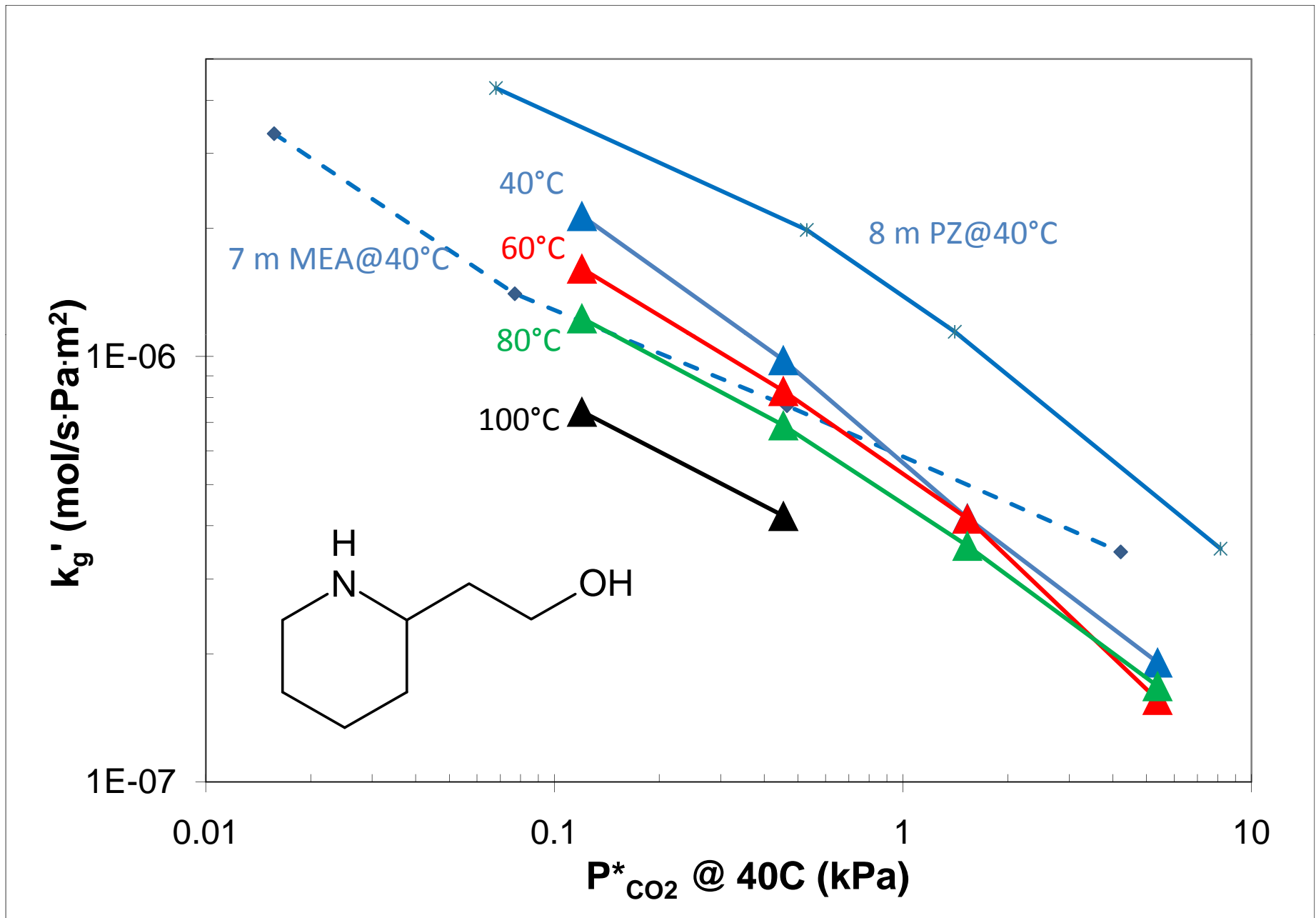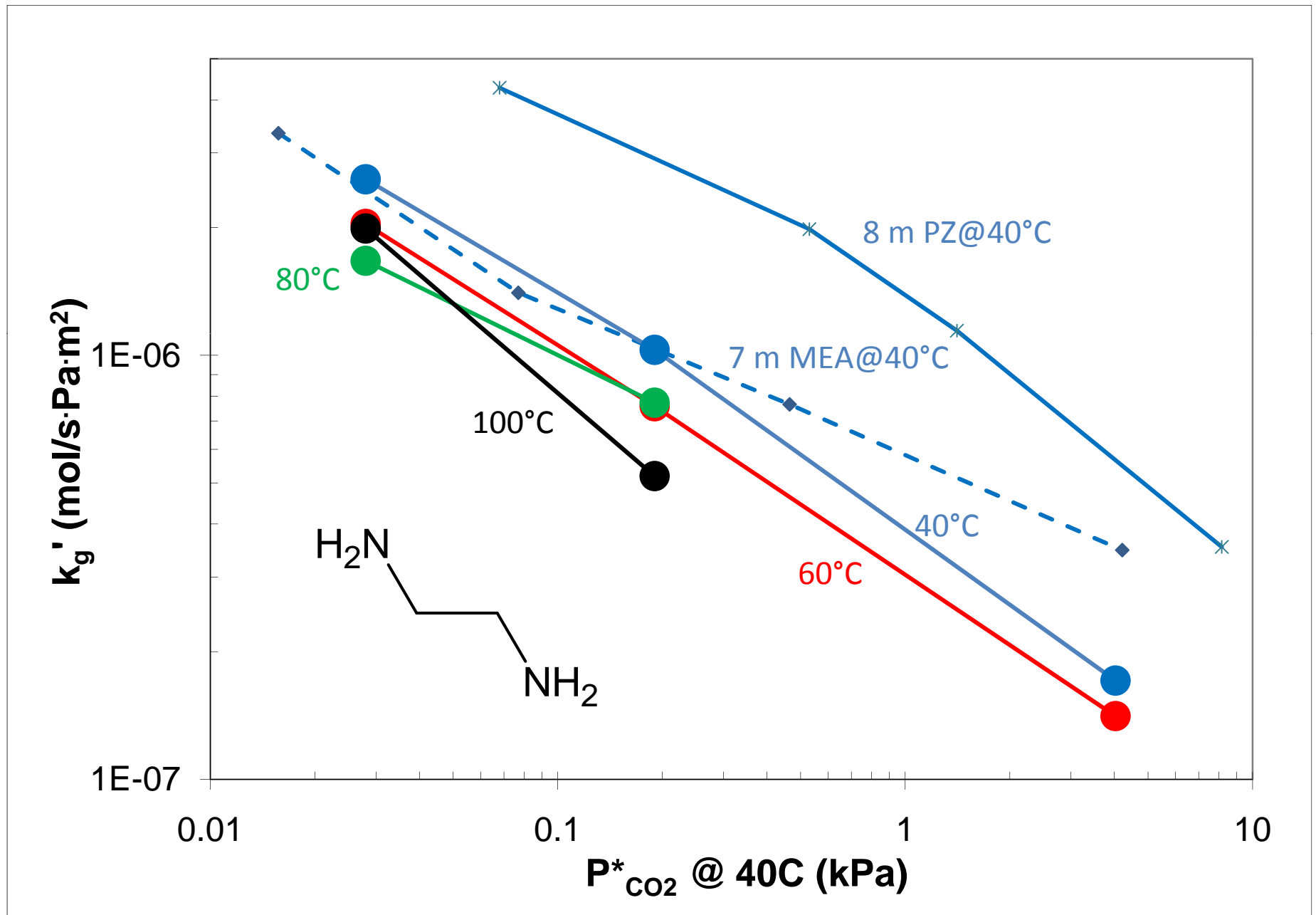
7m MDEA/2m PZ
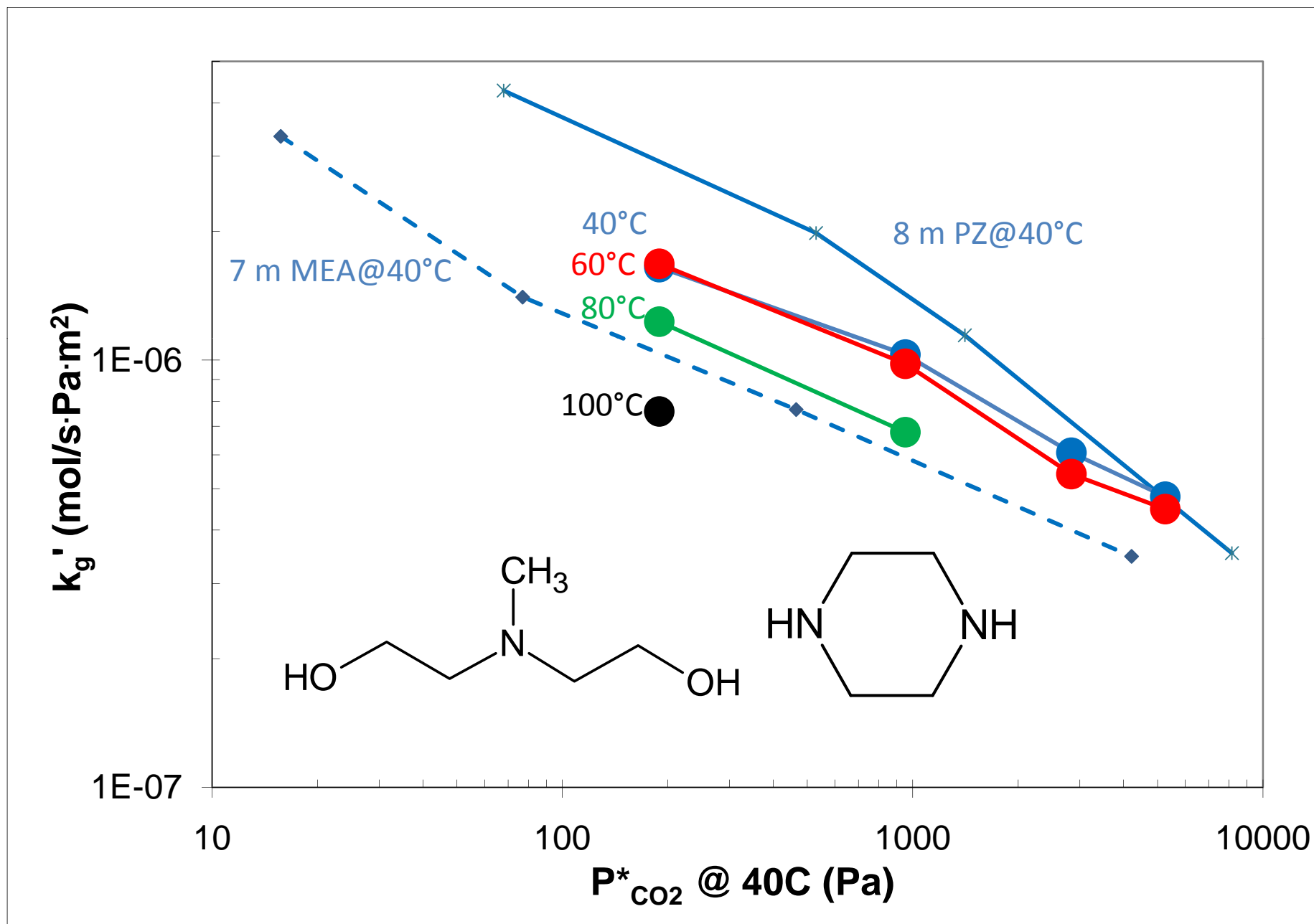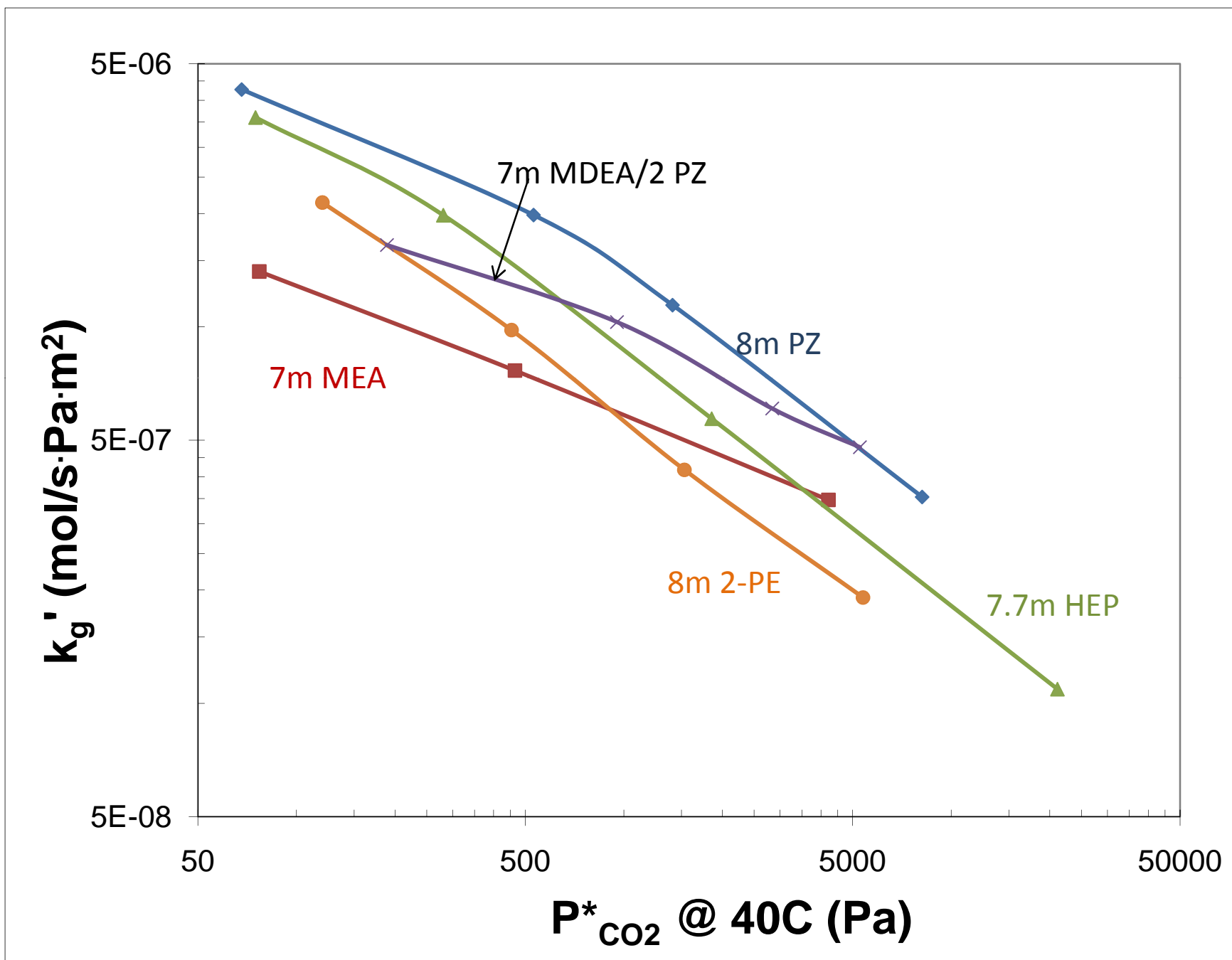
Apparent second order reaction rate of amine with CO_2

Amine	k_2 (m³/mol·s)	Source
PZ	54	(Bishnoi and Rochelle 2000)
AEP	30	(Bishnoi 2000)
HEP	12	(Bishnoi 2000)
EDA	8.8	(Sada et al. 1977)
MEA	5.9	(Blauwhoff et al. 1984)
DGA	5.1	(Pacheco 1998)
AMP	0.7	(Saha and Bandyopadhyay 1995)
2-PE	0.6	(Xu et al. 1993)
MDEA	0.005	(Versteeg and Van Swaaij 1988)
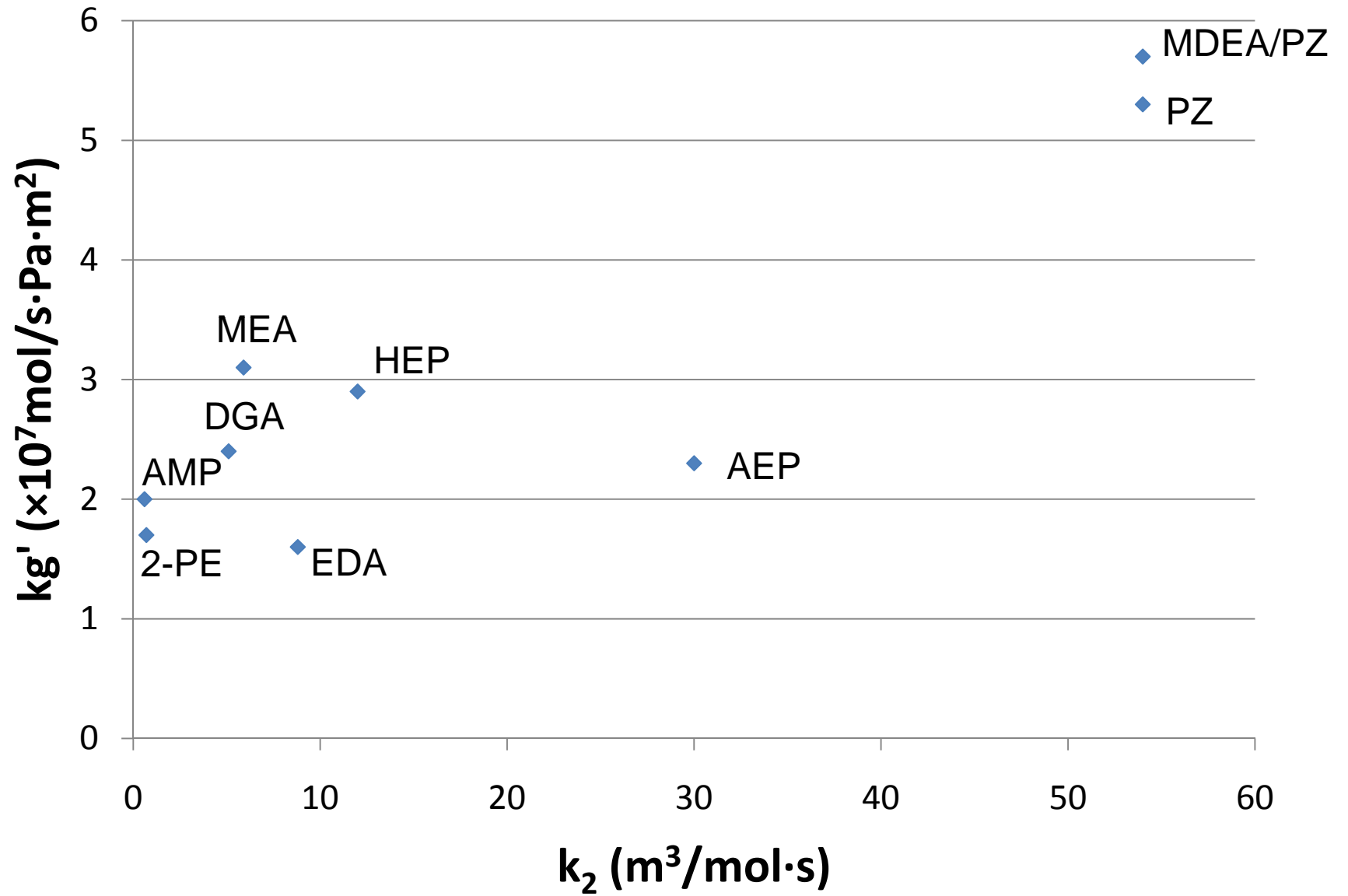
Conclusions

Fast solvents

Amine	Conc (m)	CO_2 Capacity@ $P_{CO2.lean}$=0.5kPa (mol/kg (water+amine))	k_g' @P_{CO2} =5kPa ($\times 10^7$mol/s·Pa ·m^2)	ΔH_{abs}@P_{CO2} =1.5kPa (kJ/mol)
MDEA/PZ	7/2	0.71	5.7	67
PZ	8	0.79	5.3	70
MEA	7	0.47	3.1	82
MEA	11	0.52	2.5	84

Slow solvents

Amine	Conc. (m)	CO$_2$ Capacity@ $P_{CO2,lean}$=0.5kPa (mol/kg (water+amine))	k_g' @P_{CO2} =5kPa ($\times 10^7$mol/s·Pa·m^2)	ΔH_{abs}@P_{CO2} =1.5kPa (kJ/mol)
MEA	7	0.47	3.1	82
HEP	7.7	0.68	2.9	69
DGA®	10	0.38	2.4	81
AEP	6	0.66	2.3	72
2-PE	8	1.23	2	73
AMP	4.8	0.96	1.7	73
EDA	12	0.78	1.6	80

Acknowledgement

- Luminant Carbon Management Program
- Industrial Associates Program for CO_2 Capture by Aqueous Absorption

Accurate Screening of Candidate Solvents by the Wetted Wall Column

Questions?

Xi Chen

xi@che.utexas.edu

Amine Selection to Minimize Energy for CO_2 Capture

By

Gary T. Rochelle

Luminant Carbon Management Program

Department of Chemical Engineering

The University of Texas at Austin

The Message

- Flowsheet & Reversibility – Thermal Swing

1. Greater Capacity & Reduced Exchanger ΔT
    - minimizes loss of sensible heat

2. Greater Lean Loading
    - Avoids Irreversibility of Overstripping

3. Greater ΔH_{abs} & Stripper T
    - Provide Thermal Compression

4. Reduced Thermal Degradation
    - Allows Greater Stripper T

5. Faster CO_2 Rates
    - Smaller driving forces

- Summary evaluation of 12 Solvents
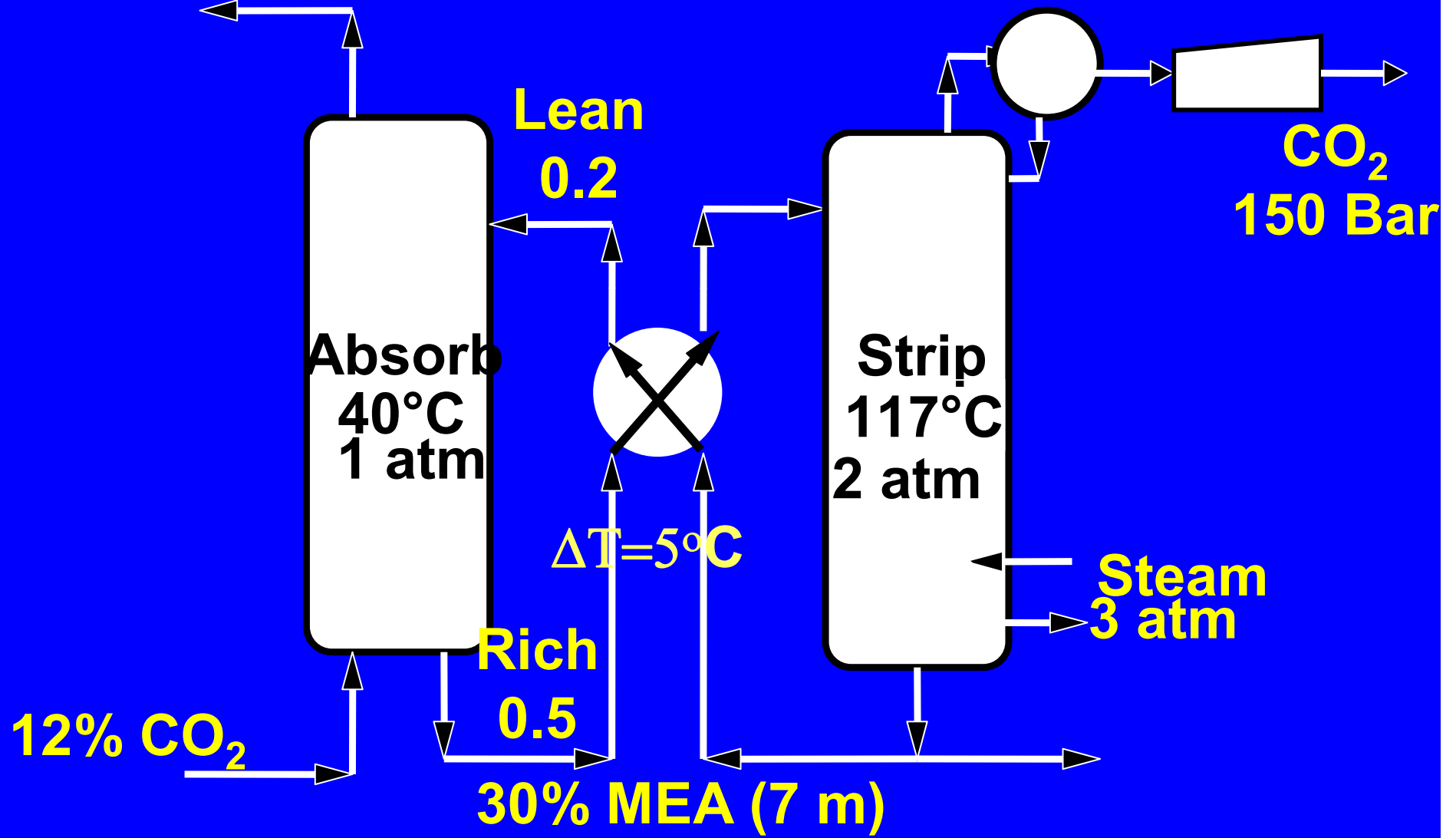
Minimum Work of Separation
Energy for separation & compression to 10 MPa
Does not include fan & pump Work

Separation Method			Total W_{eq}
			kJ/gmol CO_2
Ideal Sep., (40°C,100 kPa) Isothermal Comp.			18 (12%)
Baseline (7m MEA, 10°C, 160 kPa)			35 (23%)
Matrix (MDEA/PZ)			26 (17%)
Typical Power Plant output			150
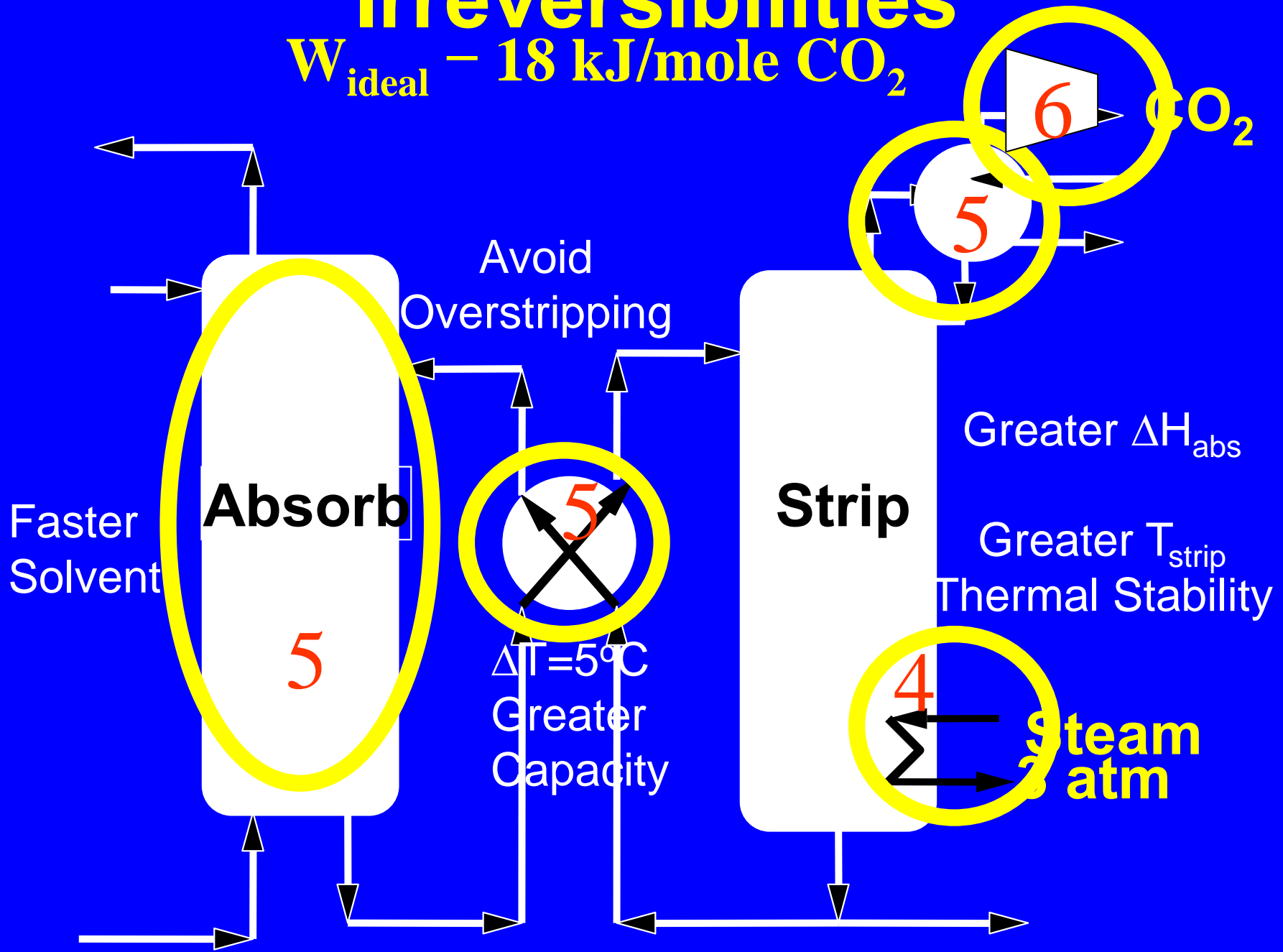
Greater Solvent Capacity & Reduced Exchanger ΔT Reduce Equivalent Work

$$Q_{sens} = \frac{C_p \left(T_{S,Bot} - T_{S,Feed} \right)}{Capacity} = \frac{3.2 \frac{kJ}{kg-K} (10K)}{1 \frac{mole\ CO_2}{kg\ solv}} = 32 \frac{kJ}{mole\ CO_2}$$

$$W_{eq} = 0.75\, Q_{sens} \frac{T_{reboiler} + 10 - 313}{T_{reboiler} + 10}$$

$$= 5 \frac{kJ}{mole\ CO_2}$$

Effect of capacity on energy requirement
(90% removal, P_{reb} = 160 kPa, ΔT = 5°C, P_{final} = 330 kPa)

	5m K$^+$/ 2.5m PZ	MDEA/PZ
ΔH_{abs} (kJ/gmol)	63	62
Capacity (mol CO_2/kg H_2O)	0.93	1.77
	Equivalent W (kJ/gmol CO_2)	
Modified baseline	22.6	17.2
Matrix	21.7	15.1

Oyenekan, 2007

CO$_2$ Solubility for 8m 2-PE

Measured in Wetted Wall Column

Capacity = 1.23 moles/kg PE + H$_2$O

ΔH_{abs} = 73 kJ/mole CO2

P* (kPa) vs CO$_2$ Loading (mol/mol alkalinity)

100 °C · 80 °C · 60 °C · 40 °C
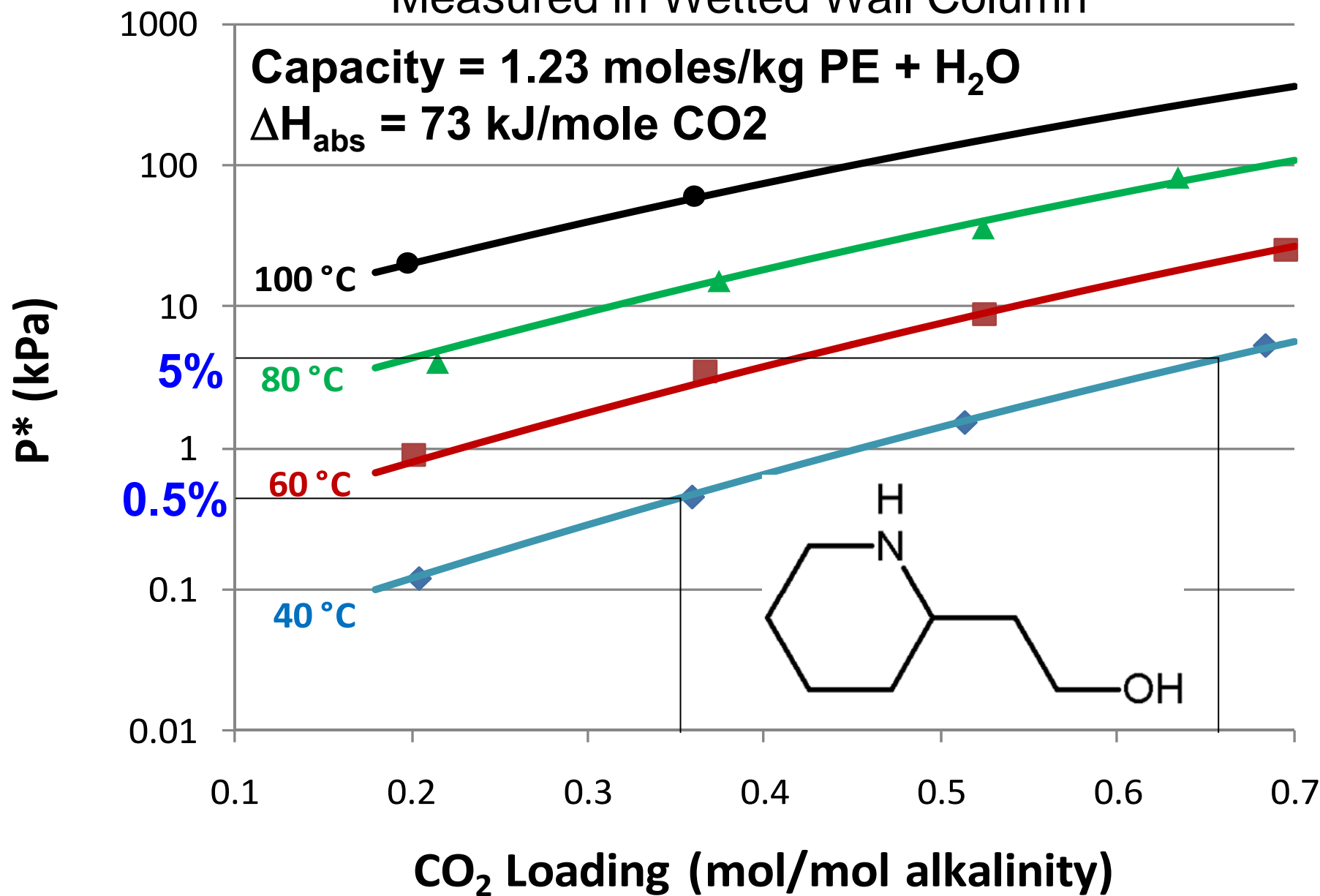
Overstripping does not reduce W
Even though it increases capacity

- With a small exchanger ΔT
- With a reversible stripper configuration
- Work/Exergy lost by excess driving force

$$W_{loss} = RT \ln\left(\frac{P_{CO_2}}{P^*_{CO_2}}\right)$$

	$P^*_{CO2,lean}$ (bar)	W_{loss} (kJ/mole CO_2)
Optimum	0.005	2.2
Overstrip	0.0005	4.6

Optimum Lean Loading with 5°C Approach
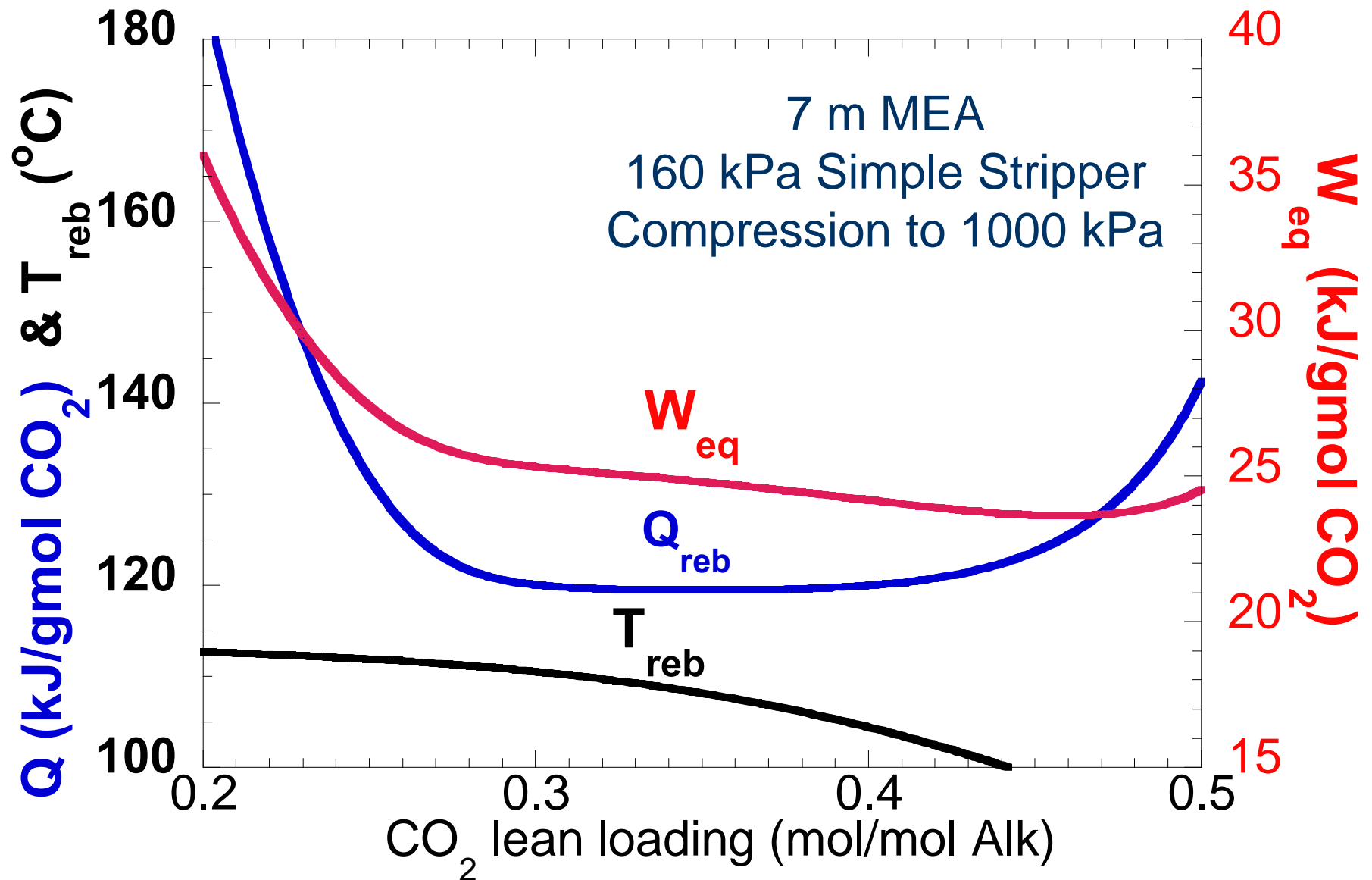
Greater Heat of CO_2 absorption and Greater Stripper T Reduce Equivalent Work

- Thermal Compression increases Stripper P at greater ΔH_{abs} &T_{strip}

$$\ln \frac{P^*_{CO_2,strip}}{P^*_{CO_2,abs}} = \frac{-\Delta H_{abs}}{R}\left[\frac{1}{T_{abs}} - \frac{1}{T_{strip}}\right]$$

- Thermal Compression reduces heat for water vapor at greater ΔH_{abs} &T_{strip}

$$\left[\frac{P_{H2O}}{P_{CO_2}}\right]_{STRIP} = \left[\frac{P_{H_2O}}{P_{CO_2}}\right]_{ABS} EXP\left[\frac{-(H_{CO2} - H_{H2O})}{R}\left(\frac{1}{T_{ABS}} - \frac{1}{T_{STRIP}}\right)\right]$$

Greater T_{strip} & ΔH_{CO2} reduce W_{eq}

ΔH_{CO2}=60 kJ/mole

90°C

70

80

150°C

Compression to 100 bar
Single Stage Flash at 90-150C

W_{eq} (kJ/mol CO$_2$)

$(\Delta H_{CO2}-\Delta H_{H20})\Delta(1/T)$ (kJ/gmol-K)
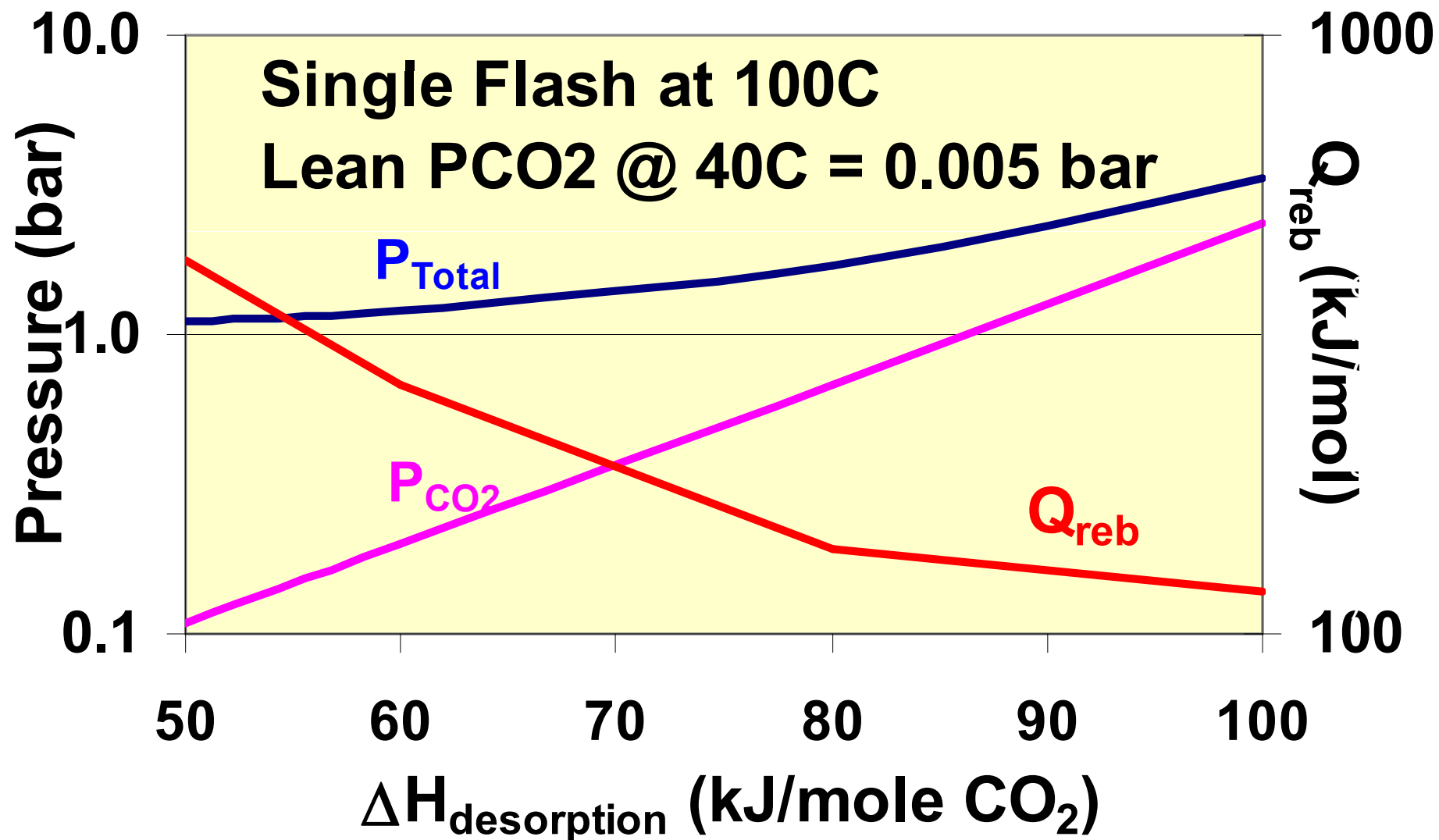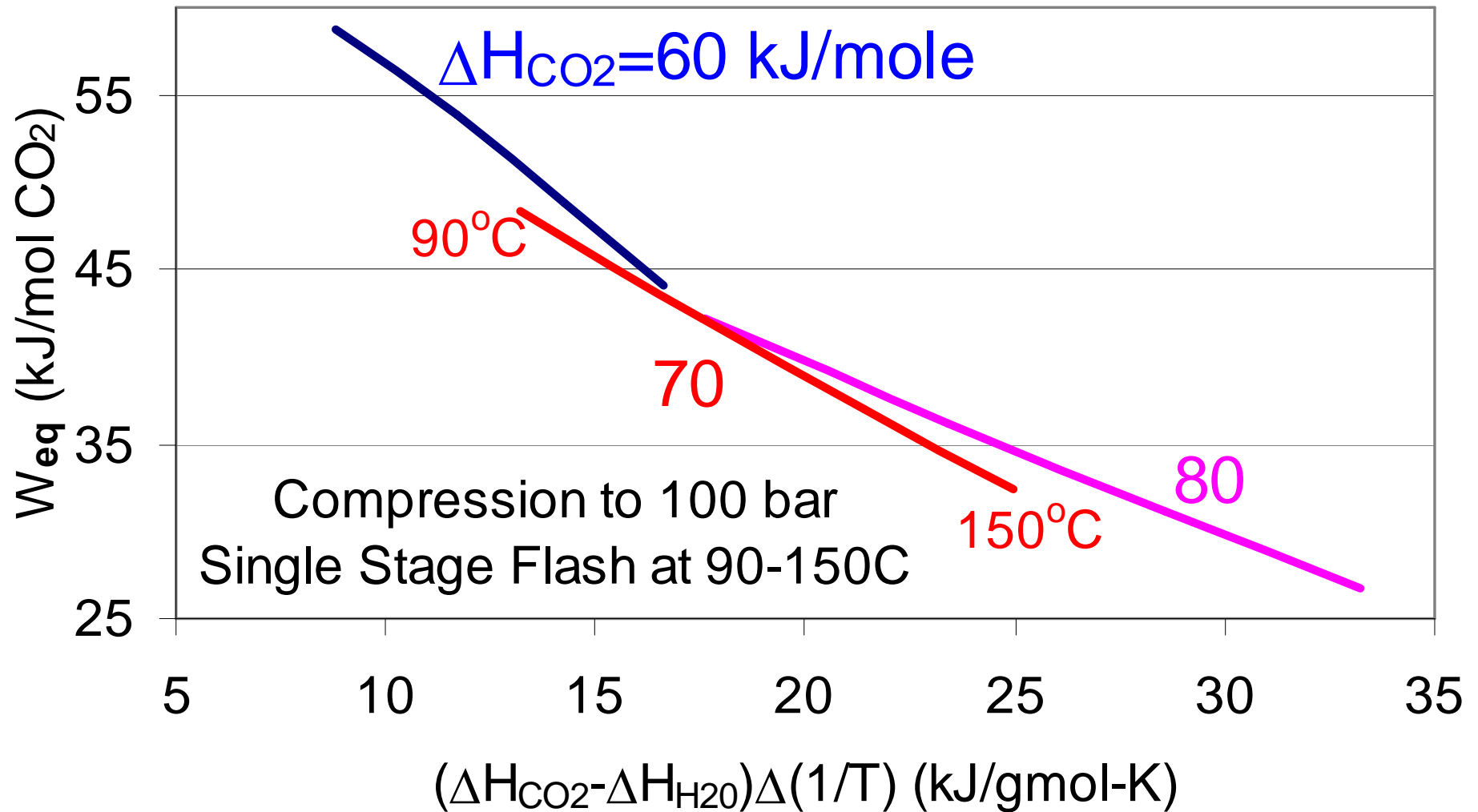
Total Equivalent Work for Generic Solvents
(Rich P_{CO_2}* = 2.5 kPa at 40°C, ΔT = 10°C)
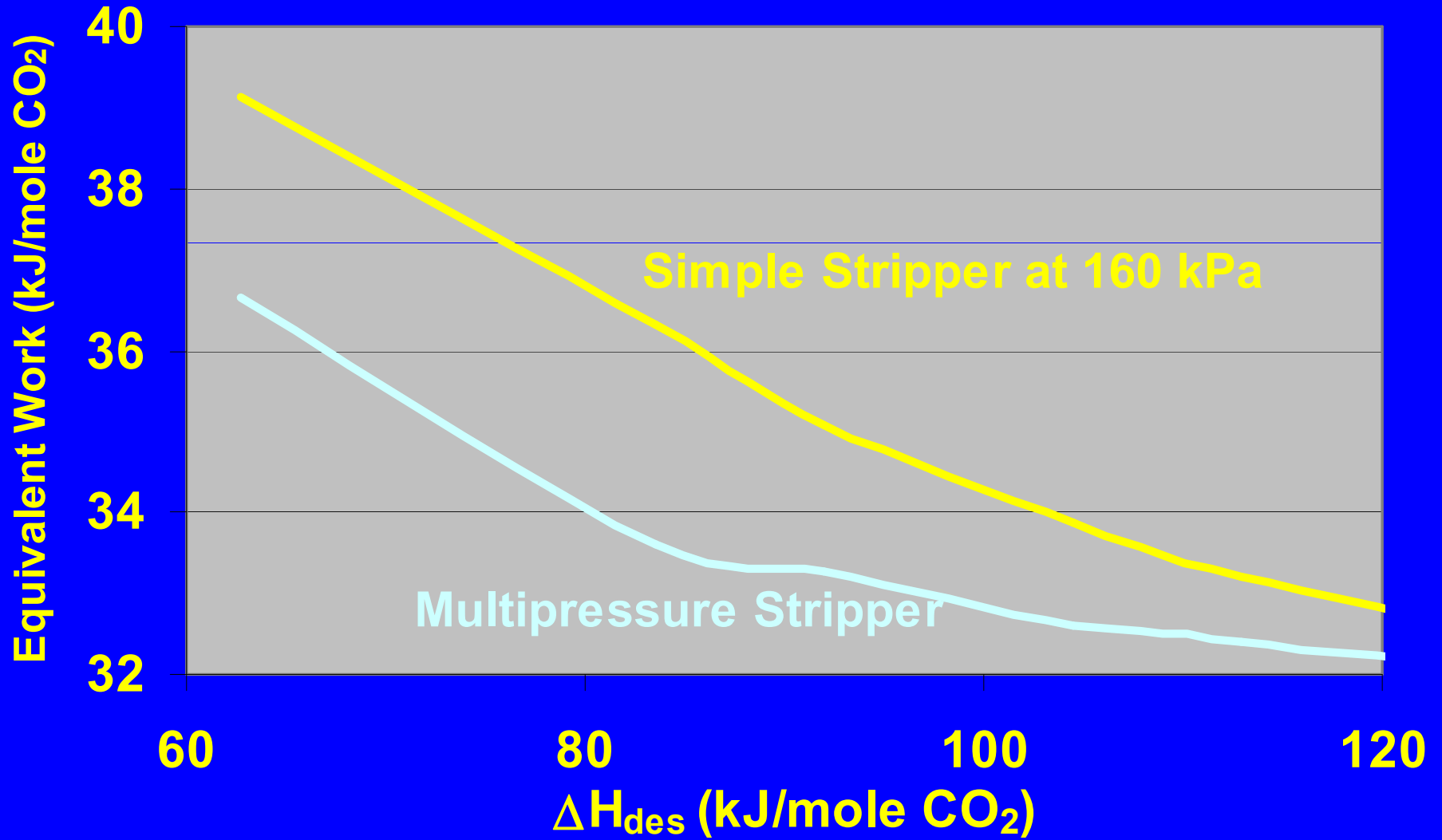
Thermal Degradation at Rich Loading

E_a=133 kJ/mol

Amine Loss (%/week)

7 m MEA

8 m PZ

10 m PZ

T (^{o}C)

CO₂ solubility in Aqueous PZ

Compressed CO_2

Multistage compressor

Water for reflux

Preheater

21.5 atm
150°C

15.5 atm
150°C

11.7 atm
150°C

Steam

Steam

Steam

Ldg=0.31
Lean
(to absorber)

Cross
heat exchanger

Rich Ldg = 0.41
(from absorber)
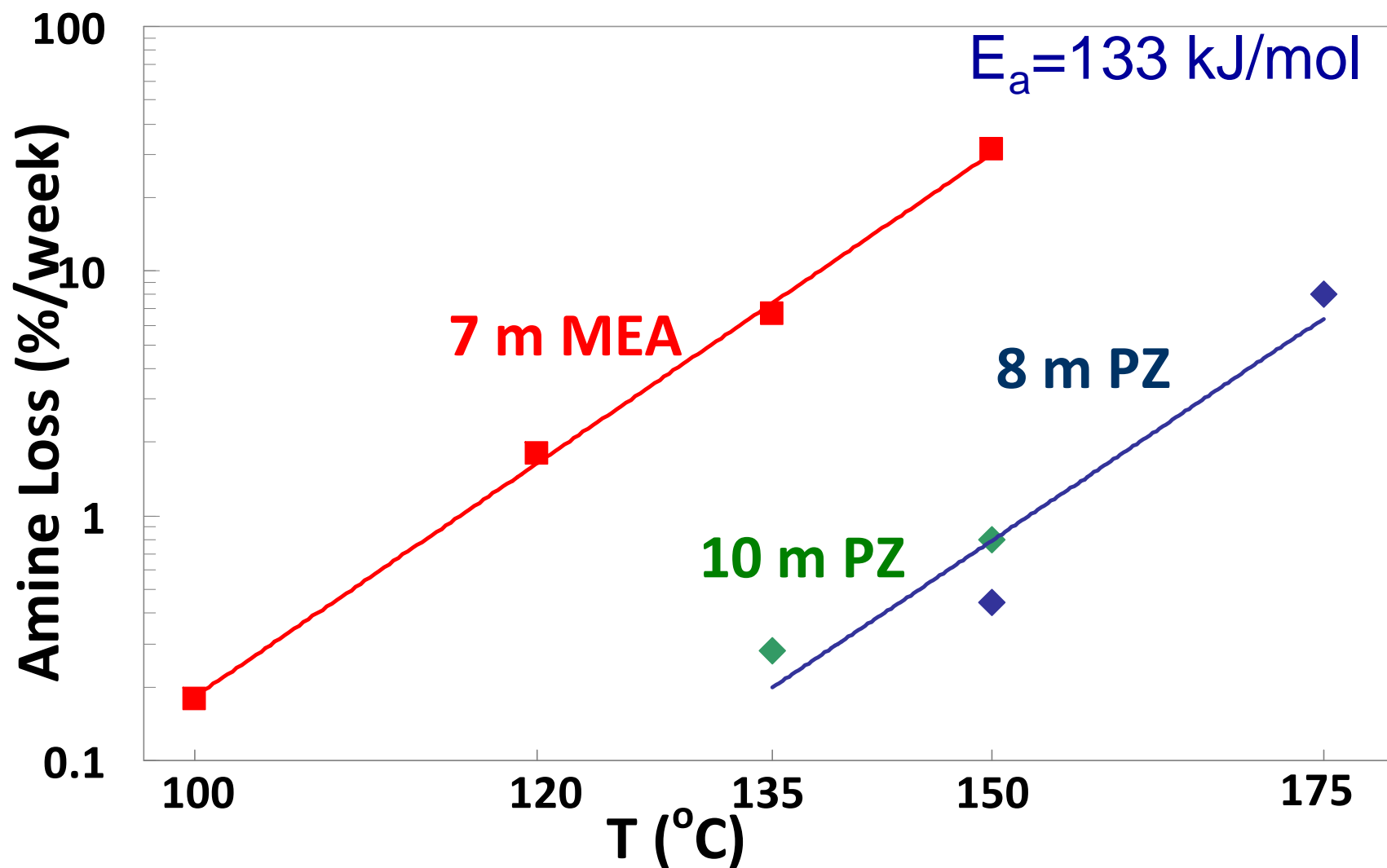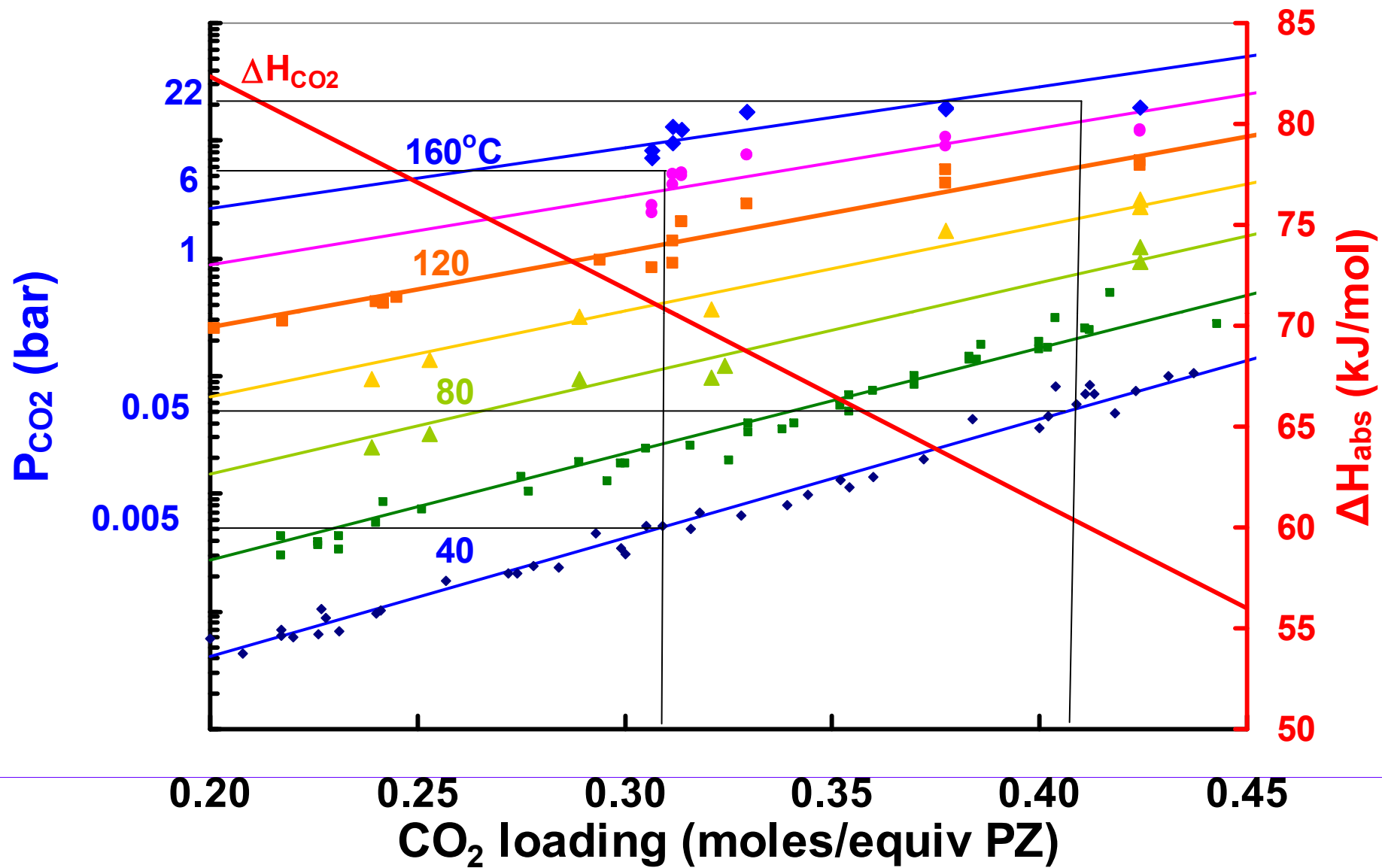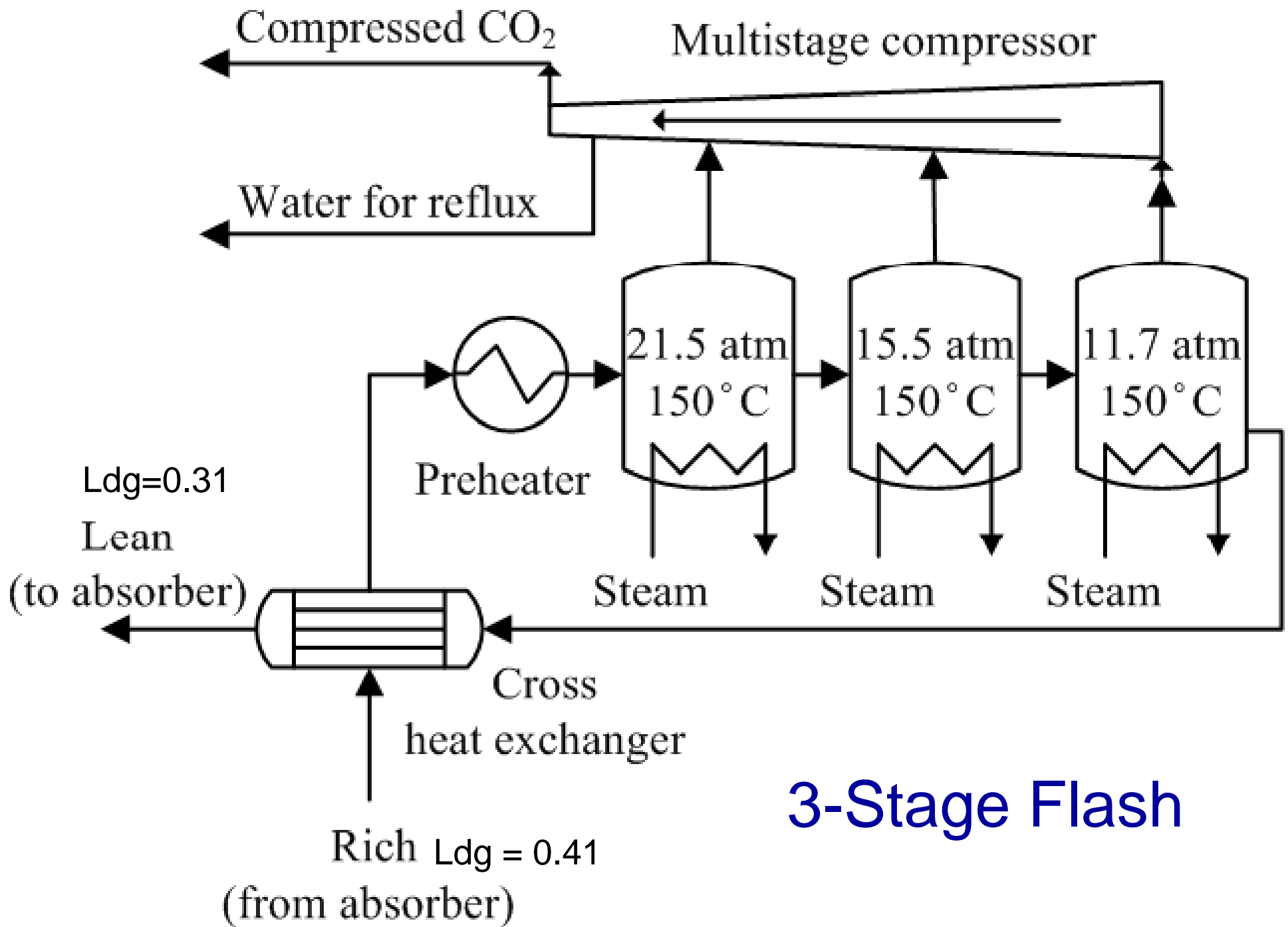
3-Stage Flash

Stripping 8 m PZ
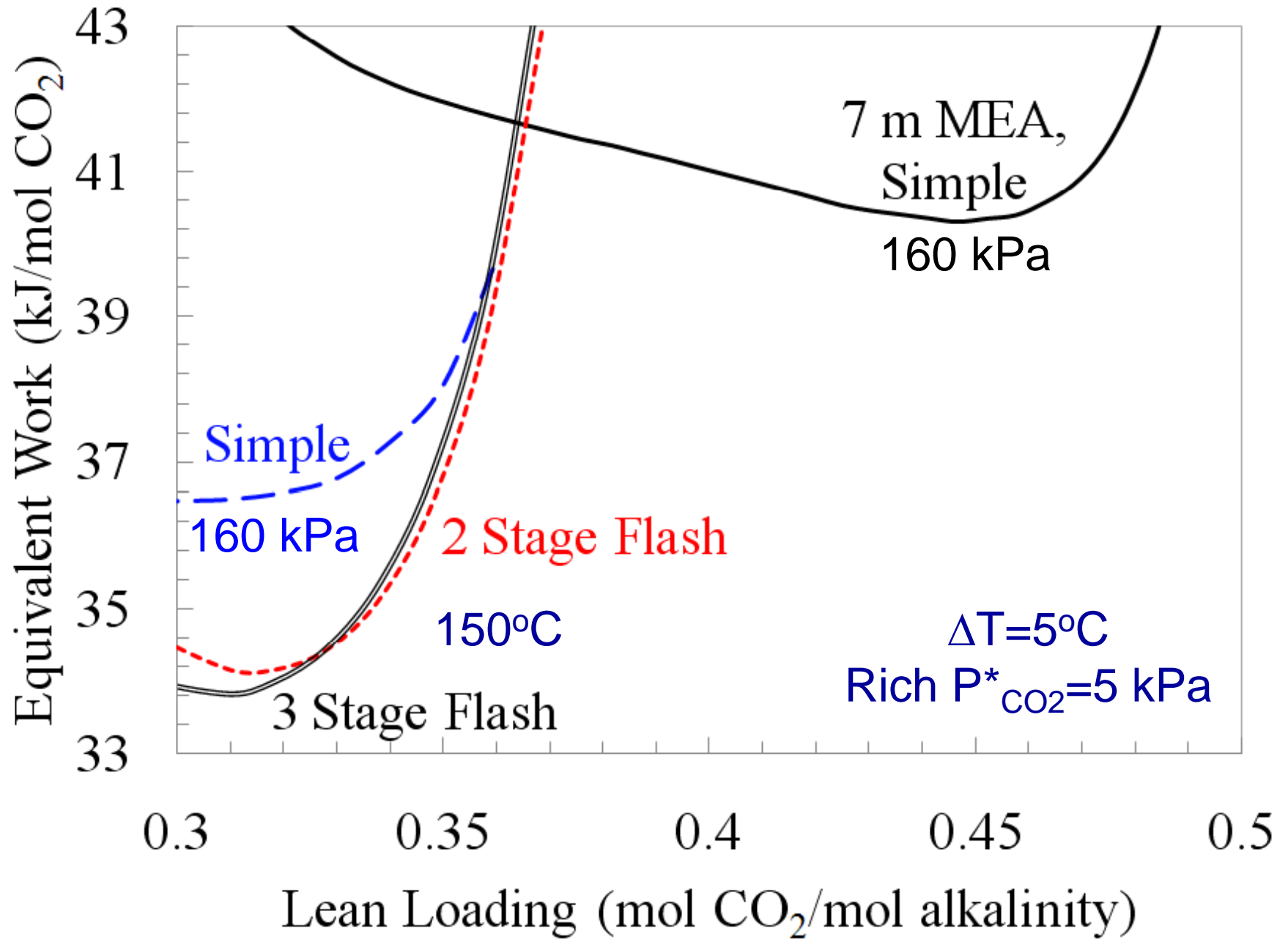
Faster Rates = Greater Reversibility Reduced Driving Force

- Closer to pinch = Greater Rich loading
  - Greater capacity
  - Greater P_{total} & P_{CO2}/P_{H2O} at Rich Stripper
- Closer to pinch = Greater Lean Loading
  - Greater P_{total} & P_{CO2}/P_{H2O} at Lean Stripper
  - Reduced Capacity, $P^*_{CO2,rich}$=0.05 bar

Faster rates increase rich & lean loading and reduce Work
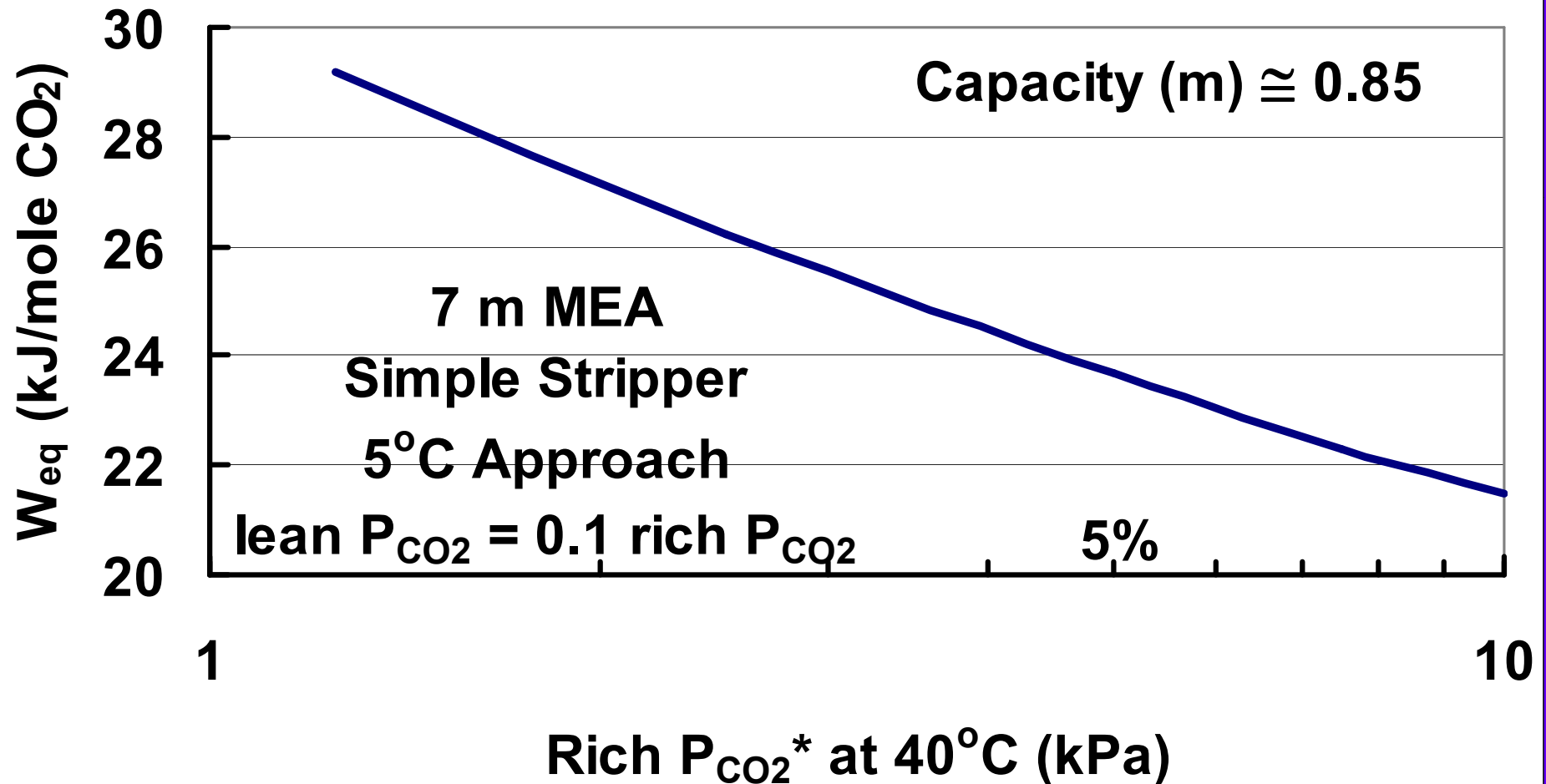
CO$_2$ Absorption Rate, 40°C

Candidate amines

MEA — HO–CH_2CH_2–NH_2

PZ — piperazine (HN, NH)

DGA — H_2N–CH_2CH_2–O–CH_2CH_2–OH

HEP — HN–piperazine–N–CH_2–CH_2OH

MDEA — HO–CH_2CH_2–$N(CH_3)$–CH_2CH_2–OH

AEP — piperazine(N, N)–CH_2CH_2–NH_2

2-PE — piperidine (N–H) with CH_2CH_2OH

AMP — HO–$C(CH_3)(CH_3)$–NH_2 (H_3C, CH_3, NH_2)

EDA — H_2N–CH_2CH_2–NH_2
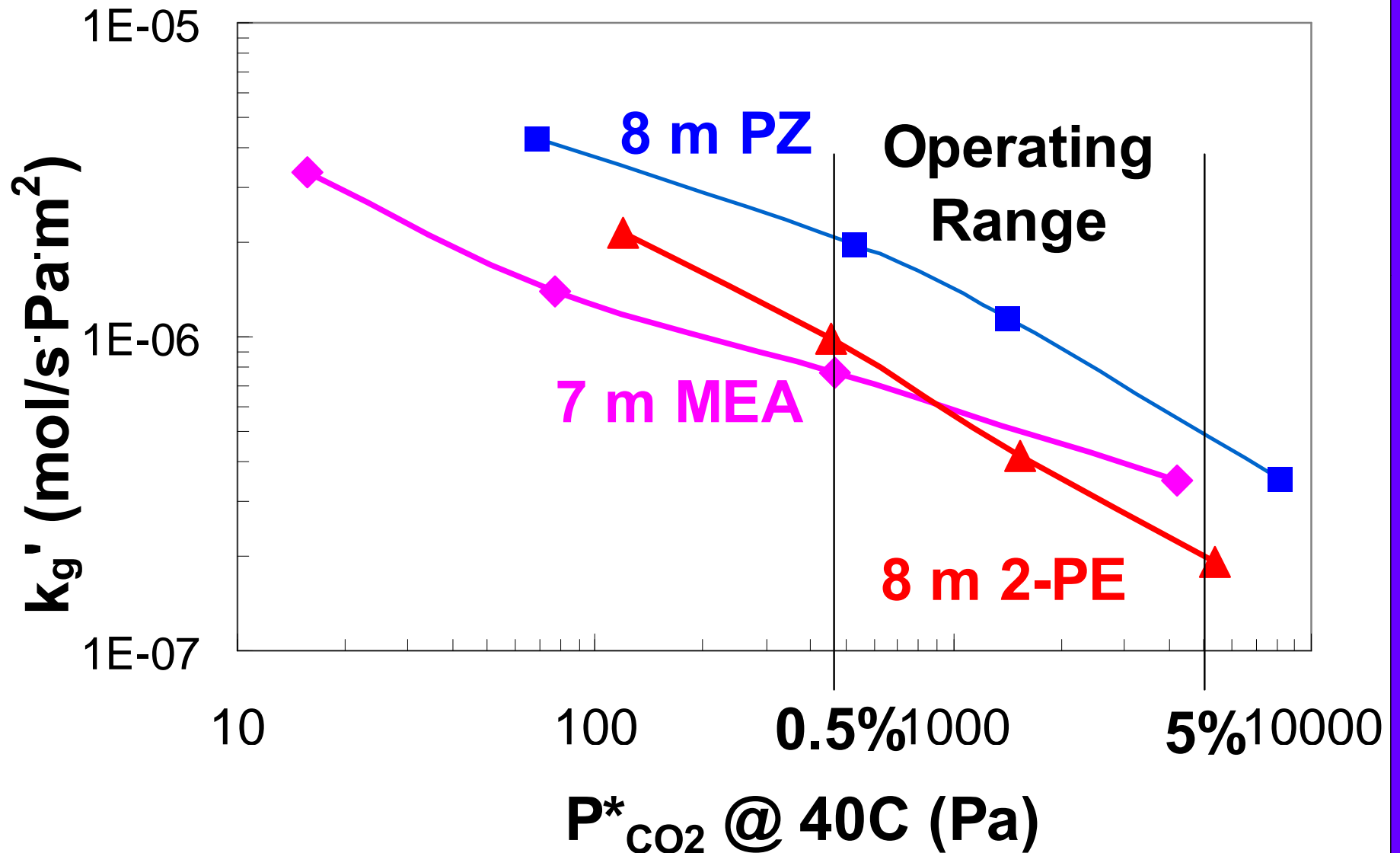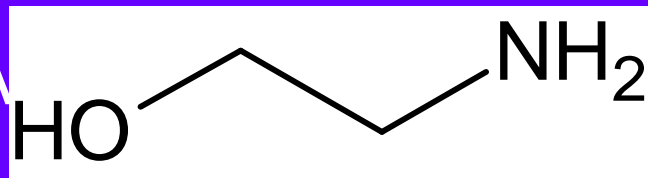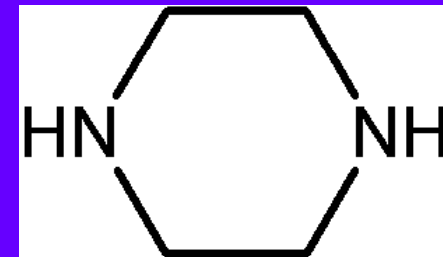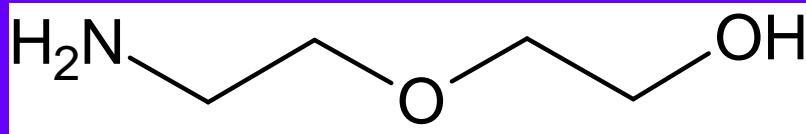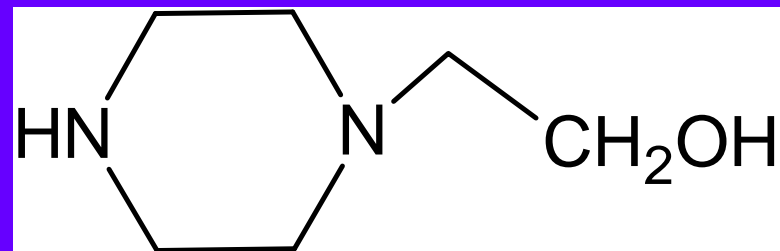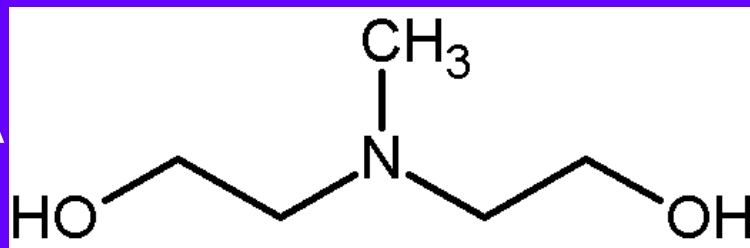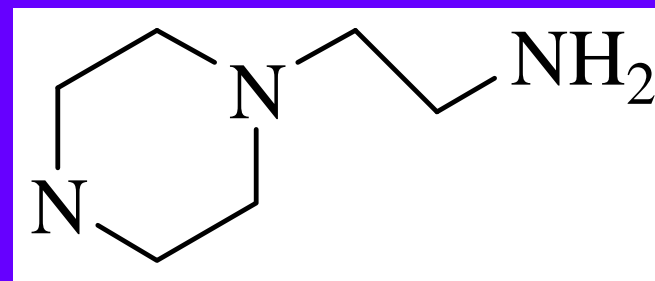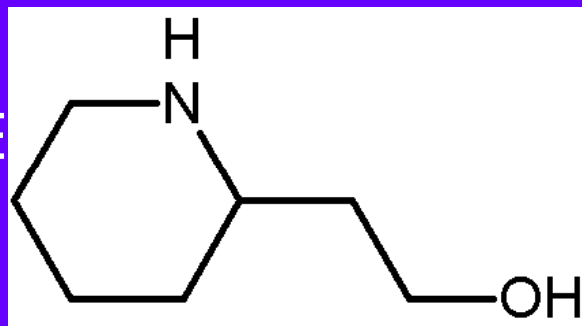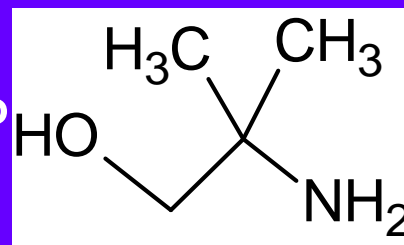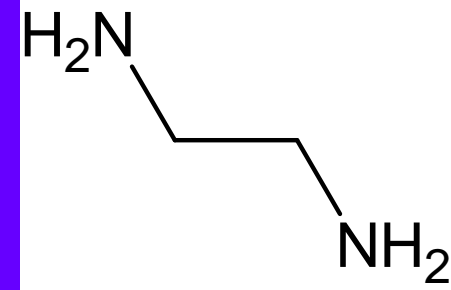
Energy Properties with Faster Solvents

Solvent	kg' x10^{10}	capacity	ΔH_{abs}	Th Deg
m	rich	5/0.5 kPa	2 kPa	135°C
	kmol/m^2.kPa.s	moles/kg	kJ/mole	%/w k
8 PZ	5.3	0.8	75	0.3
7 MDEA/2 PZ	4.5	0.8	68	5.6
5 K+/2.5 PZ	4.0	0.4	60	0.2
7.7 HEP	2.9	0.7	69	3
7 MEA	3.1	0.5	82	9

Energy Properties w Slower Solvents

Solvent	kg' x10^{10}	capacity	ΔH_{abs}	Deg rate
m	kmol/m^2.kPa.s	moles/kg	kJ/mole	%/w k
7 MEA	3.1	0.5	82	9
11 MEA	2.5	0.5	84	9
10 DGA®	2.4	0.4	81	1.8
6 AEP	2.3	0.7	72	9
7 MEA/2 PZ	2.0	0.8	70	7.7
8 2-PE	2.0	1.2	73	
4.8 AMP	1.7	1.0	73	0.8
12 EDA	1.6	0.8	75	11

Conclusions

- **Greater ΔH_{abs} is better**

  MEA>PZ,2PE>MDEA/PZ

  High pKa primary amines provide greater ΔH_{abs}

- **Greater Capacity, w/o overstripping, w small ΔT**

  2-PE > PZ,MDEA/PZ > MEA

  Hindered amines provide greater capacity

- **Fast rates are more reversible**

  PZ, MDEA/PZ > MEA, 2PE

  Sec amines in rings are fastest

- **Low Thermal Degradation allows high T/P stripper**

  PZ < AMP < MDEA/PZ < MEA

  Alkanolamines degrade faster

Acknowledgements

- Luminant Carbon Management Program
- Rate and Solubility Data
  - Ross Dugas, Xi Chen, Thu Nguyen
- Thermal Degradation
  - Jason Davis, Stephanie Freeman, Fred Closmann
- Stripper Modeling
  - Tunde Oyenekan, David Van Wagener
- High T VLE
  - Qing Xu

Effect of ΔH_{abs} on energy requirement (90% removal, $\Delta T = 5^{\circ}C$, P_{final} = 330 kPa)

	6.4m K^+/ 1.6m PZ	5m K^+/ 2.5m PZ
CO_2 Capacity (mol/kg H_2O)	0.91	0.93
ΔH_{abs}(kJ/gmol)	50	63
	Equivalent Work (kJ/gmol CO_2)	
Simple Stripper, 1.6 bar	27.4	22.6
Vacuum Stripper, 0.3 bar	23.7	23.1

Oyenekan, 2007

Overstripping Can Increase Capacity